DISS. ETH NO. 25172

Molecular Recognition with Enantiopure Alleno-Acetylenic Cage Receptors

A Dissertation submitted to attain the degree of
Doctor of Sciences of ETH Zurich
(Dr. sc. ETH Zurich)

presented by
Cornelius Immanuel Robson Gropp
M.Sc. Chemistry, ETH Zurich

born on 30.07.1988
citizen of the Federal Republic of Germany

accepted on the recommendation of
Prof. Dr. François Diederich, examiner
Prof. Dr. Erick M. Carreira, co-examiner

Zurich 2018

In Dankbarkeit an meine Familie

To our society that supports our academic adventures

Acknowledgments

I would like to express my deepest gratitude to Prof. Dr. François Diederich for providing me with an academic environment that strongly influenced my scientific and personal development. The freedom you gave me during my Ph.D., together with your enthusiasm and the people you chose to be part of your group, created a unique and inspiring working environment. I thank you for your generous support, motivation, trust and guidance, during and beyond this Thesis.

Many thanks to Prof. Dr. Erick M. Carreira for accepting the co-examination of this Thesis. During my Master studies, I had the pleasure to work in the Carreira group and experience a highly inspiring working environment. I am grateful for your support during my stay at ETH and beyond. I had the pleasure to collaborate with Dr. Stefan Fischer, a member of the Carreira group, on a project described in this Thesis.

I would like to acknowledge the Studienstiftung des Deutschen Volkes for their continuous support over the last ten years. Importantly, besides the financial support with scholarships during my B.Sc., M.Sc., abroad research stays and Ph.D., the Studienstiftung greatly helped me to explore various scientific and non-scientific areas. I am grateful for their support during the Lindau Nobel Laureate Meeting in 2017 and for traveling grants.

Special thanks go to Tamara Husch and Prof. Markus Reiher (ETHZ) with whom I had the pleasure to collaborate during my Ph.D.. Invaluable insights were gained through their theoretical studies on alleno-acetylenic cage receptors. I am looking forward to our ongoing collaboration. I thank Prof. Markus Reiher for his support during my postdoctoral application.

Many thanks to Dr. Brendan Quigley for his support and invaluable contribution during the preparation of the *Perspective Article*.

I thank all the people I had the pleasure to collaborate with during my Ph.D. (and ongoing collaborations), namely Prof. Dr. Eric Anslyn, Mario Wiesenfeldt and Prof. Dr. Frank Glorius, Prof. Dr. Günter Haufe.

I would like to thank the Small Molecule Crystallographic center of ETH Zurich, Dr. Nils Trapp, Michael Solar and Prof. Dr. Michael Wörle. Their engagement and passion for measuring and solving X-ray crystal structures contributed considerably to this Thesis.

During my Ph.D. I had the pleasure to supervise two Master students, Emmanuel Wirt and F. Wieland Goetzke. I would like to thank them for choosing a Master Thesis under

my supervision. I would like thank Wieland for his contribution to the development of water-soluble alleno-acetyleninc cage receptors, his endurance and passion for chemistry.

I am grateful for the support of the NMR service during my stay at ETH, namely Prof. Dr. Marc-Olivier Ebert, René Arnold, Rainer Frankenstein und Stephan Burkhardt.

The unique research environment at ETH is acknowledged, including the Mass Spectrometry Service, with Rolf Häflinger (MALDI), and the elemental analysis facilities with Peter Kälin.

Many thanks go to Karin Puce-Schmid and Irma Näf for taking care of all the administrative tasks. I also thank Prof. Carlo Thilgen for organizing the OCP2 practica and for fruitful discussion in nomenclature. Dr. Bruno Bernet for carefully correcting the Experimental Part of this Thesis and the manuscripts cited herein.

Chapters of this Thesis were proofread by Dr. Anatol Schwab, Dr. Geoffrey Schwertz, Dr. Levon Movsisyan, and Dr. Brendan Quigley. I thank them for their careful corrections and fruitful discussion.

I thank the people I had the chance to work with during my Master studies and who considerably influenced the path I ventured: Dr. Quentin Huchet, Dr. Igor Pochorovski, and Prof. Dr. Ori Gidron.

During my stay in the Diederich group, I met numerous inspiring personalities who created a positive atmosphere in and around the lab. I thank Dr. Anatol Schwab for assistance in HPLC seperations, as support as computer administrator and numerous scientific discussions. Cédric Schaack for his support as computer administrator and for organizing the Ski-Weekends. Many thanks to my former lab mates in G302: Dr. Tristan Reekie, Dr. Nicolas Kerisit, Dr. Oliver Dumele, Dr. Elke Persch, and my current lab mates in G322: Sophie Haberland, Leslie Riwar, Dr. Anatol Schwab, Dr. Brendan Quigley. I thank the whole Diederich group with Raoul De Gasparo, Cédric Schaack, Dr. Levon Movsisyan, Dr. Victor Garcia López, Sophie Haberland, Leslie Riwar, Dr. Brendan Quigley. I thank Geoffrey Schwertz for our memorable discussions while sharing a writing room. Dr. Michal Tichý, Dr. David Schweinfurth, Dr. Jonas Thelemann, and many more people I met during my time in the group.

I am indebted to inspiring encounters during my studies who have left a lasting impression on me: Prof. Fabien Gagosz and Prof. Samir Zard during my stay at the École Polytechnique; Pof. Phil S. Baran during my research stay at the Scripps Research Institute; Prof. Erick M. Carreira and Prof. Jack Dunitz during my Masters at ETH.

Many thanks to my all my friends who supported me during my Ph.D. Thesis. To Roland Wedekind, Gunnar Bachem, and Nina Hentzen for our friendship and to Selin Anil for being an important part of my life.

Grenzenloser Dank gilt meinen Eltern. Die Begeisterung für das Leben, die ihr an uns Kinder weitergebt, trägt wesentlich dazu bei, wer wir sind. Meinen Geschwistern sei Dank für ihre bedingungslose Unterstützung und Liebe.

Publications

I. Pochorovski, J. Milić, D. Kolarski, C. Gropp, W. B. Schweizer, F. Diederich, *J. Am. Chem. Soc.* **2014**, *136*, 3852–3858. Evaluation of Hydrogen Bond Acceptors for Redox-Switchable Resorcine[4]arene Cavitands.

C. Gropp, N. Trapp, F. Diederich, *Angew. Chem. Int. Ed.* **2016**, *55*, 14444–14449; *Angew. Chem.* **2016**, *128*, 14659–14664. Alleno-Acetylenic Cage (AAC) Receptors: Chiroptical Switching and Enantioselective Complexation of *trans*-1,2-Dimethylcyclohexane in a Diaxial Conformation.
(F1000 Prime Highlight, Pharmacology and Drug Discovery)

C. Gropp, T. Husch, N. Trapp, M. Reiher, F. Diederich, *J. Am. Chem. Soc.* **2017**, *139*, 12190–12200. Dispersion and Halogen-Bonding Interactions: Binding of the Axial Conformers of Monohalo- and (±)-*trans*-1,2-Dihalocyclohexanes in Enantiopure Alleno-Acetylenic Cages.
(*JACS* Cover Article and Spotlight)

C. Gropp, B. Quigley, F. Diederich, *J. Am. Chem. Soc.* **2018**, *140*, 2705–2717. Molecular Recognition with Resorcin[4]arene Cavitands: Switching, Halogen-Bonded Capsules, and Enantioselective Complexation.
(*JACS* Spotlight)

C. Gropp,* N. Trapp, *Chimia* **2018**, *72*. Complexation and Structure Elucidation of the Axial Conformers of Mono- and (±)-*trans*-Disubstituted Cyclohexanes by Enantiopure Alleno-Acetylenic Cage Receptors.

Manuscripts in preparation:

C. Gropp, T. Husch, N. Trapp, M. Reiher, F. Diederich, *manuscript in preparation*. Directional Hydrogen-Bonding Interactions: Molecular Recognition of Cyclic Alcohols in Enantiopure Alleno-Acetylenic Cage Receptors.

C. Gropp, S. Fischer, T. Husch, N. Trapp, M. Reiher, E. M. Carreira, F. Diederich, *manuscript in preparation*. Hydrogen-Bonding and Halogen-Bonding Interactions: Molecular Recognition and Conformational Analysis of Acyclic Alcohols in Enantiopure Alleno-Acetylenic Cage Receptors.

C. Gropp, W. Goetzke, N. Trapp, F. Diederich, *manuscript in preparation*. Enantiopure Alleno-Acetylenic Cage Receptors for Chiral Recognition in Aqueous Medium.

C. Gropp, N. Trapp, F. Diederich, *manuscript in preparation*. Enantiopure Covalently Capped Alleno-Acetylenic Cage Receptors.

Presentations

C. Gropp, T. Husch, N. Trapp, M. Reiher, F. Diederich

Chiral Recognition Purely by Dispersion and Halogen-Bonding Interactions – 150 Degrees of Cyclohexane. GDCh Scientific Forum Chemistry 2017 – Anniversary Congress "GDCh – 150 Years". Berlin, Germany, **2017**.

C. Gropp, T. Husch, N. Trapp, M. Reiher, F. Diederich

Chiral Recognition by Dispersion and Halogen-Bonding Interactions. Swiss Chemical Society, Fall Meeting. Bern, Switzerland, **2017**.

Poster Prize and Travel Award (Organic Chemistry)

C. Gropp

67th Lindau Nobel Laureate Meeting (Chemistry), Lindau, Germany, **2017**.

Funded by: Verband der Chemischen Industrie (VCI) and Studienstiftung des Deutschen Volkes

C. Gropp, T. Husch, N. Trapp, M. Reiher, F. Diederich

Alleno-Acetylenic Cage Receptors: Chiroptical Switching and Enantioselective Complexation. Gordon Research Conference (GRC), Les Diablerets, Switzerland, **2017**.

C. Gropp, N. Trapp, F. Diederich

Alleno-Acetylenic Cage Receptors: Chiroptical Switching and Enantioselective Complexation. Scholarship Fund of the Swiss Chemical Industry (SSCI), Zurich, Switzerland, **2016**.

C. Gropp, N. Trapp, F. Diederich

Molecular Recognition in Enantiopure Cage Receptors. International Symposium on Macrocyclic and Supramolecular Chemistry (ISMSC). Seoul, South Korea, **2016**.

C. Gropp, N. Trapp, F. Diederich

Alleno-Acetylenic Cage (AAC) Receptors: Molecular Recognition. Swiss Chemical Society, Spring Meeting. Zurich, Switzerland, **2016**.

Table of Contents

Abbreviations and Color Codes

°	degree
2D	two dimensional
Å	Angstrom
Ac	acetyl
aq.	aqueous
Ar	aromatic ring
ATR	attenuated total reflectance
ax or a	axial
n-BuLi	*n*-butyllithium
br.	broad
Br	bromide
Bu	butyl
C	Celsius
CAM	Coulomb-Attenuating Method
CCDC	Cambridge Crystallographic Databank
cat.	catalytic
COSY	correlated spectroscopy
CSP	Chiral Stationary Phase
CSD	Cambridge Structural Databank
δ	chemical shift (NMR)
Δ	difference
d	day(s); doublet (NMR)
DCM	dichloromethane
DEA	diethynylallene
decomp.	decomposition
DFT	density functional theory
DMF	dimethylformamide
DMSO	dimethylsulfoxide
E	Energy
ε	molar extinction coefficient (M^{-1} cm^{-1})
ECD	Electronic Circular Dichromism
e.e.	enantiomeric excess

EI	electron ionization
equiv.	equivalent
EtOAc	ethylacetate
e.r.	enaniomeric ratio
ESI	electrospray ionization
Et	ethyl
Et_2O	diethyl ether
eqiv.	equivalent
eq or e	equatorial
F	structure factor (crystallography)
FC	Flash chromatography
FT-IR	Fourier transform infrared spectroscopy
g	gram
G	Gibbs energy
gem	geminal
h	hour
H-Bond	hydrogen bond
HMBC	heteronuclear multiple bond correlation
HR-MS	high resolution mass spectrometry
HSQC	heteronuclear single quantum coherence
HPLC	High Performance Liquid Chromatography
Hz	Hertz
I	intensity (crystallography)
i	*iso-*
ITC	Isothermal Titration Calorimetry
J	coupling constant (NMR) in Hz
K_a	association constant or binding constant
λ	wavelength
LC/MS	liquid chromatography/mass spectrometry
Lit.	Literature
IR	infrared spectroscopy
m	medium
M	molecular ion peak (MS)
MALDI	Matrix Assisted Laser Desorption/Ionization

Me	methyl
mg	milligrams
mmol	millimoles
m.p.	melting point
MPLC	Medium Pressure Liquid Chromatography
MP2	second-order Moeller-Plesset perturbation theory
MW	molecular weight
N	Normal
NBS	*N*-bromosuccinimide
n-but	*n*-butyl
NMR	Nuclear Magnetic Resonance
OPR	Optical Rotatory Dispersion
ORTEP	Oak Ridge Thermal Ellipsoid Plot
PDB	Protein Data Bank
PG	Protecting Group
*i*Pr	isopropyl
Ph	phenyl
1,10-Phen	1,10-phenanthroline
ppb	parts per billion
ppm	parts per million (NMR)
PTFE	polytetrafluoroethylene
quant.	Quantitative
quint.	quintet (NMR coupling)
R	undefined substituent
R_f	retention factor (TLC)
Ref.	reference
RP	reversed phase
ROESY	rotating frame nuclear Overhauser effect spectroscopy
s	singlet (NMR); or strong (UV/Vis)
sat.	saturated
Sphos	2-Dicyclohexylphosphino-2',6'-dimethoxybiphenyl
NTf_2	bis(trifluoromethanesulfonyl)amide
THF	tetrahydrofuran
TIPS	triisopropylsilyl

TLC	thin-layer chromatography
TMS	trimethylsilane
TMEDA	*N,N,N',N'*-tetramethylethylenediamine
UV	ultraviolet
$\tilde{\nu}$	wavenumber (IR)
Vis	visible
w	weak

The international system of units (SI) is used. If not otherwise stated, the following color code has been applied for the depiction of molecular structures:

F	cyan
C	grey (or dark green if indicated)
Cl	green
Br	brown
I	purple
N	blue
O	red
S	yellow

Summary

The study of synthetic model systems and biological counterparts has developed an extraordinary symbiosis, helping to decipher important chemical phenomena observed in nature. This Thesis is dedicated to the understanding of molecular recognition processes of neutral achiral and chiral small molecules by enantiopure receptors.

Despite the progress in the design and construction of enantiopure receptors, examples of optically pure systems that effectively differentiate chiral neutral small molecules are still rare. The general notion prevails that strong directional interactions between the host and the guest are required. In order to question this idea, we constructed enantiopure alleno-acetylenic cage (AAC) receptors that bind molecules purely based on dispersion interactions largely in the absence of directional interactions. Subsequently, we extended our molecular recognition studies to halogen-bonding and hydrogen-bonding interactions.

In the second chapter, we describe the synthesis and properties of enantiopure alleno-acetylenic cage (AAC) receptors. AACs are constructed from a methylene-bridged resorcin[4]arene core to which four homochiral alleno-acetylenes with OH termini are attached to, giving access to both $(P)_4$- and $(M)_4$-configured AACs. Detailed analysis of the structure-property relationship of the receptor allowed to identify important conformational features of the receptor, enabling quantification of guest uptake and release: the receptors undergoes solvent-dependent binary conformational switching accompanied by strong changes in the associated electronic circular dichroism (ECD) spectra with $\Delta\Delta\varepsilon = 882$ M^{-1} cm^{-1} at $\lambda = 304$ nm, allowing for a sensitive spectroscopic readout of the conformational changes.

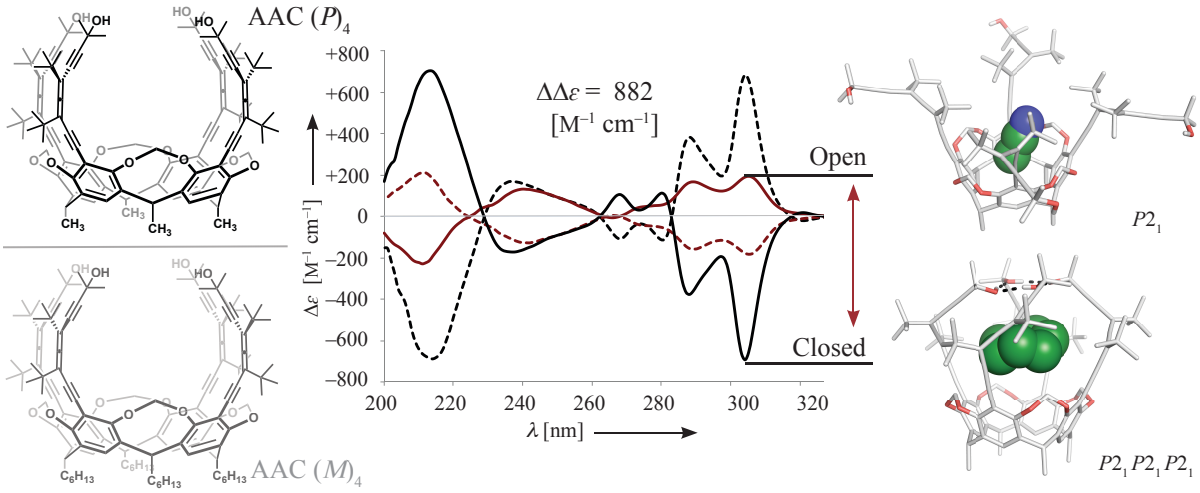

In the closed cage conformation, the OH-termini of the alleno-acetylenic arms form a cyclic four-fold hydrogen-bonding array, creating a highly confined cavity. The directional nature of the H-bonding array – clockwise for $(P)_4$-configured AACs and counter-clockwise for $(M)_4$-configured AACs – was identified to contribute to the unprecedentedly large change in chiroptical properties of the assembly. A general method to obtain single crystals of the solid-state inclusion complexes was developed and relies on the guest-induced switching of the receptor from its open state (in CH_3CN/H_2O 9:1) to the closed state upon encapsulation of guest molecules.

The combination of a highly shape-persistent, confined chiral cavity, capable of guest encapsulation, together with the spectroscopic and crystallographic readout for cage inclusion, made the AAC receptors ideal model system to study chiral recognition. We first investigated the molecular recognition of achiral and chiral cyclic alkanes, where complexation is purely based on non-directional dispersion interactions. X-ray co-crystal structures revealed a size adaptability of the receptor towards the guest, thereby optimizing the packing coefficient of the ensemble. At the optimal packing coefficient of ~55%, the enantiopure receptor showed complete selectivity towards (±)-*trans*-1,2-dimethylcyclohexane, where the $(P)_4$-configured host solely bound the (*R*,*R*)-configured guest, and the $(M)_4$-configured receptor exclusively bound the (*S*,*S*)-configured guest. X-ray co-crystal structures of the host-bound guests revealed the exclusive complexation of their higher-energy diaxial conformation, with the diaxial dihedral angle deviating strongly from the commonly accepted value of 180° down to 146°. Subsequent theoretical investigations demonstrated negligible influence of the host on the guest structures.

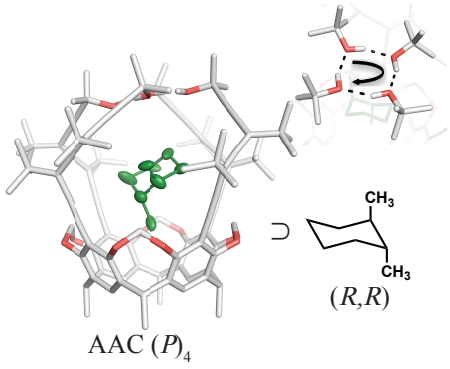

We validated the utility of the host for the structural elucidation of the (di)axial conformations of cyclohexane derivatives by expanding the series of guest molecules to monohalo- and (±)-*trans*-1,2-dihalocyclohexanes. The molecular structures of the host–guest complexes, obtained through single-crystal X-ray diffraction, showed the guests exclusively bound in their axial and diaxial chair conformation, with dihedral angles $\vartheta_{a,a}$ (X-C(1)-C(2)-H/X) deviating substantially from 180°. Increasing deviation from this angle was observed for the monohalocyclohexanes (up to 25°) to (±)-*trans*-1,2-dihalocyclohexanes (up to 33°). Substantial bond-length and bond-angle alteration in the carbon scaffold was assumed to

reduce the strain caused by the 1,3-diaxial interactions of the guests in their diaxial conformation.

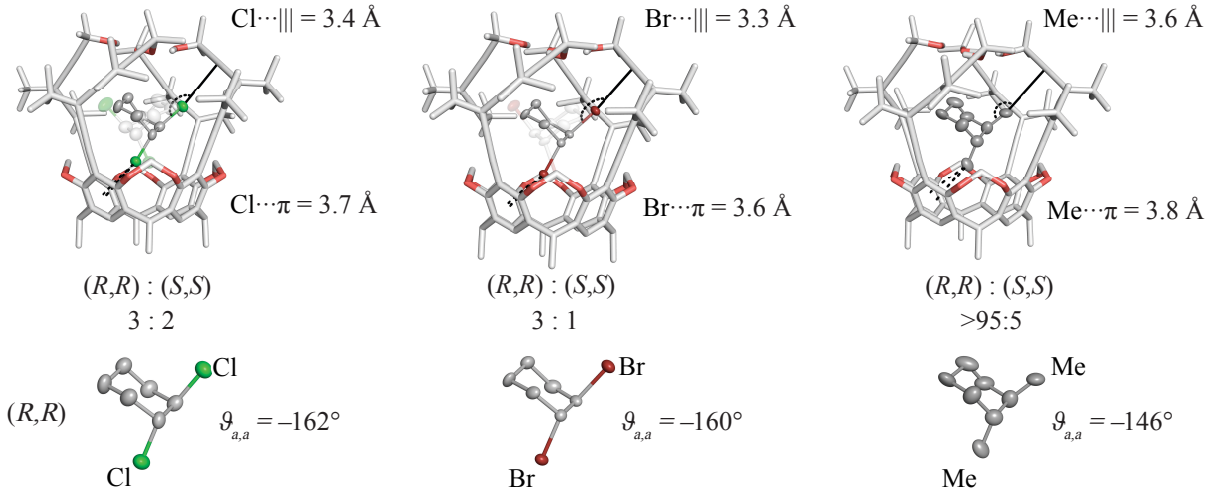

Solution complexation studies supported the exclusive complexation of the guests in their (di)axial chair conformation, where slow host–guest exchange allowed for full characterization of the guest in the interior of the host. Theoretical analysis of the isolated guest molecules showed close agreement of the complexed and the isolated guest structures, validating the utility of the AACs to capture single conformers of derivatives of cyclohexane for their structural elucidation. X-ray co-crystal structures of the host-guest complexes further revealed a yet hardly studied halogen-bonding contact: the C–X···||| contact. Theoretical studies on the C–X···||| interaction substantiated its halogen-bonding character. Solution binding constants, along with the theoretical calculations on the conformational energies (*A*-values) of the guests, indicated a contribution of the C–Br···||| halogen-bonding contact of $\Delta\Delta G_{F\rightarrow Br} = -0.9$ kcal mol^{-1}. The C–X···||| contact appeared to majorly influence the enantioselectivity of the enantiopure receptor towards the chiral guests, with increased enantioselectivity with increased halogen-bonding strength (Cl < Br). The overall enantioselectivity towards (±)-*trans*-1,2-dihalocyclohexanes was lower compared to (±)-*trans*-1,2-dimethylcyclohexanes (complete enantioselectivity). This finding was counter-intuitive considering the stronger and directional nature of halogen-bonding contacts compared to the non-directional, purely dispersion interactions, of (±)-*trans*-1,2-dimethylcyclohexanes with the host. It is in stark contrast to established concepts for enantioselective complexation of optically pure receptors with chiral guests, where more directional interactions were considered to enhance selectivity. We explained this observation with the much higher polarizability of chlorine and bromine compared to the methyl substituents.

Inspired by a crystal structure of the AAC receptor encapsulating one water molecule and two acetonitrile molecules, we expanded our series of guest molecules to cyclic and acyclic alcohols. The alcohol series formed strong directional interactions between the alcohol groups of the guest and the hydrogen-bonding array of the host. Generally, the introduction of an alcohol group increased the binding affinities of the guest to the receptors in solution by ~3–4 kcal mol^{-1}, resulting in kinetically stable host–guest complexes on the NMR time scale. Solution studies, along with structural information obtained from X-ray co-crystal structures, enabled the conformational analysis of the host-bound guests. Noteworthy was the substantial increase in binding affinity from cycloheptane to *endo*-tropine with a difference in binding affinitiy of $\Delta\Delta G_{293\,K} = -6.1$ kcal mol^{-1} ($K_a = 7.0 \cdot 10^6$ M^{-1} in *n*-octane at 293 K), allowing to detect *endo*-tropine with AACs in the part per billion regime.

The directional hydrogen-bonding interactions of the guest to the receptors generated various hydrogen-bonding motifs (4-fold to 5-fold and 6-fold), which were strongly dependent on the alcohol guest encapsulated in the interior of the host. The host–guest-complex appeared to retain some directionality of the hydrogen-bonding array, despite the disruptive nature of the directional hydrogen-bonding interactions of the guest with the host.

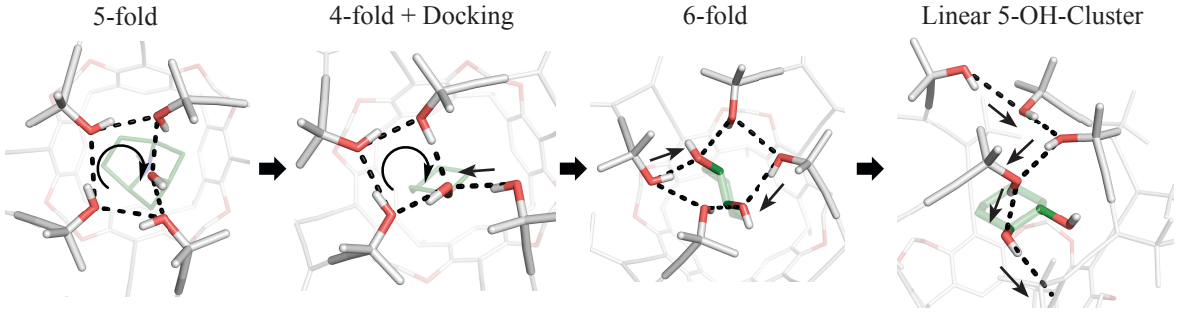

In a collaboration with Dr. Fischer and Prof. Carreira (ETHZ), supported by theoretical studies by T. Husch and Prof. Reiher (ETHZ), we studied the enantioselective binding of various acyclic alkyl and alkyl halide alcohols, undergoing dispersion and halogen-bonding interactions. The formation of diastereoisomeric complexes of the enantiopure hosts with the chiral guests enabled us to assess the enantioselectivity of the receptors towards the guests in solution and in the solid state. X-ray co-crystal structures gave insight into the conformation of the guests complexed to the interior of the host.

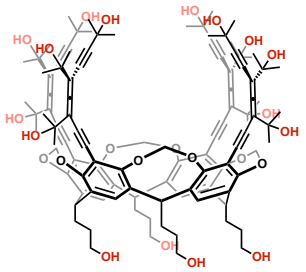
AAC $(P)_4$

In the following chapter, we describe the modular synthesis of enantiopure alleno-acetylenic cage receptors with increased surface polarity and solubility in aqueous medium. This new class of receptors revealed conformational switching from an open to a closed form upon guest complexation. The structural similarity of the hydrophobic cavity of the more polar AACs soluble in aqueous medium with the apolar AAC receptors, make them ideal to study the thermodynamic differences of enantioselective complexation in apolar and aqueous solvent systems.

The last chapter gives a brief overview on the synthesis and chiroptical properties of covalently capped alleno-acetylenic cage receptors, accessed through intramolecular oxidative dimerization. The covalent AACs showed strong absorption properties towards circulary polarized light, with hardly any temperature dependencies. X-ray co-crystal structure of the covalent $(P)_4$- and $(M)_4$-configured AACs gave insights into the volume of the cavity for molecular recognition studies. Molecular recognition studies on the covalent receptor systems are ongoing.

Zusammenfassung

Die Studie von synthetischen Modellsystemen und ihren biologischen Gegenstücken hat eine außergewöhnliche Symbiose entwickelt, die dazu beiträgt, in der Natur beobachtete chemische Phänomene zu entschlüsseln. Diese Arbeit ist dem Verständnis von molekularen Erkennungsprozessen von neutralen achiralen und chiralen kleinen Molekülen durch enantiomerenreine Rezeptoren gewidmet.

Trotz des Fortschritts bei der Entwicklung und Konstruktion enantiomerenreiner Rezeptoren sind Beispiele für optisch reine Systeme, die chirale neutrale kleine Moleküle effizient unterscheiden, noch selten. Der allgemeine Gedanke überwiegt, dass starke gerichtete Wechselwirkungen zwischen dem Wirt und dem Gast erforderlich sind. Um diese Betrachtung in Frage zu stellen, haben wir enantiomerenreine, alleno-acetylenische Käfigrezeptoren (AAKs) entworfen, die Moleküle auf der Basis von Dispersionswechselwirkungen in Abwesenheit von gerichteten Wechselwirkungen binden.

Im ersten Kapitel beschreiben wir die Synthese und Eigenschaften von enantiomerenreinen alleno-acetylenischen Käfig (AAK) Rezeptoren. AAKs sind aus einem methylen-verbrückten Resorcin[4]aren-Cavitanden aufgebaut, an dem vier homochirale Alleno-Acetylene mit OH-Termini verknüpft sind und Zugang zu sowohl $(P)_4$- als auch $(M)_4$-konfigurierten AAKs ermöglicht. Eine detaillierte Analyse der Struktur-Eigenschaft-Beziehung ermöglichte die Identifizierung wichtiger Konformationsmerkmale des Rezeptors, die die Aufnahme und Freisetzung von Gastmolekülen zu quantifizieren ermöglichte: die Rezeptoren gehen eine Lösungsmittel-abhängige binäre konformative Schaltung ein, begleitet von starken Änderungen in den elektronischen Circulardichroismusspektren (ECD) von $\Delta\Delta\varepsilon$ = 882 M^{-1} cm^{-1} bei λ = 304 nm, was ein empfindliches spektroskopisches Auslesen der Konformationsänderungen ermöglicht. In der geschlossenen Käfigform bilden die OH-Termini der alleno-acetylenischen Arme ein cyclisches vierfaches Wasserstoffbrückennetzwerk, die einen Hohlraum umschließen.

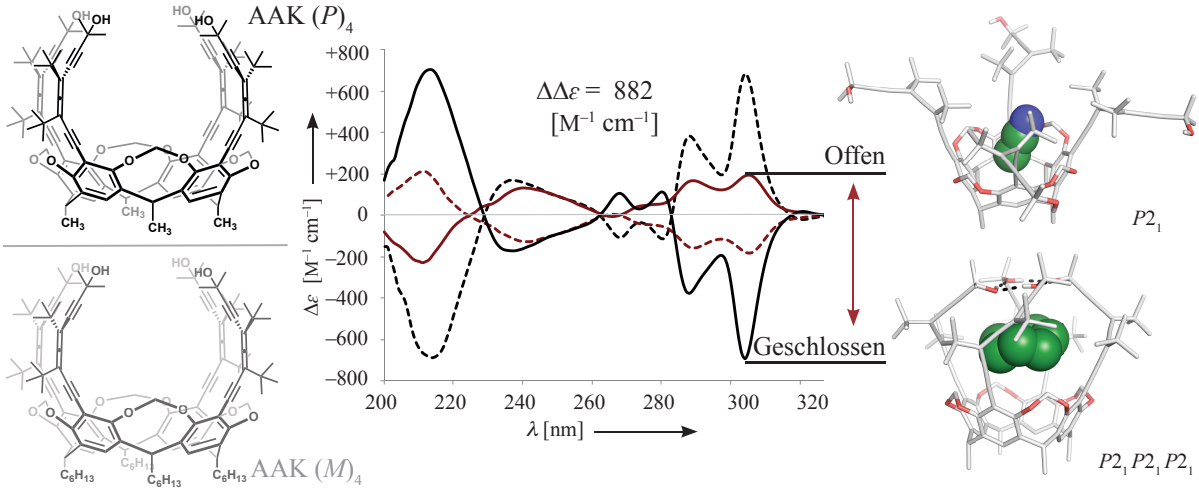

Die Ausrichtung der H-Brücken – im Uhrzeigersinn für $(P)_4$-konfigurierte AAKs und gegen den Uhrzeigersinn für $(M)_4$-konfigurierte AAKs – trägt zu der außergewöhnlich großen Änderung der chiroptischen Eigenschaften bei. Eine allgemeine Methode zur Kristallisation der Wirt-Gast-Komplexe wurde entwickelt und beruht auf dem Gast-induzierten Schalten des Rezeptors von seinem offenen Zustand (in CH_3CN/H_2O 9:1) in den geschlossenen Zustand durch die Einschließung von Gastmolekülen.

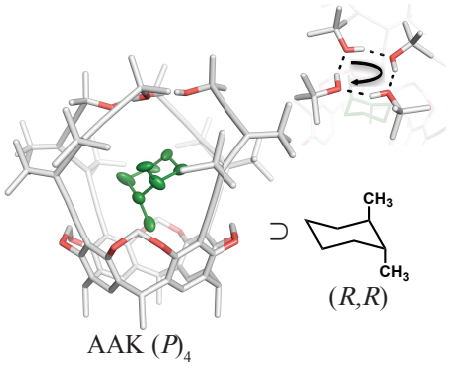

Die Kombination einer hochgradig formbeständigen, chiralen Kavität, die zur Einschließung von Gastmolekülen fähig ist, zusammen mit dem spektroskopischen und kristallographischen Nachweis für den Einschluss, macht die AAK-Rezeptoren zum idealen Modellsystem für die Untersuchung der chiralen Erkennung. Wir untersuchten zunächst die molekulare Erkennung von achiralen und chiralen cyclischen Alkanen, wobei die Komplexierung ausschließlich auf nichtgerichteten Dispersionswechselwirkungen beruht. Lösungsbindungsstudien wurden durch Strukturanalyse mittels Einkristall-Röntgenbeugung ergänzt. Die Cokristallstrukturen zeigten eine Größenanpassungsfähigkeit des Rezeptors an den Gast, wodurch der Packungskoeffizient des Ensembles optimiert wurde. Bei einem optimalen Packungskoeffizienten von ~55% zeigte der enantiomerenreine Rezeptor eine vollständige Selektivität für (±)-*trans*-1,2-Dimethylcyclohexan, wobei der $(P)_4$-konfigurierte Wirt ausschließlich den (*R*,*R*)-konfigurierten Gast und der $(M)_4$-konfigurierte Rezeptor ausschließlich den (*S*,*S*)-konfigurierten Gast band. Die Cokristallstrukturen der Wirt-gebundenen Gäste zeigten außerdem die exklusive Komplexierung der höher-energetischen diaxialen Konformation von

(*R*,*R*)- und (*S*,*S*)-*trans*-1,2-Dimethylcyclohexan mit einem diaxialen Diederwinkel, der stark von dem allgemein akzeptierten Wert von 180 ° auf 146 ° abweicht. Dies warf die Frage auf, ob der gefundene Diederwinkel das Ergebnis einer rezeptorinduzierten Abweichung ist oder seinem sich eigenen Winkel entspricht. Nachfolgende theoretische Untersuchungen zeigten einen vernachlässigbaren Einfluss des Wirts auf die Gaststrukturen.

Wir bestätigten den Nutzen des Rezeptors, schwer erfassbare (di)axialen Konformationen von Cyclohexan-Derivaten aufzuklären, indem wir die Reihe von Gastmolekülen auf Alkylhalogenide, wie Monohalogen- und (±)-*trans*-1,2-Dihalogencyclohexane, erweiterten. Das entwickelte Kristallisationsprotokoll ermöglichte es, die Strukturen der Wirt-Gast-Komplexe durch Einkristall-Röntgenbeugung zu erhalten, wobei die Gäste ausschließlich in ihrer axialen und diaxialen Sesselkonformation gebunden waren. Die diaxialen Diederwinkel $\theta_{a,a}$ (X-C-(1)-C(2)-H / X) wichen wesentlich von 180 ° ab, mit zunehmender Abweichung der Monohalogencyclohexanen (bis zu 25 °) zu den (±)-*trans*-1,2-Dihalogencyclohexanen (bis zu 33 °). Erhebliche Bindungslängen- und Bindungswinkelalternierungen im Kohlenstoffgerüst scheinen die konformationelle Energie zu reduzieren, die durch die 1,3-diaxialen Wechselwirkungen der Gäste in ihrer diaxialen Konformation verursacht wird. Lösungsmittelstudien bestätigten die ausschließliche Komplexierung der Gäste in ihrer (di) axialen Sesselkonformation, wobei der langsame Wirt-Gast-Austausch eine vollständige Charakterisierung der Wirt-Gast-Komplexe ermöglichte.

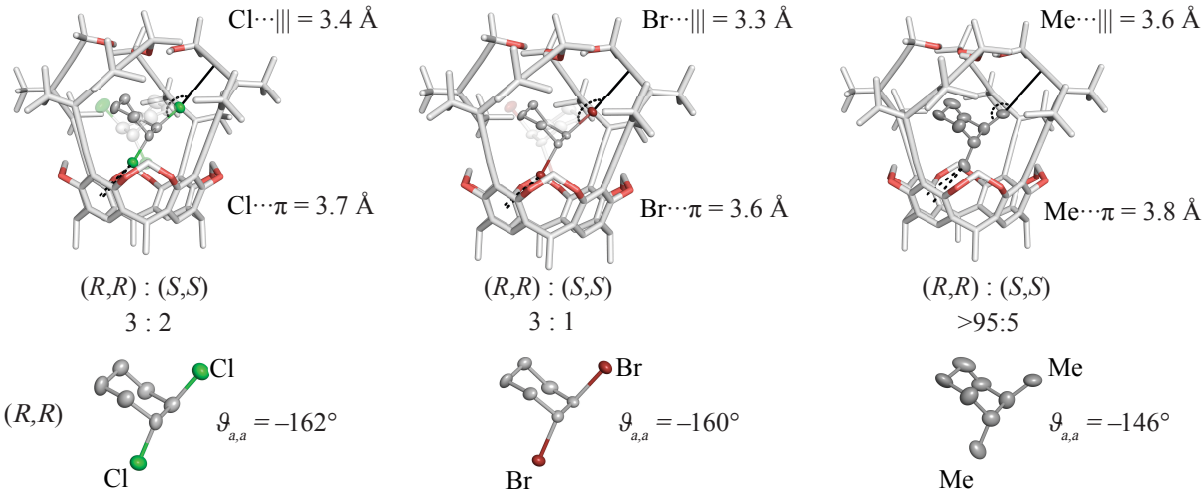

Theoretische Analyse des isolierten Gastes bestätigen eine enge Übereinstimmung der komplexierten und der isolierten Gaststrukturen. Die Cokristallstrukturen der Wirt-Gast-Komplexe zeigten einen noch wenig untersuchten Halogenbindungskontakt: den C-X···|||-Kontakt. Theoretische Studien zur C–X-Wechselwirkung bestätigten ihren Halogenbindungscharakter. Aus Bindungsstudien in Lösung zusammen mit den theoretischen

Berechnungen der Konformationsenergien (*A*-Werte) der Gäste ermittelten wir einen Beitrag des C-Br···|||-Halogenbindungskontakts von $\Delta\Delta G_{F\rightarrow Br} = -0.9$ kcal mol^{-1}. Der C-Br···|||-Kontakt scheint die Enantioselektivität des enantiomerenreinen Rezeptors gegenüber den chiralen Gästen stark zu beeinflussen. Die AAKs zeigten eine zunehmende Enantioselektivität mit zunehmender Halogenbindungsstärke (Cl < Br). Die Enantioselektivität gegenüber den (±)-*trans*-1,2-Dihalogencyclohexanen war jedoch geringer im Vergleich zu den (±)-*trans*-1,2-Dimethylcyclohexanen (vollständige Enantioselektivität). Dieser Befund war entgegen Intuition, wenn man die stärkere und gerichtete Natur von Halogenbrücken im Vergleich zu den ungerichteten rein dispersiven Wechselwirkungen von *trans*-1,2-Dimethylcyclohexanen mit dem Wirt bedenkt. Er steht im Widerspruch zu etablierten Konzepten für die enantioselektive Komplexierung von optisch reinen Rezeptoren mit chiralen Gästen, bei welcher gerichtete Wechselwirkungen zu einer Erhöhung der Selektivität führen sollten. Wir haben diese Beobachtung mit der viel höheren Polarisierbarkeit von Chlor und Brom im Vergleich zu den Methylsubstituenten begründet.

Inspiriert durch eine Kristallstruktur eines AAK-Rezeptors, der ein Wassermolekül und zwei Acetonitrilmoleküle einschloss, erweiterten wir unsere Reihe von Gastmolekülen zu cyclischen und acyclischen Alkoholen. Die Alkohole bildeten starke gerichtete Wechselwirkungen mit dem Wasserstoffbrückennetzwerk des Wirts aus. Im Allgemeinen erhöhte die Einführung einer Alkoholgruppe die Bindungsaffinitäten des Gastes an die Rezeptoren in Lösung um ~3–4 kcal mol^{-1}, was zu kinetisch stabilen Wirt-Gast-Komplexen auf der NMR-Zeitskala führte. Lösungsstudien, zusammen mit Cokristallstrukturen, ermöglichten die Konformationsanalyse der Wirt-gebundenen Gäste. Erwähnenswert ist die deutliche Zunahme der Bindungsaffinität von Cycloheptan zu *endo*-Tropin, die mit mit einem Unterschied in den Bindungsaffinitäten von $\Delta\Delta G_{293\ K} = -6.1$ kcal mol^{-1} ($K_a = 7.0\cdot10^6$ M^{-1} in *n*-Octan bei 293 K) einherging und es ermöglichte, *endo*-Tropin mit AAKs im ppb-Bereich zu detektieren. Die gerichteten Wasserstoffbrücken-Wechselwirkungen des Gastmoleküls mit den Rezeptoren führten zu verschiedenen Wasserstoffbrückenmotiven (von 4-fach bis 5-fach und 6-fach), die stark von den eingeschlossenen Alkoholen bestimmt wurden. Der Wirt-Gast-Komplex schien trotz der disruptiven Natur der gerichteten Wasserstoffbrückenwechselwirkung eine gewisse Direktionalität der Wasserstoffbrückenanordnung beizubehalten.

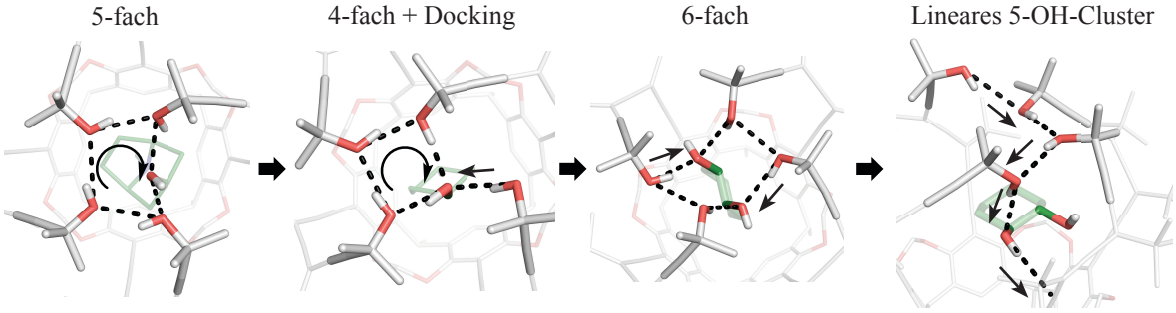

In Zusammenarbeit mit Dr. S. Fischer und Prof. E. M. Carreira (ETHZ), unterstützt durch theoretische Studien von T. Husch und Prof. M. Reiher (ETHZ), untersuchten wir die enantioselektive Bindung verschiedener acyclischer Alkyl- und Alkylhalogenidalkohole, die zusätzlich zu den gerichteten H-Bindungen dispersive und Halogen-Bindungswechselwirkungen eingehen. Durch die Bildung diastereoisomerer Komplexe der enantiomerenreinen Wirte mit den chiralen Gästen konnten wir die Enantioselektivität der AAKs gegenüber den in Lösung befindlichen Gästen bestimmen. Lösungsstudien wurden durch Cokristallstrukturen ergänzt, bei denen die Verteilung der Enantiomere des Gastmoleküls im Wirt der beobachteten Enantioselektivität in Lösung entsprach. Die Bindungsmodi der Gäste im Wirt bestätigten die beobachteten Enantioselektivitäten.

Im folgenden Kapitel beschreiben wir die modulare Synthese von enantiomerenreinen alleno-acetylenischen Käfigrezeptoren mit erhöhter Oberflächenpolarität und Löslichkeit in wässrigen Lösungsmitteln. Diese AAKs zeigten konformative Schaltung von einer offenen in eine geschlossene Form, induziert durch Gastmoleküle. Die strukturelle Ähnlichkeit des hydrophoben Hohlraums der in wässrigem Medium löslichen AAKs mit den unpolareren AAK-Rezeptoren macht sie ideal für die Untersuchung der thermodynamischen Unterschiede der enantioselektiven Komplexierung in apolaren und wässrigen Lösungsmittelsystemen.

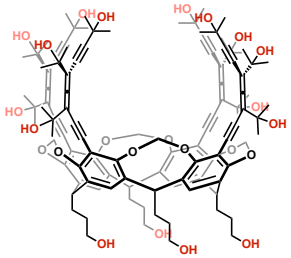
AAK $(P)_4$

Das letzte Kapitel gibt einen kurzen Überblick über die Synthese und den chiroptischen Eigenschaften von kovalent geschlossenen alleno-acetylenischen Käfigrezeptoren, die durch intramolekulare oxidative Dimerisierung zugänglich sind. Die kovalent verbrückten AAKs zeigten starke Absorptionseigenschaften gegenüber zirkular polarisiertem Licht, wobei kaum Temperaturabhängigkeiten auftraten. Die Cokristallstrukturen lieferten Einblicke in die Größe des Hohlraums für zukünftige molekulare Erkennungsstudien.

1. Introduction

Sections of this chapter where published in a recent Perspective Article in the *Journal of the American Chemical Society*: Molecular Recognition with Resorcin[4]arene Cavitands: Switching, Halogen-Bonded Capsules, and Enantioselective Complexation.[1]

1 Introduction

Structure-based ligand design in medicinal chemistry and crop protection builds on the identification and quantification of noncovalent bonding interactions.[2,3] Methods that allow to identify new interactions in chemical and biological systems comprise data base mining in structural databanks and protein and small molecule crystallography. The identification of novel interactions is followed by their quantification, involving complexation studies with proteins and synthetic model systems, accompanied by accurate computational methods. This multi-dimensional approach continues to expand our fundamental understanding of molecular recognition in biological and chemical systems, and is key in advancing modern medicinal chemistry by successfully generating and optimizing lead structures.[4]

In this regard, the study of synthetic model systems and biological systems has developed an extraordinary symbiosis, helping to decipher phenomena observed in nature. This is summarized in Cram's historical definition of host-guest chemistry, where hosts are defined as the synthetic equivalent of biological receptors, and guests as their counterparts, such as substrates, inhibitors, or co-factors.[5]

As much as the design of synthetic host systems was inspired by natural receptors, the lessons learned from synthetic systems have contributed directly to elucidating the basic principles governing the function of their biological equivalents. Prominent examples are natural ionophores, such as the membrane spanning potassium ion-channel elucidated by McKinnon and co-workers.[6-8] The principles governing the high selectivity and turnover for potassium ions compared to sodium ions were established years before the structural elucidation of the potassium ion-channel in synthetic ionophores.[9-15] A more recent example are dipolar interactions, where large increase in ligand binding potency was achieved by establishing halogen-bonding interactions between proteins and ligands.[16-18] The intrinsic strength of individual halogen bonds was established through model systems in solution.[19]

1.1 Noncovalent Interactions Studied in Model Systems

Over the past 50 years, synthetic model systems have guided chemists through the ensemble of intermolecular interactions observed in natural systems, spanning from hydrogen bonding and Coulombic interactions, to more subtle contacts, such as dipolar interactions.[4] Figure 1 gives a timeline of selected examples of interactions and concepts, which were studied in biological systems and synthetic model systems. The information that has resulted from the study of both chemical and biological systems has contributed to important guiding principles in medicinal chemistry, crop protection, supramolecular chemistry, and material science.[4]

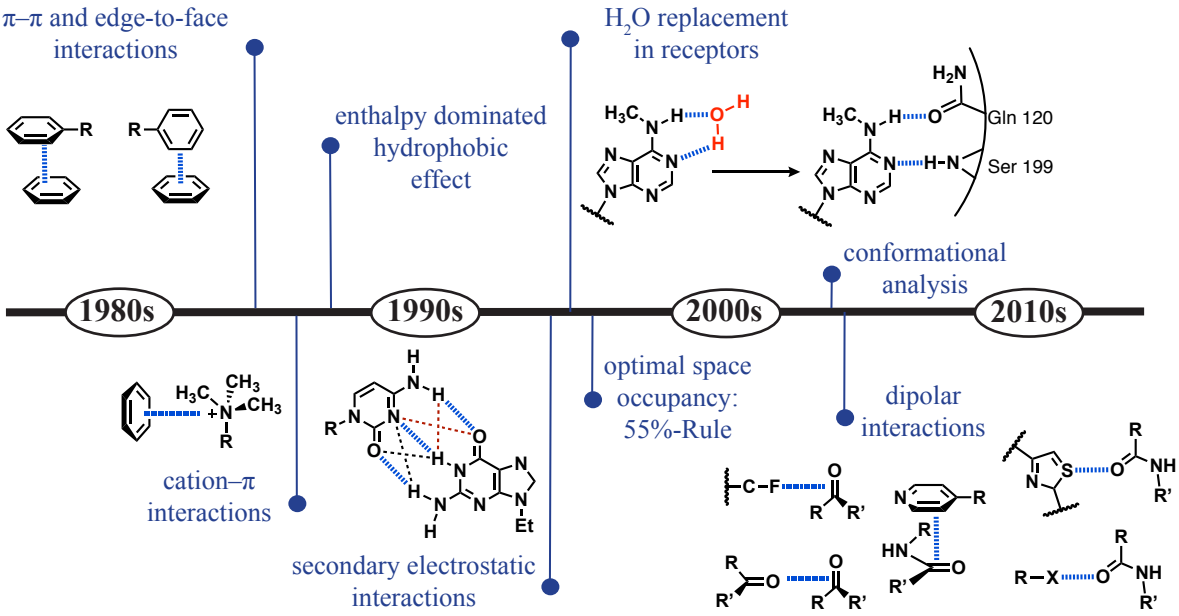

Figure 1. A timeline of selected examples of noncovalent interactions and binding concepts that where studied in chemical and biological systems (from left to right): π–π and edge-to-face aromatic interactions;[20-31] cation-π interactions;[32-39] the enthalpy dominated hydrophobic effect;[40-47] secondary electrostatic interactions;[48-50] water replacement in crystals,[51] biomolecules[52-55] and synthetic receptor systems;[4,56-58] optimal space occupancy of lipophilic molecules in apolar binding sites;[59-63] conformational analysis;[64-67] weak, unusual interactions such as dispersion,[68,69] orthogonal dipolar,[70,71] amide-π (arene/heteroarene) interactions,[72,73] halogen-bonding[74,75] and chalcogen-bonding interactions.[76,77]

In the mid 1980s, Burley and Petsko observed both π–π interactions and edge-to-face aromatic interactions in biological systems.[20,21] Subsequently, various model systems followed, including simple benzene dimers,[22] macrocyclic receptors,[23] and torsion balances[24-26] which allowed to quantify their interaction energies.[27] Substituent effects on aromatic interactions are still subject of research with different models evolving from these studies, which rationalize the electronic contributions of the substituents on the aromatic interactions.[28-31] Macrocyclic hosts, such as cyclophanes,[32] are prominent examples of early model systems, which illustrate the achievements in the complexation of aromatic molecules[33] and led to the discovery of the cation-π interaction by Dougherty and co-workers in the late 1980s.[34,35] It was found that the interaction of organic cations with aromatic functionalities can outcompete the desolvation of cations in water. The impact of these studies was significant, not only in biological receptors,[36,37] but also in many areas of chemistry, such as molecular switches[38] and small-molecule catalysis.[39] At the same time, cyclophanes enabled the investigation of enthalpically driven complexation, known as the "nonclassical" hydrophobic

effect,[40] for the tight binding of apolar substrates in hydrophobic cavities, both in organic and aqueous media.[41-44] Traditionally, the hydrophobic effect was correlated with the entropically driven release of water molecules from lipophilic surfaces (classical hydrophobic effect). Compared to the classical hydrophobic effect, the "nonclassical" hydrophobic effect is associated with an enthalpic energy gain.[45,46] The favorable enthalpic complexation was explained with a gain in van der Waals interactions and solvent cohesive interactions in the bulk phase.[47] In the beginning of the 1990s, Jorgensen and co-workers systematically studied the secondary electrostatic interactions in hydrogen bonding networks.[48] Secondary electrostatic interactions were shown to have significant influence on the stability of assemblies comprising of multiple hydrogen bonds.[49,50] In the mid 1990s, Dunitz predicted the energetic gain of releasing weakly coordinated water molecules from the interior of a protein into the aqueous bulk.[51] This prediction was later systematically studied by various groups, showing that the replacement of water molecules undergoing two or more directional interactions generally results in little gain in free enthalpic energy. In contrast, the replacement of water molecules with a single polar interaction can be accompanied with a substantial gain in free enthalpic energy.[4,52-55] The understanding of the contribution of water and water networks for the thermodynamic and structural stability of protein-ligand complexes is still subject of intense research, where further insight relies on the development of new model systems.[56-58] In the late 1990s, hydrogen-bonded supramolecular capsules pioneered by Rebek and co-workers, allowed the determination of the optimal space occupancy of 55 ± 9% for lipophilic molecules in apolar binding sites.[59,60] The authors predicted that in case of additional polar interactions, a higher occupancy can be expected, which was later confirmed by various groups.[59] This rule evolved to a guiding principle for optimal pocket filling in medicinal chemistry.[61-63] From 2000 onwards, there has been increased recognition of the importance of conformational analysis,[64,65] where various model systems allowed to gain insight into the conformation of small molecules in confined spaces.[66,67] This development can be traced back to an increasing amount of available structural information on small molecules and ligand-protein complexes. Nowadays, conformational analysis is an essential tool in structure-based design. In the last years, the field has progressed to the identification and quantification of weak, unusual interactions, such as dispersion,[68,69] orthogonal dipolar,[70,71] amide–π (of arene or heteroarene),[72,73] halogen-bonding[74,75] and chalcogen-bonding interactions.[76,77]

Halogen bonds are an interesting example that illustrate the discovery of a less obvious intermolecular interaction, where model systems have played an important role in their quantification. Halogen bonding (XB) is defined, in analogy to hydrogen bonding, by a donor

and an acceptor.[78] The halogen containing part is the donor (D) and the electron-donating part, usually a Lewis base, is the acceptor (A). With increasing polarizability of the halogens from Cl to Br to I (D) the strength of the halogen-bonding donor increases.[79,80] The growing basicity of the Lewis base results in an increase in its acceptor ability. Important criteria for XB are the precise orientation of the donor and the acceptor, with a C–D···A angle approaching 180°.[81,82] As a result of strong halogen bonding, donor and acceptor move to sub-van-der-Waals distance.[83] Within this geometrical constraints, the lone pair of the Lewis base can interact with the σ*-orbital of the C–D bond. The highly defined geometrical framework associated with halogen bonding makes it a challenging interaction to be established in solution. In consequence, XB was first discovered in precisely aligned solid state networks.[84,85] XB studies in solution only started to appear around 2010, where the intrinsic strength of a single halogen bond was established through the study of model systems in solution.[19,86,87] It was shown that the enthalpic gain for a single strong neutral halogen bond in a noncompetitive solvent environment is stronger than the energy gain of a strong neutral hydrogen bond. The rigorous geometrical requirements, however, account for large entropic costs compensating the enthalpic energy gain. In protein-ligand complexes, the entropic costs are largely paid by the binding of the ligand to the receptor through multiple, less geometrically demanding interactions, which orient the XB donor in the precise orientation to a XB acceptor site of the protein.[16,17,88]

As a result of these studies on biological systems and model systems, halogen bonds have become an important tool in medicinal chemistry. This was recently shown in structure-based design, where an increase in affinity of 55-fold was observed on establishing a halogen bond between the ligand and the receptor.[16-18]

1.2 Noncovalent Interactions in Multidentate Supramolecular Assemblies

In biological systems, the entropic costs associated with the geometrical requirements for interactions are paid through the binding event, which preorganizes the ligand within the receptor. Supramolecular chemistry was largely inspired by the concept of preorganization observed in natural systems[89] and adopted an approach coined multidentate bonding. Supramolecular capsular architectures illustrate this approach, where preorganization of the molecular subunits and the event of multiple interactions reduces the entropic costs to enable the formation of complex architectures. Figure 2 highlights three selected examples of supramolecular assemblies comprising of highly preorganized platforms that form capsular assemblies *via* multiple hydrogen bonds, dispersion and halogen-bonding interactions.

Hydrogen Bonding Dispersion Interactions Halogen Bonding

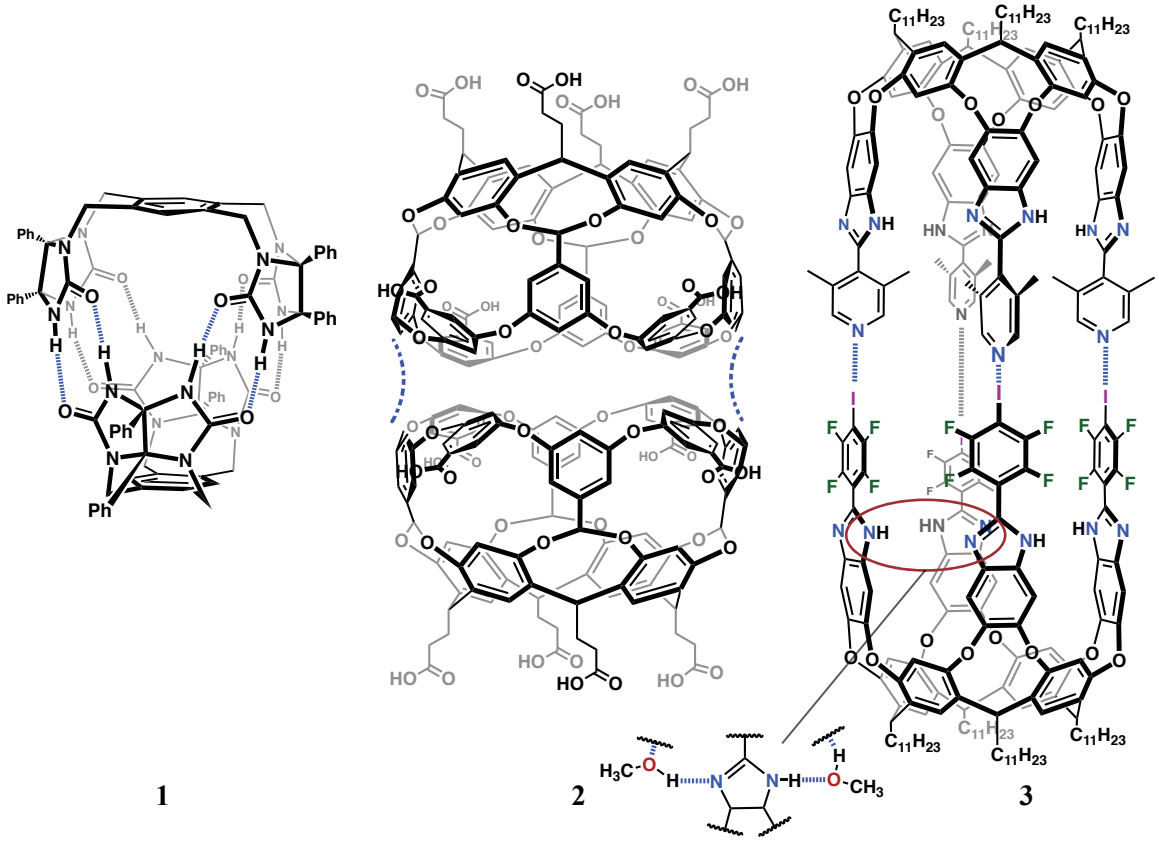

Figure 2. Noncovalent multidentate bonding in supramolecular assemblies. Selected examples employing hydrogen-bonding, [85-87] dispersion (solvent cohesive and dispersion interactions in aqueous solution) [88,89] and halogen-bonding interactions. [91,92]

Rebek and co-worker assembled the first supramolecular assembly employing hydrogen bonds **1**.[90] Structure **1** shows two glycoluril-components that form a dimer via eight complementary hydrogen bonds (Figure 2, **1**).[90] Later, hydrogen bonding architectures were also achieved with extended glycoluril-derivatives[91] and resorcin[4]arene scaffolds.[92] The stability of the assembly was strongly dependent on the nature of the hydrogen bonds and the principles of secondary electrostatic interactions, mentioned in the previous section. The curvature of the molecular subunits induces a cavity, capable of binding small molecules, such as saturated and unsaturated hydrocarbons.

Gibb and co-workers used the hydrophobic effect, which comprises of both solvent cohesive and van der Waals dispersion interactions in aqueous solution, to assemble two deep cavitands (Figure 2, **2**).[93,94] The highly rigid structure of the water-soluble deep cavitand **2** comprises of aromatic surfaces. In water, two hemispheres dimerize in head-to-head fashion to form an elongated hydrophobic cavity, capable of binding larger apolar molecules, such as steroids.[93] The dimerization of two capsules with large aromatic surfaces in organic solvents

was studied before by Cram and co-workers and was coined velcraplexes.[95] Compared to architectures assembled *via* dispersive interactions, capsular assemblies through dipolar interactions, such as halogen bonds, require precise orientation of the interacting donor and acceptor (Figure 2).[96] Compound **3** shows a halogen bonded capsular assembly of two resorcin[4]arene-based XB donor and acceptor platforms. Rigidification and preorganization of the flexible imidazole walls was ensured through the addition of alcohol molecules that bridge the walls, to form a cyclic hydrogen bonding array (see insert, Figure 2). Four neutral halogen bonds between the tetrafluoroiodophenyls (donor) and the lutidines (donor) established the assembly of **3**.[96] Exchanging the tetrafluoroiodophenyls with a stronger donor, such as (iodoethynyl)tetrafluorophenyl moieties, resulted in a large increase in association of both hemispheres, with binding constants K_a of 10^5 M^{-1}.[97] Both hemispheres were able to bind small guests, such as 1,4-dithiane and 1,4-dioxane.[97]

These three examples illustrate, how the understanding of individual interactions can provide new tools in the construction of novel molecular structures. Once an interaction is identified and quantified, it starts to be used in almost every sub-field of chemistry. With increasing directionality of the interaction, more rigorous geometrical requirements have to be met, in order to obtain the assembly in solution. However, once these requirements are met, even not so obvious interactions, such as multipolar interactions, can become an important tool in many fields of chemistry by introducing a high degree of selectivity.

1.3 Enantioselective Complexation through Noncovalent Interactions

Two enantiomers of a chiral substance in a symmetric environment have identical physicochemical properties, except their ability to rotate plane-polarized light. The latter results from the fact that a pair of enantiomers are related to each other as mirror images. The different properties of two enantiomers can, nevertheless, be expressed in their unequal interactions in an asymmetric environment (chiral recognition). The molecular mechanism of chiral recognition has been fascinating researchers since the earliest study of stereochemistry.[98,99]

A characteristic of many enzymes is their ability to distinguish between two enantiomers through multiple noncovalent interactions. Upon complexation of a ligand, the asymmetry of the active sites of these enzymes leads to the formation of diastereoisomeric complexes of the ligand with the receptor, where the overall potential energy of the diastereoisomeric complex of the receptor with one enantiomer decreases more significantly than with the other enantiomer. Understanding the processes in nature that lead to

enantioselective complexation, requires the study of attractive and repulsive intermolecular interactions at the molecular level.

In 1894, Fischer formulated the concept of shape complementarity describing the selectivity of enzymes towards their substrates through a lock-and key analogy:[100]

"…;denn die Überzeugung, dass der geometrische Bau des Moleküls selbst bei Spiegelbildformen einen so grossen Einfluss auf das Spiel der chemischen Affinität ausübe, konnte meiner Ansicht nach nur durch neue tatsächliche Beobachtungen gewonnen werden."[100]

Around 40 years later, in 1933, Easson and Stedman inferred from quantitative structure-activity relationship studies that a minimum of three attractive directional interactions are necessary for the enantioselective complexation of a ligand with a receptor.[101] This concept was later applied to enantioselective enzymatic reactions.[102] Early pioneering studies with synthetic model systems were developed by Cram *et al.*[103-105] and Prelog *et al.*[106,107] to investigate the enantioselective complexation of chiral substrates by enantiopure receptors (Figure 3).

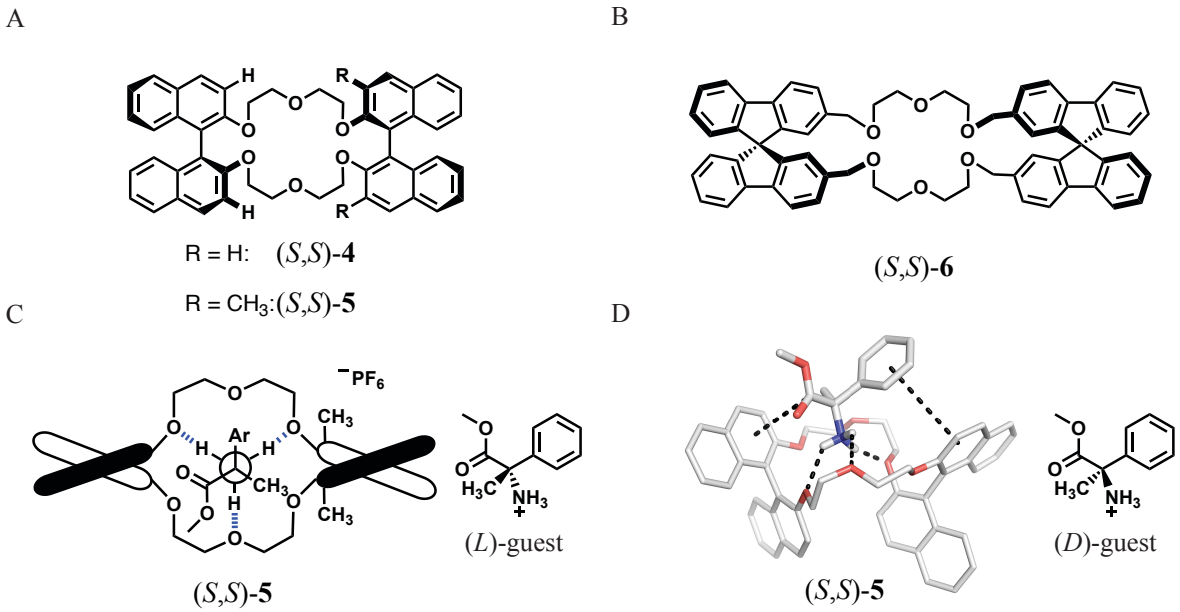

Figure 3. Cram's chiral binaphthyl crown ether receptor (A: (*S*,*S*)-**4** and (*S*,*S*)-**5**)[105] and Prelog's chiral spirobifluorene crown ether (B: (*S*,*S*)-**6**)[107] for the enantioselective complexation of chiral ammonium cations. C: Model for the formation of the more favorable diastereoisomeric complex of the (*S*,*S*)-**5** with protonated (*L*)-α-amino acid esters. D: X-ray co-crystal structure of the less favorable (from ^{1}H NMR studies in $CDCl_3$ at 283 K) obtained from (*S*,*S*)-**5** with the weaker binding (*D*)-α-amino acid ester; PF_6^- counter anion omitted for clarity.[108]

These studies mainly focused on the enantioselective binding of chiral ammonium cations of α-amino acid esters and α-aminoalcohols by optically pure crown ethers. The chirality of the receptors stems in the case of Cram's system, **4** and **5**, from the axial chirality of the binaphthyl linkers (Figure 3, A),[105] whereas Prelog's design relies on the axial chirality of the spirobifluorene moiety **6** (Figure 3, B).[107]

The complexation of the amino acid derivatives to the crown ether receptors is characterized by three points of interactions. The ammonium cation of the guest undergoes strong hydrogen-bonding and ion-dipole interactions with the crown ether of the receptor. Additionally, the ester functionality of the guests undergoes favorable π···π-interactions with the naphthyl or spirobifluorene moiety of the hosts. The aromatic substituent of the guest finally introduces steric constraints with the axial chiral moieties of the host. In extension to the three-point-interaction model, these studies revealed the importance of preorganization of the receptor to effectively differentiate between two enantiomers. While Easson and Stedman's model inferred three strong directional interactions, Cram *et al*. and Prelog *et al.* introduced steric constraints replacing one or two attractive interactions.[105,107] The co-crystal structure of the less favorable complex of (*S*,*S*)-**5** with the (*D*)-α-phenylglycine methyl ester revealed the strong directional ionic H-bonding interaction of the primary ammonium group with the crown ethers, fixating the ligand to the receptor. Additionally, the ester residue adopts favorable π···π contacts with the aromatic moieties (Figure 3, D).[108] The Ph group of the ligand oriented towards the axial chiral binaphtyl moiety, introduces steric constraints (Figure 3, D). In the more favorable diastereomeric complex of (*S*,*S*)-**5** with the (*L*)-α-phenylglycine methyl ester, this Ph group faces away from the binaphthyl groups (Figure 3, C). In case of the (*D*)- and (*L*)-α-phenylglycine methyl ester, the different interaction modes with (*S*,*S*)-**5** account for substantial differences in the stability of the diastereoisomeric complexes of up to $\Delta\Delta G^0$ = –1.9 kcal mol^{-1} (from ^{1}H NMR studies in $CDCl_3$ at 283 K).[105]

In the following years, increasing complexity of the cationic guests led to the investigation of more sophisticated and highly preorganized enantiopure receptors, such as cryptophane[109] and hemicarcerand derivatives,[110] to achieve enantioselective binding. While chiral recognition with cationic guests can be considered a mature subject, the enantioselective complexation of anionic guests emerged only recently.[111-113] The main reason lies in the solvation-related challenges associated with the complexation of anions in protic environment. Anion complexation in protic solvents requires strong Coulombic and hydrogen bonding interactions, compensating for the high costs of desolvation. Additionally, both the protonation

states of the receptor and the anion, as well as the influence of the counterions have to be taken into consideration.[111] The evolution of anion receptors parallels that for cations, with an increasing degree of sophistication and preorganization in the design of the receptor system.[111,113] Chiral versions of the azamacrocyclic receptors initially developed by Simmons and Park,[114] and Schmidtchen[115] evolved to receptors, such as the cyclic sapphyrin-based dimer $(S)_4$-**7** for the enantioselective complexation of dicarboxylate salts (Figure 4, A).[116]

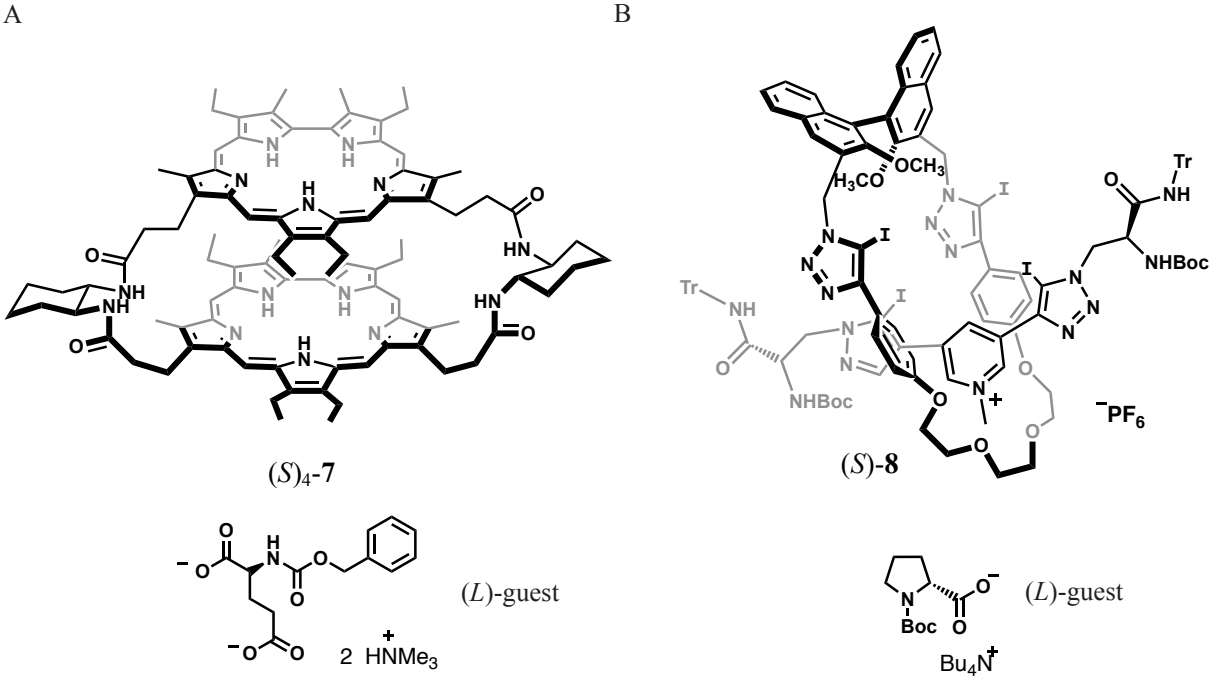

Figure 4. A: Sessler's enantiopure sapphyrin-based receptor $(S)_4$-**7** for the chiral recognition of carboxylate anions, such as the bis-trimethylammonium salts of *N*-Cbz-glutamate;[116] B: Beer's optically pure (*S*)-[2]rotaxane (*S*)-**8** for the recognition of *N*-Boc-protected amino acids, such as the hexafluorophosphate salt of *N*-Boc-proline. Tr groups represent bulky trityl-derivatives.[117]

The chirality in $(S)_4$-**7** stems from the (1*S*,2*S*)-configuration of the two 1,2-diaminocyclohexane linkers (Figure 4, A). The highest selectivity of the receptor was found with racemic *N*-Cbz-glutamate, where the *L*-configured guest was preferentially bound over the *D*-configured guest ($\Delta\Delta G^0$ = –0.84 kcal mol^{-1}; from ^{1}H NMR studies in CD_2Cl_2/d_3-methanol 95:5 at 293 K, Figure 4, A).[116]

A recent example of the mechanically interlocked (*S*)-[2]rotaxane **8**, takes advantage of ionic halogen bonding interactions in the recognition of guests, such as *N*-Boc-protected amino acids (Figure 4, B).[117] The chirality of the [2]rotaxane (*S*)-**8** originates from the (*S*)-1,1'-bi-2-naphthol (BINOL) linker. The (*S*)-configured receptor showed preferential binding of the tetrabutylammonium salt of (*L*)-*N*-Boc-protected proline carboxylate over the (*D*)-*N*-Boc-protected proline (3:1 preference of (*L*):(*D*)-guest; from ^{1}H NMR studies in d_6-

acetone/D_2O 98:2 at 298 K).[117] The [2]rotaxane was further extended to a chiral [3]rotaxane for the binding of dicarboxylate anions, such as *N*-Boc-glutamate, with high selectivity.[118] Similar to the system illustrated in Figure 4 B, the complexation of the *N*-Boc-glutamate dianion is mainly driven by ionic halogen bonds of the iodines with the carboxylate anions.[118] The enantioselectivity arises from additional steric effects induced by the interlocked arrangement. The examples shown in Figure 4 illustrate two different approaches towards highly preorganized receptors: the covalent linking of two receptor platforms (Figure 4 A, $(S)_4$-**7**) and the mechanical interlocking of two single strands (Figure 4 B, (*S*)-**8**).

In general, ion-dipole interactions dominate over other interactions in the recognition of both cationic and anionic species and allow little insight into the contribution of weaker interactions. Conversely, enantioselective recognition of neutral small molecules relies on a network of interactions and cannot be reduced to single directional interactions. In consequence, the geometrical tetrahedral point model evolved to more complex multipoint interactions models.[119] With the absence of strong directional interactions, such as ion-dipole contacts, preorganization of the receptor became even more important to achieve enantioselectivity.

Early attempts at enantioselective binding of neutral molecules utilized confined molecular cage systems. Prominent examples are hemicarcerands **9** and **10**, constructed from resorcin[4]arene platforms and enantiopure 1,1'-binaphthyl linkers, (Figure 5).[120,121] Hemicarcerand $(S)_4$-**9** was assembled from two resorcin[4]arene platforms, linked through four enantiopure 1,1'-binaphthyl linkers (Figure 5, A).[120] The steric constraints of the axial chiral binaphthyl linkers induce a highly confined chiral cavity. The authors reported the complexation of racemic dibromo butanes with generally moderate selectivity of the receptor towards one enantiomer and increasing selectivity from 1,2-dibromobutane (1.5:1) to 1,3-dibromobutane (2:1, Figure 5, A; for selectivity studies, the host $(S)_4$-**9** was dissolved in a neat guest solution and heated to 100 °C for 18 h; diastereoisomeric ratios were measured through relative rates of decomplexation by ^{1}H NMR in $CDCl_3$ at 295 K).[120] It was argued that the steric repulsion and the dipole-dipole alignments in the diastereoisomeric complexes of the host with the guest are responsible for the observed selectivity (see stick model, Figure 5, A bottom). Later, the same group replaced three of the binaphthyl linkers with achiral *n*-butyl linkers (Figure 5, B).[121] This less confined receptor (*S*)-**10** showed generally higher enantioselectivity compared to $(S)_4$-**9**, however, with overall moderate selectivity towards racemic alcohols, but remarkably high selectivity towards racemic sulfoxides (>20:1 (*R*):(*S*) in (*S*)-**10**).[121] While no explanation was found to rationalize the high enantioselectivity towards

chiral sulfoxides compared to chiral alcohols, the authors observed from molecular model examinations that the guest accesses the inside of the receptor more likely *via* the achiral openings compared to the chiral ones.[121]

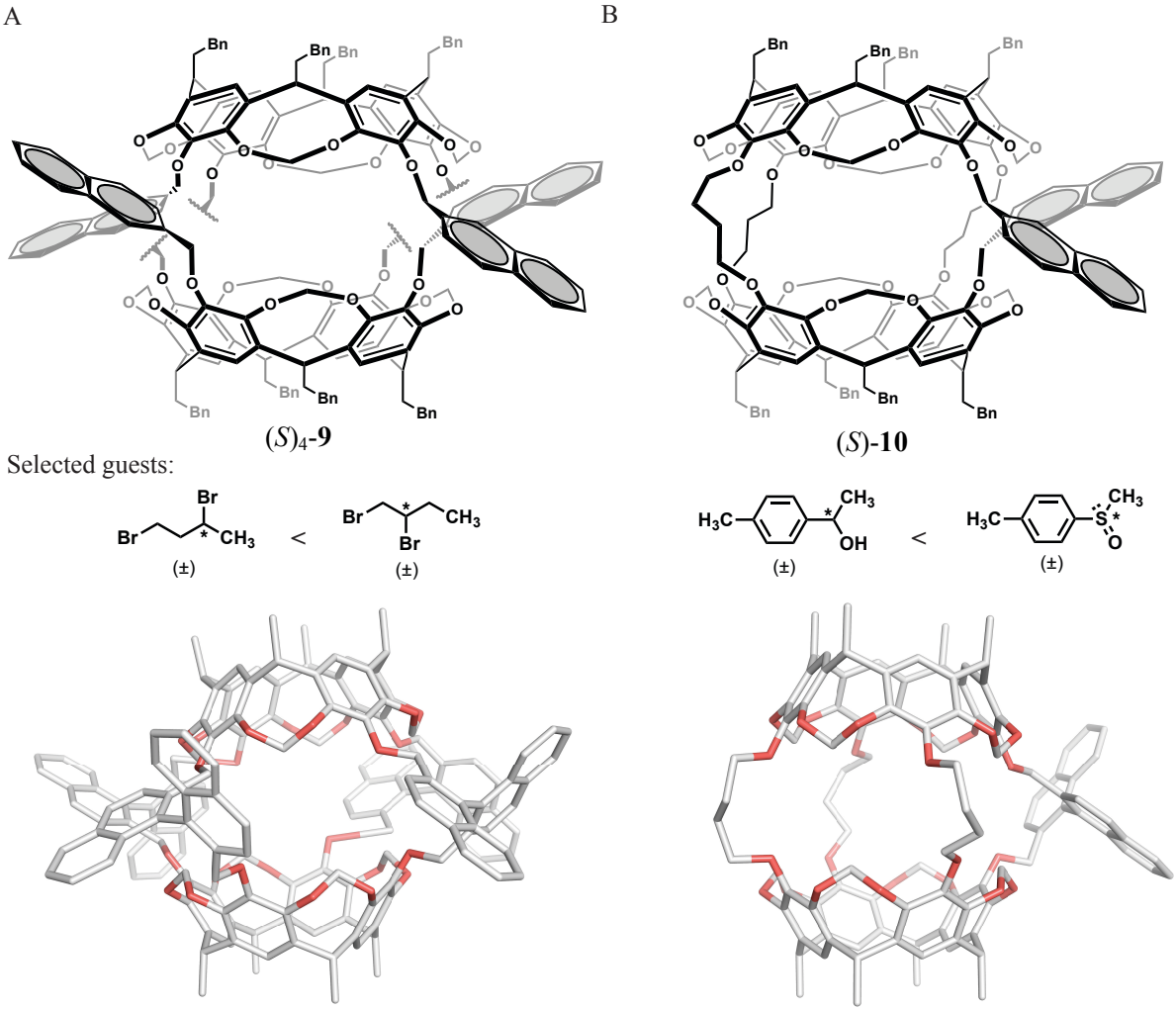

Figure 5. A: Hemicarcerand $(S)_4$-**9** comprising of two resorcin[4]arene platforms connected through four (*S*)-binaphthyl linkers (two linkers omitted for clarity); $(S)_4$-**9** showed moderate selectivity towards different chiral isomers of bromo alkanes. [120] B: Hemicarcerand (*S*)-**10** with a single (*S*)-binaphthyl linker and three butyl linkers shows moderate selectivity towards chiral alcohols, but complete selectivity towards chiral sulfoxides.[121] Below are stick models of hemicarcerands $(S)_4$-**9** and (*S*)-**10**; leg-groups and hydrogens are omitted for clarity.

A second family of optically pure cage receptors are cryptophanes, which are derived from cyclotriveratrylene (CTV) platforms and were introduced by Collet and co-workers (Figure 6, **11**).[109,122] In cryptophanes, the chirality stems from the helically chiral CTV moiety. Two CTVs are bridged through three ethyl linkers, giving $(P)_2$- and $(M)_2$-configured receptors **11**.[122] The CTV-based cryptophane **11** served as host for the chiral (±)-

CHBrClF guest, which is considered to be one of the simplest possible stable chiral molecules.[122] The authors envisioned the enantioselective complexation and elucidation of the absolute configuration of the guest. The thermodynamic stereoselectivity observed towards (±)-CHBrClF was approximated to be $\Delta\Delta G^0 = -0.26$ kcal mol^{-1} at 339 K and is comparable to the selectivity Cram *et al.* observed for the complexation of brominated *n*-butanes with hemicarcerand hosts.[120,122]

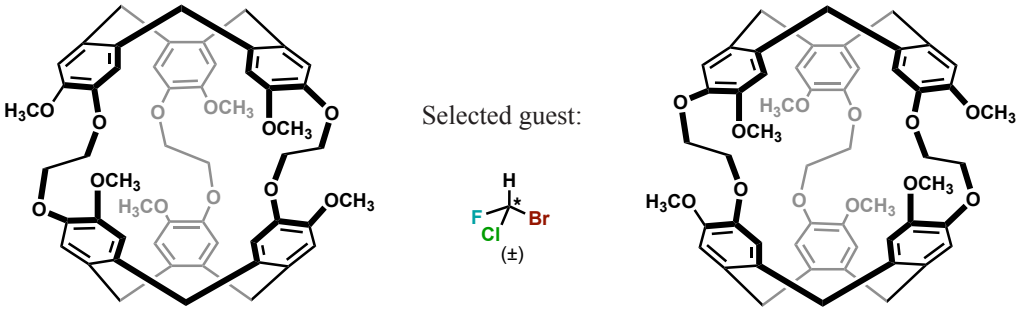

$(M)_2$-**11** $(P)_2$-**11**

Figure 6. Collet's enantiopure (*M*)- and (*P*)-configured cryptophane **11** for the chiral recognition of (±)-CHBrClF.[122,123]

The two early examples of optically pure host systems illustrate the general approach towards enantiopure receptors. The chirality in hemicarcerands results from the enantiopure binaphthyl linkers connecting two achiral platforms,[110] while in cryptophanes the enantiopure CTV platforms are linked through achiral alkyl chains.[109] Later, a combination of enantiopure platforms with enantiopure linkers was pursued by different groups with varying success in chiral recognition studies.[124-127] An important lesson learned from these studies is that preorganization and confinement are crucial for enantioselective binding, but have to be balanced with flexibility and porosity for guest uptake and release.

After these early studies, noncovalent, mainly hydrogen bonded assemblies,[128-135] metal-mediated (metal–organic cages),[136-139] and dynamic covalent assemblies[140-144] have emerged in the construction of optically pure cage receptors. The dynamic nature of the assemblies allows a more facile access to complex enantiopure architectures, compared to covalently assembled receptors. However, few of the reported receptors have been applied to chiral recognition studies and, with the exception of isolated examples, only moderate enantioselective guest complexation was achieved in most cases. Presumably, due to the difficulty of achieving the necessary preorganization and confinement for chiral recognition of neutral molecules in a dynamic assembly. The following examples will demonstrate the challenges in designing optically pure receptors assembled through noncovalent interactions, suitable for chiral recognition studies.

Rebek and co-workers described the assembly of a hydrogen-bond-mediated pseudospherical assembly of extended asymmetric glycolurils **12** (Figure 7).[130]

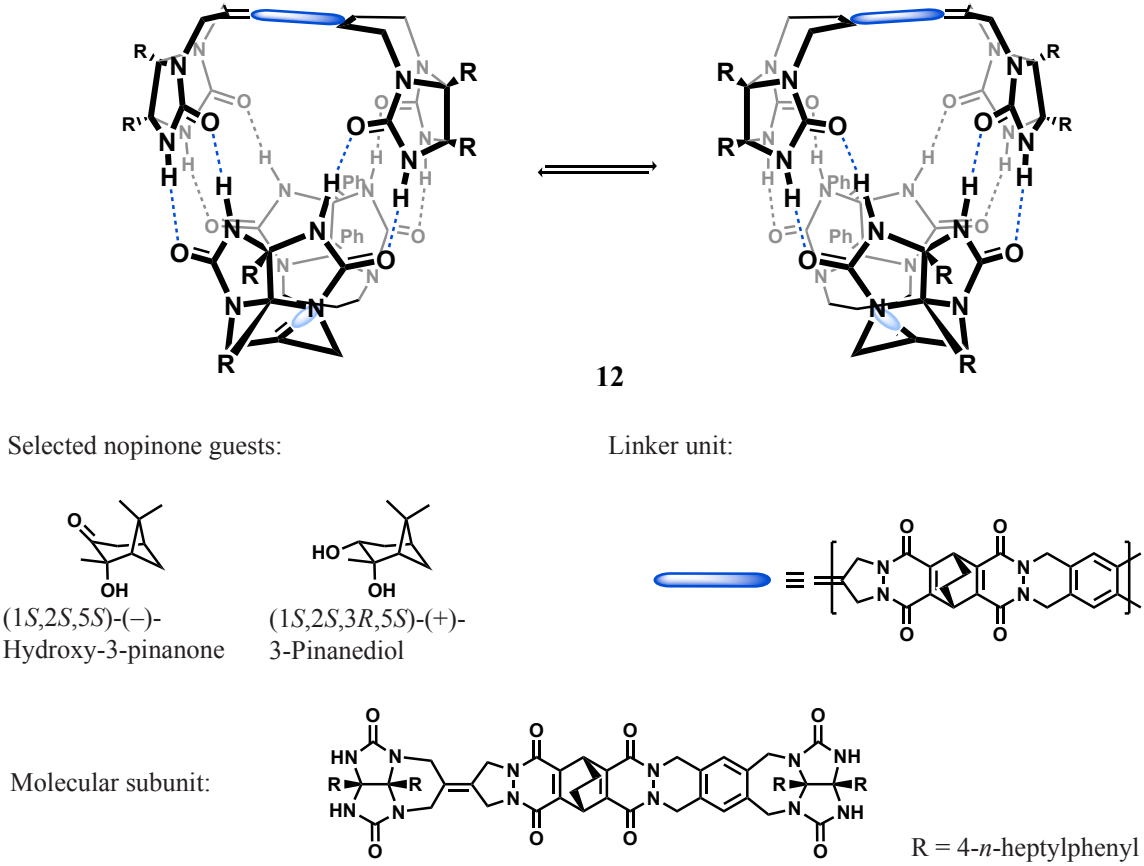

Figure 7. Rebek's racemic hydrogen bonded assembly **12** of two asymmetric extended glycouril molecular subunits. The two enantiomeric assemblies interconvert rapidly in solution. Complexation with chiral guests shifts the equilibrium towards the formation of the favorable diastereoisomeric complex.[130]

The asymmetry of the glycoluril backbone leads to the formation of a racemic dimer **12** in solution, where both enantiomeric capsules interconvert rapidly. The curvature of the molecular subunits produces an asymmetric cavity capable of guest encapsulation. Through guest complexation, the equilibrium between the enantiomeric dimers is shifted towards the favorable diastereoisomeric complex.[130] With smaller guests, such as nopinones, no selectivity was observed. (1*S*,2*S*,5*S*)-(–)2-Hydroxy-3-pinanone induced a moderate diastereoselectivity of $\Delta\Delta G$ = –0.2 kcal mol^{-1}, increasing up to $\Delta\Delta G$ = –0.4 kcal mol^{-1} for (1*S*,2*S*,3*R*,5*S*)-(+)-pinanediol (from ^{1}H NMR studies in *p*-xylene-d_{10} at 295 K, Figure 7).[130] Based on this work, Mastalerz and co-workers recently used a similar hydrogen bonding motif to assemble a large racemic octameric hydrogen bonded capsule from optically pure tripodal subunits.[145] The capsule was not subjected to chiral recognition studies.

Bergmann, Raymond, and co-workers reported on a tetrahedral coordination assembly of M_4L_6 stoichiometry, where four metal atoms (M = Ga^{3+}, Al^{3+}, In^{3+}, or Fe^{3+}) are situated at the corners of a tetrahedron and are bridged by bis-bidentate catechol ligands.[136,146] The negatively charged (–12 overall charge) and water-soluble assembly consists of a hydrophobic cavity, capable of incorporating organometallic complexes. Figure 8 shows the $[(\Lambda)_4\text{-}Ga_4L_6]^{12-}$-**13** tetrahedral host, encapsulating unsymmetrically substituted chiral ruthenium half-sandwich complexes of the general formula Cp*Ru(diene)X (Cp* = η^5-$C_5(CH_3)$; X = Cl).[146] In water, the complexes undergo halide dissociation to form cationic solvated ruthenium species. In a series of 1- and 2-subsituted diene complexes, a high degree of size and shape selectivity was observed (Figure 8, Table).[146] The host-guest complex K_{11}[Cp*Ru(isoprene) (H_2O) ⊂**13**] showed only moderate diastereoselectivity (52:48). Exchanging the methyl substitutent of isoprene to an ethyl substituent on the R_2 position, resulted in a significantly augmented difference in the diastereoisomeric complexes of 85:15.[146]

Host:

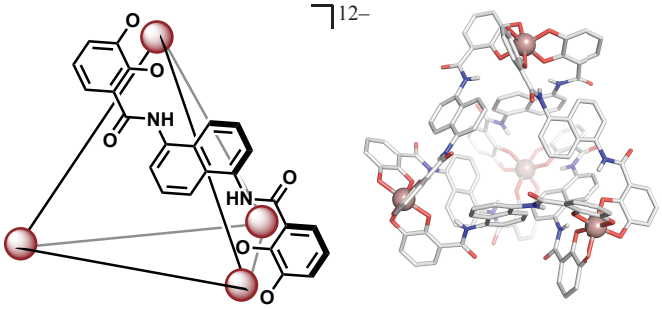

$[(\Lambda)_4\text{-}Ga_4L_6]^{12-}$-**13**

Guest:

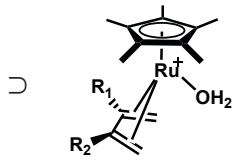

[Cp*Ru (R_1,R_2-diene) H_2O]$^+$

Cp* = η^5-$C_5(CH_3)_5$

Selected host-guest complexes:

[Cp*Ru (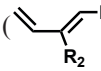

) (H_2O) Ga_4L_6]$^{11-}$

R_1	R_2	*dr*
H	Me	52 : 48
H	Et	85 : 15
H	*i*-Pr	63 : 37
H	*n*-Pr	82 : 18
Me	H	58 : 42
Et	H	59 : 41

Figure 8. Bergman and Raymond's tetrahedral coordination complex of $[(\Lambda)_4\text{-}Ga_4L_6]^{12-}$-**13** encapsulating chiral ruthenium half-sandwich complexes of the general formula Cp*Ru(diene)X (Cp* = η^5-$C_5(CH_3)$; X = Cl) in water. An adapted stick representation of the X-ray co-crystal structure is shown: $[(\Lambda)_4\text{-}Ga_4L_6]^{12-}$-**13**; guest molecules and counter anions are omitted for clarity. The table shows the observed diastereoisomeric ratios (*dr*) of the host-guest complexes of $[(\Lambda)_4\text{-}Ga_4L_6]^{12-}$-**13**.[146]

Comparable selectivity was observed for the *n*-propyl substituent. The authors reported a loss in selectivity upon exchanging the ethyl substituent from the R_1 to the R_2 group (Figure 8, Table).[146] Although the selectivity seems modest compared to conventional

reagents, the diastereoisomeric ratios of the respective complexes compare favorably to those seen in other self-assembled host-systems in which recognition relies solely on van der Waals dispersion and hydrogen-bonding interactions.

Recently, Cui and co-workers used an enantiopure atropisomeric 1,1'-biphenyl-2,2'-diol based linker to assemble a Fe^{3+}-mediated tetrahedral complex **14**, reminiscent of those reported by Bergman and Raymond (Figure 9).[147]

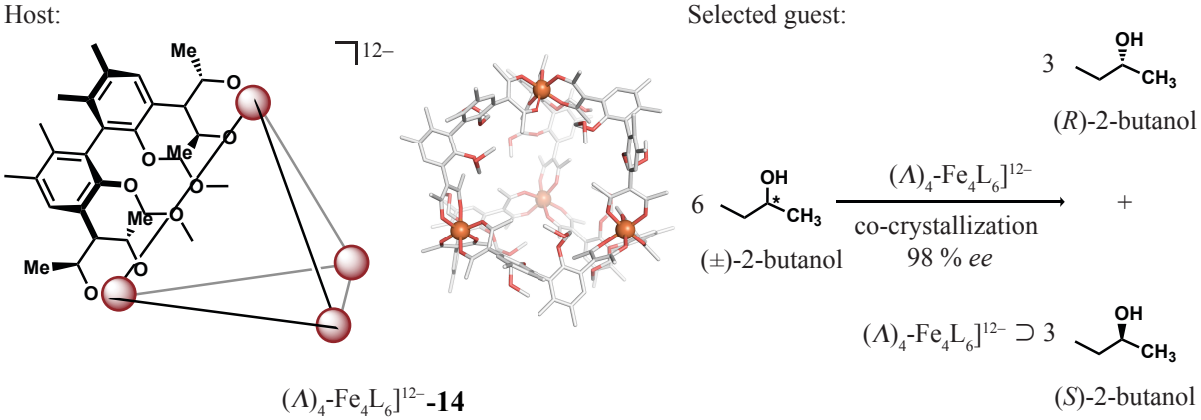

Figure 9. Cui's tetrahedral coordination complex of $[(\Lambda)_4\text{-}Fe_4L_6]^{12-}$**-14** for the enantioselective complexation of (*S*)-2-butanol. An adapted stick representation of the X-ray co-crystal structure is shown: $[(\Lambda)_4\text{-}Fe_4L_6]^{12-}$**-14**; guest molecules and counter anions are omitted for clarity.[147]

In co-crystallisation experiments, the $[(\Lambda)_4\text{-}Fe_4L_6]^{12-}$**-14** tetrahedral host showed high enantioselectivity towards the (*S*)-configured 2-butanol (98.8 *ee* from GC analysis on a chiral support).[147] Similar enantioselective behavior was observed towards (±)-3-methyl-2-butanol. While the reported enantioselectivity is remarkable, the absence of structural information on the host-guest complexes make it difficult to rationalize the observed selectivity, especially considering the 1:3 stoichiometry of the host-guest assembly. Based on these findings, the same group reported later on a chiral metallosalen-based octahedral coordination complex for asymmetric cataylsis and applied the system to the oxidative kinetic resolution of racemic secondary alcohols with high enantioselectivity.[148]

Despite recent advances in the construction of receptor systems through noncovalent, metal-ligand, and dynamic covalent interactions, enantiopure receptors for the selective binding of chiral neutral small molecules still remain relatively scarce. Mainly, due to the difficulty in synthesizing chiral cages in optically pure form with cavities suitable for selective guest encapsulation. The results from chiral recognition studies over the last years inferred important criteria for the desired high difference in stability between the diastereoisomeric complexes of an optically pure receptor and the enantiomers of a chiral

guest: (*a*) the receptor has to be rigid and preorganized with the necessary flexibility to allow guest uptake and release and (*b*) the noncovalent interactions in the asymmetric environment of the receptor have to be differentially effective for both enantiomers. For the latter, it was assumed that strong directional interactions (such as reported in the three-point-interactions model and deviations thereof) are essential to ensure significant enantioselectivity.

In this context, the question arose at the beginning of this Thesis, if enantioselective complexation can occur in the absence of strong directional interactions. We therefore sought to construct enantiopure cage receptors with highly confined hydrophobic cavities and to apply these to recognition studies with small molecule hydrocarbons and derivatives. Our approach towards optically pure cage receptors was based on an axially chiral building block, 1,3-diethynylallenes (DEAs), the development and application of which will be subject of the next section.

1.4 1,3-Diethynylallenes: From a Building Block to Supramolecular Chemistry

The development of new allenic structures has to be understood in the context of a general search for all-carbon and carbon rich scaffolds for their potential application in materials with high stability and interesting electrical and optical properties.[149,150]

1.4.1 1,3-Diethynylallenes: An Axially Chiral Building Block

Especially, the interest in tetraethynylallene fuelled research in this area, as a potential precursor for a new polymeric carbon allotrope.[151] Appropriately substituted allenes are axially chiral as a consequence of the 90° twist about the *sp*-hybridized central carbon (Figure 10, Left).[152,153]

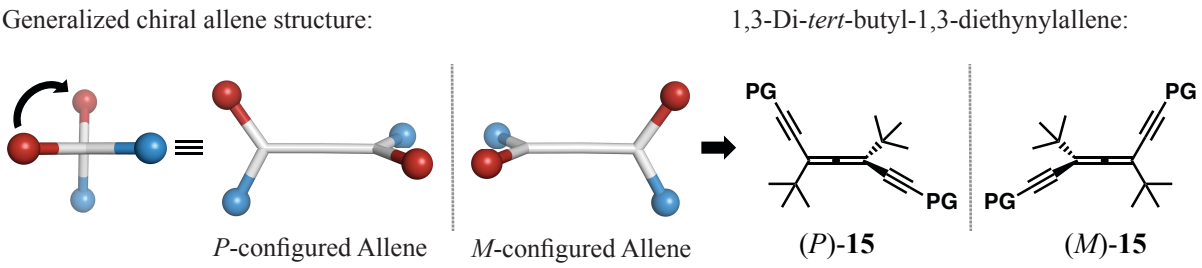

Figure 10. Left: Illustrative stick representation of a chiral allene containing substituents of different priority (red over blue) on the terminal carbon atoms. Looking along the chirality axis, the descriptors *P* and *M* designate clockwise and counter clockwise orientation of the substituents. Right: (*P*)- and (*M*)-1,3-di-*tert*-butyl-1,3-diethynylallene **15** introduced as a racemic mixture in 2002. PG = protecting groups.[154,155]

DEAs are axially chiral molecules with two acetylenic functionalities departing from the 1,3-positions. These functionalities allow to introduce these building blocks into various extended structures through cross-coupling or oxidative coupling procedures.[156] The 1,3-di-*tert*-butyl-groups of 1,3-di-*tert*-butyl-1,3-diethynylallenes (±)-**15** shield the allenic core and render these DEAs optically and thermally stable.[155] Extensive investigations showed that the 1,3-diethynylallene core is stable against [2+2] cycloaddition, when shielded by sterically demanding groups, such as the 1,3-di-*tert*-butyl-groups and if extended π-electron delocalization of the allene functionality is avoided.[155] Later, it was found that one methyl substituent of the 1,3-di-*tert*-butyl-groups can be replaced with aromatic groups or ether functionalities, such as in (±)-**16**, without significant loss in optical or thermal stability (Scheme 1, Left).[156]

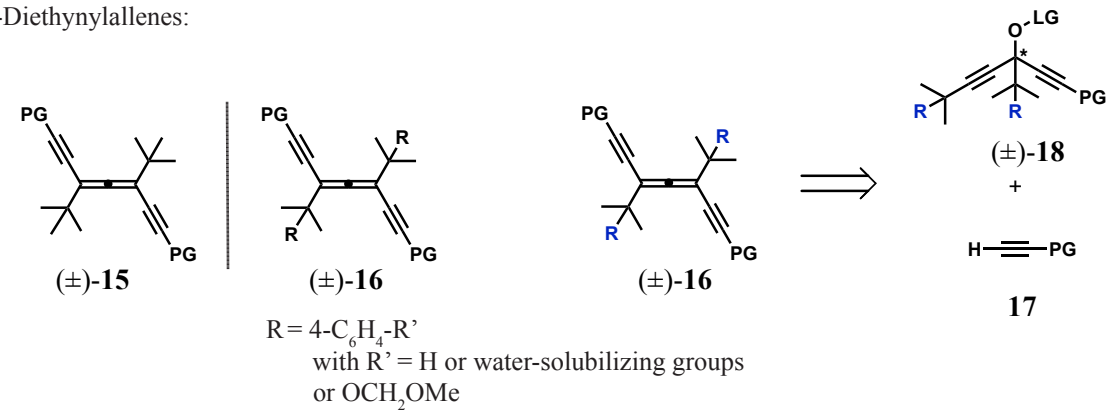

Scheme 1. The initially developed 1,3-di-*tert*-butyl-1,3-diethynylallenes (±)-**15** was extended to 1,3-diethynylallenes (±)-**16** bearing aromatic and water solubilizing groups such as ethers replacing one methyl group (representative examples of stable DEAs). The key step in the formation of the allene-core consists of a Pd(0) and Cu(I) catalyzed reaction. LG: leaving group; PG: protecting group.[156]

The lean all-carbon backbone is a distinctive feature of DEAs, compared to other widely used and sterically demanding axially chiral scaffolds, such as axially chiral 1,1'-binaphthyls.[156] The general retrosynthetic analysis pursued in the Diederich group for differently substituted DEAs consists of the formation of the allene core involving a terminal alkyne, such as 2-methyl-3-butyn-2-ol **17**, and a bispropargylic alcohol, such as (±)-**18**, functionalized with a leaving group (Scheme 1). The leaving group in the bispropargylic precursor (±)-**18** can consist of different functionalities, such as epoxides, carbonates, or carboxylates.[155] The best results were obtained with a perfluorobenzoate leaving group.[157,158] The synthesis of the bispropargylic alcohol as the allene precursor was first described in this context in 2001 and was optimized for differently substituted DEAs over the following years.[154] The key step for the formation of the allene core comprises of a

palladium(0) and copper(I) catalyzed reaction, which presumably follows a S_N2' type mechanism involving a sequence of oxidative addition, transmetalation and reductive elimination (Scheme 2).

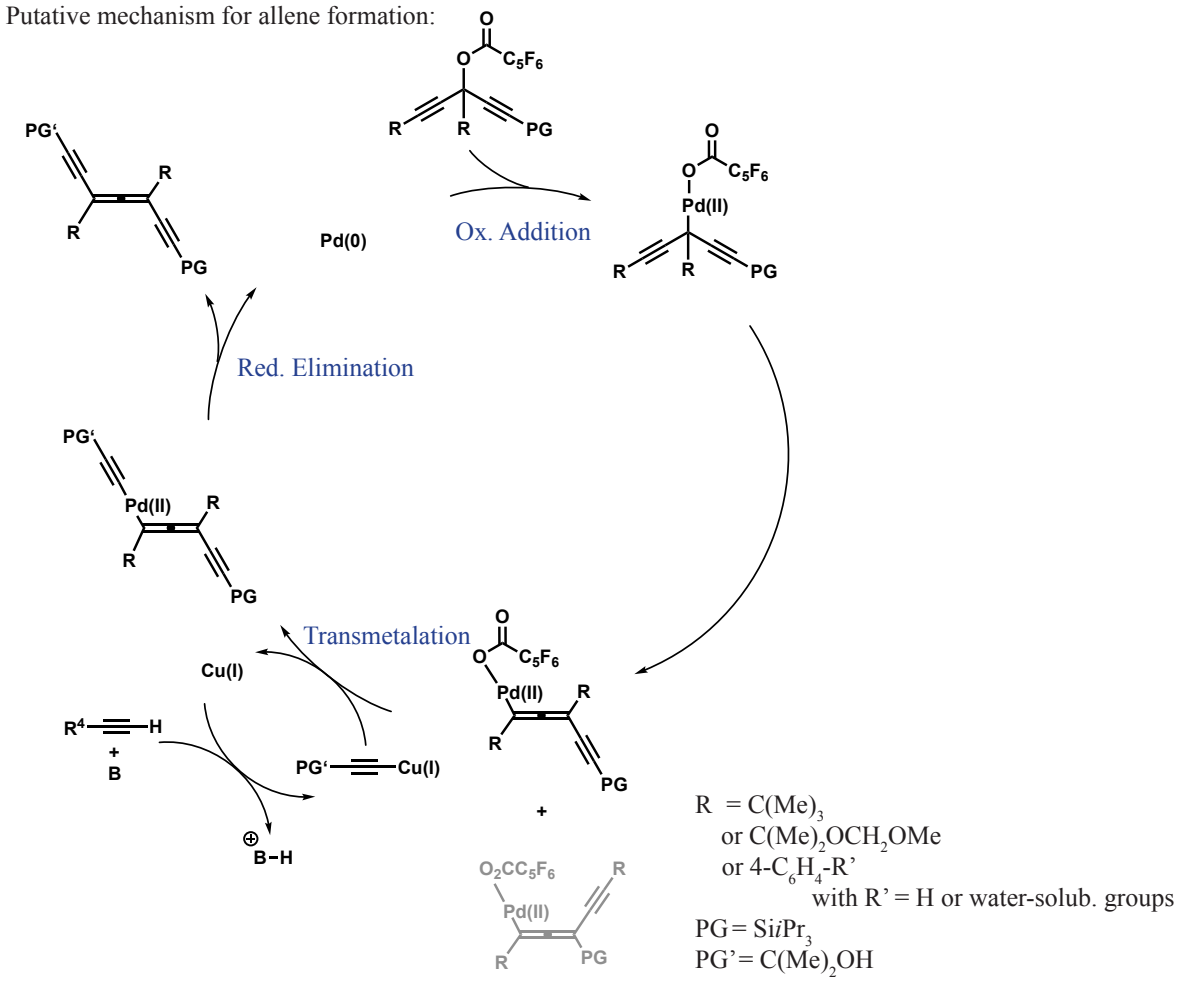

Scheme 2. Putative mechanism for the palladium(0) and copper(I) mediated allene formation, following a S_N2' type mechanism. B: Base, such as iPr$_2$NEt.

The transmetalation step is generally considered to be the rate-determining step for Sonogashira reactions.[159] The sterically demanding protecting group triisopropyl sily ether (PG) was postulated to be a potential factor determining the regioselectivity of the reaction during the allylic rearrangement (Scheme 2). Complete 1,3-regioselectivity was observed in the final allene products featuring the triisopropyl sily ether group (PG, Scheme 2, unobserved regioisomer in grey).[155]

One of the signatures of DEAs is their axial chirality along with their strong chiroptical properties in their enantiopure form.[156] Since the first report of the synthesis of the racemic 1,3-di-*tert*-butyl-1,3-diethynylallenes, stereoselective synthetic and preparative separation methods by chiral HPLC were explored.[158] The synthetic approach relied on the

preparation of optically pure bispropargylic precursors (*R*)-(+)-**19** and (*S*)-(–)-**19** (Scheme 3).[158] To this extend, the racemic bispropargylic tertiary alcohol (±)-**20** was functionalized with enantiopure (*S*,*R*)-camphanic esters, to form a mixture of diastereomers of bispropargylic camphanic esters, (*R*,*S*,*R*)- and (*S*,*S*,*R*)-**21** (Scheme 3).[158]

Stereoselective Synthesis of DEAs:

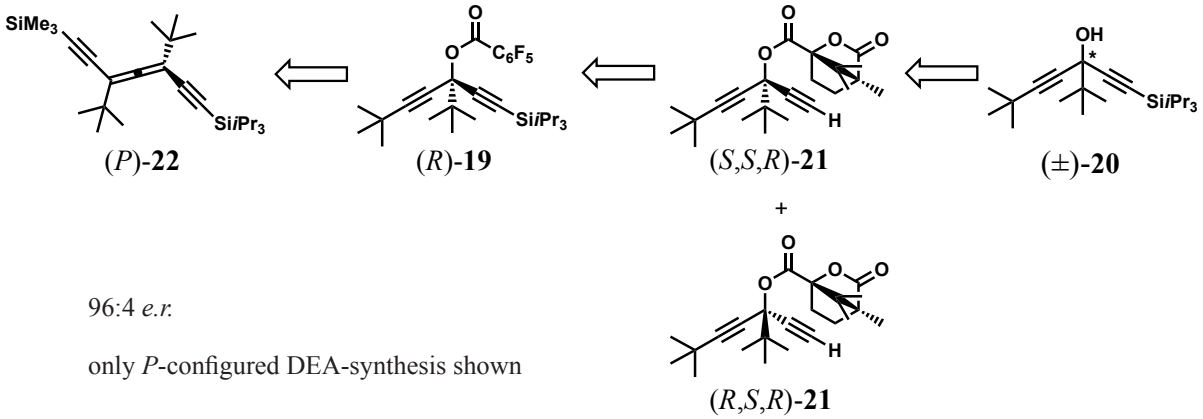

Scheme 3. Stereoselective synthesis of DEA **22** in 96:4 *e.r.* ((*P)* : (*M*)) from racemic bispropargylic alcohol **(±)-20** through functionalization with enantiopure camphanic esters and subsequent fractional crystallization to afford (*R*,*S*,*R*)- and (*S*,*S*,*R*)-**21**. Final separation of enantiomerically enriched DEAs afforded enantiopure (*P*)-and (*M*)-configured **22**.[158]

The diastereoisomers **21** were subsequently separated by fractional crystallization from CH_2Cl_2/cyclohexane (the relative configuration was confirmed by single-crystal X-ray analysis).[158] After removal of the chiral ester groups and subsequent functionalization with the pentafluorobenzoate leaving group, the enantiopure bispropargylic ester was converted into the enantiomerically enriched DEA (only (*P*)-(+)-**22** shown*; e.r*. 96:4).[158] Final resolution on a chiral preparative HPLC afforded (*P*)- and (*M*)-configured DEA **22** in its optically pure form. Later, the synthetic procedure was optimized and the chiral DEAs **22** were separated into their enantiomers by a chiral phase (CSP Diacel Chiralpak IA®) HPLC to afford both enantiomers of DEA in their optically pure form.[160] The current synthetic protocol, optimized in this Thesis for the synthesis of optically pure 1,3-di-*tert*-butyl-1,3-diethynylallenes, is described in Scheme 4.

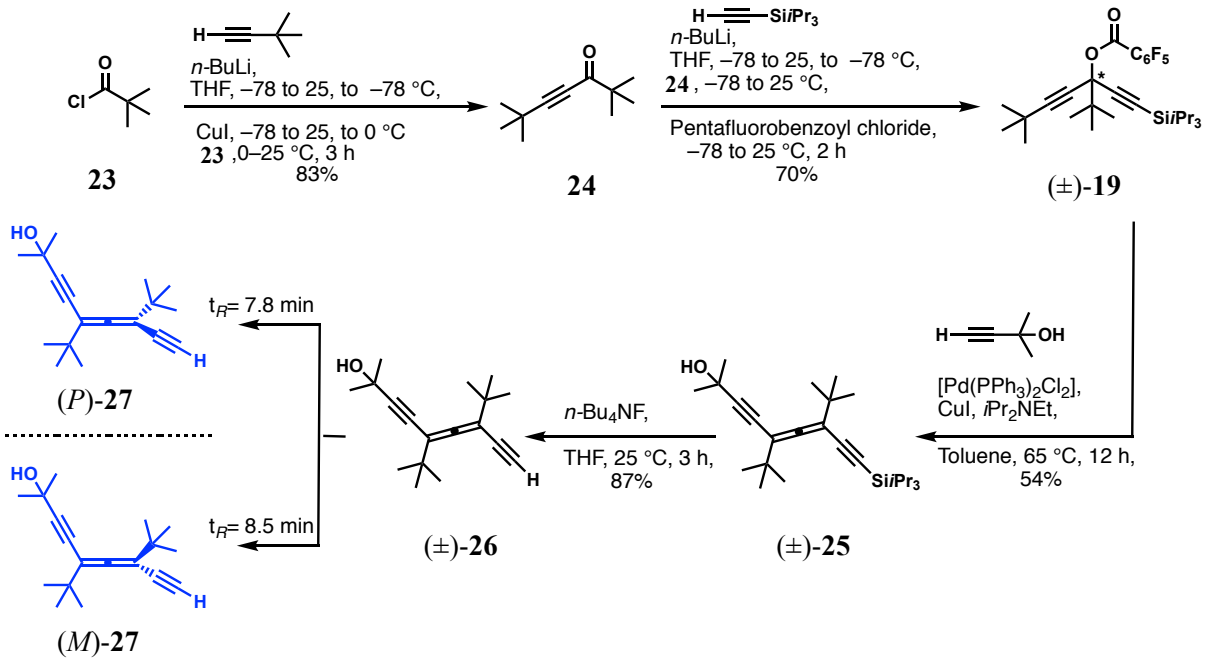

Scheme 4. Efficient Synthesis of (±)-**27** in four synthetic steps (27% overall yield), followed by the separation of (±)-**27** into the (*M*)- and (*P*)-configured enantiomers. t_R designates the retention time of the respective enantiomers by preparative HPLC with a CSP Diacel Chiralpak® IA in *n*-hexane/*i*PrOH 99.2:0.8.

The tertiary alcohol group of (±)-**27** was initially introduced as an alkyne protecting group to facilitate the enantiomeric separation on the chiral phase HPLC.[161] The efficient synthetic procedure together with the separation protocol, enabled the incorporation of DEAs into extended alleno-acetylenic structures and the study of their physical organic properties. It should be noted, that several achiral and chiral allenes with various substitution patterns have been incorporated into oligomeric and macrocyclic structures, such as allenophanes, but were obtained in most cases only as their diastereoisomeric mixtures.[157,158,162-165] Since 2008, enantiopure DEAs have been incorporated into various oligomeric and macrocyclic structures with exceptional chiroptical properties (Figure 11).

1.4.2 1,3-Diethynylallenes in Monodisperse Oligomers and Macrocycles

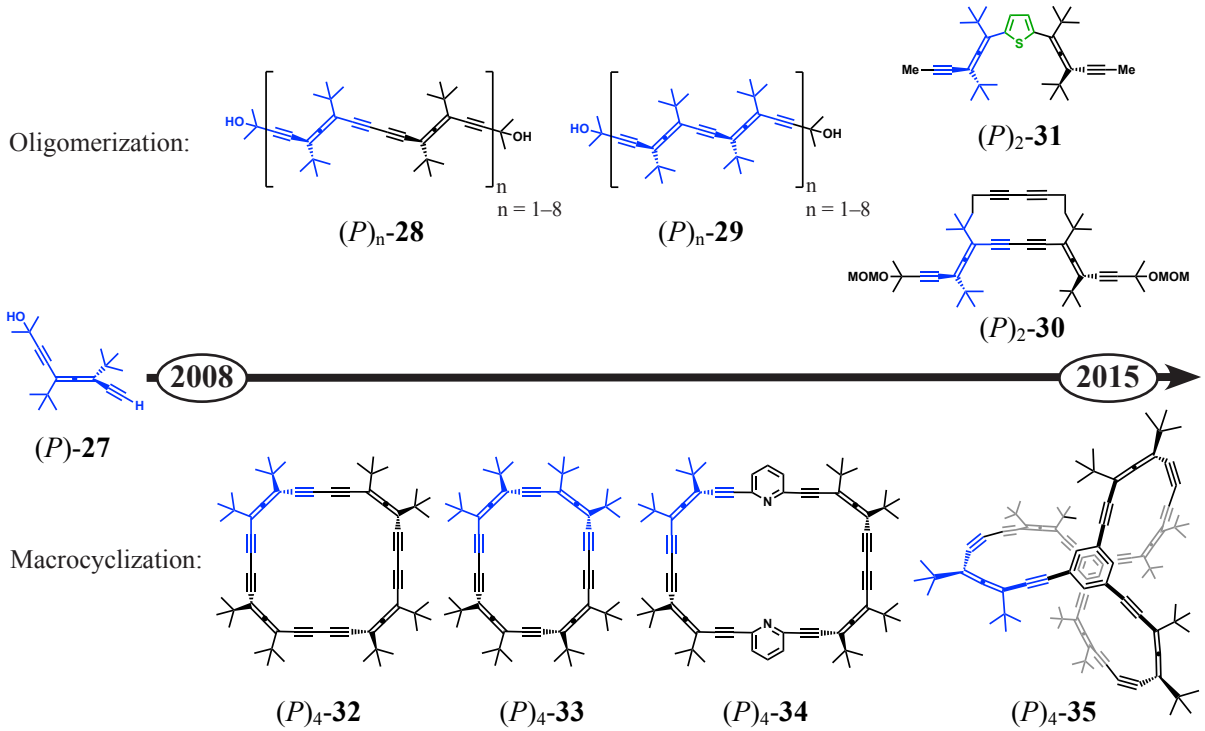

Figure 11. From the enantiomerically pure DEA building block (*P*)-**27** to optically pure dimers, oligomers, and macrocyclic structures (**28**–**35**) with strong chiroptical properties (references are included in the text).[162,168–174]

The oligomerization of (*P*)- and (*M*)-DEA **27** through oxidative homocoupling gave monodisperse, enantiopure alleno-acetylenic oligomers (*P*)$_n$- and (*M*)$_n$-**28** with n = 1–8.[166] Electronic circular dichroism (ECD) and optical rotation of the open chain oligomers showed nonlinear enhancement of the chiroptical properties with increasing length of the oligomer. The ECD traces showed strong increase in the intensities of (*P*)$_n$- and (*M*)$_n$-**28** from $\Delta\varepsilon = \pm 9$ M^{-1} cm^{-1} at $\lambda = 225$ nm for the monomeric DEA to $\Delta\varepsilon = \pm 825$ M^{-1} cm^{-1} at $\lambda = 225$ nm for the octamer (n = 4, Figure 12).[166] The hexadecamers (*P*)$_8$- and (*M*)$_8$-**28** were reported to display longest wavelength Cotton effects, defined as a maximum or minimum in the ECD traces, which were among the strongest ever reported ($\Delta\varepsilon = \pm 1360$ M^{-1} cm^{-1} at $\lambda = 266$ nm, Figure 12, B).[166] This corresponds to an increase in the intensities of the Cotton effects at the respective wavelength by an approximate factor of 150.

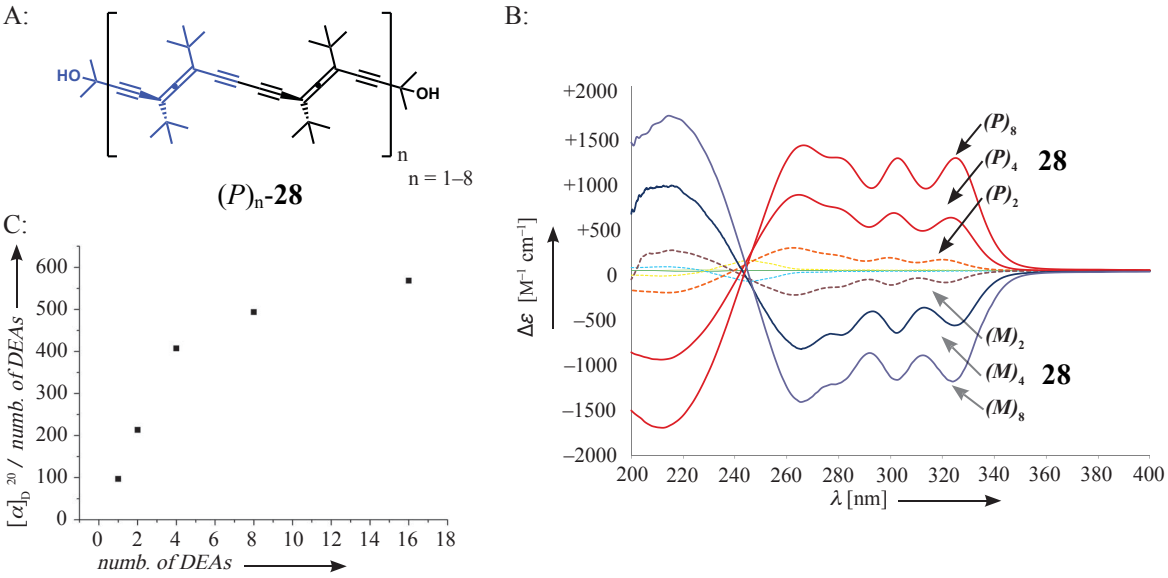

Figure 12. Enantiopure (*P*)- and (*M*)-configured alleno-acetylenic oligomers **28**. A: only $(P)_n$-configured oligomer **28** depicted. B: ECD traces of (*P*)- and (*M*)-configured alleno-acetylenic oligomers **28**; measurements were done in *n*-hexane at 293 K. C: optical rotation $[\alpha]_D^{20}$ normalized by the number of DEA units in the oligomer **28** as a function of the oligomeric length.[166]

This amplification suggested a conformational preference of the alleno-acetylenic oligomeric structures $(P)_n/(M)_n$-**28**. Initial calculations[166] and an X-ray crystal structure[167] substantiated the preference of alleno-acetylenic oligomers to adopt a secondary helical structure. While alleno-acetylenic oligomer $(P)_n/(M)_n$-**28** initially showed a nonlinear increase in their chiroptical properties with the addition of chiral chromophoric units, the chiroptical properties saturated with increasing oligomeric length (Figure 12, C).[166] In an effort to further study the contribution of the conformational rigidity to the amplified Cotton effects, stapling of the oligomers through ring closing metathesis was reported ($(P)_n/(M)_n$-**30**).[168] An alternative approach investigated the modification of the alleno-acetylenic backbone through postfunctionalization of the 1,3-diyne linker into heteroaryls, such as thiophenes ($(P)_n/(M)_n$-**31**).[169] This modification resulted in a substantial loss in the chiroptical properties of the DEAs, suggesting that the 1,3-dyine linker is critical for strong Cotton effects. The introduction of an alternating acetylene (–C≡C–)-diacetylene (–C≡C–C≡C–) motif, replacing the all-buta-1,3-diynediyl linkers, resulted in an increase in the chiroptical properties (Figure 11, $(P)_n/(M)_n$-**29**).[167] This confirmed the initial hypothesis that the amplified chiroptical properties of alleno-acetylenic oligomers are a result of their preferential helical secondary structure and that the chiroptical properties can be further enhanced through rigidification of the alleno-acetylenic backbone by stabilizing the helical secondary structure, which was seen in a X-ray co-crystal structure.[167]

The study on the alleno-acetylenic oligomers demonstrated that, despite the generally strong chiroptical properties, the inherent flexibility of larger oligomers is counterproductive to achieve materials with amplified chiroptical properties.[166,167]

Alleno-acetylenic macrocycles allowed to follow up on these findings through in-depth studies of the interplay between symmetry and conformational rigidity towards their exceptionally strong chiroptical properties.[170] Generally, the macrocyclic analogs of the acyclic alleno-acetylenic oligomers showed amplified chiroptical properties, presumably due to the enhanced rigidity (Figure 13).[167,170]

Backbone Rigidification:

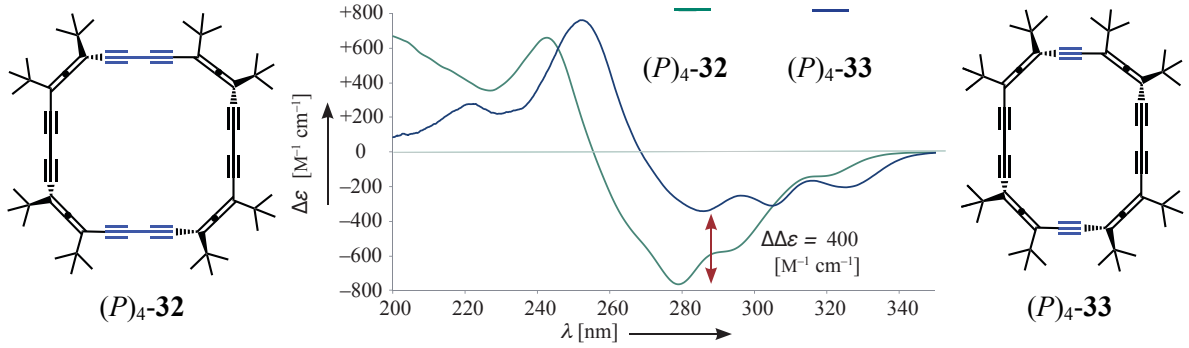

Figure 13. Comparision of the chiroptical properties (ECD traces) of shape persistent macrocycle $(P)_4$-**32** with $(P)_4$-**33**. Rigidification of the backbone by replacing the all-buta-1,3-dyinediyl linkers in $(P)_4$-**32** with alternating acetylene (–C≡C–)-diacetylene (–C≡C–C≡C–) linkers in $(P)_4$-**33** augmented the higher wavelength Cotton effects by $\Delta\Delta\varepsilon = 400$ M^{-1} cm^{-1}; measured in *n*-hexane at 293 K.[167,170]

Additional rigidification of the backbone of the macrocycles replacing the all-buta-1,3-diynediyl linkers of $(P)_4/(M)_4$-**32** with alternating actetylene (–C≡C–) and diacetylene (–C≡C–C≡C–) linkers in $(P)_4/(M)_4$-**33** further increased the higher wavelength Cotton effects by $\Delta\Delta\varepsilon = 400$ M^{-1} cm^{-1} (Figure 13).[167,170]

In a series of alleno-acetylenic macrocycles with variable number of monomeric DEA units, it was demonstrated that the increasing number of chiral chromophores only showed amplified chiroptical properties when the overall macrocyclic structure was shape-persistent.[160] In the series of cyclooligomers containing three, four, and five alleno-acetylenic units, the Cotton effects increased at the respective wavelength from three to four chiral chromophoric units, but decreased from four to five units (Figure 14, see reference for ECD traces).[160] The X-ray crystal structures of this series illustrated the increasing flexibility of the macrocycles with increasing size.[160] Additionally, it was shown that the symmetry of the molecular structures contributes substantially towards the magnitude of their Cotton effects. Generally, D_n symmetric macrocycles were found to optimize the angle between the electronic

transition and magnetic transition dipolar moments, enhancing the strength of the chiroptical properties.[160] While structures $(P)_3/(M)_3$-**36** and $(P)_4/(M)_4$-**32** show D_n symmetry with strong chiroptical properties, the macrocyclic structure $(P)_5/(M)_5$-**37** is not in D_n-, but rather C_2-symmetric, and weaker chiroptical properties are observed. Noteworthy is the change in the sign of the optical rotation (from – → +) with increasing size of the macrocycle from (*P*,*P*,*P*)-(–)-**36** and (*P*,*P*,*P*,*P*)-(–)-**32** to (*P*,*P*,*P*,*P*,*P*)-(+)-**37** (Figure 13).[160]

It was noted that the sensitivity of the optical properties towards conformational changes could be exploited through incorporation of these devices into molecular switches.[160]

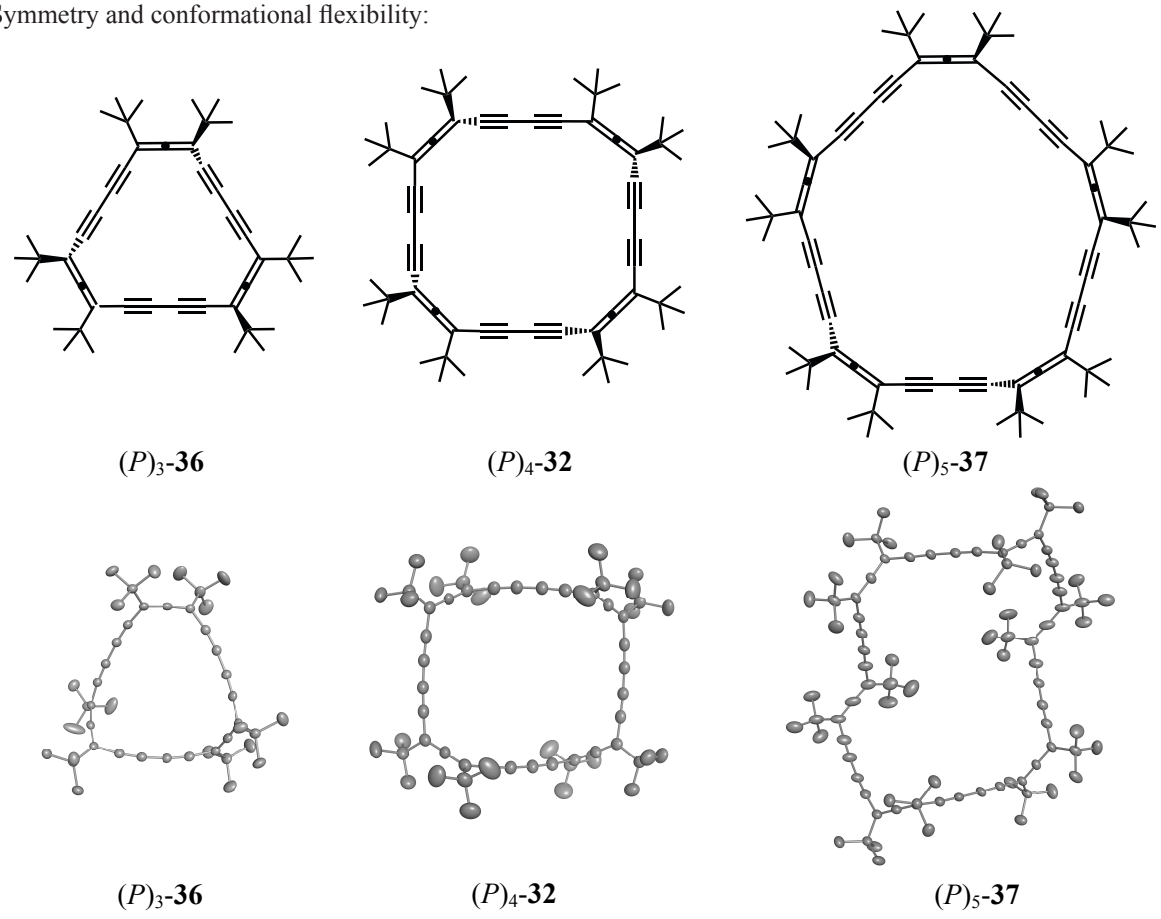

Figure 14. Alleno-acetylenic cyclooligomers containing three $(P)_3$-**36**, four $(P)_4$-**32**, and five $(P)_5$-**37** alleno-acetylenic units. (*P*)-Configured Lewis structures are shown on top and (*M*)-configured X-ray crystal structures are shown below. Note the change in the sign of the optical rotation with increasing size if the cyclooligomers. X-ray crystal structures are shown in ellipsoid representation at 50**%** probability level for structures $(P)_3$-**36** and $(P)_4$-**32**, and 40% probability level for $(P)_5$-**37**.[160]

In 2014, an example was reported, where two pyridine moieties were incorporated into the backbone of an enantiopure alleno-acetylenic macrocycle to complex an iodinated small molecule.[171] The macrocycle $(P)_4/(M)_4$-**34** formed a 1:1 complex with octafluoro-1,4-diiodobutane (Figure 15).[171] The formation of the complex, together with the association

constant, were recorded by NMR spectroscopy (K_a = 4.2 M^{-1} in C_6D_6 at 293 K). The X-ray crystal structures shows close contacts between the nitrogen of the pyridine group and the iodine at heavy atom distances of 3.0 Å, indicating favorable halogen-bonding interactions (Figure 15).[171]

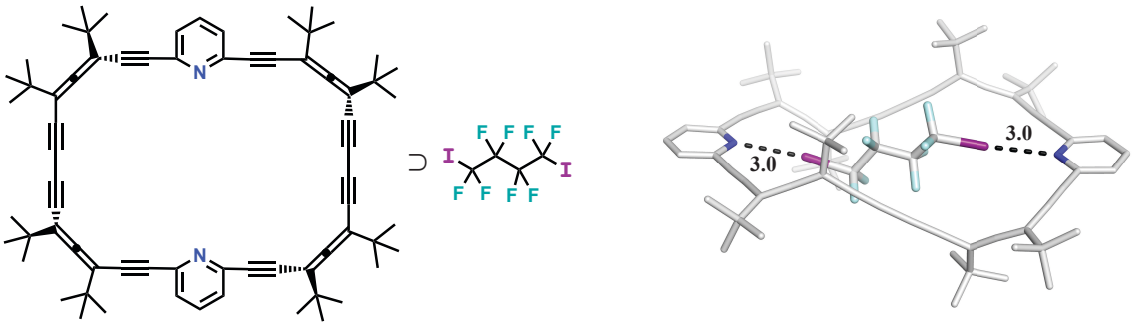

$(P)_4$-**34** $(M)_4$-**34**

Figure 15. Halogen-bonding interactions in a pyridine functionalized enantiopure alleno-acetylenic macrocycle $(P)_4$/$(M)_4$-**34**; (*P*)-configured structure depicted on the left. The stick representation of the X-ray co-crystal structure indicates a 1:1 complex of the (*M*)-configured macrocycle with octafluoro-1,4-diiodobutane (right).[171]

This represents one of the first examples, where the shape persistency in alleno-acetylenic macrocylces was exploited for the complexation of small molecules.[171] Later, the two-dimensional macrocycles were expanded to a three dimensional one, where two tripodal alleno-acetylenic scaffolds were oxidatively coupled to form the three-dimensional $(P)_6$- and $(M)_6$-configured **35** with 55% yield in the final step (Figure 16).[172]

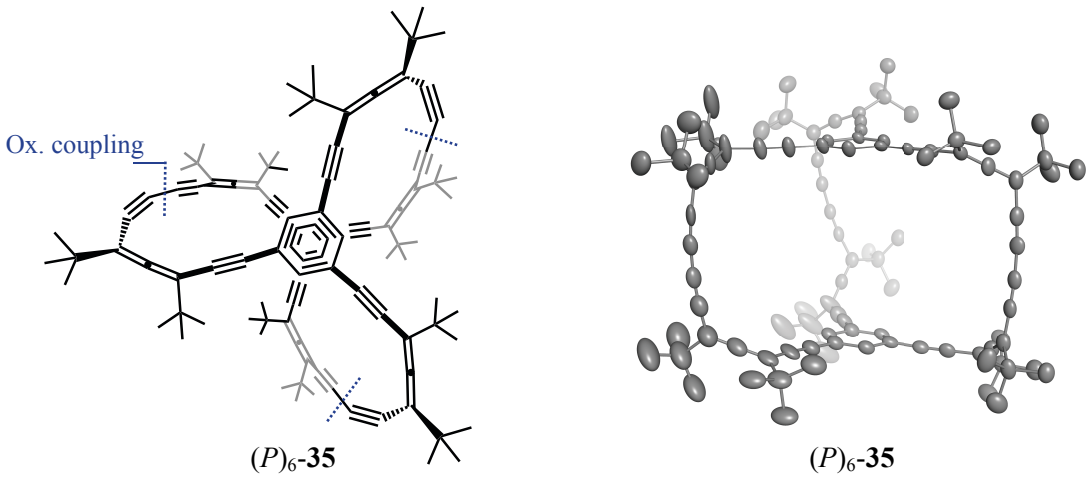

$(P)_6$-**35** $(P)_6$-**35**

Figure 16. Enantiopure alleno-acetylenic tricycle $(P)_6$-**35** containing six alleno-acetylenic moieties. Blue lines indicate points of disconnection for the oxidative coupling. X-ray crystal structure of $(M)_6$-**35** is shown on the right in ellipsoid representation at 30% probability level.[172]

The enantiopure tricyclic structure $(P)_6$-**35** showed weak affinity towards ferrocenium hexafluorophosphate ($K_a = 22\ M^{-1}$ in acetone-d_6 at 293 K).[172] Complexation was presumably driven through cation-π interactions of the positively charged cyclopentadienyl group of the ferrocenium guest with the aromatic moiety of the host. The inherent porosity of this system explained the low affinity of even highly charged guests towards the tricycle.[172]

In both the macrocyclic system $(P)_4/(M)_4$-**34**, complexing the diiodinated derivative, and the tricyclice $(P)_6/(M)_6$-**35**, alleno-acetylenes were employed as shape-persistent scaffolds with a ~90° dihedral angle. Their axial chirality along with their chiroptical properties, however, remained unexploited.[171,172]

1.4.3 From Oligomers and Macrocycles to Supramolecular Chemistry

The two previous sections illustrated the development of 1,3-diethynylallenes as axially chiral building blocks, followed by the study of the underlying physical organic properties of DEAs in oligomeric and macrocyclic structures. It is important to mention that the lessons learned from the initial physical organic studies on alleno-acetylenic oligomers and macrocycles, especially the contribution of rigidity and symmetry towards the chiroptical properties, have been crucial for the transition towards exploiting the unique chiroptical properties of DEAs in supramolecular assemblies and host-guest chemistry. The last two examples of the previous section illustrate this development.[171,172] Since 2013, alleno-acetylenic architectures include noncovalent assemblies and metal-mediated assemblies (Figure 16).

Lateral functionalization of the enantiopure DEA scaffold with aromatic groups, such as phenyl, biphenyl and naphthyl groups ((*P*)/(*M*)-**42**) afforded molecules that were effective chiral inducers of a cholesteric liquid crystalline phase.[173] The highest cholesteric induction was observed with the biphenyl substituent and showed comparable induction strength compared to conventional cholesteric inducers, such as axially chiral 1,1'-binaphthyl derivatives.[173] Importantly, this report established the synthetic methods for terminally functionalized DEAs with aromatic substituents under Sonogashira cross-coupling conditions and with triazoles derivatives *via* Cu(I)-mediated cycloaddition of azides to the terminal alkine of the DEAs.[173]

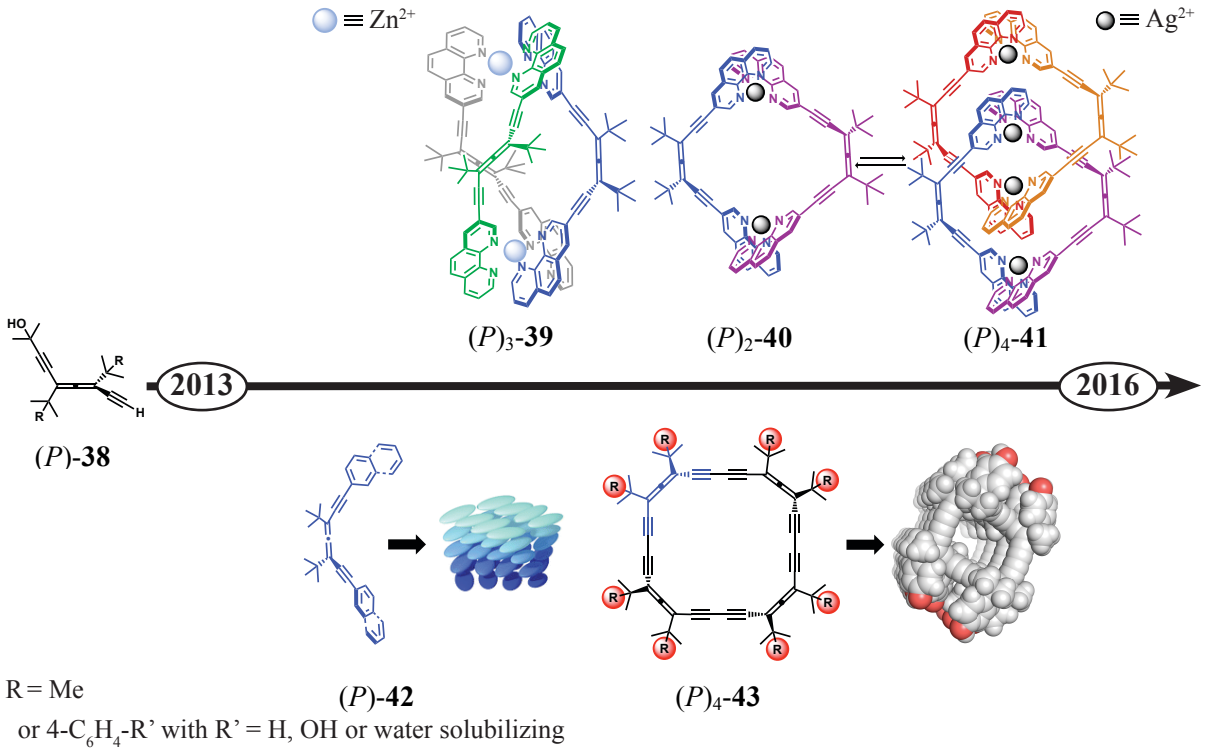

Figure 17. More recently, DEAs were incorporated into metal-mediated assemblies (top) and assemblies driven by noncovalent interactions (bottom). Selected examples are shown and are discussed in the following section (references are included in the text).[173–178]

During the same time, alleno-acetylenic macrocycles were peripherally functionalized with aromatic groups, such as phenols, and water-solubilizing groups.[174,175] The goal was to introduce functionalities on the periphery of the enantiopure shape-persistent macrocycles that would induce self-assembly into ordered super-structures in organic and aqueous solvent systems. It was generally observed that the strength of the Cotton effects decreased upon peripheral functionalization of the macrocycles compared to their all *tert*-butyl analogues, presumably due the increased conformational flexibility of the introduced functionalities and "dilution" of chirality.[174,175] Nevertheless, the intensities of the Cotton effects remained pronounced. Enantiopure macrocycles with two phenol groups per DEA unit ((*P*)$_4$/(*M*)$_4$-**43**) form a two-dimensional lateral network through intermolecular H-bonding between the phenolic groups.[174] Additionally, the two-dimensional extended structures stacked into three-dimensional perfectly eclipsed columnar structures. The three-dimensional crystalline architecture shows porous voids of approximate dimensions of 5.2 Å x 7.1 Å (xy-axis, Figure 18).[174]

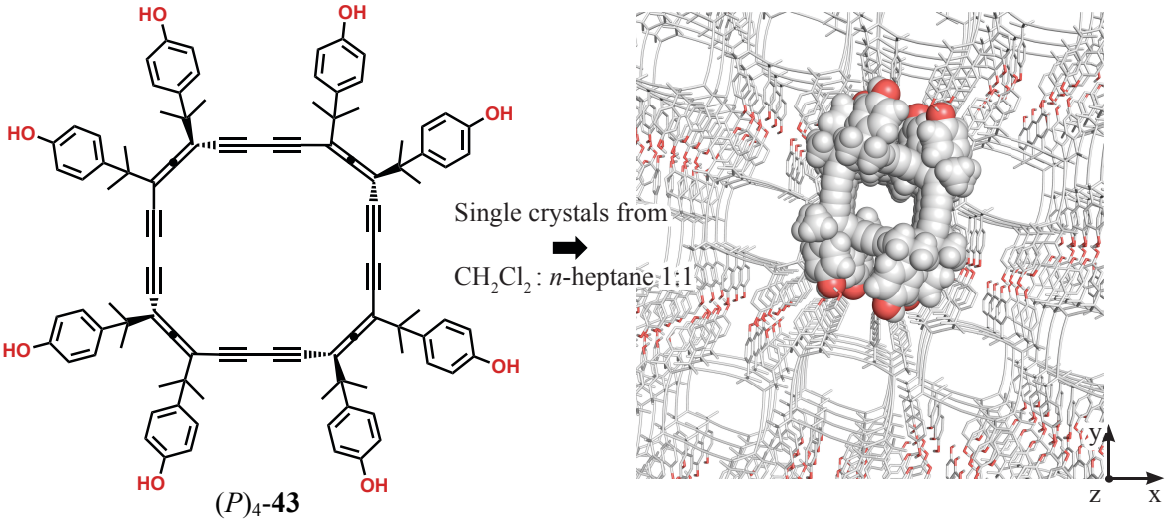

Figure 18. Phenol-substituted enantiopure alleno-acetylenic macrocycles $(P)_4/(M)_4$-**43** form homochiral pores in the single crystal solid state structure through eclipsed stacking of the macrocycles (only (*P*)-configured macrocycle shown). Lateral intermolecular H-bonding establishes additional two-dimensional networks in the xy-plane. *n*-Heptane molecules filling the voids are omitted for clarity.[174]

These voids extend to form homochiral pores along the z-axis. As the single crystals were formed from an CH_2Cl_2-*n*-heptane (1:1), one *n*-heptane per macrocycle molecule fills the void. These are omitted for clarity in Figure 18.[174]

Further functionalization of the phenol-substituted alleno-acetylenic macrocycles with water-solubilizing groups afforded enantiopure $(P)_4$-**44** and $(M)_4$-**44**, which formed homochiral vesicles and tubular fibres built from macrocyclic stacks in aqueous solution that interacted through hydrophobic interactions (deduced from cryo-TEM images Figure 19).[175]

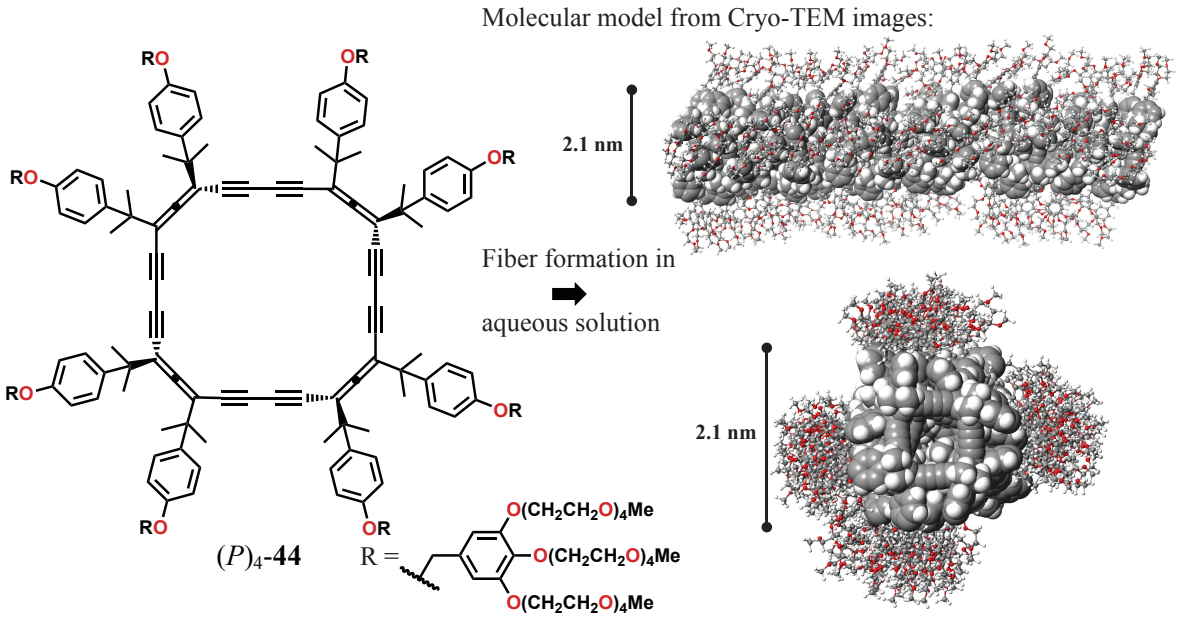

Figure 19. Water-soluble alleno-acetylenic macrocycles $(P)_4$- and $(M)_4$-**44** form tubular fibres in water built from macrocyclic stacks that interact through hydrophobic interactions (molecular models from cryo-TEM images).[175]

In 2014, DEAs were terminally functionalized with phenanthrolines to afford enantiopure alleno-acetylenic ligands (*P*)- and (*M*)-**45**.[176] Upon addition of Zn(II) salts these ligands formed diastereoselectively triple-stranded helicates $(P)_3/(M)_3$-**39** (Figure 20).[176] The racemic mixture of the phenanthroline-based ligands self-sorted to form exclusively the respective homochiral $(P)_3$- and $(M)_3$-configured assembly **39**. The lean, all-carbon backbone of the triple-stranded helicates formed a cavity, which demonstrated to be suitable for guest inclusion (see X-ray co-crystal structure of $(M)_3$-**39** with 1,4-dioxane, Figure 20).[176] Small heterocycles, such as 1,4-dioxanes, coordinatively aligned in the cavity of the helicates, with binding constants in aqueous solution of up to 1800 M^{-1} (from ^1H NMR studies in D_2O/CD_3OD 1:1 at 298 K).[176] The Zn(II) hexacoordinate assembly is quite flexible and the angles adjust to the guest, which is reflected by the guest specific changes of the exciton chirality coupling band at the longest ECD wavelength ($\Delta\Delta\varepsilon = -75$ M^{-1} cm^{-1} at 365 nm upon addition of 1% (*v*/*v*) of dioxane in methanol). Upon coordinative alignment of 1,4-dioxane, with both oxygens pointing towards the zinc(II)-centers (heavy atom distances of 5.3 Å), the overall assembly is stabilized, leading to strong amplification of the Cotton effects. [176]

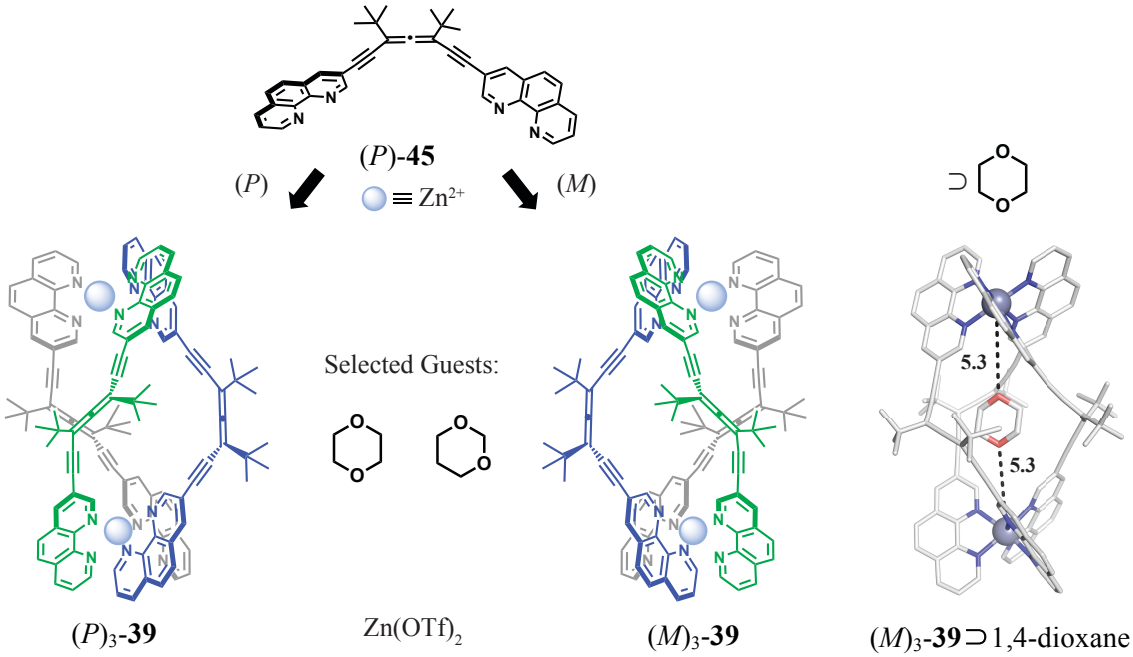

Figure 20. Phenanthroline functionalized alleno-acetylenic ligands (*P*)/(*M*)-**45** formed diastereoselectively triple-stranded (*P*)$_3$- and (*M*)$_3$-configured helicates **39** upon addition of $Zn(OTf)_2$ (3:2 ratio of salt:ligand) in acetonitrile. X-ray co-crystal structure of the 1:1 complex of (*M*)$_3$-**39**⊃1,4-dioxane; heavy atom distances are given in Å; counter anions are omitted for clarity: ($[(ClO_4)_4]^{2-}$).[176]

The guest induced ECD signals led to the detection of non-chromophoric small molecules at the part-per-million (ppm) regime in aqueous solution and to the differentiation of two different structural isomers through ECD (1,4-dioxane over 1,3-dioxane).[176]

This example illustrates how the extremely sensitive nature of the chiroptical properties towards induced structural changes can be exploited to quantify guest binding.[176] Later, this system was expanded to contain two binding sites formed by trinuclear triple-stranded helicates.[177] Binding studies confirmed the ability of the internal binding sites to coordinatively align 1,4-dioxane molecules, accompanied by strong amplification of the ECD signals upon guest complexation. No positive allosteric effects were observed between the two binding sites of the helicate.[177] In both systems, enantioselective complexation was not effective, due to lack of preorganization and insufficient confinement of the chiral cavities.[176,177]

Addition of silver(I) salts in CH_2Cl_2 or $C_2H_2Cl_4$ to homochiral ligands containing alternating alleno-acetylenes and either two ((*P*)/(*M*)-**45**) or three phenanthroline moieties ((*P*)$_2$/(*M*)$_2$-**46**) led to the respective diastereoselective assembly of dinuclear ((*P*)$_2$/(*M*)$_2$-**40**) and trinuclear ((*P*)$_4$/(*M*)$_4$-**47**) double stranded helicates (Figure 21).[178]

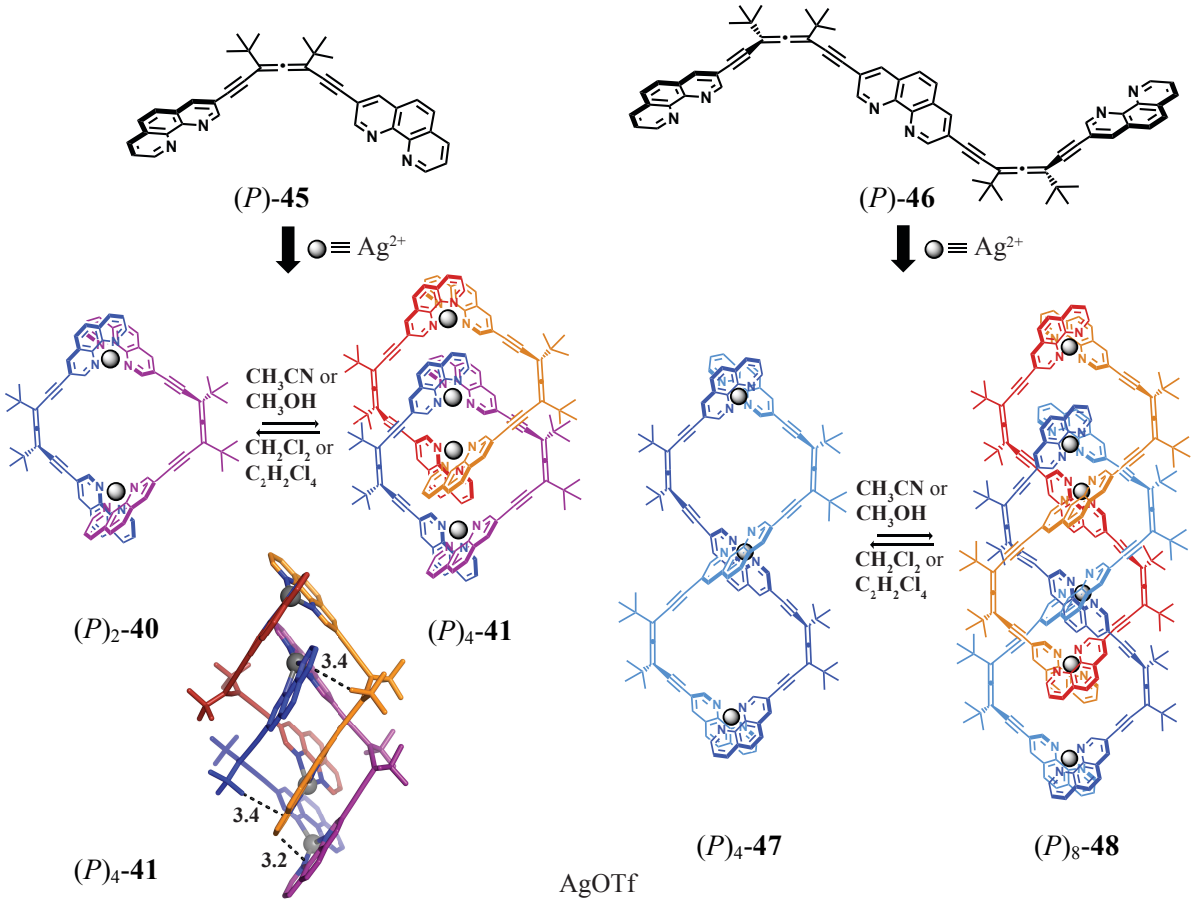

Figure 21. Homochiral ligands containing alternating alleno-acetylenes and either two ((*P*)/(*M*)-**45**) or three (*P*)/(*M*)-**46**) phenanthroline groups form dinuclear ((*P*)$_2$/(*M*)$_2$-**40**) and trinuclear ((*P*)$_4$/(*M*)$_4$-**47**) double stranded helicates upon addition of AgOTf in in CH_2Cl_2 or $C_2H_2Cl_4$. In more polar solvents, such as MeCN or MeOH, the di-and trinuclear double stranded helicates assembled to [2]catenanes ((*P*)$_4$/(*M*)$_4$-**41**) and bis[2]catenanes ((*P*)$_8$/(*M*)$_8$-**48**). Only (*P*)-configured structures shown; counter ions $[OTf]^-$ omitted for clarity. Below: single crystal X-ray structure of (*P*)$_2$-**41** with distances given in Å.[178]

Upon increasing of the solvent polarity to MeCN or MeOH the di-and trinuclear double stranded helicates formed [2]catenanes ((*P*)$_4$/(*M*)$_4$-**41)** and bis[2]catenanes ((*P*)$_8$/(*M*)$_8$-**48**). Remarkably, when the same experiment was done with the racemic mixtures of both short ((*P*)$_2$/(*M*)$_2$-**45)** and long ((*P*)$_4$/(*M*)$_4$-**46**) alleno-acetylenic ligands, complete enantioselective and stereoselective self-sorting towards the double stranded helicates ((*P*)$_2$/(*M*)$_2$-**40** and (*P*)$_4$/(*M*)$_4$-**47**) or the respective catenanes ((*P*)$_4$/(*M*)$_4$-**41** and ((*P*)$_8$/(*M*)$_8$-**48**) was observed.[178] For the bis[2]catenanes ((*P*)$_8$/(*M*)$_8$-**48** the assembly involves 14 chiral elements (6 for the Ag(I) metal centers and 8 for the axially chiral alleno-acetylenes). The ECD traces of both the shorter and longer ligands showed significant amplification of the strength of the Cotton effects upon transition from the single ligands to the helicates and the catenanes.[178] This trend indicated

increasing stabilization of the helical secondary structure. The X-ray diffraction of the single crystal of the $(P)_4$-configured [2]catenane **41** shows a perfect fit of the interlocked strands, demonstrating favorable intermolecular parallel-displaced π···π-interactions (heavy atom distances of 3.2 Å) and CH_3···π-interactions of the *tert*-butyl groups with the phenthroline (heavy atom distances of 3.4 Å), substantiating the significant increase in ECD signal intensities upon catenation (Figure 21, structure obtained from single crystal X-ray diffraction).[178]

In this recent development towards supramolecular chemistry, alleno-acetylenes have demonstrated to be useful, shape-persistent building blocks for the construction of macrocycles that form to columnar stacks and for metal-mediated assembly to helicates and catenanes. The lean all-carbon backbone of alleno-acetylenes introduced pores and cavities into the assemblies, capable of binding small molecules. Additionally, their strong chiroptical properties with the sensitivity towards guest-induced conformational changes in their enantiopure form enabled to monitor structural changes and guest complexation optically.

In this regard, it became apparent that alleno-acetylenes could be useful building blocks for enantiopure receptors in order to study enantioselective complexation of small molecules. While there are several motifs apart from stereogenic centers that introduce chirality into a receptor, such as spirocyclic systems and appropriately substituted biaryls, few are sterically less demanding than the lean all-carbon alleno-acetylenic backbone.[156] For strong molecular recognition abilities of a potential receptor system containing alleno-acetylenes, the subtle balance between flexibility that confers adaptability and guest uptake, and preorganization that confers selectivity, would have to be taken into account (see Section 1.3). The rational design of a receptor for the selective complexation of small molecules had to include information of the complexation process to be transduced in form of a quantifiable signal. Taking the dynamic nature of host-guest complexes into account, the investigation of the complexion process can be challenging and requires precise techniques.

1.5 Monitoring Host-Guest Recognition Processes.

Molecular recognition events refer to the interactions between a guest molecule and a receptor. Over the last decades, various methods have been established to determine the kinetic and thermodynamic quantities of host-guest complexation.[179] A general way of evaluating the formation and strength of a host-guest complex in a quantitative fashion is through determination of the association constant (K_a) of the guest with the host.[180] The definition of

the thermodynamic quantities of a host-guest complex, such as K_a, is based on a binding equilibrium model:

$$a\cdot[H] + b\cdot[G] \rightleftarrows [HG] \tag{1.5.1}$$

where are a and b are defined as the stoichiometric factors and [H], [G], and [HG] as the concentration of the host, guest, and host-guest complex in the equilibrium model.[180]
The association constant K_a can be determined from this equilibrium as follows:

$$K_a = \frac{[HG]}{[H]^a\cdot[G]^b} \tag{1.5.2}$$

where the total concentration of the respective host and guest is defined as:

$$[H]_0 = [H] + a\cdot[HG] \text{ and } [G]_0 = [G] + b\cdot[HG] \tag{1.5.3}$$

From the equations (1.5.1) and (1.5.2), the following equation can be deduced:

$$K_a = \frac{[HG]}{([H]_0 - a[HG]^a)\cdot([G]_0 - b[HG]^b)} \tag{1.5.4}$$

The free enthalpy (or Gibbs free energy) of complexation, ΔG, is derived from K_a:

$$\Delta G = -RT\cdot\ln K_a = \Delta H - T\cdot\Delta S \tag{1.5.5}$$

where R is the gas constant and T the temperature.[180]
In order to determine the binding constant and the free enthalpy of complexation, the binding stoichiometry, namely a and b, has to be determined together with the unknown quantity [HG]. In this Thesis, we will only consider a 1:1 binding stoichiometry of host and guest, with $a = b = 1$, and its determination will be discussed in detail where needed. Generally, the continuous variation method (Job's Plot) was used at fast exchange on the NMR timescale and integration of the respective host and guest peaks gave the respective stoichiometry at slow exchange in solution. [181-183] Additionally, determination of the X-ray co-crystal structure indicated the stoichiometry of the host-guest complex in the solid state.

The remaining unknown quantity, namely the concentration of the host-guest complex [HG], is proportional to measurable changes in spectroscopic properties.[180] When

monitoring the changes in spectroscopic properties, the kinetics of the complexation and decomplexation processes can be either fast or slow on the measured spectroscopic time scale. At slow exchange, separate diagnostic signals are observed and at fast exchange the signals of the free and bound states are averaged. The structural features of the host system, in our context the chiral receptor, together with the magnitude of K_a and the physical properties dictate the spectroscopic techniques to analyze the host-guest complex. In the following, only techniques which were relevant in this context are briefly discussed.

Nuclear magnetic resonance (NMR) spectroscopy is one of the most used methods to determine the thermodynamic quantities of host-guest complexes.[180] It allows to deduce some structural information of the host-guest complex during the determination of the association constant. Host concentrations are normally in the region of ~1–10 mM with a guest-to-host ratio of ~1–100.[180] Generally, association constants in the region of ~1–10 000 can be reliably determined. The slow or fast complexation and exchange process on the NMR timescale are determined by a number of factors, such as the magnetic field (usually 500 or 600 MHz in this Thesis), the magnitude of the binding constant, and the change in the chemical shifts of the respective signals. At fast exchange on the NMR timescale, signals of the free and bound states are averaged. Through variation of the [HG] concentration (see equation 1.5.4) and monitoring of isolated signals, the association constant can be determined by non-linear least square curve fitting of the signal changes (see Experimental Part for details).[180]

Slow exchange process on the NMR time scale results in the observation of separated diagnostic signals for the free and the complexed species. The association constant can be determined through integration of the respective signals.

In case of an enantiopure host, the complexation of a chiral guest at slow exchange leads to the formation of diastereoisomeric signals between the host and the two enantiomers of the guest. Integration of these signals (if separated) allows to evaluate the enantioselectivity of the host towards the specific guest.

Fourier-transform infrared spectroscopy and *Fourier-transform raman spectroscopy* can generally be employed to determine association constants, by monitoring changes in signal intensities. In this Thesis both spectroscopic techniques were used to determine conformational states of the receptor and host-guest contacts. In general, IR and Raman spectroscopic studies are done at ~0.1–10 mM [HG] concentration.

Electronic circular dichroism (ECD or CD) spectroscopy is a chiral variant of the absorption spectroscopy in the ultraviolet-visible (UV-Vis) region.[184] The differentiation of

circularly polarized light is an inherent property of enantiopure materials, and ECD measures the differences between the absorption of left and right handed circularly polarized light. The individual ECD traces are characterized by the position (λ in nm) and the intensity of their maxima ($\Delta\varepsilon$ in M^{-1} cm^{-1}).[184] The differential nature of ECD spectroscopy results in the possibility that bands can have negative or positive signs depending on the absolute configuration and conformation of the studied molecule.[184] This makes ECD a powerful technique to elucidate configurations and conformation of chiral molecules.[185,186] Because of its sensitive nature towards conformational changes, ECD spectroscopy has more recently been used for determining association constants of host-guest complexes.[187] A prerequisite is the strong absorption of the host towards polarized light, characteristic for alleno-acetylenic structures. For strong chiral chromophores, ECD traces are measured at very low concentrations between 0.01–0.001 mM. In principle, this allows to assess association of the host and the guest at very high dilution, such as in the parts-per-million (ppm) or parts-per-billion (ppb) regime. Association constants in the region of ~1–10^7 can be reliably determined.

Isothermal titration calorimetry (ITC) measures the heat that evolves or is consumed in the process of the host-guest complexation event.[188] Alike to ECD spectroscopy, calorimetry reports on the ensemble averaged over time. This allows to characterize the thermodynamics of the studied system. The heat evolution in an ITC experiment is measured at constant atmospheric pressure and at constant, normally slightly above ambient, temperature.[188] The measured heat thus represents a change in enthalpy, ΔH. From a single calorimetric titration experiment, the thermodynamic parameters ΔH, ΔG, and ΔS are accessible (equation 1.5.5).[188] This is a major advantage compared to spectroscopic techniques, where entropy has to be elaborately determined through van't Hoff analysis.[189] In general, measurements are done at $[H]_0$ concentrations of ~0.1–1 mM. Association constants in the region of ~$5 \cdot 10^4$ – 10^6 were reliably determined.

These tools are just a selection of multiple techniques to quantify host-guest interactions, but allowed to accurately quantify the thermodynamics of the investigated host-guest interactions for this Thesis. Additionally, structural insight of the host-guest complexes was obtained by single crystal X-ray diffraction.[190] Theoretical chemistry provided efficient and accurate methods for the structural and physiochemical characterization of host-guest complexes and complemented insight obtained from experimental techniques.[191] This multi-dimensional approach towards the study of supramolecular systems was essential to fully understand the interactions in detail.

1.6 Project Goal and Outline

We dedicated this Thesis to improve the understanding of molecular recognition processes of neutral achiral and chiral small molecules with enantiopure receptors.

First, we sought to address the open question, if enantioselective complexation can occur in the absence of strong directional interactions. To this extent we developed enantiopure cage receptors with confined hydrophobic cavities. The first chapter guides through the design and synthesis of different alleno-acetylene derived systems, eventually leading to the discovery of an enantiopure alleno-acetylenic (AAC) cage receptor that obeys the stringent design criteria for enantioselective complexation of neutral small molecules. Detailed analysis of the structure-property relationship of the receptor allowed to identify important conformational features that enable to quantify guest uptake and release. In order to gain insight into the molecular complexes on the atomic level of detail, we set out to develop a general method to obtain the solid-state inclusion complexes.

Subsequently, we addressed the molecular recognition of achiral and chiral cyclic hydrocarbons, where intermolecular interactions are purely based on dispersion interactions. The goal was to investigate the general notion that strong directional interactions between the host and the guest are necessary for effective enantioselective complexation. Solution and solid-state studies allowed to challenge this notion, describing the first example of enantioselective complexation purely based on dispersion interactions. X-ray co-crystal structures of the host–guest complexes enabled the structure elucidation of *trans*-1,2-dimethylcyclohexane in a higher energy diaxial conformation, demonstrating large deviations of their dihedral angles from the commonly accepted value of 180°. We sought to validate the utility of the receptors to structurally elucidate single (di)axial conformers of substituted cyclohexane, in expanding the guest complexation studies to monohalo- and (±)-*trans*-1,2-dihalocyclohexanes. X-ray co-crystal structures and extensive solution complexation studies enabled the investigation of the exclusive complexation of the guests in their (di)axial chair conformation. Theoretical analysis of the isolated guest molecules further allowed us to compare the complexed and the isolated guest structures in order to test the hypothesis that the host is an ideal means to study the elusive (di)axial conformers of cyclohexane. Next to the structural elucidation of the dihedral angles, we investigated the halogen-bonding interactions between the alkyl halides and the receptor. The more directional nature of halogen-bonding further expanded our chiral recognition studies to more directional interactions. We were

especially interested to study the overall enantioselectivity of the enantiopure receptors towards (±)-*trans*-1,2-dihalocyclohexanes compared to (±)-*trans*-1,2-dimethylcyclohexanes, as more directional interactions are generally considered to enhance enantioselective binding.

Inspired by a co-crystal structure of the AAC encapsulating one water and two acetonitrile molecules, we considered the replacement of the water molecule by alcohol containing guests. We were interested to study the gain in binding energy by introducing one or two directional hydrogen-bonding interactions, in comparison to the previously studied series of purely hydrophobic guests. Depending on the guest molecules, various interaction modes of the alcohol groups with the H-bonding array of the host were imaginable. Strong directional hydrogen-bonding interactions between the guest and the receptor would also compensate for the conformational entropic penalty of complexation, allowing us to study the complexation and crystallization of acyclic guest molecules.

In order to extend molecular recognition studies to a solvent environment comparable to natural systems, we set out to develop AAC receptors, which would be soluble in aqueous medium. We envisioned a modular synthesis of enantiopure alleno-acetylenic cage receptors with increased surface polarity and solubility in aqueous medium. Conformational analysis of the receptors in solution was pursued. Preliminary guest binding studies revealed the ability of the receptors to complex small molecules in aqueous medium. Quantitative binding studies are ongoing.

The last chapter addresses the synthesis and structure-property relationship of covalent alleno-acetylenic cage receptors, accessed through intramolecular oxidative dimerization. The robust nature of covalent cage receptors was imagined to decrease the dependency of the cavity to external stimuli, such as temperature and the solvent identity.

2. Development of Enantiopure Alleno-Acetylenic Cage (AAC) Receptors

Parts of this chapter were published in a communication in *Angewandte Chemie International Edition* and *Angewandte Chemie*: Alleno-Acetylenic Cage (AAC) Receptors: Chiroptical Switching and Enantioselective Complexation of *trans*-1,2-Dimethylcyclohexane in a Diaxial Conformation.[192] Small-molecule single crystals were mounted by M. Solar, and X-ray structures were resolved by Dr. Nils Trapp (ETHZ).

2 Development of Enantiopure Alleno-Acetylenic Cage (AAC) Receptors

The introduction into enantioselective binding of chiral small molecules illustrated selective examples that advanced the understanding of enantioselective complexation of charged and neutral small molecules by synthetic receptors systems. Despite the apparent progresses in the design and construction of enantiopure receptors, examples of optically pure systems that effectively differentiate chiral neutral small molecules are still rare. The general notion prevails that strong directional interactions between the host and the guest are required. In order to question this notion, we set out to design enantiopure receptors that would bind molecules purely based on dispersion interactions in the absence of directional interactions.

The quantification of individual intermolecular interactions contributing to a binding event is rendered challenging through the competition of solvation. This implies careful design of the receptor systems. The important design criteria for enantioselective complexation evolved out of pioneering studies (see Introduction) and can be pinpointed to comprise of (a) a highly preorganized and confined hydrophobic cavity with an asymmetric interior allowing for the effective differentiation between two enantiomers; (b) a balance of confinement and flexibility to allow guest uptake and release; (c) transduction of the complexation process in form of a quantifiable signal, such as through NMR or ECD spectroscopy.

Throughout this chapter, the reader is guided through the initial design considerations of optically pure receptors for the complexation of neutral small molecules. Selected original targets of cage receptors are shown. The synthetic course of the targeted receptors eventually led to a new class of cage receptors with remarkable physicochemical and guest binding properties.

2.1 Alleno-Acetylenes as Axially Chiral Building Blocks for Enantiopure Receptors

In the evolution of the alleno-acetylenes – from their development as synthetic building blocks to their incorporation into more complex supramolecular structures – their unique features as axially chiral building blocks became apparent. The lean all-carbon backbone together with the 90° dihedral angle, made their incorporation into receptors system attractive.[176,177] Additionally, the strong chiroptical properties allowed for monitoring conformational changes through a sensitive spectroscopic output (Figure 22).[156]

1,3-Di-*tert*-butyl-1,3-diethynylallene:

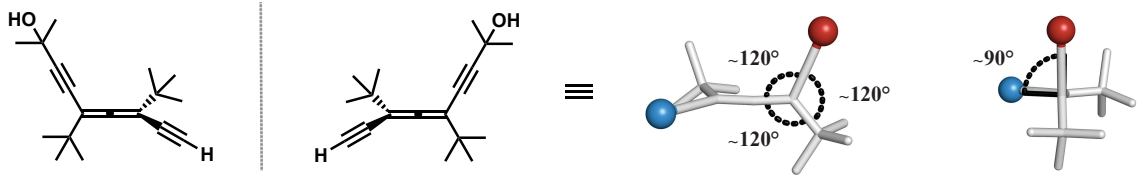

(*P*)-**27** (*M*)-**27**

Figure 22. Geometric properties and considerations of 1,3-di-tert-butyl-1,3-diethylynallenes (*P*)/(*M*)-**27**. Model of the (*M*)-configured 1,3-di-tert-butyl-1,3-diethylynallene **27** displayed on the right.[156,160]

The initially reported synthesis of DEA (±)-**27** was optimized in this Thesis and is summarized in Scheme 4 in the Introduction.[160] The synthesis comprises of four steps with an overall yield of 27%, followed by enantiomeric separation on a stationary chiral phase HPLC.

With the chiral building blocks (*P*)- and (*M*)-**27** at hand, we searched for platforms, which would complement the geometric features of the alleno-acetylenic building block (Figure 22). Various classes of preorganized macrocyclic receptors have been employed in the construction of enantiopure receptors for neutral small molecules.[1] Among these macrocycles, resorcin[4]arenes scaffolds have demonstrated particular utility, due to their synthetic tunability, which allows to access structures with precisely defined geometries.[1]

2.2 Alkyl-Bridged Resorcin[4]arenes as Macrocyclic Platforms

The common method for the preparation of resorcin[4]arenes is the Brønsted-acid-catalyzed condensation of resorcinol and an aldehyde.[193,194] Modular post-functionalization methods provide access to various resorcin[4]arene based structures with widespread applications in host–guest chemistry (Figure 23).[195-197] These synthetic methods have been extensively reviewed[198] and only key structural aspects are highlighted.

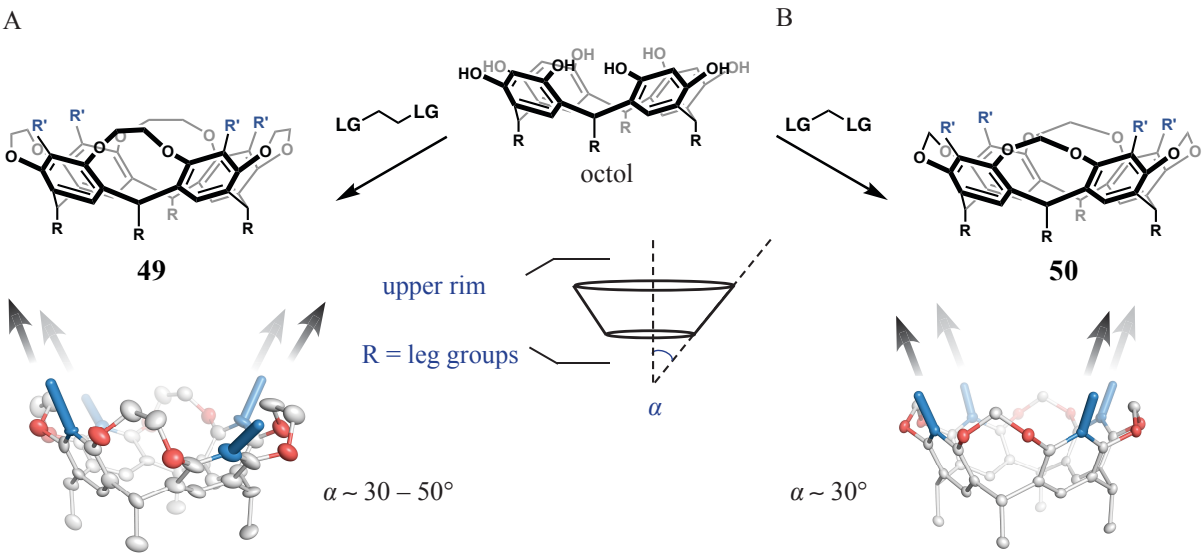

Figure 23. Functionalization of the resorcin[4]arene scaffold with the geometrical implications of alkyl-bridging. A: Ethane-1,2-diyl-bridged compound **49** adopts a near-C_2-symmetric conformation with exit vectors of ~30–50°. B: Methylene-bridging leads to a near-C_4-symmetric conformation with rigid exit vectors of ~30° (**50**). The leg groups allow to tune the solubility of the scaffold. LG: leaving group. Representative models were extracted from X-ray crystal structures and are depicted below each structure (CCDC = 137143 (left) and 1496457 (right)).[110,197,199,200]

While the product of the condensation reaction of the aldehyde with the resorcinol, referred to as octol, is highly flexible and adopts multiple conformations, bridging of the phenolic groups with alkyl groups results in rigidified bowl-shaped macrocycles.[110] Two types of alkyl-bridging have been widely employed over the years.[110,197,198] The ethane-1,2-diyl-bridging of the parent octol results in a near-C_2-symmetric conformation, where the exit vectors departs from the aryl rings in the 1-position at an angle α ranging from ~30–50° with respect to the principle axis of the molecule (**49**, Figure 23).[200] Conversely, the methylene-bridged compound **50** is held in a near-C_4-symmetric conformation with a rigid exit vector α of ~30°.[200] While both types of bridging enhance the conformational preorganization of the resulting cavitand, we selected the methylene-bridged near-C_4-symmetric resorcin[4]arene platform to complement the geometrical features of the alleno-acetylenes.

Another major advantage of resorcin[4]arenes over other potential platforms, is the ability to tune the solubility properties by varying the leg groups (Figure 23).[198] The latter are typically introduced through the corresponding aldehyde in the octol synthesis.[198] Longer alkyl groups generally render resorcin[4]arenes more soluble in apolar solvents.[201] Shorter alkyl chains enable solubility in more polar solvents.[202,203] The incorporation of polar neutral and charged groups provides solubility in aqueous environment.[204-206] Additionally, through

the incorporation of binding groups, such as thiols, at the leg termini, resorcinarene-based receptors can be immobilized on surfaces.[207]

n-Hexyl groups were chosen as leg groups in order to ensure solubility in apolar solvents. Shorter alkyl groups, such as methyl groups were envisaged to additionally facilitate crystallization.

2.2.1 Activation of the Methyl-Bridged Resorcin[4]arenes

We envisaged two different reaction classes for the attachment of the alleno-acetylenic moieties to the resorcin[4]arene platform. Cross-coupling of the activated methylene bridged resorcin[4]arene with the terminal acetylene of the axial chiral building block would preserve the exit vector α of ~30° (Figure 24, left). Alternatively, we imagined a 1,3-dipolar cycloaddition of an azide functionalized resorcin[4]arene with the terminal acetylene of the alleno-acetylene (Figure 24, right), resulting in a slight increase of the exit vector α of ~30°. Additionally, the 1,3-dipolar cycloaddition would result in the formation of a triazole moiety, giving rise to additional functional groups in the final cage receptor (Figure 24, right).

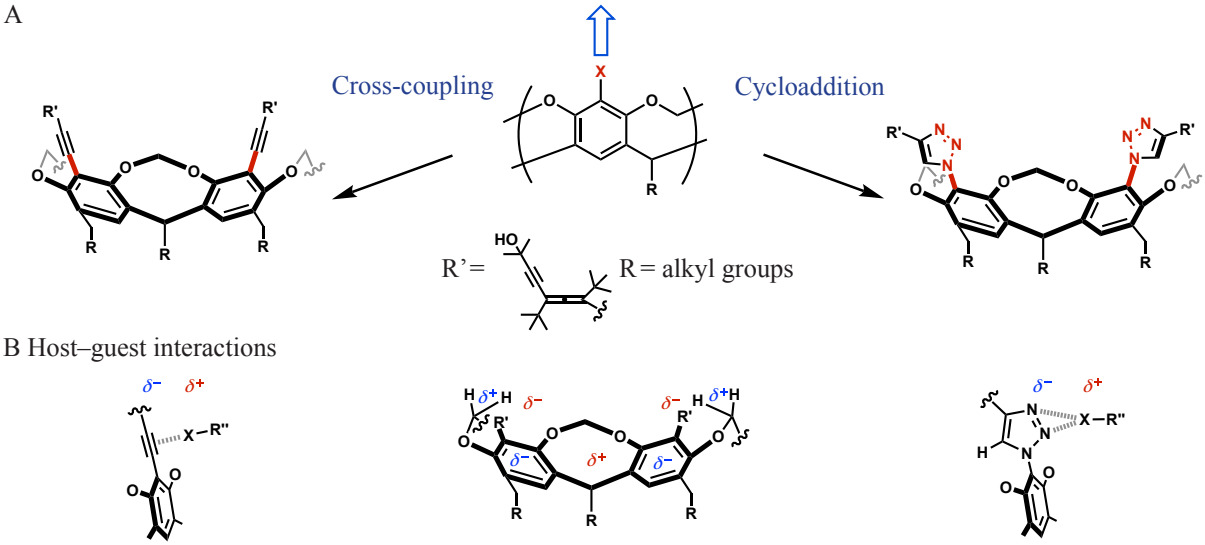

Figure 24. A: Two types of reaction classes were envisaged to functionalize the methylene-bridged resorcin[4]arene with the axial chiral alleno-acetylene: cross-coupling (top left) and 1,3-dipolar cycloaddtion (top right). Both reaction classes would enable to access a diversity of potential receptor systems. B: The acetylenic functionality as well as the triazole group would introduce additional possibilities for host–guest interactions. The complementary polarization of the guests in order to interact with the host structures is shown in red. Blue designates the polarization of the receptor core.

Both reaction classes enable to access a high structural diversity for potential receptors systems. Especially, the thermal 1,3-dipolar cycloaddition, initially developed by R. Huisgen,[208] which was further advanced to a highly regioselective copper-catalyzed variant

by the group of K. B. Sharpless,[209,210] finds today broad application in chemistry and biology.[211-213]

2.3 Initial Design Ideas of Optically Pure Alleno-Acetylenic Cage Receptors

Various receptor systems were imagined to be accessed out of the combination of the alleno-acetylenes with the methylene-bridged resorcin[4]arene scaffold, either through cross-coupling or through 1,3-dipolar cycloadditions. A selection of the initial ideas is displayed in Figure 25 to illustrate potential target structures, such as (*P*)- and (*M*)-configured **51**–**55**.

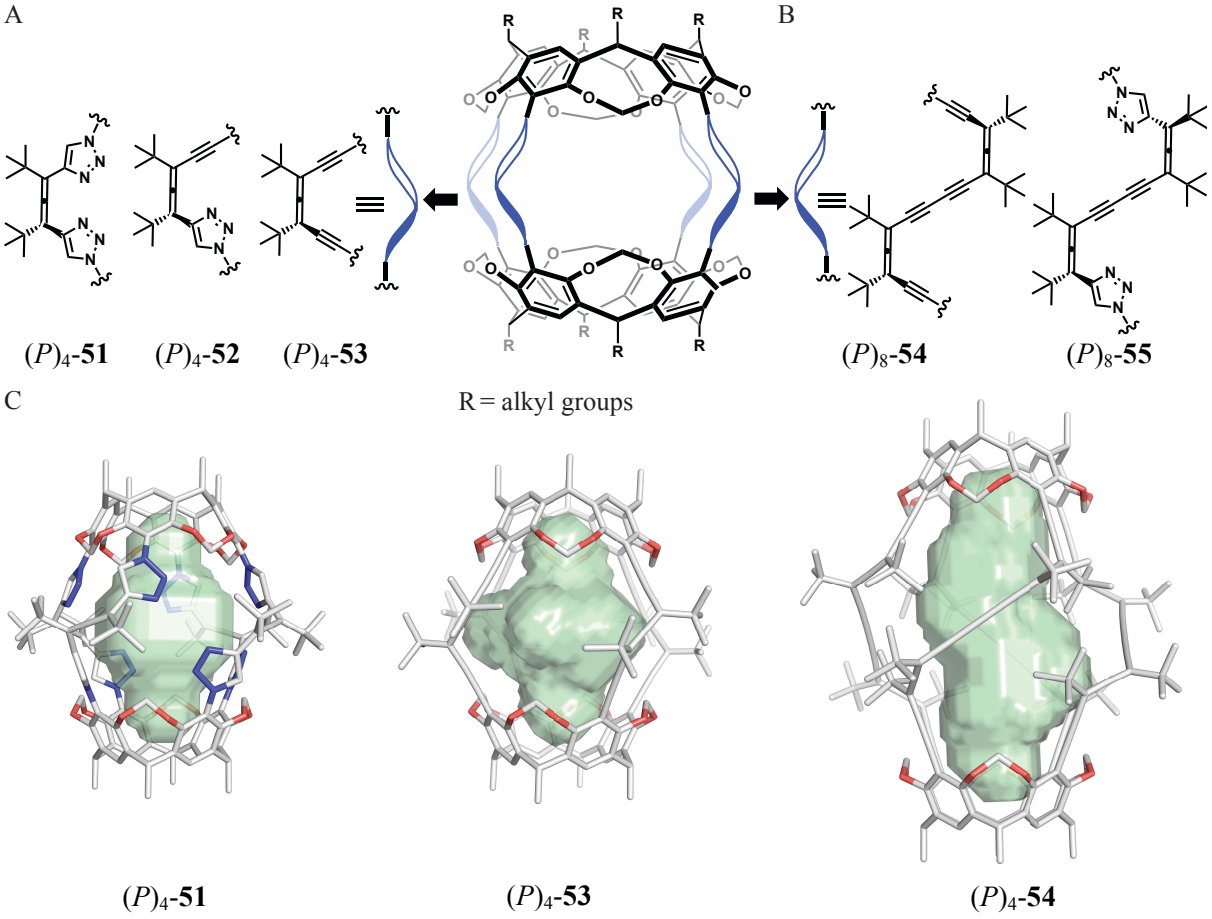

Figure 25. Selected examples of enantiomerically pure cage receptors, which were imagined to be accessed through cross-coupling or 1,3-dipolar cycloaddition of the alleno-acetylene (*P*)/(*M*)-**27** with the methylene-bridged resorcin[4]arene **50**. A: Selected combinations of (*P*)-configured cage receptors **51**–**53**; B: Expanded optically pure cage receptors (*P*)$_8$-**54** and (*P*)$_8$-**55**. C: Model structures of selected examples (*P*)$_4$-**51**, (*P*)$_4$-53, and (*P*)$_8$-**54**; the interior of the model is visualized in green and gives rise to cavity sizes ranging from 300–400 Å^3, as calculated with VOIDOO.[214]

The receptors displayed in Figure 25 consist of two resorcin[4]arene receptor hemispheres linked through either four monomeric or dimeric alleno-acetylenes with cavity sizes ranging from 300–400 Å^3 (Figure 25). We imagined the twist of the receptor hemispheres of up to 38° ((*P*)$_4$-**51**) to result in an asymmetric interior capable of differentiating enantiomers.

The dynamics of the systems (breathing), especially for receptors $(P)_8$-**54** and $(P)_8$-**55**, would enable guest uptake and release. Changes in the ECD signals through the conformational changes induced in the receptor upon guest uptake and release would allow us to precisely quantify guest complexation.

2.4 Synthesis of the Resorcin[4]arene Platforms

With the original synthetic targets in mind, we set out to synthesize the resorcin[4]arene platforms. Retrosynthetically, the cross-coupling approach would rely on a halogen-activated resorcin[4]arene scaffold, while the 1,3-dipolar cycloaddition approach would lead through a azide-functionalized resorcin[4]arene. The synthesis of the halogen-activated resorcin[4]arenes was reported for different alkyl leg groups, but no literature report on a tetraazide-functionalized macrocycle was found. [215-217]

The preparation of tetrabromo-resorcin[4]arene **58** relies on the Brønsted-acid-catalyzed condensation of resorcinol with heptanal to afford octol **56**. Selective bromination led to **57**, and subsequent methylene-bridging of the phenolic groups afforded the rigid cavitand **58** (Scheme 5).

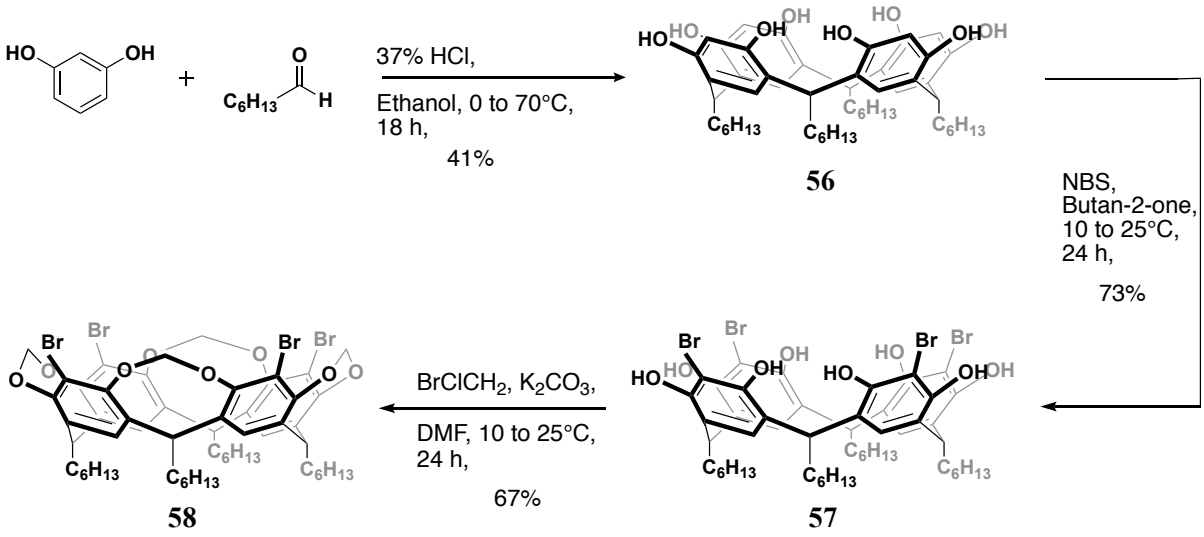

Scheme 5. Synthesis of resorcin[4]arene cavitand **58** from resorcinol and heptanal.[215-217]

In order to further activate the resorcin[4]arene core, we subsequently lithiated **58** at –100 °C followed by iodination to afford tetraiodo-cavitand **59** in 80% yield (Figure 26).[218] While lithiation of **58** followed by addition of different azide sources gave a mixture of one-, two-, three- and four-fold azide functionalization, bromine-lithium exchange of **58** at –100 °C and subsequent treatment with pure tosylazide gave tetraazido-cavitand **60** in 58% yield (Figure 26). Both thermogravimetric analysis and differential scanning calorimetry confirmed

the stability of the tetraazide **60** under normal laboratory conditions. The carbon nitrogen ratio of 5.3 additionally supported its stability.

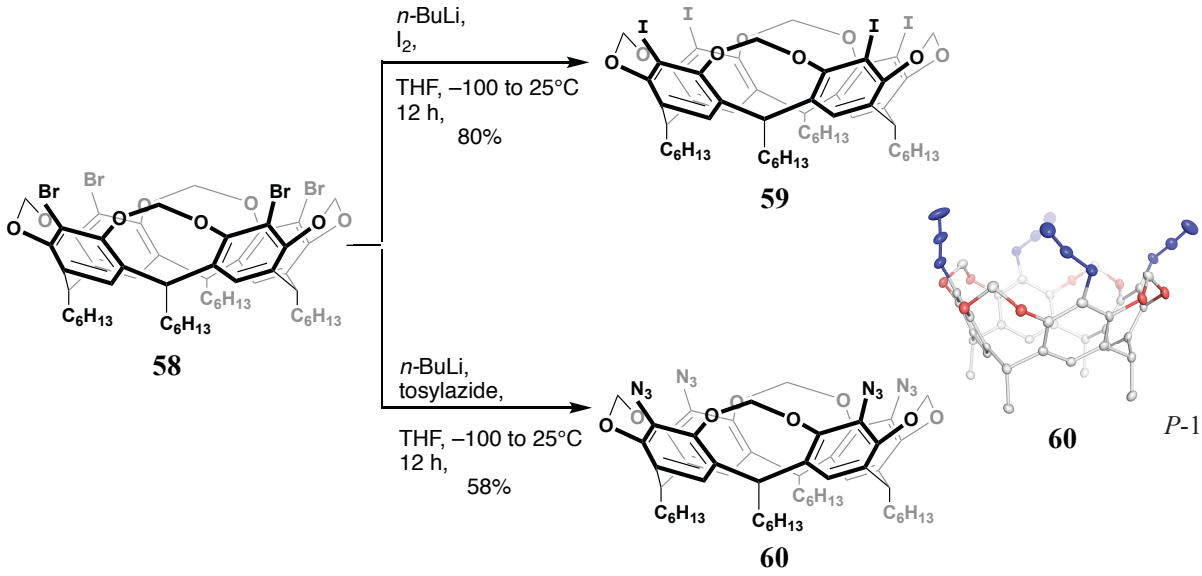

Figure 26. Synthesis of tetraiodo cvitand **59** and tetraazido cavitand **60**. Single crystal X-ray structure of tetraazide **60** is shown on the right. *n*-Hexyl chains are omitted for clarity.[218]

With the coupling and the cycloaddition molecules at hand, we set out to develop methods to attach the enantiopure alleno-acetylenes (*P*)- and (*M*)-**27** to the cavitands.

2.5 Towards Alleno-Acetylenic Cage Receptors

The attachment of the alleno-acetylenes (*P*)- and (*M*)-**27** to the resorcin[4]arene platform relied on a four-fold cross-coupling or dipolar cycloaddition. In order to obtain significant yields, each single reaction had to proceed with yields of above 80%.

2.5.1 Alleno-Acetylenic Cage Receptors *via* 1,3-Dipolar Cycloaddition

We decided to focus on the four-fold 1,3-dipolar cycloaddition of the alleno-acetylenes (*P*)- and (*M*)-**27** to the tetraazido resorcin[4]arene **60**, as cooperativity of the copper-catalyzed cycloadditon was expected to enhance the overall yield of the four-fold cycloaddition.[219,220] A selected screening of adapted literature procedures on racemic (±)-**27** with **60** is shown in Table 1.[219-223]

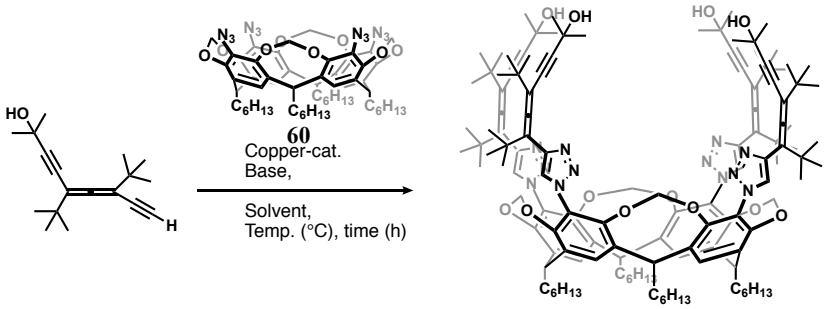

(±)-**27** (±)-**61**

Table 1. Selected reaction conditions adapted from the literature for the four-fold copper-mediated 1,3-dipolar cycloaddition of tetraazide **60** with 4.0 equiv. DEA (±)-**27**. SIPr = 1,3-bis(2,6-diisopropylphenyl)imidazolinium; SIMes = 1,2-bis(2,4,6-trimethylphenyl)-4,5-dihydroimidazol-2-ylidene; THF = tetrahydrofurane; DMSO = dimethylsulfoxide.[219,221-223]

Entry	Copper-Cat.	Solvent	Base	t/h	T/°C	Conversion
1	CuI	THF	DIPEA	24	25	0%
2	[Cu(SIPr)]Cl	CH_2Cl_2/MeOH 4:1	-	24	25	0%
3	$[Cu(SIMes)_2]Cl$	THF	-	24	25	10%
4	$[Cu(SIMes)_2]BF_4$	DMSO	-	24	25	12%
5	$[Cu(SIMes)_2]BF_4$	Aceton	-	24	25	10%
6	$[Cu(CH_3CN)_4]PF_6$ Cu	CH_2Cl_2/MeOH 4:1	DIPEA	24	25	53%
7	$[Cu(CH_3CN)_4]PF_6$ Cu	CH_2Cl_2/MeOH 4:1	DIPEA	60	25	80%

The best result was obtained with the $[Cu(CH_3CN)_4]PF_6$ and elemental copper powder as catalyst in a solvent mixture of CH_2Cl_2/MeOH 4:1.[223] After 60 h at 25 °C, the racemic mixture of (±)-**61** was obtained in an overall yield of 80%, corresponding to a yield of 95% for each cycloaddition. This procedure was subsequently applied for the coupling of the enantiopure alleno-acetylenes (*P*)- and (*M*)-**27** with the tetraazide functionalized cavitand **60** to afford the optically pure alleno-acetylenic cage receptors $(P)_4$- and $(M)_4$-**61** (Scheme 6).

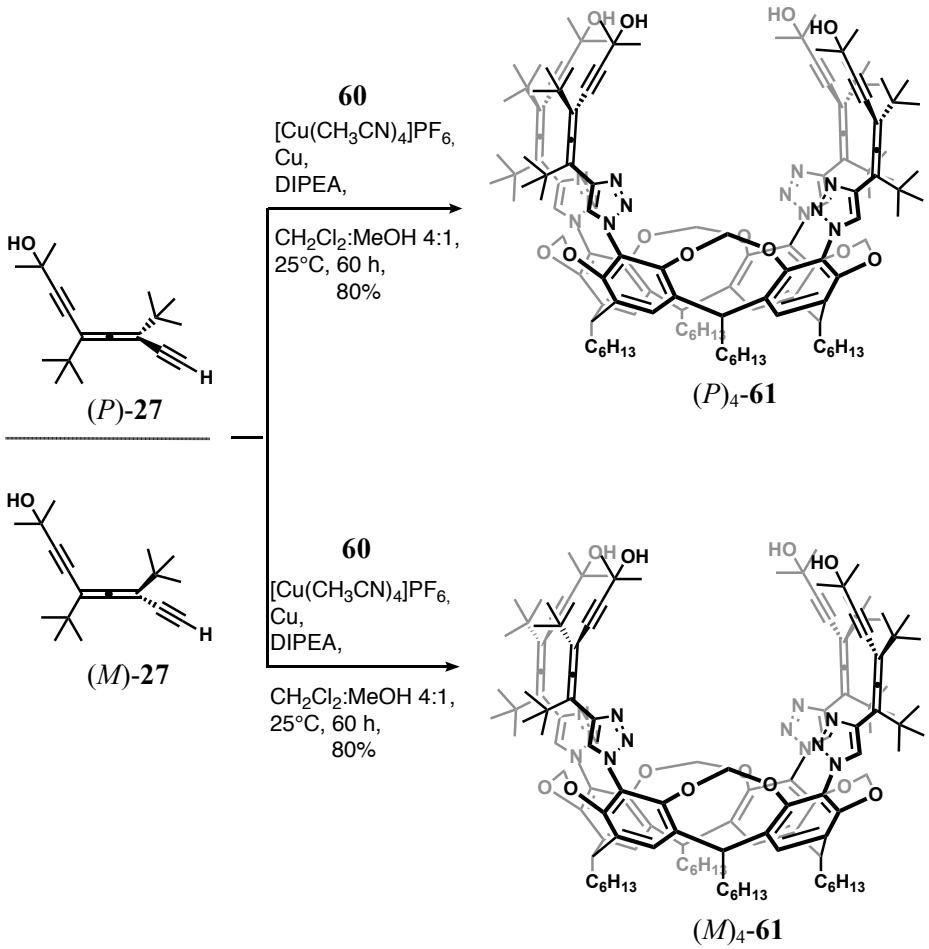

Scheme 6. Synthetic procedure of Entry 7 (Table 1) was applied for the synthesis of optically pure $(P)_4$- and $(M)_4$-configured AACs **61** from enantiopure DEA **27** (4.0 equiv.) and tetraazido-cavitand **60** (1.0 equiv.).

Having established high-yielding conditions for the four-fold 1,3-dipolar cycloaddition of the DEAs to the resorcin[4]arene core, we pursued the preparation of the AACs through cross-coupling, in order to compare their chiroptical properties.

2.5.2 Alleno-Acetylenic Cage Receptors *via* Sonogashira Cross-Coupling

We decided to focus on Sonogashira cross-coupling conditions for the coupling of the tetraiodo-activated resorcin[4]arene cavitand **59** with racemic DEAs (±)-**27**. As cooperativity effects are less known for the palladium-catalyzed cross-coupling reactions, we expected lower overall yields. Table 2 shows a selected screening of adapted literature procedures.[224]

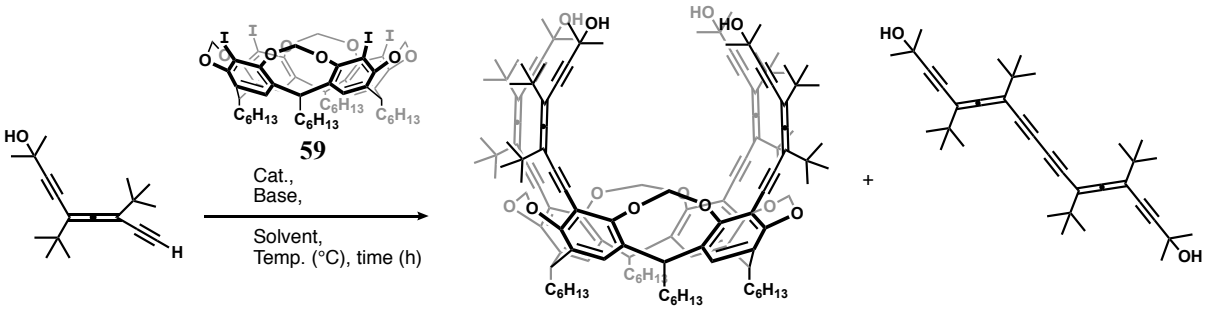

(±)-**27** (±)-**62** (±)-**63**

Table 2. Selected reaction conditions adapted from the literature for the four-fold Sonogashira cross-coupling of tetraiodo cavitand **59** with 5.0 equiv. DEA (±)-**27**. XPhos = 2-dicyclohexylphosphino-2',4',6'-triisopropylbiphenyl.[224]

Entry	Cat.	Ligand	Solvent	Base	t/h	T/°C	(±)-**63**	(±)-**62**
1	$[Pd(Ph_3P)_2]Cl_2$, CuI	–	Et_2NH	Et_2NH	6	50	97%	0%
2	$[Pd(Ph_3P)_2]Cl_2$, CuI	–	THF	iPr_2NH	6	60	90%	0%
3	$[Pd(Ph_3P)_2]Cl_2$, CuI	PPh_3	THF	iPr_2NH	6	60	70%	21%
4	$[Pd(Ph_3P)_2]Cl_2$, CuI, Cu	PPh_3	THF	iPr_2NH	6	60	95%	0%
5	$[Pd(CH_3CN)_2]Cl_2$,	XPhos	CH_3CN/THF 9:1	Cs_2CO_3	6	80	65%	0%
6	$[Pd(CH_3CN)_2]Cl_2$,	XPhos	DMSO	K_3PO_4	6	80	70%	0%
7	$[Pd(Ph_3P)_4]$, CuI	–	Et_3N	Et_3N	6	100	40%	54%
8[1]	$[Pd(Ph_3P)_4]$, CuI	–	Et_3N	Et_3N	12	100	4%	96%

[1]Et_3N was distilled prior to use, and the reaction was performed under argon atmosphere.

One of the challenges was to find conditions, which did not favor the oxidative homocoupling of the DEAs yielding (±)-**63**. While this side reaction could not completely be eliminated, even in the absence of Cu(I),[225] the reaction in freshly distilled Et_3N with $[Pd(Ph_3P)_4]$ and CuI as catalyst (each 10 mol%) under argon atmosphere yielded 96% of

racemic AAC (±)-**62**. The high yield was surprising, considering this corresponded to yields above 99 % per C_{sp}–C_{sp2} bond formation.[192]

We subsequently applied the synthetic protocol to the synthesis of the optically pure AACs and obtained both $(P)_4$- and $(M)_4$-configured AAC **62** in high yields (Scheme 7).

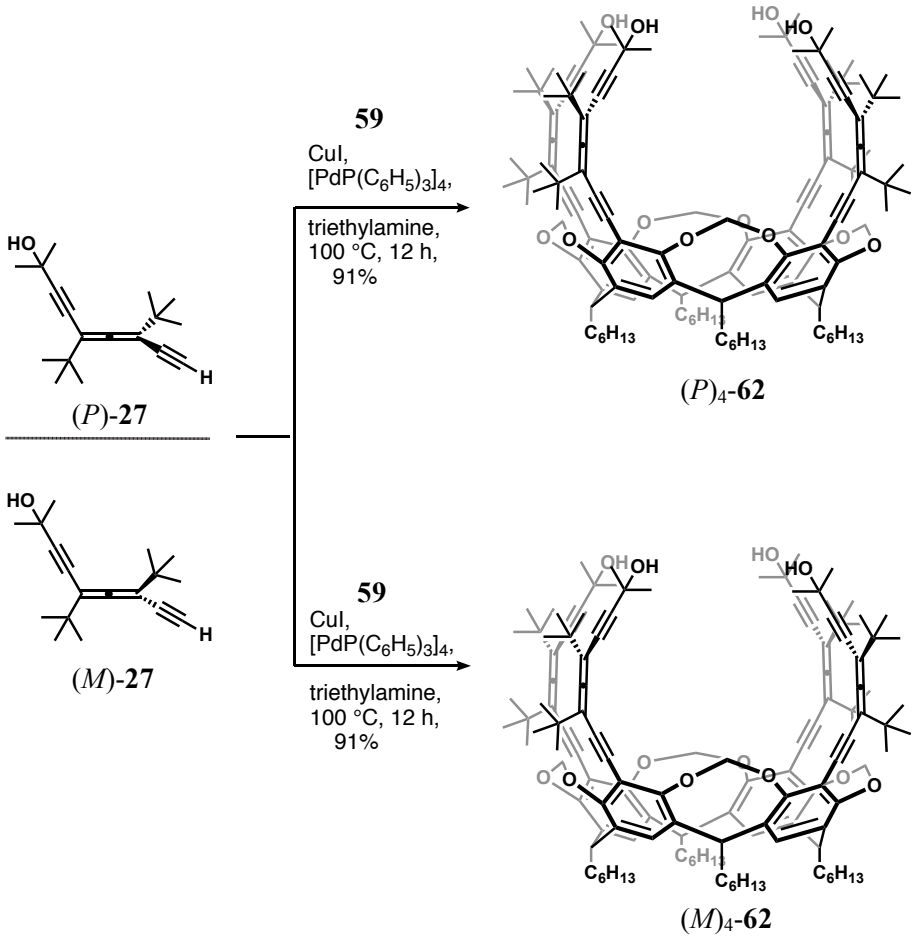

Scheme 7. Synthetic procedure of Entry 8 (Table 2) was applied for the synthesis of optically pure $(P)_4$- and $(M)_4$-configured AACs **62** from enantiopure DEA **27** (5.0 equiv.) and tetraiodo-cavitand **59** (1.0 equiv.). The solvent was distilled prior to use and the reaction was performed under argon atmosphere.[192]

With both the enantiopure four-fold cycloaddition product $(P)_4$- and $(M)_4$-**61** and the cross-coupling product $(P)_4$- and $(M)_4$-**62** in hand, we set out to study their photophysical properties.

2.5.3 ECD and UV/Vis Properties of Enantiopure AACs $(P)_4$- and $(M)_4$-61 and 62

In order to evaluate the chiroptical properties of the optically pure AACs $(P)_4$/$(M)_4$-**61** and -**62**, we measured their ECD and UV/Vis properties. Figure 27 (left) shows the ECD traces at 293 K in acetonitrile of both $(P)_4$- and $(M)_4$-configured AACs **61** and **62**. UV/Vis traces of the $(P)_4$-AACs **61** and **62** are displayed on the right (Figure 27).

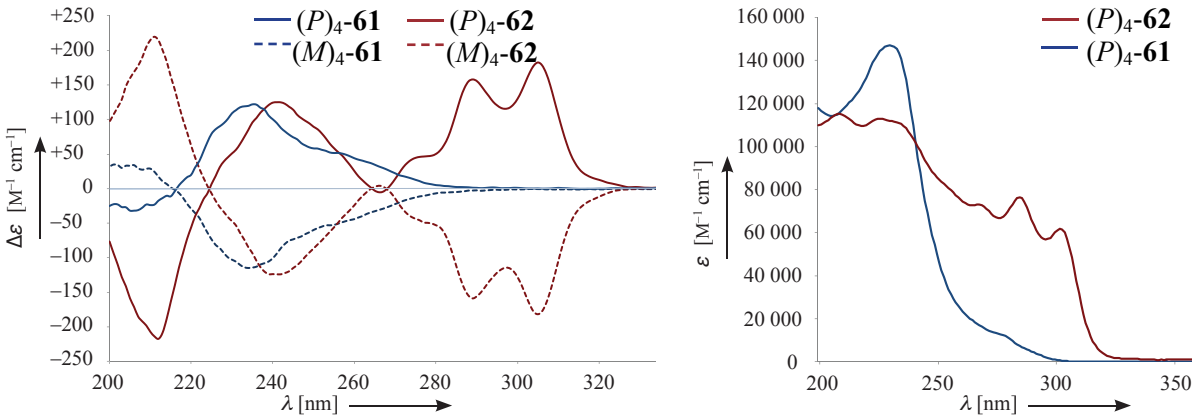

Figure 27. ECD (left) traces of AACs $(P)_4$-**61** and **62** (solid lines) and $(M)_4$-**61** and **62** (dashed lines) at 293 K in acetonitrile. UV/Vis (right) traces of the $(P)_4$-configured AACs **61** and **62**.

Both ECD and UV/Vis traces showed large differences in the optical properties of the enantiopure AACs $(P)_4/(M)_4$-**61** and -**62**. Cage receptor $(P)_4$-**62**, obtained by the four-fold Sonogashira cross-coupling reaction, displayed large Cotton effects of $\Delta\varepsilon = -231$ M^{-1} cm^{-1} at $\lambda = 214$ nm and $\Delta\varepsilon = +191$ M^{-1} cm^{-1} at $\lambda = 304$ nm and the $(M)_4$-configured enantiomer showed mirror image traces. In contrast, the product of the 1,3-dipolar cycloaddition $(P)_4$-**61** displayed weakened ECD intensities with maximums at $\Delta\varepsilon = +121$ M^{-1} cm^{-1} at $\lambda = 236$ nm and a completely attenuated signal in the region of $\lambda = 304$ nm. Also, the UV/Vis traces of the AACs $(P)_4$-and $(M)_4$-**61** showed a substantial decrease in the absorption intensities around $\lambda = 304$ nm.

In order to gain further insight into the molecular structures of AACs $(P)_4/(M)_4$-**61** and -**62**, we optimized their structure computationally at a PM6//OPLS2005 level of theory.[226] Figure 28 shows the optimized $(P)_4$-configured enantiomer of **61** and **62**. The triazole group in $(P)_4$-**61** is rotated out of the aryl plane, disrupting the conjugation and thus explained the lower intensities in the ECD and UV/Vis spectra (Figure 28, right). In contrast, the lean acetylenic functionality in $(P)_4$-**62**, bridging the cavitand core with the allene strands, seemed to preserve conjugation.

PM6//OPLS2005 optimized AACs:

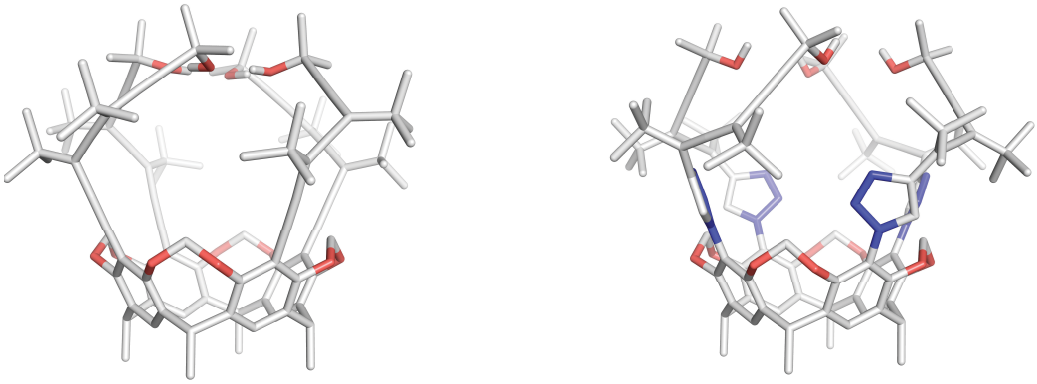

$(P)_4$-**62** $(P)_4$-**61**

Figure 28. Optimized $(P)_4$-configured AACs **62** (left) and **61** (right) on a PM6//OPLS2005 level of theory.[226] The tertiary alcohols in $(P)_4$-**62** converge into a four-fold hydrogen bonding array.

Additionally, the model of $(P)_4$-**61** showed that the triazole-group increased the exit vector α (see Figure 23) of the alleno-acetylene with respect to the principle axis of the molecule, resulting in a distance of the tertiary alcohols (d_{O-O}) of around 4.5 Å. Surprisingly, the intact exit vector α of 30° in AACs $(P)_4$-**62** seemed to result in a perfect distance between the tertiary alcohol groups of the alleno-acetylenes to form a four-fold hydrogen bonding array (d_{O-O} = 2.8 Å). The model also shows the formation of a hydrogen-bonding array closing the receptor. In order to further investigate the structure obtained by calculations, we set out to study the physicochemical properties of the AACs $(P)_4$-and $(M)_4$-**62** in depth.

2.6 AACs $(P)_4$- and $(M)_4$-62: Binary Conformational Switching in Solution

2.6.1 Hypothesis

Initial ECD studies on the AACs $(P)_4$ and $(M)_4$-**62** showed strong solvent dependencies of the absorption properties. From the calculated model (Figure 28, left), we hypothesized a solvent induced conformational switching.[192] Two discrete conformations were suggested and supported by calculations: a closed conformation with the alleno-acetylenic arms oriented inward and the tertiary alcohols converging into a circular hydrogen-bonding array, and an open conformation where the alleno-acetylenes are oriented outwards (Figure 29).

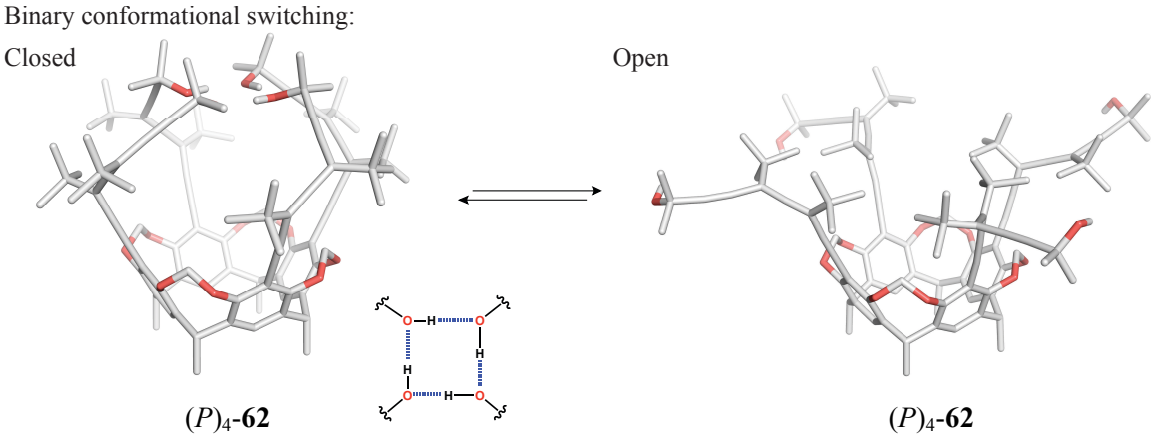

Figure 29. Hypothesized binary conformational switching of AACs $(P)_4$-**62** in solution between a closed cage conformation (left) and an open conformation (right).

The conformational switching was postulated to be the result of differences in solvent size and polarity. Large apolar solvents were anticipated to stabilize the closed conformation, while smaller more polar solvents were expected to stabilize the open conformation. In order to test this hypothesis, a "monomeric" model system was prepared (2,6-dimethoxyphenyl-substituted DEA (*P*)- and (*M*)-**64**, see Scheme 8), which served as comparison for solution studies and later for the photophysical properties.

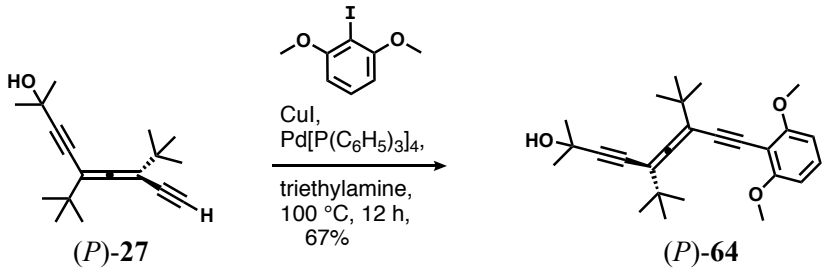

Scheme 8. Reagents and conditions for the synthesis of the "monomeric" model system (*P*)-**64** corresponding to approximately a fourth of the molecular structure of the AAC $(P)_4$-**62**. Only (*P*)-configured structure shown. (*M*)-configured **64** were obtained from (*M*)-configured DEA **27**.[192]

It is noteworthy that the synthetic yield of the cross-coupling to afford the monomeric "model system" (*P*)-**64** with DEA (*P*)-**27** was substantially lower (67%) compared to the four-fold cross-coupling reaction to afford $(P)_4$-**62** (98% per C_{sp}–C_{sp2}-bond formation), indicating some cooperativity in the formation of the AACs $(P)_4$-**62**.

2.6.2 NMR Spectroscopic Study of the Conformational Switching of AACs $(P)_4$- and $(M)_4$-62

The solvent-dependent switching of the AACs $(P)_4/(M)_4$-**62** between the open and the closed conformation was studied by ^{1}H NMR and 2D ROESY NMR in $CDCl_3$ and cyclohexane-d_6.[192]

^{1}H NMR spectra were measured in $CDCl_3$ and cyclohexane-d_6, and the shifts of the OH resonances of the tertiary alcohol moieties ($C(Me)_2OH$) in the solvents were compared (Figure 30).

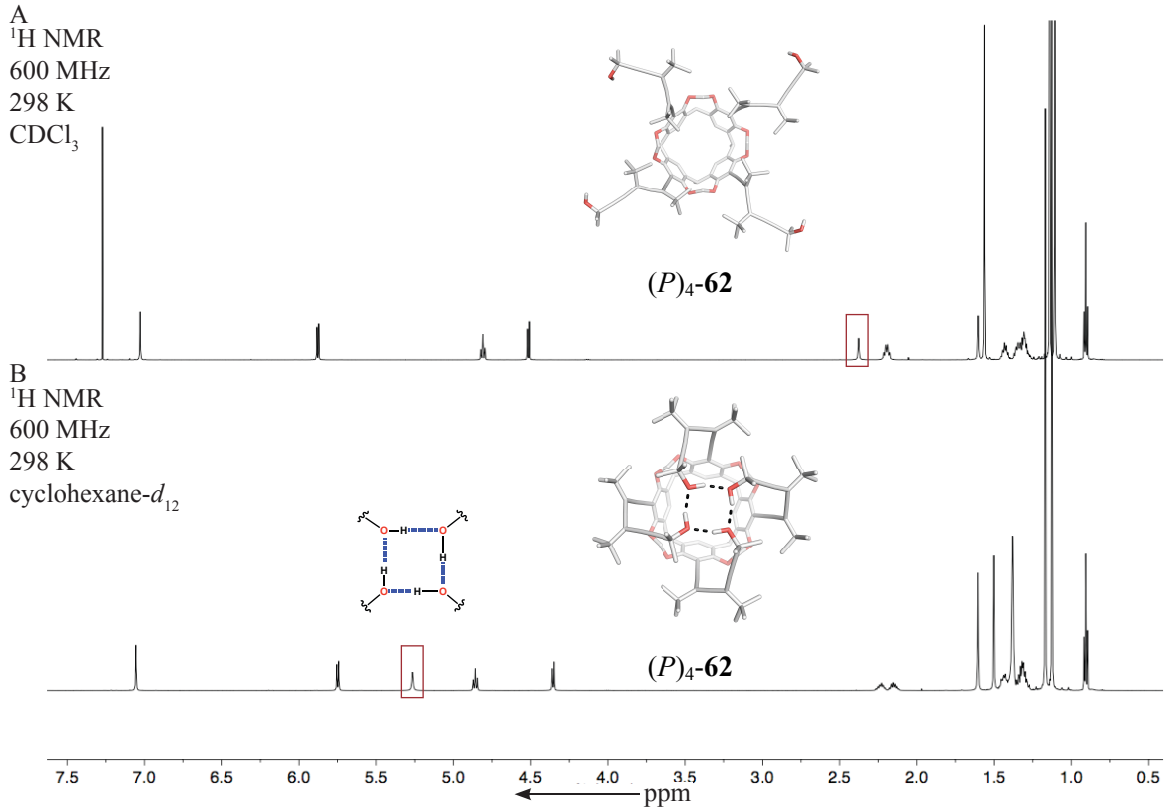

Figure 30. A: ^{1}H NMR resonances of the OH groups of AAC $(P)_4$-**62** in $CDCl_3$; B: cyclohexane-d_{12} at 298 K. The downfield shift $\Delta\partial_{OH}$ corresponds to +2.9 ppm.

A strong solvent-dependent downfield shift of 2.9 ppm of the OH signal $\Delta\delta_{OH}$ upon exchanging the solvent from $CDCl_3$ to cyclohexane-d_6 was observed and indicated the formation of the circular four-fold hydrogen-bonding array in cyclohexane-d_6 compared to the free OH signal in $CDCl_3$. Hardly any solvent-dependent shifts of the OH signal was observed for the "monomeric" alleno-acetylenic model system (*P*)-**64** with $\Delta\delta_{OH}$ = +0.03 ppm (Figure 31).

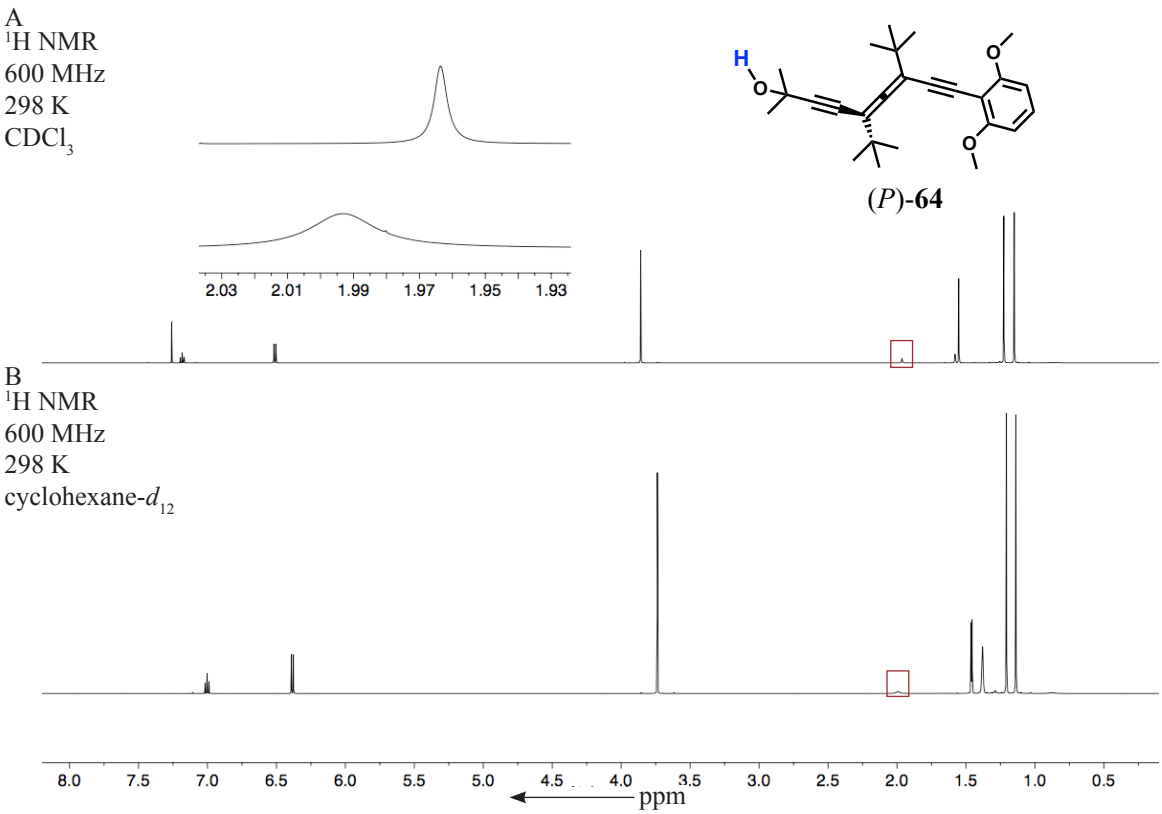

Figure 31. A: Chemical shift of the OH of (*P*)-**64** in $CDCl_3$; B: in cyclohexane-d_{12} at 298 K. An unsignificant downfield shift of $\Delta\partial_{OH} = +0.03$ ppm is observed.

The rigid and preorganized nature of AACs $(P)_4$- and $(M)_4$-**62** in the closed conformation in cyclohexane-d_6 was further supported by 2D ROESY NMR studies. Figure 32 indicates the expected cross signals in the NMR experiments.

In cyclohexane-d_6, one Me group (light green) of the tertiary alcohols (C(*Me*)$_2$OH) of AAC $(P)_4$-**62** showed through-space correlation with one neighboring *tert*-butyl group (C*(Me)*$_3$, blue, Figure 33. The second Me group (dark green) showed two through space correlations: one with the neighboring *tert*-butyl group (C*(Me)*$_3$, blue) and a second one with the spatial proximate *tert*-butyl group (C*(Me)*$_3$, violate). The latter cross signal was absent in both the AACs $(P)_4$-**62** in $CDCl_3$ (open conformation) and the model system (*P*)-**64** (Figure 34).

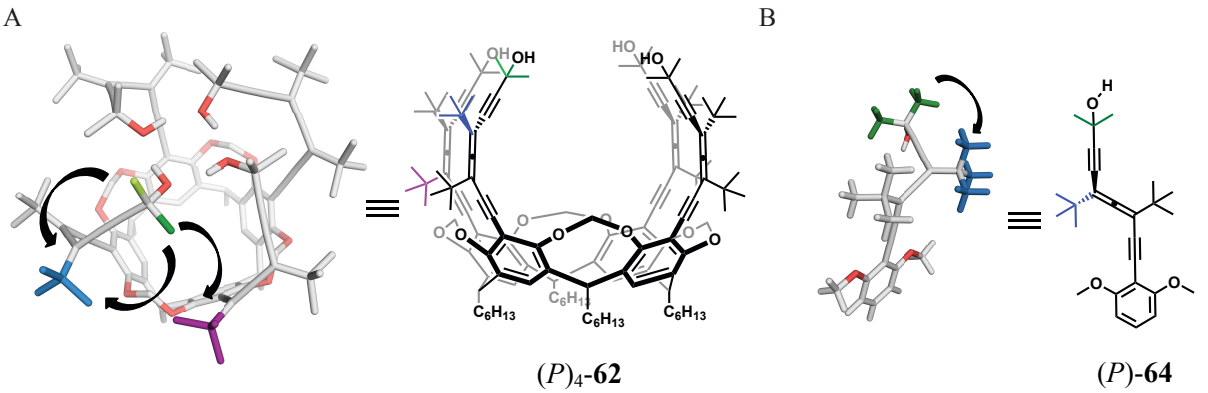

Figure 32. 2D ROESY NMR cross signals (black arrows) for A: AAC $(P)_4$-**62** in the closed conformation stabilized by the circular hydrogen-bonding array and B: in the model system (*P*)-**64**.

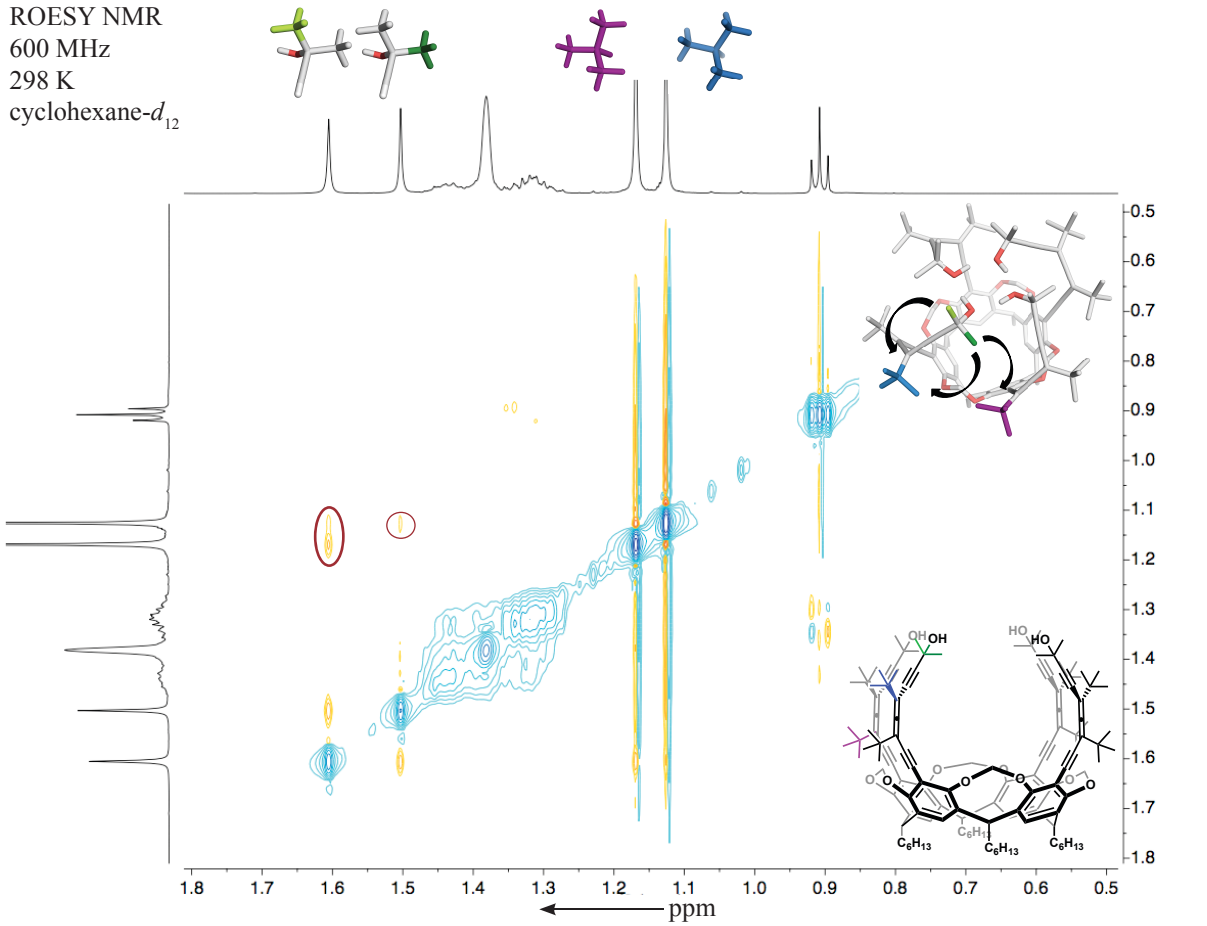

Figure 33. 2D ROESY NMR traces of AAC $(P)_4$-**62** in cyclohexane-d_{12} at 298 K with cross signals of the Me of the tertiary alcohol (C(*Me*)$_2$OH, dark green) with one neighboring *tert*-butyl group (C*(Me)*$_3$, blue) and one spatial proximate *tert*-butyl group (C*(Me)*$_3$, violet) of a second DEA arm. Cross signals circled in red.

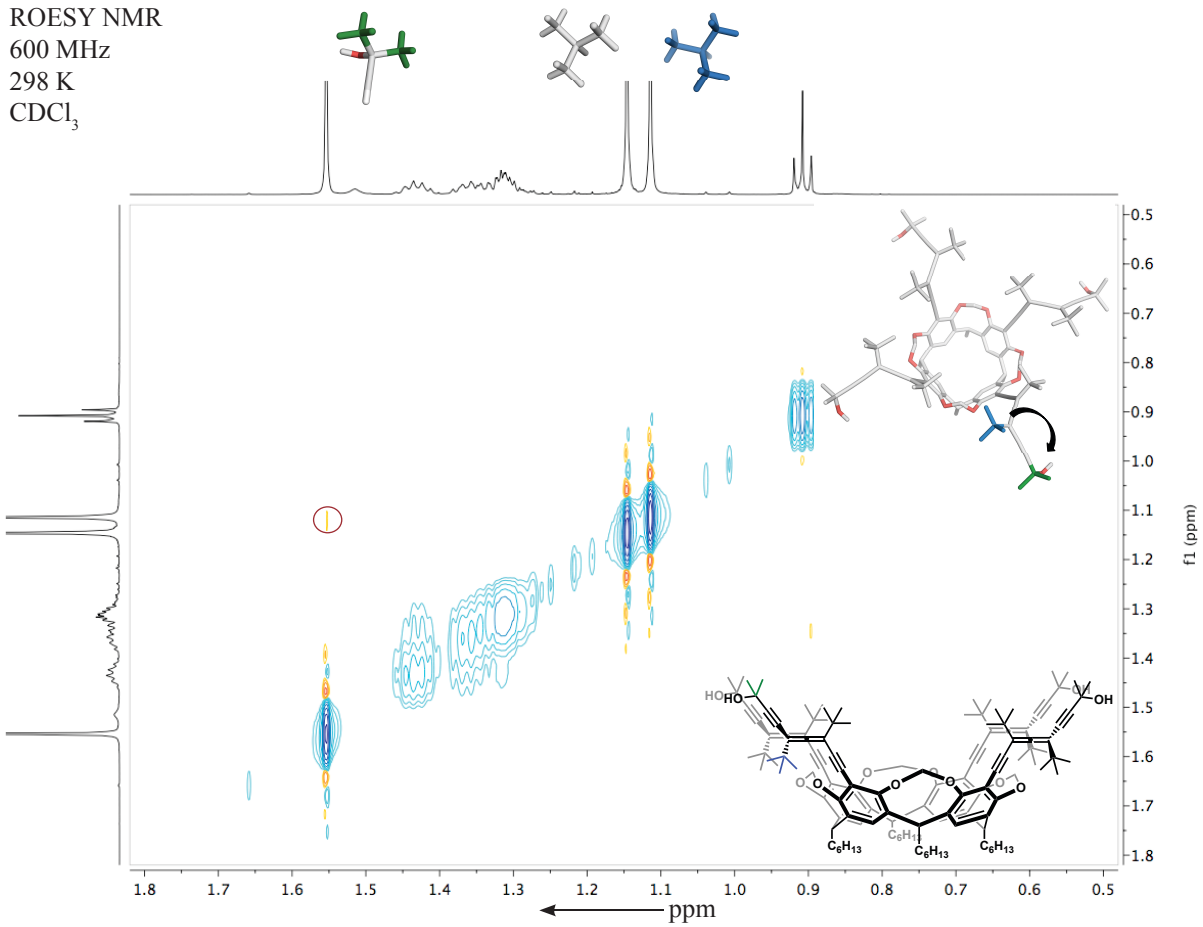

Figure 34. 2D ROESY NMR traces of AAC $(P)_4$-**62** in $CDCl_3$ at 298 K showing only one cross signal between the Me of the tertiary alcohol ($C(Me)_2OH$, dark green) and the neighboring *tert*-butyl-group ($C(Me)_3$, blue). Cross signals circled in red.

2.6.3 IR Spectroscopic Study of the Conformational Switching of $(P)_4$- and $(M)_4$-62

Similarly, a large shift of the OH wavenumber $\tilde{\nu}_{OH}$ to lower energy was recorded in IR solution studies. Upon changing the solvent from CH_2Cl_2 to cyclohexane a shift from $\tilde{\nu}_{OH}$ = 3600 cm^{-1} to 3370 cm^{-1} was observed, accompanied by broadening of the signal (Figures 35 and 36). Importantly, the value of $\tilde{\nu}_{OH}$ was largely independent of concentrations for both the open and the closed conformation of $(P)_4$- and $(M)_4$-**62**.

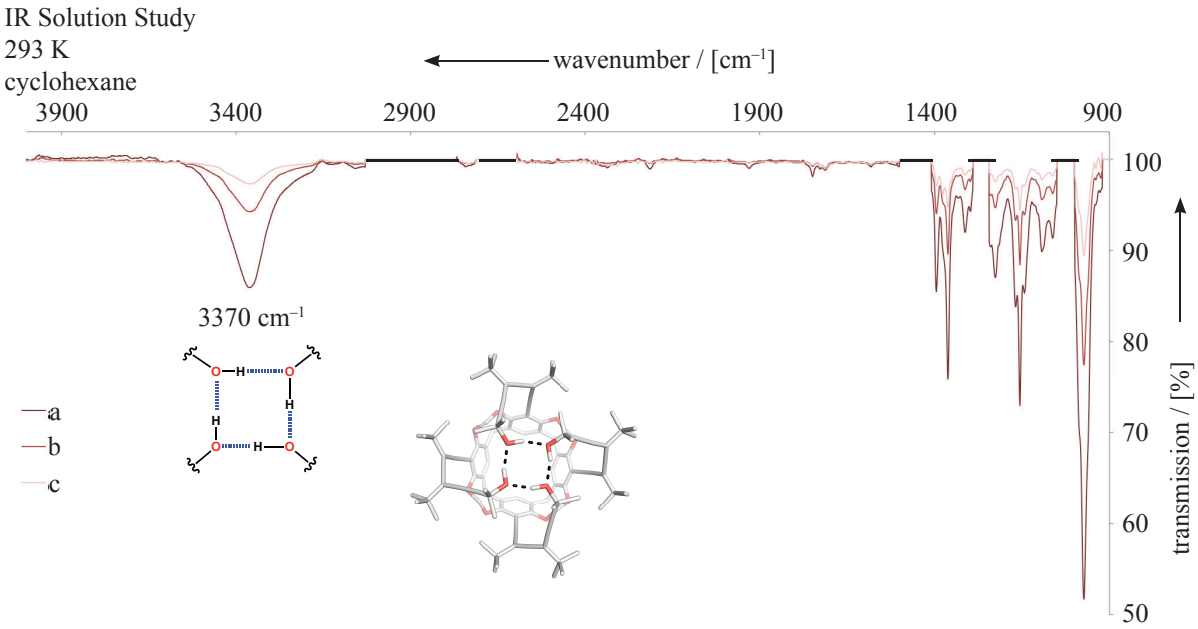

Figure 35. IR dilution study of AAC $(P)_4$-**62** in cyclohexane at 293 K displaying the characteristic cyclic OH hydrogen-bonding band at 3370 cm^{-1}. Concentration range: 10^{-3} to 10^{-4} M. Corresponding solvent bands are subtracted and marked in black.

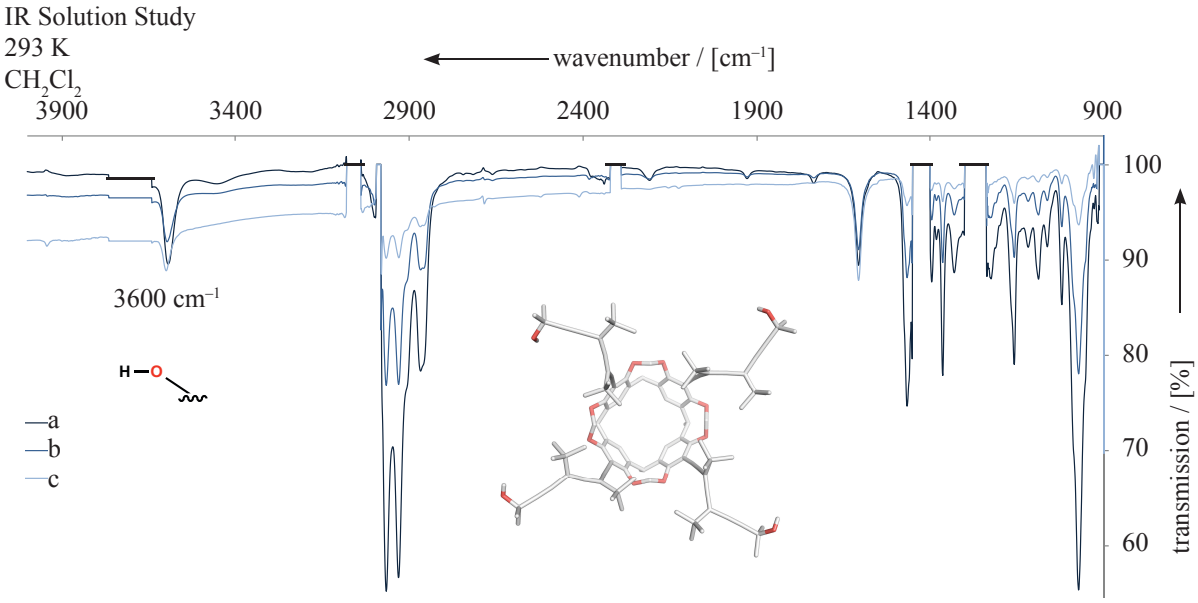

Figure 36. IR dilution study of AAC $(P)_4$-**62** in dichloromethane at 293 K displaying the characteristic free OH band at 3600 cm^{-1}. The band at 3690 cm^{-1} corresponds to traces of H_2O in the solvent. Concentration range: 10^{-3} to 10^{-4} M. Corresponding solvent bands are subtracted and marked in black.

2.6.4 ECD and UV/Vis Study on Conformational Switching of AACs $(P)_4$- and $(M)_4$-62

As conformation and symmetry are known to have large impact on the on the chiroptical properties (see Introduction, Figure 14), we expected the enantiopure AACs $(P)_4$/$(M)_4$-**62** to

display strong excitonic coupling of the alleno-acetylenic chromophores.[160] The ECD and UV/Vis spectra of both enantiomers of AACs $(P)_4$/$(M)_4$-**62** were recorded in cyclohexane and acetonitrile (Figure 37).

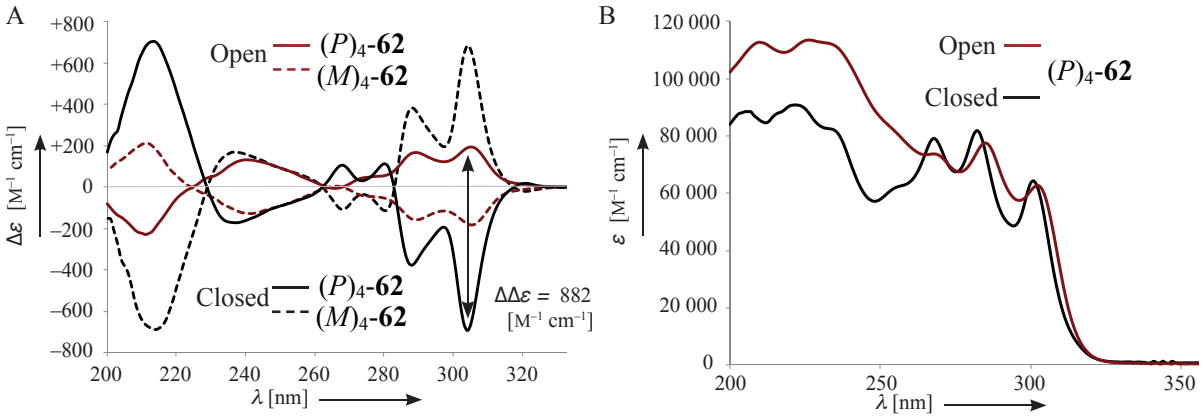

Figure 37. A: ECD spectra of AAC $(P)_4$-**62** (solid lines) AAC $(M)_4$-**62** (dotted lines) at 293 K. Spectra in red display AAC $(P)_4$-**62** and $(M)_4$-**62** in acetonitrile and spectra in black display corresponding traces in cyclohexane. Switching between the open and closed conformation results in $\Delta\Delta\varepsilon$ = 882 M^{-1} cm^{-1} at λ = 304 nm. B: UV/Vis spectra of AAC $(P)_4$-**62** in acetonitrile (red) and cyclohexane (black) at 293 K.

AAC $(P)_4$-**62** showed very large Cotton effects in cyclohexane at $\Delta\varepsilon$ = +700 M^{-1} cm^{-1} at λ = 214 nm and $\Delta\varepsilon$ = –691 M^{-1} cm^{-1} at λ = 304 nm (Figure 37, A). Upon changing the solvent from cyclohexane to acetonitrile, the Cotton effects inverted with lower absolute value in intensities: $\Delta\varepsilon$ = –231 M^{-1} cm^{-1} at λ = 214 nm and $\Delta\varepsilon$ = –191 M^{-1} cm^{-1} at λ = 304 nm (Figure 37, A). The $(M)_4$-configured enantiomer displayed mirror image ECD traces. This solvent-induced switching resulted in a very high value of $\Delta\Delta\varepsilon$ = 882 M^{-1} cm^{-1} at λ = 304 nm between the open and the closed conformation. Conformational stability in the closed H-bonded structure contributes to the exceptionally strong ECD properties of AAC $(P)_4$-**62** in cyclohexane. This effect decreased in the open, non-hydrogen-bonded conformation of AAC $(P)_4$-**62** in acetonitrile; the main difference certainly originating from the presence of the structure-rigidifying circular H-bonding array in the closed form and its absence in the open form. Importantly, the absorption of non-polarized light (through UV/Vis spectroscopy) was hardly affected by the nature of the solvent (Figure 37, B). This excluded the possibility of the formation of structures of higher order in any of the solvents.

In order to study the origin of the outstanding chiroptical properties, we analyzed the *g*-factor, which is defined as the ratio between the molar circular dichromism $\Delta\varepsilon$ and the molar extinction coefficient ε. AAC $(P)_4$-**62** showed Δg-factor values of 1.7×10^{-2} (cyclohexane → acetonitrile) at 304 nm (Figure 38). The larger *g*-factor value at 304 nm for the closed conformation clearly indicated a stronger contribution of the magnetic transition dipole

moment compared to the electric transition dipole moment. The obtained value is amongst the highest measured for pure organic compounds.[227,228]

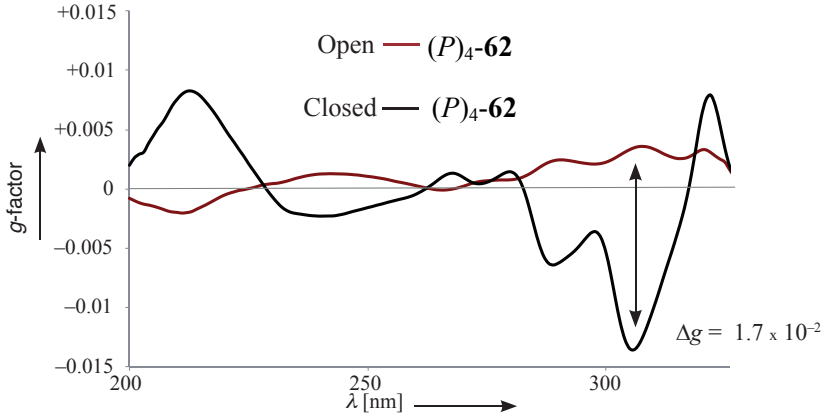

Figure 38. *g*-Factor plots ($\Delta\varepsilon/\varepsilon$) of AAC $(P)_4$-**62** in cyclohexane (solid black) and acetonitrile (solid red) with a maximum value of Δg of 1.7×10^{-2} at $\lambda = 304$ nm. Only $(P)_4$-configured enantiomers shown, (*M*)-configured AAC **62** display mirror image traces.

The comparison of AAC $(P)_4$-**62** with the "monomeric" model compound (*P*)-**64** (4x (*P*)-model system **64** ≈ AAC $(P)_4$-**62**) further substantiated the strong supramolecular chirality of the AAC enforced by the circular H-bonding array (Figure 39). While the (*P*)-model system **64** showed no solvent-dependent ECD properties with relatively low absorption, AAC $(P)_4$-**62** showed substantial solvent dependencies featuring strong absorption properties with $\Delta\varepsilon_{max}$ intensities around 100 time larger than its monomeric analogue (*P*)-**64**. The absorption intensities of non-polarized light (UV/Vis) of the model system (*P*)-**64** compared to the AACs $(P)_4$-**62**, however, were approximately the sum of the contributions of the four "monomeric" units (Figure 39, B).

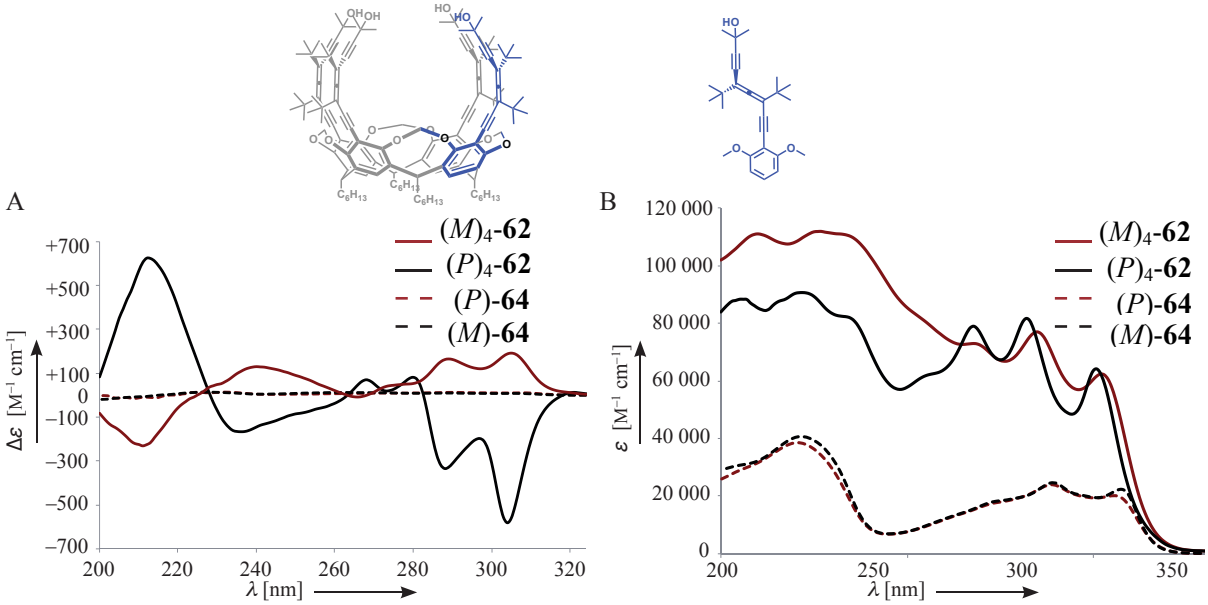

Figure 39. A: Overlay of ECD spectra of $(P)_4$-**62** in *n*-hexane (solid black) and acetonitrile (solid red) with (*P*)-model system **64** in *n*-hexane (dashed black) and acetonitrile (dashed red) at 293 K. Only (*P*)-configured enantiomers shown, *M*-configured structures displaed a mirror image traces. B: Overlay of UV/Vis spectra of $(P)_4$-**62** in *n*-hexane (solid black) and acetonitrile (solid red) with *P*-model system **64** in *n*-hexane (dashed black) and acetonitrile (dashed red) at 293 K.

2.6.5 Contribution of the Circular Hydrogen-Bonding Array to the Chiroptical Properties of AACs $(P)_4$- and $(M)_4$-62

In order to evaluate the contribution of the circular four-fold hydrogen-bonding array to the strong chiroptical properties of AACs, methylated analogues, namely AAC-$(OMe)_4$ $(P)_4$- and $(M)_4$-**65**, were prepared (Scheme 9).

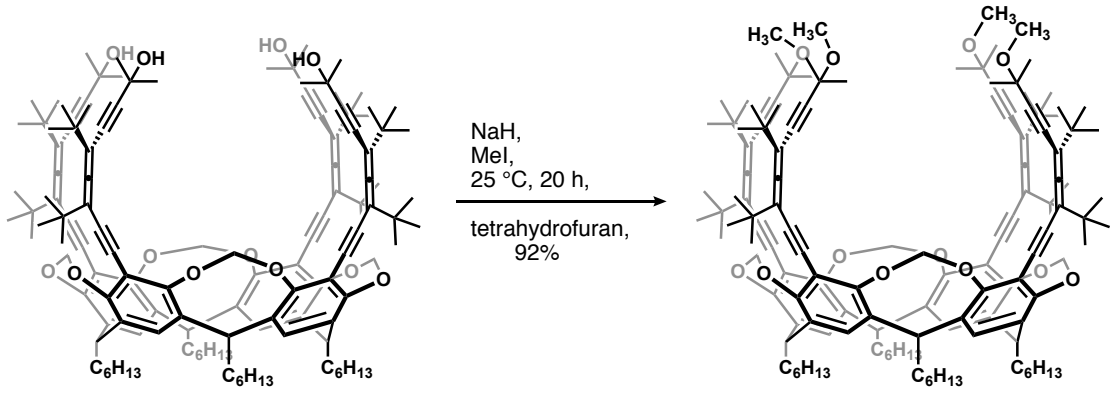

$(P)_4$-**62** $(P)_4$-**65**

Scheme 9. Reagents and conditions for the synthesis of the methylated analogues of AAC: (OMe)-AAC $(P)_4$-**65**. Only $(P)_4$-configured structure shown. $(M)_4$-configured **65** was obtained from $(M)_4$-configured AAC **62**.[192]

ECD properties of both compounds were compared in *n*-hexane, revealing a substantial difference in ECD intensities corresponding to $\Delta\Delta\varepsilon$ = 623 M^{-1} cm^{-1} at λ = 304 nm (Figure 40).

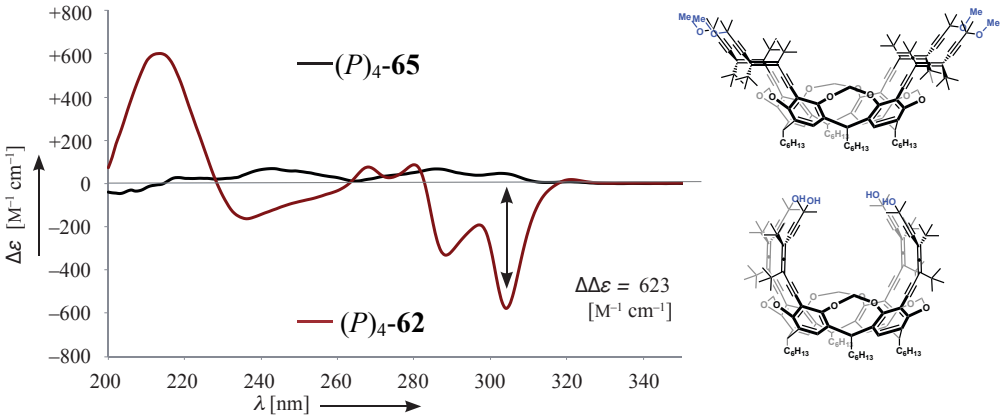

Figure 40. Evaluation of the contribution of the circular OH hydrogen-bonding array: ECD spectra of AAC $(P)_4$-**62** in *n*-hexane (solid red) and $(OMe)_4$-AAC $(P)_4$-**65** acetonitrile (solid black). Spectra measured at 293 K. Only *P*-configured enantiomer traces shown.

These results clearly showed that the methylated derivative $(OMe)_4$-AACs $(P)_4$- and $(M)_4$-**65** cannot be switched into the closed state, underlining the importance of the four-fold hydrogen-bonding array for the formation of the cage structure, contributing to the exceptional chiroptical properties.

2.6.6 Temperature-Dependence of the ECD Properties of AACs $(P)_4$- and $(M)_4$-62

Temperature-dependent ECD studies gave qualitative insight into the shape-persistency of the compounds of interest. The ECD traces of AAC $(P)_4$- and$(M)_4$-**62** were therefore recorded in a temperature range of 0–60 °C in acetonitrile (open conformation) and in *n*-hexane (closed cage conformation, Figure 41).

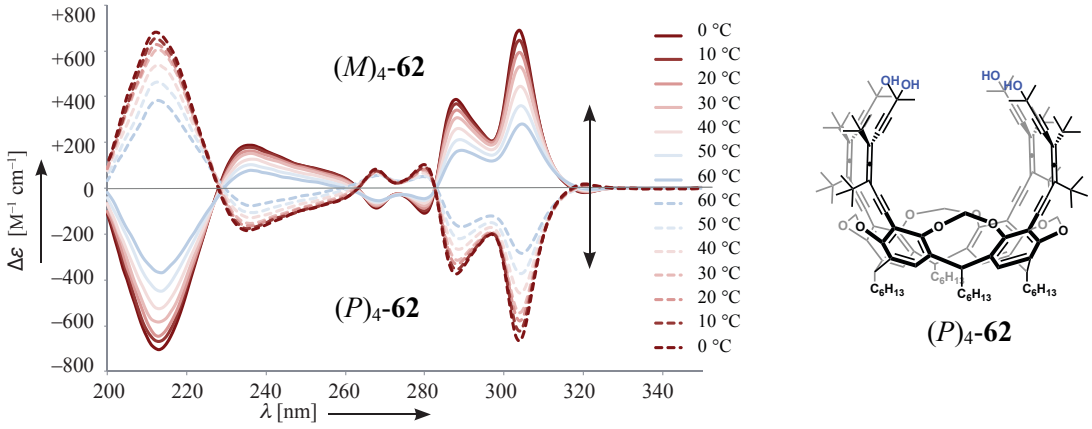

Figure 41. Overlay of ECD spectra of AACs $(P)_4$-**62** and $(M)_4$-**62** in *n*-hexane measured in the temperature range of 0–60 °C.

While AACs $(P)_4$- and$(M)_4$-**62** did not show significant temperature dependence in acetonitrile, strong temperature dependency was observed in *n*-hexane. In the temperature range of 0–60 °C, the ECD values decreased from 689 M^{-1} cm^{-1} to 275 M^{-1} cm^{-1} at 304 nm. This effect can be attributed to the fact that lower temperatures stabilize the closed hydrogen-bonded conformation while higher temperatures decrease the stabilization of the hydrogen-bonded array through increased "conformational wiggling" at elevated temperatures.

2.6.7 Solvent-Contribution to Conformational Switching of AACs $(P)_4$- and $(M)_4$-62

Although the increase in temperature weakened the ECD intensities of the AACs $(P)_4$- and $(M)_4$-**62**, it did not induce the conformational switching we had observed in changing the solvent from cyclohexane to acetonitrile (see Figure 37). To further elucidate the nature of the conformational switching, we measured ECD traces of AACs $(P)_4$- and $(M)_4$-**62** in solvents of varying polarity and size, assuming that both properties would contribute to the conformational preference of the receptor system.[192]

ECD signal intensities varied strongly with the solvents of different size and bulk dielectric properties (Figure 42).[229]

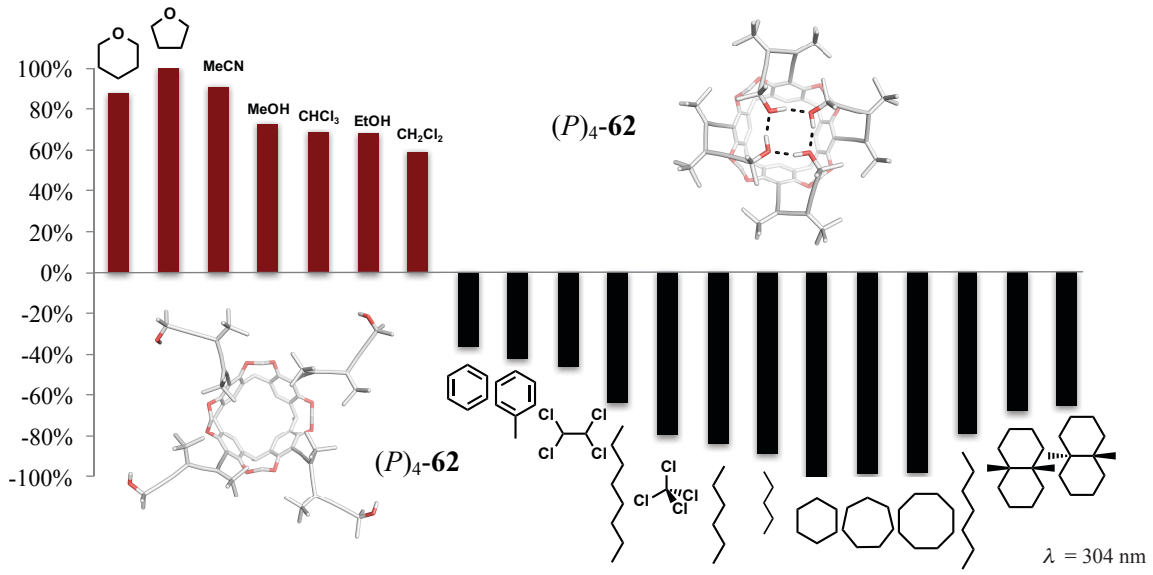

Figure 42. Conformational excess (*CE*, %) of AAC $(P)_4$-**62** in various solvents (relative values taken at λ = 304 nm). The ECD absorption AAC $(P)_4$-**62** at λ = 304 nm in cyclohexane for the closed conformation and in tetrahydrofuran for the open conformation was defined as maximum (100%, respectively).

The absorption of AAC $(P)_4$-**62** reached a maximum in the closed conformation with apolar solvents such as cyclohexane (ε_r = 2.02), cycloheptane (ε_r = 2.07), and cyclooctane (ε_r = 2.12, dielectric constants from Ref.[229]). Increasing the size further to decahydronaphthalenes (*cis*-decalin, ε_r = 2.20) decreased the ECD intensities. Smaller and

more polar solvents, such as tetrahydrofuran (ε_r = 7.58), stabilized the open conformation. Interestingly, the switching properties could not be reduced to the bulk properties of the solvent, but the size of the solvent, stabilizing one of the two conformations, had a considerable contribution. The conformational excess (*CE*, %) in each solvent was plotted in order to better visualize this effect and illustrate the solvent-induced conformational preferences. For this analysis, ECD absorption at λ = 304 nm were normalized and the intensities in cyclohexane (ε_r = 2.02) for the closed conformation and in acetonitrile (ε_r = 35.94) for the open conformation were set as their respective maximum (*CE* = +100 % and –100 %, respectively, Figure 42).

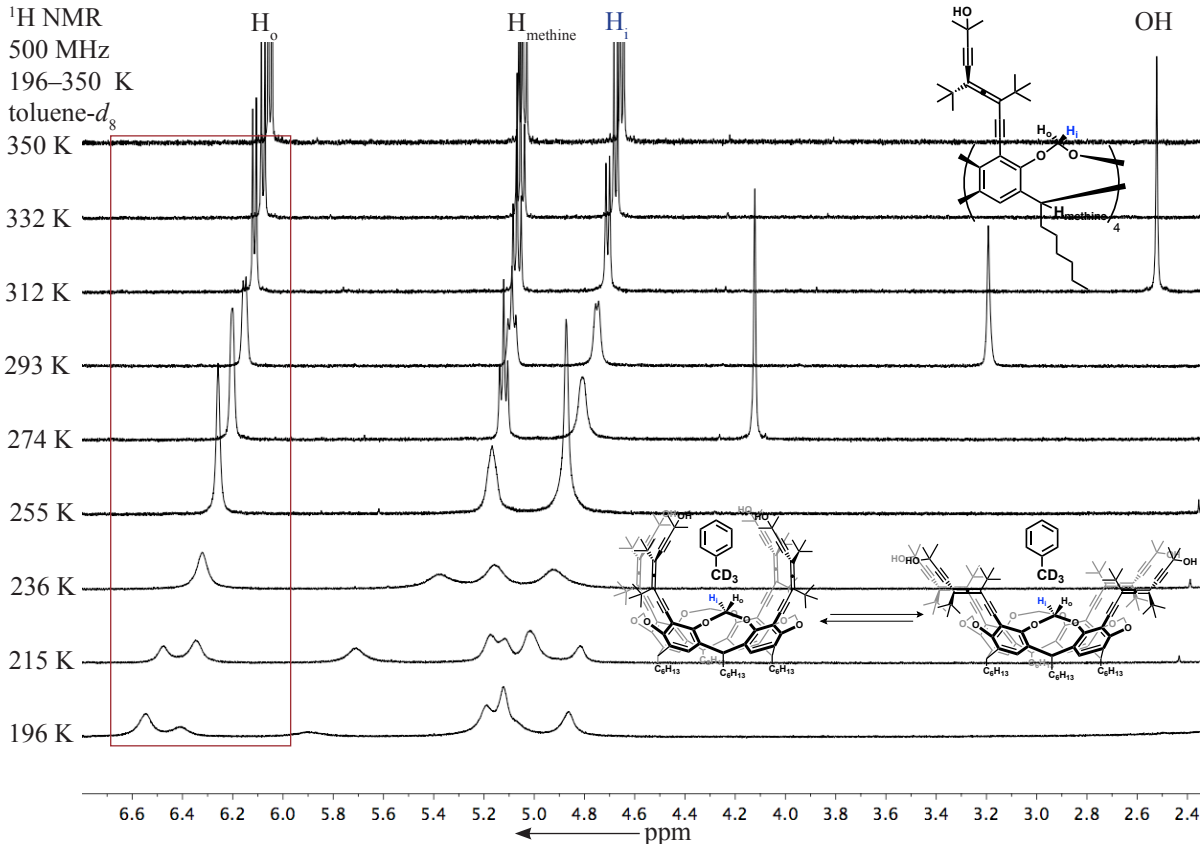

Figure 43. Temperature-dependent ^{1}H NMR study of AAC $(P)_4$-**62** in toluene-d_8 (from 350–196 K). At lower temperatures (215 and 196 K), the two discreet conformations of AAC $(P)_4$-**62** in toluene-d_8 appear. H_i = inside protons and H_o = outside protons of the methylene bridges.

Importantly, the solvent nature had little effect on the absorption of non-polarized light (UV/Vis traces). The predominant conformation in solution seemed to be determined both by solvent size and bulk dielectric properties (ε_r = 2.38), in agreement to binding to the closed or open state of the receptor. To further substantiate the effect of the solvent size, we compared AAC $(P)_4$-**62** and $(OMe)_4$-AAC $(P)_4$-**65** in different solvents of varying size.

2.6.8 Contribution of Solvent Size to Conformational Switching of AACs $(P)_4$- and $(M)_4$-62

Three exemplary ECD studies were undertaken with AAC $(P)_4$-**62** and $(OMe)_4$-AAC $(P)_4$-**65**.[192] Changing the solvent from *n*-hexane (ε_r = 1.88) to cyclohexane (ε_r = 2.02) increased the intensities of the ECD traces at λ = 304 nm (Figure 44, left).

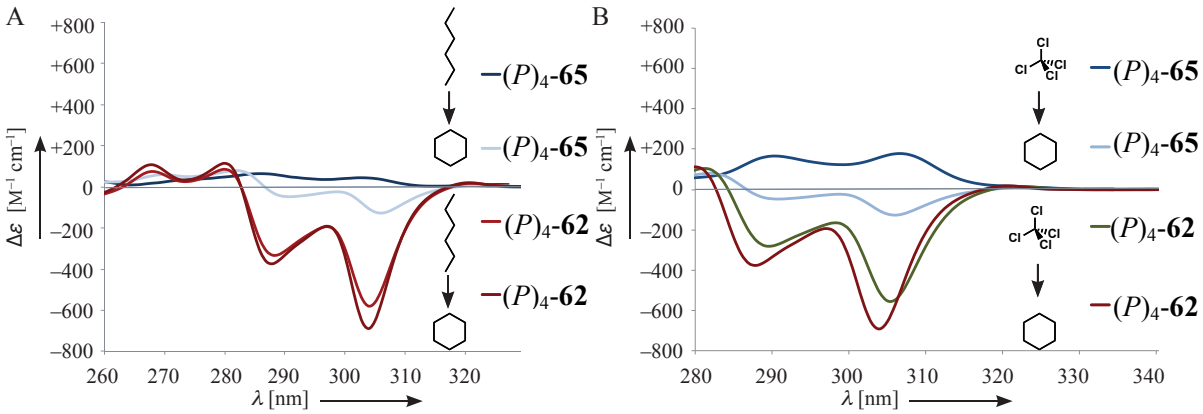

Figure 44. A: Evaluation of the contribution of solvent size by comparing *n*-hexane and cyclohexane with AAC $(P)_4$-**62** and -$(OMe)_4$-AAC $(P)_4$-**65**. B: Comparison of ECD spectra of AAC $(P)_4$-**62** and -$(OMe)_4$-AAC $(P)_4$-**65** in tetrachloromethane and cyclohexane. Spectra were measured at 293 K. Only (*P*)-configured enantiomer traces are depicted.

Both in the AAC $(P)_4$-**62** as well as its methylated analogue $(P)_4$-**65** the change in solvent favored the closed conformation, presumably due to better shape complementarity of cyclohexane within the interior of the receptor. A similar trend was observed in changing the solvents from tetrachloromethane (ε_r = 2.24) to cyclohexane (ε_r = 2.38). Again, cyclohexane appeared to have better shape complementarity. Most pronounced was the contribution of the solvent size to the conformational preferences of the receptor in the comparison of dichloromethane (ε_r = 8.93) and 1,1,2,2-tetrachloroethane (ε_r = 8.08, Figure 45). Although both solvents have comparable bulk properties, a switch from the open towards the closed state was observed with $\Delta\Delta\varepsilon$ = 453 M^{-1} cm^{-1} at λ = 304 nm.

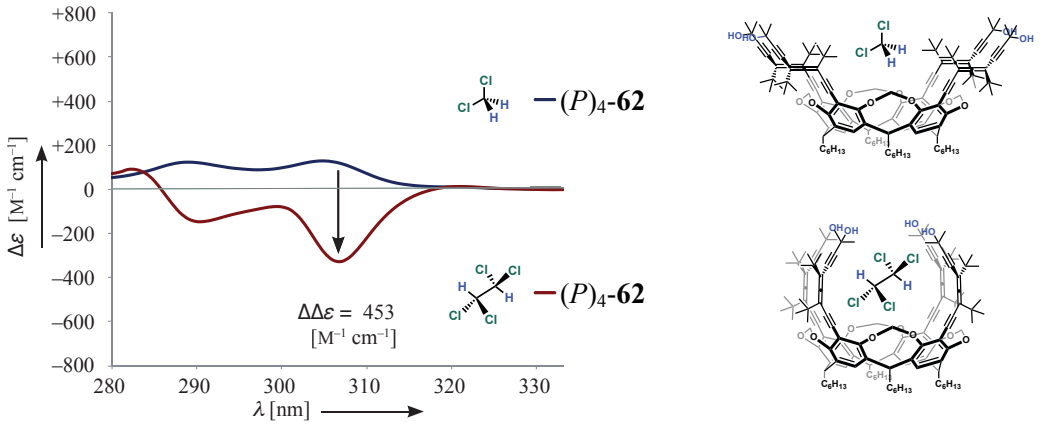

Figure 45. Comparison of ECD spectra of AAC $(P)_4$-**62** in dichloromethane (solid blue) and tetrachloroethane (solid red). While maintaining comparable bulk properties a size-induced conformational change corresponding to $\Delta\Delta\varepsilon = 453$ M^{-1} cm^{-1} was observed. Spectra measured at 293 K. Only (*P*)-configured enantiomer traces are depicted.

We concluded from these experiments that the bulk dielectric properties, shape complementarity and structural preorganization of the solvent determine the host conformation and the chiroptical properties of AACs $(P)_4$- and $(M)_4$-**62** in solution.

2.7 Single Crystal X-Ray Analysis of Binary Conformational States of AACs $(P)_4$- and $(M)_4$-62

Despite the constantly evolving techniques to characterize molecular structures, single crystal X-ray diffraction remains the most important method to provide accurate structural information with atomic resolution.[230-233] In order to substantiate the binary conformational switching also in the solid state, we set out to obtain single crystals suitable for X-ray diffraction from acetonitrile (open conformation in solution) and cycloheptane (closed conformation in solution).[192]

While the *n*-hexyl chains on the resorcin[4]arene cavitand ensured solubility in a wide range of organic solvents in solution, we envisaged shortening of the alkyl groups, such as to methyl groups, to aid crystallization. Accordingly, the tetramethyl footed cavitand **69** was synthesized following the protocol described for **59** (Scheme 10).

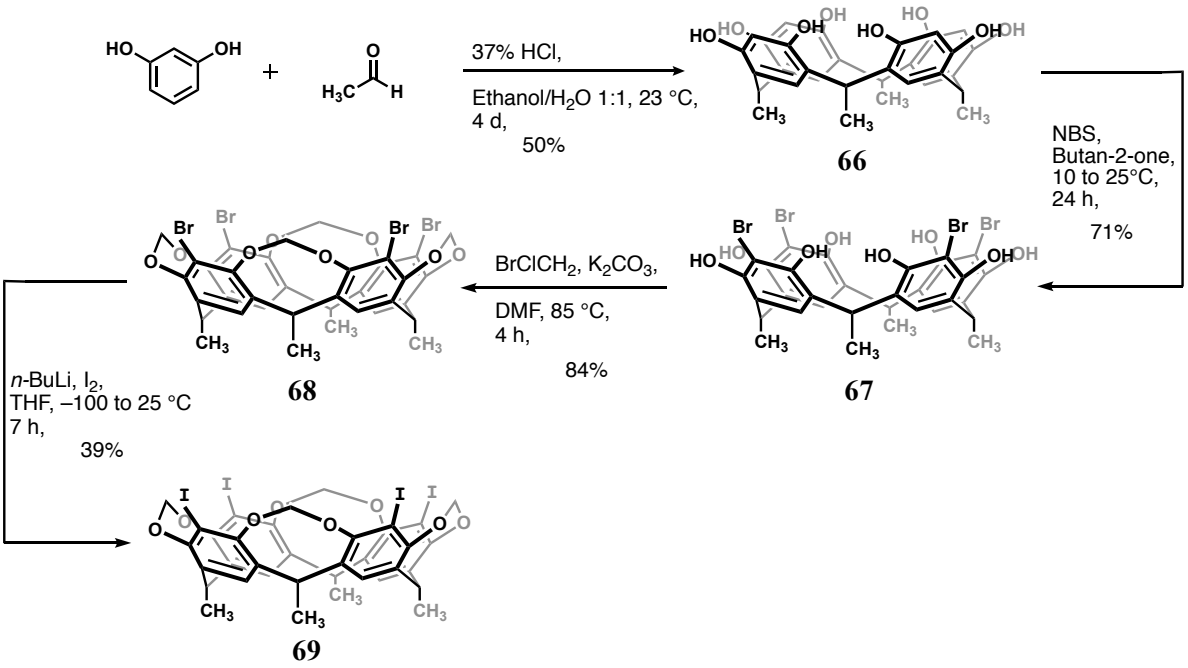

Scheme 10. Synthesis of tetraiodo resorcin[4]arene cavitand **69** from resorcinol and acetaldehyde.[216,217]

Condensation of acetaldehyde with resorcinol yielded octol **66**, which was subsequently brominated and methylene-bridged with 1,1'-bromochloromethane to afford cavitand **68**. Subsequent lithium-iodine exchange converted the tetrabrominated cavitand into the tetraiodo cavitand **69** in overall 12% yield. The preparation of **69** was then followed by Sonogashira cross-coupling with enantiopure DEA (*P*)- and (*M*)-**27** to afford AACs $(P)_4$- and $(M)_4$-**70** (Scheme 11).

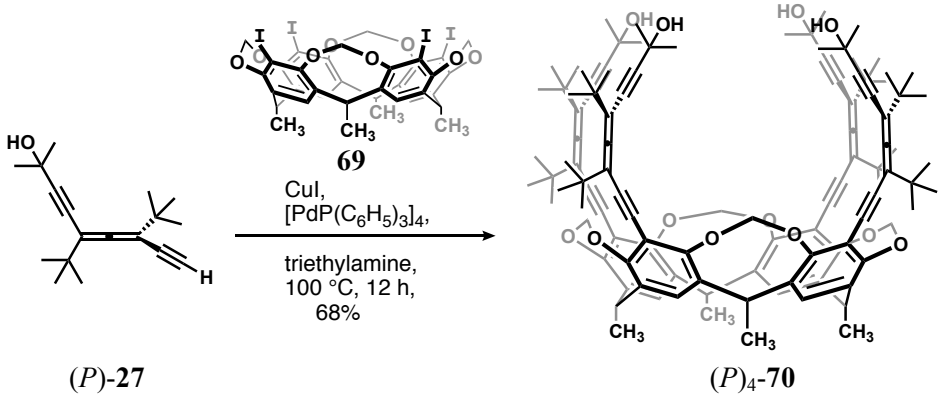

Scheme 11. Reagents and conditions for the synthesis tetramethyl-footed AAC $(P)_4$-**70** corresponding. Only (*P*)-configured structure shown. (*M*)-configured **70** were obtained from (*M*)-configured DEA **27**.

The yields of the four-fold cross-coupling of the DEA (*P*)- and (*M*)-**27** to the tetraiodo cavitand **69** were lower compared to the ones obtained for the synthesis of the hexyl-footed analogue (Scheme 7, 91%), presumably due to enhanced solubility of the hexyl-footed

cavitand **59** in triethylamine. The chiroptical properties in solution were comparable between AACs $(P)_4$- and $(M)_4$-**62** and **70** (see Experimental Part).

Both $(P)_4$- and $(M)_4$-configured **62** and **70** proved to be well soluble in organic solvents, but hardly soluble in water. In a first attempt to obtain single crystals suitable for X-ray diffraction of the cage receptors in the open conformation, we chose a mixture of acetonitrile/water, where acetonitrile was selected as a solvent that stabilizes the open conformation. Slow evaporation of acetonitrile increased the water content and induced crystallization. While methyl-footed AACs $(P)_4$- and $(M)_4$-**70** only gave microcrystalline materials, hexyl-footed AACs $(P)_4$- and $(M)_4$-**62** gave single crystals suitable for X-ray diffraction. The X-ray crystal structure of AAC $(P)_4$-**62** with one acetonitrile molecule occupying the open cavity is shown in Figure 46, A.

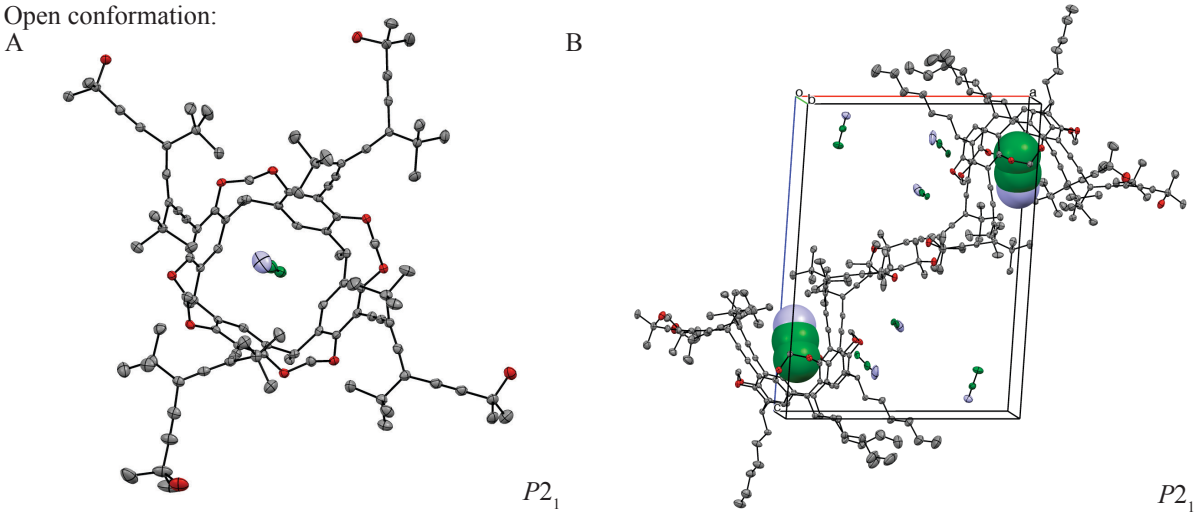

Figure 46. A: Top view of AAC $(P)_4$-**62** in the open conformation with one acetonitrile occupying the cavity (green). *n*-Hexyl-chains are omitted for clarity. B: Packing of AAC $(P)_4$-**62**⊃acetonitrile. Encapsulated acetonitrile is presented in the space filling representation. Space group: $P2_1$.

X-ray crystal structure of AAC $(P)_4$-**62** in the open conformation features the alleno-acetylenes moieties oriented outwards with their respective *tert*-butyl groups of the alleno-acetylenic backbone facing into the cavity (see Figure 46, A). The packing representation shows the AAC $(P)_4$-**62** engaged in intermolecular hydrogen bonding, resulting in the formation of two-dimensional hydrogen-bonded layers (Figure 46, B and Experimental Part).

Crystallization from an acetonitrile/water mixture with small amounts of cycloheptane resulted in the formation of single crystals of AACs $(P)_4$-**62** encapsulating one cycloheptane molecule (Figure 47). Again, only hexyl-footed $(P)_4$- and $(M)_4$-**62** resulted in the

formation of single crystals suitable for X-ray diffraction. Methyl-footed AACs $(P)_4$- and $(M)_4$-**70** formed microcrystalline material, which was unsuitable for X-ray diffraction.

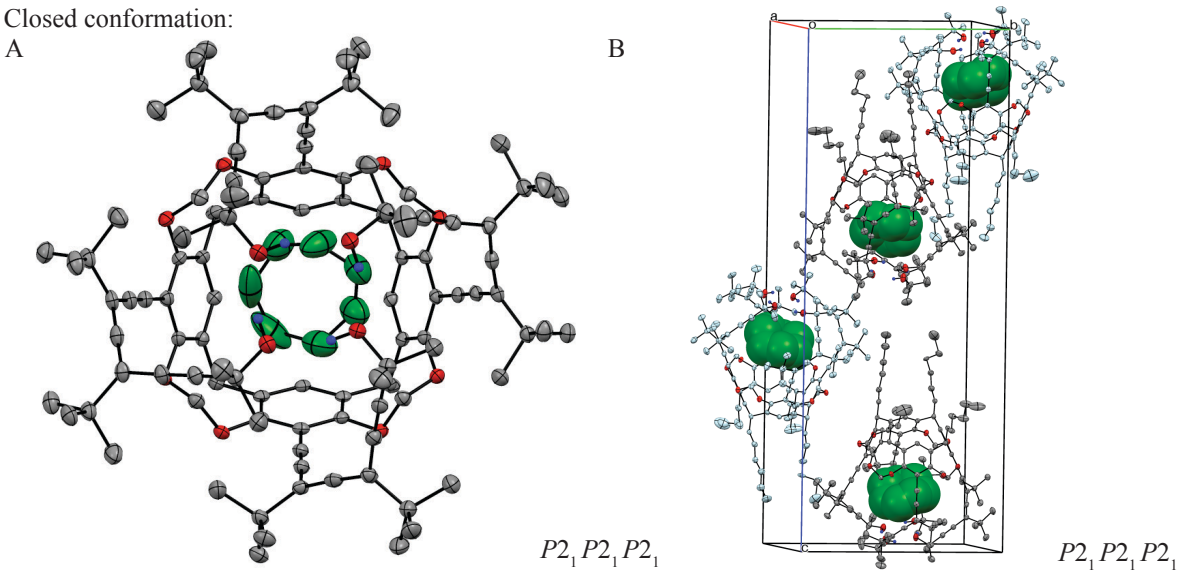

Figure 47. A: Top view of the AAC $(P)_4$-**62** in the closed hydrogen-bonded conformation with cycloheptane occupying the cavity (green). The circular hydrogen-bonding array is highlighted in dark blue. *n*-Hexyl chains are omitted for clarity. B: Packing of AAC $(P)_4$-**62**⊃cycloheptane; packing of the crystal structure of the AAC $(P)_4$-**62** in the closed hydrogen-bonded conformation with encapsulated cycloheptane shown in space filling representation. $(P)_4$-**62** are packed in a head-to-tail fashion with hydrophobic contacts. Residual acetonitrile molecules are omitted for clarity. Space group: $P2_1P2_1P2_1$.

X-ray co-crystal structure of AAC $(P)_4$-**62**⊃cycloheptane revealed the closed conformation, where the alleno-acetylenes are oriented inwards with the tertiary alcohols converging in a circular hydrogen-bonding array (Figure 47, A). The importance of the *n*-hexyl chains in the formation of the single crystals became apparent in analyzing the packing of $(P)_4$-AAC **62** (Figure 47, B). AAC $(P)_4$-**62** are aligned in a head-to-tail fashion with hydrophobic contacts of the *n*-hexyl chains with the alleno-acetylenic backbone. The absence of these contacts may explain the formation of microcrystalline material, unsuitable for X-ray diffraction, for the tetramethyl-footed AACs compared to tetrahexyl AACs $(P)_4$- and $(M)_4$-**62**.

The X-ray crystal structures of AACs $(P)_4$- and $(M)_4$-**62** confirmed our hypothesis of the binary conformational switching in the solid state and allowed us to obtain the molecular structures of both discrete states (Figure 48).

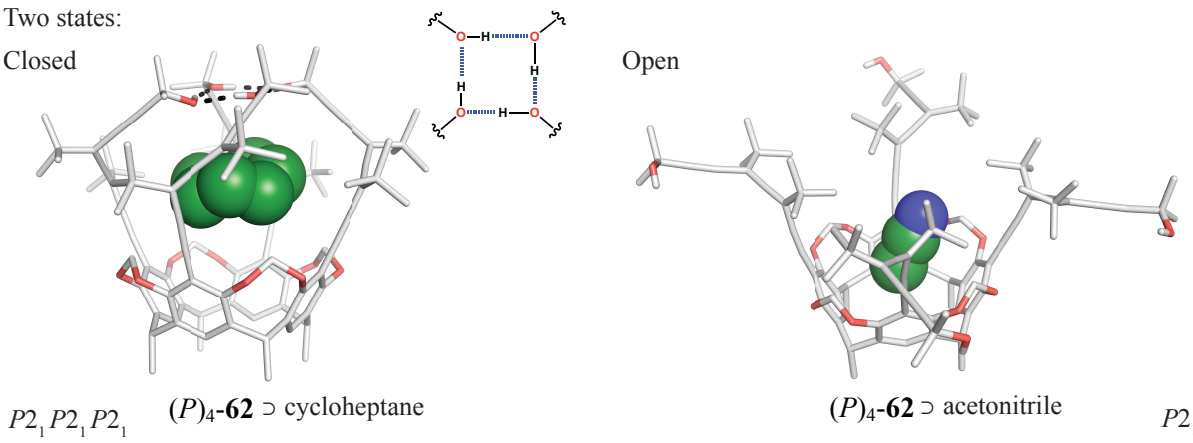

Figure 48. X-ray co-crystal structures of AAC $(P)_4$-**62** in the closed hydrogen-bonded conformation with cycloheptane occupying the cavity (left) and in the open state with acetonitrile occupying the cavity. *n*-Hexyl chains are omitted for clarity.

Our initial crystallization of AACs $(P)_4$- and $(M)_4$-**62** with cycloheptane resulted in the formation of co-crystals of the host–guest complexes, which enabled high-resolution structure determination of both the host and the encapsulated guest. A more general crystallization method was imagined to enable a crystallographic readout with information of the guest molecules in the interior of the receptor, complementary to our solution studies. The protocol we developed is based on the guest-induced binary conformational switching from the open to the closed state of the receptor. In acetonitrile/water 9:1 the AACs $(P)_4$- and $(M)_4$-**62** are in their open conformation. Upon addition of the guest molecules, e.g cycloheptane, AACs $(P)_4$- and $(M)_4$-**62** undergo conformational switching to the closed state encapsulating the cycloheptane and burying the polar tertiary alcohols in the hydrogen-bonding array. Sparing solubility of the closed receptor in acetonitrile/water facilitates nucleation of the host–guest complexes. A schematic representation is given in Figure 49.

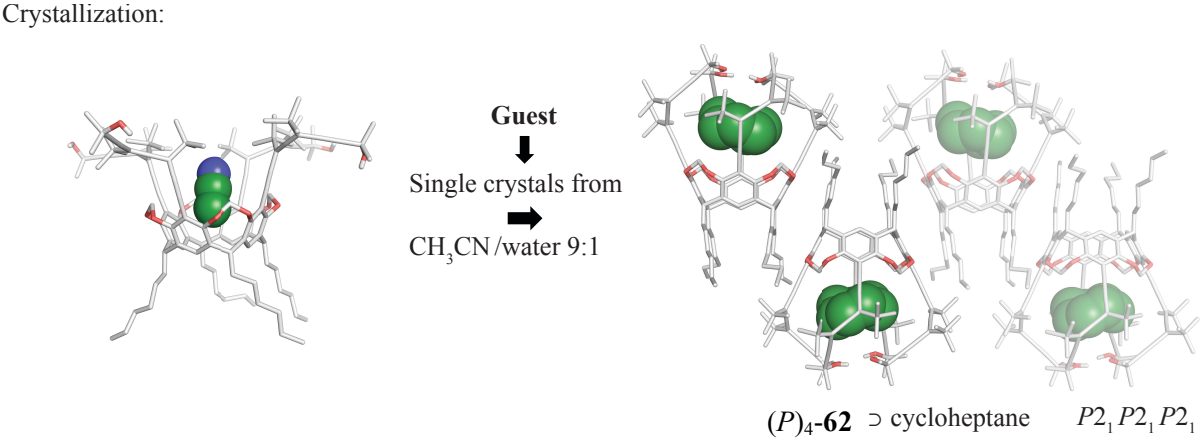

Figure 49. Schematic representation of the crystallization protocol developed for the complexation and crystallization of small molecules. Exemplary shown for AAC $(P)_4$-**62**.

The nature of the crystallization implies generally high occupancies for the guest molecules inside the cavity which constitutes a major advantage compared to other currently used host systems for the structure elucidation of small molecules.[234]

While most molecules and molecular complexes can in principle be crystallized, the disorder in their solid-state assemblies often prevents the determination of high-resolution structures.[231,232,235] Early techniques, such as clathrate-type inclusion into porous complexes, were developed to overcome these challenges.[236,237] Through inclusion into host lattices, the guest molecules interacted with the host, which could result in an ordering and lowering of their motional degrees of freedom. The effective decrease of the orientational disorder led in some cases to the structure determination of the ordered guest.[236,237] Prominent examples are the dianine complexes illustrated in Figure 50.[236]

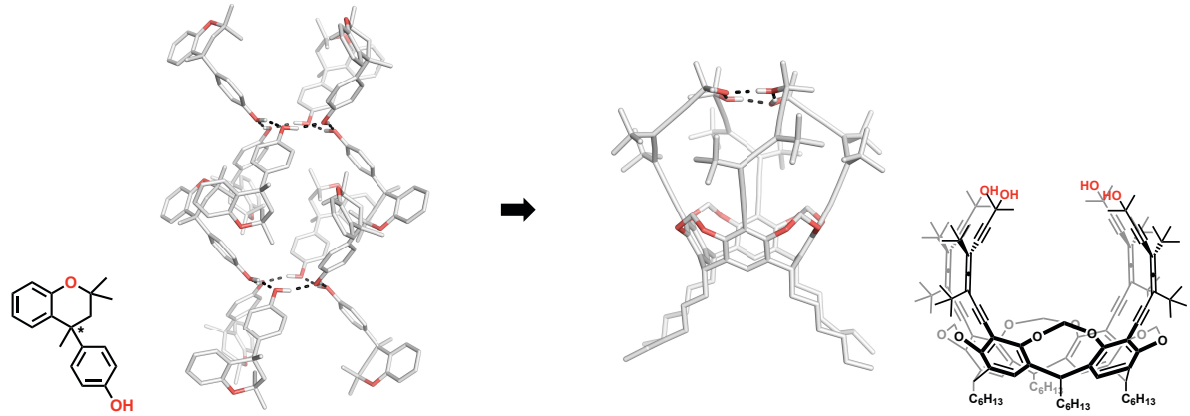

Figure 50. Comparison of clathrate-type inclusion complexation with (±)-4-*p*-hydroxyphenyl-2-2-4-trimethylchroman (left) and AAC receptors $(P)_4$-**62** (right). Guests are omitted for clarity.[192,236]

The formation of the racemic porous complexes in the solid state through the formation of a six-fold hydrogen-bonding is somewhat reminiscent of the AAC receptor system $(P)_4$- and $(M)_4$-**62**. More recently, coordination[238] or soaking of small molecules into crystalline metal–organic frameworks (MOFs) emerged as alternatives.[239] The main difference to the clathrate-type inclusion complexation and host-guest complexation is that the single crystals are formed prior to guest complexation. Suitable single crystals are subsequently soaked with the guest or the guests are coordinatively aligned into the host framework. The porous nature of the framework often results in large and open voids, capable of incorporating a large variety of molecules. The drawback remains that the porous nature often results in lower occupancies of the guest molecules and subsequent potential lower resolution.[234] In this context, molecular receptors which can form stable 1:1 host–guest

complexes and facilitate the structural elucidation of small molecules can be advantageous.[234,240]

2.8 Summary and Conclusion on Enantiopure AAC Receptors (*P*)$_4$- and (*M*)$_4$-62

Enantiopure alleno-acetylenic cage (AAC) receptors (*P*)$_4$- and (*M*)$_4$-**62** were constructed from a methylene-bridged resorcin[4]arene core to which four homochiral alleno-acetylenes with OH termini were attached to by four-fold Sonogashira cross-coupling, giving access to (*P)*$_4$- and (*M*)$_4$-configured AACs **62**.

The AAC receptors (*P*)$_4$- and (*M*)$_4$-**62** underwent solvent-dependent binary conformational switching between a closed cage conformation and an open state by rotation around a C–C bond. Both states were characterized in solution by NMR, IR, UV/Vis, and ECD spectroscopic studies and by single crystal X-ray diffraction in the solid state. In the closed cage conformation, the OH-termini of the alleno-acetylenic arms form a cyclic four-fold hydrogen-bonding array, which creates a highly confined cavity. The binary conformational switching was accompanied by strong changes in the associated ECD spectra with $\Delta\Delta\varepsilon$ = 882 M^{-1} cm^{-1} at λ = 304 nm, allowing for a sensitive spectroscopic readout of the conformational changes. The formation of the four-fold hydrogen-bonding array for the cage structure was identified to contribute to the exceptional chiroptical properties.

We concluded from ECD studies on AAC (*P*)$_4$-**62** and its methylated analogue (OMe)$_4$-AAC (*P*)$_4$-**70** that both shape complementarity and structural preorganization of the solvent determine the host conformation and the chiroptical properties of AACs (*P*)$_4$- and (*M*)$_4$-**62** in solution.

The combination of an interior capable of guest complexation together with the highly sensitive optical readout through ECD, along with crystallographic readout through the developed protocol, make AACs (*P*)$_4$- and (*M*)$_4$-**62** ideal receptor system for enantioselective complexation.

3. AAC Receptors: Enantioselective Complexation through Dispersion and Halogen-Bonding Interactions

The first part of this chapter was published as a communication in *Angewandte Chemie International Edition* and *Angewandte Chemie*: Alleno-Acetylenic Cage (AAC) Receptors: Chiroptical Switching and Enantioselective Complexation of *trans*-1,2-Dimethylcyclohexane in a Diaxial Conformation.[192] The second part of this chapter was published in a full article in the *Journal of the American Chemical Society*: Dispersion and Halogen-Bonding Interactions: Binding of the Axial Conformers of Monohalo- and (±)-*trans*-1,2-Dihalocyclohexanes in Enantiopure Alleno-Acetylenic Cages.[241] A recent review was published in *Chimia*: Complexation and Structure Elucidation of the Axial Conformers of Mono- and (±)-*trans*-1,2-Disubstituted Cyclohexanes in Enantiopure Alleno-Acetylenic Cage Receptors.[242] Theoretical studies were done by T. Husch and Prof. M. Reiher (ETHZ). Small-molecule single crystals were mounted by M. Solar, and X-ray structures were resolved by Dr. N. Trapp (ETHZ).

3 Enantioselective Complexation through Dispersion Interactions and Halogen-Bonding Interactions

Chapter 2 described the discovery of the enantiopure $(P)_4$- and $(M)_4$-configured AAC receptors **62** (Figure 51).[192] Its binary conformational switching accompanied by strong changes in the associated electronic circular dichroism (ECD) spectra of the AACs $(P)_4$- and $(M)_4$-**62** introduced a sensitive spectroscopic readout to identify and quantify guest binding in solution. Additionally, the developed crystallization protocol allowed us to obtain structural information of the complexed guest molecules (Figure 51, B). In order to get first insights into the interior of AAC $(P)_4$-**62** we calculated the electrostatic potential map (Figure 51, C).[241]

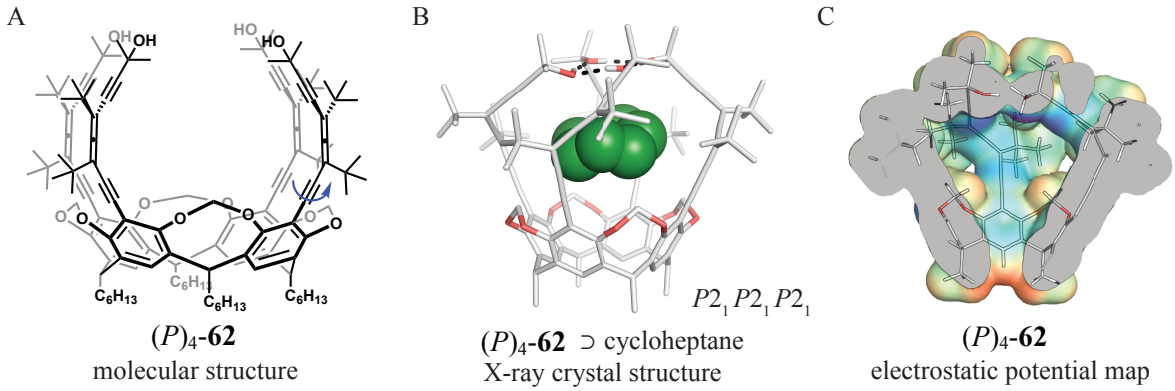

Figure 51. A: Molecular structure of AAC $(P)_4$-**62**; blue arrow indicates conformational switching towards the open state (around the C–C bond). B: X-ray co-crystal structure of AAC $(P)_4$-**62**⊃cycloheptane; hydrogen atoms and *n*-hexyl chains are omitted for clarity; cycloheptane in green (sphere representation). C: electrostatic potential map of AAC $(P)_4$-**62** based on the data calculated in Ref.[241]

On the outer surface, the receptor is largely characterized by a neutral electrostatic potential, while the interior of the receptor contains areas of more negative electrostatic potential associated with the alcohols in the closed form, and with the aromatic and acetylenic moieties within the host. This analysis enabled first insights that guests, such as pure hydrocarbons and alkyl halides, could interact favorably with the interior of the receptor.

3.1 Enantioselective Complexation through Dispersion Interactions

In the recognition of pure hydrocarbons, host–guest interactions solely rely on relatively weak dispersive interactions and CH···π contacts. The absence of directional interactions makes shape complementarity of the guest to the interior of the host crucial. Based on the structural information obtained from AAC $(P)_4$-**62** encapsulating cycloheptane, we chose a series of larger, mainly six and seven membered cyclic hydrocarbons for the closed cage and smaller,

five-membered hydrocarbons to study the binding of the cage receptor in the open conformation (Figure 52).[192]

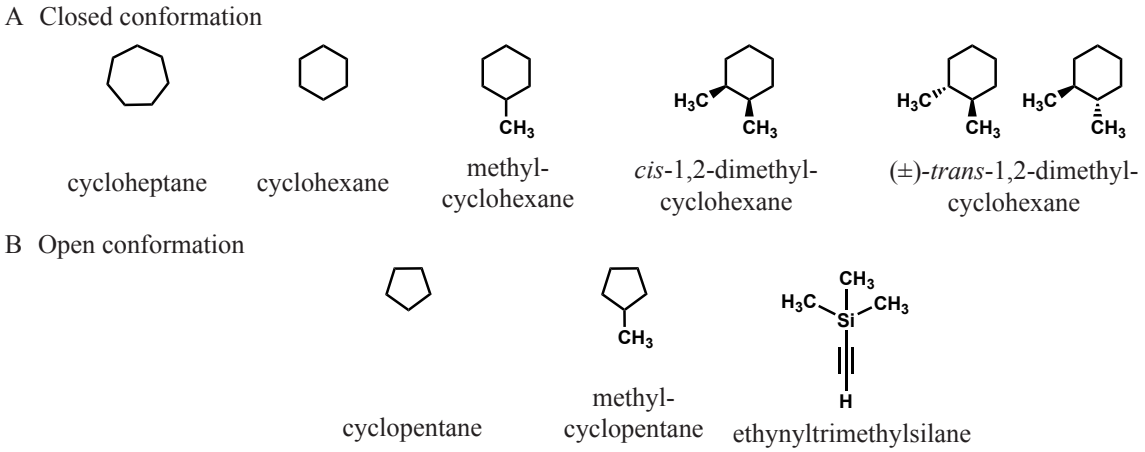

Figure 52. Structures of selected hydrocarbons for the complexation studies of AAC $(P)_4$/$(M)_4$-**62** in the open and in the closed conformation.

3.1.1 Solution Binding Studies of Hydrocarbons with AACs $(P)_4$- and $(M)_4$-62

Development of the solvent system

The choice of an appropriate solvent was evaluated prior to ECD and NMR titration experiments. The crucial factor was believed to be the use of non- or weakly competitive solvents, nonetheless maintaining some preorganization of either host conformation. Importantly, for ECD titrations it was necessary to choose UV/Vis-silent solvents (~200 nm–250 nm). We chose *n*-octane as apolar solvent, which was too large and too dynamic to fully enable the closed conformation, but nevertheless assured a certain degree of preorganization of the cage form (*CE* = –79%, Figure 42 and 53). *n*-Octane gave similar binding isotherms compared to the well-established mesitylene as non-competitive solvent for binding studies with resorcin[4]arene cavitands. An exemplary comparison of the binding isotherms was made for cycloheptane in both mesitylene and *n*-octane giving similar values. Methanol (*CE* = +72%, Figure 42 and 53) was chosen to provide some degree of preorganization to the open form, as tetrahydrofuran was too competitive as guest for the open conformation.

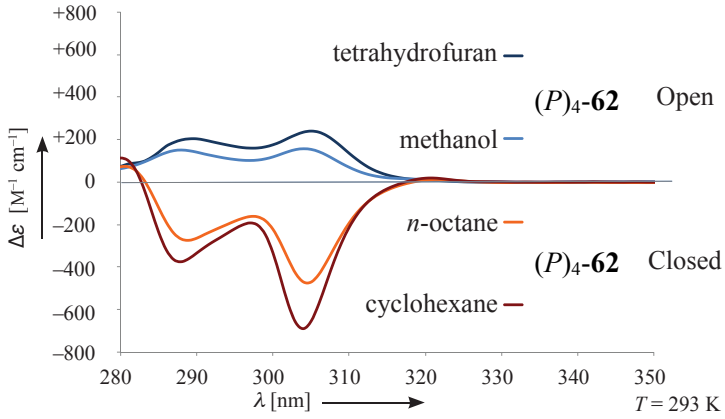

Figure 53. *n*-Octane and methanol were chosen as solvents for ECD and NMR studies. The size and polarity make them relatively weak competitive solvents. As UV/Vis-silent solvents they allow measurements down to 200 nm in ECD. Only traces of $(P)_4$-configured AAC **62** are shown.

Determination of Dimerization:

In order to compare binding isotherms which were to be acquired at different concentrations by NMR (~10 mM) and ECD (~10 μM) spectroscopies, dilution studies were performed on AAC $(P)_4$-**62** in both methanol and *n*-octane. Although various mechanisms of aggregation are possible, we assumed, if at all, dimerization to occur. For a detailed description of the dimerization studies, see the Experimental Part. AAC $(P)_4$-**62** in *n*-octane-d_{18} gave a dimerization constant of K_{dim} = 101 M^{-1} and in CD_3OD of K_{dim} = 293 M^{-1}. Although, the dimerization constants are relatively weak, they cannot be neglected for weaker binding guests, such as pure hydrocarbons. We therefore refer to apparent association constants whenever discussing weaker binding guests.

Determination of the Binding Stoichiometry

In order to determine the binding constants and the free enthalpy of complexation, the binding stoichiometry had to be established. X-ray co-crystal structure of AAC $(P)_4$-**62**⊃cycloheptane indicated 1:1 binding stoichiometry in the solid state. For solution studies, we applied the Job's method of continuous variations by the ^{1}H NMR spectroscopy (Figure 54).[181-183] A more detailed description is given in the Experimental Part. The maximum at around 0.5 indicates 1:1 host to guest stoichiometry.

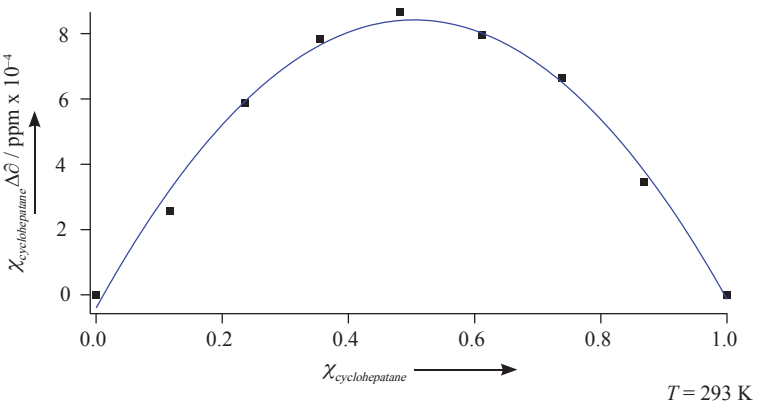

$\chi_{Cyclohept}$	$\chi_{Cyclohept}$ ($\Delta\delta_{Hi}$)
0	0
0.12	2.56 x 10^{-4}
0.24	5.89 x 10^{-4}
0.36	7.82 x 10^{-4}
0.48	8.66 x 10^{-4}
0.61	7.95 x 10^{-4}
0.74	6.65 x 10^{-4}
0.87	3.47 x 10^{-4}
1.00	0

Figure 54. Job's plot of binding between AAC $(P)_4$-**62** and cycloheptane in *n*-octane-d_{18} at 293 K.

Determination of the Binding Constants through ^{1}H NMR and ECD Spectroscopy

The determination of the apparent binding constant via NMR spectroscopy is explained in detail in the Experimental Part. Proton resonances depicted in Figure 55 were followed during NMR spectroscopic titrations. The apparent binding constants were determined by non-linear least-square curve fitting of the observed changes in $\Delta\delta$ (ppm) of the identified protons and plotted against the respective guest concentration at fast host–guest exchange on the NMR timescale.

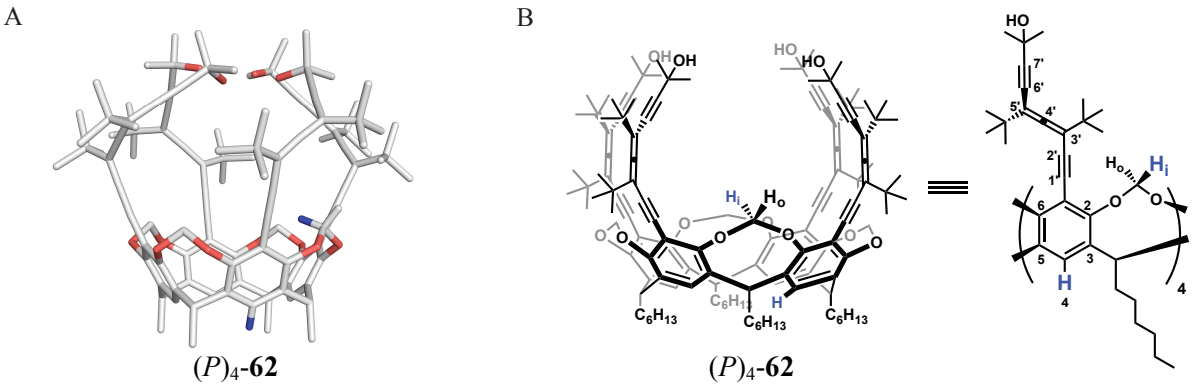

Figure 55. A and B: Protons of AAC **62**, which were followed for the determination of the apparent binding constants by NMR spectroscopy, are highlighted in blue. Only (*P*)-configured structures are shown.

During ECD titrations, the change in $\Delta\Delta\varepsilon$ (M^{-1} cm^{-1}) at 304 nm was followed and plotted against the respective guest concentration. Non-linear square curve fitting, assuming a 1:1 binding enabled determination of the corresponding binding constants.

Summary of Apparent Binding Constants of AACs $(P)_4$- and $(M)_4$-62

As a general note, the ECD titrations had much higher accuracy and provided more reliable data since the large changes in band intensity were recorded in all titrations while the observed changes in chemical shift in the ^{1}H NMR spectra were smaller and therefore more error prone

(see Experimental Part).[192] The difference in binding constants obtained by ^{1}H NMR and ECD measured in deuterated and non-deuterated *n*-octane was explained by the concentration-dependent self-dimerization (Table 3). We restrict our discussion of the binding data to the values obtained through ECD spectroscopy. AAC $(P)_4$-**62** in the open conformation in methanol showed only weak complexation of cyclopentane, methylcyclopentane, and triisopropylsilylacetylene with K_{app} = 6–19 M^{-1} (Table 3).

Table 3. Apparent binding constants (K_{app}) at 293 K determined by ^{1}H NMR and ECD spectroscopies for various guests by $(P)_4$-AAC **62** in the closed (*n*-octane or *n*-octane-d_{18}) and open (methanol or methanol-d_4) conformation.[192]

Guest	^{1}H NMR K_{app} [M^{-1}]	^{1}H NMR[a] $\Delta G_{293\ K}$ [kcal mol^{-1}]	ECD K_{app} [M^{-1}]	ECD[a] $\Delta G_{293\ K}$ [kcal mol^{-1}]
in *n*-octane: closed conformation				
cyclohexane	<1	–	<1	–
Cycloheptane	60[b]	–2.4	141	–2.9
Methylcyclohexane	28	–1.9	22	–1.8
Cis-1,2-dimethylcyclohexane	173	–3.0	347	–3.4
(±)-*Trans*-1,2-dimethylcyclohexane	67[c]	–2.4	107[c]	–2.7
in methanol: open conformation				
Cyclopentane	2	–0.4	6	–1.0
Methylcyclopentane	7	–1.1	8	–1.2
Triisopropylsilyl-acetylene	17	–1.7	19	–1.7

The overall error was estimated to be in the range of 20%. [a] The Gibbs binding energy was calculated from $K_{app\ 293\ K}$. [b] Cycloheptane bound in mesitylene-d_{12} with 59 M^{-1}. [c] Binding of (±)-*trans*-1,2-dimethylcyclohexane with $(M)_4$-**62** gave comparable values compared to AAC $(P)_4$-**62**: K_{app} = 66 M^{-1} by ^{1}H NMR and 148 M^{-1} by ECD.

The observed complexation was presumably largely driven by the hydrophobic effect of the guests in methanol. The binding data confirmed the weak complexation ability of the receptor in the open conformation. Binding affinities of AAC $(P)_4$-**62** in the closed conformation in *n*-octane were significantly enhanced. With the absence of polar solvents, the

apparent binding constants K_{app} can be largely attributed to favorable dispersive interactions of the guest with the host. While cyclohexane did not show any measurable binding to $(P)_4$-**62**, methylcyclohexane and cycloheptane gave binding constants of K_{app} = 22 M^{-1} and 140 M^{-1}, respectively. *cis*-1,2-Dimethylcyclohexane showed enhanced binding of K_{app} = 341 M^{-1}. The increase can be explained with the better size-complementarity from methylcyclohexane to *cis*-1,2-dimethylcyclohexane. The binding of the *trans*-isomer of (±)-1,2-dimethylcyclohexane, however, showed weaker binding to AAC $(P)_4$-**62** of K_{app} = 107 M^{-1}. The (*M*)-configured receptor **62** gave comparable binding affinities to the racemic (±)-*trans*-1,2-dimethylcyclohexane (see Table 3). The decrease in binding affinity from *cis*-1,2-dimethylcyclohexane to (±)-*trans*-1,2-dimethylcyclohexane by a factor of three was intriguing and we set out to obtain the crystal structures of this series of host–guest complexes.

X-Ray Co-crystal Structures Obtained from AAC $(P)_4$- and $(M)_4$-62 with the Guests

Single crystals of AACs $(P)_4$- and $(M)_4$-**62** with co-crystalized guests were obtained following the protocol described in Chapter 2.[192] Slow diffusion of H_2O into a solution of acetonitrile/H_2O/guest/host (8.9:1:0.1:0.01) at 25 °C over three to fourteen days gave single crystals of the host–guest complexes as colorless plates or needles. For this compound class, the presented X-ray co-crystal structures show comparatively high resolution and low *R* values, meeting generally accepted small molecule crystal structure publication standards (see Experimental part for detailed description). Figure 56 shows the X-ray co-crystal structures of AAC $(P)_4$-**62** with cyclohexane, methylcyclohexane, and *cis*-1,2-dimethylcyclohexane.

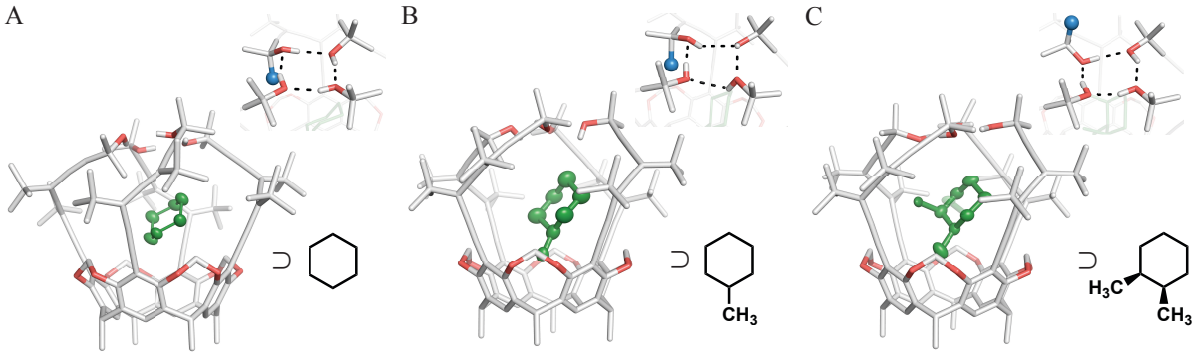

$(P)_4$-**62** $(P)_4$-**62** $(P)_4$-**62**

Figure 56. X-ray co-crystal structures of AAC $(P)_4$-**62**⊃guests (space group); A: AAC $(P)_4$-**62**⊃cyclohexane ($P2_1P2_1P2_1$); B: AAC $(P)_4$-**62**⊃methylcyclohexane($P2_1$); AAC $(P)_4$-**62**⊃*cis*-1,2-dimethylyclohexane ($P2_1P2_1P2_1$). Guests are shown in green in their ellipsoid representation. *n*-Hexyl chains are omitted for clarity. The four-fold circular hydrogen bonding array is shown for all complexes. Depending on the size of the guest, the receptor compensates for the missing space filling of the guest by rotating one methyl group into the cavity (highlighted as blue ball in A–C).[192]

In this series, the AAC $(P)_4$-**62** showed an interesting feature, where the receptor adjusted the size and shape of the cavity to the guest. For cyclohexane and methylcyclohexane the host compensated for the missing shape complementarity by rotating one of the methyl groups of the tertiary hydrogen-bonding array into the cavity. The rotated methyl group is highlighted as a blue ball (Figure 56). By introducing an additional methyl group, such as in *cis*-1,2-dimethylcyclohexane and thereby increasing the size of the guest further, the guest properly filled the cavity and all methyl groups of the H-bonding array were rotated outside of the cavity (Figure 56, C).

In order to further evaluate the adaptable nature of the host to optimize the packing coefficient of the ensemble, we calculated the packing coefficients from the crystallographic data (*PC*, see Experimental Part for description of the method). A total of six volumes were calculated for the closed cage conformer with three different probe sizes of 1.0 Å, 1.2 Å and 1.4 Å. Table 4 gives the values of the calculated cavity volumes with the probe sizes of 1.0 Å and the obtained packing coefficients.[214] The volumes of the guests were calculated using the same software.[214] The choice of the adequate probe size was essential for satisfying volume estimations. In this case, a probe size of 1.0 Å was in best agreement with the Mecozzi-Rebek volume occupancy rule of 55%, originally derived for apolar capsules (Table 4).[59]

Table 4. Calculated packing coefficients of the X-ray co-crystal structures of AAC $(P)_4$-**62** with cyclohexane, methylcyclohexane, and *cis*-1,2-dimethylcyclohexane from the crystallographic data (Figure 56). The radius of the probe size is given in brackets. Packing coefficients (*PC*, ratio of guest volume to host volume) are given in %.[214]

	AAC $(P)_4$-**62**	AAC $(P)_4$-**62**	AAC $(P)_4$-**62**	AAC $(P)_4$-**62**
		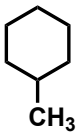		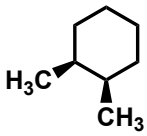
Cavity V/(Å^3) (1.0 Å)	191	190	220	221
Guests V/(Å^3)	94	111	109	128
PC /% (1.0 Å)	**49**	**58**	**50**	**58**

With a probe size of 1.0 Å, volumes of the host $(P)_4$-**62** of 190–223 Å^3 were calculated, resulting in packing coefficients ranging from 49–58%. An increase in guest size from e.g. methylcyclohexane to *cis*-1,2-dimethylcyclohexane was accompanied by an increase in host volume of 14% (ca. 190 Å^3 → 220 Å^3), thus optimizing space filling of the ensemble

in maintaining the ideal packing coefficient of *ca.* 55%.[59] Figure 57 illustrates this size adaptability of the receptor with cyclohexane and *cis*-1,2-dimethylcyclohexane complexed by AAC $(P)_4$-**62**.

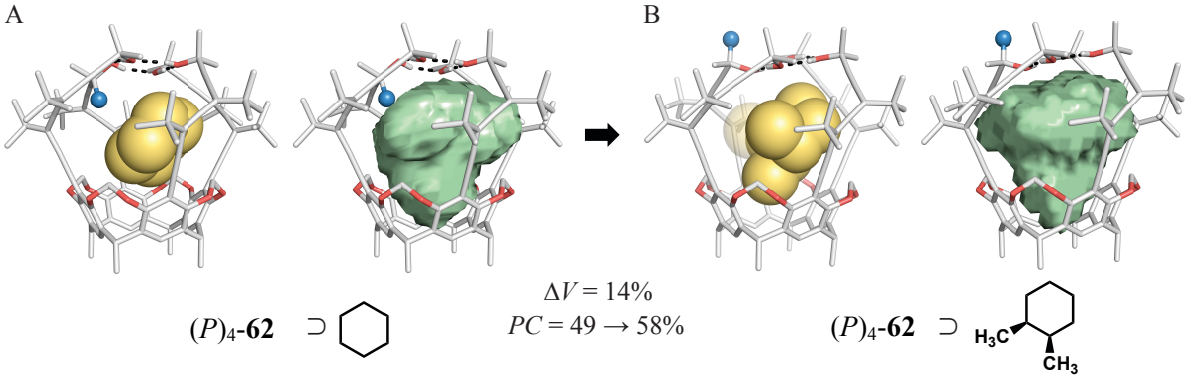

Figure 57. AAC $(P)_4$-**62** with encapsulated cyclohexane (A) and *cis*-1,2-dimethylcyclohexane (B) in the spherical model representation in yellow (taken from the X-ray co-crystal structures) and visual representation of the volume in green calculated by VOIDOO.[214] Probe size with a radius of 1.0 Å was chosen. A cavity volume difference of 14% was measured with *PC* increasing from 49 to 58%.

With *cis*-1,2-dimethylcyclohexane, we had identified a guest molecule, which optimally filled the cavity of the AACs $(P)_4/(M)_4$-**62** (*PC* = 58%).

It was long postulated that the enantiomers of *cis*-1,2-dimethylcyclohexane, which rapidly interconvert at room temperature via an achiral transition state yielding an achiral structure, cannot be individually isolated.[98,243] Only at low temperatures (ca. –150 °C) the isolation of both enantiomers has been proposed, but was never reported, probably due to technical challenges.[98] The X-ray co-crystal structure of AAC $(P)_4$-**62** with *cis*-1,2-dimethylcyclohexane showed two equally populated (50:50%) occupancies of the guest molecule (Figure 56). The two populations of the guest observed in the X-ray crystal structure arises from the two individually observed enantiomers in the cage. While AAC $(P)_4$-**62** did not show any selectivity towards one enantiomer (50:50%), this was the first experimental observation of both enantiomeric conformers of *cis*-1,2-dimethylcyclohexane.[192] It can be assumed that the interconversion of the enantiomeric conformers via the achiral transition state also occurs in the capsule. No X-ray crystal structure of this compound has been previously reported. The *gauche* torsional angle Me–C(1)-C(2)-Me of the enantiomeric conformer corresponded to –67.6° and +57.7°, respectively. For details of the guest conformation see the Experimental Part.[192]

At the optimal packing coefficient, dispersion interactions are optimized and we were curious to study the enantioselectivity of the receptors towards chiral cyclic alkanes.[59]

Compared to the overall achiral *cis* isomer, the enantiomers of (±)-*trans*-1,2-dimethylcyclohexane do not interconvert at room temperature. Each enantiomer of (±)-*trans*-1,2-dimethylcyclohexane has two conformers, the more stable diequatorial and the less stable diaxial one (Figure 58, middle). We set up crystallization of both the (*P*)- and the (*M*)-configured AACs **62** with the racemic (±)-*trans*-1,2-dimethylcyclohexane. Figure 58 shows the obtained X-ray co-crystal structures.

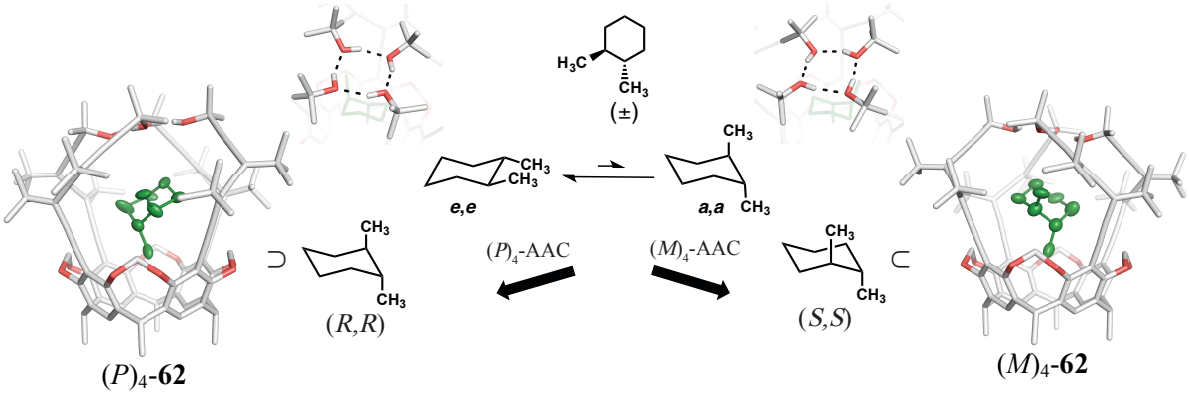

Figure 58. Left: X-ray co-crystal structure of AAC (*P*)$_4$-**62**⊃(*R*,*R*)-*trans*-1,2-dimethylcyclohexane with complete enantioselectivity. Right: Left: X-ray co-crystal structure of AAC (*M*)$_4$-**62**⊃(*S*,*S*)-*trans*-1,2-dimethylcyclohexane with complete enantioselectivity. The *trans*-1,2-dimethylcyclohexane is complexed in the higher energy diaxial conformation. Space groups: $P2_1P2_1P2_1$.[192]

AAC (*P*)$_4$-**62** co-crystallized selectively with only (*R*,*R*)-*trans*-1,2-dimethylcyclohexane highly selective, while AAC (*M*)$_4$-**62** selectively formed co-crystal structures only with (*S*,*S*)-*trans*-1,2-dimethylcyclohexane. The complete selectivity (≥ 95:5 according to residual electron density) was remarkable, considering the absence of directional interactions, making dispersive interactions solely responsible for the observed selectivity. To the best of our knowledge, this constituted the first report on the complete enantioselective complexation of a pure hydrocarbon molecule.[192] We explained the complete enantioselectivity with perfect shape complementarity of the guest with the interior of the host and with the formation of the circular hydrogen-bonding array, ensuring rigidity and preorganization. The calculated *PC* of AAC (*P*)$_4$-**62** with (*R*,*R*)-*trans*-1,2-dimethylcyclohexane and AAC (*M*)$_4$-**62** with (*S*,*S*)-*trans*-1,2-dimethylcyclohexane corresponded to 56 and 57%, respectively.[214] When examining the circular hydrogen-bonding array for the (*P*)- and (*M*)-configured ACCs **62**, we found that all AAC (*P*)$_4$-**62** show a clockwise orientation of the alcohol groups in the circular H-bonding array, whereas AAC (*M*)$_4$-**62** showed only counter-clockwise orientation (Figure 59).

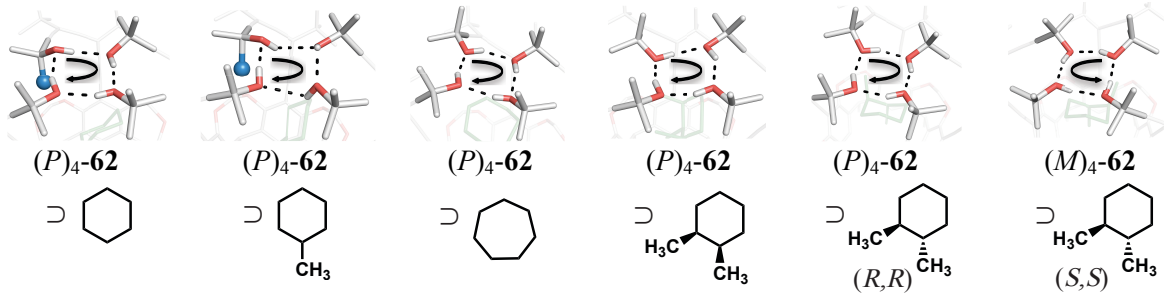

Figure 59. Top view on the fourfold hydrogen-bonding array of AAC $(P)_4$-**62** and AAC $(M)_4$-**62** encapsulating various hydrocarbons. In all complexes of $(P)_4$-configuration, the hydrogen-bonding array follows a clockwise orientation. For AAC $(M)_4$-**62**, the hydrogen-bonding array follows counter-clockwise orientation. Highlighted in blue is one of the methyl groups of the tertiary alcohol (C(*Me*)$_2$OH) of the alleno-acetylenic moiety.[192]

The fixed orientation of the H-bonding array, observed in the solid-state structures, appears to be dictated by the $(P)_4$- or $(M)_4$-configuration of the receptor **62** and is independent on the configuration of the encapsulated guest. This handedness was assumed to stabilize the cage form and contribute to the strong enantioselective and chiroptical properties of the AACs $(P)_4$- and $(M)_4$-**62**. Even more intriguing was the finding that the enantiomers of *trans*-1,2-dimethylcyclohexane were complexed in their diaxial conformation (Figure 58). In 1983, Eliel and co-workers,[244] as well as Booth and Grindley[245] determined the steric energy of the diaxial conformation experimentally by direct determination of the diequatorial (*e*,*e*) → diaxial (*a*,*a*) equilibrium (Figure 58). The energy difference between the two conformers was determined as $\Delta\Delta G^0_{298\ K\ e,e \rightarrow a,a}$ = 2.74 kcal mol^{-1} (11.5 kJ mol^{-1}), leading to the Boltzmann distribution of 99% *e*,*e* to 1% *a*,*a*.[98] This distribution may explain why no crystal structure of the diaxial conformer of *trans*-1,2-dimethylcyclohexane has been obtained until now. Figure 60 displays the diaxial torsional angles of both enantiomers of *trans*-1,2-dimethylcyclohexane. A full description is given in the Experimental Part.[192]

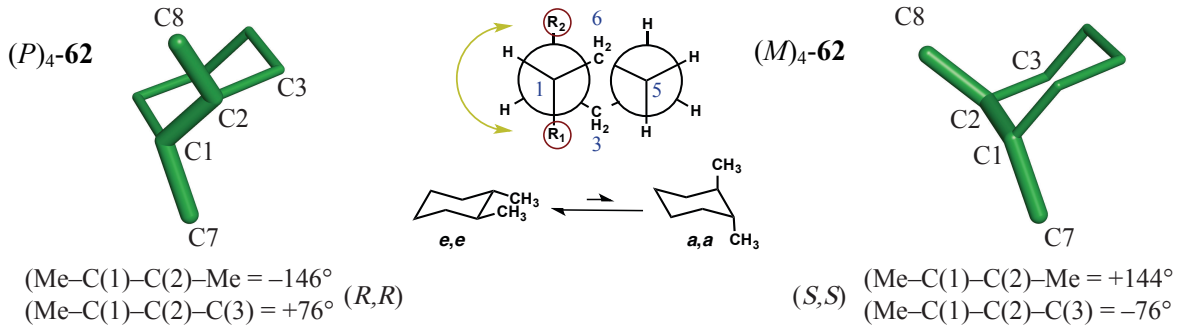

Figure 60. Selected geometric parameters of (*R*,*R*)-*trans*-1,2-dimethylcyclohexane (CCDC-1496462) and (*S*,*S*)-*trans*-1,2-dimethylcyclohexane (CCDC-1496460); space groups: $P2_1P2_1P2_1$. Selected torsion angles are given in °.[192]

With the *trans*-1,2-dimethylcyclohexane in the chair conformation, the two methyl groups approach a *trans*-diaxial alignment. The dihedral torsion angles (Me-C(1)-C(2)-Me) correspond to –146° and +144 degrees for the (*R*,*R*)- and the (*S*,*S*)-enantiomer, respectively. The deviation from the perfect dihedral angle of 180° is accompanied by flattening of the ring dihedral angles (Me-C(1)-C(2)-C(3) = +76°). The substantial bond-length and bond-angle alteration (see Experimental Part)[192] was hypothesized to reduce the strain caused by the 1,3-diaxial interactions. The significant deviation of the bond lengths and bond angles, however, also raised the question of how much the host affects the structure of the encapsulating guests. The crystallographic data already suggested that this effect is likely to be small, with the observed host–guest contacts exceeding the sum of their respective van der Waals radii (heavy atom distances ≤ 3.50 Å; Figure 61C). In order to gain further insight into the influence of the host on the guest structures, the host–guest contacts were analyzed through noncovalent interaction measures.[241]. Figure 61 displays the calculated isosurface of the reduced density gradient *s*(r) of density functional theory for *s*(r) = 0.55 between AAC $(P)_4$-**62** and methylcyclohexane (A) and AAC $(P)_4$-**62** and (*R*,*R*)-*trans*-1,2-dimethylcyclohexane (B) within a radius of 4.5 Å around the centroid of the guest molecules.[241]

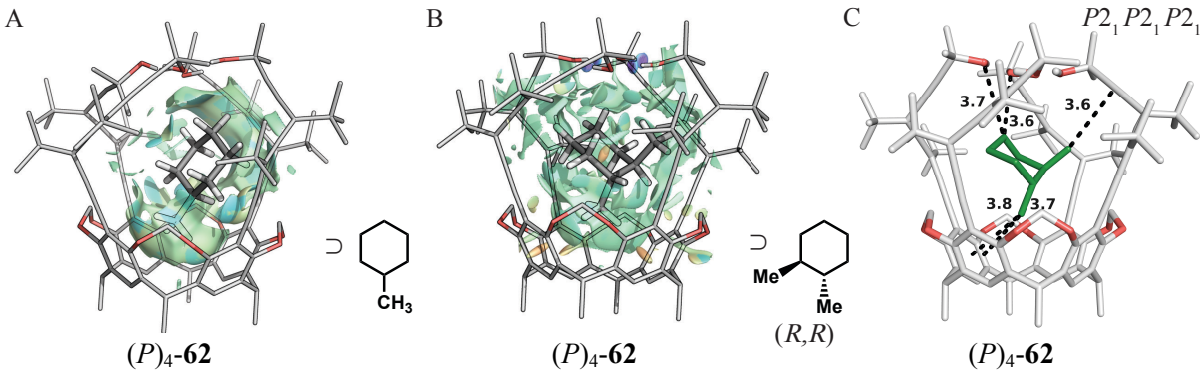

Figure 61. A–B: isosurface of the reduced density gradient s(r) of density functional theory for s(r) = 0.55 revealing the interaction between between methylcyclohexane and AAC $(P)_4$-**62** (A) and (*R*,*R*)-*trans*-1,2-dimethylcyclohexane and AAC $(P)_4$-**62** (B) and within a radius of 4.5 Å around the centroid of the guest molecule based on the data calculated in Ref.[241] The surfaces are colored on a blue-green-red scale according to the type of interactions with which they are associated: blue indicates strongly attractive interactions such as hydrogen-bonding, and green indicates dispersive interactions; red would indicate steric clashes, but no such red regions emerged in the analysis. We refer to Ref.[241] for a detailed discussion on how the types of interaction are assigned. Element color code: carbon in host, light gray; carbon in guest, dark gray; oxygen, red; hydrogen, white. Hydrogen atoms of the host are omitted for clarity. C: X-ray co-crystal structure of AAC $(P)_4$-**62**⊃(*R*,*R*)-*trans*-1,2-dimethylcyclohexane (Space group: $P2_1P2_1P2_1$); distances are given in Å; *n*-hexyl chains and hydrogens are omitted for clarity.

The calculations revealed the overall enveloping dispersive interactions of the guests with the interior of the receptor in absence of strong repulsive (or attractive) interactions and suggested that the trapped guest structures are hardly affected by the receptor.

The initial studies on the host–guest interactions implied that the AACs $(P)_4$- and $(M)_4$-**62** could be an ideal means to trap elusive diaxial conformers of cyclohexane derivatives in order to analyse their diaxial conformation on the atomic level of detail. We therefore set out to expand our series of pure cyclic hydrocarbons to cyclic alkyl halides.

3.2 Enantioselective Complexation through Dispersion and Halogen-Bonding Interactions

The isolation and characterization of single conformers of mono- and (±)-*trans*-1,2-disubstituted cyclohexanes is considered challenging due to the rapid isomerization process between their (di)equatorial and (di)axial conformers (ca. 2 x 10^5 s^{-1} at room temperature).[98] The existence of both conformers together with their respective preference for either conformation has previously been studied in solution by IR and at low temperature by NMR spectroscopies (near –150 °C), and enabled the quantitative determination of their

conformational energies (*A*-values).[246,247] While the equatorial conformations are generally preferred for monosubstituted cyclohexanes (positive *A*-values), the diaxial conformation becomes the more stable conformation for (±)-*trans*-1,2-dihalocyclohexanes (negative *A*-values).[98] This is in stark contrast to the previously described (±)-*trans*-1,2-dimethylcyclohexane, where the diequatorial conformation is strongly favored (positive *A*-value with $\Delta\Delta G^0_{298\ K}$ *e,e* → *a,a* = +2.74 kcal mol^{-1}).[244,245] Despite continuous research on substituted cyclohexanes, no conformational isomer of the mono- or (±)-*trans*-1,2-disubstituted cyclohexanes has ever been isolated at ambient temperatures in solution, and only few X-ray co-crystal structures have been reported.[98,243,248-252] In this context, we sought to utilize AACs $(P)_4$- and $(M)_4$-**62** as receptors to trap the single conformers of monosubstituted cyclohexanes (methyl-, fluoro-, chloro-, bromo- and iodocyclohexane) and selected (±)-*trans*-1,2-disubstituted analogs ((±)-*trans*-1,2-dichloro-, -dibromo-, -bromofluoro- and -dimethylcyclohexane) in solution and in the solid state.[241] The selected guest molecules are depicted in Figure 62.

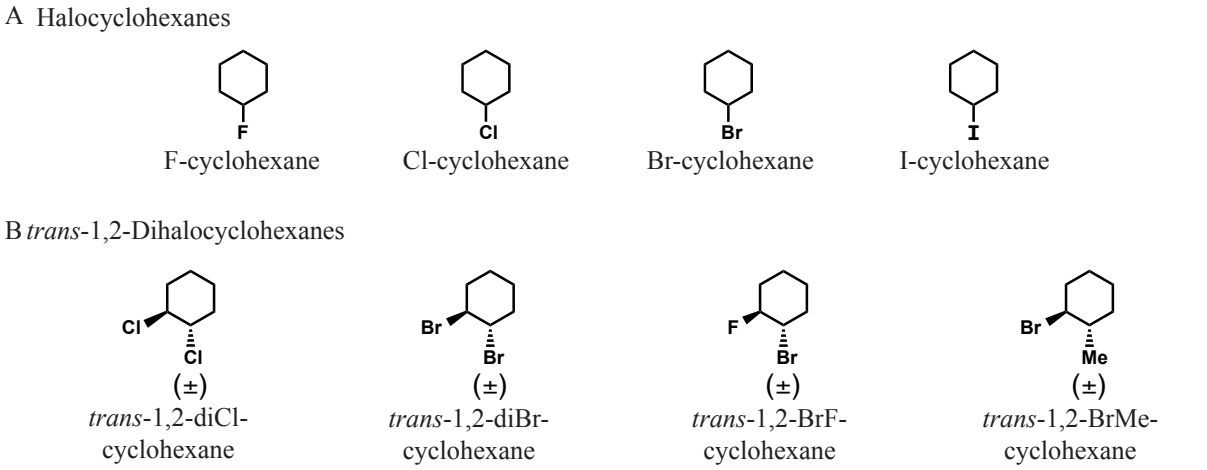

Figure 62. Summary of monohalo- and (±)-*trans*-1,2-dihalocyclohexanes for solid state and solution complexation studies with AACs $(P)_4$/$(M)_4$-**62**.

For this study, we collaborated with Tamara Husch and Prof. Markus Reiher (ETHZ), who supported our experimental findings theoretically.[241]

3.2.1 X-Ray Co-crystal Structures of Monohalocyclohexanes bound to AACs $(P)_4$-62

We obtained X-ray co-crystal structures of AAC $(P)_4$-**62** with the above depicted series of monohalocyclohexanes following the previously described protocol (Figure 49). All X-ray co-crystal structures show the guest molecules in their higher-energy axial conformation (Figure 63).

The halogens of the guest molecules are in close distance to the four electron-rich aromatic rings of the resorcin[4]arene core. The averaged distance of the halogens to the centroids of the four aromatics decreases (C–X···π) from fluorocyclohexane (4.6 Å), chlorocyclohexane (4.0 Å), bromocyclohexane (3.9 Å), to iodocyclohexane (3.8 Å). The decreasing distance of the halogens to the centroids of the aromatic groups with increasing size and polarizability of the halogens (F < Cl < Br < I) demonstrated the increasing strength of the halogen-bonding interaction to the π-rings as acceptors. This observation was later supported by increasing binding affinities of the monohalocyclohexanes from F to Cl to Br to I.

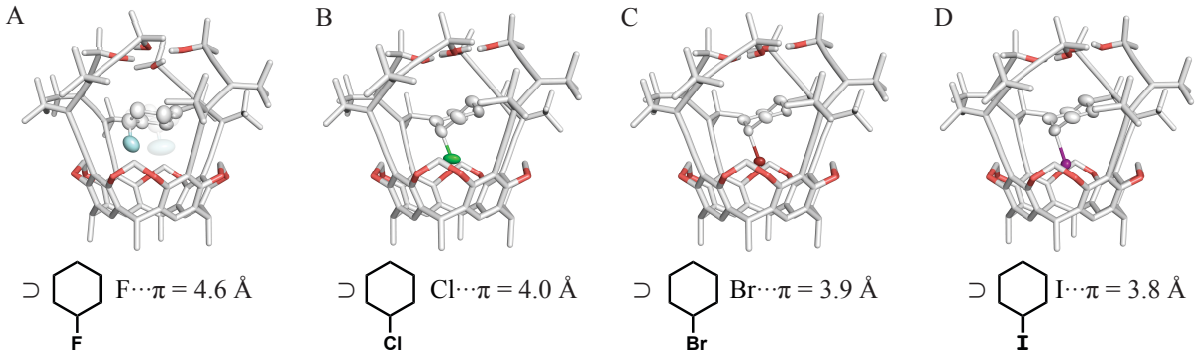

Figure 63. X-ray co-crystal structures of AAC $(P)_4$-**62** ⊃ X-cyclohexanes: X = fluoro (A), chloro (B), bromo (C) and iodo (D). C–X···π contacts are averaged distance of the halogens to the centroids of the four aromatics. The complexed guests are in their high-energy axial conformation with ellipsoids set at 50% probability at 100 K. Space groups: $P2_1P2_1P2_1$. *n*-Hexyl chains of the receptor $(P)_4$-**62** and hydrogens are omitted for clarity.[241]

In recent theoretical and experimental studies on C–X···π-contacts, it was recognized that aromatic groups can serve as halogen-bonding acceptors.[253-258] The interaction of the alkyl halides with the AACs $(P)_4$- and $(M)_4$-**62** was also studied theoretically (PBE-D3 optimized) and could confirm the decreasing distance of the higher halogens to the resorcin[4]arene core (for computational methods, see the Experimental Part).[241] The interaction energy difference for iodocyclohexane with AAC $(P)_4$-**62** compared to fluorocyclohexane was calculated to 6.7 kcal mol^{-1} and is in good agreement with the experimentally obtained results.

Dihedral Angles of Halocyclohexanes Bound to AACs $(P)_4$-62 in the Solid State

All X-ray co-crystal structures of halocyclohexanes complexed by AAC $(P)_4$-**62** show the guest in the higher-energy axial conformation allowing for a detailed analysis of the dihedral torsional angles. The axial dihedral angles $\vartheta_{a,a}$ (X-C(1)-C(2)-H) along with the torsional angle ϱ (X-C(1)-C(2)-C(3)) are displayed in Figure 64.

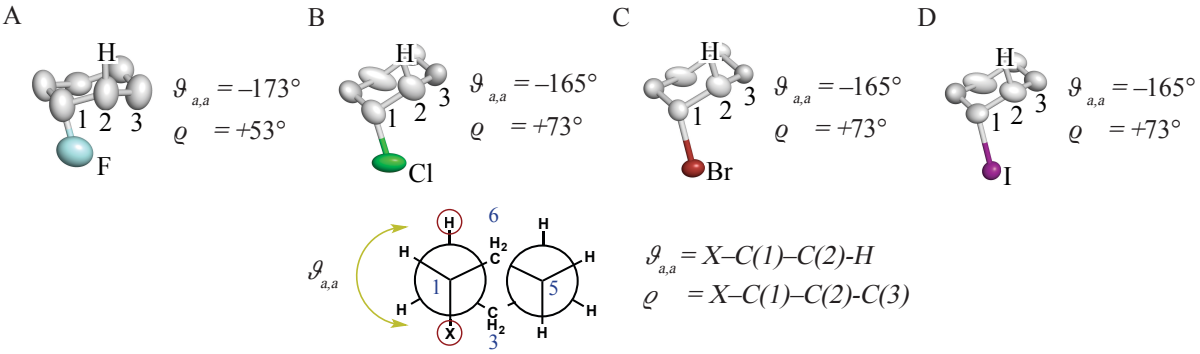

Figure 64. Dihedral angles $\vartheta_{a,a}$ and ϱ are given for monohalocyclohexanes complexed by AAC $(P)_4$-**62**: (X-C(1)-C(2)-H) and (X-C(1)-C(2)-C(3)). X = F, cyan; Cl, green; Br, brown; I, purple.[241]

The axial dihedral angle $\vartheta_{a,a}$ (X–C(1)–C(2)–H) decreases from –173° for fluorocyclohexane (near 180°) to –165° for chloro-, bromo- and iodocyclohexane (Figure 64). This decrease in the dihedral angle is accompanied by a flattening of the ring torsional angles ϱ (X–C(1)–C(2)–C(3)) from +53° for fluorocyclohexane to +73° for iodocyclohexane. The analysis allowed for the first time to study the axial dihedral angles of a series of monosubstituted halocyclohexanes in their axial conformation and raised the open question, why fluorocyclohexane deviates strongly from the other monohalocyclohexanes.[241]

3.2.2 X-Ray Co-Crystal Structures of *trans*-1,2-Dihalocyclohexanes bound to AACs $(P)_4$- and $(M)_4$-62

Compared to monohalocyclohexanes, (±)-*trans*-1,2-dihalocyclohexanes are chiral. The two enantiomers of the (±)-*trans*-1,2-dihalocyclohexanes are in equilibrium between their diaxial and their diequatorial conformation, with a general preference for the diaxial conformation.[98,259-262] If complexed to the AACs $(P)_4$- and $(M)_4$-**62** in their diaxial conformation, we imagined the two halogens to form one halogen bond to the aromatic moieties of the resorcin[4]arene scaffold (C–X···π) and a second one to the acetylene functionality of the alleno-acetylenic arms (C–X···|||). The latter was hitherto little studied with some reports in the literature on solid state assemblies.[19,263,264]

We assumed that the C–X···|||-contact (observed as C–H···|||-contact for AAC $(P)_4$-**62**⊃(*R*,*R*)-*trans*-1,2-dimethylcyclohexane, Figure 61) would largely determine the enantioselectivity of the $(P)_4$- and $(M)_4$-configured AACs **62** towards (±)-*trans*-1,2-dihalocyclohexanes. X-ray co-crystal structures of both $(P)_4$- and $(M)_4$-configured AACs **62** with *trans*-1,2-dichloro-, *trans*-1,2-dibromo-, and *trans*-1,2-bromofluorocyclohexane are depicted in Figure 65 (only AAC $(P)_4$-**62** shown, for AAC $(M)_4$-**62** see Experimental Part).

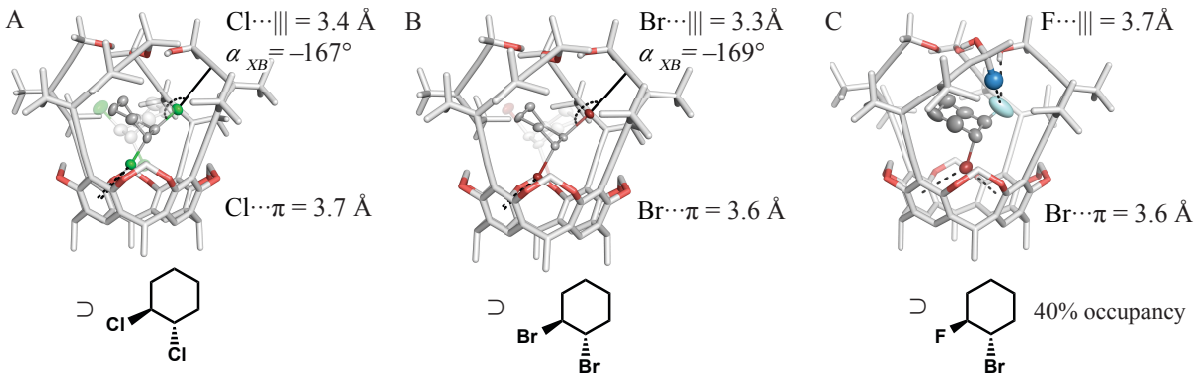

Figure 65. X-ray co-crystal structures of AAC $(P)_4$-**62**⊃*trans*-1,2-dihalocyclohexanes: *trans*-1,2-dichlorocyclohexane (A), *trans*-1,2-dibromocyclohexane (B), *trans*-1,2-bromofluorocyclohexane (C). C–X···π-contacts are averaged distances of the halogens to the centroids of the two indicated aromatics. The complexed guests are in their high-energy axial conformation with thermal ellipsoids set at 50% probability at 100 K. Space groups: $P2_1P2_1P2_1$. *n*-Hexyl chains of the receptor $(P)_4$-**62** and hydrogens are omitted for clarity.[241]

trans-1,2-Dichloro-, *trans*-1,2-dibromo-, and *trans*-1,2-bromofluorocyclohexane are complexed in their diaxial chair conformation. As anticipated, both the chloro and the bromo derivatives show close C–X···π-contacts of the halogen with the resorcin[4]arene scaffold, decreasing from 3.7 Å for *trans*-1,2-dichlorocyclohexane to 3.6 Å for *trans*-1,2-dibromocyclohexane and *trans*-1,2-bromofluorocyclohexane (Figure 65 A, B, and C). Additionally, *trans*-1,2-dichlorocyclohexane and *trans*-1,2-dibromocyclohexane engage in C–X···||| interactions with the alleno-acetylenic arm of the host with distances of 3.4 Å and 3.3 Å, respectively. The angles α_{XB} (C–X···C≡C) approach 167° for *trans*-1,2-dichlorocyclohexane and 169° for *trans*-1,2-dibromocyclohexane, which is in good agreement with halogen bonding criteria. This contact is lost with *trans*-1,2-bromofluorocyclohexane, where the fluorine faces away from the acetylenic functionality. The missing space occupancy of this compound is compensated by the host through rotation of one methyl group of the tertiary alcohol (CMe_2OH) into the cavity (Figure 65, C indicated in blue).

Enantioselective Complexation of (±)-trans-1,2-Dihalocyclohexanes by $(P)_4$- and $(M)_4$-AACs 62

The X-ray co-crystal structures of $(P)_4$- and $(M)_4$-configured AACs **62** encapsulating *trans*-1,2-dichloro- and *trans*-1,2-dibromocyclohexane display two populations of the guest in the host, which correspond to the guest enantiomers (Figure 66).

The population ratio relates to the enantioselectivity of the $(P)_4$- and $(M)_4$-configured AACs **62** towards the (*R*,*R*) and (*S*,*S*) enantiomers of (±)-*trans*-1,2-

dihalocyclohexanes observed in the solid state. Comparison of the enantiomeric ratios enabled us to approximate the enantioselectivity of the receptor towards the chiral guests. The enantiomeric ratio ((*R*,*R*):(*S*,*S*)) of the guest bound to AAC (*P*)$_4$-**62** increased from 3:2 for *trans*-1,2-dichlorocyclohexane to 3:1 for *trans*-1,2-dibromocyclohexane. The inverse ratios were observed for AAC (*M*)$_4$-**62**. The increasing selectivity was rationalized with the shorter contacts of the bromine substituent compared to the chlorine with stronger halogen-bonding contacts. Within the same halogen substituent, the (*R*,*R*)-enantiomer of the guest undergoes more favorable halogen-bonding contacts with the host compared to the weaker binding (*S*,*S*)-enantiomer.

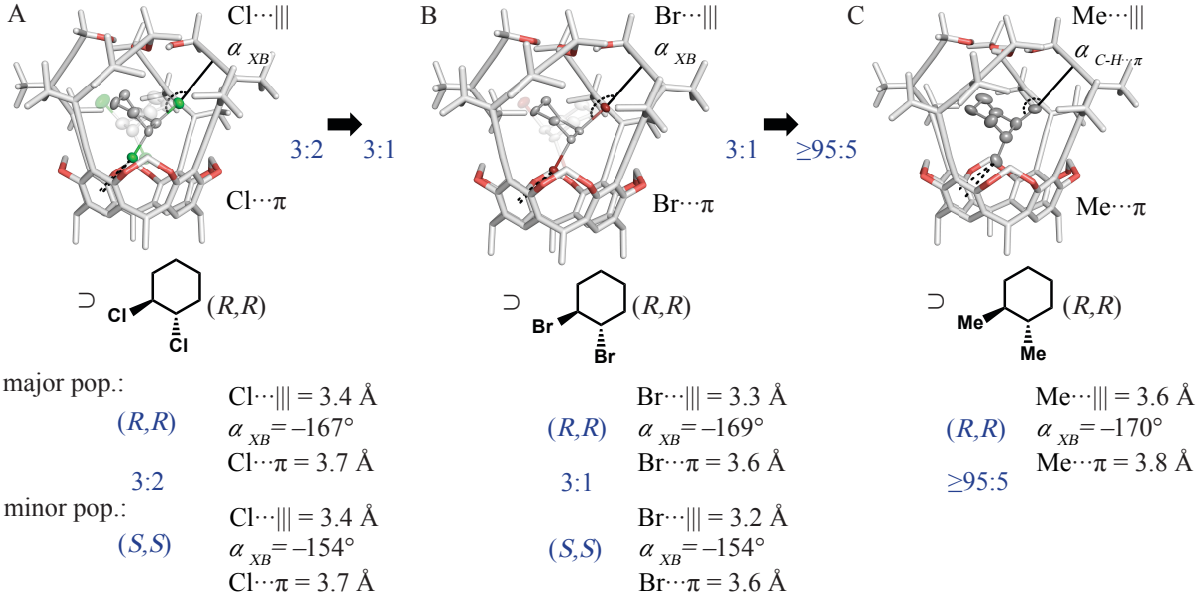

Figure 66. X-ray co-crystal structures of AAC (*P*)$_4$-**62**⊃*trans*-1,2-disubstituted cyclohexanes: *trans*-1,2-dichlorocyclohexane (A), *trans*-1,2-dibromocyclohexane (B), *trans*-1,2-dimethylclohexane (C). C–X···π- and C–H···π-contacts are averaged distances of the carbon or halogens to the centroids of the two indicated aromatics. Close contacts are given in Å. Close contacts and angles of the minor populated enantiomer of the guest are given below. Thermal ellipsoids are set at 50% probability at 100 K. *n*-Hexyl chains of the receptor (*P*)$_4$-**62** and hydrogens are omitted for clarity. Space group: $P2_1P2_1P2_1$.[241]

The (*R*,*R*)-*trans*-1,2-dichlorocyclohexane bound to AAC (*P*)$_4$-**62** displayed C–Cl···π-contacts of one chlorine with the resorcin[4]arene scaffold of 3.7 Å. The second chlorine undergoes C–Cl···||| interactions facing towards the alleno-acetylenic arm of the host of 3.4 Å (Figure 66), with an angle α_{XB} (C–Cl···C≡C) of 167°. The weaker binding (*S*,*S*)-*trans*-1,2-dichlorocyclohexane displayes equivalent halogen-bonding distances to the aromatic and acetylenic functionality, but the α_{XB} (C–Cl···C≡C) decreased down to 154°. For the (*R*,*R*)-*trans*-

1,2-dibromocyclohexane bound to AAC $(P)_4$-**62**, shorter halogen-bonding contacts of the C–Br···π-distance to the resorcin[4]arene scaffold at 3.6 Å were observed, together with short C–Br···|||-contacts of 3.3 Å with α_{XB} (C– Br···C≡C) = 169° (Figure 66, B). In the minor populated (*S*,*S*)-enantiomer, the C– Br···|||-contact decreased to 3.2 Å, significantly below the sum of the van der Waals radii of the heavy atoms, with α_{XB} (C– Br···C≡C) decreasing to 154°.

While the AAC $(P)_4$-**62** showed an increasing enantioselective preference for the (*R*,*R*)-configured *trans*-1,2-dihalocyclohexanes for the dichloride (3:2) and the dibromide derivative (3:1), the overall enantioselectivity towards the *trans*-1,2-dihalocyclohexanes was lower compared to the *trans*-1,2-dimethylcyclohexanes (complete enantioselectivity, Figure 66, C). This finding is counter-intuitive considering the stronger and directional halogen-bonding contacts of the *trans*-1,2-dihalocyclohexanes to the receptor compared to the non-directional dispersion interactions of *trans*-1,2-dimethylcyclohexanes with the host. It is also in conflict with established concepts for enantioselective complexation of optically pure receptors with chiral guests, where more directional interactions are considered to enhance selectivity (see Introduction). We explained this observation with the much higher polarizability and the larger distortions of the electron densities of chlorine and bromine compared to the methyl substituents.[265] The closer contacts of the halogen-derivatives with the receptor decreased their overall space occupancies within the host compared to the *trans*-1,2-dimethyl derivative. The *PC*s increased from 51% for *trans*-1,2-dichlorocyclohexane within AAC $(P)_4$-**62** to 56% for *trans*-1,2-dibromocyclohexane and 57% for *trans*-1,2-dimethylcyclohexane.

To further substantiate the enantioselective binding of the AACs $(P)_4/(M)_4$-**62** towards the (±)-*trans*-1,2-dihalocyclohexanes, the electronic energy differences of the differently substituted guests within the $(P)_4$-configured receptor **62** were determined and compared to the experimentally instable *trans*-1,2-diiodocyclohexane. In close agreement with the experimental results, the (*R*,*R*)-configured guests bound favorably to the receptor compared to the (*S*,*S*)-configured guests, with energy differences of 0.6 kcal mol^{-1} for (±)-*trans*-1,2-dichlorocyclohexane and 1.1 kcal mol^{-1} for (±)-*trans*-1,2-dibromocyclohexane. This difference increased substantially for the experimentally unstable (±)-*trans*-1,2-diiodocyclohexane to 2.8 kcal mol^{-1}.

The noncovalent interactions between the receptor and the guest were visualized in terms of the reduced density gradient proposed by Yang and co-workers.[266] The

comparison between AAC $(P)_4$-**62**⊃(*R*,*R*)-*trans*-1,2-dibromocyclohexane with AAC $(P)_4$-**62**⊃(*R*,*R*)-*trans*-1,2-dimethylcyclohexane is shown in Figure 67.

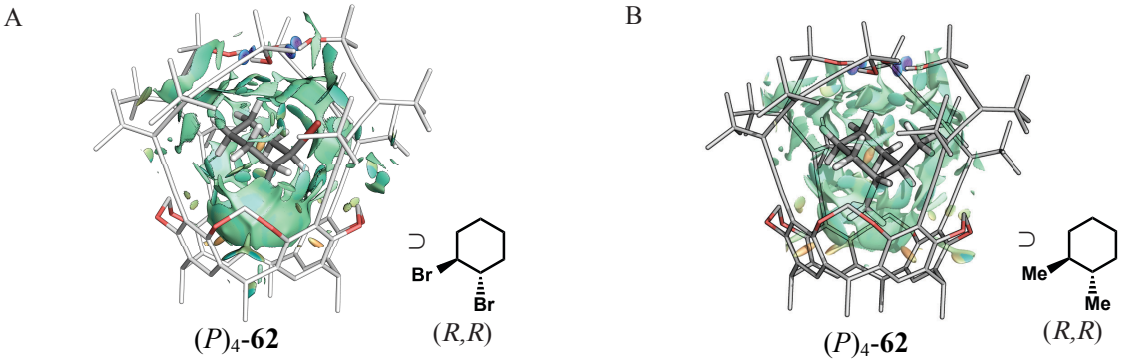

Figure 67. Isosurface of the reduced density gradient *s*(r) of density functional theory for *s*(r) = 0.55 revealing the interaction between (*R*,*R*)-*trans*-1,2-dibromocyclohexane and AAC $(P)_4$-**62** (A), and (*R*,*R*)-*trans*-1,2-dimethylcyclohexane with AAC $(P)_4$-**62** (B) within a radius of 4.5 Å around the centroid of the guest molecule based on the data calculated in Ref.[241] The surfaces are colored on a blue-green-red scale according to the type of interactions with which they are associated: blue indicates strongly attractive interactions such as hydrogen-bonding, and green indicates dispersive interactions; red would indicate steric clashes, but no such red regions emerged in the analysis.[241,266]

The analysis illustrates the perfect shape-complementarity of the guests with the host, without any apparent major steric clashes. The all-over enveloping dispersive interactions emerged in green (Figure 67).

Variable-Temperature X-Ray Diffraction of trans-1,2-Dibromocyclohexane Bound to AAC $(P)_4$-62

In order to further study the preference of AAC $(P)_4$-**62** towards one enantiomer of (±)-*trans*-1,2-dibromocyclohexane, we measured the co-crystal structure (CCDC-1549646) with a (*R*,*R*) : (*S*,*S*)-guest ratio of 3:1 at temperatures between 100 K and 280 K in steps of 20 K (Figure 68). We expected the stronger binding (*R*,*R*)-guest to show suppressed thermal motion and disorder visualized in the size of the thermal ellipsoids compared to the weaker binding (*S*,*S*)-enantiomer.[267] Figure 68 shows that the ellipsoids of the (*S*,*S*)-enantiomer increase stronger with temperature compared to the (*R*,*R*)-enantiomer. At 220 K, a second population of the (*S*,*S*)-enantiomer appeared rotated 90° clockwise. Weak residual densities pointing towards the remaining two acetylenic bonds, which can be interpreted as additional bromine positions, appeared above 260 K (not shown for clarity). Qualitatively, this can be interpreted as preferential binding of the (*R*,*R*)-enantiomer in the $(P)_4$-configured host, associated with a lowered rotational barrier for the (*S*,*S*)-enantiomer. The comparison of the temperature dependent average sphere volumes (volume of the anisotropic displacement

parameters) of AAC $(P)_4$-**62**⊃*trans*-1,2-dibromocyclohexane is displayed in the Experimental Part.[241]

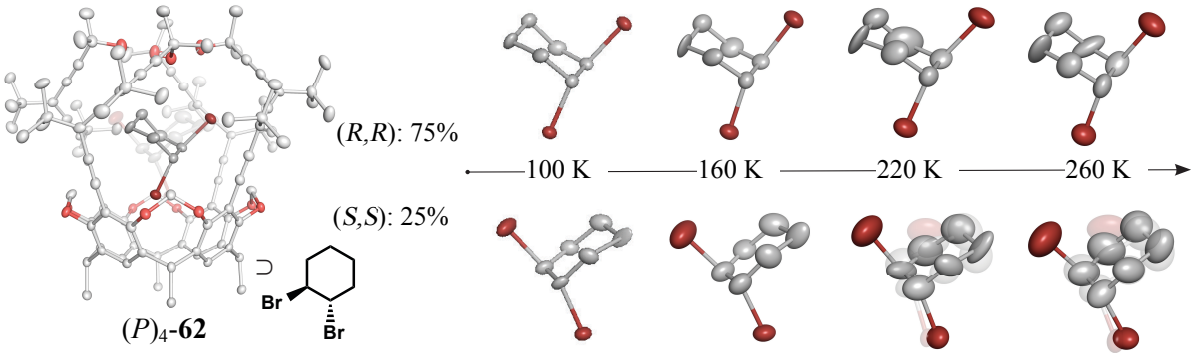

Figure 68. X-ray co-crystal structure of AAC $(P)_4$-**62**⊃*trans*-1,2-dibromocyclohexane crystallized from racemic *trans*-1,2-dibromocyclohexane and $(P)_4$-AAC at 25 °C (left). Variable-temperature X-ray diffraction revealed the stronger binding of (*R*,*R*)-*trans*-1,2-dibromocyclohexane (right). Space group: $P2_1P2_1P2_1$.[241]

The C–X···|||-Contact: Theoretical Analysis of the Geometrical Requirements of a Novel Halogen-Bonding Interaction

In a theoretical study, Riley *et al.* investigated the orientation dependence of the C–X···π-contact through a simplified model system consisting of a halocarbon relative to a benzene moiety.[257] They concluded that tilting and shifting of the halocarbon relative to the benzene hardly affects the C–X···π interaction strength.[257] This implied low geometrical requirement of this type of halogen-bonding interaction.[257] These results could be transferred to our series of guests undergoing C–X···π contacts of the halogens with the aromatic moieties of the resorcin[4]arene core. However, no such study had been done for C–X···|||-type halogen-bonding interactions. The model system we set up consisted of a halomethane and a 2-butyne molecule, simplifying the interactions we observed in the AACs $(P)_4/(M)_4$-**62**, where the halomethane served as model system for the halogen-bonding donor and the 2-butyne as model system for the alleno-acetylenic functionality (Figure 69).[241]

In accordance with the stringent geometrical requirements of halogen-bonding interactions (see Introduction), the chlorine, bromine, and iodine derivatives displayed minimum energy structures at C–X···|||-distances of 3.4–3.5 Å and α_{XB} (C–X···C≡C) angles of 179–180°. Fluorine did not show any halogen-bonding interactions. Changing the C–X···|||-distances between 3.3–3.9 Å at a fixed α_{XB} (C–X···C≡C) angle of 180° decreased the halogen-bonding strength for all halogen substituents up to 0.5 kcal mol^{-1}. Tilting of the halomethane

at a fixed distance of 3.5 Å similarly resulted in a gradual decrease of the halogen-bonding interaction. At an angle of 145°, the interaction of the halomethane with the 2-butyne decreased by 0.3 kcal mol^{-1} for the chloromethane, by 0.7 kcal mol^{-1} for the bromomethane, and by 1.4 kcal mol^{-1} for the iodomethane. The contacts became repulsive for distances smaller than 3.2 Å and large deviations from α_{XB} (C–X···C≡C) angle below 160°. Iodomethane displayed the strongest interaction with 2-butyne and the highest geometrical dependence of the interacting molecules.

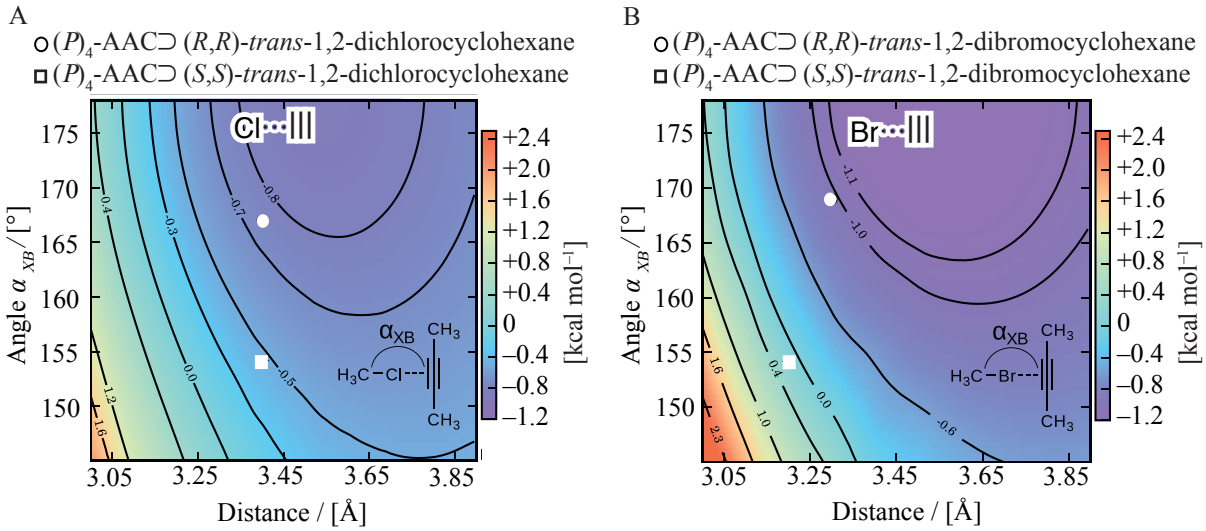

Figure 69. SCS-MP2 potential energy surface [kcal mol^{-1}] for C–Cl···||| and C–Br···||| halogen bonding interactions. Distances are given in Å and angles in °.[241]

Figure 69 also shows the experimentally observed values for the C–X···|||-distances and α_{XB} angles of (*R*,*R*)- (white circle) and (*S*,*S*)-enantiomers (white square) of *trans*-1,2-dichloro- and *trans*-1,2-dibromocyclohexane bound to AAC $(P)_4$-**62**. Within the model, the decrease in α_{XB} (C–Cl···C≡C) between (*R*,*R*)- (white circle) and (*S*,*S*)-*trans*-1,2-dichlorocyclohexane (white square) resulted in an energy difference of 0.4 kcal mol^{-1}. The change in C–Br···|||-distances (3.3 → 3.2 Å), together with the deviation of the angle α_{XB} (C–Br···C≡C, –169° → –154 Å) for the (*R*,*R*)- (white circle) and (*S*,*S*)-*trans*-1,2-dibromocyclohexane (white square) gave an energy difference of 1.0 kcal mol^{-1}. The theoretical results are consistent with the experimentally observed preferential binding of the enantiomers with the same absolute configuration of the optically pure AACs $(P)_4$/$(M)_4$-**62**.

Dihedral Angles of trans-1,2-Dihalocyclohexanes Bound to AACs (P)$_4$-and (M)$_4$-62 in the Solid State

The molecular structures obtained from single-crystal X-ray diffraction show the exclusive complexation of the diaxial conformers of the series of (±)-*trans*-1,2-dihalocyclohexanes. The

dihedral angles $\vartheta_{a,a}$ (X-C(1)-C(2)-X) deviate substantially from 180° accompanied by flattening of the ring dihedral angles ϱ (X-C(1)-C(2)-C(3)). For (*R*,*R*)-*trans*-1,2-dichlorocyclohexane bound to AAC $(P)_4$-**62** $\vartheta_{a,a}$ corresponds to –162° and decreased to –160° for (*R*,*R*)-*trans*-1,2-dibromocyclohexane (Figure 70).

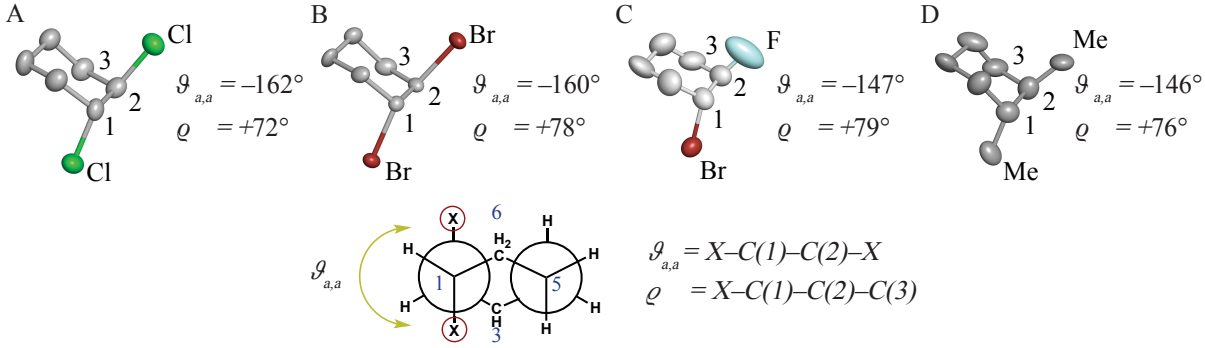

Figure 70. Dihedral angles $\vartheta_{a,a}$ (X-C(1)-C(2)-X) and ϱ (X-C(1)-C(2)-C(3) are given for (*R*,*R*)-*trans*-1,2-disubstituted cyclohexanes complexed by AAC $(P)_4$-**62**; X = F, cyan; Cl, green; Br, brown; C, grey.[241]

(*R*,*R*)-*trans*-1,2-Bromofluorocyclohexane showed an even stronger deviation from 180° for $\vartheta_{a,a}$ down to –147°. Similarly low dihedral angles $\vartheta_{a,a}$ were observed for the diastereomeric complexes of *trans*-1,2-dimethylcyclohexane, with $\vartheta_{a,a}$ = –146° for the (*R*,*R*)-enantiomer. The decrease in the dihedral angle $\vartheta_{a,a}$ is accompanied by flattening of the ring dihedral angles and substantial bond-length alteration. ϱ (X-C(1)-C(2)-C(3)) increased from +72° for (*R*,*R*)-*trans*-1,2-dichlorocyclohexane to +76° for (*R*,*R*)-*trans*-1,2-dimethylcyclohexane and +79° for (*R*,*R*)-*trans*-1,2-bromofluorocyclohexane. Comparable values were obtained for the (*S*,*S*)-configured guests bound the AAC $(M)_4$-**62**. The X-ray crystallographic data suggest hardly any influence of the receptor on the guest structures, as no strong repulsive or attractive interactions were observed.

In general, crystallographic data on *trans*-1,2-disubstituted cyclohexanes are extremely limited and the co-crystallization of *trans*-1,2-disubstituted cyclohexanes within AACs **62** allowed us to obtain structural information of this series for the first time.

3.2.3 Theoretical Investigation of the Dihedral Angle $\vartheta_{a,a}$ in Cyclohexane Derivatives

In order to validate the hypothesis that the complexed molecular structures of the cyclohexane derivatives can be transferred directly to their isolated (uncomplexed) structures, we investigated the structures of the host–guest complexes and of the isolated guests with quantum chemical methods.[241]

Comparison of the Dihedral Angle $\vartheta_{a,a}$ of Monosubstituted and trans-1,2-Disubstituted Cyclohexanes Encapsulated by AACs $(P)_4$-and $(M)_4$-62 and in their Uncomplexed Form

The influence of the receptor on the guest conformations can be directly probed by quantum chemical optimization and comparison of the isolated and encapsulated guest structures (Figure 71, A).

We found that the root-mean-square deviations of the atomic positions in the isolated (blue circles) and encapsulated guest structures (red squares and black crosses) did not exceed 0.02 Å, which indicated that the trapped guest structures closely resembled the isolated ones (Figure 71, A). Consequently, the differences of the dihedral angles $\vartheta_{a,a}$ in the isolated and complexed guest structures are small (on average 1°, Figure 71, A).[241] A direct comparison of the measured and calculated dihedral angle $\vartheta_{a,a}$ in the host–guest complexes showed a satisfactory agreement for the (±)-*trans*-1,2-dihalocyclohexanes (Figure 71, A) and larger deviations of up to 15° for (±)-*trans*-1,2-dimethylcyclohexane and some monohalocyclohexanes (Figure 71, A).[241] While this disagreement seems large, it can be traced back to the flexibility of the cyclohexane scaffold. Figure 71, B displays the relative electronic energies in [kcal mol^{-1}] for the dihedral angle $\vartheta_{a,a}$ of (*R*,*R*)-*trans*-1,2-dimethylcyclohexane in its isolated form (DF-LCCSD(T0)-F12b//PBE-D3, black crosses and PBE-D3, blue triangles) and bound to the AAC $(P)_4$-**62** (red squares). A decrease in $\vartheta_{a,a}$ for AAC $(P)_4$-**62** ⊃ (*R*,*R*)-*trans*-1,2-dimethylcyclohexane by up to 15° requires less than 1 kcal mol^{-1}.

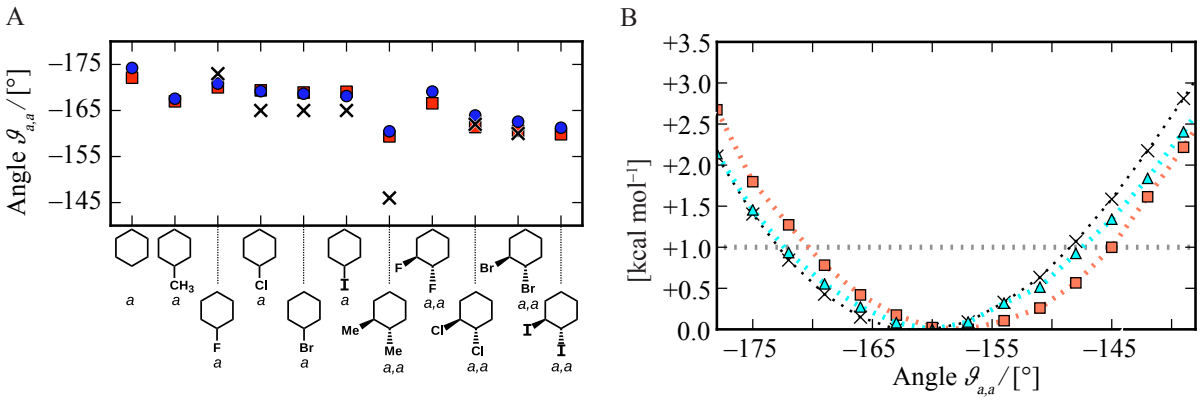

Figure 71. A: Calculated dihedral angles $\vartheta_{a,a}$ [°] in the isolated cyclohexane derivatives (blue circles) or as their host–guest complexes (red squares) in their axial (a) conformation reproduced from data presented in Ref.[241] in comparison to the experimental values (black crosses). B: Relative electronic energies in [kcal mol^{-1}] for the dihedral angle $\vartheta_{a,a}$ [°] of (*R*,*R*)-*trans*-dimethylcyclohexane in its isolated form (DF-LCCSD(T0)-F12b//PBE-D3, black crosses and PBE-D3, blue triangles) and complexed to the $(P)_4$-configured AAC **62** (red squares).[241]

The theoretical results indicated that the strong deviation of $\vartheta_{a,a}$ from the idealized angle of 180° is not the result of encapsulation, but rather represents the innate conformations of the substituted cyclohexane derivatives.

Conformational Energies (A-values) of Monosubstituted and trans-1,2-Disubstituted Cyclohexanes

While the X-ray co-crystal structures of the AACs $(P)_4/(M)_4$-**62** with mono- and *trans*-1,2-disubstituted cyclohexanes show the guest in their (di)axial conformation (with the exception of methylcyclohexane), their conformational preference in solution is highly substituent dependent. Figure 72 displays a comparison between the experimentally obtained literature values (red ranges) and the calculated Gibbs energy differences ($\Delta G = G_{(di)axial} - G_{(di)equatorial}$; calculated in the gas phase at 293 K) between the (di)axial and the (di)equatorial conformers of mono- and *trans*-1,2-disubstituted cyclohexanes.[98,262,268-270]

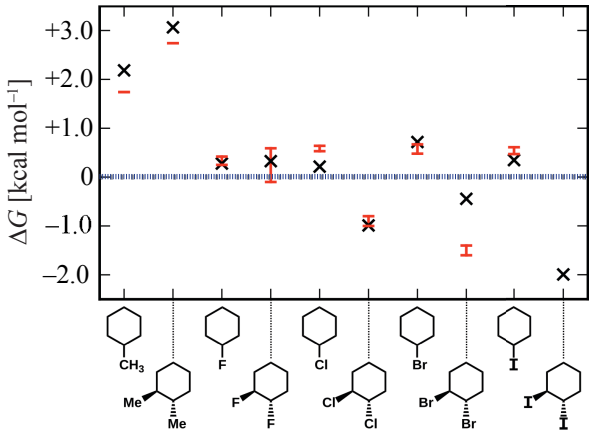

Figure 72. Calculated (black crosses) and experimentally derived (red ranges) Gibbs free energie differences ($\Delta G_{293\ K}$) in the gas phase between the (di)axial and (di)equatorial conformers of monosubstituted and *trans*-1,2-disubstituted cyclohexane derivatives. Note: the experimental values (derived from the literature) were often extrapolated from lower temperatures to 293 K and to the gas phase.[98,262,268-270]

For a detailed description of the theoretical methods, the reader is referred to Ref.[241] Despite necessary approximations, ΔG is largely dominated by the electronic energy differences between the two conformations. Monosubstituted cyclohexanes generally showed a preference for the equatorial conformation with *A*-values ranging from ΔG = +0.2 kcal mol^{-1} for chlorocyclohexane up to +2.2 kcal mol^{-1} for methylcyclohexane (Figure 72). The calculated *A*-values correspond well to the experimentally obtained ones and deviate on average by only 0.2 kcal mol^{-1}. While *trans*-1,2-dimethylcyclohexane showed a strong preference for the diequatorial conformation (ΔG = +3.0 kcal mol^{-1}), it decreased substantially

for *trans*-1,2-difluorocyclohexane (ΔG = +0.4 kcal mol^{-1}, Figure 72). *trans*-1,2-Dichlorocyclohexane already showed a strong preference for the diaxial conformation with ΔG = –1.0 kcal mol^{-1}. This value decreased for *trans*-1,2-dibromocyclohexane (ΔG = –0.5 kcal mol^{-1}).

We rationalized the increasing preference for the diaxial conformations (negative *A*-values) with increasing atomic number in terms of electronic dipole moment, intramolecular dispersion interactions, and steric contributions. The calculated differences in the dipolar moments are displayed in Ref.[241] While methylcyclohexane and *trans*-1,2-dimethylcyclohexane showed small differences in their dipole moments ($\Delta\mu$ = $\mu_{(di)axial}$ – $\mu_{(di)equatorial}$ in [Debeye]) of –0.06 and –0.08, respectively, the differences in dipole moments increased substantially for *trans*-1,2-dibromocyclohexane (–2.40) and *trans*-1,2-difluorocyclohexane (–2.58).[241] Additionally, dispersion interactions of the substituent with the methylene groups in the 1,3-positions becomes favorable in the (di)axial conformation with increasing size and polarizability of the substituent. On the other hand, with increasing van der Waals radii of the substituents, the repulsion in the diequatorial conformation increases.

We imagined the strong substituent-dependent conformational preferences of the mono- and *trans*-1,2-disubstituted cyclohexanes to have significant influence on the guest binding properties in solution.

3.2.4 Solution Binding Studies of Halocyclohexanes and (±)-*trans*-1,2-Dihalocyclohexanes with AACs $(P)_4$/$(M)_4$-62

Following the analysis of the solid state molecular structures obtained by X-ray diffraction, along with theoretical investigations on the host–guest complexes and the isolated guest molecules, we were interested in how the conformational preferences (*A*-values) of the monosubstituted and 1,2-disubstituted cyclohexanes, with their ability to undergo dispersion and halogen-bonding interactions, would affect the binding constants. We expected an increase in binding in the order of Me < F < Cl < Br < I, based on the increasing dispersion and halogen-bonding interactions.[241]

Solution complexation studies of the guests and AAC $(P)_4$-**62** were conducted by ^{1}H NMR and ECD spectroscopic titrations in a non-competitive solvent (*n*-octane-d_{18} and *n*-octane) at 293 K (for experimental details, see the Experimental Part).[192] Binding constants were obtained by non-linear least-squares fitting of NMR and ECD spectroscopic titrations and fitted to a 1:1 binding isotherm. The host-guest stoichiometry was deduced from Job plot analysis at fast host-guest exchange on the NMR timescale. Stronger binding guests showed

slow exchange on the NMR timescale, and the NMR binding stoichiometry and constants were deduced from the ratio of the bound and free host-to-guest signals. In general, NMR and ECD spectroscopic titrations gave similar values, although binding constants obtained through ECD have higher accuracy, due to the large changes in band intensities. 2D NMR spectroscopic studies were conducted on all host–guest complexes in solution. 2D ROESY NMR spectroscopy confirmed their encapsulation by the receptor. Slow exchange of the stronger binding guests towards AAC $(P)_4$-**62** on the NMR timescale, such as the iodocyclohexane (277 K, 1 equiv. of host and 2.7 equiv. of guest), *trans*-1,2-bromofluorocyclohexane (277 K, 14 equiv. of guest), *trans*-1,2-dichlorocyclohexane (277 K, 14 equiv. of guest), *trans*-1,2-bromomethylcyclohexane (277 K, 13 equiv. of guest), and *trans*-1,2-dibromocyclohexane (277 K, 2.5 equiv. of guest), enabled the characterization of the inclusion complexes in solution. 1D and 2D NMR spectroscopy proved to be a powerful method to elucidate the stereochemistry of the cyclohexyl derivatives, as protons in the axial positions generally resonate upfield compared to the equatorial protons, along with larger *J*-couplings (or bandwidth if the coupling is not resolved). While the free guest showed broader bandwidths due to the equilibrium between the (di)equatorial and (di)axial conformation in solution, the complexed guests show narrower bandwidths indicating the (di)axial conformation in the AACs $(P)_4$/$(M)_4$-**62**.

Solution Binding Studies of Halocyclohexanes with AACs $(P)_4$- and (M)-62

Table 5 gives a summary of the obtained binding constants of monosubstituted cyclohexanes and *trans*-1,2-disubstituted cyclohexanes with AAC $(P)_4$-**62**, together with their corresponding calculated conformational energies (*A*-values, Table 5).

The binding affinities for monosubstituted cyclohexanes increased with the substituent in the order of Me < F < Cl < Br < I from 22 M^{-1} for methylcyclohexane up to 18 000 M^{-1} for iodocyclohexane (Table 5). Apart from methylcyclohexane, the series of monosubstituted cyclohexanes have comparable conformational energies with *A*-values ranging from +0.2 kcal (chlorocyclohexane) mol^{-1} to +0.7 kcal mol^{-1} (bromocyclohexane). Consequently, the substantial increase in the binding affinities of 270 M^{-1} for fluorocyclohexane (*A*-values = +0.2 kcal) to 18 000 M^{-1} for iodocyclohexane (*A*-values = +0.3 kcal) can be pinpointed to the favorable C–X···π halogen-bonding interactions of the iodine with the aromatic moieties of the resorcin[4]arene receptor and results in a gain in binding affinity of $\Delta\Delta G$ = –2.4 kcal mol^{-1}. This corresponds to $\Delta\Delta G$ = –0.6 kcal mol^{-1} per C–X···π_{Ar} halogen-bonding contact of the iodine with each aromatic group of the resorcin[4]arene (2.4 kcal mol^{-1} / 4).

Table 5. Summary of binding constants K_a (293 K) and Gibbs free energies for the complexation of monosubstituted and (±)-*trans*-1,2-disubstituted cyclohexanes by $(P)_4$-AAC **62** in *n*-octane.[241]

Guest	NMR K_a / 10^3 [M^{-1}]	ECD K_a / 10^3 [M^{-1}]	ECD [a] $\Delta G_{293\ K}$ [kcal mol^{-1}]	*A*-values[b] $\Delta G_{293\ K}$ [kcal mol^{-1}]
Monosubstituted Cyclohexanes				
Me-cyclohexane	0.014	0.022	–1.8	+2.2
F-cyclohexane	0.23	0.27	–3.3	+0.3
Cl-cyclohexane	1.1	1.1	–4.1	+0.2
Br-cyclohexane	5.3	5.1	–5.0	+0.7
I-cyclohexane	18	18	–5.7	+0.3
(±)-*trans*-1,2-Disubstituted Cyclohexanes				
(±)-*trans*-1,2-diCl-cyclohexane	3.7	3.8	–4.8	–1.0
(±)-*trans*-1,2-diBr-cyclohexane	29	29	–6.0	–0.5
(±)-*trans*-1,2-BrF-cyclohexane	1.1	1.8	–4.4	+0.2
(±)-*trans*-1,2-BrMe-cyclohexane	2.3	2.1	–4.5	+2.3
(±)-*trans*-1,2-diMe-cyclocyclohexane	0.07	0.11	–2.7	+3.0

[a] The Gibbs free energy of binding was calculated from $K_{a\ 293\ K}$. [b] *A*-values (conformational energies) were calculated as described in the Ref [241] at 293 K.

The strong binding constant of iodocyclohexane to AAC $(P)_4$-**62**, resulting in slow host-guest exchange on the NMR timescale, allowed for the assignment of the signals corresponding to the axially bound molecule. Figure 73 shows the ^{1}H NMR spectrum of AAC $(P)_4$-**62**⊃iodocyclohexane (2.7 equiv.) in *n*-octane-d_{18} at 277 K. The iodocyclohexane gave a broad and unresolved peak (4.23–4.34 ppm) due to the gauche coupling with the neighboring pairs of diastereotopic CH_2 groups in both equilibrating axial and equatorial conformations. The peak width is much narrowed (4.19–4.21 ppm) for the bound iodocyclohexane in the axial conformation, in which the C*H*I proton undergoes four gauche couplings.

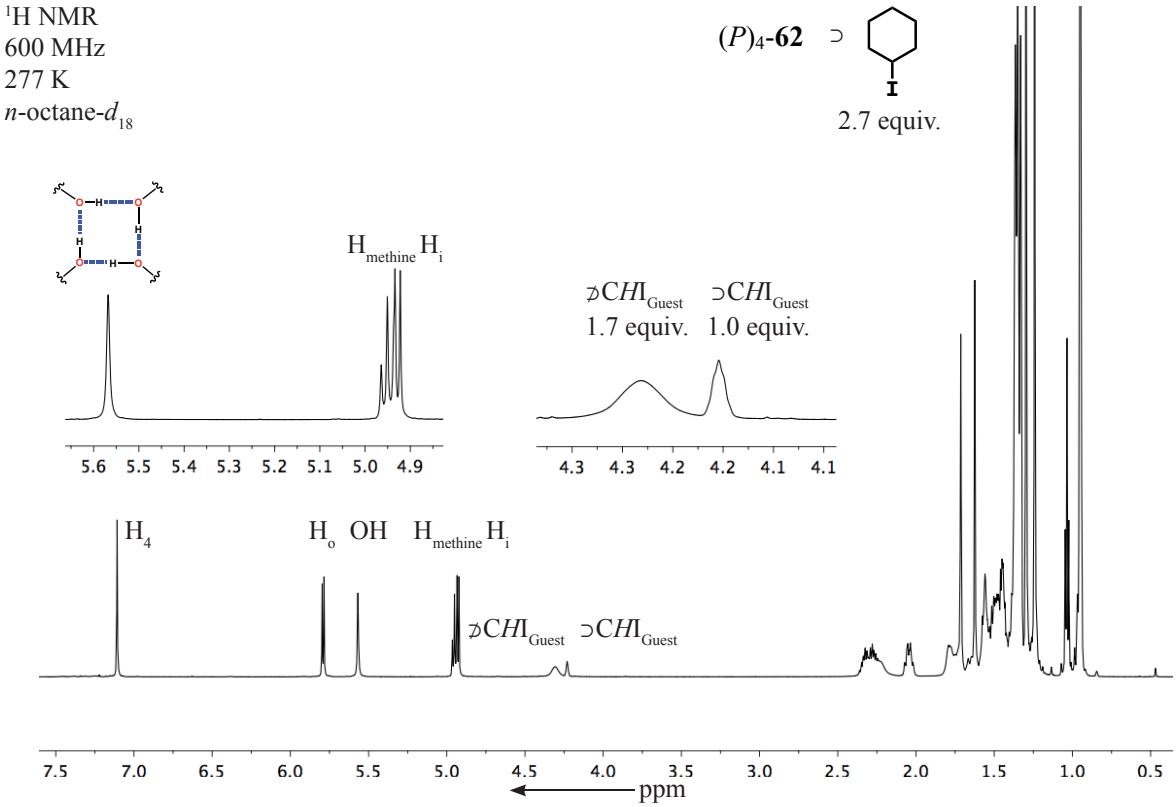

Figure 73. ^{1}H NMR traces of AAC (*P*)$_4$-**62** (6.7 mM) in *n*-octane-d_{18} at 277 K with 2.7 equiv. of iodocyclohexane. One equivalent is complexed while the 1.7 equiv. of the guest are free in solution. The insert shows the line narrowing of the C*H*I resonances of the complexed guest compared to the free guest. Host-resonances: H_{inside} = inside protons and H_o = outside protons of the methylene bridges; H_4 = aromatic proton.

The substantial narrowing of the signal width corresponding to the *C*HI resonances of the bound iodocyclohexane (⊃) compared to the free iodocyclohexane (⊅) was also observed in the ^{13}C NMR spectrum (Figure 74).

The 2D ROESY NMR spectrum of AAC (*P*)$_4$-**62**⊃iodocyclohexane (2.7 equiv.) in *n*-octane-d_{18} at 277 K is shown exemplary. Only significant through-space correlation of the guest (C*H*I) with the H_i-protons of the host were observed for the complexed guest (Figure 75, highlighted in red).

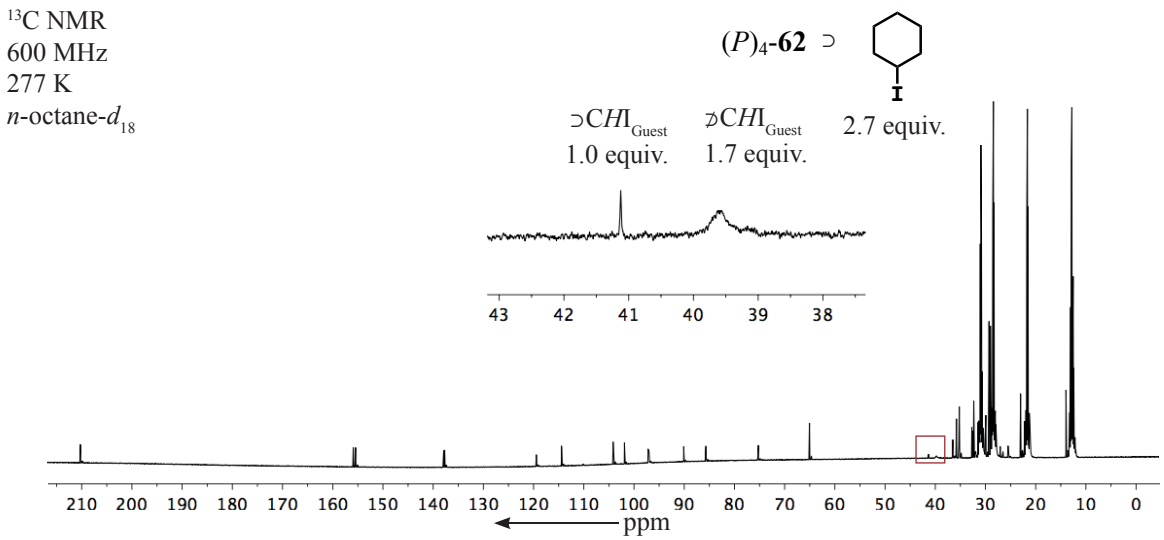

Figure 74. ^{13}C NMR traces of AAC (*P*)$_4$-**62** (6.7 mM) in *n*-octane-d_{18} at 277 K with 2.7 equiv. of iodocyclohexane. The insert shows the line narrowing of the *C*HI resonances of the complexed guest (1.0 equiv.) compared to the free guest (1.7 equiv.).

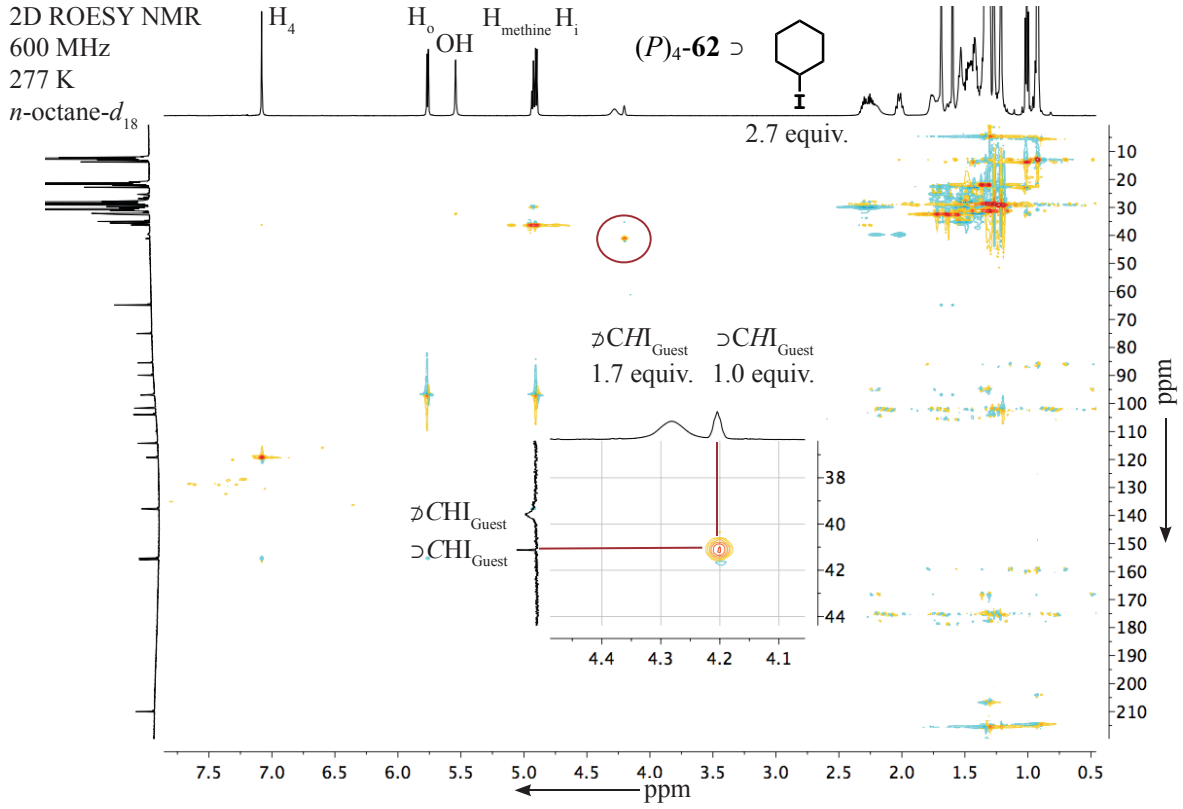

Figure 75. 2D ROESY NMR traces of AAC (*P*)$_4$-**62** in *n*-octane-d_{18} at 277 K with 2.7 eq. of iodocyclohexane. Host-resonances: H_{inside} = inside protons and H_o = outside protons of the methylene bridges; H_4 = aromatic proton.

During the ECD titrations of AAC $(P)_4$-**62** with iodocyclohexane, UV/Vis active guest in the region of 250 nm, a strong induced circular dichroism (ICD) signal was observed (Figure 76).

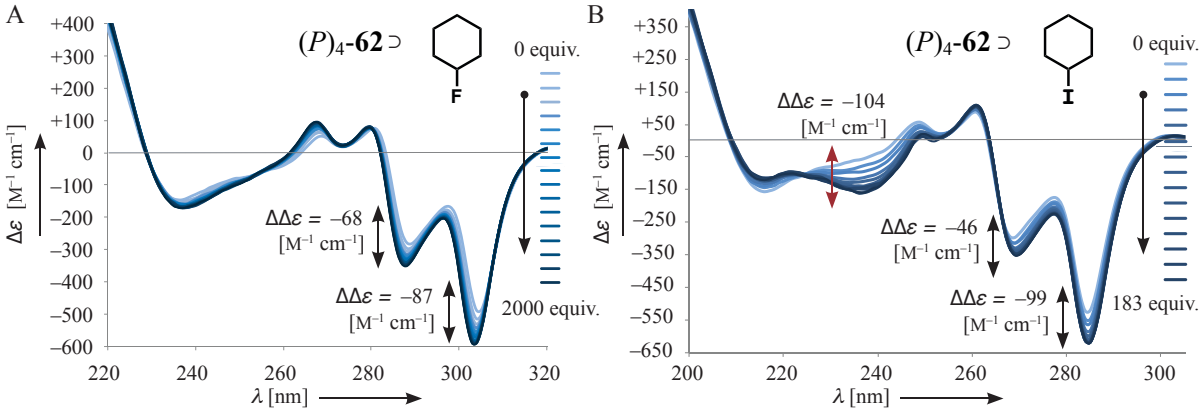

Figure 76. A: ECD titration of AAC $(P)_4$-**62** with fluorocyclohexane in *n*-octane at 293 K. B: ECD titration of AAC $(P)_4$-**62** with iodocyclohexane in *n*-octane at 293 K. Strong ICD is observed for iodocyclohexane (–104 M^{-1} cm^{-1} at 257 nm).

While fluorocyclohexane did not show any absorption in the region of 220–260 nm, a new ECD band emerged for iodocyclohexane at 254 nm with $\Delta\Delta\varepsilon$ = –104 M^{-1} cm^{-1} (Figure 76). This new band stems from the chiral induction (asymmetry information transfer process) of the optically active receptor to the bound guest.[185,186] With stronger binding and more polarizable guest molecules, the signal corresponding from the chiral induction becomes more pronounced.

Solution Binding Studies of (±)-trans-1,2-Dihalocyclohexanes with AACs (P)$_4$- and (M)-62

A strong contribution of both the conformational energies and favorable halogen-bonding interactions (C–X···π and C–X···Ⅲ) to the binding affinity was observed in the series of (±)-*trans*-1,2-disubstituted cyclohexanes. (±)-*trans*-1,2-Dimethylcyclohexane bound with K_a = $1.1 \cdot 10^2$ M^{-1} to AAC $(P)_4$-**62**. The strong diequatorial conformational preference in solution (*A*-value = +3.0 kcal mol^{-1}, Table 5), implies a high energetic penalty involved with accessing the, for binding necessary, diaxial conformation. The binding strength increased substantially for (±)-*trans*-1,2-dichlorocyclohexane (K_a = $3.8 \cdot 10^3$ M^{-1}) and (±)-*trans*-1,2-dibromocyclohexane (K_a = $2.9 \cdot 10^4$ M^{-1}). The strong increase in complexation strength was explained with the conformational preferences of the *trans*-1,2-dihalocyclohexanes for the diaxial conformation together with the favorable C–X···π and C–X···Ⅲ-halogen-bonding contacts between the host and the guest. The negative *A*-values of (±)-*trans*-1,2-dichlorocyclohexane (*A*-value = –1.0) and (±)-*trans*-1,2-dibromocyclohexane (*A*-value = –0.5) indicated a preference for the diaxial

conformation, which is the favorable binding conformation. The difference in conformational energy, together with the favorable halogen-bonding contacts of the bromines with the π-system of the receptor translated into the large increase in binding affinity of $\Delta\Delta G_{293\,K} = -3.3$ kcal mol^{-1} ((±)-*trans*-1,2-dimethylcyclohexane → (±)-*trans*-1,2-dibromocyclohexane)). Consequently, the binding constant decreased for (±)-*trans*-1,2-bromofluorocyclohexane with $K_a = 1.8 \cdot 10^3$ M^{-1} (*A*-value = +0.2), where the bromine underwent C–Br···π contacts with the resorcin[4]arene core, while the fluorine faces away from the acetylenic group. The comparison of the binding constants together with the *A*-values of (±)-*trans*-1,2-dibromocyclohexane ($K_a = 1.8 \cdot 10^3$ M^{-1} with $\Delta G = -6.0$ kcal mol^{-1}; *A*-value = +0.2) with (±)-*trans*-1,2-bromofluorocyclohexane ($K_a = 2.9 \cdot 10^4$ M^{-1} with $\Delta G = -4.4$ kcal mol^{-1}; *A*-value = –0.5) indicated a contribution of the C–Br···|||-halogen-bonding contact of 0.9 kcal mol^{-1}.

The C–Br···||| contact was further substantiated by FT-Raman spectroscopy, where the wavenumbers of the acetylenic band and the allenic band of the crystalline host–guest complexes and of the solution state complexes in *n*-octane were monitored (Figure 77). While the allenic frequencies did not change, the acetylenic frequencies shifted from 2210 cm^{-1} for iodocyclohexane to 2206 cm^{-1} for *trans*-1,2-dibromocyclohexane (Figure 77, A). This trend was also observed in *n*-octane, when changing the guest from bromocyclohexane to *trans*-1,2-dibromocyclohexane, and indicates a slight weakening of the acetylenic bond, which is expected upon establishing the C–Br···||| contact (Figure 77, B).

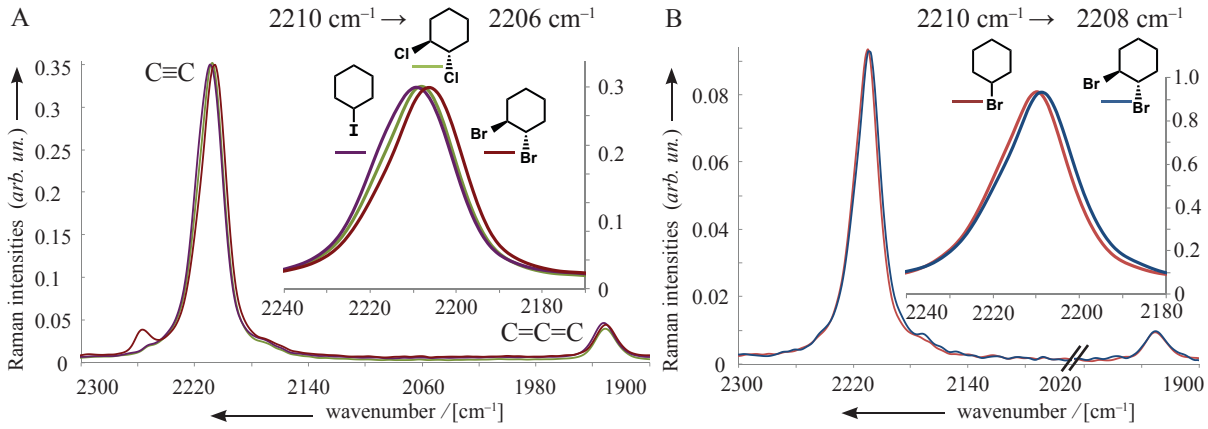

Figure 77. A: Raman spectra for the crystals of AAC $(P)_4$-**62** with iodocyclohexane (violet), *trans*-1,2-dichlorocyclohexane (green) and *trans*-1,2-dibromocyclohexane (brown). B: Raman spectra for AAC $(P)_4$-**62** with bromocyclohexane (red) and *trans*-1,2-dibromocyclohexane (blue) in *n*-octane at ca. 20 mM of the host and 100 mM of the guest.

Upon replacement of one bromine substituent in (±)-*trans*-1,2-dibromocyclohexane with one methyl group, the *A*-value increases considerably to +2.3

kcal mol^{-1} accompanied with a decrease in binding strength to K_a = 2.1·10^3 M^{-1}. The lower binding constant of (±)-*trans*-1,2-bromomethylcyclohexane compared to the (±)-*trans*-1,2-dibromocyclohexane is again in good agreement with the calculated conformational energies and halogen-bonding contact.

(±)-*trans*-1,2-Bromomethylcyclohexane additionally provided strong evidence for the exclusive complexation of the guest in the diaxial conformation in solution. This compound also underwent slow host–guest exchange with AAC (*P*)$_4$-**62** in *n*-octane-d_{18} at 277 K (Figure 78). The ^{1}H NMR spectrum of a solution with receptor and guest (13 equiv.) showed the free guest exclusively present in the diequatorial conformation, as expected from its large *A*-value (+2.3 kcal mol^{-1}). The signal of C*H*Br in the free guest gave a highly resolved coupling pattern, featuring a triplet of doublets ranging from 3.56–3.65 ppm (Figure 78, B). The triplet originates from two large coupling constants, J_{ax} = 11.7 Hz and J_{ax} = 10.4 Hz, and the doublet from the additional gauche-coupling with the equatorial proton of the neighboring C*H*$_2$ (J_{gauche} = 4.2 Hz), (Figure 78, B). In the complex, two much narrower and less resolved coupling patterns were observed for the C*H*Br proton in a ratio of 2:1. This suggested that two diastereoisomeric complexes form in a 2:1 ratio. This ratio is also supported by the ^{13}C NMR and 2D HSQC spectra. The much narrower (3.42 ppm–3.46 ppm), less resolved coupling pattern supported that the C*H*Br proton in the complex is in an equatorial position and that its resonance is split by three weaker gauche couplings (Figure 78).

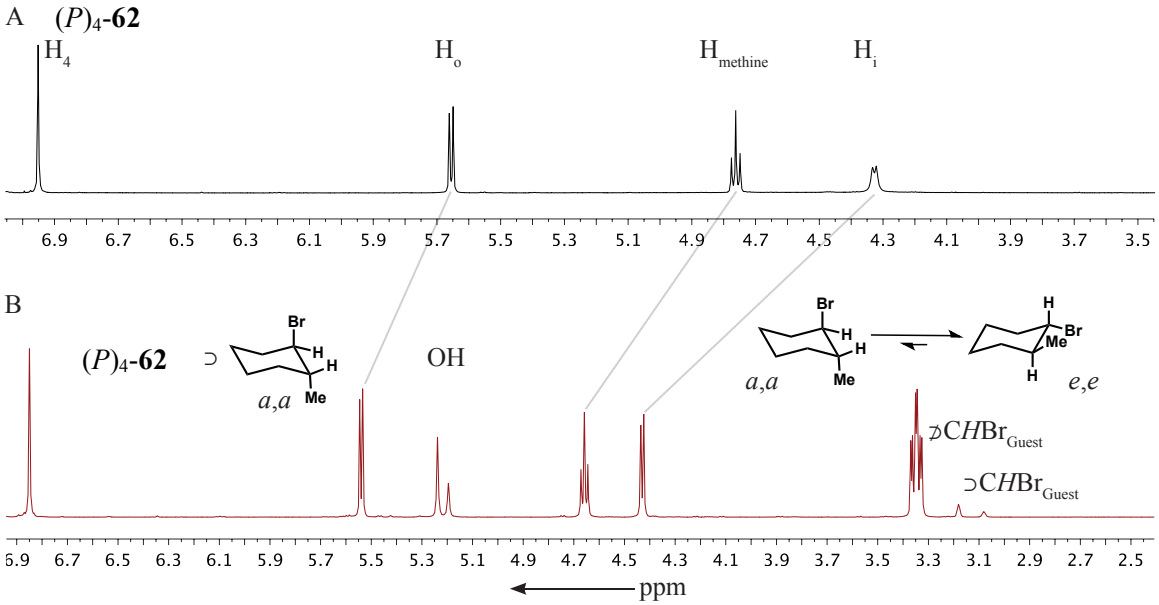

Figure 78. Overlay of ^{1}H NMR (600 MHz, 277 K, *n*-octane-d_{18}) spectra of pure AAC (*P*)$_4$-**62** (A) and AAC (*P*)$_4$-**62**⊃*trans*-1,2-bromomethylcyclohexane (13 equiv. of guest). Host-resonances: H$_{inside}$ = inside protons and H$_o$ = outside protons of the methylene bridges; H$_4$ = aromatic proton.

Enantioselective Complexation of (±)-trans-1,2-Dihalocyclohexanes with AACs $(P)_4$- and $(M)_4$-62 in Solution

The hydrogen-bonding array of the enantiopure $(P)_4$- and $(M)_4$-configured receptors encapsulating the achiral monohalocyclohexanes showed one single peak in the ^{1}H NMR spectra (in *n*-octane-d_{18}). Upon changing to the guests to the chiral (±)-*trans*-1,2-dihalocyclohexanes, a splitting of the H-bonding array was observed (Figure 79).

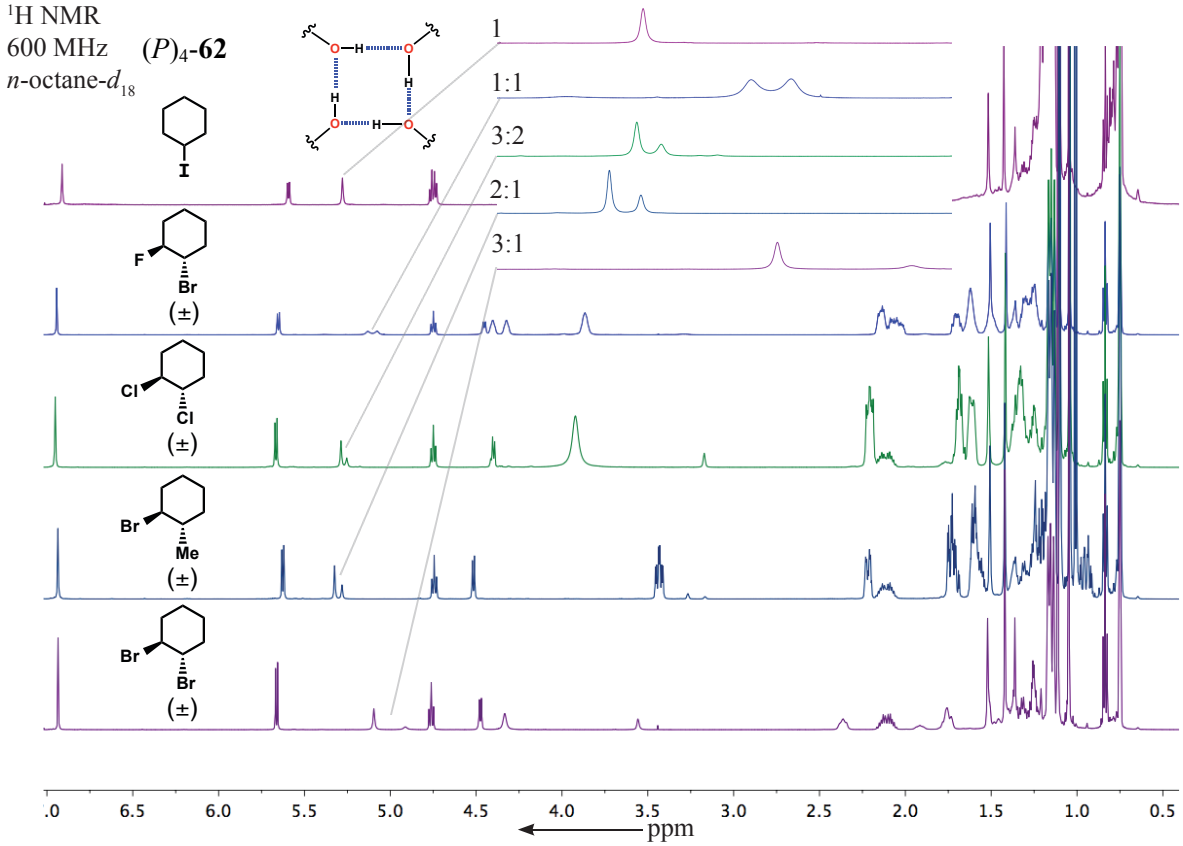

Figure 79. ^{1}H NMR of AAC $(P)_4$-**62** (6–8 mM, 1 equiv.) with guests (2.5–14 equiv. of guest) in *n*-octane-d_{18} at 277 K. The ratio of the split OH-array corresponds to the ration of (*R*,*R*):(*S*,*S*)-enantiomers observed in the co-crystal structures.

The splitting resulted from the formation of diastereomeric complexes between the enantiopure hosts and the chiral guest. The ratio of the splitting corresponded well to the enantiomeric ratios of the gest observed in the X-ray co-crystal structures (see above) and allowed for a direct comparison of the enantioselctivity in solution and in the solid state.

A summary of the enantiomeric ratios deduced from the splitting of the H-bonding array is given in Figure 79. This finding gave us a fast readout of the enantioselectivity of the AACs $(P)_4$- and $(M)_4$-**62** towards chiral guests based on NMR spectroscopy, reminiscent of chiral shift reagents. The splitting of the host–guest signals was also observed in the ^{13}C

spectra, further validating the preferential binding of the enantiomers with the same absolute configuration of the optically pure AACs $(P)_4$- and $(M)_4$-**62**.

3.3 Summary and Conclusion on Enantioselective Complexation through Dispersion and Halogen-Bonding Interactions

In the first part of this chapter, we presented a systematic study on the molecular recognition of achiral and chiral cyclic alkanes by enantiopure alleno-acetylenic cage (AAC) receptors. Solution binding studies were complemented by structural information obtained from single crystal X-ray diffraction of the host–guest complexes. The X-ray co-crystal structures revealed a size adaptability of the receptor towards the guest, in order to optimize the packing coefficient of the ensemble. At the optimal packing coefficient of ~55 %, the enantiopure receptor showed complete selectivity towards (±)-*trans*-1,2-dimethylcyclohexane, where the $(P)_4$-configured host only bound the (*R*,*R*)-configured guest, whereas the $(M)_4$-configured receptor selectively bound the (*S*,*S*)-configured guest. X-ray co-crystal structures of the host-bound guests revealed the exclusive complexation of the higher-energy diaxial conformation of *trans*-1,2-dimethylcyclohexane. This was the first time that the structure of *trans*-1,2-dimethylcyclohexane in its diaxial chair conformation was structurally elucidated. Remarkably, the dihedral angle in the diaxial *trans*-1,2-dimethylcyclohexane deviated strongly from the commonly accepted value of 180° down to 146°, posing the question, if the discovered dihedral angle is the result of receptor induced deviation. Subsequent theoretical investigations demonstrated negligible influence of the host on the guest structures.

In order to further validate the utility of the host to elucidate the elusive (di)axial conformations of cyclohexane derivatives, we expanded the initial study to the molecular recognition of monohalo- and *trans*-1,2-dihalocyclohexanes by enantiopure AACs $(P)_4$- and $(M)_4$-**62**. The developed crystallization protocol allowed us to obtain the molecular structures of the host–guest complexes through single-crystal X-ray diffraction. The series of guests are exclusively bound in their axial and diaxial chair conformation. The dihedral angles $\vartheta_{a,a}$ (X-C(1)-C(2)-H/X) deviated substantially from 180°, with increasing deviation from the monohalocyclohexanes (up to 25°) to *trans*-1,2-dihalocyclohexanes (up to 33°). The decrease in the dihedral angle $\vartheta_{a,a}$ was accompanied by flattening of the ring dihedral angles ϱ (X-C(1)-C(2)-C(3)) from 53° (fluorocyclohexane) to 79° (*trans*-1,2-bromofluorocyclohexane).

Theoretical analysis of the isolated guest molecules showed close structural similarity of the complexed and the isolated guest structures, demonstrating negligible influence of the host on the structure of the guest molecules. This further validated the utility

of the AACs to capture single conformers of derivatives of cyclohexane for their structural elucidation.

X-ray co-crystal structures of the host-guest complexes revealed two types of halogen-bonding contacts of the halogen substituents of the guest with the host (C–X···π and C–X···|||). One halogen pointed towards the four aromatic surfaces of the resorcin[4]arene core with decreasing distance from F < Cl < Br < I (C–X···π). The second halogen in the *trans*-1,2-disubstituted cyclohexanes pointed towards the acetylenic moiety, a hitherto little studied halogen-bonding contact (C–X···|||). Theoretical studies on the C–X···||| interaction substantiated its halogen bonding character. The C–X···||| contact appeared to majorly influence the enantioselectivity of the enantiopure receptor towards the chiral guests. The AACs $(P)_4$- and $(M)_4$-**62** showed preference for one enantiomer in the series of (±)-*trans*-1,2-dihalocyclohexanes with increasing enantiomeric ratio with increasing halogen-bonding strength (Cl < Br). The overall enantioselectivity towards the (±)-*trans*-1,2-dihalocyclohexanes was lower compared to the (±)-*trans*-1,2-dimethylcyclohexanes (complete enantioselectivity). This finding was counter-intuitive considering the stronger and directional nature of halogen-bonding contacts compared to the non-directional purely dispersion interactions of *trans*-1,2-dimethylcyclohexanes with the host. It was also in stark contrast to established concepts for enantioselective complexation of optically pure receptors with chiral guests, where more directional interactions are considered to enhance selectivity (see Introduction). We explained this observation with the much higher polarizability and larger distortion of the electron density of chlorine and bromine ("soft") compared to the methyl substituents ("hard").

Solution complexation studies supported the exclusive complexation of the guests in their (di)axial chair conformation, where slow host–guest exchange allowed the full characterization of the host–guest complexes. Solution binding constants, along with the theoretical calculations on the conformational energies (*A*-values), allowed to quantify the halogen-bonding contacts between the guests and the receptor. Comparison of fluorocyclohexane with iodocycloehxane revealed a gain in binding affinity of $\Delta\Delta G_{293\ K}$ = 2.4 kcal mol^{-1}, the result of the favorable C–X···π halogen-bonding interactions of the iodine with the aromatic moieties of the resorcin[4]arene receptor (0.6 kcal mol^{-1} per C–X···π_{Ar} halogen-bonding contact). Similarly, comparison of (±)-*trans*-1,2-dibromocyclohexane (K_a = $1.8\cdot10^3$ M^{-1} with $\Delta G_{293\ K}$ = –6.0 kcal mol^{-1}; *A*-value = +0.2) with (±)-*trans*-1,2-bromofluorocyclohexane (K_a = $2.9\cdot10^4$ M^{-1} with $\Delta G_{293\ K}$ = –4.4 kcal mol^{-1}; *A*-value = –0.5)

indicated a contribution of the C–Br···||| halogen-bonding contact of 0.9 kcal mol^{-1}. The difference in conformational energy, together with the favorable halogen bonding interactions, resulted in large increase in binding affinities of $\Delta\Delta G_{293\,K} = -3.3$ kcal mol^{-1} for (±)-*trans*-1,2-dibromocyclohexane compared to (±)-*trans*-1,2-dimethylcyclohexane. The enantiomeric ratios of the host–guest complexes, observed in the solid state, were also substantiated in solution, where the formation of diastereomeric complexes resulted in the splitting of the OH-array proton resonances.

4. AAC Receptors: Introducing Directional Hydrogen-Bonding Interactions – Rational Guest Design

This chapter was done in collaboration with T. Husch and Prof. M. Reiher (ETHZ). The theoretical results of Tamara Husch and Prof. M. Reiher are only briefly mentioned. Small-molecule single crystals were mounted by M. Solar, and X-ray crystal structures were solved by Dr. Nils Trapp (ETHZ).

4 AAC Receptors: Introducing Directional Hydrogen-Bonding Interactions – Rational Guest Design

The binding studies on guest molecules purely based on dispersive interaction, followed by dispersive interactions and halogen-bonding, allowed us to gain insight into the contribution of these apolar or weakly polar interactions to the enantioselective complexation with $(P)_4$- and $(M)_4$-configured AACs **62** (Chapter 3). Solution binding studies, along with the structural information obtained from X-ray co-crystal structure analysis, revealed that differences in conformational energy, along with highly directional halogen-bonding interactions, contribute to an increase in binding affinities to the receptors of up to $\Delta\Delta G = -3.3$ kcal mol^{-1} ((±)-*trans*-1,2-dimethylcyclohexane → (±)-*trans*-1,2-dibromocyclohexane).

In subsequent crystallization experiments of AAC $(P)_4$-**62** from pure acetonitrile and acetonitrile/water (9:1), we obtained two solvent enclosed X-ray crystal structures depicted in Figure 80 (slow evaporation over 1–3 days, 25 °C).

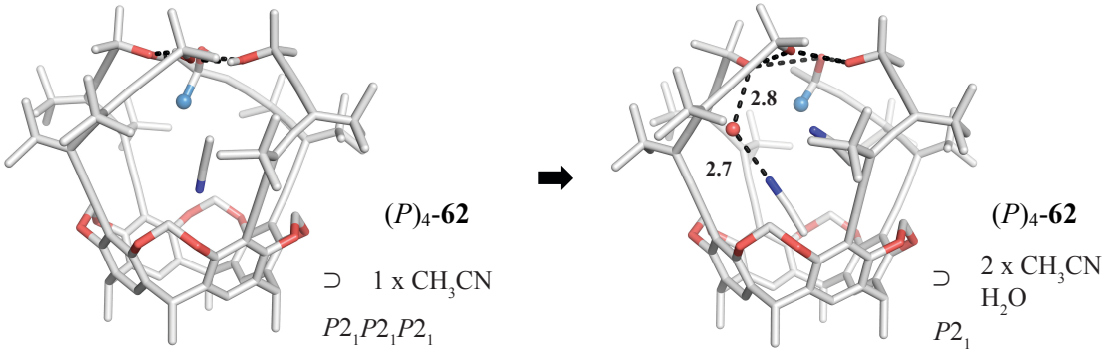

Figure 80. X-ray co-crystal structures of AAC $(P)_4$-**62** ⊃ CH_3CN (left) and AAC $(P)_4$-**62** ⊃ 2 x CH_3CN; H_2O (right). Distances are given in Å. *n*-Hexyl chains of the receptor **62** and hydrogens are omitted for clarity. One inside rotated methyl group of the tertiary alcohols (CMe_2OH) is highlighted as a blue ball.

Both X-ray crystal structures show one methyl group of the tertiary alcohol (CMe_2OH) rotated into the cavity compensating for the missing space occupancy of the solvent. The structure obtained from pure acetonitrile shows one molecule of acetonitrile occupying the interior of the host (Figure 80, left). The guest is disordered over two positions and only one acetonitrile position is shown. When adding water to the same crystallization experiment, we obtained the X-ray co-crystal structure with two acetonitrile and one water molecules occupying the cavity, where the water molecule bridges the H-bonding array to the acetonitrile molecules (Figure 80, right).

The bridging of the H-bonding array of the host with the encapsulated solvent through a single water molecule is reminiscent of the bridging of polar groups through water molecules in hydrophobic enzyme pockets[4] and led us to investigate the replacement of the water molecule by polar alcohol groups in the guest molecules. We were especially interested to study the gain in binding energy by introducing one or two directional hydrogen-bonding interactions, in comparison to the previously studied series with largely hydrophobic guests. Depending on the guest molecules, various interaction modes of the alcohol groups with the H-bonding array of the host were imaginable.

Over the course this chapter, the reader is led from the binding of purely hydrophobic guests by AACs $(P)_4$- and $(M)_4$-**62** to guest molecules containing one or two alcohol functionalities. In a rational design approach, we sought to demonstrate that the contribution of both directional interactions and perfect shape complementarity would yield high binding affinities of the guest towards the host. Finally, we explored the enantioselective complexation of chiral alcohols.

4.1 Expanding the Hydrogen-Bonding Array: Binding of Cyclic Alcohols through Directional Hydrogen-Bonding Interactions and Dispersion Interactions

In order to study the contribution of directional hydrogen-bonding to the binding affinity of guests to receptors $(P)_4$- and $(M)_4$-**62**, we selected four different series of cyclic alcohols (Figure 81).

A From Cyclohexane to *trans*-4-Methylcyclohexanol and *trans*-4-(Trifluoromethyl)cyclohexanol

B From Cyclohexane to Norbornane to *endo*-Norborneol

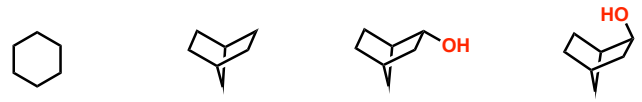

C From Cycloheptane to Tropane and *endo*-Tropine

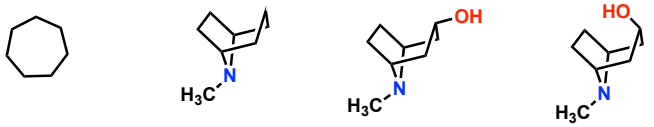

D From Cyclohexane to Cyclohexanol and *trans*-1,2-Cyclohexanediol

Figure 81. Summary of the structures of selected cyclic alcohols for the complexation studies with AACs $(P)_4$- and $(M)_4$-**62**.

The first series parallels the binding study with cyclohexane and methylcyclohexane reported in Chapter 3 and expands to *cis*-, *trans*-4-methylcycohexane and its trifluoromethyl derivative (Figure 81, A). In a second series, we studied the bridging of cyclohexane to norbornane and introduction of the alcohol group in *exo*- and *endo*-norborneol (Figure 81, B). Starting from the X-ray co-crystal structure of AAC $(P)_4$-**62**⊃cycloheptane, we rationally expanded the guest molecules to tropane and *endo*- and *exo*-tropine (Figure 81, C). Finally, the enantioselective binding of (*S*,*S*)- and (*R*,*R*)-configured *trans*-1,2-cyclohexanediol was studied.

In order to compare the binding affinities of the alcohol series to the previously studied hydrophobic molecules, we used *n*-octane as solvent for NMR and ECD binding titrations (see Chapter 2 and in the Experimental Part). 2D NMR studies substantiated the complexation of the guests in the interior of the optically pure AACs $(P)_4$- and $(M)_4$-**62**. For stronger binding guests, such as in Figure 81 C, ITC was additionally employed to obtain the entropic and enthalpic contributions to the complexation event.

4.1.1 From Cyclohexane to Cyclohexanol and *trans*-4-Methylcyclohexanol: Binding to AACs $(P)_4$- and $(M)_4$-62

In the study from cyclohexane and methylcyclohexane to *cis*- and *trans*-4-methylcyclohexanol, we were interested to explore the increase in binding affinity through H-bonding interactions (cyclohexane → cyclohexanol), with the contribution of a methyl group in the 4-position, allowing for favorable C-H···π contacts.

In our previous study on cycloalkanes, we showed that cyclohexane did not have measurable binding affinity to AACs $(P)_4$- and $(M)_4$-**62**, while methylcyclohexane already showed weak complexation with $\Delta G_{293\ K} = -1.8$ kcal·mol^{-1} (Table 6).

Table 6. Summary of binding constants (K_a at 293 K) and Gibbs free energies for the complexation of alkyl cyclohexanols by AAC $(P)_4$-**62** in *n*-octane. Only K_a obtained from ECD titrations are shown.

Host:	$(P)_4$-**62** ⊃	$P)_4$-**62** ⊃	$(P)_4$-**62** ⊃	$(P)_4$-**62** ⊃	$(P)_4$-**62** ⊃	$(P)_4$-**62** ⊃
Guest:		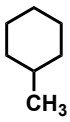	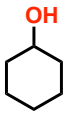	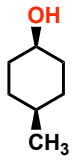	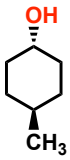	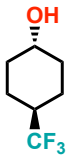
ECD K_a [M^{-1}]	< 1	2.2·10	6.7·10^3	2.8·10^4	1.0·10^5	1.8·10^3
$\Delta G_{293\ K}$ [kcal mol^{-1}]	–	–1.8	–5.1	–6.0	–6.7	–4.4

We rationalized the increase in association strength with increasing dispersion interactions (C-H···π contacts) of the methyl group of methylcyclohexane to the aromatic resorcin[4]arene core of the receptor. When introducing the alcohol functionality, such as in cyclohexanol, the binding strength increased substantially from <1 M^{-1} for cyclohexane to 6.7·10^3 M^{-1} ($\Delta G_{293\ K} = -5.1$ kcal mol^{-1}) for cyclohexanol (Table 6). Similarly, changing the guest from methylcyclohexane to *cis*-4-dimethylcyclohexane resulted in an increase in affinity from 2.2·10 M^{-1} ($\Delta G_{293\ K} = -1.8$ kcal mol^{-1}) to 2.8·10^4 M^{-1} ($\Delta G_{293\ K} = -6.0$ kcal mol^{-1}), translating to a difference in binding strength of $\Delta\Delta G_{293\ K} = -4.2$ kcal mol^{-1}. The diastereoisomer of *cis*-4-methylcyclohexanol, *trans*-4-methylcyclohexanol, further augmented the affinity to AAC $(P)_4$-**62** to 1.0·10^5 M^{-1} ($\Delta G_{293\ K} = -6.7$ kcal mol^{-1}). Substitution of the methyl group with a trifluoromethyl group decreased the binding affinity for cage inclusion by $\Delta\Delta G_{293\ K} = +2.3$ kcal mol^{-1} (Table 6). This decrease was in line with favorable C-H···π contacts

of the methyl group to the aromatic resorcin[4]arene core compared to unfavorable C-F···π proximities.

Figure 82 depicts the X-ray co-crystal structures of *cis*- and *trans*-4-methylcyclohexanol with AAC $(P)_4$-**62**.

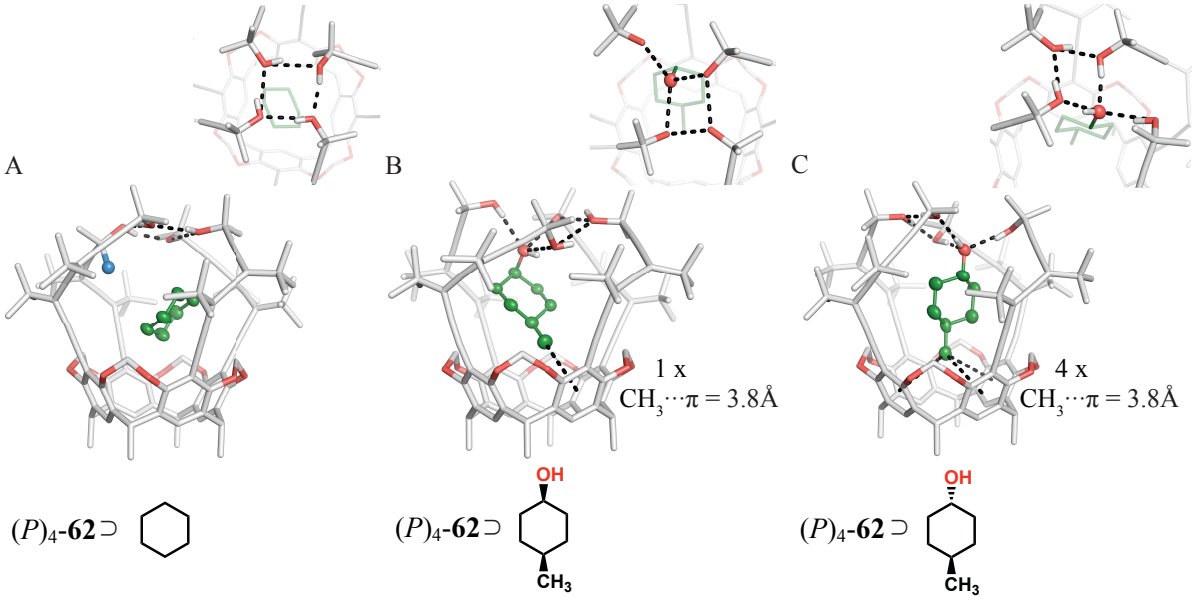

Figure 82. X-ray co-crystal structures of AAC $(P)_4$-**62**⊃cyclohexane (A), AAC $(P)_4$-**62**⊃*cis*-4-methylcyclohexanol (B) and AAC $(P)_4$-**62**⊃*trans*-4-methylcyclohexanol (C). For AAC $(P)_4$-**62**⊃ *cis*-4-methylcyclohexanol, hydrogens of the OH groups were modelled. Distances are given in Å. *n*-Hexyl chains of the receptor and hydrogens are omitted for clarity.

The alcohol group of the guests engage in H-bonding to the cyclic H-bonding array, expanding it to a five-OH-interaction network. The guest participates in a cooperative fashion, both accepting and donating a H-bond (Figure 82).[271,272] The optimized C-H···π contacts of *trans*-4-methylcyclohexanol (4 x C-H···π of 3.8 Å) compared to *cis*-4-methylcyclohexanol (1 x C-H···π of 3.8 Å) rationalized the lower binding constant of the latter ($\Delta\Delta G_{293\ K}$= +0.7 kcal mol^{-1}). The trifluoromethyl derivative *trans*-4-(trifluoromethyl)-cyclohexanol showed weakened association, since the F atoms avoid contacts with electron-rich surfaces, such as aromatic rings.[273]

4.1.2 From Cyclohexane to Norbornane and *endo*-Norborneol: Binding to AACs $(P)_4$- and $(M)_4$-62

Solution binding studies in *n*-octane at 293 K of norbornane, *exo*- and *endo*-norborneol with AAC $(P)_4$-**62** confirmed the increase in binding affinity through the introduction of one alcohol group on the guest (Table 7).

Table 7. Binding constants K_a (293 K) and Gibbs free energies for the complexation of cyclohexane, norbornane, *exo*- and *endo*-norborneol by AAC $(P)_4$-**62** in *n*-octane. Only binding constants (K_a) obtained from ECD titrations are shown.

Host: Guest:	$(P)_4$-**62** ⊃ 	$P)_4$-**62** ⊃ 	$(P)_4$-**62** ⊃ 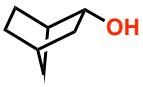	$(P)_4$-**62** ⊃ 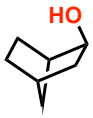
ECD K_a [M^{-1}]	< 1	$8.6 \cdot 10$	$1.7 \cdot 10^4$	$3.1 \cdot 10^4$
$\Delta G_{293\ K}$ [kcal mol^{-1}]	–	–2.6	–5.7	–6.0

The binding strength increased from cyclohexane to methylcyclohexane and norbornane ($\Delta G_{293\ K}$ = ~ 0 → –1.8 kcal mol^{-1} → –2.6 kcal mol^{-1}). The introduction of the alcohol group augmented the affinity further to $K_a = 1.7 \cdot 10^4$ M^{-1} ($\Delta G_{293\ K}$ = –5.7 kcal mol^{-1}) for *exo*-norborneol and to $3.1 \cdot 10^4$ M^{-1} ($\Delta G_{293\ K}$ = –6.0 kcal mol^{-1}) for *endo*-norborneol. The transition from norbornane to *endo*-norborneol translates to an increase in association strength of $\Delta\Delta G_{293\ K}$ = –3.4 kcal mol^{-1}. Compared to the *cis*- and *trans*-4-methylcyclohexanol, the norbornane series does not undergo favorable C-H···π contacts with the host. The gain in Gibbs free energy of $\Delta\Delta G_{293\ K}$ = –3.4 kcal mol^{-1} from norbornane to *exo*- and *endo*-norborneol can therefore be traced back to the single hydrogen-bonding contact.

The co-crystal structure of AAC $(P)_4$-**62**⊃norbornane, depicted in Figure 83, demonstrates the absence of significant C-H···π contacts.

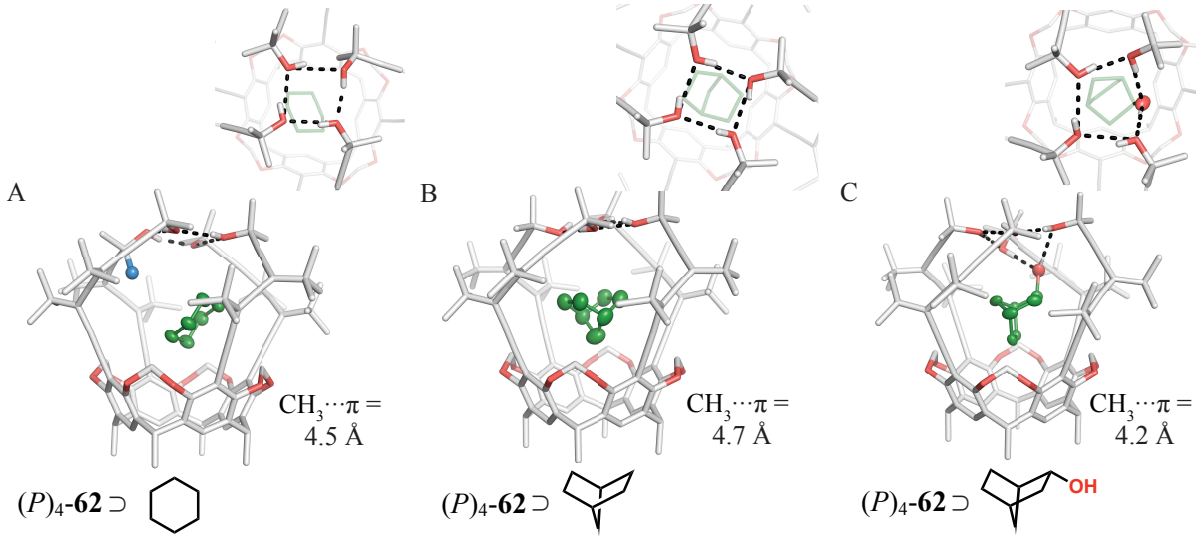

Figure 83. X-ray co-crystal structures of A: AAC $(P)_4$-**62**⊃cyclohexane; B: AAC $(P)_4$-**62**⊃norbornane; C: AAC $(P)_4$-**62**⊃*exo*-norborneol. For AAC $(P)_4$-**62**⊃ cyclohexane, one methyl group of the tertiary alcohols of the receptor is rotated into the cavity. *n*-Hexyl chains of the receptor **62** and hydrogens are omitted for clarity. Space groups: $P2_1P2_1P2_1$.

In the X-ray co-crystal structure of AAC $(P)_4$-**62**⊃cyclohexane, one methyl group of the tertiary alcohols (CMe_2OH) is rotated into the cavity. This methyl group is rotated outside for the seven-carbon containing norbornane encapsulated by AAC $(P)_4$-**62**. The complexed norbornane shows disorder over two positions (70:30, only the 70% are depicted in Figure 83), indicating lower shape complementarity, compared to guests, such as cycloheptane (see Figure 48). In the X-ray co-crystal structure of *exo*-norborneol complexed to AAC $(P)_4$-**62**, the alcohol group of the guest forms a five-fold hydrogen-bonding array with the host (Figure 83, C). The guest shows two populations (50:50) rotated 180° to each other around the C–O-bond-axis of the guest, indicating little favorable interactions of the norbornane core with the resorcin[4]arene core of the host. Crystallization of *endo*-norborneol with AAC $(P)_4$-**62** is ongoing. The series of cyclohexane, norbornane, *exo* and *endo*-norborneol illustrates the contribution of preorganization of the guests and directional hydrogen-bonding to the binding affinities towards the host.

4.1.3 From Cycloheptane to Tropane and *endo*-Tropine: Binding to AACs $(P)_4$- and $(M)_4$-62

In a structure-based design series, we sought to optimize space filling, dispersive interactions, and directional hydrogen-bonding interactions of the guest with the host. Starting from the co-crystal structure of AAC $(P)_4$-**62**⊃cycloheptane, we imagined to build up tropanes, a class of bicyclic[3.2.1] alkaloids, which can be found as core structure in molecules, such as cocaine

or atropine.[274] With increasing binding strength of the guest to the receptor, the sensitivity of the optical output (ECD) would allow us to detect minute amounts of the guest in solution. Moreover, the tight binding of tropane and its derivatives would allow us to study the *N*-methyl-inversion of the guests inside the host.[275] In solution studies and by X-ray co-crystal structure analysis, we explored the conformational preferences of the complexed *endo*-tropine and *exo*-tropine.

The series of cycloheptane, tropane and *exo*- and *endo*-tropine showed a large increase in binding affinity with increasing size, dispersive interactions, and hydrogen-bonding strength of the guest to the receptor (Table 8). The bicyclic[3.2.1] alkaloid tropane bound to AAC $(P)_4$-**62** with $K_a = 2.9 \cdot 10^4$ M^{-1} ($\Delta G_{293\ K} = -6.0$ kcal mol^{-1}), by $\Delta\Delta G_{293\ K} = -3.1$ kcal mol^{-1} stronger compared to cycloheptane. *exo*- and *endo*-Tropine further increased the binding strength substantially to $K_a = 2.8 \cdot 10^6$ M^{-1} ($\Delta G_{293\ K} = -8.4$ kcal mol^{-1}) and $K_a = 7.0 \cdot 10^6$ M^{-1} ($\Delta G_{293\ K} = -9.0$ kcal mol^{-1}), respectively. The binding strength of both tropines was remarkable and is comparable to binding affinities found for substrates of this size in natural receptors.[45] The contribution of the alcohol group interacting with the hydrogen-bonding array, corresponded to $\Delta\Delta G_{293\ K} = -2.4$–$3.0$ kcal mol^{-1}, depending on the *exo*- or *endo*-configuration of the diastereoisomeric alcohol.

Table 8. Binding constants K_a (293 K) and Gibbs free energies for the complexation of cycloheptane, tropane, *exo*- and *endo*-tropine by AAC $(P)_4$-**62** in *n*-octane. K_a values obtained from ECD titrations are shown.

AAC Host:	$(P)_4$-**62** ⊃	$P)_4$-**62** ⊃	$(P)_4$-**62** ⊃	$(P)_4$-**62** ⊃
Guest:		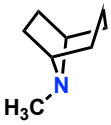	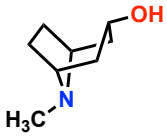	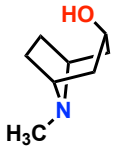
ECD K_a [M^{-1}]	$1.4 \cdot 10^2$	$2.9 \cdot 10^4$	$2.8 \cdot 10^6$	$7.0 \cdot 10^6$
$\Delta G_{293\ K}$ [kcal mol^{-1}]	–2.9	–6.0	–8.4	–9.0

Tropane (8-methyl-8-azabicyclo[3.2.1]octane) and its derivatives undergo fast *N*-methyl inversion in solution, resulting in equatorial and axial diastereisomers.[275] The equatorial diastereoisomer is defined as the structure, where the *N*-methyl group is facing away from the alcohol group (as drawn in Table 8). In the axial diastereoisomer, the *N*-methyl group

is oriented towards the alcohol.[274] ^{13}C NMR solution studies in methanol-d_3 at low temperature (–90 °C) allowed for quantification of the conformer distribution, where a preference for the equatorial conformer was detected (30:1).[275] In 1D and 2D ROESY NMR studies, we were interested to explore the conformation of the *N*-methyl group of encapsulated *endo*-tropine. Figure 84 shows the NMR spectroscopic traces of AAC $(P)_4$-**62**⊃*endo*-tropine. The ^{1}H NMR signals (Figure 84) and ^{13}C NMR traces (Figure 85) of the complexed *endo*-tropine (⊃) are well separated from the signals of the free *endo*-tropine (⊅) and allowed complete assignment of both species.

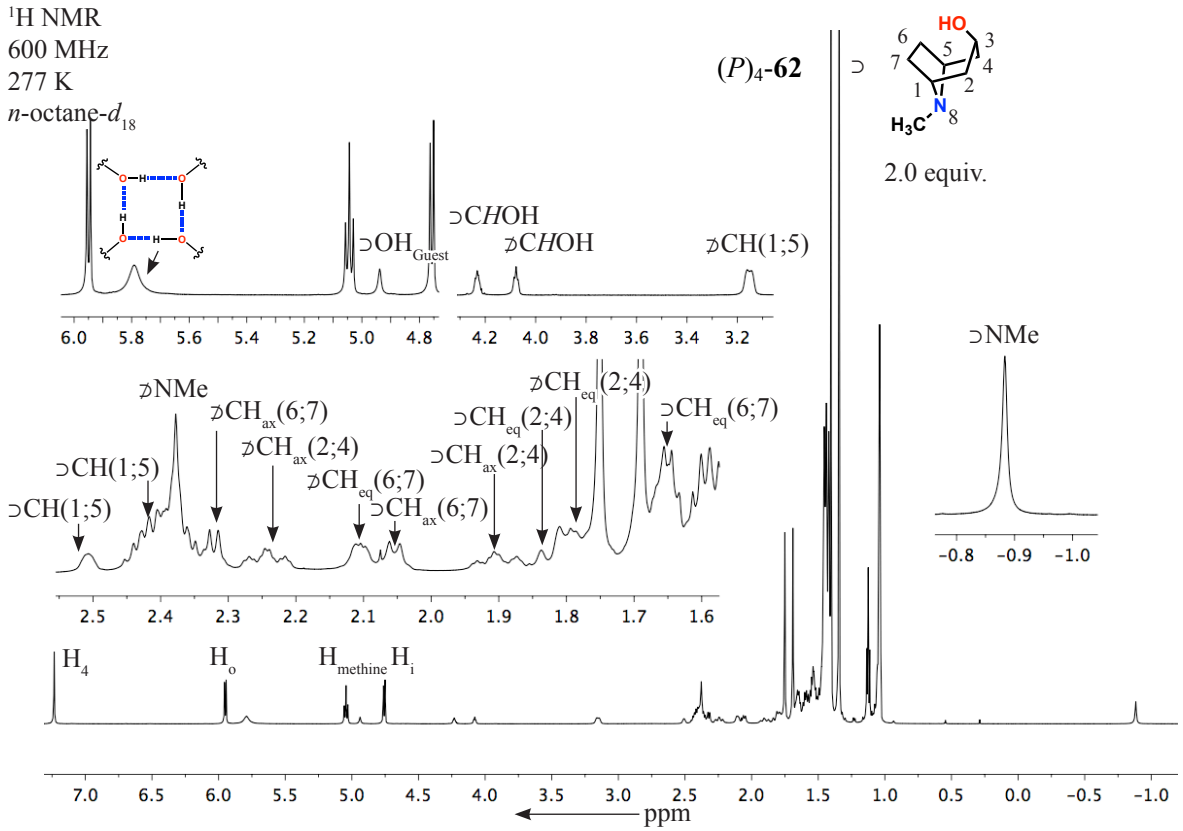

Figure 84. ^{1}H NMR traces of AAC $(P)_4$-**62** (7.1 mM) in *n*-octane-d_{18} at 277 K with 2.0 equiv. of *endo*-tropine. One equivalent is complexed while the second equiv. of the *endo*-tropine is unbound in solution. The ⊃ denotes complexed guest molecule and ⊅ denotes free guest *endo*-tropine. Host-resonances: H_{inside} = inside protons and H_o = outside protons of the methylene bridges; H_4 = aromatic proton.

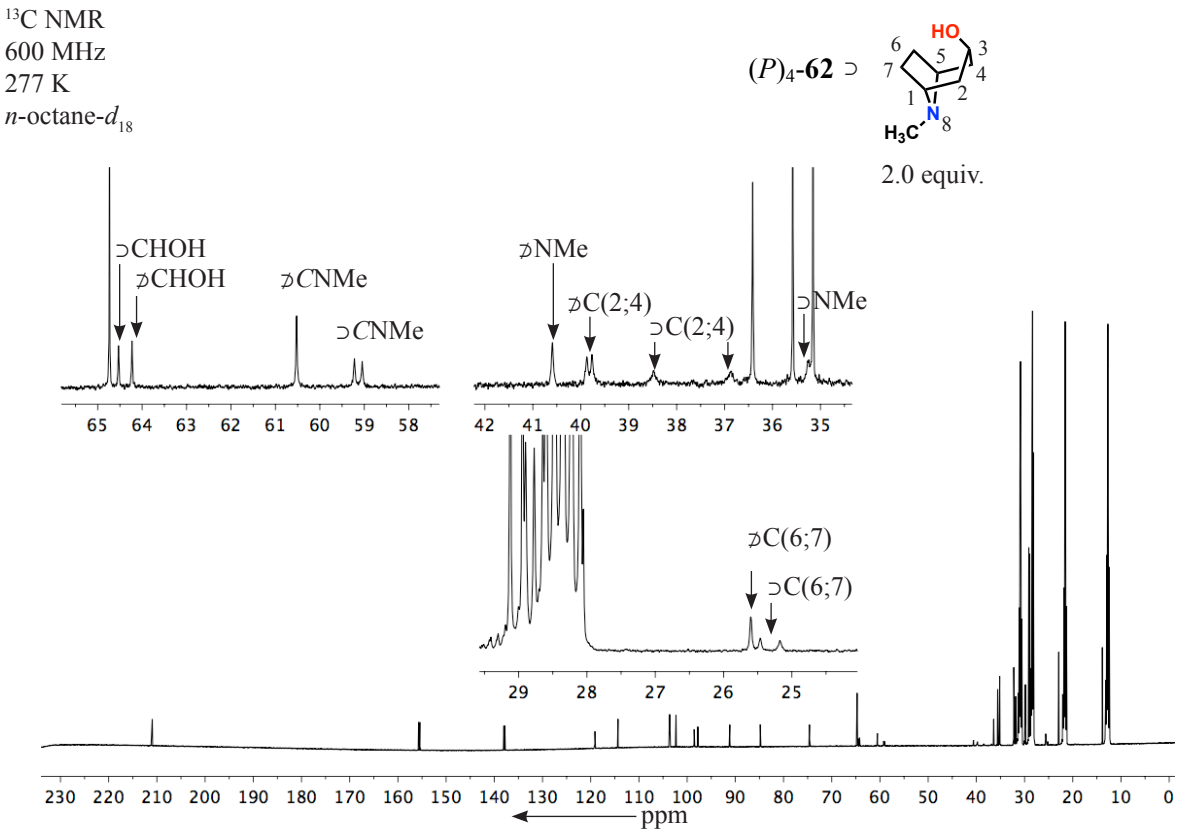

Figure 85. ^{13}C NMR traces of AAC (*P*)$_4$-**62** (7.1 mM) in *n*-octane-d_{18} at 277 K with 2.0 equiv. of *endo*-tropine. One equivalent is complexed while the second equiv. of the *endo*-tropine is unbound in solution. The ⊃ denotes complexed guest molecule and ⊅ denotes free guest *endo*-tropine.

Interestingly, a desymmetrization of the carbon resonances corresponding to the encapsulated guests was observed (Figure 85). In order to investigate if the desymmetrization is the result of the *N*-methyl inversion in the complexed guests, we measured the cross peaks of the *N*-methyl groups with the proximate CH_{eq} (2;4) and CH_{eq} (6;7) protons in the 2D ROESY NMR experiments (in *n*-octane-d_{18} at 277 K, Figure 86). The NMe group showed through-space correlation only with the equatorial protons of CH_{eq} (6;7), whereas no such cross peaks were observed with the equatorial protons CH_{eq} (2;4).

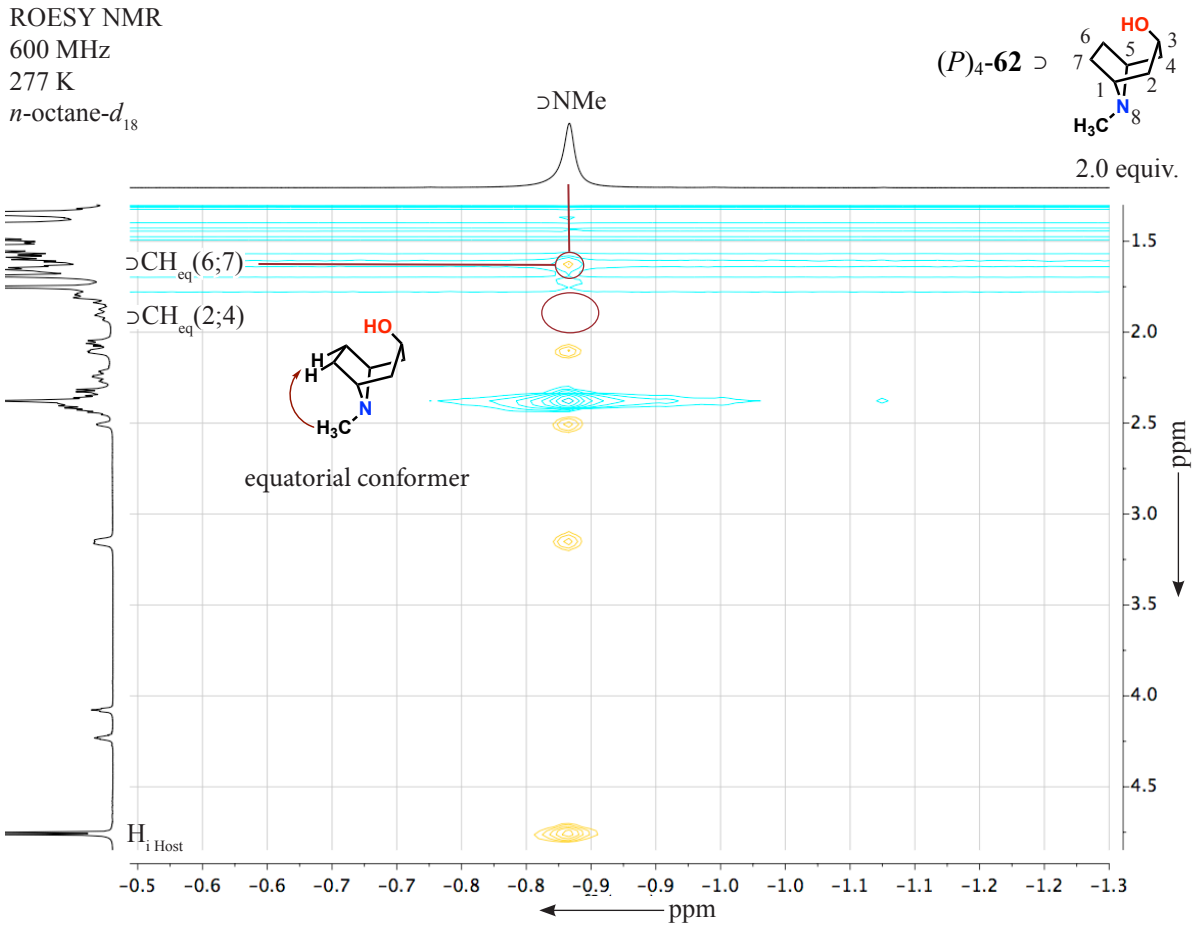

Figure 86. 2D ROESY NMR spectrum of AAC $(P)_4$-**62** (7.1 mM) in *n*-octane-d_{18} at 277 K with 2.0 equiv. of *endo*-tropine. Cross signals circled in red.

Additionally, the NMe group of the free *endo*-tropine showed cross peaks with both the CH_{eq} (2;4) and the CH_{eq} (6;7) equatorial protons. This indicated preferential complexation of the equatorial conformer of *endo*-tropine. 1D NOE NMR spectroscopic experiments are ongoing to confirm the observed diastereomeric selectivity inside the host.

The high binding affinities of tropane, *exo*- and *endo*-tropine to AAC $(P)_4$-**62** allowed us to study the thermodynamic parameters of their binding by isothermal titration calorimetry (ITC). The ITC traces of *exo*- (A) and *endo*-tropine (B) are shown exemplary in Figure 87.

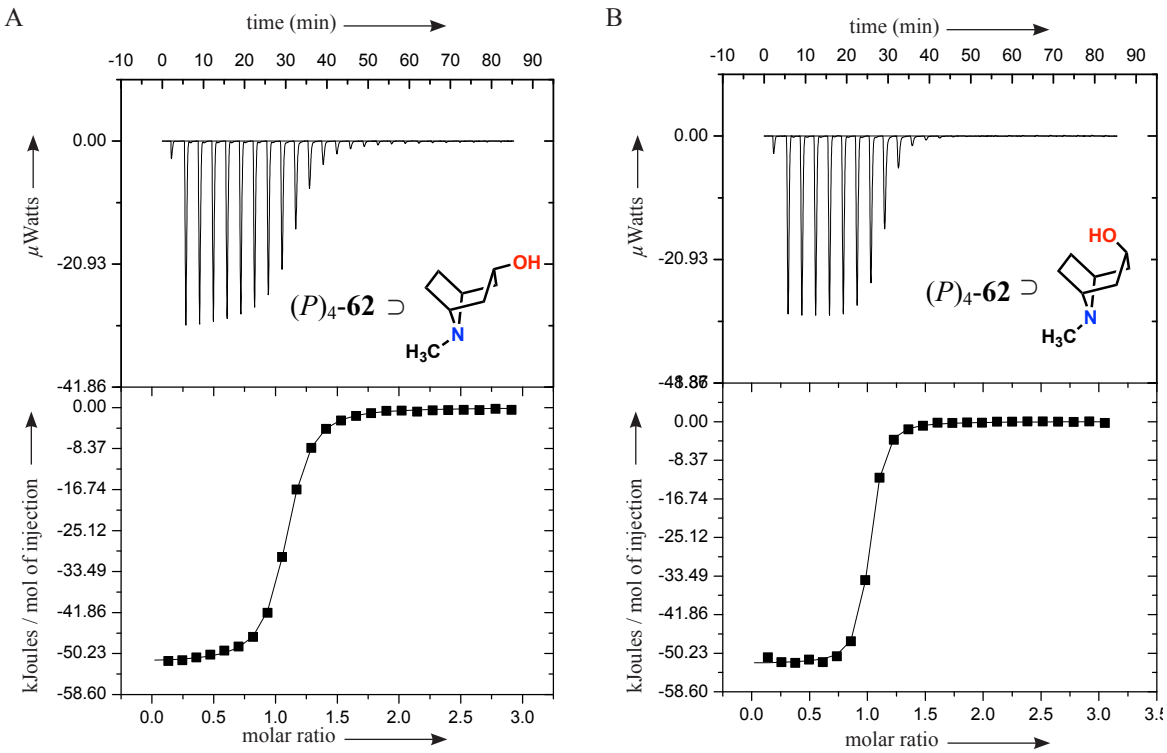

Figure 87. ITC binding isotherms for AAC $(P)_4$-**62** in *n*-octane at 303 K with *exo*- (A) and *endo*-tropine (B).

The corresponding thermodynamic data is shown in Table 9 and compared to the binding constants obtained by ECD spectroscopy. Both methods gave comparable values (Table 9). Tropane and *exo*- and *endo*-tropine show large enthalpic contributions to the Gibbs free energy of complexation, with only small entropic penalties. The contribution of the alcohol interacting with the H-boding array of the receptor corresponds to a remarkable ~4 kcal mol^{-1} (tropane → *exo*-/ *endo*-tropine). The increase in binding energy through the directional hydrogen bonding of *exo*- and *endo*-tropine is counterbalanced by small entropic costs of ~1–2 kcal mol^{-1} (tropane → *exo*-/ *endo*-tropine).

Table 9. ECD and ITC binding isotherms for AAC $(P)_4$-**62** in *n*-octane at 293 K (ECD) and 303 K (ITC) with tropane, *exo*- and *endo*-tropine.

Guest	ECD $K_{a\ 293\ K}$ [M^{-1}]	ITC $K_{a\ 293\ K}$ [M^{-1}]	ITC $\Delta G_{303\ K}$ [kcal mol^{-1}]	ITC $\Delta H_{303\ K}$ [kcal mol^{-1}]	ITC $-T\Delta S_{303\ K}$ [kcal mol^{-1}]
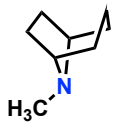	$2.9\cdot10^4$	$3.1\cdot10^4$	–5.95	–8.23	+2.28
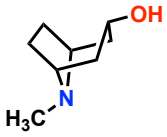	$2.8\cdot10^6$	$2.2\cdot10^6$	–8.36	–12.33	+4.08
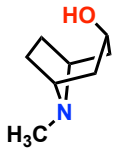	$7.0\cdot10^6$	$6.3\cdot10^6$	–9.01	–12.55	+3.54

To demonstrate the high binding affinity of *endo*-tropine to AAC $(P)_4$-**62** in *n*-octane, we measured ECD spectroscopic changes at very high dilution of the host ($1.0\cdot10^{-6}$ M^{-1}) with the guest ($1.0\cdot10^{-9}$ M^{-1}, Figure 88).

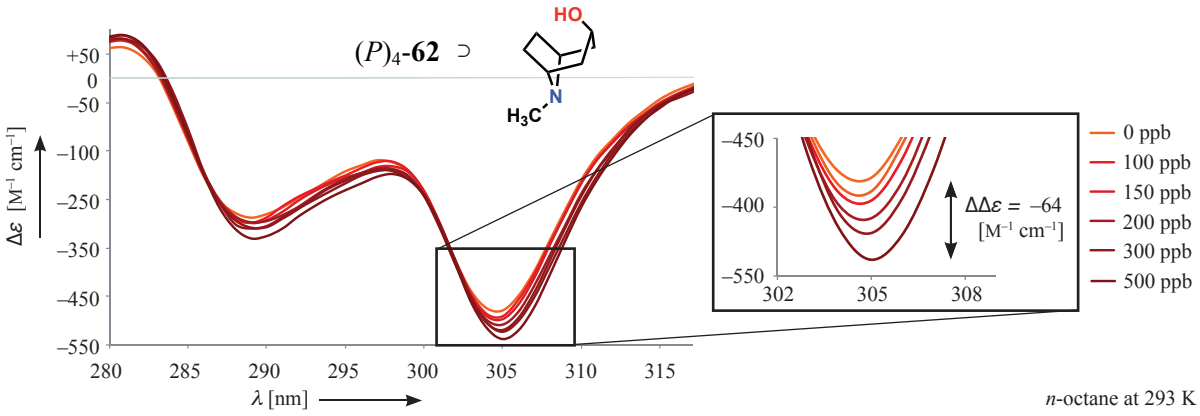

Figure 88. ECD traces of AAC $(P)_4$-**62** (1.0 μM) in *n*-octane at 293 K with *endo*-tropine (titrated at $1.0\cdot10^{-9}$ M^{-1}).

Already in the parts per billion regime (below 100 ppb) of the guest in solution, we observed induced ECD (ICD) intensities (Figure 88). At 500 ppb of the guest, an induced circular dichroism of $\Delta\Delta\varepsilon = -64$ M^{-1} cm^{-1} at 304 nm was measured. The high affinity combined with the extremely sensitive optical output of the AAC receptors $(P)_4$- and $(M)_4$-**62** was remarkable, considering the high dilution of the guest (ppb). It exemplifies the potential

applicability of the AACs $(P)_4$- and $(M)_4$-**62** for the detection of non-chromophoric small molecules.[176]

The configuration of the *N*-methyl group of different derivatives of tropine varies in reported crystal structures. The crystal structure of cocaine displayed the *N*-methyl group in the equatorial conformation,[276] whereas scopolamine for example showed the *N*-methyl group in the axial conformation.[277] In 1967, Laan *et. al.* reported the crystal structure of *exo*-tropine, with the *N*-methyl group in the equatorial conformation.[278] To the best of our knowledge, no crystal structure of *endo*-tropine has been reported to date.

In order to determine the binding mode of the series of tropane and *exo*- and *endo*-tropine to AAC $(P)_4$-**62** in the solid state, we set up crystallization experiments following the described protocol. X-ray co-crystal structures of *endo*- and *exo*-tropine with AAC $(P)_4$-**62** are depicted in Figure 89.

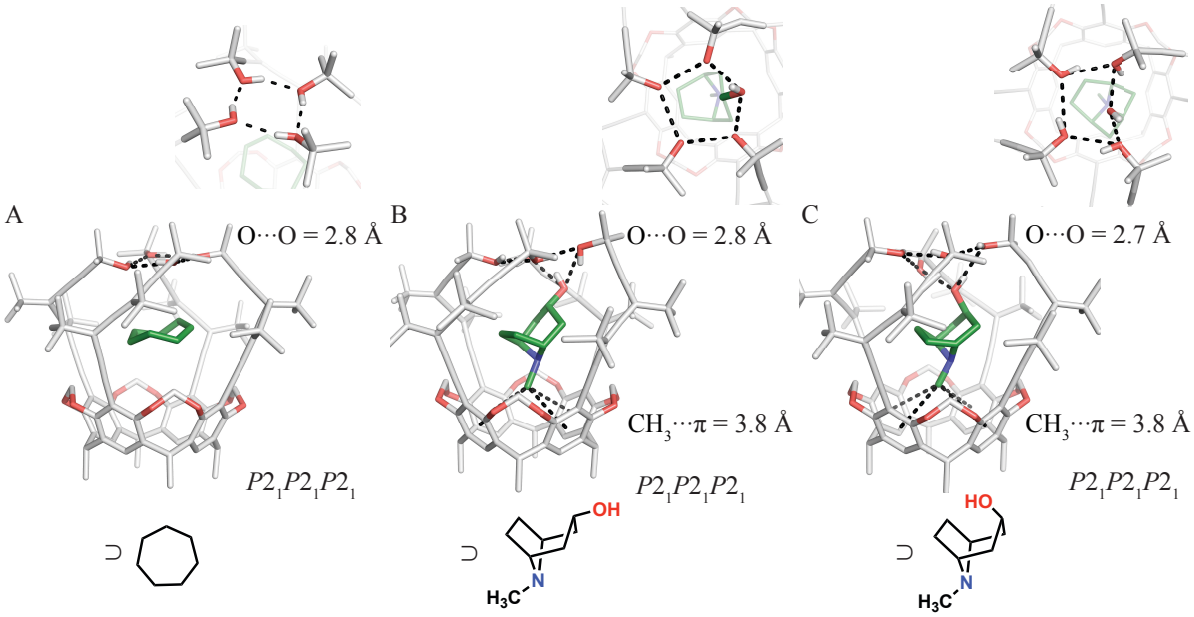

Figure 89. X-ray co-crystal structures of AAC $(P)_4$-**62**⊃cycloheptane (A), AAC $(P)_4$-**62**⊃*exo*-tropine (B) and AAC $(P)_4$-**62**⊃*endo*-tropine (C). For structures in B and C the protons of the OH groups were modelled. Guest structures in B and C show disorder over two positions, only one is shown here. Distances are given in Å. *n*-Hexyl chains of the receptor **62** and hydrogends are omitted for clarity. Guests are shown in stick representation. Space groups: $P2_1P2_1P2_1$.

Compared to the X-ray co-crystal structures obtained with the cyclohexanol derivatives (Figure 82), where the guests formed a four-fold hydrogen-bonding array with three tertiary alcohol groups of the host, the alcohol groups of *exo*- and *endo*-tropinol engaged cooperatively in a five-fold hydrogen-bonding array (Figure 89). The *N*-methyl group in both *exo*- and *endo*-tropinol undergoes favorable C-H···π interactions at 3.8 Å. The change in the

configuration of the alcohol in the tropines from *exo* to *endo* appeared to shorten the O···O contacts in the five-fold hydrogen-bonding array (Figure 89, B and C). *exo*-Tropine complexed to AAC $(P)_4$-**62** showed disorder over two positions, with the distribution of the *N*-methyl group in the equatorial (40%) and axial position (60%), respectively. Figure 88 only shows the equatorial conformer (40% populated). Contrarily, *endo*-Tropine complexed to AAC $(P)_4$-**62** exclusively displayed the equatorial conformer. This observation confirms the solution complexation studies and indicated a preferential binding of the equatorial conformer of *endo*-tropine in the solid state.

4.1.4 From Cyclohexanol to (*S*,*S*)- and (*R*,*R*)-*trans*-1,2-Cyclohexanediol: Enantioselective Binding to AACs $(P)_4$- and $(M)_4$-62

With the directionality of the four-fold hydrogen bonding array depending on the configuration of the host, we were curious to investigate the enantioselective binding through directional hydrogen-bonding interactions. *trans*-1,2-Cyclohexanediol exists as the (*S*,*S*)- and the (*R*,*R*)-configured enantiomers. To study the enantioselective binding of enantiopure AACs $(P)_4$- and $(M)_4$-**62** towards chiral cyclohexanediols undergoing directional hydrogen-bonding interactions, we set up solution studies and crystallization experiments with the commercially available (*S*,*S*)- and the (*R*,*R*)-configured enantiomers of *trans*-1,2-cyclohexanediol.

Table 10 displays the binding constants of the (*S*,*S*)- and the (*R*,*R*)-*trans*-1,2-cyclohexanediol along with those of cyclohexane and cyclohexanol. We observed an increase in binding affinity from cyclohexanol to (*S*,*S*)-*trans*-1,2-cyclohexanediol by $\Delta\Delta G_{293\ K} = -1.4$ kcal mol^{-1}. The stronger binding (*R*,*R*)-enantiomer showed $K_a = 3.4 \cdot 10^5$ M^{-1} ($\Delta G_{293\ K} = -7.4$ kcal mol^{-1}). The difference in binding energy between the two enantiomers to AAC $(P)_4$-**62** corresponds to $\Delta\Delta G_{293\ K} = -0.9$ kcal mol^{-1}. The observed enantioselectivity is high, considering that it exclusively results from the directional hydrogen-binding interactions of the diol, without additional strong attractive or repulsive interactions of the cyclohexane core.

Table 10. Binding constants K_a (293 K) and Gibbs free energies for the complexation of cyclohexane, cyclohexanol, (*S,S*)- and (*R,R*)-*trans*-1,2-cyclohexanediol by AAC $(P)_4$-**62** in *n*-octane. Only K_a values obtained from ECD titrations are shown.

AAC Host:	$(P)_4$-**62** ⊃	$P)_4$-**62** ⊃	$(P)_4$-**62** ⊃	$(P)_4$-**62** ⊃
Guest:		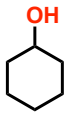	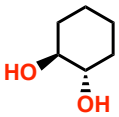 (*S,S*)	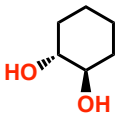 (*R,R*)
ECD K_a [M^{-1}]	< 1	$6.7 \cdot 10^3$	$7.5 \cdot 10^4$	$3.4 \cdot 10^5$
$\Delta G_{293\ K}$ [kcal mol^{-1}]	–	–5.1	–6.5	–7.4

In order to obtain further insight into the different binding modes of (*S,S*)- and (*R,R*)-*trans*-1,2-cyclohexanediol towards the enantiopure $(P)_4$-configured receptors **62**, we set up co-crystallization experiments. Figure 90 illustrates the co-crystal structures of (*S,S*)- (A) and the (*R,R*)-*trans*-1,2-cyclohexanediol (B) with AAC $(P)_4$-**62**.

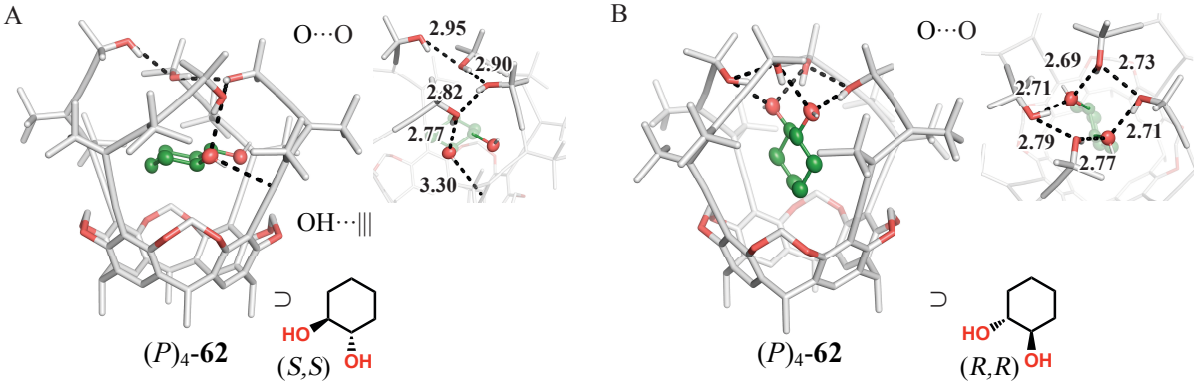

Figure 90. X-ray co-crystal structures of AAC $(P)_4$-**62**⊃(*S,S*)-*trans*-1,2-cyclohexanediol (A) and AAC $(P)_4$-**62**⊃(*R,R*)-*trans*-1,2-cyclohexanediol (B). Distances are given in Å. *n*-Hexyl chains of the receptor **62** are omitted for clarity. Guests are shown in ellipsoids representation (50% probability). Space groups: $P2_1P2_1P2_1$.

The X-ray co-crystal structure of AAC $(P)_4$-**62**⊃(*S,S*)-*trans*-1,2-cyclohexanediol shows the cyclohexane core of the guest parallel to the hydrogen bonding array. The four-fold hydrogen bonding array is disrupted and instead host and guest form a linear (unidirectional) hydrogen-bonding "chain" (Figure 90, A top view). The O···O distances vary between 2.77–

2.95 Å. Additionally, the guest undergoes OH···||| contacts with the alleno-acetylenic arms of the receptor (Figure 90, A). The closest OH···||| contact is 3.30 Å. This binding mode is in stark contrast to the binding mode of the (*R*,*R*)-configured guest enantiomer, where the cyclohexane core is perpendicular to the hydrogen bonding array and the diols expand the former four-fold hydrogen-bonding array to a remarkable six-fold one (Figure 90, B).[58,279,280] NMR spectroscopic studies to substantiate the two binding modes in solution are ongoing.

4.2 Clockwise and Counter-Clockwise Directionality of the H-Bonding Array in AACs (*P*)$_4$- and (*M*)$_4$-62

In our previous studies (see Chapter 3) we found that the four-fold hydrogen-bonding array adopts a fixed orientation in their solid-state structures. The directionality (clockwise and counter-clockwise) appeared to be dictated by the (*P*)$_4$- or (*M*)$_4$-configuration of the receptor **62** and was independent on the configuration of the encapsulated guest. This handedness of the H-bonding array, reminiscent of earlier works by Rebek,[281,282] Atwood[128,283] and Szumna,[284,285] was assumed to stabilize the cage form and contribute to the strong enantioselective and chiroptical properties of the AACs (*P*)$_4$- and (*M*)$_4$-**62**. Comparable achiral systems undergoing cyclic hydrogen-bonding networks were reported to undergo simultaneous tunnelling of the protons in the solid state at low temperatures.[286-289] In a collaboration with theoretical chemists, T. Husch and Prof. M. Reiher (ETHZ), we set out to study the inversion barrier for the four-fold hydrogen-bonding array. The investigations are still ongoing, but preliminary results indicate a high energy barrier for inversion.

With directional hydrogen-bonding interactions of the guest to the receptors (see Chapter 4), the four-fold hydrogen-bonding array is expanded or disrupted and various hydrogen-bonding motifs were discovered. The observed motif is strongly dependent on the alcohol guest encapsulated by the host. Figure 91 shows selected hydrogen-bonding motifs.

Remarkably, the host–guest-complex appeared to retain some directionality of the hydrogen-bonding array, despite the disruptive nature of the directional hydrogen-bonding interactions of the guest with the host (Figure 91).

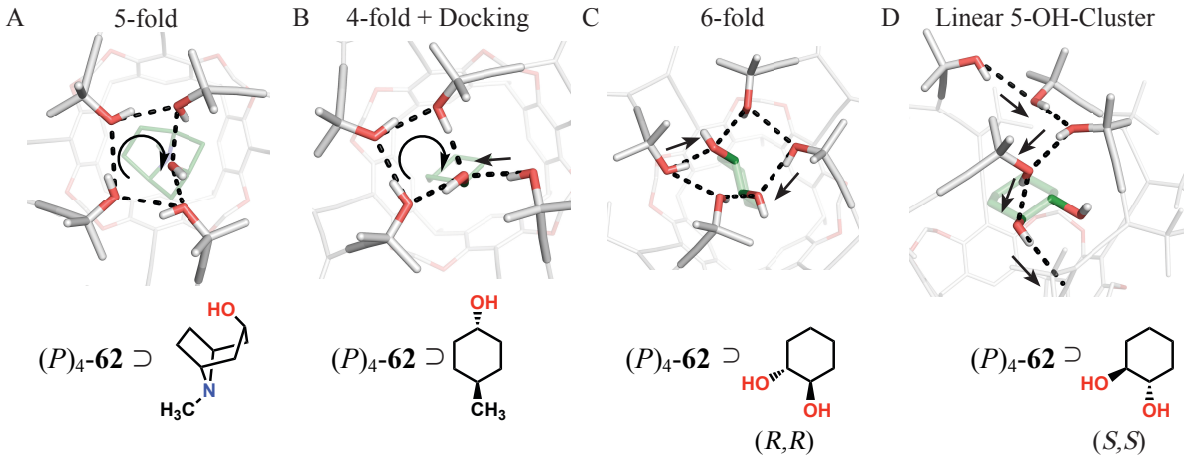

Figure 91. Top view on the hydrogen-bonding array of AAC $(P)_4$-**62** ⊃*endo*-tropine (A), ⊃*trans*-4-methylcyclohexanol (B) and ⊃(*R*,*R*)-*trans*-1,2-cyclohexanediol (C) and ⊃(*S*,*S*)-*trans*-1,2-cyclohexanediol (D). In all complexes of $(P)_4$-configuration, the hydrogen-bonding array some clockwise directionality. For AAC $(M)_4$-**62**, the hydrogen-bonding array follows the counter-clockwise orientation.

We are currently studying the preference for unidirectional hydrogen-bonding networks experimentally and theoretically.

4.3 Summary and Conclusion on the Directional Hydrogen-Bonding Interactions and Rational Design of Guest Molecules

Inspired by a crystal structure of AACs $(P)_4$- and $(M)_4$-**62** encapsulating one water molecule and two acetonitrile molecules, in which a water molecule bridges the H-bonding array of the host with the acetonitrile, we expanded our series of guest molecules to alcohols.

The alcohol guests formed strong directional interactions with the hydrogen-bonding array of the host. Generally, the introduction of an alcohol group increased the binding affinities of the guest to the receptors in solution by ~3–4 kcal mol^{-1}, resulting in kinetically stable host–guest complexes on the NMR time scale. Solution studies, along with structural information obtained from X-ray co-crystal structures, enabled the conformational analysis of the host-bound guests. Noteworthy is the substantial increase in binding affinity from cycloheptane to *endo*-tropine with a difference in Gibbs energies of $\Delta\Delta G_{293\,K} = -6.1$ kcal mol^{-1}, translating to binding constants of $K_a = 7.0 \cdot 10^6$ M^{-1} (in *n*-octane at 293 K). These remarkably high binding affinities allowed to detect *endo*-tropine with $(P)_4$-AACs **62** in the part per billion regime (Figure 88). X-ray co-crystal structures and 2D NMR spectroscopic solution studies indicated a preferential binding of *endo*-tropine to $(P)_4$-AACs **62** with the *N*-methyl group in the equatorial conformation (Figure 84–86). In enantioselective complexation studies, the

strongest differentiation was observed for *trans*-1,2-cyclohexanediol, where the (*R*,*R*)-enantiomer bound by $\Delta\Delta G_{293\ K} = -0.9$ kcal mol^{-1} stronger compared to the (*S*,*S*)-enantiomer. X-ray co-crystal structures substantiated their different binding modes (Figure 90).

With directional hydrogen-bonding interactions of the guest to the receptors, the four-fold hydrogen-bonding array was disrupted and various hydrogen-bonding motifs were discovered. The observed motif was strongly dependent on the encapsulated alcohol guest. Figure 91 shows selected hydrogen-bonding motifs. Remarkably, the host–guest-complex appeared to retain some directionality of the hydrogen-bonding array, despite the disruptive nature of the directional hydrogen-bonding interactions of the guest with the host (Figure 91).

5. AAC Receptors: Hydrogen-Bonding, Dispersion and Halogen-Bonding Interactions – Conformational Analysis of Encapsulated Acyclic Guests

This chapter was done in collaboration with Dr. S. Fischer and Prof. E. M. Carreira (ETHZ). Dr. S. Fischer synthesized the indicated alcohols as racemates. Experimental studies were complemented by theoretical studies by T. Husch and Prof. M. Reiher (ETHZ). Small-molecule single crystals were mounted by M. Solar, and X-ray crystal structures were solved by Dr. Nils Trapp (ETHZ).

5 AAC Receptors: Hydrogen-Bonding, Dispersion and Halogen-Bonding Interactions – Conformational Analysis of Encapsulated Acyclic Guests

The alcohol guests formed strong directional hydrogen-bonding interactions with the H-bonding array, which closes the host. Depending on the nature of the guests, different modes of interaction with the array were observed (Figure 91). Generally, the introduction of an alcohol group increased the binding affinities of the guest to the receptors by ~3–4 kcal mol^{-1}, resulting in kinetically stable host–guest complexes on the NMR time scale. Solution studies, along with structural information obtained from X-ray co-crystal structures, enabled insight into the binding modes of the host-bound guests.

In a collaborative effort with Dr. S. Fischer and Prof. E. M. Carreira (ETHZ), we sought to expand the series of cyclic alcohols to achiral and chiral acyclic aliphatic alcohols and alkyl haloalcohols. These targeted guest molecules were inspired by the work of the Carreira group on fluoro-, chloro- and bromodanicalipin A and consist largely of fragments of the aforementioned (Figure 92).[290-293]

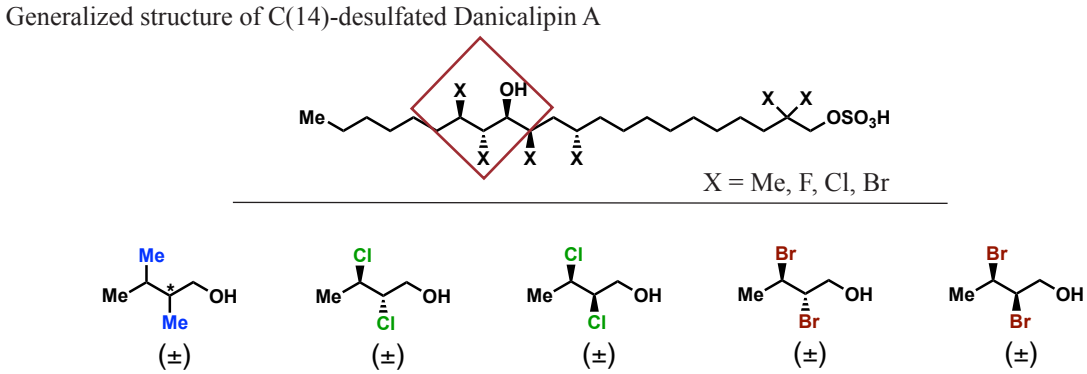

Figure 92. General structure of Danicalipin A (top) and fragments thereof, which were selected as potential guest molecules (highlighted in a red square). [290,292]

We were especially interested to study the conformation of a series of aliphatic and alkyl haloalcohols in a confined hydrophobic cavity. Solution studies of kinetically stable host–guest complexes, along with analysis of the X-ray co-crystal structures, would enable us to obtain structural information of the host-bound molecules. The formation of diastereoisomeric complexes between the enantiopure receptors and the chiral guests would allow us to investigate enantioselective binding based on dispersive and halogen-bonding interactions, complementing the insight gained from the alicyclic series of guest molecules (Chapter 3). A summary of the selected guest structures is given in Figure 93.

A H-bonding and dispersion interactions

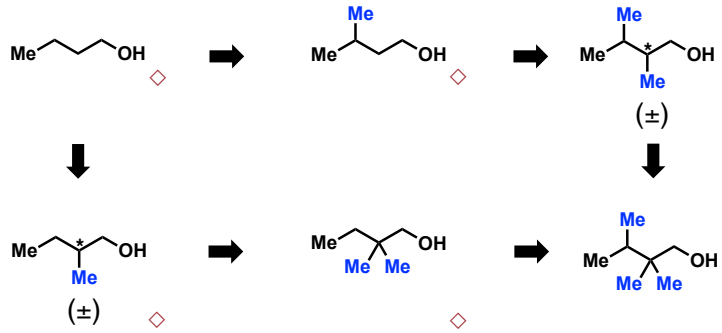

B H-bonding, dispersion and halogen-bonding interactions

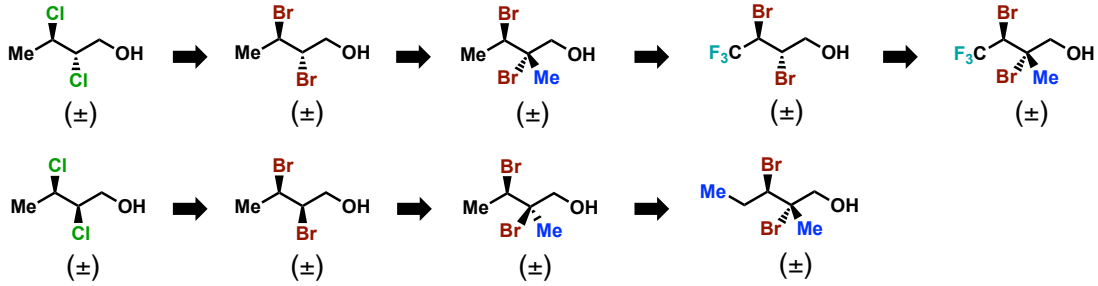

Figure 93. Structures of guest molecules selected for complexation studies with enantiopure AACs $(P)_4$- and $(M)_4$-**62**. Apart from the molecules designated with a square (◇), all molecules were prepared in a racemic fashion by Dr. Stefan Fischer (ETHZ).

The molecules designated with a red ◇ are commercially available, the rest of the series was prepared by Dr. Stefan Fischer as a racemate (Figure 93).[294] When possible, the racemic mixture was separated into their corresponding enantiomers by preparative HPLC with a CSP Diacel Chiralpak® IA in *n*-hexane/ethanol (see Experimental Section). The association constants of the guests to the receptor were obtained through ECD spectroscopic titrations and ITC. 1D and 2D NMR studies allowed the full characterization of the free and the host-bound complexes in *n*-octane-d_{18} at temperature between 277–293 K. The formation of diastereoisomeric complexes of the enantiopure hosts with the chiral (racemic) guests resulted in splitting of the 1D NMR signals of the host and the guests. The diagnostic splitting of the signals, reminiscent of the effects of chiral NMR shift reagents, allowed us to evaluate the enantioselectivity of the $(P)_4$- and $(M)_4$-configured AACs **62** to the guests in solution. Where applicable, splitting in the ^{1}H, ^{13}C, and ^{19}F NMR traces was observed. NMR solution studies were complemented by X-ray co-crystal structures, where the distributing of the enantiomers of the guest in the host (with 100% occupation) matched the observed enantioselectivity in solution. In total, 15 X-ray co-crystal structures of the achiral or racemic guests bound to the $(P)_4$- or $(M)_4$-configured receptor **62** were obtained, with more in preparation. Theoretical studies, conducted by T. Husch and Prof. M. Reiher (ETHZ), allowed us to further evaluate

the host-bound guest conformations theoretically. The confined nature of the host was found to create an environment where predictions of the guest conformations matched well with the ones obtained from X-ray co-crystallization experiments. In future, this will allow us to evaluate potential binding of guests to the host prior to experimental complexation studies.

The collaborative work with the groups of Prof. Carreira and Prof. M. Reiher are ongoing and only selected and representative examples will be discussed in this Thesis.

5.1 H-Bonding and Dispersion Interactions: Binding of Acyclic Alkyl Alcohols to AACs $(P)_4$- and $(M)_4$-62

Figure 93, A, summarizes the selected guest molecules, which were imagined to bind to the $(P)_4$- or $(M)_4$-configured receptor **62** based on directional H-bonding interactions and dispersion interactions. We expected the association constant of the guests to the receptor to increase from *n*-butanol to 2,2,3-trimethylbutanol with increasing shape complementarity of the guests to the host (Figure 93, A).

The association constants of the selected guests were obtained from ECD spectroscopic titrations and ITC titrations in *n*-octane at 293 K and 303 K, respectively. Although, the magnitude of the binding constants of the alkyl alcohols did not allow for evaluation of the exact enthalpic and entropic contribution to binding with high accuracy, the binding constants obtained from ITC titrations matched well with the values obtained from ECD titrations. Table 11 summarizes the binding constants of the guests to AAC $(P)_4$-**62**.

As anticipated, the binding affinity increased with increasing size and space occupancy of the guest molecules. While *n*-butanol did not show quantifiable association to the receptor, 3-methylbutanol and 2-methylbutanol showed enhanced binding of $\Delta G_{293\ K}$ = –4.3 kcal mol^{-1} and –4.5 kcal mol^{-1}, respectively. The addition of one more methyl substituent to 3-methylbutanol and 2-methylbutanol, such as in 2,3-dimethylbutanol, further increased the binding strength to $\Delta G_{293\ K}$ = –5.4 kcal mol^{-1}, indicating a contribution of $\Delta\Delta G_{293\ K}$ = –0.9–1.1 kcal mol^{-1} for the additional methyl substituent. The association strength for 2,2,3-trimethylbutanol, however, did not further increase, but gave a comparable binding constant to 2,3-dimethylbutanol of $\Delta G_{293\ K}$ = –5.2 kcal mol^{-1}.

Table 11. ECD and ITC binding isotherms for AAC $(P)_4$-**62** in *n*-octane at 293 K (ECD) and 303 K (ITC) with selected alkyl alcohols.

Host: AAC $(P)_4$-**62** Guest:	ITC K_a $[M^{-1}]$	ECD K_a $[M^{-1}]$	ECD [a] $\Delta G_{293\ K}$ [kcal mol^{-1}]
	<1	<1	–
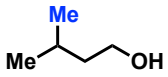	$1.4 \cdot 10^3$	$1.5 \cdot 10^3$	–4.3
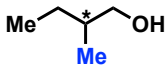 (±)	$4.6 \cdot 10^3$	$2.3 \cdot 10^3$	–4.5
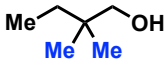	n.a.[b]	n.a.[b]	n.a.[b]
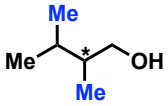 (±)	$5.9 \cdot 10^3$	$9.9 \cdot 10^3$	–5.4
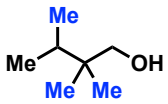	$8.2 \cdot 10^3$	$6.9 \cdot 10^3$	–5.2

[a] The Gibbs free energy of binding was calculated from $K_{a\ 293\ K}$ of ECD data. [b] Binding titrations are ongoing.

The association constants of the guest towards the receptor $(P)_4/(M)_4$-**62** are not only the result of enhanced dispersion interactions with the interior of the receptor, but are also influenced by the conformational energy, which the guest has to pay for adopting the host-preferred conformation.

2D NMR experiments allowed to gain insight into the binding mode of the guests inside the host. Figure 94 shows the complexed 2,2,3-trimethylbutanol to AAC $(P)_4$-**62** in *n*-octane-d_{18} at 277 K and an insert of the ^{1}H NMR traces at 238 K. At 277 K, the uncomplexed 2,2,3-trimethylbutanol displays two singlets for the four methyl substituents. The resonances corresponding to the methyl substituents of the host-bound guest are broad and upfield shifted to the ppm range of +0.19 to +0.73 compared to the signals of the free guest. No coupling constants are visible for the methyl groups in the 3-positions ($C(3)HMe_2$), indicating the dynamic nature of the assembly. At lower temperatures, the terminal methyl groups of the complexed guest shift further upfield to +0.21 and –0.36 ppm, displaying a doublet of the methyl groups in the 3-position (Figure 94, insert). The doublet is only observed for the

complexed molecule and not for the free 2,2,3-trimethylbutanol. The upfield shift of the terminal methyl groups of the bound guest indicated shielding by the acetylenic groups of the host.

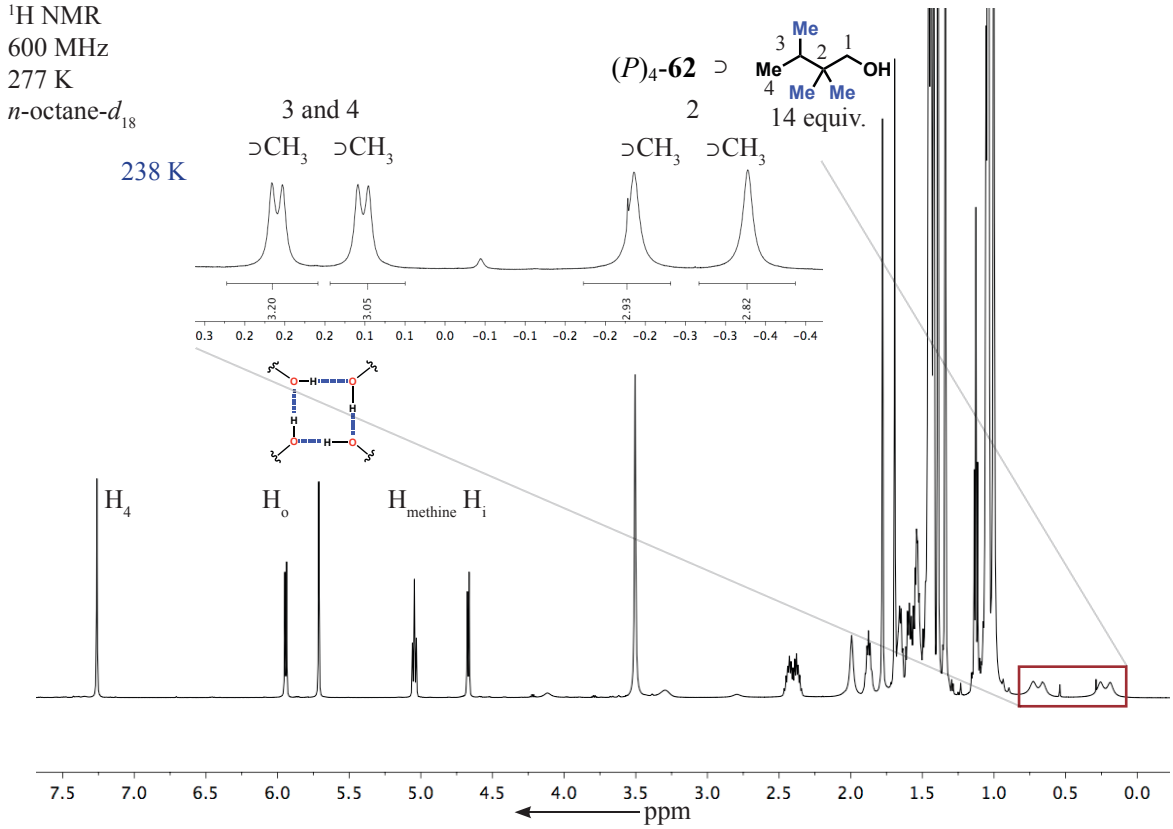

Figure 94. ^{1}H NMR traces of AAC (*P*)$_4$-**62** (6.8 mM) in *n*-octane-d_{18} at 277 K with 14.0 equiv. of 2,2,3-trimethylbutanol. One equivalent is complexed while the remaining 13.0 equiv. of the guest are free in solution. The ⊃ denotes the terminal methyl groups of the complexed guest molecule. Host-resonances: H_{inside} = inside protons and H_o = outside protons of the methylene bridges; H_4 = aromatic proton.

The diagnostic splitting of the four-fold hydrogen-bonding array as a result of the formation of the diastereoisomeric complexes of the enantiopure (*P*)$_4$-configured AACs **62** with chiral guests, enabled us to quantify the enantioselectivity towards the enantiomers of (±)-2-methylbutanol and (±)-2,3-dimethylbutanol. While AAC (*P*)$_4$-**62** did not show significant selectivity towards (±)-2-methylbutanol, we observed enhanced selectivity of 2:1 towards (±)-2,3-dimethylbutanol. This increase in selectivity in introducing one more methyl group was remarkable, considering the weak dispersion interactions of the guest with the host.

In order to verify the conformation of the host-bound guest molecule, we set up crystallization experiments with the series of alkyl alcohol and (*P*)$_4$-configured AACs **62** (see Experimental Part). The crystallization experiments were in itself intriguing as, to the best of

our knowledge, no crystal structure of the series of butanol derivatives has been reported to date. Figure 95 displays the X-ray co-crystal structures of AAC $(P)_4$-**62**⊃2,2-dimethylbutanol and AAC $(P)_4$-**62**⊃2,2,3-trimethylbutanol (Figure 95).

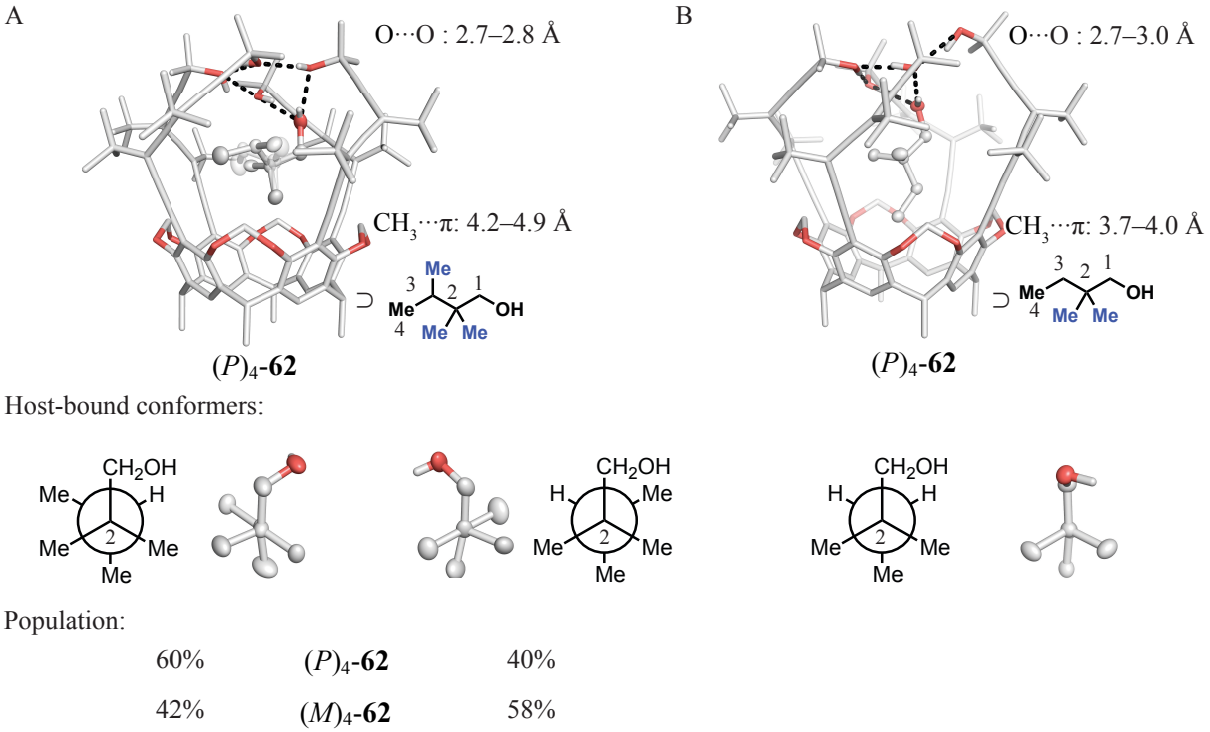

Figure 95. A: X-ray co-crystal structures of AAC $(P)_4$-**62**⊃2,2,3-trimethylbutanol; the guest is bound in two enantiomeric conformations (depicted below). B: AAC $(P)_4$-**62**⊃2,2-dimethylbutanol. Distances are given in Å. *n*-Hexyl chains of the receptor $(P)_4$-**62** and hydrogens are omitted for clarity. Guests are shown in ellipsoids representation (50% probability).

2,2,3-Trimethylbutanol forms a five-fold hydrogen-bonding array with the host, with three methyl substituents pointing to the acetylenic functionalities of the alleno-acetylenes (3.5–3.8 Å). One methyl group in the 2-position points towards the aromatic resorcin[4]arene core (4.2–4.9 Å). Remarkably, the guest is complexed in two conformations, which are enantiomers of each other. One of the conformational enantiomers is preferentially bound to the host (Figure 95, A). The distribution of the conformer populations in the host is 60:40 for the $(P)_4$-configured receptor. The ratio inverts in the X-ray crystal structure with the $(M)_4$-configured host, exemplifying the highly asymmetric environment of the interior of the host. In the X-ray co-crystal structure of AAC $(P)_4$-**62**⊃2,2-dimethylbutanol, the guest forms a four-fold hydrogen-bonding array with the tertiary alcohols of the receptor, with one tertiary alcohol coordinating to the hydrogen-bonding array. The *n*-butanol chain of the guest is bound perpendicular to the H-bonding array, contrarily to 2,2,3-trimethylbutanol. This results in

closer contacts of the terminal methyl group of the *n*-butanol chain to the resorcin[4]arene core. NMR spectroscopic studies confirmed this conformation in solution, where a strong upfield shift of the terminal methyl group was observed.

These two exemplary X-ray crystal structures demonstrate the complementarity of the solution studies with the structures obtained from single crystal X-ray diffraction.

5.2 H-Bonding, Dispersion and Halogen-Bonding Interactions: Binding of Acyclic Alkyl Haloalcohols to AACs $(P)_4$- and $(M)_4$-62

In the series of the alkyl haloalcohols we imagined that the halogen substituents would adopt the positions of the methyl groups, undergoing halogen-bonding interactions with the acetylenic functionalities and the resorcin[4]arene core of the receptor (see Chapter 2).

We chose to study *anti*- and *syn*-configured 2,3-dihalogen substituted *n*-butanols (Figure 93, B). Figure 93 B, top row (*anti*) and bottom row (*syn*), shows the set of molecules with both dichloro- and dibromo-derivatives. Additional methyl groups and trifluoromethyl groups would allow us to probe the influence of size to the association of the guests to the receptors. We were especially keen on studying the changes in enantioselectivity with increasing shape complementarity and interaction strength of the guest towards the host. Intuitively, one would assume that the guest with the highest association strength would also show the highest enantioselectivity towards the enantiopure host.

Solution binding studies were initially conducted with the racemic mixture of the guests with enantiopure $(P)_4$- and $(M)_4$-configured AAC **62**. Guests with enhanced enantioselectivity towards the receptors were separated by preparative HPLC with a CSP Diacel Chiralpak® IA in *n*-hexane/ethanol (see Experimental Section). 1D and 2D NMR experiments of the host-guest complexes were conducted with all compounds and selected examples will be discussed.

Generally, we expected an increase in association strength of the guests towards the AACs $(P)_4$/$(M)_4$-**62** from the chloro to the bromo derivatives. Additional methyl groups and optimizing space filling and dispersion interactions were envisioned to contribute to increasing binding strength. Table 12 summarizes the association constants of the guest with the $(P)_4$-AAC **62** measured by ECD spectroscopic and ITC titrations.

Generally, the association constants of the 2,3-dihalo alcohols bound with higher association constants compared to their aliphatic analogues and, with the exception of entry 9 (Table 12), showed slow exchange on the NMR timescale at 277 K.

Table 12. ECD and ITC binding isotherms for AAC $(P)_4$-**62** in *n*-octane at 293 K (ECD) and 303 K (ITC) with selected alkyl haloalcohols.

	Host: AAC $(P)_4$-**62**	ITC	ECD	ECD [a]
Entry	(±)-Guest:	K_a [M^{-1}]	K_a [M^{-1}]	ΔG_{293}[kcal mol^{-1}]
1	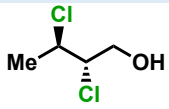 (±)	$1.8 \cdot 10^4$	$1.5 \cdot 10^4$	–5.4
2	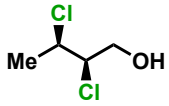 (±)	$8.9 \cdot 10^4$	$7.0 \cdot 10^4$	–6.5
3	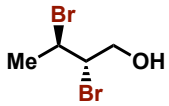 (±)	$6.6 \cdot 10^4$	$7.6 \cdot 10^4$	–6.5
4	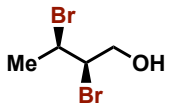 (±)	$4.8 \cdot 10^5$	n.a.[b]	–7.6[c]
5	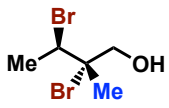 (±)	$1.4 \cdot 10^5$	$1.2 \cdot 10^5$	–6.8
6	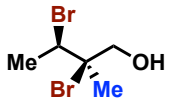 (±)	$7.4 \cdot 10^5$	n.a.[b]	–7.9[c]
7	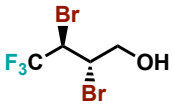 (±)	$1.7 \cdot 10^4$	n.a.[b]	–5.7[c]
8	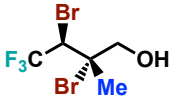 (±)	$1.8 \cdot 10^4$	n.a.[b]	–5.7
9	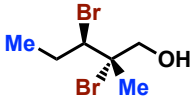 (±)	$6.7 \cdot 10^3$	$3.5 \cdot 10^3$	–4.8

[a] The Gibbs binding energy was calculated from $K_{a\,293\,K}$ ontained from ECD spectroscopic titrations. [b] Binding titrations are ongoing. [c] The Gibbs binding energy was obtained by ITC.

The binding strength increased from the chloro- to the bromo-derivatives and was enhanced for all *syn*-configured 2,3-dihalo alcohols compared to the *anti*-configured analogues. (±)-*anti*-1,2-Dichlorobutanol bound with $\Delta G_{293\ K} = -5.4$ kcal mol^{-1} to AAC $(P)_4$-**62**. The inversion of one stereocenter, affording the *syn*-conformer, resulted in an enhanced binding strength of $\Delta G_{293\ K} = -6.5$ kcal mol^{-1}. Similarly, (±)-*syn*-1,2-dibromobutanol bound by $\Delta\Delta G_{293\ K} = -1.1$ kcal mol^{-1} stronger to AAC $(P)_4$-**62** compared to (±)-*anti*-1,2-dibromobutanol (–6.5 kcal mol^{-1} → –7.6 kcal mol^{-1}). The binding affinity further increased with the addition of a methyl group in the 2-position, resulting in Gibbs free energies of binding of $\Delta G_{293\ K} = -6.8$ kcal mol^{-1} for *anti*-2,3-dibromo-2-methylbutanol (entry 5) and $\Delta G_{293\ K} = -7.9$ kcal mol^{-1} for *syn*-2,3-dibromo-2-methylbutanol. The binding affinitiy in the series reached its maximum with the latter, translating to a binding constant of $K_a = 7.4 \cdot 10^5$ M^{-1} at 293 K, a surprisingly high value for an acyclic alcohol undergoing only one strong hydrogen-bonding interaction. Interestingly, the inversion of one stereocenter from *anti* to *syn* consistently increased the binding affinity by –1.1 kcal mol^{-1} (Table 12). The introduction of one terminal trifluoromethyl group (entry 7 and 8, Table 12), decreased the affinity by ~ +1.0 kcal mol^{-1} (entry 3 → entry 7 $\Delta\Delta G_{293\ K} = +0.8$ kcal mol^{-1} and entry 5 → entry 8 $\Delta\Delta G_{293\ K} = +1.1$ kcal mol^{-1}). Unfavorable interactions of the F-atom with the electron-rich aromatic rings and the alleno-acetylenes must be assumed.[273] Also, the elongated *n*-pentyl chain, such as in entry 9, substantially decreased the binding affinities to AAC $(P)_4$-**62** by $\Delta\Delta G_{293\ K} = +2.0$ kcal mol^{-1} (entry 5 → entry 9).

In Chapter 3, we established that the contribution of the C–Br···||| halogen-bonding contact translates to an increase in binding affinity of ~1.0 kcal mol^{-1}.

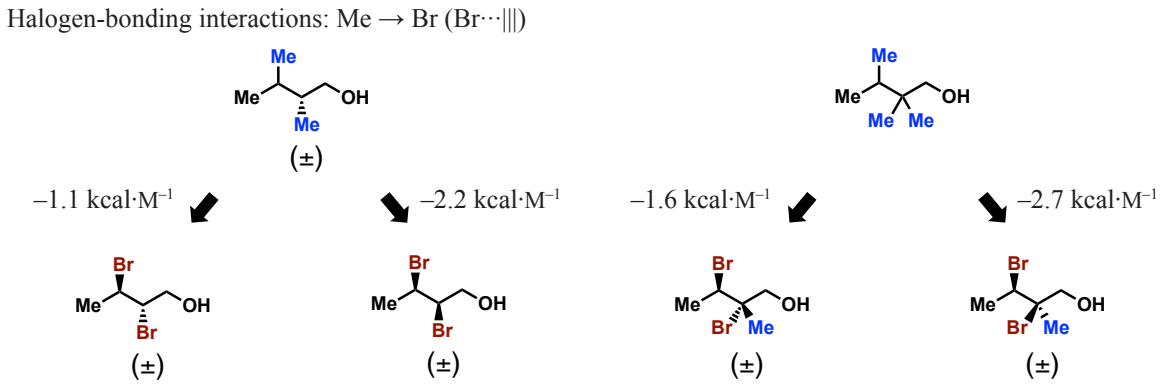

Figure 96. Comparison of the Gibbs free energies of binding $\Delta\Delta G_{293\ K}$ in kcal mol^{-1} obtained from ECD spectroscopic titrations of the 2,3-dimethylbutanol (left) and 2,2,3-trimethylbutanol bound to AAC $(P)_4$-**62** with their *anti*- and *syn*-configured bromo analogues.

Figure 96 displays the difference in Gibbs free energies of binding for 2,3-dimethylbutanol (left) and 2,2,3-trimethylbutanol bound to AAC $(P)_4$-**62** with their *anti*- and *syn*-configured bromo analogues. The differences in binding affinities of the aliphatic alcohols compared to their haloalkyl analogues accounts for both the difference in conformational energy and increasing halogen-bonding interactions; therefore, they have to be discussed with caution. Nevertheless, substitution of the methyl groups with bromides resulted in an increase in binding affinities of up 0.6–1.4 kcal mol^{-1} per methyl substitution. In collaboration with Tamara Husch and Prof. M. Reiher (ETHZ), the contribution of the halogen-bonding interactions is being theoretically investigated.

In order to investigate the enantioselective binding of the series of alkyl haloalcohols towards $(P)_4$- and $(M)_4$-configured AACs **62**, we first measured the ^{1}H NMR traces of the racemic alcohols with the enantiopure receptors. The formation of the diastereoisomeric complexes was observed in the diagnostic splitting of the H-bonding array of the host. Figure 97 displays the observed splitting of the H-bonding array, corresponding to the indicated enantioselectivities. On a sidenote, no such splitting was observed in the ^{1}H NMR traces of enantiopure guests with the optically pure hosts.

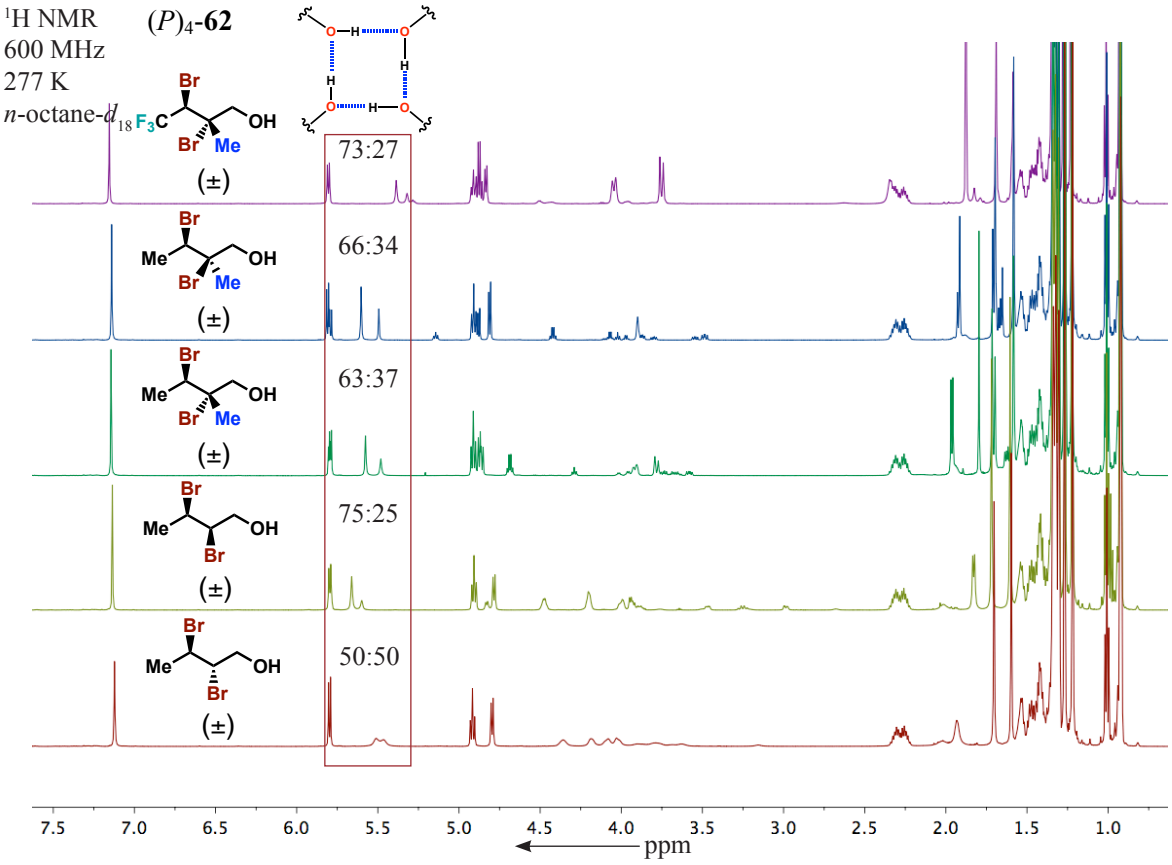

Figure 97. Diagnostic splitting of the H-bonding array of the host AAC $(P)_4$-**62** upon complexation of the racemic guests, as observed in the ^{1}H NMR spectroscopic traces.

The enantiomerically pure guests further allowed us to assign the respective resoncances to the corresponding enantiomer. While $(P)_4$-AACs **62** did not show significant enantioselectivity towards *anti*-2,3-dibromobutanol (50:50 ratio of the ^{1}H NMR signals at 5.5 ppm, see Figure 97), the preferential binding of one enantiomer increased substantially towards its *syn*-configured analogue (75:25). Surprisingly, *anti*- and *syn*-2,3-dibromo-2-methylbutanol displayed lower enantioselective binding compared to *anti*- and *syn*-2,3-dibromobutanol (63:37 and 66:34, respectively). The introduction of the terminal trifluoromethyl group (Table 12, entry 8) increased the preferential binding and resulted in a 73:27 ratio of the diastereoisomeric H-bonding resonances. The diagnostic splitting of the signals in the NMR traces was not only observed in the ^{1}H NMR spectra, but also in the ^{13}C and, where applicable, in the ^{19}F NMR traces. Figure 98 shows exemplary the set of diastereomeric signals of (±)-*anti*-2,3-dibromo-2-(trifluoromethyl)butanol complexed to AAC $(P)_4$-**62**, where signal splitting (73:27 ratio) was observed consistently in the ^{1}H, ^{13}C and ^{19}F NMR traces.

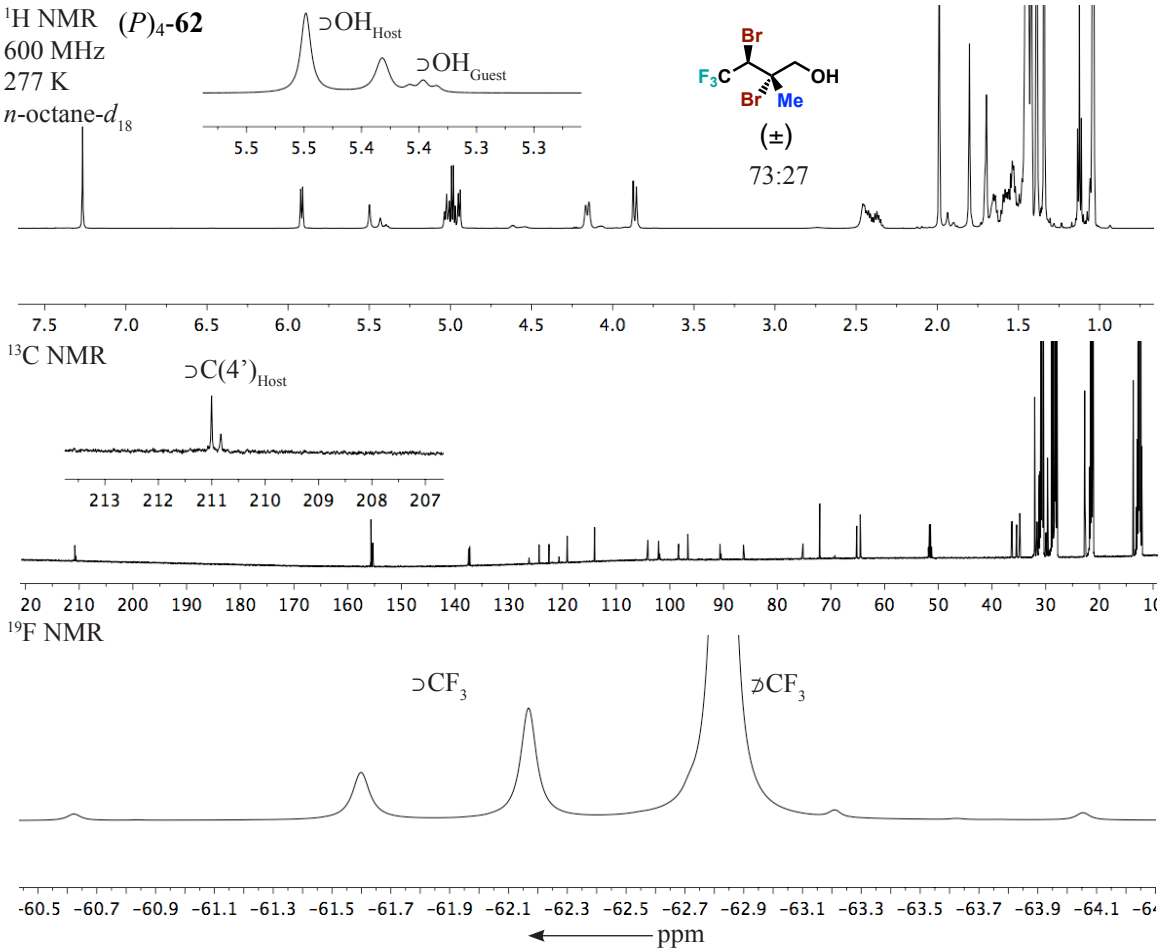

Figure 98. ^{1}H, ^{13}C, and ^{19}F NMR traces of (±)-*anti*-2,3-dibromo-2-(trifluoromethyl)butanol complexed to AAC $(P)_4$-**62** in *n*-octane-d_{18} at 277 K. Diagnostic splitting of the H-bonding array of the host upon complexation of the racemic guests, as observed in the ^{1}H NMR spectroscopic traces.

The enantioselectivities of the racemic guests toward the enantiopure hosts, observed through the formation of diastereomeric complexes, was surprising, as they did not correlate with the binding strength or optimal space filling of the guests with the host. The highest enantioselectivities were observed for smaller guests, such as *syn*-2,3-dibromobutanol and for larger guests, such as for *anti*-2,3-dibromo-2-(trifluoromethyl)butanol (Figure 97). In accordance with the observed enantioselctivities in *trans*-disubstituted cyclohexanes (see Chapter 2), stronger directional interactions did not result in stronger preferential binding of one guest enantiomer over the other (such as for 2,3-dimethylbutanol (65:35) compared to *anti*-2,3-dibromobutanol (50:50)).

In order to further substantiate the enantioselectivities of the guest displayed in Figure 97, we separated the racemic mixtures of the guests into their enantiomers by preparative HPLC with a CSP Diacel Chiralpak® IA in *n*-hexane/ethanol (see Experimental Section). Each enantiomer was titrated to the enantiopure $(P)_4$- and $(M)_4$-configured host **62** in *n*-octane at 293 K (ECD) or at 303 K (ITC). Binding isotherms were determined by ECD spectroscopic titration and by ITC. The high binding affinities allowed to obtain reliable thermodynamic data from ITC titrations.

An exemplary ITC titration is depicted in Figure 99, displaying binding isotherms obtained from $(P)_4$-AAC **62** and (*S*,*S*)- and (*R*,*R*)-2,3-dibromo-2-methylbutanol. The enthalpy $\Delta H^0_{303\ K}$ of binding of both (*S*,*S*)- and (*R*,*R*)-2,3-dibromo-2-methylbutanol is higher compared to the *exo*- and *endo*-tropines. The large enthalpic contribution is however counterbalanced by a larger entropic contribution, since the acyclic guests lack the degree of preorganization compared to the bicyclic ones (Figure 99 and Table 9). The acyclic haloalcohols can better accommodate to establish optimized interactions with the host, but at the prize of conformational entropy loss.

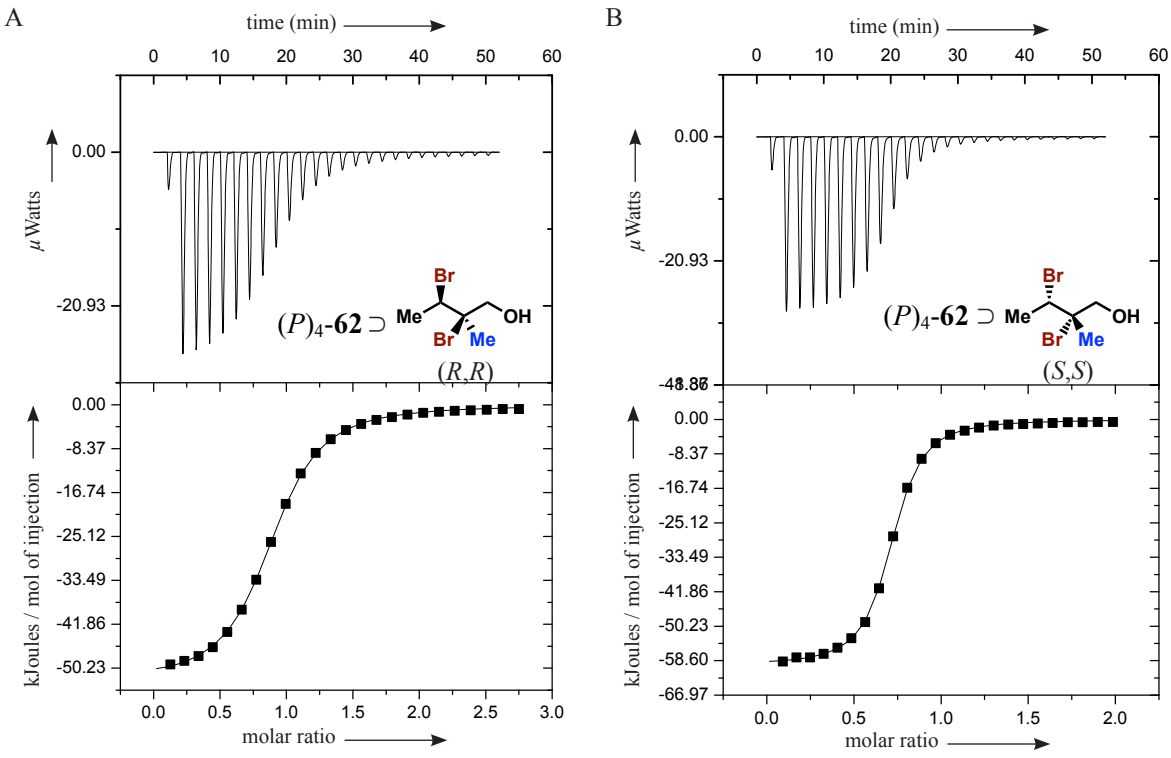

	ITC K_a [M^{-1}]	$\Delta G^0_{303\,K}$ [kcal·M^{-1}]	$\Delta H^0_{303\,K}$ [kcal·M^{-1}]	$-T\Delta S^0_{303\,K}$ [kcal·M^{-1}]
(*R*,*R*)	$2.4 \cdot 10^5$	–8.10	–14.28	+6.19
(*S*,*S*)	$6.8 \cdot 10^5$	–7.46	–12.61	+5.16

Figure 99. ITC binding isotherms for AAC $(P)_4$-**62** in *n*-octane at 303 K; A: with (*S*,*S*)-*syn*-2,3-dibromo-2-methylbutanol; B: (*R*,*R*)-*syn*-2,3-dibromo-2-methylbutanol.

A complete summary of the binding constants of the enantiopure guests with $(P)_4$-configured host **62** is given in Figure 100.

	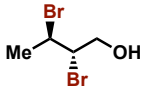 (*S*,*R*)	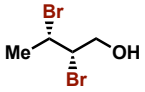 (*S*,*S*)	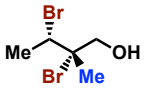 (*S*,*S*)	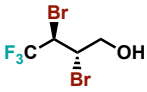 (*S*,*R*)	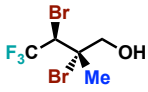 (*S*,*R*)
ECD K_a [M^{-1}]	$6.1 \cdot 10^4$	$1.2 \cdot 10^6$	$2.0 \cdot 10^6$	$7.7 \cdot 10^3$	$7.0 \cdot 10^3$
ITC K_a [M^{-1}]	$6.1 \cdot 10^4$	$1.2 \cdot 10^6$	$1.6 \cdot 10^6$	$1.3 \cdot 10^4$	$1.2 \cdot 10^4$
$\Delta\Delta G_{293\,K}$ [kcal·M^{-1}]	⬇ 0	⬇ –0.9	⬇ –0.3	⬇ +0.4	⬇ +0.6
	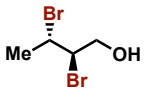 (*R*,*S*)	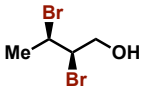 (*R*,*R*)	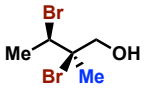 (*R*,*R*)	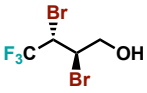 (*R*,*S*)	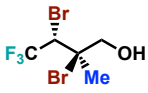 (*R*,*S*)
ECD K_a [M^{-1}]	$6.0 \cdot 10^4$	$2.8 \cdot 10^5$	$1.3 \cdot 10^6$	$1.5 \cdot 10^4$	$1.8 \cdot 10^4$
ITC K_a [M^{-1}]	$4.9 \cdot 10^4$	$3.6 \cdot 10^5$	$4.9 \cdot 10^5$	$2.0 \cdot 10^4$	$2.8 \cdot 10^4$

Figure 100. Summary of association constants of enantiopure *anti*- and *syn*-configured 2,3-dibromoalcohols with AAC $(P)_4$-**62** in *n*-octane at 293 K (ECD) and 303 K (ITC). $\Delta\Delta G_{293\,K}$ calculated from ECD titrations.

The Gibbs energy differences of binding to AAC $(P)_4$-**62** correspond well to the ones obtained from ^{1}H NMR solution studies (Figure 97). Noteworthy is the inversion of the selectivities towards the enantiomers of the alcohols with one terminal trifluoromethyl group.

A yet unaddressed question concerned the binding mode of the guest molecules inside the host. 2D NMR studies enabled the complete assignment of the host-bound guests. The chemical shifts indicated a binding geometry of the guest with the *n*-butanol core in perpendicular alignment to the hydrogen-bonding array of the host and the alcohol group of the guests involved in the hydrogen-bonding array. Depending on the association strength of the guest towards the host, the host-bound guest peaks were more or less resolved. Figures 101 and 102 exemplify the structural assignment by ^{1}H and ^{13}C NMR spectroscopy of a strongly binding guest, enantiopure (*S*,*S*)-2,3-dibromobutanol, encapsulated in AAC $(P)_4$-**62**.

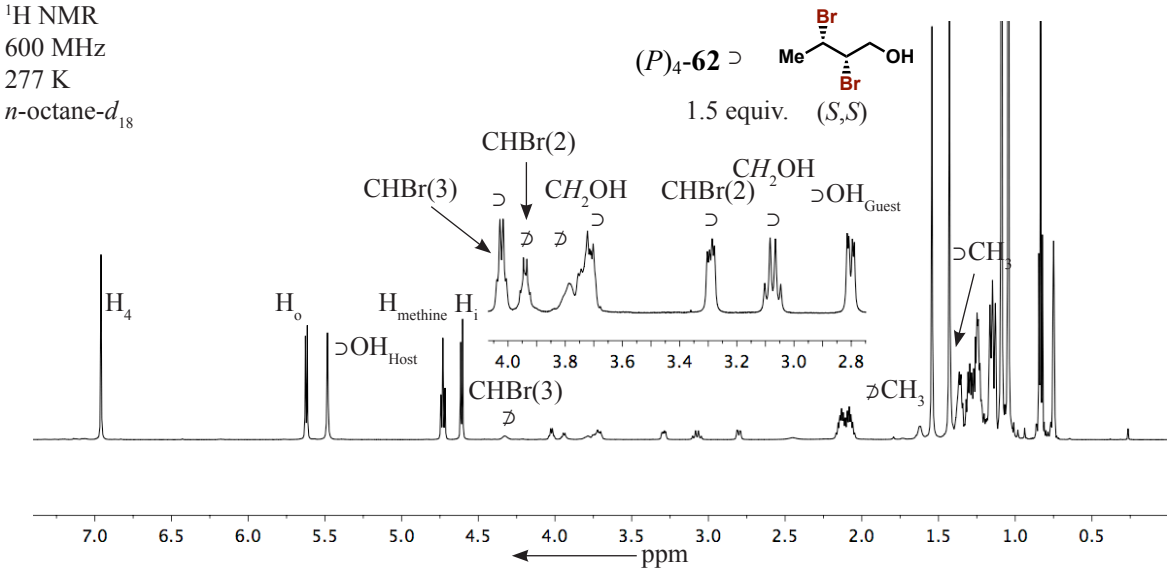

Figure 101. ^{1}H NMR traces of AAC (*P*)$_4$-**62** (35 mM) in *n*-octane-d_{18} at 277 K with 1.5 equiv. of (*S*,*S*)-2,3-dibromobutanol. One equivalent is complexed, while the 0.5 equiv. of the guest are free in solution. The ⊃ denotes the signals corresponding to the complexed guest molecule and ⊅ to the signals corresponding to the free guest molecule. Host-resonances: H_{inside} = inside protons and H_o = outside protons of the methylene bridges; H_4 = aromatic proton.

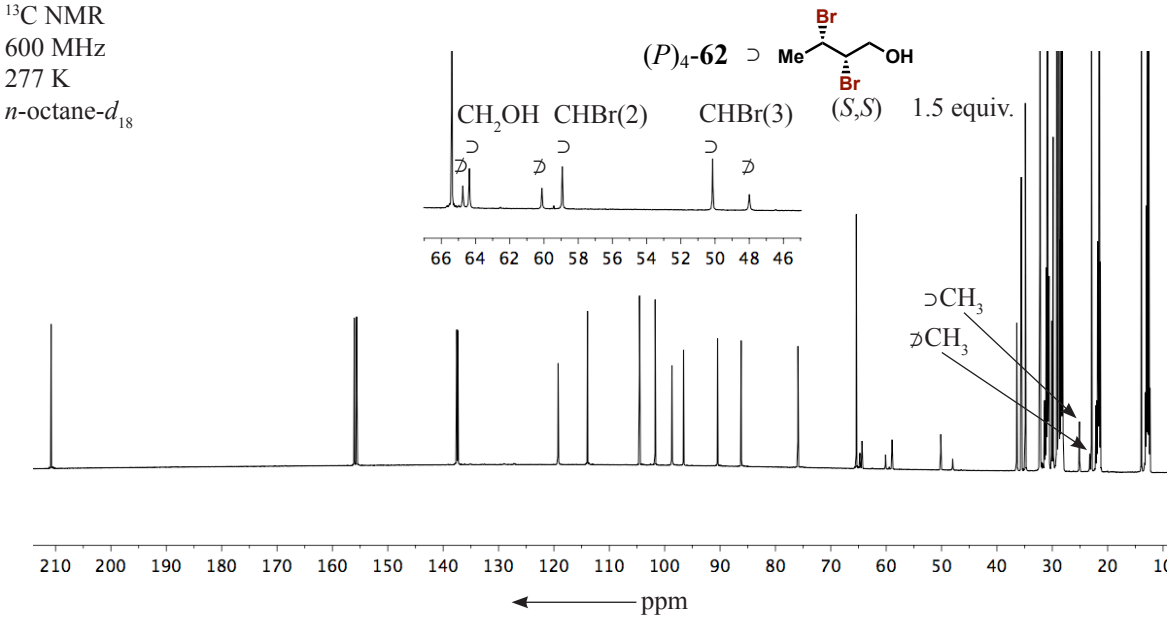

Figure 102. ^{13}C NMR traces of AAC (*P*)$_4$-**62** (35 mM) in *n*-octane-d_{18} at 277 K with 1.5 equiv. of (*S*,*S*)-2,3-dibromobutanol. One equivalent is complexed, while the 0.5 equiv. of the guest are free in solution. The ⊃ denotes the signals corresponding to the complexed guest molecule and ⊅ to the signals corresponding to the free guest molecule.

NMR solution studies were complemented by X-ray co-crystal structures, for which the enantiopure $(P)_4$- and $(M)_4$-configured AACs **62** were crystallized with the racemic guest molecules (see Experimental Part). The X-ray co crystal structures allowed to analyze the complexation geometry of the host-bound guest molecules in the solid state. Theoretical studies on the host–guest complexes are ongoing and indicated that the binding mode of the guests observed in the solid-state structure matches well with the lowest energy conformations calculated for the gas phase (T. Husch and Prof. M. Reiher, ETHZ). We were especially interested to study the different binding mode of the enantiomeric pairs of guests.

The distribution of the enantiomers of the guest in the host (with 100% occupation) allowed additionally to estimate the enantioselectivity of the host towards the guest. The observed enantioselectivity in the solid-sate structures matched well with the observed enantioselectivity in solution. Here, we show only selected examples to highlight the complementary information obtained from the X-ray co-crystal structures. On a side note, very few X-ray crystal structure of comparable small molecule alkyl and alkyl halide alcohols have been reported, presumably due to the difficulty in crystallizing them.

Remarkably, all X-ray co-crystal structures of the alkyl halide guest molecules (Table 12, entry 1–6) with both the AACs $(P)_4$- and $(M)_4$-**62** showed the guest in a similar binding mode with the alcohol engaged in the hydrogen-bonding array of the host and one halogen pointing towards the aromatic moieties of the resorcin[4]arene core, while the second halogen pointed towards the acetylene functionality of the alleno-acetylenic arm (Figure 103).

Figure 103 shows an overlay of the X-ray co-crystal structures of the host–guest complexes obtained from enantiopure AAC $(P)_4$-**62** with the racemic alcohols. Every X-ray co-crystal structure shows the pair of guest enantiomers in different populations, depending on the enantioselective preference towards the receptor. Figure 103 A depicts higher populated and stronger binding (*S*,*S*)- and (*S*,*R*)-enantiomers of the guests, while Figure 103 B shows the generally lower populated and weaker binding (*R*,*R*)- and (*R*,*S*)-enantiomers (displayed with decreased transparency in Figure 103, B).

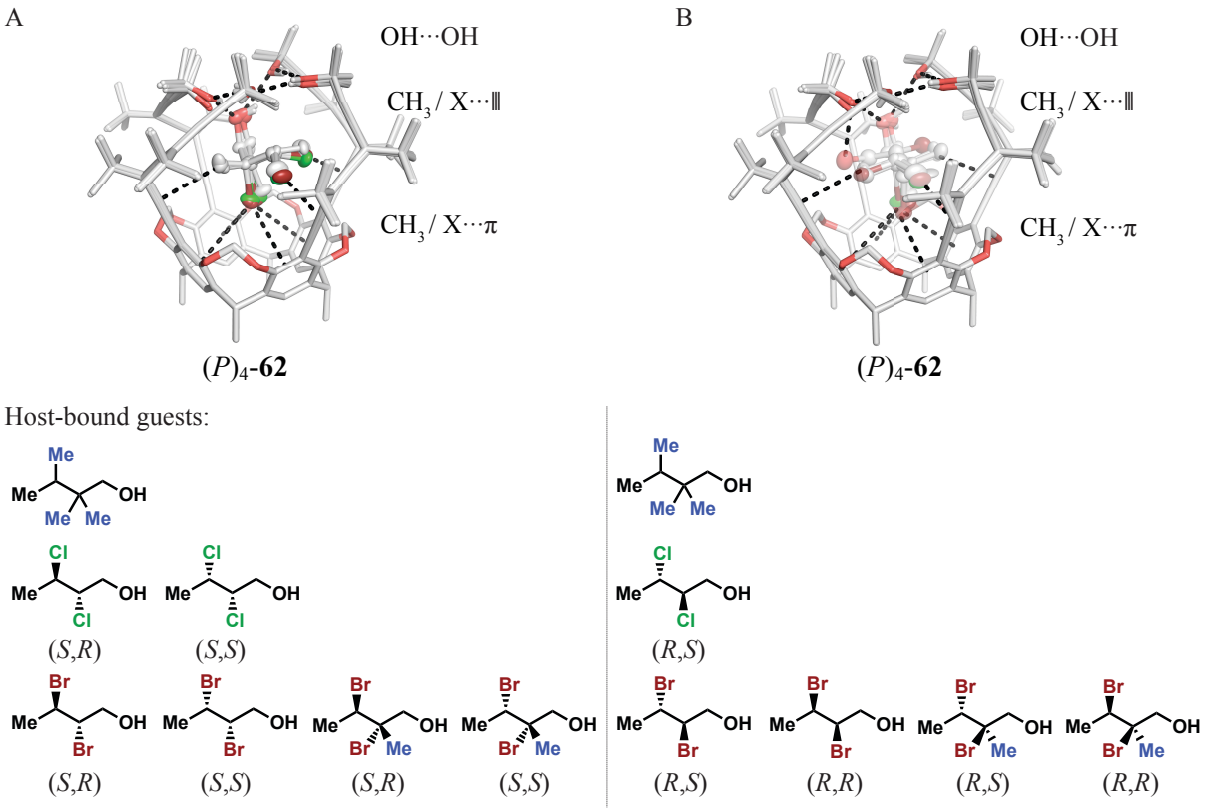

Figure 103. Overlay of X-ray co-crystal structures obtained from of AAC $(P)_4$-**62** with the selected series of racemic alcohols. Depending on the guests, different populations of the enantiomers were observed. A: the stronger binding (*S*,*S*)- and (*S*,*R*)-enantiomers of the guests are depicted. B: the weaker binding (*R*,*R*)- and (*R*,*S*)-enantiomers of the guests are depicted (decreased transparency). *n*-Hexyl chains of the receptor $(P)_4$-**62** are omitted for clarity. Guests are shown in ellipsoids representation (50% probability).

In the overlay of the host–guest complexes, the host shows hardly any structural flexibility (Figure 103). Only small deviations are observed in the tertiary alcohols groups, closing the interior cavity of the host. The guest molecules barely differ in their binding mode, undergoing one directional hydrogen-bonding and X···π and X···Ⅲ interactions with the host. Depending on the nature of the halogen and on its *anti*- or *syn*-configuration, the X···π and X···Ⅲ distances vary. However, all X···Ⅲ interactions show heavy atom contacts below their van der Waals radii. The respective enantiomers of the guest molecules bind in their mirror image conformation, with only a single exception. In the following we will discuss the X-ray co-crystal structure of the weakest binding ligand in solution of the series of alkyl halide alcohols, namely AAC $(P)_4$-**62**⊃*anti*-2,3-dichlorobutanol ((*S*,*S*) : (*R*,*R*) = 58:42), and compare it to the strongest binding ligands, namely AAC $(P)_4$-**62**⊃*syn*-2,3-dibromo-2-methylbutanol ((*S*,*S*) : (*R*,*R*) = 65:35) and AAC $(P)_4$-**62**⊃*syn*-2,3-dibromobutanol ((*S*,*S*) : (*R*,*R*) = 68:32). The latter

illustrates the exception, where the two enantiomeric guest pairs bind in a different conformation. For a full description of all host–guest complexes, see Appendix.

Figure 104 shows the X-ray co-crystal structure of AAC $(P)_4$-**62**⊃*anti*-2,3-dichlorobutanol ((*S*,*S*) : (*R*,*R*) = 58:42) and AAC $(P)_4$-**62**⊃*syn*-2,3-dibromo-2-methylbutanol ((*S*,*S*) : (*R*,*R*) = 65:35).

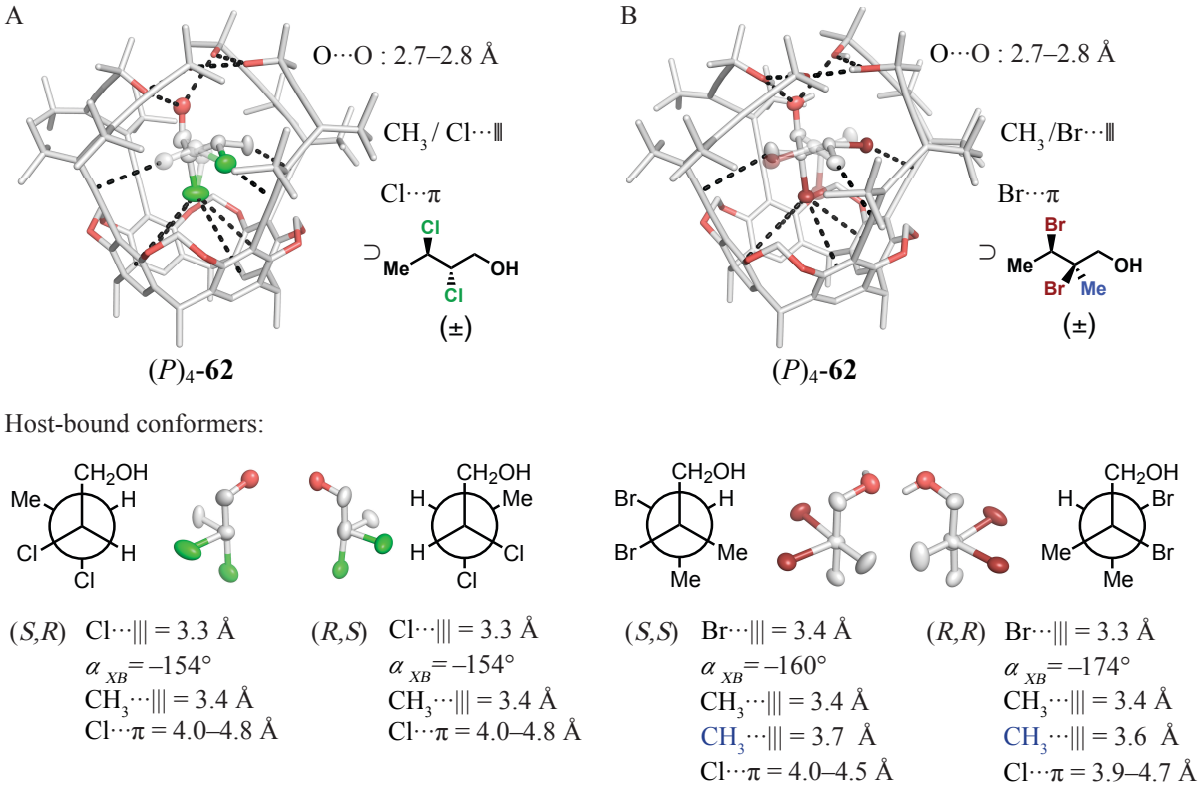

Figure 104. X-ray co-crystal structures of A: AAC $(P)_4$-**62**⊃*anti*-2,3-dichlorobutanol ((*S*,*S*) : (*R*,*R*) = 58:42); B: AAC $(P)_4$-**62**⊃*syn*-2,3-dibromo-2-methylbutanol ((*S*,*S*) : (*R*,*R*) = 65:35). The stronger binding enantiomers are the (*S*,*R*)- and (*S*,*S*)-configured guests. The weaker binding (*R*,*S*)- and (*R*,*R*)-enantiomers of the guests are depicted with decreased transparency. The host-bound conformations of the guests are illustrated below, along with the host–guest contacts. *n*-Hexyl chains of the receptor $(P)_4$-**62** are omitted for clarity. Guests are shown in ellipsoids representation (50% probability).

In both crystal structures, the enantiomeric pairs of the guest molecules bind in their mirror image conformation. The adopted conformation in the cage receptor is higher in energy (*gauche*) compared to the lower energy conformer adopted in solution (*periplanar*). The (*S*,*S*)- and the (*R*,*R*)-configured enantiomers of *anti*-2,3-dichlorobutanol show comparable host–guest contacts with Cl···Ⅲ contacts at 3.3 Å ($\alpha_{XB} = -154°$) and multiple CH_3···π / Ⅲ contacts (Figure 104, below). In solution, (±)-*syn*-2,3-dibromo-2-methylbutanol is bound by –2.5 kcal mol^{-1} stronger compared to (±)-*anti*-2,3-dichlorobutanol (Table 12). The X-ray co-

crystal structure of AAC $(P)_4$-**62**⊃*syn*-2,3-dibromo-2-methylbutanol ((*S*,*S*) : (*R*,*R*) = 65:35) shows the enantiomeric pairs bound in their mirror image conformation, with the bromo- and the methyl-substituents *gauche* to each other. In solution, the guests adopt two equally populated conformers, where the bromo- and the methyl-substituents are *gauche* to each other. The cage receptor binds one of the two lower energy conformations in solution. The guest inside the host shows multiple favorable contacts with the host, where the distances slightly differ between the enantiomers ((*S*,*S*): Br···||| = 3.4 Å with $\alpha_{XB} = -160°$ and (*R*,*R*): Br···||| = 3.3 Å with $\alpha_{XB} = -174°$). The additional methyl group in the 2-position undergoes favorable CH_3···||| contacts at 3.4 Å. Overall, the small differences in the contacts between the receptor and each enantiomers result in a slight preferential binding of the receptor for the (*S*,*S*)-configured guests enantiomer.

In solution, (±)-*syn*-2,3-dibromobutanol displayed similar binding affinities compared to (±)-*syn*-2,3-dibromo-2-methylbutanol ($\Delta G_{293\ K}$ = –7.6 kcal mol^{-1} and –7.9 kcal mol^{-1}, respectively, Table 12). The X-ray co-crystal structure of AAC $(P)_4$-**62**⊃*syn*-2,3-dibromobutanol shows the guest bound to the host in the lower energy conformation with the bromo-substituents *gauche* to each other (Figure 105).

Also in solution, this was observed to be the preferred conformation. Although both enantiomers of the guest bound in their *gauche* conformation, the binding mode of the enantiomeric pairs differed. The alcohol group of the (*S*,*S*)-configured enantiomer forms a five-fold hydrogen-bonding array with the host and additional Br···||| contacts at 3.3 Å ($\alpha_{XB} = -160°$) and multiple CH_3/Br···||| contacts are established. In contrast, the alcohol group of the (*R*,*R*)-configured enantiomer coordinates to the hydrogen-bonding array of the host from below. Additionally, the bromo-substituent in the 2-position forms Br···||| contacts at 3.7 Å ($\alpha_{XB} = -144°$), whereas the bromine in the 3-position is engaged in Br···π contacts with the resorcin[4]arene core. The inverse was observed for the stronger binding (*S*,*S*)-configured enantiomer. This difference in binding mode between the enantiomeric pairs presumably contributes to the largest ratio between the enantiomeric pairs of the guests ((*S*,*S*) : (*R*,*R*) = 68:32 in the solid state and ((*S*,*S*) : (*R*,*R*) = 75:25 in *n*-octane).

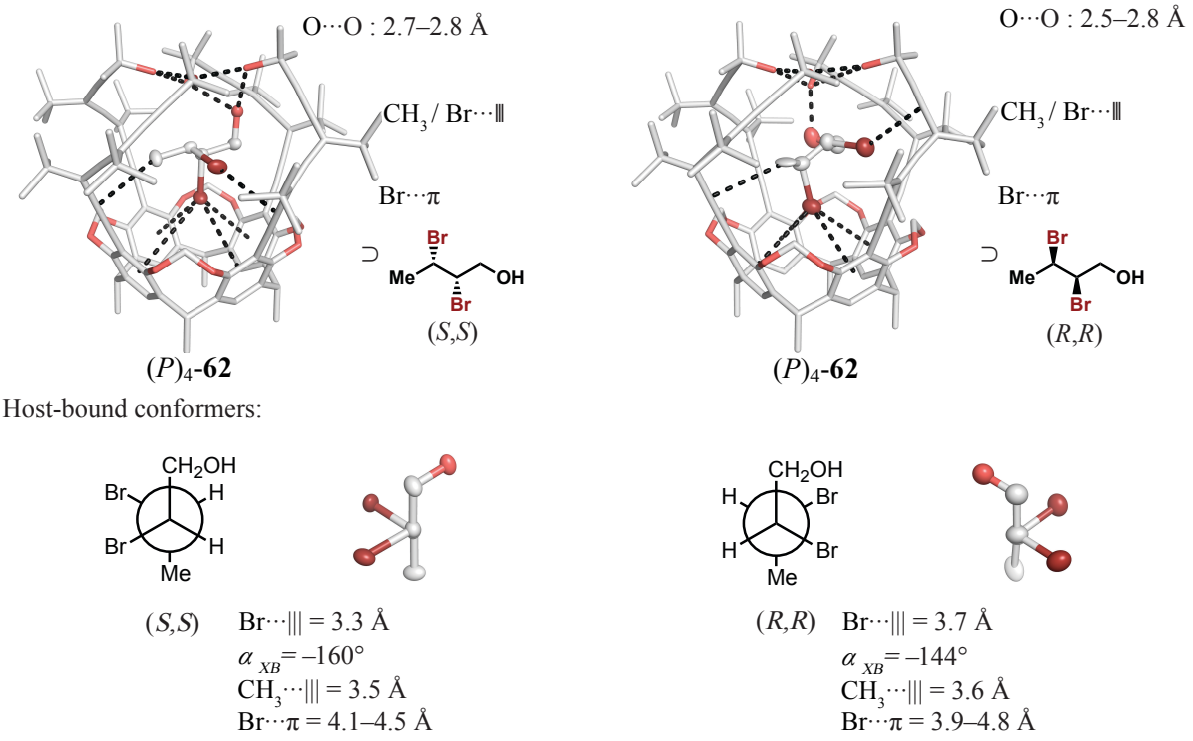

Figure 105. X-ray co-crystal structures of AAC $(P)_4$-**62**⊃*syn*-2,3-dibromobutanol ((*S*,*S*) : (*R*,*R*) = 68:32). A: AAC $(P)_4$-**62**⊃(*S*,*S*)-2,3-dibromobutanol; B: AAC $(P)_4$-**62**⊃(*R*,*R*)-2,3-dibromobutanol, with the stronger binding (*S*,*S*)-configured enantiomer (A) and the weaker binding (*R*,*R*)-enantiomer (B). The host-bound conformations of the guests are illustrated below, along with the host–guest contacts. *n*-Hexyl chains of the receptor $(P)_4$-**62** are omitted for clarity. Guests are shown in ellipsoids representation (50% probability).

The binding modes of the guests inside the host were highly reproducible in the X-ray co-crystal structures of the $(M)_4$-configured receptor. Additionally, theoretical calculations on the host-bound structures match well with the ones observed in the solid-state structures. This allowed us to start to predict the host-bound guest-conformation, along with their enantioselectivities prior to solution studies and crystallization experiments. This collaborative project between the groups of Prof. Reiher, Prof. Carreira and Prof. Diederich is ongoing.

5.3 Summary and Conclusion on H-Bonding, Dispersion and Halogen-Bonding Interactions

In a collaboration with Dr. Fischer and Prof. Carreira (ETHZ), supported by theoretical studies by T. Husch and Prof. Reiher (ETHZ), we expanded the cyclic alcohol series to acyclic alkyl alcohols and alkyl haloalcohols. The guest molecules were inspired by the work of the Carreira group on fluoro-, chloro-, and bromodanicalipin A, and consist largely of fragments of the aforementioned (Figure 92). In solution studies with AACs $(P)_4$- and $(M)_4$-**62**, we investigated the binding affinities of the chiral guests towards the host, along with the conformations of the

host-bound structures. Remarkable high binding affinities were observed for the alkyl haloalcohols, such as for (±)-*syn*-2,3-dibromo-2-methylbutanol ($\Delta G_{293\ K} = -7.9$ kcal mol^{-1}, $K_a = 7.4 \cdot 10^5$ M^{-1} Table 12). 1D and 2D NMR studies allowed the full characterization of the free and the host-bound complexes in *n*-octane-d_{18} at temperature between 277–293 K. The formation of diastereoisomeric complexes of the enantiopure hosts with the chiral (racemic) guests resulted in splitting of the 1D NMR signals of the host and the guests. The diagnostic splitting of the signals, reminiscent of the effect of chiral NMR shift reagents, allowed us to evaluate the enantioselectivity of the AACs $(P)_4$- and $(M)_4$-**62** to the guests in solution. The highest selectivities were observed for *syn*-2,3-dibromobutanol ((*S*,*S*) : (*R*,*R*) = 75:25 with AAC $(P)_4$-**62**) and *anti*-2,3-dibromo-2-trifluoromethylbutanol ((*S*,*R*) : (*R*,*S*) = 73:27 with AAC $(P)_4$-**62**). The enantioselectivities of the racemic guests towards the enantiopure hosts were surprising, as they did not correlate with the binding strength or optimal space filling of the guests with the host. The highest enantioselectivities were observed for smaller guests (*syn*-2,3-dibromobutanol) and larger guests, such as for *anti*-2,3-dibromo-2-(trifluoromethyl)butanol (Figure 97).

NMR solution studies were complemented by X-ray co-crystal structures, where the distribution of the enantiomers of the guest in the host (with 100% occupation) matched the observed enantioselectivity in solution. In total, 15 X-ray co-crystal structures of the achiral or racemic guests bound to the $(P)_4$- or $(M)_4$-configured receptor were obtained, with more in preparation. The X-ray co-crystal structure of AAC $(P)_4$-**62**⊃*syn*-2,3-dibromobutanol showed the two enantiomers differing in their binding mode to the receptor, further substantiating the observed enantioselectivities. Theoretical studies, conducted by Tamara Husch (ETHZ), allowed us to evaluate the host-bound guest conformations theoretically. The confined nature of the interior of the host creates an environment where predictions of the guest conformations matched well with the ones obtained from X-ray co-crystallization experiments. In future, this will allow us to evaluate potential binding of guests to the host prior to experimental complexation studies.

6. Development of Alleno-Acetylenic Cage (AAC) Receptors for Molecular Recognition in Aqueous Medium

This project was designed as part of the Master Thesis of Wieland Goetzke. He contributed to the synthesis of the receptor systems described herein. We thank Dr. A. Schwab for assistance with HPLC separation.

6 Development of Alleno-Acetylenic Cage (AAC) Receptors for Molecular Recognition in Aqueous Medium

Complexation of small molecules in aqueous medium is highly challenging and differs fundamentally from complexation in organic solvents.[4] The entropic and enthalpic contributions of hydrophobic interactions in water are still poorly understood and highly controversial.[4,280,295] Both the "classical" and the "nonclassical hydrophobic effect" (see Introduction, Section 1.1) play an important role for the strong binding and selectivity of ligands to natural receptors in water.[45,46] A solid understanding of the role of water in molecular recognition is crucial for better understanding biological processes for rational structure-based design in medicinal chemistry as well as agrochemical applications.[4,46]

Aqueous model systems were already applied successfully to study salt bridges, ion pairs, cation–π, dispersive, stacking and hydrophobic interactions (for references, see Introduction). The study by Dougherty and co-workers on cation-π interactions exemplifies the impact of model systems on the recognition and quantification of interactions observed in nature.[34,35,189,296,297]

Hydrophobic and well-defined cavities in aqueous medium represent a highly challenging structural motif.[298-300] $(P)_4$- and $(M)_4$-configured alleno-acetylenic cage (AAC) receptors proved to be ideal model systems to study the interplay between space occupancy, conformation, and chiral recognition in apolar organic solvents (Chapter 3–5).[192] In order to study molecular recognition in a solvent environment comparable to natural systems, we set out to develop enantiopure AAC receptors, which would be soluble in aqueous medium. A potential water-soluble receptor system would have to display more polar groups on the surface. We envisioned replacement of the tertiary butyl groups of the alleno-acetylenic backbone with more polar tertiary alcohols (Figure 106, B).

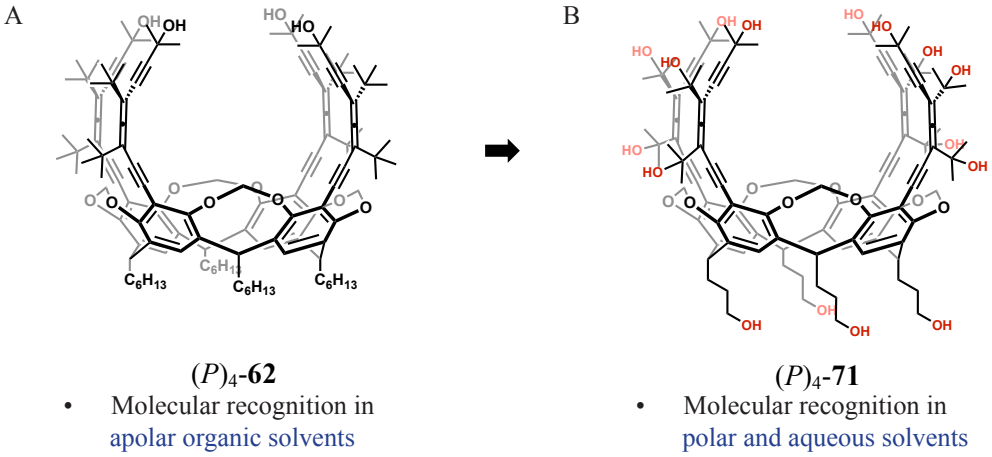

Figure 106. A: Enantiopure $(P)_4$- and $(M)_4$-configured alleno-acetylenic cage (AAC) receptors **62**, which are soluble in organic solvents, have proven to be ideal to study molecular recognition in apolar organic solvents, such as *n*-octane. B: Targeted $(P)_4$- and $(M)_4$-configured alleno-acetylenic cage (AAC) receptors **71** with improved solubility in polar solvents for molecular recognition studies in aqueous medium.

A modular synthetic approach was designed to additionally allow the introduction of polar leg groups.[204,301,302] Herein, we describe a new class of highly polar AAC receptors. Conformational analysis of the receptors in solution is discussed. Preliminary guest binding studies demonstrated the ability of the receptors to complex small molecules in aqueous medium. Further studies, including quantitative binding studies, are ongoing.

6.1 Overview of Targeted Enantiopure AAC Receptors with Polar Functional Groups

In order to gradually increase the solubility in polar solvents and to study the corresponding optical properties of the synthesized AACs, we decided to pursue a modular synthetic approach. Figure 107 shows the targeted $(P)_4$-configured AACs, as a product of the alleno-acetylenic building blocks and resorcin[4]arene scaffolds.

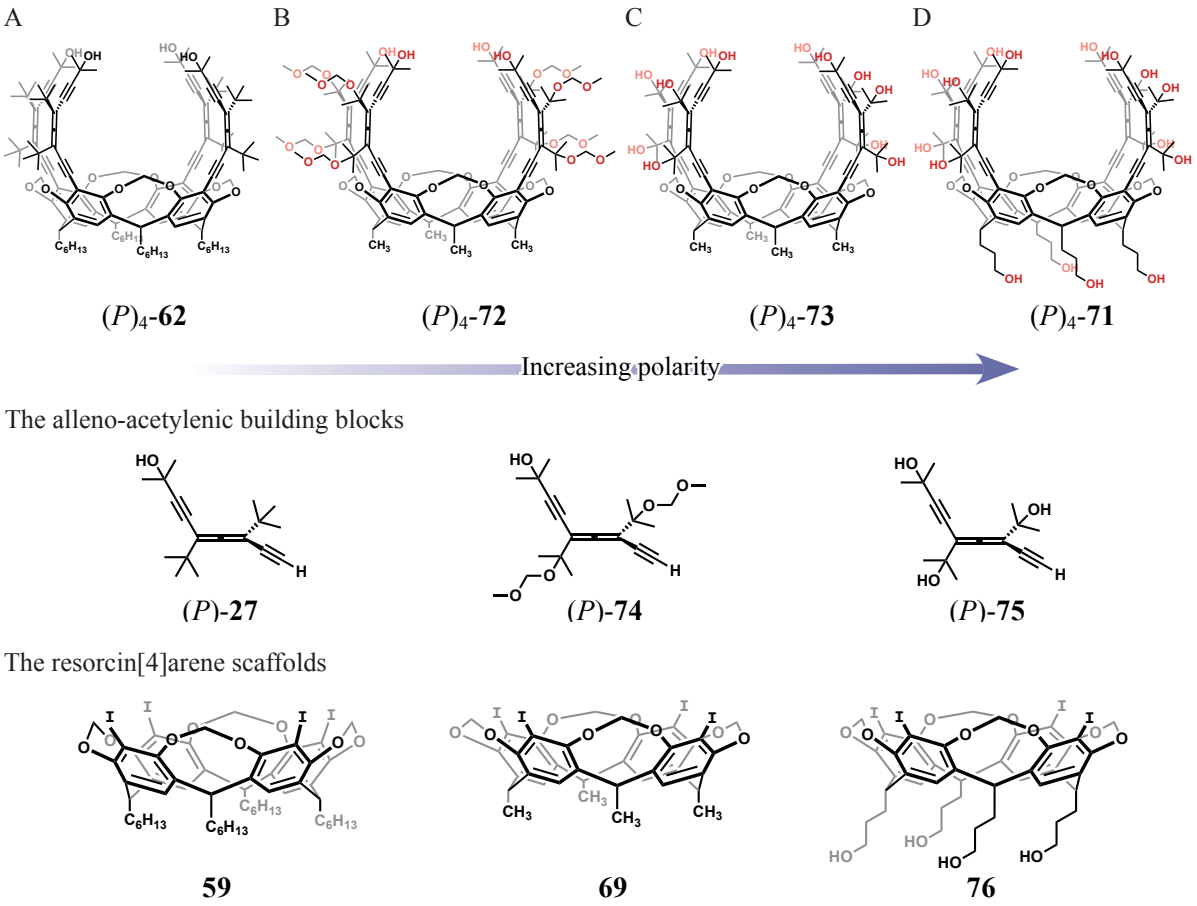

Figure 107. Overview of targeted enantiopure AAC $(P)_4$-**71**–**73** receptors with increasing solubility in polar and aqueous media. A divergent synthetic approach was envisaged consisting of the enantiopure alleno-acetylenic building blocks and different resorcin[4]arene scaffolds. Only $(P)_4$-configured receptors are shown. $(M)_4$-configured receptors were to be synthetized accordingly from the enantiopure (*M*)-configured alleno-acetylenes.

The synthetic approach relied on the four-fold Sonogashira cross-coupling developed for AACs $(P)_4$- and $(M)_4$-**62**.[192] We therefore set out to synthesize enantiopure alleno-acetylenes (*P*)- and (*M*)-**74** and **75** and the iodinated resorcin[4]arene scaffold **76**.

6.2 Synthesis of Enantiopure 1,3-Diethynylallenes (*P*)/(*M*)-74 and -75

The synthesis of 1,3-diethynylallene (DEA) (±)-**74** was previously developed in the group from commercially available ethyl 2-hydroxy-2-methyl-propionate (**77**, Scheme 12) and was optimized in this Thesis.[303] The synthesis was performed on a multi-gram scale and (±)-**74** was obtained in 31% yield over seven linear synthetic steps.

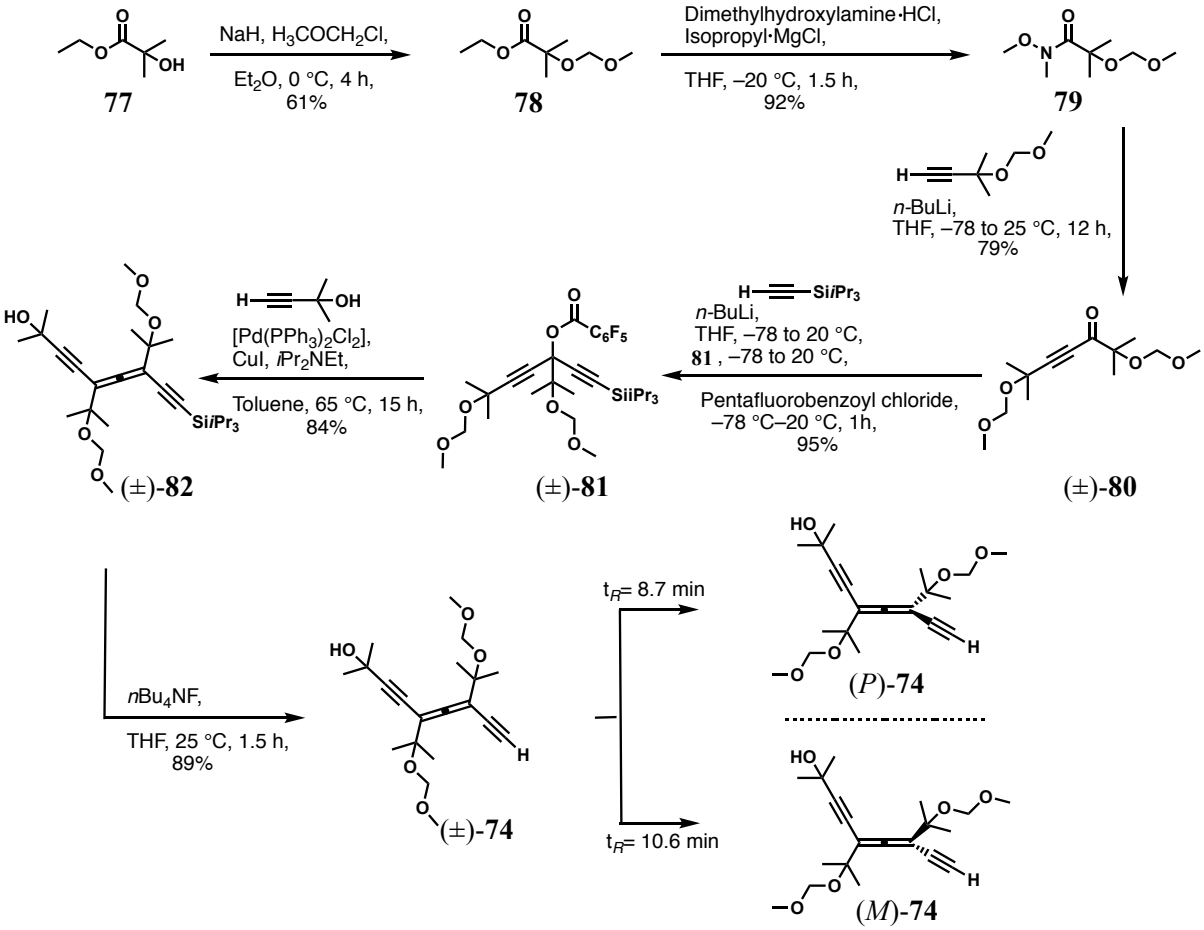

Scheme 12. Synthesis of (*P*)- and (*M*)-configured enantiomers of **74**. Six synthetic steps (27% overall yield) are followed by separation of (±)-**74** into the enantiomers. t_R designates the retention time of the respective enantiomers by preparative HPLC on a CSP Diacel Chiralpak® IA column, using in *n*-hexane/*i*PrOH 99.2:0.8.[303]

The key synthetic step for the synthesis of DEA (*P*)- and (*M*)-**74** consists of allene formation via the palladium(0) and copper(I) mediated S_N2' reaction of (±)-**81** with 2-methylbut-3-yn-2-ol to afford (±)-**82** (Scheme 12). Compound (±)-**81** was constructed by two formal acetylation reactions of Weinreb amide **79**, via compound **80**. The Weinreb amide was accessed in two steps from compound **77** and **78**. For a detailed synthetic protocol, see the Experimental Part.

Enantiopure alleno-acetylenic triol (*P*)-(+)-**75** was obtained by deprotection of (*P*)-(+)-**74** in 84% yield (Scheme 13).

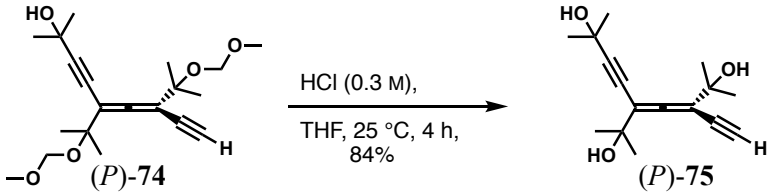

Scheme 13. Deprotection of enantiopure alleno-acetylene (*P*)-**74** to obtain enantiopure alleno-acetylenic triol (*P*)-**75**. Only (*P*)-configured **75** are shown. (*M*)-configured **75** was synthetized accordingly from the enantiopure (*M*)-configured alleno-acetylene **74**.

Methoxymethyl deprotection was achieved under mild conditions with HCl in MeOH (0.3 M), and (*P*)-(+)-**75** was isolated in 83% within 4 hours of reaction time. The same synthetic procedure was applied to the (*M*)-(–)-configured enantiomer. On a side note, an increase in temperature and molarity of the acid ($HCl_{aqueous}$) during evaporation under reduced pressure led to significant elimination of the tertiary alcohols (observed by ^{1}H NMR). This undesired side-reaction was avoided by an aqueous work-up prior to solvent concentration *in vacuo*.

With an efficient synthetic protocol for enantiopure alleno-acetylenes (*P*)- and (*M*)-**74** and -**75** in hand, we set out to synthesize the iodo-activated resorcin[4]arene scaffolds.

6.3 Synthesis of Resorcin[4]arene Scaffold 76

The synthesis of tetramethyl tetraiodo resorcin[4]arene **69** was described in Scheme 10 (Chapter 1). Tetraiodo resorcin[4]arenes **76** and **83** were synthesized in four steps, followed by adapting a previously reported procedure (Figure 108).[304,305]

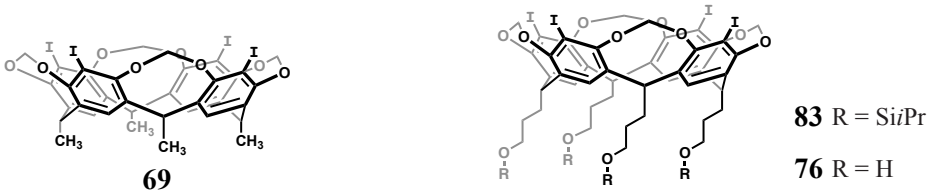

Figure 108. Tetraiodo resorcin[4]arene scaffolds **76** and **83**. [304,305]

Octol **84** was synthesized from resorcinol and 2,3-dihydrofuran followed by bromination with *N*-bromosuccinimide. Scheme 14 summarizes the synthesis of tetraiodo resorcin[4]arene cavitands **83** in four steps.[305]

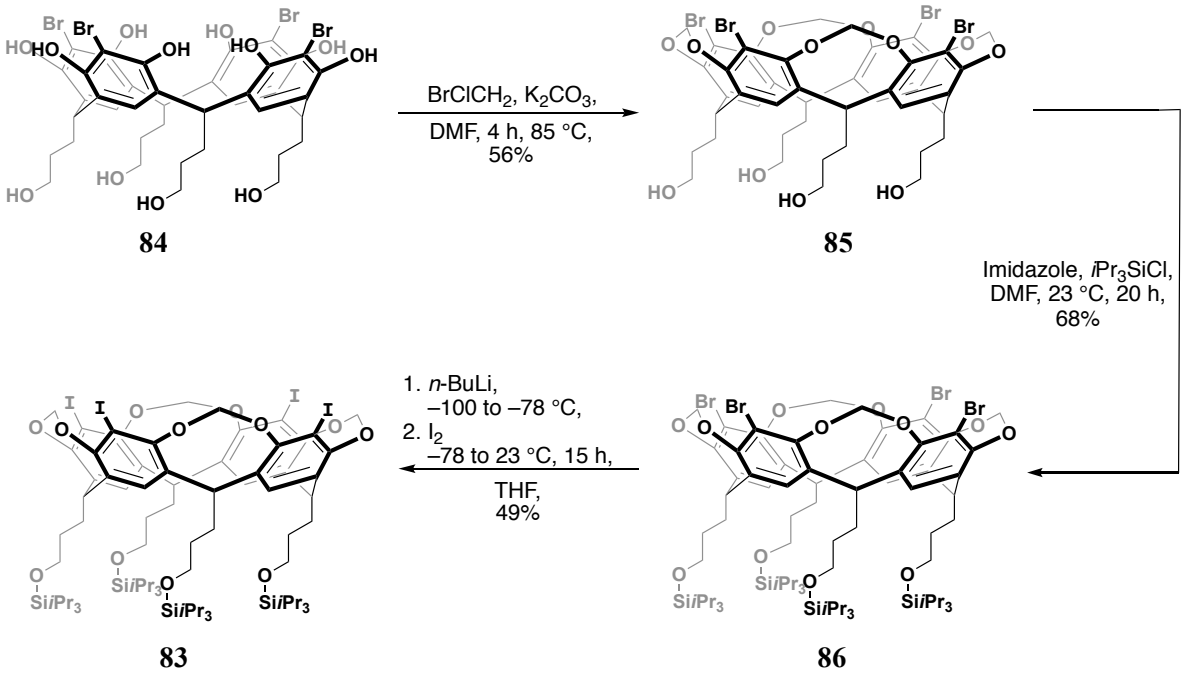

84 **85** **86** **83**

Scheme 14. Synthetic procedure for tetraiodo resorcin[4]arene scaffolds **83** from tetrabromooctol **84**.[305]

Methylene bridging of **84** with $ClBrCH_2$ and K_2CO_3 in DMF afforded **85** in 56% yield. A first attempt at direct lithiation followed by iodination resulted in a complex mixture of products presumably due to partial dehalogenation. Therefore, a protecting group strategy for the four hydroxyl groups was required. The triisopropylsilyl protecting group can be cleaved under mild acidic conditions, harsh alkaline conditions, or with *n*-tetrabutylammonium fluoride.[306] We envisioned the selective triisopropylsilyl deprotection with *n*-tetrabutylammonium fluoride facilitating post-modification of hydroxyl-footed alleno-acetylenic cages. Triisopropylsilyl-protected cavitand **83** was prepared following a literature procedure with triisopropylsilyl chloride and imidazole in DMF in 68% yield. [305] Finally, tetrabromide **86** was lithiated with *n*-butyllithium at –100 °C, followed by treatment with I_2, which yielded the product **83** in 49% yield (Scheme 14).

6.4 Synthesis of AAC Receptors $(P)_4$-71, $(P)_4$-72, and $(P)_4$-73 containing Polar Functional Groups

With enantiopure polar 1,3-diethynylallenes (DEAs (*P*)/(*M*)-**74** and -**75**) and tetraiodo resorcin[4]arene building blocks (**76** and **83**) at hand, we investigated suitable conditions for the Sonogashira cross-coupling and strategies for the removal of the protecting groups. We herein report on the synthesis of three novel polar alleno acetylenic cage receptors $(P)_4$-**71**, $(P)_4$-**72**, and $(P)_4$-**73** (Figure 109), and their corresponding $(M)_4$-configured structures.

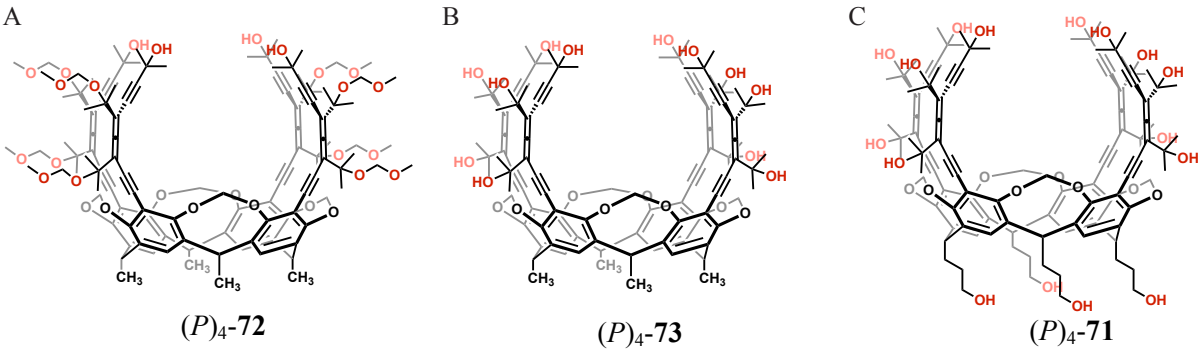

Figure 109. A–C: Summary of synthesized enantiopure AACs $(P)_4$- and $(M)_4$-**71**–**73** bearing polar functional groups. Only $(P)_4$-configured receptors are shown. $(M)_4$-configured receptors were synthetized accordingly from the enantiopure (*M*)-configured alleno-acetylenes.

AAC $(P)_4$-**71** was synthesized by a fourfold Sonogashira coupling reaction between alleno-acetylene (*P*)-**74** and tetraiodo resorcin[4]arene **69**, by applying the previously developed conditions for AACs $(P)_4$/$(M)_4$-**62** (Scheme 15).

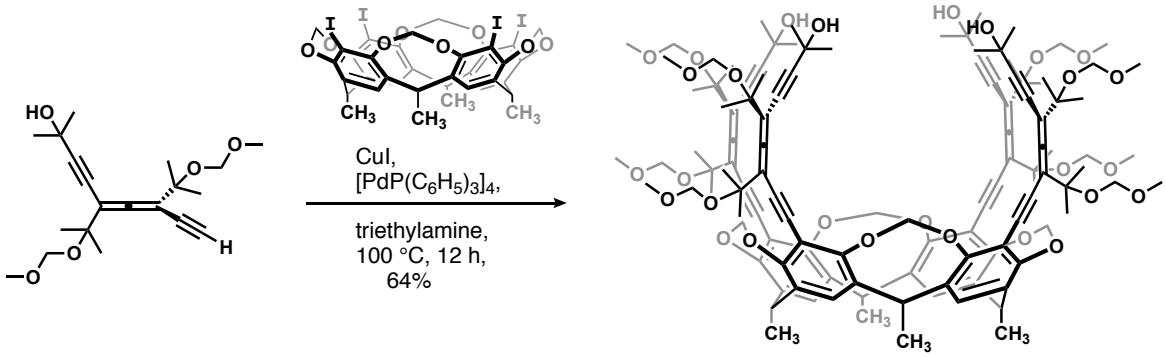

Scheme 15. Reagents and conditions for the synthesis tetramethyl-footed AAC $(P)_4$-**72**. Only (*P*)-configured structure shown. $(M)_4$-configured **72** was obtained from (*M*)-**74**.

The direct synthesis of AAC $(P)_4$-**72** by Sonogashira cross-coupling reaction between the enantiopure alleno-acetylenic triol (*P*)-**75** and tetraiodo resorcin[4]arene **69** failed. Instead, we observed the exclusive oxidative dimerization of the terminal acetylenic functionalities to afford the alleno-acetylenic dimer. Presumably, this resulted from the low solubility of the polar alleno-acetylene (*P*)-**75** in triethylamine. Previous studies showed that the oxidative homocoupling competes with the Sonogashira cross-coupling pathway and can dominate if the oxidative addition and transmetalation steps are slow.[307,308] We therefore pursued cross coupling with the protected alleno-acetylene (*P*)-**74,** which afforded AAC $(P)_4$- and $(M)_4$-**72**. Subsequent methoxymethyl deprotection of AACs $(P)_4$-**72** with HCl in MeOH

(0.3 M; 23 °C, 3 h), followed by RP-HPLC (LiChrospher® 100 CN (5 μm) column; eluent: $CH_3CN:H_2O$ 1:1), afforded AAC $(P)_4$-**71** in 66% yield (Scheme 16).

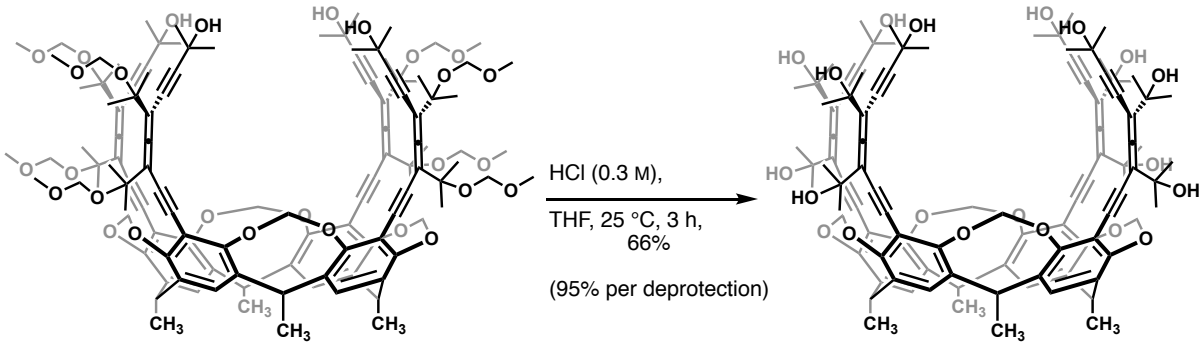

$(P)_4$-**72** $(P)_4$-**73**

Scheme 16. Deprotection of AAC $(P)_4$-**72** to obtain $(P)_4$-enantiopure AAC **73**. Only $(P)_4$-configured receptors are shown. $(M)_4$-configured receptor was synthetized analogously from the enantiopure $(M)_4$-configured AAC **72**.

The isolated yield of 66% corresponds to 95% yield per deprotection reaction. The same synthetic procedure was applied for AAC $(M)_4$-**73**. Importantly, the enantiopure AACs **73** did not racemize under acidic conditions and proved to be both optically and thermally stable, an essential prerequisite for further studies.

In order to obtain the AACs $(P)_4/(M)_4$-**71** with further enhanced solubility in polar solvents, tetraisopropylsilyl protected resorcin[4]arene **83** was subjected to the established coupling procedure with MOM-protected enantiopure alleno-acetylene (*P*)/(*M*)-**74**. The tetraisopropylsilyl-protected cage AAC $(P)_4$-**87** was purified by a filtration through silica and was directly subjected to the deprotection conditions (HCl in MeOH; 0.3 M, 23 °C, 3 h; Scheme 17). The deprotection was monitored by ^{1}H NMR spectroscopy, and AAC $(P)_4$-**71** was isolated in 40% yield over two steps (Scheme 17).

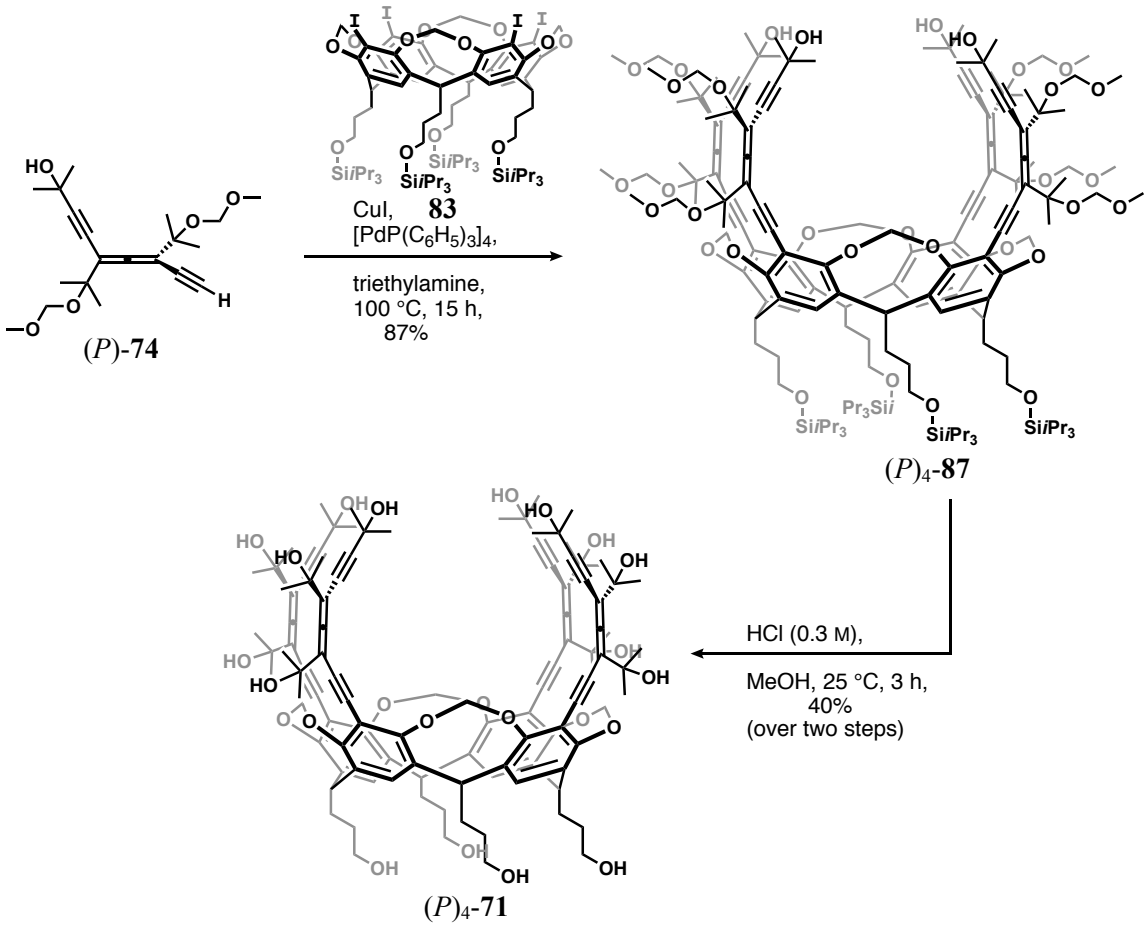

Scheme 17. Reagents and conditions for the synthesis AAC $(P)_4$-**71**. The coupling to afford AAC $(P)_4$-**87** was followed by deprotection of to obtain enantiopure $(P)_4$-AAC **71**. Only $(P)_4$-configured receptors are shown. The corresponding $(M)_4$-configured receptor was synthetized analogously from the enantiopure $(M)_4$-configured AAC **87**.

The lower temperature and the selected solvent (methanol) for the simultaneous deprotection of the triisopropylsilyl and the methoxymethyl groups were found to be crucial. The tertiary alcohols can form a carbenium ion under the acidic conditions, which can subsequently undergo elimination.

With the new series of enantiopure AACs bearing polar functional groups, we studied their solution-state properties by ECD, UV/Vis, and NMR spectroscopies.

6.5 Solution Studies of AAC $(P)_4$- and $(M)_4$-72

We were especially interested to study the conformational switching behavior of the AACs $(P)_4/(M)_4$-**71**–**73** between open and closed conformational states, similar to what we had observed for AACs $(P)_4/(M)_4$-**62**. We therefore conducted ECD, UV/Vis, and NMR spectroscopic studies in solvents of different bulk dielectric properties. With ECD and UV/Vis, we monitored the solvent dependent absorption properties. For solvents in which we observed

strong changes in the chiroptical properties of the AACs, we monitored the solvent-dependent chemical shifts with NMR spectroscopy.

While the ECD traces of the enantiopure cage receptors showed generally strong solvent dependencies, hardly any changes in the UV/Vis absorption was observed. This supported the notion that changes in the chiroptical properties were related to solvent-dependent conformational changes in solution.

6.5.1 ECD and UV/Vis Spectroscopic Properties of AACs (*P*)$_4$- and (*M*)$_4$-72

The least polar receptor of the series, AAC (*P*)$_4$/(*M*)$_4$-**72**, showed solubility in both apolar and polar organic solvents. Little solubility in aqueous solvents was observed. In cyclohexane, AAC (*P*)$_4$-**72** displayed large Cotton effects $\Delta\varepsilon = -133$ M^{-1} cm^{-1} at $\lambda = 307$ nm (Figure 110). Changing the solvent to acetonitrile inverted the Cotton effect to $\Delta\varepsilon = +94$ M^{-1} cm^{-1} at $\lambda = 304$ nm with a difference of $\Delta\Delta\varepsilon = +227$ M^{-1} cm^{-1}.

The ECD traces of the (*M*)$_4$-configured enantiomer displayed mirror image traces. In analogy to AAC (*P*)$_4$-**62**, this result indicated stronger stabilization of a closed cage conformation in cyclohexane and stabilization of an open conformation in acetonitrile. The large difference in ECD originates from the different conformations in solution between the closed cage and the open conformation. Importantly, UV/Vis traces did not show significant solvent dependencies.

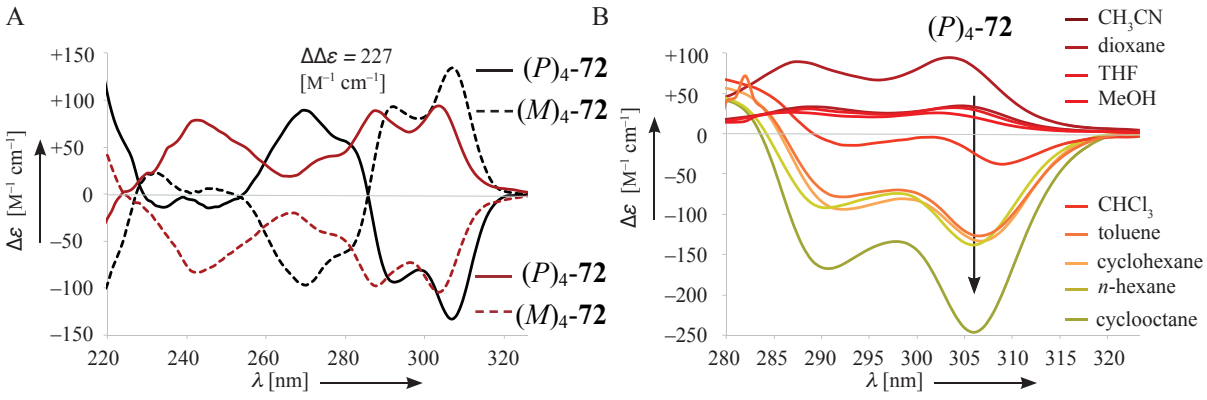

Figure 110. A: ECD spectra of AAC (*P*)$_4$-**72** (solid lines) and AAC (*M*)$_4$-**72** (dotted lines) at 293 K. Spectra in red display AAC (*P*)$_4$-**72** and AAC (*M*)$_4$-**72** in acetonitrile and spectra in black display corresponding traces in cyclohexane. Switching between the open and closed conformation results in $\Delta\Delta\varepsilon = 227$ M^{-1} cm^{-1} at $\lambda = 304$–307 nm. B: ECD traces of AAC (*P*)$_4$-**72** in different solvents of varying polarities.

6.5.2 NMR Spectroscopic Properties of AACs (*P*)$_4$- and (*M*)$_4$-72

Additional to ECD spectroscopic studies, ^{1}H NMR spectra of AAC (*P*)$_4$-**72** were measured in cyclohexane-d_{12} and acetonitrile-d_3. A downfield shift of the tertiary alcohol moieties

($C(Me)_2OH$) by +0.9 ppm was observed by changing the solvent from acetonitrile-d_3 (δ_{OH} = 3.62 ppm) to cyclohexane-d_{12} (δ_{OH} = 4.51 ppm). The downfield shift in cyclohexane indicated larger stabilization of the closed conformation over the open conformation. The observed downfield shift of the OH-protons in the hydrogen-bonding array were consistent with the ECD spectroscopic interpretation that apolar solvents stabilize the closed cage form while polar solvents favor the open conformation.

^{1}H NMR spectra measured in both cyclohexane-d_{12} and acetonitrile-d_3 showed distinct chemical shifts for each of the eight methoxymethyl (OCH_2OMe) groups, further indicating the presence of discrete conformational states on the ^{1}H-NMR spectroscopic time scale. NMR spectroscopic studies will be subject for further investigations.

6.5.3 ECD and UV/Vis Spectroscopic Properties of AACs (*P*)$_4$- and (*M*)$_4$-73

With increasing polarity of the enantiopure receptor system to AAC (*P*)$_4$-**73**, lower solubility in apolar solvents was observed, along with enhanced solubility in more polar solvents. AAC (*P*)$_4$-**73** was hardly soluble in apolar solvents and well soluble in more polar solvents, such as tetrahydrofuran, acetonitrile, dioxane and methanol.

ECD traces of AAC (*P*)$_4$-**73** in acetonitrile were comparable to the ones measured for its methoxymethyl protected analogue AAC (*P*)$_4$-**72** (Figure 111).

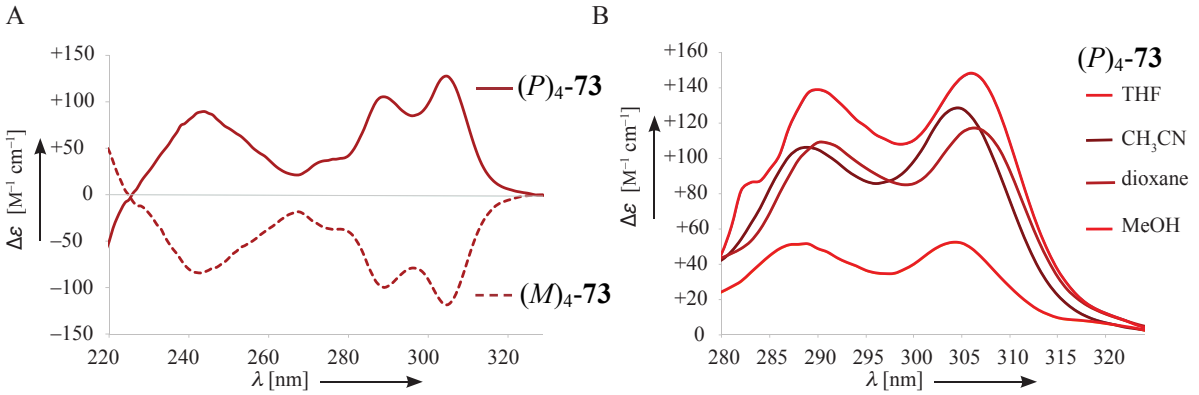

Figure 111. A: ECD spectra of AAC (*P*)$_4$-**73** (solid lines) and AAC (*M*)$_4$-**73** (dotted lines) at 293 K in acetonitrile. B: ECD traces of AAC (*P*)$_4$-**73** in different solvents of varying polarities.

In acetonitrile, AAC (*P*)$_4$-**73** displayed large Cotton effects, with $\Delta\varepsilon$ = +127 M^{-1} cm^{-1} at λ = 304 nm (Figure 111). The (*M*)$_4$-configured enantiomers showed mirror image traces. Acetonitrile, dioxane, and tetrahydrofuran induced comparable Cotton effects at λ = 307–304 nm. In methanol, AAC (*P*)$_4$-**73** showed significantly decreased absorption of $\Delta\varepsilon$ = +52 M^{-1} cm^{-1} at λ = 304 nm. The weakening of ECD intensity indicated that methanol is a poorer solvent for solubilizing either conformation. Although AAC (*P*)$_4$-**73** was not soluble

in pure water at 10^{-5} M concentration, methanol as a non-competitive co-solvent (40 vol%; 10^{-5} M) brought sufficient solubility in aqueous medium.

6.5.4 NMR Spectroscopic Properties of AACs $(P)_4$- and $(M)_4$-73

In ^{1}H NMR spectroscopic measurements in acetonitrile-d_3, the tertiary alcohol moieties ($C(Me)_2OH$) of AAC $(P)_4$-**73** appeared at $\delta_{OH} = 3.87$ ppm, comparable to the shift of the tertiary alcohol moieties of AAC $(P)_4$-**72**.

6.5.5 ECD and UV/Vis Spectroscopic Properties of AACs $(P)_4$- and $(M)_4$-71

Enantiopure AACs $(P)_4$/$(M)_4$-**71** were soluble only in low polarity solvents, such as protic and aprotic organic solvents.

ECD traces of AAC $(P)_4$-**71** in acetonitrile were comparable to the ones measured for AACs $(P)_4$-**72** and $(P)_4$-**73**, with Cotton effects of $\Delta\varepsilon = +127$ M^{-1} cm^{-1} at $\lambda = 305$ nm (Figure 112).

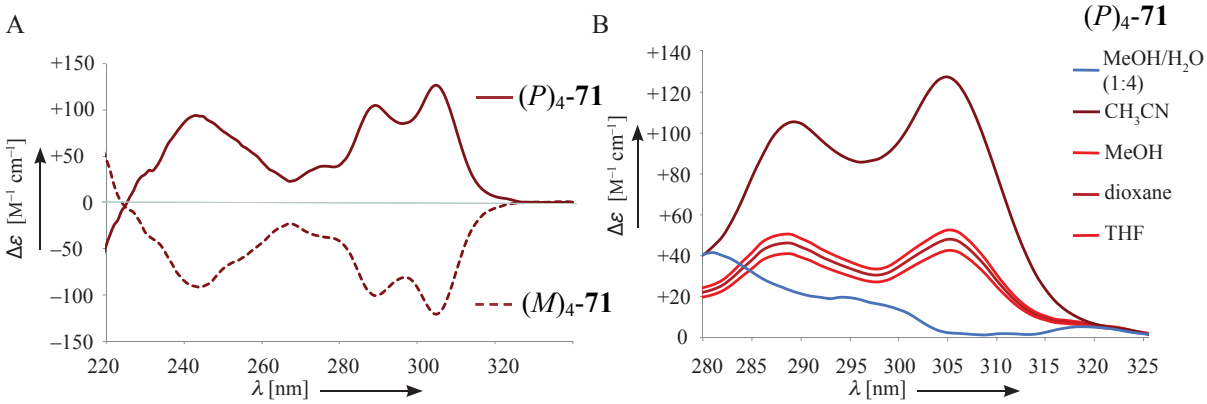

Figure 112. A: ECD spectra of AAC $(P)_4$-**71** (solid lines) and AAC $(M)_4$-**71** (dotted lines) at 293 K in acetonitrile. B: ECD traces of AAC $(P)_4$-**71** in different solvents of varying polarities.

The $(M)_4$-configured enantiomers showed mirror images traces. The introduction of four additional alcohols groups, 3-hydroxypropyl chains at the resorcin[4]arene receptor, strongly influenced the ECD traces of AAC $(P)_4$-**71** in tetrahydrofuran and dioxane, weakening the intensities to $\Delta\varepsilon = +50$ M^{-1} cm^{-1} at $\lambda = 305$ nm. While AAC $(P)_4$-**71** showed low solubility in pure water, 20vol% of methanol were sufficient to achieve solubility in aqueous medium. Interestingly, ECD traces showed a strong decrease in intensities in H_2O/methanol (4:1) (Figure 112), indicating little stabilization of either conformation in this solvent system. Again, UV/Vis traces did not show significant solvent dependencies.

6.5.6 NMR Spectroscopic Properties of AACs (*P*)$_4$- and (*M*)$_4$-71

In ^{1}H NMR studies in acetonitrile-d_3, small amounts (2 vol%) of water were required to for full solubility. The tertiary alcohol moieties (C(Me)$_2$OH) in acetonitrile-d_3 (2 vol% H_2O) appeared at δ_{OH} = 4.14 ppm, strongly indicating their involvement in hydrogen-bonding.

6.5.7 Conclusion on Solution Studies of AACs (*P*)$_4$- and (*M*)$_4$-71–73

The newly described enantiopure cage receptors (*P*)$_4$- and (*M*)$_4$-configured **71**–**73** proved to be configurationally, optically and thermally stable. Large Cotton effects in their ECD traces with strong solvent dependencies in their chiroptical absorption intensities, indicated conformational switching behavior, reminiscent of AACs (*P*)$_4$- and (*M*)$_4$-**62**. Little solvent dependencies were observed in their UV/Vis traces, further substantiating their conformational switching in solution.

In comparison to the previously developed system AACs (*P*)$_4$- and (*M*)$_4$-**62**, (*P*)$_4$- and (*M*)$_4$-configured **71**–**73** showed generally attenuated ECD intensities across a variety of solvents of different bulk dielectric properties. We attributed the weaker ECD intensities to a conformationally more dynamic system induced by large substituents at the allene backbone that possibly compete with guest binding. These findings hinted that large substituents at both the allene-backbone and the recorcin[4]arene receptor have to be avoided in order to enable efficient guest-induced conformational switching.

While AACs (*P*)$_4$- and (*M*)$_4$-**73** showed hardly any solubility in water, AACs (*P*)$_4$- and (*M*)$_4$-**71** showed good solubility in aqueous-organic solvents (water/methanol 4:1). This solvent system did not exclusively stabilize the open conformation of the cage, facilitating guest-induced conformational switching.

6.6 Guest-Binding Induced Conformational Switching of AACs (*P*)$_4$- and (*M*)$_4$-71

In guest-binding studies, we focused on the enantiopure (*P*)$_4$-and (*M*)$_4$-configured AACs **71** in the non-competitive and highly polar solvent system of water/methanol (4:1). We expected guest-induced conformational switching towards the closed-cage conformation, with the guest stabilizing the hydrophobic interior of the host or vice-versa.

In analogy to AACs (*P*)$_4$- and (*M*)$_4$-**62**, we expected the changes in ECD intensities to correlate with guest binding affinity. Prior to quantitative complexation studies, we monitored guest-induced ECD changes in order to assess qualitative binding. Generally, we expected stronger binding for more hydrophobic guests (due to the hydrophobic effect in water/methanol) compared to guest molecules containing polar functional groups, where encapsulation is accompanied with desolvation of the polar functional groups.

For the screening, a host solution of AAC $(P)_4$-**71** at a concentration of 8.5 μM L^{-1} in aqueous medium (H_2O/MeOH 4:1) was prepared. The parent solution was used to prepare the host–guest solution (1.0 mg guest per 1.0 mL host solution). After addition of the guest, the ECD spectrum was recorded. The change in ECD intensity ($\Delta\Delta\varepsilon$) between the host–guest solution and the pure host solution was followed at λ = 304–307 nm to obtain a qualitative guest affinity to the receptor (Figure 113).

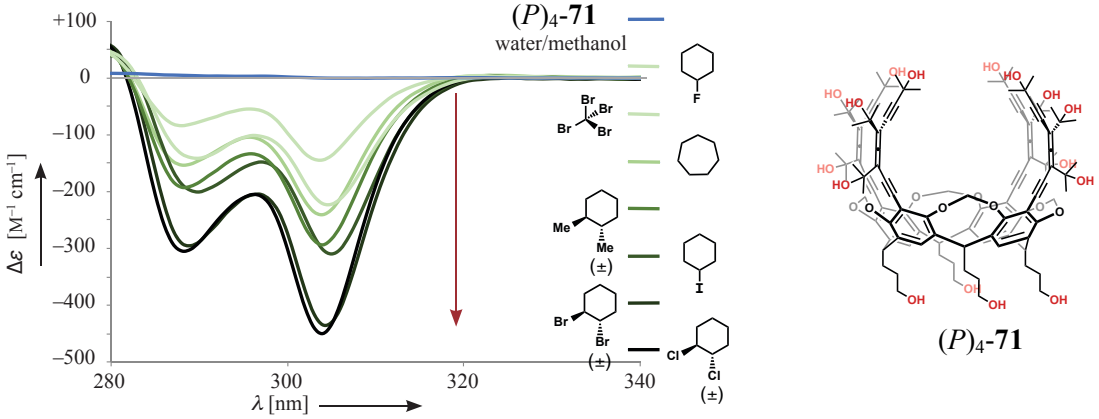

Figure 113. Guest-induced changes in the ECD traces of AAC $(P)_4$-**71** in water/methanol (4:1) at 293 K. Cyclic alkanes and alkyl halides induced strong ICD of up to $\Delta\Delta\varepsilon$ = –450 M^{-1} cm^{-1} at λ = 304 nm.

Figure 113 shows the induced ECD traces of AAC $(P)_4$-**71** in water/methanol (4:1) with a series of alkanes and alkyl halides. While AAC $(P)_4$-**71** displayed hardly any absorption in the ECD traces in water/methanol (4:1), small amounts of guest induced large changes in the band intensity at 304 nm. The most significant changes were observed for guests that bound strongly in the previously studied AACs $(P)_4$- and $(M)_4$-**62** (Figure 113). (±)-*trans*-1,2-Dichlorocyclohexane and (±)-*trans*-1,2-dibromocyclohexane induced very strong changes in ECD intensity at λ = 304 nm of $\Delta\Delta\varepsilon$ = –450 M^{-1} cm^{-1} and $\Delta\Delta\varepsilon$ = –435 M^{-1} cm^{-1}, respectively. This finding was indicative of alkane and alkyl halide guests inducing conformational switching of an open receptor conformation to a closed cage form.

In a second series of potential guest molecules, we monitored the conformational changes induced by molecules bearing polar functional groups, such as alcohols or amines. We expected the desolvation of polar guest molecules to result in weaker binding affinities to the AAC receptors $(P)_4$-**71**. Figure 114 displays the ICD traces upon addition of the guest molecules to AAC $(P)_4$-**71** in water/methanol (4:1).

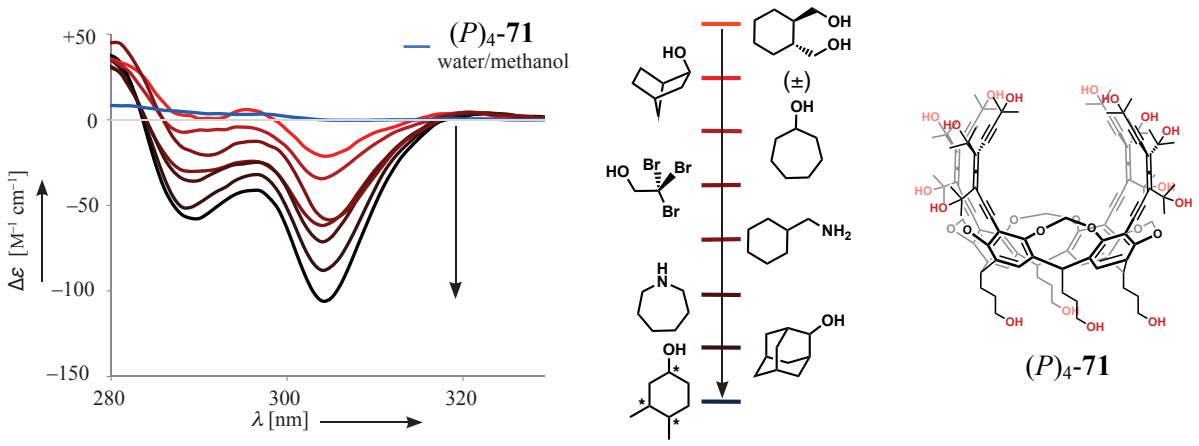

Figure 114. Guest-induced changes in the ECD traces of AAC $(P)_4$-**71** in water/methanol (4:1) at 293 K. Guests with alcohol and amine functionalities resulted in strong ICD of up to $\Delta\Delta\varepsilon$ =–106 M^{-1} cm^{-1} at λ = 304 nm.

Generally, guest molecules bearing polar functional groups induced smaller changes in the ECD traces of AAC $(P)_4$-**71** in water/methanol (4:1). The strongest ICD of $\Delta\Delta\varepsilon$ = –106 M^{-1} cm^{-1} at λ = 304 nm was observed for 3,4-dimethylcyclohexanol (mixture of enantiomers and diastereomers) (Figure 114). The intensity was five times weaker than that observed for (±)-*trans*-1,2-dichlorocyclohexane, indicating weaker binding affinities (Figure 113). The weaker binding of molecules bearing polar functional groups was rationalized with the enthalpic cost of desolvation involved in complexation with the receptor. NMR spectroscopic studies are ongoing to further quantify guest binding to AACs $(P)_4$- and $(M)_4$-**71**.

An exemplary binding study with AAC $(P)_4$-**71** and iodocyclohexane in D_2O/methanol-d_3 (3:2) was carried out by NMR spectroscopic titration (Figure 115). A higher fraction of methanol was required to maintain full solubility at the higher host concentration used for NMR spectroscopic experiments. For iodocyclohexane, fast exchange kinetics on the ^{1}H NMR time scale were observed. Upon guest addition, a downfield shift of the H_{in} protons was observed, accompanied by a smaller upfield shift of the H_4 protons (Figure 115). Furthermore, the methyl groups of the tertiary alcohol moieties in the allene-backbone ($C(Me)_2OH$; δ = 1.5–1.3 ppm) showed an increased splitting upon guest complexation, presumably due to stabilization of a more rigid cage conformation. An association constant of K_a = $1.03 \cdot 10^3$ M^{-1} (determined as arithmetic mean from H_4 and H_{in}), was observed for iodocyclohexane, translating to a Gibbs free energy of $\Delta G_{293\,K}$ = 4.0 kcal mol^{-1}.

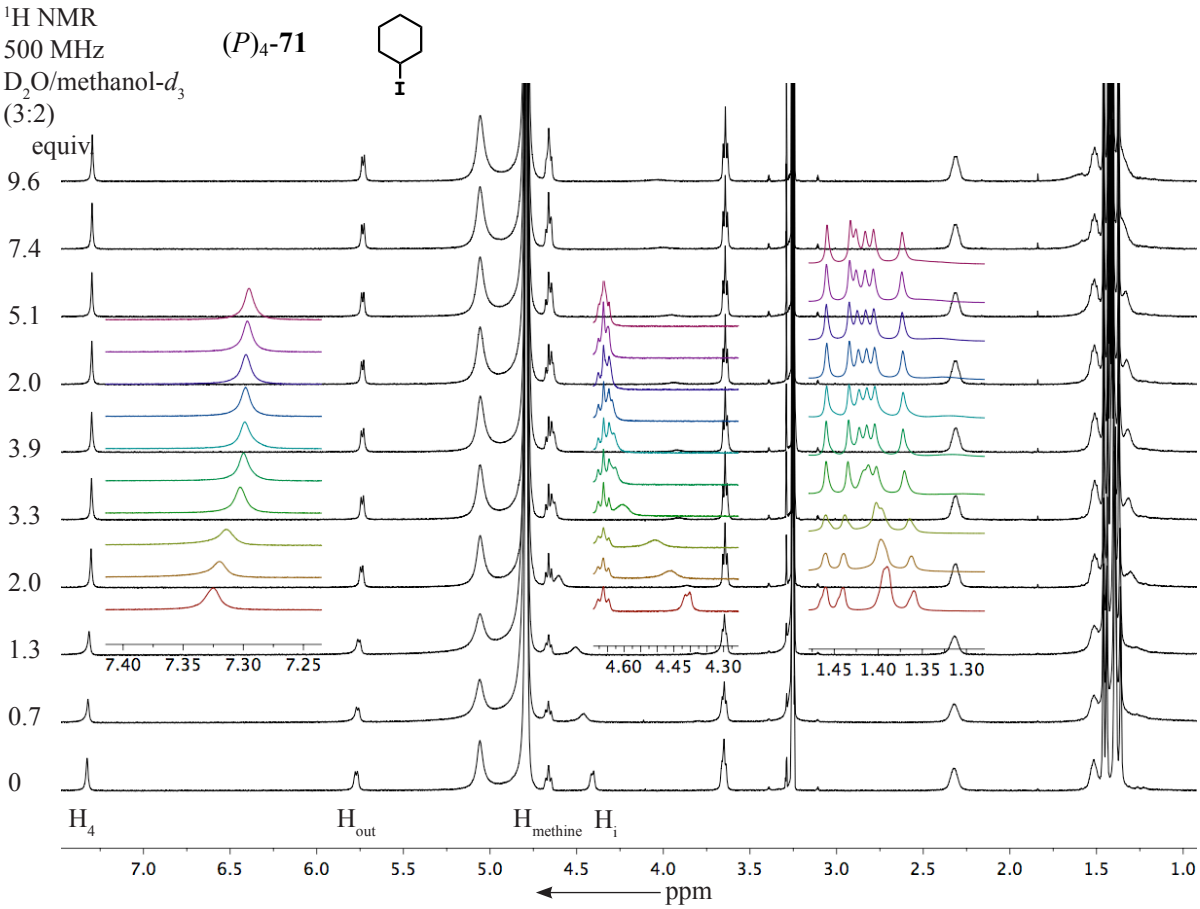

Figure 115. ^{1}H NMR titration of AAC $(P)_4$-**71** (6–8 mM) with iodocyclohexane (0–9.6 equiv.) in D_2O/methanol-d_3 (3:2) at 293 K. A binding affinity of $K_a = 1.03 \cdot 10^3$ $M^{-1}$was determined following the chemical shifts of the host signals 4.3–4.6 ppm. Inserts display the chemical shifts of the host-guest solution with increasing guest concentration (0 → 9.6 equiv.).

6.7 Summary and Conclusion on Alleno-Acetylenic Cage (AAC) Receptors for Molecular Recognition in Aqueous Medium

We developed an efficient and modular synthesis of alleno-acetylenic cage receptors with increased surface polarity, bearing alcohol groups on the alleno-acetylenic backbone and on the resorcin[4]arene scaffold. The modular construction of the $(P)_4$-and $(M)_4$-configured AACs **71**–**73** involved a high-yielding Sonogashira cross-coupling between iodo-activated resorcin[4]arenes and enantiopure alleno-acetylenes, followed by subsequent deprotection. The synthetic approach yielded three new enantiopure AAC receptors, which were soluble in polar and aqueous solvent systems.

ECD, UV/Vis and NMR spectroscopic solution studies revealed increasing solubility in polar, aqueous solvents from$(P)_4$-and $(M)_4$-**71**–**73**. Strongly solvent-dependent ECD absorptions were detected for all AACs, with hardly any solvent dependencies in the

UV/Vis spectroscopic traces, indicating conformational changes depending on the nature of the solvent.

The strong chiroptical properties of the receptors allowed for sensitive detection of guest binding through induced ECD intensities. AACs $(P)_4$-and $(M)_4$-**71** revealed guest-induced switching to a closed conformation in water/methanol (4:1) upon addition of apolar guests and guest molecules bearing alcohol or amine functionalities. An exemplary NMR spectroscopic binding study with iodocyclohexane and AAC $(P)_4$-**71** in D_2O/methanol-d_3 (3:2) further substantiated guest binding in solution.

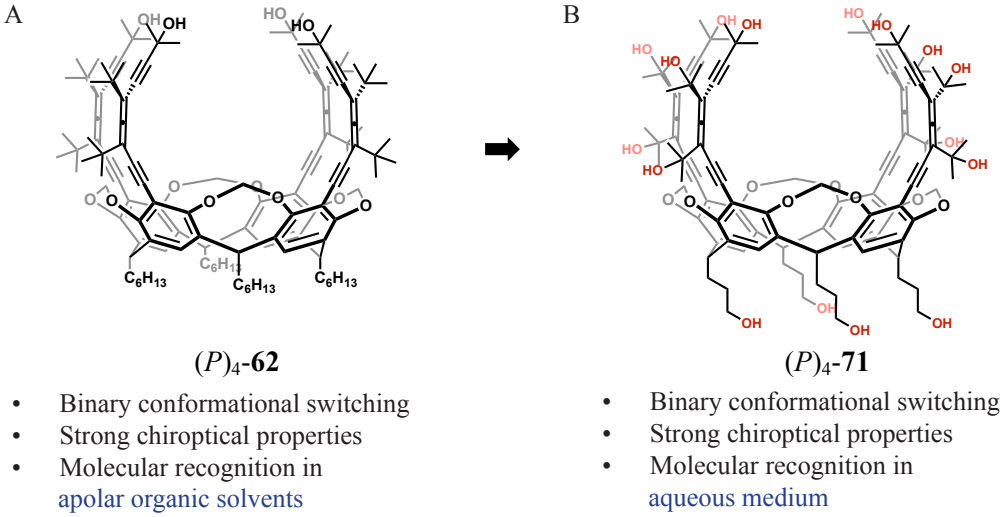

Figure 116. A: Enantiopure alleno-acetylenic cage (AAC) receptors $(P)_4$/$(M)_4$-**62** soluble in organic solvents, ideal to study molecular recognition in apolar organic solvents, such as *n*-octane. B: Alleno-acetylenic cage (AAC) receptors $(P)_4$/$(M)_4$-**71** soluble in aqueous medium for molecular recognition studies in aqueous medium.

Quantitative binding studies of the AACs $(P)_4$-and $(M)_4$-**71** with a variety of polar organic small molecule guests are ongoing. Additionally, development of crystallization conditions will enable insights in the solid-state structure of the receptor systems. While the outer surface of the AACs has been significantly altered by the replacement of *tert*-butyl groups with alcohol containing groups, the properties of the interior surface remains largely conserved, making them ideal to compare enantioselective complexation in apolar and aqueous solvent systems. In future, we would like to expand the extensive molecular recognition studies described in Chapter 2 and 3 to AACs $(P)_4$-and $(M)_4$-**71** in aqueous medium.

7. Brief Overview towards Covalent Alleno-Acetylenic Cage Receptors

Small-molecule single-crystals were mounted by M. Solar, and X-ray crystal structures were solved by Dr. Nils Trapp (ETHZ).

7 Brief Overview on Covalent Alleno-Acetylenic Cage Receptors

This chapter will give a brief overview on the synthesis and properties of covalent alleno-acetylenic cage receptors. A detailed description was not included in this Thesis. Detailed synthetic protocols are described in the Experimental Part. The project is ongoing. The X-ray co-crystal structures obtained of $(P)_4$- and $(M)_4$-configured enantiopure covalent organic cages **88** are described in the Appendix.

7.1 Enantiopure Covalent Alleno-Acetylenic Cage Receptors

Covalent organic cage receptors offer well-defined structures with cavity sizes that emerge from the topology and shape of their molecular building blocks.[110,142,309,310] Compared to the previously described enantiopure alleno-acetylenic cage receptors that undergo binary conformational switching (Chapter 2), covalent enantiopure AACs lock the receptor in its closed cage conformation.

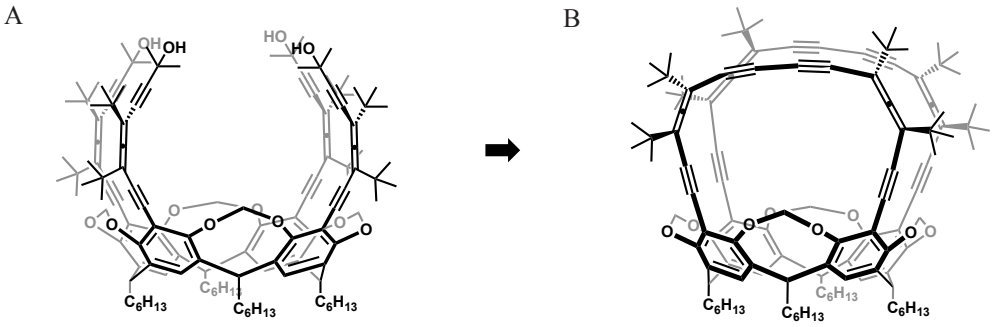

Figure 117. Comparison of enantiopure hydrogen-bonded AACs $(P)_4$- and $(M)_4$-**62** undergoing binary conformational switching (A) with covalent AACs receptors $(P)_4$- and $(M)_4$-**88** (B). Only $(P)_4$-configured receptors shown.

Strong covalent bonds (C≡C–C≡C) replace the four-fold hydrogen-bonding array and ensure high thermal stability and continuous porosity. In pursuit of the series of covalent AAC receptors described in Section 2 of the Introduction (Figure 25), we investigated intramolecular oxidative dimerization of the deprotected terminal acetylenes to obtain enantiopure $(P)_4/(M)_4$-**88** (Figure 117).[307,311-314]

The synthesis involves the deprotection of the terminal tertiary alcohols of **62** to afford enantiopure AACs $(P)_4/(M)_4$-**89** (see Experimental Part). $(P)_4/(M)_4$-**89** are subsequently converted into the enantiopure covalent AAC receptors $(P)_4/(M)_4$-**88**, employing oxidative

dimerization conditions reported by Breslow et. al.[311] and Cram et. al..[312] Enantiopure $(P)_4$- and $(M)_4$-configured cages **88** were obtained (Scheme 18).

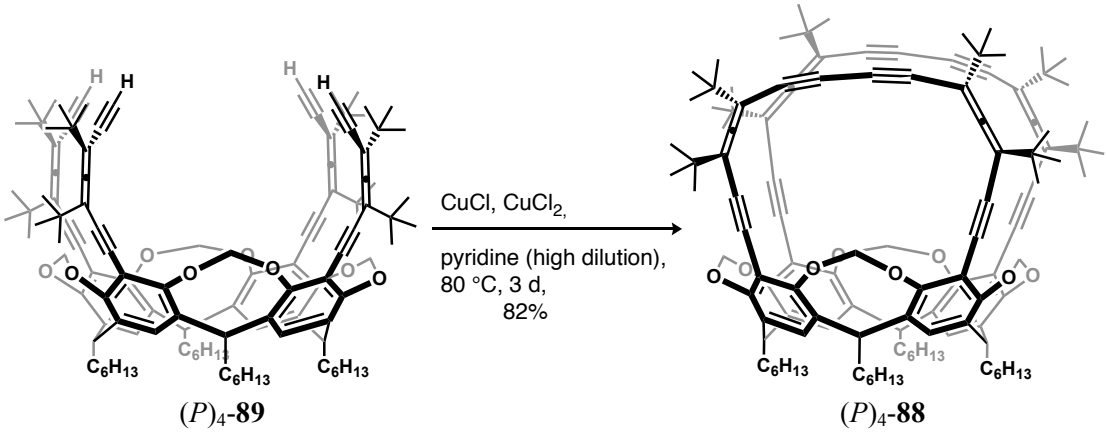

Scheme 18. Reagents and conditions for the synthesis AAC $(P)_4$-**88**. Final intramolecular oxidative dimerization is shown. Only (*P*)-configured structure shown. (*M*)-configured **88** was obtained from (*M*)-configured AAC **89**.

In ECD studies, $(P)_4$- and $(M)_4$-configured AACs **88** showed strong absorption properties towards circularly polarized light (Figure 118, A). Figure 118 shows the overlay of the ECD traces of AACs $(P)_4$-**62** and $(P)_4$-**88** in *n*-hexane at 293 K.

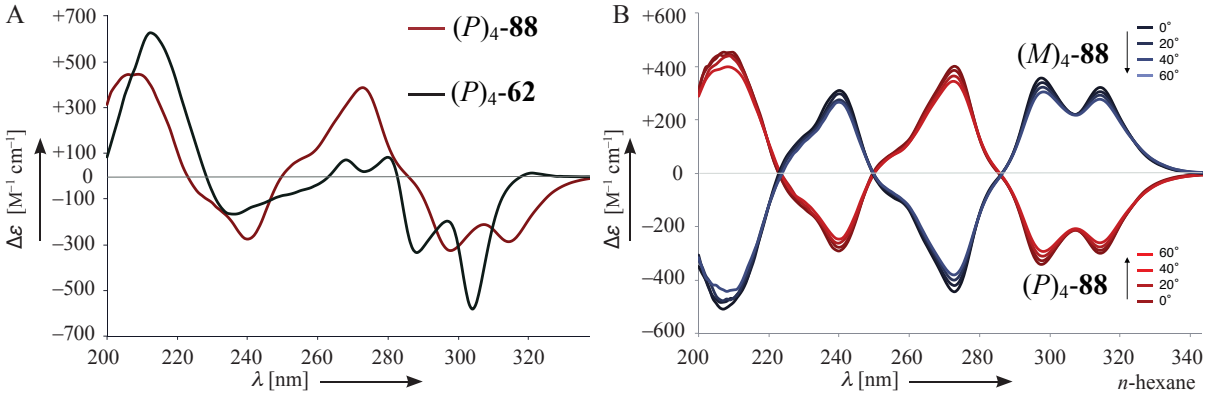

Figure 118. A: Overlay of ECD traces of hydrogen-bonded $(P)_4$-**62** (blue lines) and covalent AAC $(P)_4$-**88** (red lines) in *n*-hexane at 293 K. B: variable-temperature ECD traces of covalent $(P)_4$- (red lines) and $(M)_4$-**88** (blue lines) in *n*-hexane.

While AAC $(P)_4$-**88** displayed strong temperature-dependent chiroptical properties (Figure 41), AAC $(P)_4$-**88** showed very little temperature-dependent ECD traces (Figure 118, B). This additionally confirmed the rigid nature of the covalent cage system in solution.

Gas-absorption studies are ongoing to substantiate the continuous porosity of AACs $(P)_4$/$(M)_4$-**88**. The high crystallinity allowed us to obtain single crystal X-ray co-crystal structures with alkyl halides complexed in the interior of the cage (Figure 119).

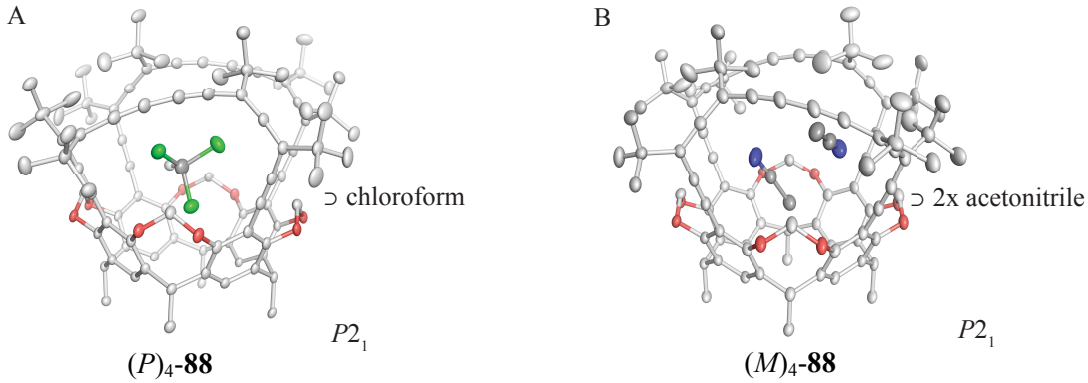

Figure 119. X-ray co-crystal structures of AAC $(P)_4$-**88**⊃chloroform (A) and AAC $(M)_4$-**88**⊃2 x acetonitrile (B). *n*-hexyl chains and hydrogens omitted for clarity; space group: $P2_1$.

7.2 Summary and Outlook on Enantiopure Covalent Alleno-Acetylenic Cage Receptors

Oxidative intramolecular dimerization of deprotected of AACs $(P)_4/(M)_4$-**89** yielded enantiopure covalent AAC receptors $(P)_4$- and $(M)_4$-**88** with strong absorption properties towards circulary polarized light and hardly any temperature dependencies. The high thermal stability makes $(P)_4$- and $(M)_4$-configured AACs **88** interesting receptor systems. X-ray co-crysral structures of $(P)_4$- and $(M)_4$-configured AACs **88** gave insights into the volume of the cavity for future molecular recognition studies. Our previous research on dispersion and halogen-bonding interactions of alkyl halides with AACs $(P)_4/(M)_4$-**62** (Chapter 3), established alleno-acetylenes as unique recognition motifs for guests undergoing dispersion and halogen-bonding interactions. We are currently pursuing the optical resolution of small alkyl halides, such as (±)-fluorochlorobromomethane (see Introduction).

8. Conclusions and Outlook

8 Conclusions and Outlook

8.1 Summary and Conclusion

The study of synthetic model systems and biological counterparts has developed an extraordinary symbiosis, helping to decipher important chemical phenomena observed in nature. We dedicated this Thesis to the understanding of molecular recognition processes of neutral achiral and chiral small molecules by enantiopure receptors.

Despite the apparent progress in the design and construction of enantiopure receptors, examples of optically pure systems that effectively differentiate chiral neutral small molecules are still rare. The general notion prevails that strong directional interactions between the host and the guest are required. In order to question this idea, we set out to design enantiopure receptors that would bind molecules purely based on dispersion interactions, largely in the absence of directional interactions.

In the Introduction to this Thesis, we illustrated important design criteria for enantiopure cage receptors for neutral small molecules, which evolved out of pioneering studies. They can be pinpointed to comprise of (a) a highly preorganized and confined hydrophobic cavity with an asymmetric environment, thereby allowing for the effective differentiation between two enantiomers; (b) a balance of confinement and flexibility to allow guest uptake and release; (c) transduction of the complexation process in the form of a quantifiable signal, such as through NMR or ECD spectroscopies.

The first chapter illustrates our initial design ideas, leading to the development of enantiopure alleno-acetylenic cage (AAC) receptors $(P)_4$/$(M)_4$-**62**. The key synthetic step consists of the four-fold Sonogashira cross-coupling of four axially homochiral 1,3-diethynylallenes with OH termini to a tetraiodo-activated tetramethylene-bridged resorcin[4]arene platform, giving access to AACs $(P)_4$- and $(M)_4$-**62** (Figure 120).

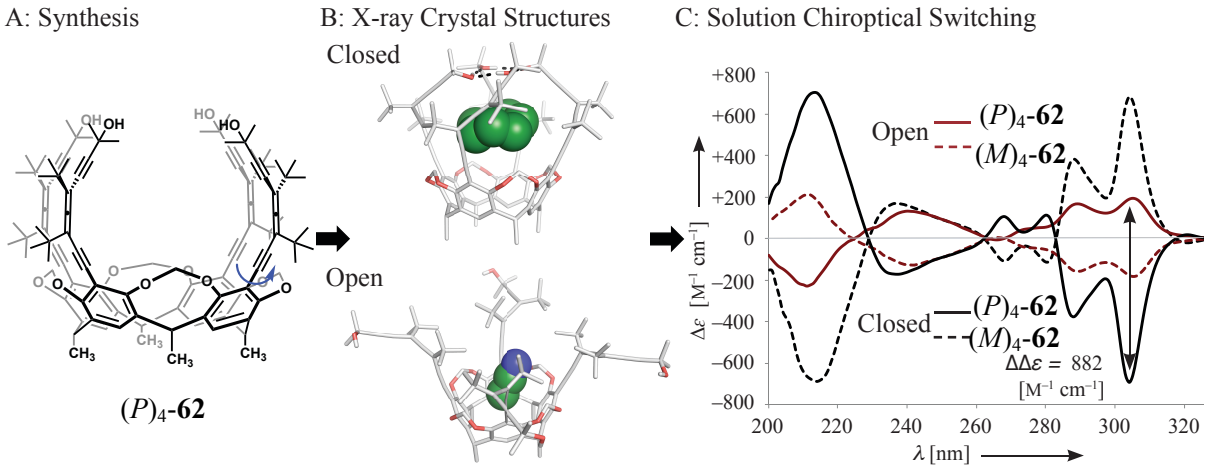

Figure 120. Enantiopure alleno-acetylenic cage (AAC) receptors **62**. A: Synthesis of $(P)_4$- and $(M)_4$-configured AACs **62**; B: co-crystal structures obtained from single-crystal X-ray diffraction of the open and the closed conformation of AAC $(P)_4$-**62**; C: solution-state chiroptical switching between the closed-cage state and the open conformation of $(P)_4$- and $(M)_4$-configured AACs **62**.

The AAC receptors $(P)_4/(M)_4$-**62** undergo solvent-dependent binary conformational switching between a closed-cage conformation and an open state by rotation around a C–C bond. Small polar solvents, such as tetrahydrofuran, acetonitrile, small alcohols and halomethanes favor the open conformation. Larger, less polar solvents, such as *n*-alkanes, cycloalkanes and tetrachloromethane favor the closed conformation. Both states were characterized in solution by NMR-, IR-, UV/Vis- and ECD-spectroscopic studies and by single-crystal X-ray diffraction in the solid state. The binary conformational switching is accompanied by strong changes in the associated electronic circular dichroism (ECD) spectra with $\Delta\Delta\varepsilon = 882$ M^{-1} cm^{-1} at $\lambda = 304$ nm, allowing for a sensitive spectroscopic readout of the conformational changes. In the closed cage conformation, the OH-termini of the alleno-acetylenic arms form a cyclic four-fold hydrogen-bonding array, creating a highly confined cavity. The formation of the four-fold hydrogen-bonding array for the cage structure was identified to contribute to the exceptional chiroptical properties. We concluded from ECD studies on $(P)_4$-AAC **62** and its methylated analogue $(P)_4$-$(OMe)_4$-AAC **70** that both shape complementarity and structural preorganization of the solvent determine the host conformation and the chiroptical properties of AACs $(P)_4$- and $(M)_4$-**62** in solution. The combination of an interior capable of guest complexation together with the highly sensitive optical readout through ECD, along with the crystallographic readout, made AACs $(P)_4$- and $(M)_4$-**62** an ideal receptor system to study enantioselective complexation.

In the following chapter, we investigated the molecular recognition of achiral and chiral cyclic alkanes and alkyl halides by enantiopure alleno-acetylenic cage (AAC) receptors.

Solution-state binding studies were complemented by molecular structures obtained from single crystal X-ray diffraction of the host–guest complexes. The X-ray co-crystal structures revealed size adaptability of the receptor towards the guest, thereby optimizing the packing coefficient of the ensemble. At the optimal packing coefficient of ~55%, the enantiopure receptor showed complete selectivity towards (±)-*trans*-1,2-dimethylcyclohexane, where the $(P)_4$-configured host only bound the (*R*,*R*)-configured guest and the $(M)_4$-configured receptor selectively bound the (*S*,*S*)-configured guest (Figure 121, C).

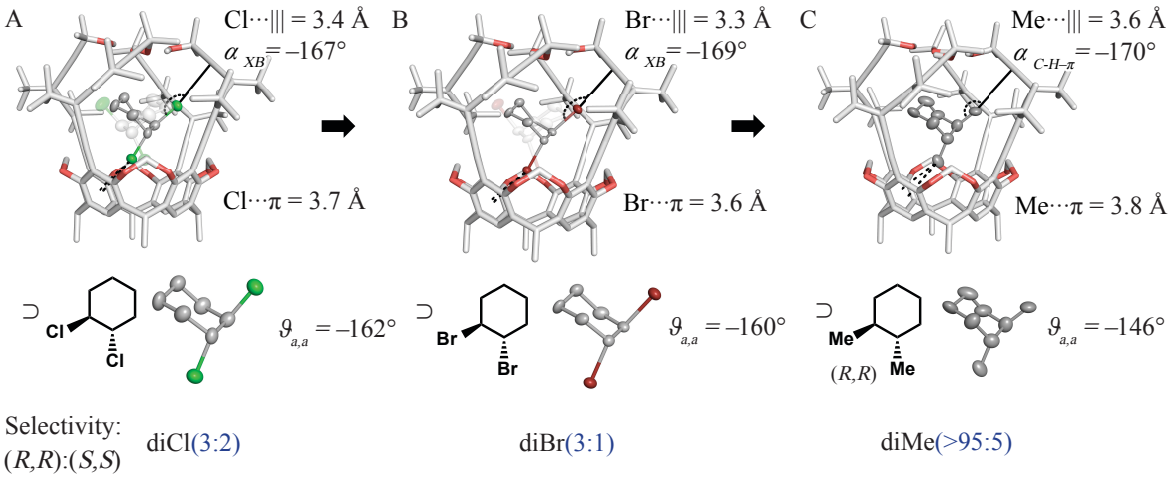

Figure 121. X-ray co-crystal structures of A: AAC $(P)_4$-**62** with *trans*-1,2-dichlorocyclohexane; B: with *trans*-1,2-dibromocyclohexane; C: with *trans*-1,2-dimethylcyclohexane. Enantioselectivities towards the guest molecules are given below. Guest molecules are complexed in their diaxial conformation, dihedral angles $\vartheta_{a,a}$ (R-C(1)-C(2)-R) are given; R = Cl, green; Br, brown; C , grey. Ellipsoids are set at 50% probability at 100 K. *n*-Hexyl chains of the receptor are omitted for clarity.

X-ray co-crystal structures of the host-bound guests further revealed exclusive complexation of the higher-energy diaxial conformation of (*R*,*R*)- and (*S*,*S*)-*trans*-1,2-dimethylcyclohexane (Figure 121C). This was the first time that the structure of (±)-*trans*-1,2-dimethylcyclohexane in its diaxial chair conformation has been structurally elucidated. Remarkably, the dihedral angle of the diaxial *trans*-1,2-dimethylcyclohexane deviated strongly from the commonly accepted value of 180° down to 146°, raising the question, if the discovered dihedral angle is the result of receptor induced deviation. Subsequent theoretical investigations demonstrated negligible influence of the host on the guest structures.

We validated the utility of the host to elucidate the elusive (di)axial conformations of cyclohexane derivatives by expanding the series of guest molecules to monohalo- and *trans*-1,2-dihalocyclohexanes. The developed crystallization protocol allowed us to obtain the molecular structures of the host–guest complexes through single-crystal X-ray diffraction. The

series of guests were exclusively bound in their axial or diaxial chair conformation. The dihedral angles $\vartheta_{a,a}$ (X-C(1)-C(2)-H/X) deviated substantially from 180°, with increasing deviation from the monohalocyclohexanes (up to 25°) to (±)-*trans*-1,2-dihalocyclohexanes (up to 33°). The decrease in the dihedral angle $\vartheta_{a,a}$ was accompanied by flattening of the ring dihedral angles ϱ (X-C(1)-C(2)-C(3)) from 53° (fluorocyclohexane) to 79° ((*R*,*R*)- and (*S*,*S*)-*trans*-1,2-bromofluorocyclohexane). Theoretical analysis of the isolated guest molecules showed close agreement of the complexed and the isolated guest structures, suggesting negligible influence of the host on the structure of the guest molecules. This further validated the utility of the AACs $(P)_4$- and $(M)_4$-**62** to capture single conformers of cyclohexane derivatives for their structural elucidation.

X-ray co-crystal structures of the host-guest complexes revealed a little studied halogen-bonding contact of the guest with the host: the C–X···||| contact. Theoretical studies on this C–X···||| interaction substantiated its halogen-bonding character. The C–X···||| contact appeared to majorly influence the enantioselectivity of the enantiopure receptor towards the chiral guests. The AACs $(P)_4$- and $(M)_4$-**62** showed increased enantioselectivity with increased halogen-bonding strength (Cl < Br). The overall enantioselectivity towards the (±)-*trans*-1,2-dihalocyclohexanes was lower compared to the (±)-*trans*-1,2-dimethylcyclohexane (complete enantioselectivity, Figure 121, C). This finding was counter-intuitive considering the stronger and more directional nature of halogen-bonding contacts compared to the non-directional purely dispersion interactions of *trans*-1,2-dimethylcyclohexanes with the host, and is in stark contrast to established concepts for enantioselective complexation of chiral guests with optically pure receptors, where more directional interactions were considered necessary to enhance selectivity (see Introduction). We explained this observation with the much higher polarizability and ease of distortion of their electron density of chlorine and bromine compared to the methyl substituents.

Solution complexation studies supported the exclusive complexation of the guests in their (di)axial chair conformation, where slow host–guest exchange allowed the full characterization of the host–guest complexes. Solution binding constants, along with the theoretical calculations on the conformational energies (*A*-values), allowed us to quantify the halogen-bonding contacts between the guests and the receptor. Comparison of the binding constants of the guests indicated a contribution of the C–Br···||| halogen-bonding contact of $\Delta\Delta G_{293\ K} = -0.9$ kcal mol^{-1}. This difference in conformational energy, together with the favorable halogen bonding interactions, resulted in a large increase in binding affinities of

$\Delta\Delta G_{293\ K}$ = –3.3 kcal mol^{-1} for (±)-*trans*-1,2-dimethylcyclohexane compared to (±)-*trans*-1,2-dibromocyclohexane. The enantiomeric ratios of the host–guest complexes, observed in the solid state, were confirmed in solution, where the formation of diastereoisomeric complexes resulted in the splitting of the OH-array proton resonances.

Inspired by a crystal structure of AAC $(P)_4$-**62** encapsulating one water molecule and two acetonitrile molecules, we expanded our series of guest molecules to cyclic and acyclic alcohols (Chapters 4 and 5). The alcohol series formed strong directional interactions between the alcohol groups of the guest and the hydrogen-bonding array of the host. Generally, the introduction of an alcohol group increased the binding affinities of the guest to the receptors in solution by ~3–4 kcal mol^{-1}, resulting in kinetically stable host–guest complexes on the NMR timescale. Solution studies, along with structural information obtained from X-ray co-crystal structures, enabled the conformational analysis of the host–bound guests. Noteworthy, was the substantial increase in binding affinity from cycloheptane to *endo*-tropine with a difference in binding affinities of $\Delta\Delta G_{293\ K}$ = –6.0 kcal mol^{-1}, translating to binding affinities of K_a = $7.0 \cdot 10^6$ M^{-1} (from ITC in *n*-octane at 293 K). The remarkably high binding affinities allowed detection of *endo*-tropine by AAC $(P)_4$-**62** in the part per billion regime. X-ray co-crystal structures and 2D-NMR spectroscopic solution studies indicated a preferential binding of *endo*-tropine to AAC $(P)_4$-**62** with the *N*-methyl group in the equatorial conformation.

The directional hydrogen-bonding interactions of the guest to the receptors generated various hydrogen-bonding motifs, which were strongly dependent on the specific alcohol guest encapsulated by the host. Remarkably, the host–guest-complex appeared to retain some directionality of the hydrogen-bonding array, despite the disruptive nature of the directional hydrogen-bonding interactions of the guest with the host (Figure 122).

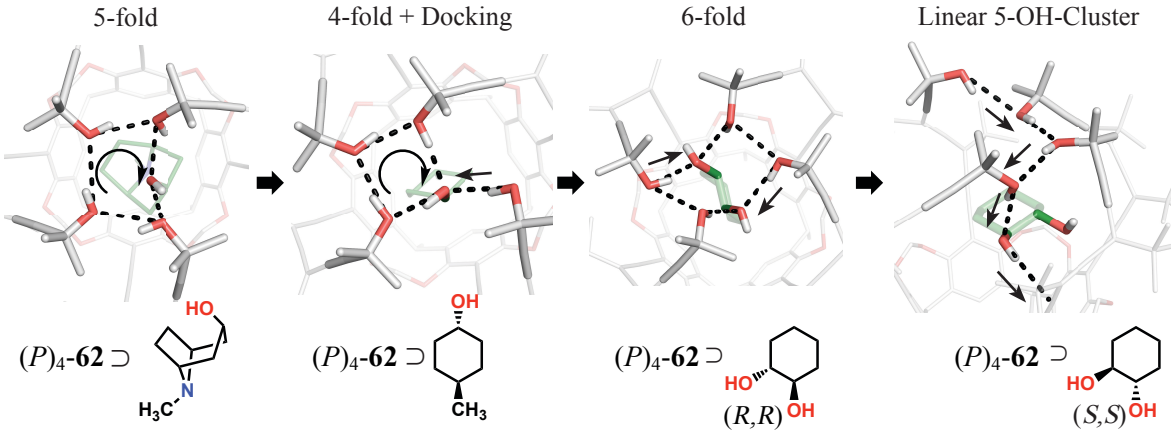

Figure 122. Top view on the hydrogen-bonding array of the X-ray co-crystal structures of $(P)_4$-AAC **62**⊃*endo*-tropine (A), ⊃*trans*-4-methylcyclohexanol, ⊃(*R*,*R*)-*trans*-1,2-cyclohexanediol (C) and ⊃(*S*,*S*)-*trans*-1,2-cyclohexanediol (D).

In a collaboration with Dr. Fischer and Prof. Carreira (ETHZ), supported by theoretical studies by T. Husch and Prof. Reiher (ETHZ), we expanded the cyclic alcohol series to acyclic alkyl and alkyl halide alcohols. In solution studies with AACs $(P)_4$- and $(M)_4$-**62**, we investigated the binding affinities of the chiral guests towards the host, along with the conformations of the host-bound structures. High binding affinities were observed for the alkyl haloalcohols, such as for (±)-*syn*-2,3-dibromo-2-methylbutanol ($\Delta G_{293\,K} = -7.9$ kcal mol^{-1}, $K_a = 7.4 \cdot 10^5$ M^{-1}). 1D- and 2D-NMR studies allowed the full characterization of the free and the host-bound complexes in *n*-octane-d_{18} at temperatures between 277–293 K. The formation of diastereoisomeric complexes of the enantiopure hosts with the chiral (racemic) guests resulted in splitting of the 1D NMR signals of the host and the guests. The diagnostic splitting of the signals allowed us to evaluate the enantioselectivity of the AACs $(P)_4$- and $(M)_4$-**62** in guests binding in solution. The highest enantioselectivities were observed for guests below optimal space occupancy (*syn*-2,3-dibromobutanol) and for guests which exceeded the optimal space occupancy, such as for *anti*-2,3-dibromo-2-trifluoromethylbutanol. NMR solution studies were complemented by X-ray co-crystal structures, where the relative distribution of the enantiomers of the guest in the host (with 100% occupation) matched the observed enantioselectivity in solution. In total, fifteen X-ray co-crystal structures of the achiral or racemic guests bound to the $(P)_4$- or $(M)_4$-configured receptor were obtained, with more in preparation. The X-ray co-crystal structure of AAC $(P)_4$-**62**⊃*syn*-2,3-dibromobutanol gave insight into the binding modes of the guests to the host, further substantiating the observed enantioselectivities (Figure 123).

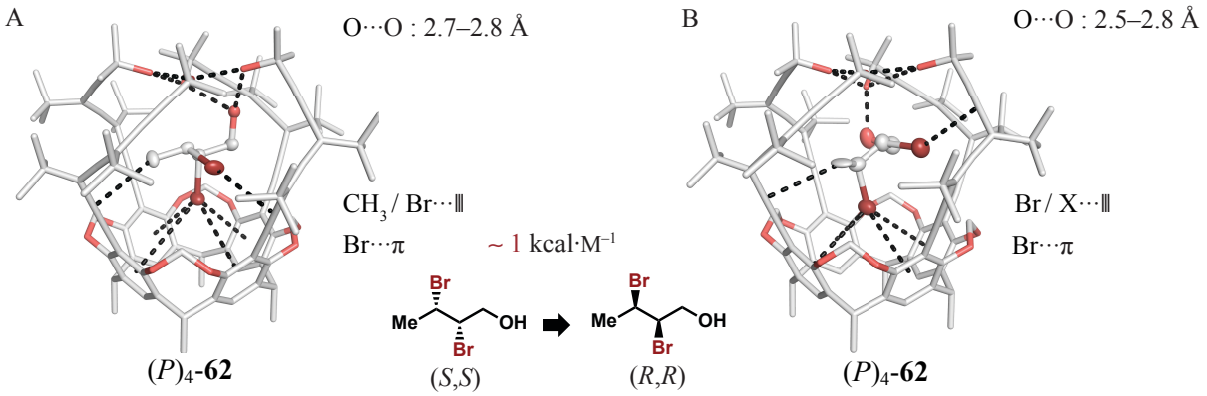

Figure 123. X-ray co-crystal structures of $(P)_4$-AAC **62**⊃*syn*-2,3-dibromobutanol ((*S*,*S*) : (*R*,*R*) = 68:32). A: $(P)_4$-AAC **62**⊃(*S*,*S*)-2,3-dibromobutanol; B: $(P)_4$-AAC **62**⊃(*R*,*R*)-2,3-dibromobutanol.

In Chapter 6, we described the efficient and modular synthesis of alleno-acetylenic cage receptors with increased surface polarity. Enantiopure $(P)_4$/$(M)_4$-configured AACs **71**–**73** were prepared which were soluble in polar and aqueous solvent systems (Figure 124).

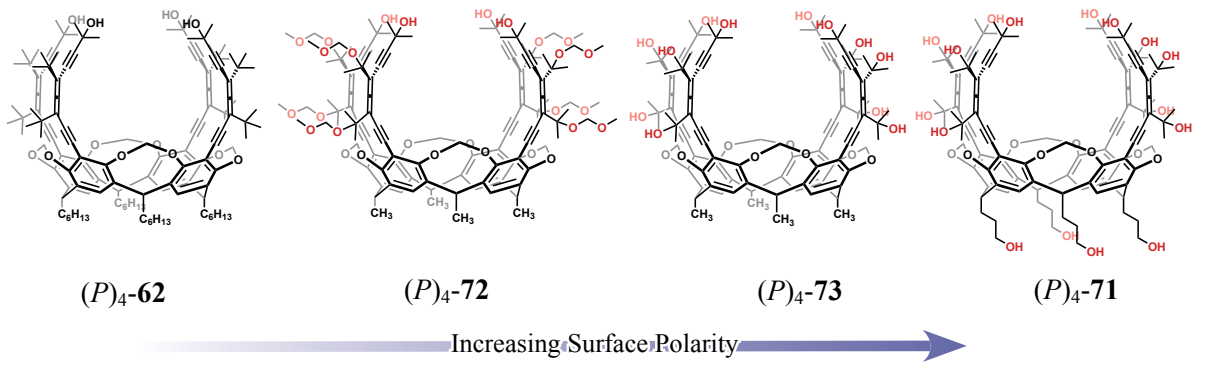

Figure 124. Summary of synthesized enantiopure AACs $(P)_4$- and $(M)_4$-**62** and **-71**–**73** with increasing surface polarity. Only $(P)_4$-configured receptors are shown.

The strong chiroptical properties of the receptors allowed us to assess guest binding through induced ECD intensities. AACs $(P)_4$- and $(M)_4$-**71** revealed guest-induced switching to a closed conformation in water/methanol (4:1) upon addition of apolar guests and guest molecules bearing alcohol or amine functionalities. An exemplary NMR spectroscopic binding study with iodocyclohexane and AAC $(P)_4$-**71** in D_2O/methanol-d_4 (3:2) substantiated guest binding in solution. The structural similarity of the interior of the AACs soluble in aqueous medium with the more apolar AAC receptors make them ideal to study the thermodynamic differences of enantioselective complexation in apolar and aqueous solvent systems.

En route to covalently locked AAC receptors (Chapter 7) we prepared enantiopure $(P)_4$- and $(M)_4$-configured AAC receptors **88** through intramolecular oxidative dimerization. The AACs $(P)_4$- and $(M)_4$-**88** showed strong absorption properties towards circulary polarized

light, but with much lower temperature dependency than their noncovalent counterparts. X-ray co-crystal structure of $(P)_4$- and $(M)_4$-configured AACs **88** gave insights into the volume of the cavity for molecular recognition studies. Molecular recognition studies on the covalently capped receptor systems are ongoing.

8.2 Outlook

Single crystal X-ray diffraction is a powerful method to unambiguously characterize the structure of molecules with atomic resolution. Despite the constantly evolving techniques to obtain structural information through X-ray diffraction, the dynamic nature of molecules often prevents the determination of high-resolution X-ray crystal structures. In this context, molecular receptors, which can form stable 1:1 host–guest complexes, can facilitate the structural elucidation of small molecules.[234,240] Alleno-acetylenic cage receptors $(P)_4$- and $(M)_4$-**62** have proven useful to elucidate elusive (di)axial conformations of cyclohexane derivatives. Reminiscent of early clathrate type inclusion complexation, structural elucidation through host–guest chemistry can complement other currently used host systems for structural elucidation of otherwise challenging small molecules. More recent methods include coordination[238] or soaking of small molecules into crystalline metal–organic frameworks (MOFs, Figure 125).[239]

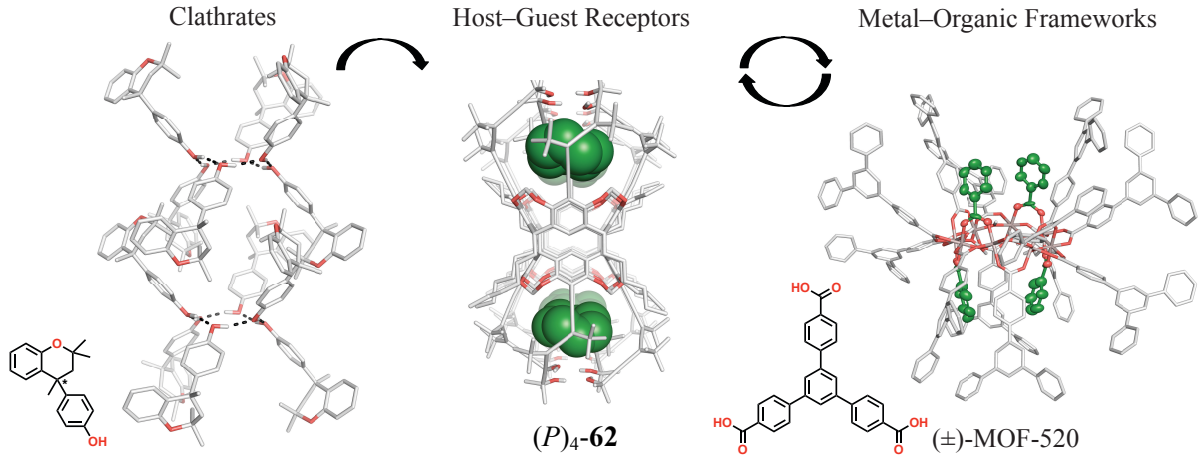

Figure 125. X-ray crystal structure elucidation through encapsulation or coordination: from clathrate-type inclusion complexation (left) to host–guest chemistry (middle) and metal–organic frameworks (right).

In a collaboration with the group of Prof. F. Glorius (University of Münster), we set out to obtain single crystal X-ray structures of a series of *cis*-fluorinated cycloalkanes through co-crystallization in AACs $(P)_4$- and $(M)_4$-**62** (Figure 126).[315]

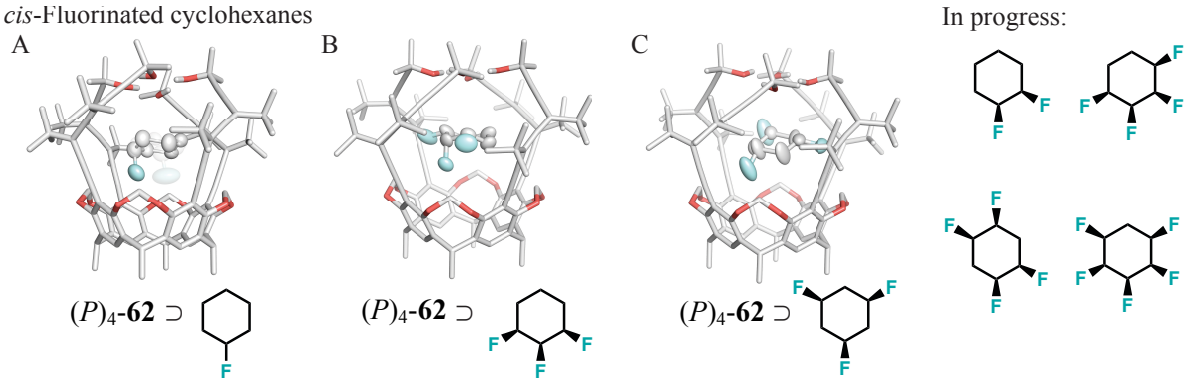

Figure 126. Structural elucidation of *cis*-fluorinated cyclohexanes through co-crystallization in AAC (*P*)$_4$-**62**.[315]

Figure 126 depicts the obtained co-crystal structures of fluorocyclohexane (axial), *cis*-1,2,3-trifluorocyclohexane (equatorial-axial-equatorial) and *cis*-1,3,5-trifluorocyclohexane (all equatorial) encapsulated by AAC (*P*)$_4$-**62**. Further crystallization experiments are in progress. This collaboration further illustrates the utility of AACs (*P*)$_4$-**62** to obtain single crystal X-ray structures of small molecules and we are working with the Small Molecule Crystallography Center (SMoCC, ETHZ) to continue such collaborations.

The enantiopure AACs displayed solvent- and guests-induced binary conformational switching between a closed cage conformation and an open state. The introduction of a binary conformational switching mechanism, enabling guest uptake and release, circumvented the trade-off of confinement versus porosity. The combination of a highly shape-persistent, confined chiral cavity together with the chiroptical readout for the inclusion complexation, make this system ideal to study chiral recognition. In an effort to make the switching mechanism largely solvent-independent, we sought to introduce pH-dependent hydrogen-bonding groups or redox-active functionalities.[1]

As pH-dependent hydrogen-bonding groups, we introduced carboxylic acid groups through lithiation of enantiopure AAC (*P*)$_4$-**89** and subsequent quenching with CO_2 to afford (*P*)$_4$-**90** (Figure 127).

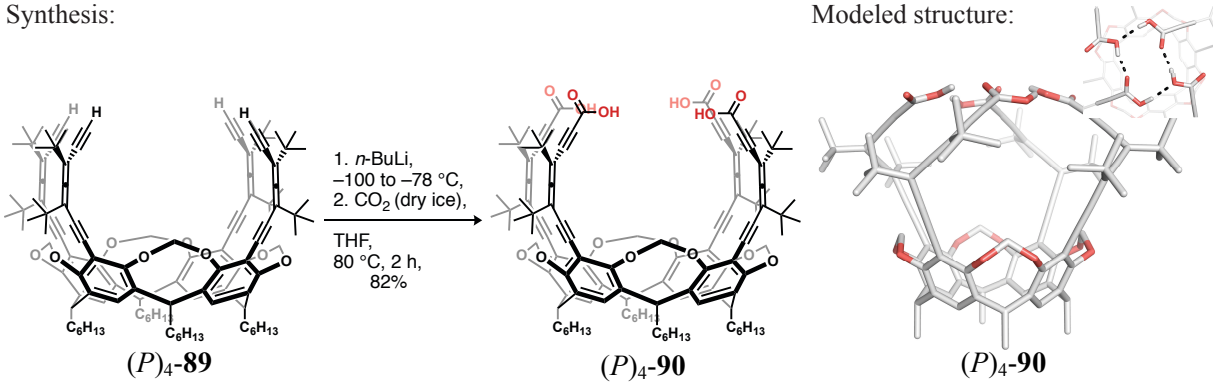

Figure 127. Synthesis of enantiopure tetracarboxyl AACs *(P)*$_4$-**90** from AAC *(P)*$_4$-**89**. Synthetic procedures are described in the Experimental Part. Only (*P*)-configured structures shown. Calculated structure for the AAC *(P)*$_4$-**90** (HF//PM6); H-bonding array shown in inset.

The detailed synthetic procedure is described in the Experimental Part. Preliminary modeling (HF//PM6) of the AACs bearing four carboxylic acid is displayed in Figure 127, displaying the carboxylic acid engaged in a hydrogen-bonding network to form a closed cage. Upon addition of base, we expected opening of the cage due to the repulsive nature of the carboxylate anions. While the synthesis of the pH-dependent AACs (*P*)$_4$-and (*M*)$_4$-**90** is established, conformational studies are ongoing. The carboxylate groups could also enable metal coordination, allowing us to explore complexation and asymmetric modification of host-bound guests.

Another cage receptor with a switchable closure was also targeted, wherein the alcohols would be replaced by thiols. Disulfide bonds are usually formed from the oxidation of thiols.[316] In replacing the tertiary alcohols of AACs (*P*)$_4$-and (*M*)$_4$-**62** with tertiary thiols, such as in AACs (*P*)$_4$-and (*M*)$_4$-**91**, one could imagine a reversible, redox-active switching mechanism involving the formation and cleavage of thiols to disulfides (Figure 128).

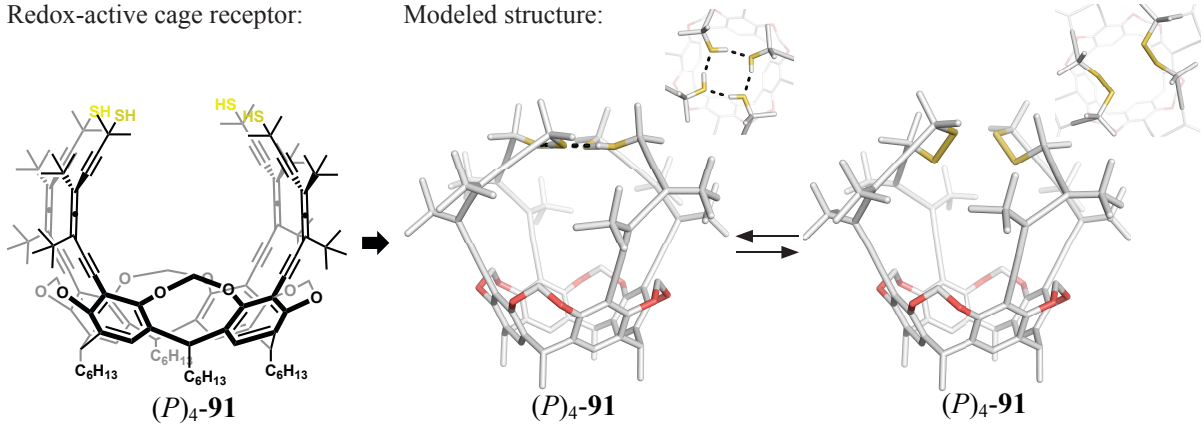

Figure 128. Proposed structure of AAC (*P*)$_4$-**91** with four tertiary thiols replacing the tertiary alcohols in AAC (*P*)$_4$-**62**. Calculated model of the AAC (*P*)$_4$-**91** (PM6); H-bonding array displayed above.

The synthesis could follow a similar route as described for the tetracarboxylate AACs $(P)_4$-and $(M)_4$-**90**, with quenching of the lithiated species with thioacetone to afford $(P)_4$- and $(M)_4$-configured AAC **91**. The covalent nature of the disulfide bonds would enable the complexation through guest-induced conformational switching, in analogy to AACs $(P)_4$-and $(M)_4$-**62**, with subsequent oxidation of the thiols to disulfides, encarcerating the complexed guest molecule. Under reductive conditions, the cage would open and release the guest. This switching mechanism, especially in combination with the water-soluble receptor system $(P)_4$- and $(M)_4$-**71** described in Chapter 6, could be a promising carrier for biological applications.[317]

Along the lines of expanding the application of AACs $(P)_4$-and $(M)_4$-**62** for the detection of minute quantities of guest molecules, we started a collaboration with Prof. Anslyn (University of Texas, Austin, Figure 129).

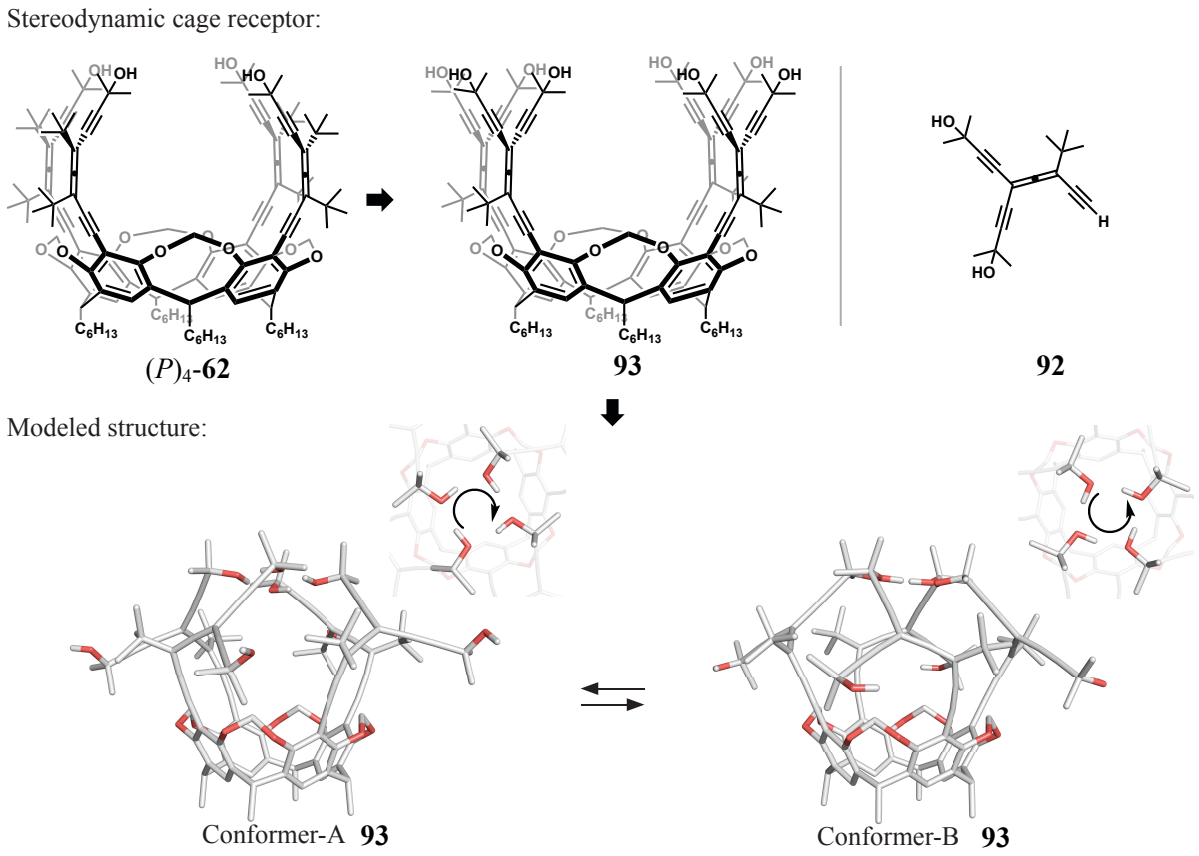

Figure 129. From enantiopure AAC $(P)_4$-**62** to stereodynamic AAC **93**. The synthesis of the AAC **93** is based on the development of the 1,1,3-triethynylallene **92**. The dynamic interconversion of the two enantiomeric conformers of AAC **93** is depicted below.

Prof. Anslyn developed an ECD-based spectroscopic method for the quantitative detection of chiral molecules bearing functional groups.[318] The detection of small molecules without polar functional groups, such as cyclic and acyclic alkanes and alkyl halides remains challenging. We therefore set out to design a racemic AAC receptor that would enable the

quantitative detection of enantiopure cyclic and acyclic alkanes and alkyl halides. Previously, we described enantiopure hosts that could differentiate between chiral (racemic) guests. The new approach inverts the concept, consisting of achiral host **93**, where only one enantiomer of the host complexes the enantiopure guest (Figure 129).

The complexation process is transduced in form of a quantifiable ECD signal. Figure 129 illustrates the proposed achiral AAC receptor **93**. The two conformers of the receptor are in enantiotopic relationship to each other, resulting in an overall achiral structure. The addition of a chiral guest with only a small excess of one enantiomer will shift the equilibrium of the interconverting conformers to one side, resulting in a solely induced ECD signal. The synthesis of this receptor system is underway and builds on the synthesis of the 1,1,3-triethynylallene **92**.[155,319,320]

In the evolution of the alleno-acetylenes – from its development as a synthetic building block to its incorporation into more complex supramolecular structures – the extraordinary chiroptical properties, stemming from the axial chiral allene core, have become a signature. This Thesis, with selected examples in the Outlook, highlights the diversity of potential applications open to alleno-acetylenic cage receptors in many different areas of molecular recognition. The choice of an adequate platform to which alleno-acetylenes are attached to or are incorporated into, will continue to play an important role. For our studies, we chose the resorcin[4]arene cavitands for the construction of a supramolecular receptors. Routes to efficiently access higher resorcin[n]arenes (n = 5, 6) would allow to study receptors with larger internal cavities, further broadening the scope of their applications. Alleno-acetylenic receptors are, however, not limited to resorcinarene scaffolds. Many more assemblies are imaginable, where the exceptional properties of alleno-acetylenes can contribute significantly. We hope that the unique properties of alleno-acetylenes continue to inspire their incorporation into a wide array of structures and applications.

9. Experimental Part

9 Experimental Part

9.1 Materials and Experimental Methods

Solvents and reagents: Reagents (ABCR, Acros, Sigma Aldrich, Fluka, TCI) were used without prior purification. Solvents of technical grade were used. Air and moisture sensitive reactions were carried out in anhydrous solvents, purified by a solvent drying system (LC Technology Solutions Inc. Sp-105) under nitrogen atmosphere (H_2O content < 10 ppm as determined by Karl-Fischer titration). Concentration under reduced pressure was performed by rotary evaporation at 40 °C. Purified compounds were further dried under high vacuum. All reactions under exclusion of air or water were performed in standard glassware and under nitrogen atmosphere unless stated otherwise.

Chromatography: For chromatographic purifications, technical-grade solvents were used. Flash column chromatography was performed on SiO_2 60 (particle size 0.040–0.063 mm, 230-400 mesh ASTM; Fluka) or neutral Al_2O_3 (particle size 0.050–0.200 mm, 70–290 mesh ASTM; Fluka) and was run on a maximum head pressure of 0.2 bar. Thin Layer Chromatography (TLC) was performed on glass-backed plates pre-coated with silica (*Merck Silica Gel 60 F254 TLC plates*), which were developed using standard visualizing agents: UV fluorescence (254 & 366 nm) and $KMnO_4$ oxidation (5 g $NaHCO_3$ and 1.5 g $KMnO_4$ in 400 mL H_2O).

High Pressure Liquid Chromatography **(HPLC)** was run on a Merck-Hitachi LaChrom D-Line system equipped with a D-7000 Interface pump, and a L-7400 UV-detector.

Medium Pressure Liquid Chromatography **(MPLC)** was carried out with SiO_2 or basic Al_2O_3 columns (particle size 0.040–0.063 mm, 230–400 mesh; Silica Flash F60) performed on a *CombiFlashRf* machine version 1.8.3 with a fraction collector version 00.00.85, detector version USB4000: 0.99.1, and a pump version: B5, B3.

Liquid Chromatography-Mass Spectrometry (LC-MS) was performed using an Ultimate 3000 series LC intrument combined with an MSQ Plus mass spectrometer from Dionex, using Zorbax Eclipse Plus C18 column (30 x 3 mm; 3.5 μm pore size) from Agilent.

^{1}H NMR spectra were recorded on a *Varian Mercury 300* (300 MHz, ^{1}H) or a *Gemini 400* (400 MHz, ^{1}H) instrument at 298 K. Chemical shifts (δ_H) are quoted in parts per million (ppm),

referenced to the residual solvent peak ($CDCl_3$, δ_H 7.226). Coupling constants (*J*) are reported to the nearest 0.5 Hz. Multiplicities are reported as follows: s = singlet, d = doublet, t = triplet, q = quartet, m = multiplet, or as a combination of them. Coupling constants *J* are given in Hertz (Hz).

^{13}C NMR spectra were recorded on a *Bruker DRX 400* (100 MHz, ^{13}C) instrument. Chemical shifts (δ_C) are quoted in ppm referenced to the appropriate solvent peak ($CDCl_3$, δ_C 77.0 ppm).

Infrared spectra (IR) were recorded on a *Perkin-Elmer 1600 FT-IR spectrometer (ATR, Golden State)*. Only selected absorbances (υ_{max}) are reported. The samples are reported as absorption maxima in cm^{-1} with corresponding relative intensities described as sh (shoulder), s (strong), m (medium), and w (weak).

Raman spectra *(FT-Raman)* were recorded on a *Bruker Vertex 70 FT-Raman* spectrometer (RAM II, RockSolid Interferometer). Only selected frequencies (υ) are reported. Scan settings were chosen for 4 cm^{-1} spectral resolution.

UV/Vis spectra were recorded on a *Varian Cary-500 Scan spectrophotometer*. The spectra were measured in a quartz cuvette (1 cm) at 293 K. The absorption wavelength is reported in nm with the molar extinction coefficient ε ($dm^3\ mol^{-1}\ cm^{-1}$).

Isothermal Titration Calorimetry (ITC) were performed on a MicroCal VP-ITC calorimeter. 25 portions of 10 µL "guest"-solution was added to a "host"-solution at intervals of 240 s. The power (*P*) that was consumed to keep the sample temperature at 303 K was monitored. The heat of dilution of "guest"-solution added to pure solvent was measured and subtracted. The Origin 7 software was used for data treatment.

Electronic Circular Dichroism **(ECD)** were recorded on on a *JASCO Corp. J-715, Rev. 1.00 instrument*. The spectra were measured in a quartz cuvette (1 cm) at 293 K. The absorption wavelength is reported in nm with the molar extinction coefficient $\Delta\varepsilon$ ($dm^3\ mol^{-1}\ cm^{-1}$).

Optical Rotation was recorded on a Perkin-Elmer 1600 FT-IR spectrometer 241 polarimeter.

High Resolution Mass spectra **(HR-MS)** measurements were performed by the MS service at the Laboratory of Organic Chemistry of ETH Zurich. EI‑MS: *Waters Micromass AutoSpe-Ultima spectrometer*; ESI-MS: *Bruker maXis spectrometer*. HR‑MALDI: *Varian IonSpec* FT‑ICR; Masses are reported in *m/z* units as the molecule ion M^+, $[M + H]^+$, $[M + Na]^+$, $[M + K]^+$, with the corresponding intensities in %.

X-ray Intensity Data were measured on a Rigaku XtaLAB Synergy diffractometer equipped with a Dectris Pilatus 300K hybrid pixel array detector, using microfocus sealed-tube Cu-*K*α radiation with mirror optics (λ = 1.54184 Å) at the given temperature. Samples were mounted on MiTeGen Micromount Kapton sample holders in perfluoroalkyl ether oil. Collected data were processed with the CrysAlisPro[321] software package and corrected for absorption effects using the multi-scan or Gaussian method, or a combination thereof. Structures were solved and refined using the OLEX2[322] and SHELX[323] software packages. Generally, wherever relative occupancies (in %) within disordered regions are discussed in the Thesis, they are directly taken from the refined free variables. The authors are aware that this method can be rather unreliable due to a variety of reasons, and hence for all purposes of discussion we assumed an error margin of ± 5%. It should be noted that relative occupancies were highly reproducible in multiple repeat experiments (from different crystallization attempts) and control experiments (AACs $(P)_4$ vs. $(M)_4$). Additionally, care was taken not to over-restrain disorder of the guest molecules. Only soft similar distance restraints (SADI) and enhanced rigid bond restraints (RIGU) were applied in this region, except in the variable temperature study where at higher temperatures harder restraints (DFIX, ISOR) were needed. Their usage was kept at the practicable minimum.

Supplementary data for the X-ray co-crystal structures can be obtained free of charge from The Cambridge Crystallographic Data Centre, 12 Union Road, Cambridge CB2 1EZ, UK (fax: +44(1223)-336-033; e-mail: deposit@ccdc.cam.ac.uk), or online via https://www.ccdc.cam.ac.uk/getstructures. HKL data and refinement instructions, as well as applied restraints, are included with the deposited files.

9.2 Synthetic Procedures

9.2.1 Synthesis of 1,3-Diethynylallenes (*P*)- and (*M*)-27

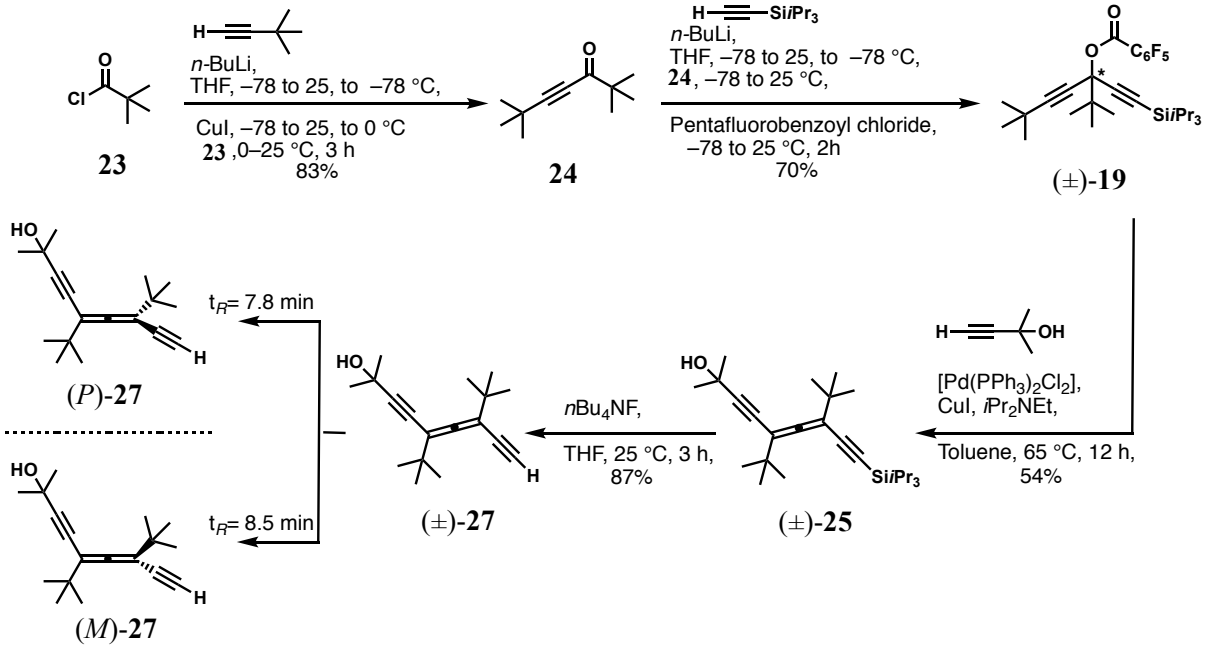

Scheme 19. Optimized synthetic route and resolution on a chiral phase preparative HPLC to enantiopure 1,3-diethynylallene (*P*)- and (*M*)-**27**. Spectroscopic properties of **23**–**27** were identical to those previously reported.[154,155,157,158,160]

(±)-5,7-Di-*tert*-butyl-2-methylnona-5,6-dien-3,8-diyn-2-ol ((±)-27)

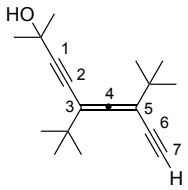

A solution of the triisopropylsilyl-protected alleno-acetylene (3 g, 7.23 mmol) in wet THF (96 mL) was treated with tetrabutylammonium fluoride (7.23 ml, 7.23 mmol). The mixture was stirred at 25 ºC for 1 h, washed with a sat. aq. solution of NaH_4Cl (4 x 20 mL), and the aqueous phase was extracted with EtOAc (3 x 20 mL). The combined organic layers were washed with brine, and dried over $MgSO_4$, and the solvent was evaporated *in vacuo*. Purification by MPLC (RediSep Column: SiO_2 80 g; 60 ml/min; cyclohexane/EtOAc 100:0 to 80:20, 16 min) gave (±)-**27** (1.83 g, 7.09 mmol, 98 % yield) as a pale yellow oil.

Enantiomers (*P*)-(+)-**27** and (*M*)-(–)-**27** were resolved by preparative HPLC using the CSP Chiralpak® IA (Diacel Chemical Industries Ltd.). Elution was performed with *n*-hexane/*i*PrOH 99.2:0.8 at a flow of 18 mL min^{-1}. Under these conditions, 0.8 mL of a solution of (±)-**27** in *n*-hexane (10 mg/mL) was injected.

(*P*)-(+)-**27**: t_R = 7.56 min, e.r. > 99:1; $[\alpha]_D^{20}$ = +112.5 (*c* = 1.2 in *n*-hexane)

(*M*)-(–)-**27**: t_R = 8.53 min, e.r. > 99:1; $[\alpha]_D^{20}$ = –98.9 (*c* = 1.2 in *n*-hexane)

R_f = 0.22 (SiO_2; hexane/EtOAc 9:1, UV);

^{1}H NMR (400 MHz, $CDCl_3$, 25 °C): δ = 2.99 (s, 1 H; C≡C–H0), 1.95 (s, 1 H; OH), 1.55 (s, 6 H; C*Me*$_2$OH), 1.14 (s, 9 H; Me_3), 1.12 ppm (s, 9 H, Me_3); ^{13}C NMR (101 MHz, 25 °C, $CDCl_3$): δ = 211.7 (C(4)), 103.2 (C(3)), 102.3 (C(5)), 97.5 (C(2)), 80.4 (C(6)), 77.5 (C(7)), 75.7 (C(1)), 65.9 (*C*(Me)$_2$OH), 35.6 (*C*–Me_3)), 35.3 (*C*–Me_3), 31.6 (C(*Me*)$_2$OH), 29.0 (Me_3), 28.9 ppm (Me_3); IR (ATR): $\tilde{\nu}$ = 3314 (sh, m), 2964 (s), 2927 (m), 2903 (m), 2868 (m), 2090 (w), 1929 (w), 1475 (m), 1459 (m), 1392 (m), 1362 (s), 1244 (m), 1224 (m), 1201 (m), 1163 (s), 1140 (m), 1069 (m), 1024 (w), 954 (s), 895 (m), 848 (m), 817 (w), 758 (m), 695 (m), 642 cm^{-1} (s); HR-MS-EI: *m*/*z* : 258.1974 [*M*]$^+$, calcd for $C_{18}H_{27}O^+$: 258.1979).

9.2.2 Synthesis of Cavitand Scaffold

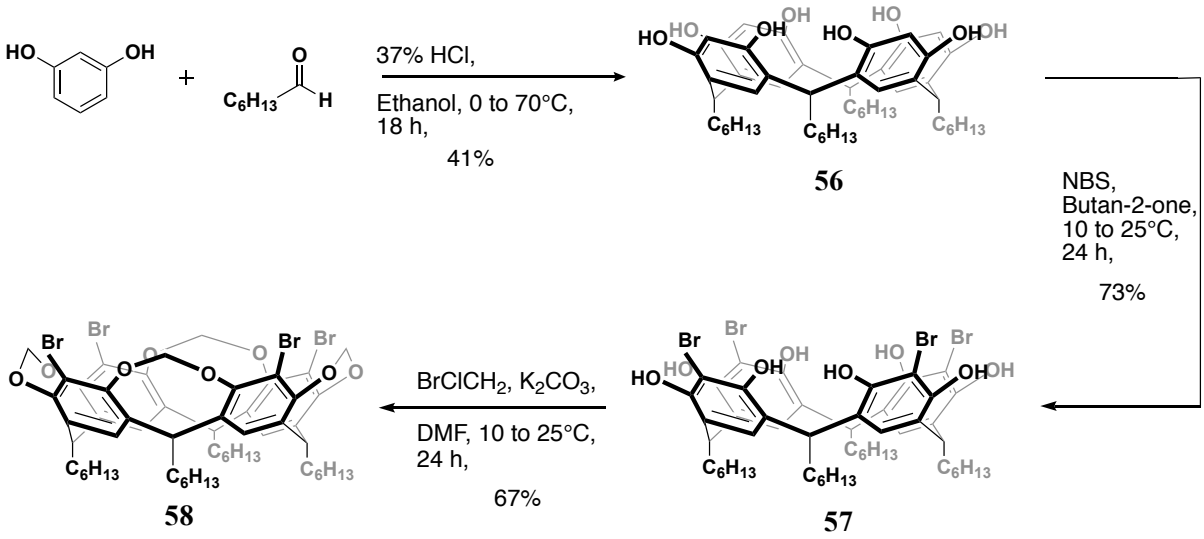

Scheme 20. Synthesis of resorcin[4]arene cavitand **58** from resorcinol and heptanal.[215-217]

7,11,15,28-Tetrabromo-1,21,23,25-tetrahexyl-2,20:3,19-dimethano-1*H*,21*H*,23*H*,25*H*-bis[1,3]dioxocino[5,4-*i*:5',4'-*i*]benzo[1,2-*d*:5,4-*d*']bis[1,3]benzodioxocin (58)

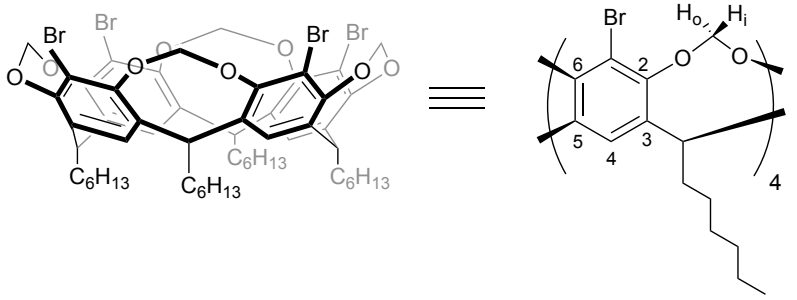

The procedure was adapted from the literature.[217] DMF (88 ml) was added to the reaction flask and degassed for 30 min by bubbling argon through it. Tetrabromo octol **57** (6 g, 5.26

mmol) was added, followed by K_2CO_3 (11.63 g, 84 mmol). The mixture was stirred until a homogeneous solution was obtained. Bromochloromethane (1.5 mL) was added under vigourous stirring to the solution. The mixture was heated to 40 °C, stirred for 24 h, treated with bromochloromethane (1.5 mL), stirred at 65 °C for 24 h bromochloromethane (1.5 mL), treated with bromochloromethane (1.5 mL), and stirred at 65 °C and 24 h at 25 °C. The solid was filtered off by a filter funnel, washed with DMF (2 x 10 mL), distilled water (3 x 40 mL), and methanol (2 x 10 mL). The residue was dried under high vacuum at 100 °C for 5 h. Flash column chromatography (cyclohexane/CH_2Cl_2 6:4 to 2:8) gave as a crystalline white solid. Traces of water were removed by azeotropic destillation from dry benzene (4 mL) and dry THF (4 mL). Drying under high vacuum at 110 °C for 24 h gave tetrabromo tetrahexyl cavitand **58** (4.2 g, 67%) as white crystalline solid.

R_f = 0.42 (SiO_2; cyclohexane/CH_2Cl_2 1:1, UV); m.p. 158 °C (Lit.[216]: 200–205 °C); ^{1}H NMR (400 MHz, $CDCl_3$, 25 °C; assignments based on HSQC spectra): δ = 7.03 (s, 4 H; 4 H–C(4)), 5.96 (d, J = 7.3 Hz, 4 H; 4 H_{out} of OCH_2O), 4.85 (t, J = 8.1 Hz, 4 H; 4 $H_{methine}$C–C(3)), 4.39 (d, J = 7.3 Hz, 4 H; 4 H_{in} of OCH_2O), 2.17–2.23 (m, 8 H; 4 CH_2(CH$_2$)$_4$Me), 1.25–1.47 (m, 32 H; 4 CH$_2$(CH_2)$_4$Me), 0.90 ppm (t, J= 6.7 Hz, 12 H; 4 Me); ^{13}C NMR (101 MHz, $CDCl_3$, 25 °C, assignments based on HMBC NMR spectra): δ = 152.2 (4 C(2,6)), 139.4 (4 C(3,5)), 119.2 (4 C(4)), 113.7 (4 C(1)), 98.6 (4 OCH_2O), 37.8 (4 *C*H–C(3,5)), 32.0, 30.0, 29.5, 27.9 (C(1,2,3,4) of 4 hexyl), 22.8 (C(5) of 4 hexyl), 14.2 (C(6) of 4 hexyl); IR (ATR): $\tilde{\nu}_{max}$ = 2925 (m, br), 2855 (m), 1466 (s), 1449 (s), 1415 (m), 1299 (m), 1227 (m), 1142 (w), 1019 (m), 958 (s), 790 (m), 664 (w), 620 cm^{-1} (w); HR-MALDI-MS: m/z (%): 1184.1622 (18, $[M]^+$, calcd. for $C_{56}H_{68}{}^{79}Br_4O_8{}^+$: 1184.1642), 1185.1508 (25), 1185.1740 (12), 1186.1598 (70), 1187.1464 (36), 1187.1695 (47) 1188.1568 (100), 1188.1798 (19), 1189.1426 (27), 1189.1654 (73), 1190.1538 (64), 1190.1749 (24), 1191.1616 (51), 1192.1512 (16); anal. calc. for $C_{56}H_{68}Br_4O_8$ (1188.76): C 56.58, H 5.77, O 10.77, Br 26.89; found: C 56.82, H 5.81, O 10.84.

7,11,15,28-Tetrazido-1,21,23,25-tetrahexyl-2,20:3,19-dimethano-1*H*,21*H*,23*H*,25*H*-bis[1,3]dioxocino[5,4-*i*:5',4'-*i*]benzo[1,2-*d*:5,4-*d*']bis[1,3]benzodioxocin (60)

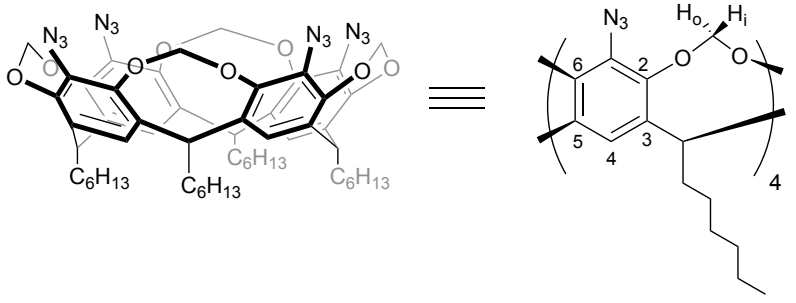

A solution of tetrabromo tetrahexyl cavitand **58** (500 mg, 0.42 mmol) in dry THF (7 mL) under an argon atmosphere was cooled to –100 °C (methanol/N_2(*l*)) and treated dropwise with 1.6 M *n*-BuLi (2.63 mL, 4.21 mmol) while maintaining –100 °C. The solution was warmed to –78 °C over 30 min, treated with a solution tosylazide (1.0 g, 5.05 mmol) in dry THF (4 mL), warmed to 25 °C over 20 h, and diluted with H_2O (20 mL). The aqueous phase was extracted with EtOAc (3 x 20 mL). The combined organic layers were washed with brine, dried over Na_2SO_4, and concentrated *in vacuo*. Flash column chromatography (SiO_2; cyclohexane/CH_2Cl_2 100:0 to 4:6) afforded the **60** (252 mg, 58%) as a white solid.

The stability of the product was immediately tested by differential scanning calorimetry (DSC) and thermogravimetric analysis (TGA). Decomposition took place at 184 °C (–10 % of the molecular weight and at 415 °C (–45 % of the molecular weight).

R_f = 0.30 (SiO_2; cyclohexane/CH_2Cl_2 4:6, UV); m.p. 163 °C; ^{1}H NMR (400 MHz, $CDCl_3$, 25 °C; assignments based on HSQC NMR spectra): δ = 6.85 (s, 4 H; 4 H–C(4)), 5.83 (d, J = 7.0 Hz, 4 H; 4 H_{out} of OCH_2O), 4.74 (t, J = 8.1 Hz, 4 H; 4 $H_{methine}$C–C(3,5)), 4.40 (d, J = 7.1 Hz, 4 H; 4 H_{in} of OCH_2O), 2.13–2.19 (m, 8 H; 4 CH_2(CH$_2$)$_4$Me), 1.26–1.44 (m, 32 H; 4 CH$_2$(CH_2)$_4$Me, 0.90 ppm (t, J = 6.8 Hz, 12 H; 4 Me); ^{13}C NMR (101 MHz, $CDCl_3$, 25 °C; assignments based on COSY, HSQC, and HMBC NMR spectra): δ = 147.4 (4 C(2,6)), 139.1 (4 C(3)), 125.9 (4 C(4)), 115.8 (4 OCH_2O), 100.3 (4 C(1)), 37.0 (4 *C*H–C(3)), 32.0, 29.9, 29.5, 27.9 (*C*(1,2,3,4) of 4 hexyl), 22.8 (C(5) of 4 hexyl), 14.2 ppm (4 Me); IR (ATR): $\tilde{\nu}_{max}$ = 2963 (m), 2935 (m), 2860 (m), 2102 (s), 1600 (w), 1578 (m), 1462 (s), 1435 (s), 1337 (m), 1296 (m), 1225 (m), 1191 (w), 1146 (w), 1093 (m), 1021 (m), 956 (s), 870 (w), 819 (w), 809 (w), 791 (w), 719 (w), 676 (w), 668 cm^{-1} (w); HR-MALDI-MS: *m*/*z* (%): 1059.5177 (100, [M + Na]$^+$, calcd. for $C_{56}H_{68}N_{12}NaO_8^+$: 1059.5175), 1060.5213 (66), 1061.5236 (23).

7,11,15,28-Tetraiodo-1,21,23,25-tetrahexyl-2,20:3,19-dimetheno-1*H*,21*H*,23*H*,25*H*-bis[1,3]dioxocino[5,4-*i*:5',4'-*i*]benzo[1,2-*d*:5,4-*d*']bis[1,3]benzodioxocin (59)[216]

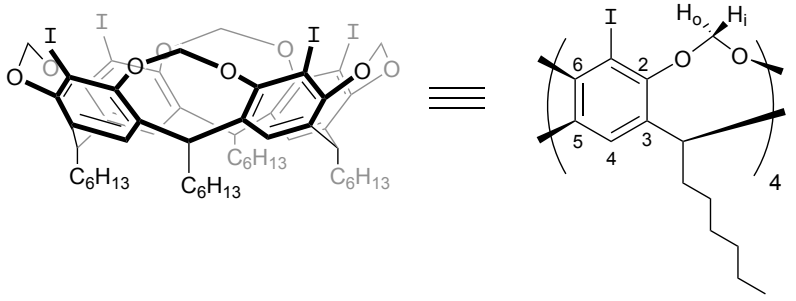

The procedure was adapted from the literature.[218] A solution of tetrabromo tetrahexyl cavitand **58** (500 mg, 0.42 mmol) was dissolved in THF (14 mL) under argon, cooled to –100 °C

(methanol/N_2(*l*)) and treated dropwise with 1.6 M *n*-BuLi (2.63 mL, 4.21 mmol) while maintaining –100 °C. The solution was warmed to –70 °C over 30 min, treated with iodine (1.28 g, 5.05 mmol), and the solution slowly warmed to 25 °C over 20 h. A sat. aq. $Na_2S_2O_3$ solution was added and vigorously stirred for 10 min. The aqueous layer was extracted with CH_2Cl_2 (3 x 15 mL). The combined organic phases were washed with 20% aqueous $NaHSO_3$ (20 mL), brine, dried over Na_2SO_4, and the solvent was evaporated. Flash column chromatography (SiO_2; cyclohexane/CH_2Cl_2 8:2 to 4:6) afforded **59** (465 mg, 80%) as a white solid.

R_f = 0.38 (SiO_2; cyclohexane/ CH_2Cl_2 1:1, UV); m.p. 182 °C (no m.p. previously reported); ^{1}H NMR (400 MHz, $CDCl_3$, 25 °C; assignments based on HSQC NMR spectra): δ = 7.06 (s, 4 H; 4 H–C(4)), 5.97 (d, J = 7.4 Hz, 4 H; 4 H_{out} of OCH_2O), 4.85 (t, J = 8.1 Hz, 4 H; $H_{methine}C$–C(3,5)), 4.32 (d, J = 7.4 Hz, 4 H; 4 H_{in} of OCH_2O), 2.17–2.22 (m, 8 H; 4 CH_2(CH_2)$_4$Me), 1.25–1.47 (m, 32 H; 4 CH_2(CH_2)$_4$Me, 0.90 ppm (t, J= 6.7 Hz, 12 H; 4 Me); ^{13}C NMR (101 MHz, $CDCl_3$, 25 °C; assignments based on COSY, HSQC, and HMBC NMR spectra): δ = 155.0 (4 C(2,6)), 138.9 (4 C(3,5)), 120.8 (4 C(4)), 98.6 (4 OCH_2O), 93.2 (4 C(1)), 38.1 (4 *C*H–C(3)), 32.0, 30.3, 29.5, 27.9 (C(1,2,3,4) of 4 hexyl), 22.8 (C(5) of 4 hexyl), 14.2 ppm (4 Me); IR (ATR): $\tilde{\nu}_{max}$ = 2924 (m, br.), 2854 (m), 1466 (s), 1443 (s), 1411 (m), 1297 (m), 1225 (m), 1172 (w), 1149 (w), 1085 (m), 1017 (m), 955 (s), 777 (w), 754 (w), 731 (w), 659 (w), 641 cm^{-1} (w); HR-MALDI-MS: *m*/*z* (%): 1399.0978 (100, $[M + Na]^+$, calcd. for $C_{56}H_{68}I_4NaO_8^+$: 1399.0985), 1400.1013 (62).

AACs (P)$_4$-and (M)$_4$-61

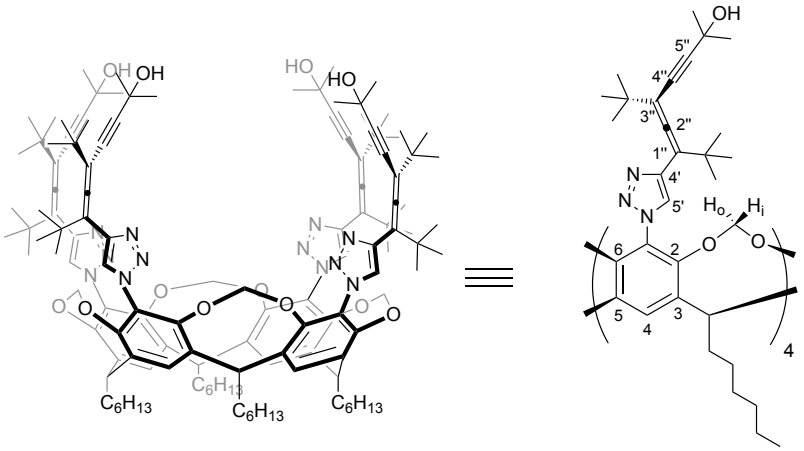

A 50 mL two-necked flask was loaded with tetraazido tetrahexyl cavitand **60** (50 mg, 48 µmol) and (*P*)-**27** (125 mg, 0.48 mmol). A mixture of dry CH_2Cl_2 (3.5 mL) and dry methanol (0.9 mL) was added, and the solution was degassed for 20 min with argon. Diisopropylethylamine

(3.5 µL, 0.19 mmol), copper powder (1.5 mg, 24 µmol), and $[Cu(CH_3CN)_4]\cdot PF_6$ (9.0 mg, 24 µmol) were added, and the mixture was stirred for 20 h at 25 °C. Additional copper (1.5 mg, 24 µmol) and $[Cu(CH_3CN)_4]\cdot PF_6$ (9.0 mg, 24 µmol) were added. The mixture was stirred for 20 h, diluted with EtOAc (10 mL), and filtered over Celite. Evaporation of the filtrate and flash column chromatography (SiO_2; cyclohexane/EtOAc 9:1 to 7:3) afforded the $(P)_4$-AAC-**61** (80%, 90 mg) as a white solid and recovered (*P*)-**27** (62 %, 78 mg).

The same synthetic procedure was applied for $(M)_4$-configured enantiomer.

(*P*)-**61**: $[\alpha]_D^{22} = +194.8$ (*c* = 0.22 in acetonitrile)

(*M*)-**61**: $[\alpha]_D^{20} = -184.7$ (*c* = 0.22 in acetonitrile)

R_f = 0.33 (SiO_2; cyclohexane/EtOAc 7:3, UV); m.p. 146 °C; ^{1}H NMR (400 MHz, $CDCl_3$, 25 °C; assignments based on DQF COSY and HSQC NMR spectra): δ = 7.52 (s, 4 H; 4 H–C(5')), 7.34 (s, 4 H; 4 H–C(4)), 5.33 (d, *J* = 7.8 Hz, 4 H; 4 H_{out} of OCH_2O), 4.90 (t, *J* = 8.1 Hz, 4 H; 4 $H_{methine}$C–C(3)), 4.64 (d, *J* = 7.8 Hz, 4 H; 4 H_{in} of OCH_2O), 2.27–2.38 (m, 8 H; 4 C*H*$_2$(CH$_2$)$_4$Me), 2.08 (br s, 4 H, 4 OH), 1.53 (s, 24 H, C*Me*$_2$OH), 1.33–1.51 (m, 32 H; 4 CH$_2$(C*H*$_2$)$_4$Me, 1.31 (s, 36 H, 4 C*Me*$_3$), 1.12 (s, 36 H, 4 C*Me*$_3$), 0.92 ppm (t, *J* = 6.8 Hz, 12 H; 4 Me); ^{13}C NMR (101 MHz, $CDCl_3$, 25 °C, assignments based on COSY, HSQC, and HMBC NMR spectra): δ = 206.5 (4 C(2'')), 149.7 and 149.4 (4 C(2,6)), 143.1 (4 C(4'), 139.1 and 139.0 (4 C(3,5)), 125.3 (4 C(1)), 124.8 (4 C(5'), 121.0 (4 C(4)), 109.2 (4 C(1'')), 102.4 (3'' C(5')), 100.9 (4 OCH_2O), 96.8 (4 C(5'')), 76.5 (4 C(4'')), 65.8 (4 *C*Me$_2$OH), 37.2 (4 *C*H–C(3)), 35.6 (4 *C*Me$_3$), 35.1 (4 *C*Me$_3$), 32.0 (4 C(1) of 4 hexyl), 31.7 and 31.6 (4 C*Me*$_2$OH), 30.1 and 29.6 (C(2,3) of 4 hexyl), 29.9 and 29.3 (8 C*Me*$_3$), 28.0 (C(4) of 4 hexyl), 22.8 (C(5) of 4 hexyl), 14.2 ppm (4 Me); IR (ATR): $\tilde{\nu}_{max}$ = 3391 (w, br.), 2961 (m), 2930 (m), 2864 (m), 2123 (w), 1475 (m), 1456 (m), 1409 (w), 1390 (w), 1361 (m), 1306 (w), 1226 (m), 1151 (m), 1086 (m), 1028 (w), 1014 (m), 951 (s), 891 (m), 835 (w), 810 (w), 755 (m), 741 (m), 723 (m), 674 (m), 659 (w), 632 (w) cm^{-1} (w); HR-MALDI-MS: *m*/*z* (%): 2092.3110 (68, $[M]^+$, calcd. for $C_{128}H_{172}N_{12}NaO_{12}^+$: 2092.3110), 2093.3128 (100), 2094.3162 (74).

AACs $(P)_4$-and $(M)_4$- AAC-62

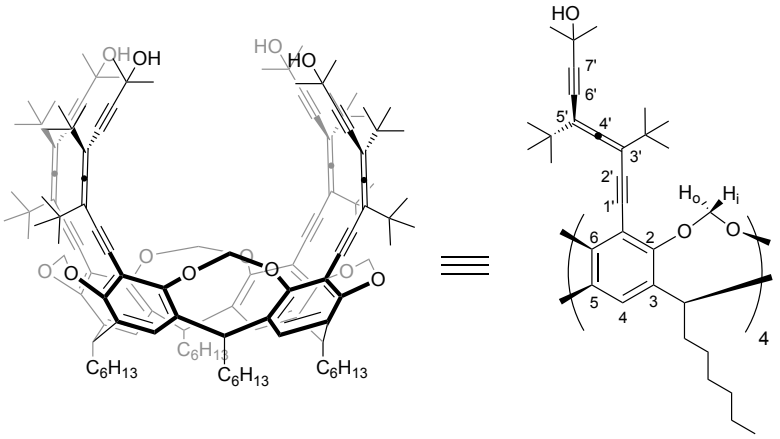

A 10 mL Schlenk tube was loaded with tetraiodo tetrahexyl cavitand **59** (100 mg, 73 µmol) and $[Pd(Ph_3P)_4]$ (8.39 mg, 7.26 µmol) and flushed with N_2. Triethylamine (1.5 mL) was added, and the solution was subjected to a freeze/pump/N_2 cycle. CuI (2 mg, 10 µmol) was added, and the solution was again subjected to freeze/pump/N_2 cycles (2x). A second 10 mL Schlenk tube was charged with (*P*)-(+)-**27** (94 mg, 0.36 mmol) and flushed with N_2. Triethylamine (0.6 mL) was added. The solution was subjected to a freeze/pump/N_2 cycle, before adding it dropwise into the first Schlenk tube. The resulting mixture was heated to 100 °C under N_2 for 8 h and then washed with a sat. aq. NH_4Cl solution. The aqueous phase was extracted with EtOAc (3 x 20 mL). The combined organic phases were washed with brine, dried over Na_2SO_4, and concentrated *in vacuo*. Flash column chromatography (SiO_2; cyclohexane/EtOAc 9:1 to 7:3) afforded the $(P)_4$-**62** (91 mg, 91%,) as a white solid.

The same synthetic procedure was applied for the $(M)_4$-configured enantiomer.

(*P*)-**62**: $[\alpha]_D^{20}$ = –621.5 (*c* = 0.26 in *n*-hexane) and +518.7(*c* = 0.26 in acetonitrile)

(*M*)-**62**: $[\alpha]_D^{20}$ = +648.9 (*c* = 0.27 in *n*-hexane) and –517.6 (*c* = 0.26 in acetonitrile)

R_f = 0.28 (SiO_2; cyclohexane/EtOAc 8:2, UV); m.p. 150 °C; ^{1}H NMR (400 MHz, $CDCl_3$, 25 °C; assignments based on DQF COSY and HSQC NMR spectra): δ = 7.02 (s, 4 H; 4 H–C(4)), 5.87 (d, *J* = 7.2 Hz, 4 H; 4 H_{out} of OCH_2O), 4.80 (t, *J* = 8.1 Hz, 4 H; 4 $H_{methine}C$–C(3)), 4.50 (d, *J* = 7.2 Hz, 4 H; 4 H_{in} of OCH_2O), 2.34 (br. s, 4 H, 4 OH), 2.15–2.21 (m, 8 H; 4 $CH_2(CH_2)_4Me$), 1.55 (s, 24 H, 4 CMe_2OH), 1.25–1.44 (m, 32 H; 4 $CH_2(CH_2)_4Me$), 1.14 (s, 36 H, 4 CMe_3), 1.12 (s, 36 H, 4 CMe_3), 0.90 ppm (t, *J* = 6.7 Hz, 12 H; 4 Me); ^{13}C NMR (101 MHz, $CDCl_3$, 25 °C; assignments based on COSY, HSQC, and HMBC NMR spectra): δ = 211.7 (4 C(4')), 155.3 and 155.2 (4 C(2,6)),138.5 and 138.4 (4 C(3,5)), 120.0 (4 C(4)), 113.6 (4 C(1)), 103.4 (4 C(3')), 103.0 (4 C(5')), 98.6 (4 OCH_2O), 97.4 (4 C(7')), 91.7 (4 C(1')), 84.3

(4 C(2'), 75.6 (4 C(6')), 65.8 (4 *C*Me$_2$OH), 36.7 (4 *C*H–C(3)), 35.7 (4 *C*Me$_3$), 35.6 (4 *C*Me$_3$), 32.0 (C(1) of 4 hexyl), 31.7 and 31.6 (4 C*Me*$_2$OH), 29.7 and 29.5 (C(2,3) of 4 hexyl), 29.2 and 29.1 (8 C*Me*$_3$, 27.9 (C(4) of 4 hexyl), 22.8 (C(5) of 4 hexyl), 14.2 (4 Me of hexyl); IR (ATR): $\tilde{\nu}_{max}$ = 3365 (w, br.), 2962 (m), 2928 (m), 2864 (m), 2210 (w), 1978 (w), 1929 (w), 1466 (m), 1447 (m), 1393 (w), 1361 (m), 1225 (m), 1156 (m), 1087 (m), 1020 (m), 968 (s), 904 (m), 805 (w), 731 (m), 702 (w), 675 (w), 635 cm^{-1} (w); HR-MALDI-MS: *m*/*z* (%): 1897.2534 (71, $[M]^+$, calcd. for $C_{128}H_{168}O_{12}^+$: 1897.2530), 1898.2569 (100), 1899.2608 (72), 1900.2644 (35).

(*P*)- and (*M*)-5,7-di-*tert*-butyl-9-(2,6-dimethoxyphenyl)-2-methylnona-5,6-dien-3,8-diyn-2-ol (64)

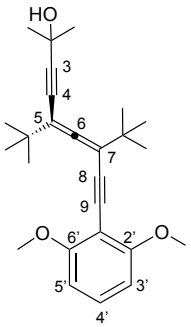

A 10 mL Schlenk tube was loaded with 2-iodo-1,3-dimethoxybenzene (30 mg, 114 µmol) and [Pd(Ph$_3$P)]$_4$ (13 mg, 11 µmol) and flushed with N_2. Triethylamine (1.5 mL) was added, and the solution was subjected to a freeze/pump/N_2 cycle. CuI (2 mg, 11 µmol) was added and the solution was again subjected to freeze/pump/N_2 cycles (2 x). A second 10 mL Schlenk was charged with alleno-acetylene (*P*)-(+)-**27** (32 mg, 12.5 µmol) and flushed with N_2. Triethylamine (0.6 mL) was added, and the solution was subjected to a freeze/pump/N_2 cycle before adding it dropwise to the first Schlenk tube. The resulting mixture was heated to 100 °C under argon for 6 h and diluted with a sat. aq. NH_4Cl solution. The aqueous phase was extracted with EtOAc (3 x 20 mL). The combined organic layers were washed with brine, dried over Na_2SO_4, and concentrated *in vacuo*. Flash column chromatography (SiO_2; cyclohexane/EtOAc 9:1 to 7:3; then CH_2Cl_2) afforded *P*-(+)-**64** (30 mg, 67%) as a white solid. The same procedure was applied for the *M*-configured enantiomer.

(*P*)-(+)-**64**: $[\alpha]_D^{20}$ = +292.5 (*c* = 0.29 in *n*-hexane).

(*M*)-(–)-**64**: $[\alpha]_D^{20}$ = –269.6 (*c* = 0.27 in *n*-hexane).

R_f = 0.40 (SiO_2; cyclohexane/ EtOAc 7:3, UV); R_f = 0.40 (SiO_2; CH_2Cl_2, UV); m.p. 47 °C; ^{1}H NMR (400 MHz, $CDCl_3$, 25 °C, assignments based on DQF COSY and HSQC NMR spectra): δ = 7.18 (t, *J* = 8.4 Hz, 1 H; H–C(4')), 6.51 (d, *J* = 8.4 Hz, 2 H; H–C(3',5')), 3.86 (s, 6 H; 2

OMe), 1.96 (br. s, 1 H; OH), 1.55 (s, 6 H; C*Me*$_2$OH), 1.23 (s, 9 H; CMe$_3$), 1.15 (s, 9 H; CMe$_3$) ppm. ^{13}C NMR (101 MHz, $CDCl_3$; 25 °C,assignments based on COSY, HSQC, and HMBC NMR spectra): δ = 211.1 (C(6)), 161.41 (C(2',6')), 129.5 (C(4')), 104.3 (C(7), 103.7 (C(3',5')), 102.5 (C(1') and C(5)), 96.9 (C(3)), 92.0 C(9), 85.4 (C(8), 76.5 (C(4)), 65.9 (*C*Me$_2$OH), 56.2 (2 OMe), 36.1 (*C*Me$_3$), 35.7 (*C*Me$_3$), 31.7 (C*Me*$_2$OH), 29.2 ppm (2 C*Me*$_3$); IR (ATR): $\tilde{\nu}_{max}$ = 3343 (w, br), 2963 (s), 2928 (m), 2902 (m), 2866 (w), 2836 (w), 2195 (w), 1988 (w), 1925 (w), 1581 (s), 1473 (s), 1431 (s), 1361 (m), 1254 (s), 1229 (m), 1164 (m), 1109 (s), 1032 (m), 954 (m), 895 (m), 859 (w), 775 (m), 724 (m), 635 cm^{-1} (w); HR-ESI-MS: *m*/*z* (%): 395.2579 (100, $[M+H]^+$, calcd. for $C_{26}H_{35}O_3^+$: 395.2581), 396.2614 (29).

AAC (*P*)$_4$-and (*M*)$_4$-65

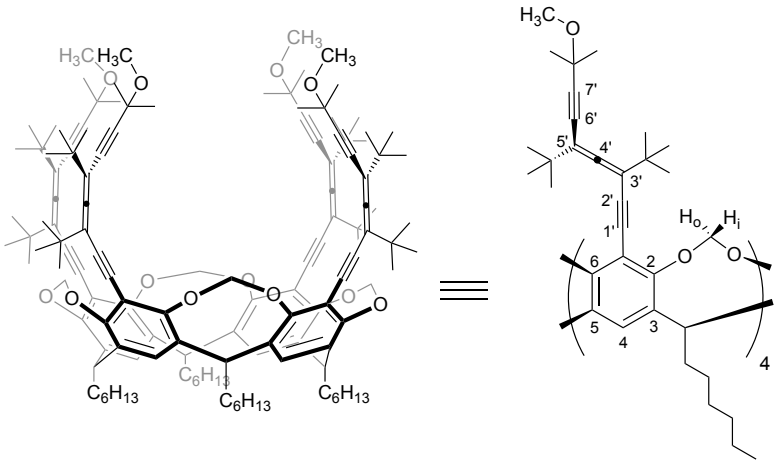

A 10 mL round bottom flask was loaded with 60% NaH in mineral oil (4 mg, 0.11 mmol) and dry THF (1.8 mL). The suspension was cooled to 0 °C, treated with (*P*)$_4$-**62** (20 mg, 10.5 µmol) at 0 °C, stirred for 30 min at 0 °C, warmed to 25 °C, and stirred for an additional 2 h. MeI (13 µL, 0.21 µmol) was added. The solution was stirred for 20 h at 25 °C and diluted with H_2O. The aqueous phase was extracted with EtOAc (3 x 10 mL). The combined organic phases were washed with brine, dried over Na_2SO_4, and concentrated *in vacuo*. Flash column chromatography (SiO_2; cyclohexane/EtOAc 95:5 to 9:1) afforded (OMe)$_4$-AAC (*P*)$_4$-**65** (18 mg, 92%) as a white solid.

The same synthetic procedure was applied for the (*M*)$_4$-configured enantiomer.

(OMe)$_4$-AAC (*P*)$_4$-**65**: $[\alpha]_D^{20}$ = +283.4 (*c* = 0.26 in *n*-hexane).

(OMe)$_4$-AAC (*M*)$_4$-**65**: $[\alpha]_D^{20}$ = –268.0 (*c* = 0.26 in *n*-hexane).

R_f = 0.25 (SiO_2; cyclohexane/EtOAc 9:1, UV); m.p. 232 °C; ^{1}H NMR (400 MHz, $CDCl_3$, 25 °C; assignments based on DFQ COSY and HSQC NMR spectra): δ = 7.02 (s, 4 H; 4 H–C(4)), 5.87 (d, *J* = 7.2 Hz, 4 H; 4 H_{out} of OCH_2O), 4.80 (t, *J* = 8.1 Hz, 4 H; 4 $H_{methine}$C–C(3,5)), 4.50

(d, J = 7.2 Hz, 4 H; 4 H_{in} of OCH_2O), 3.36 (s, 12 H; OMe), 2.16–2.21 (m, 8 H; 4 CH_2(CH_2)$_4$Me), 1.48 (s, 6 H; CMe_2OMe), 1.47 (s, 6 H; CMe_2OMe), 1.26–1.41 (m, 32 H; 4 CH_2(CH_2)$_4$Me, 1.12 (s, 36 H, C(H_3)$_3$)), 1.10 (s, 36 H; CMe_3), 0.89 ppm (t , J = 6.7 Hz, 12 H; 4 Me); ^{13}C NMR (101 MHz, $CDCl_3$, 25 °C; assignments based on DFQ COSY, HSQC and HMBC NMR spectra): δ = 211.5 (4 C(4')), 155.3 and 155.2 (4 C(2,6)), 138.5 and 138.4 (4 C(3,5)), 120.0 (4 C(4)), 113.6 (4 C(1)), 103.2 (4 C(3')), 103.1 (4 C(5')), 98.6 (4 OCH_2O), 94.9 (4 C(7')), 91.7 (4 C(1')) and 84.2 (4 C(2')), 77.7 (4 C(6')), 71.22 (4 CMe$_2$OMe)), 51.8 (4 OMe)), 36.7 (4 CH–C(3)), 35.7 and 35.6 (8 CMe$_3$)), 32.0 (C(1) of 4 hexyl), 29.7 and 29.5 (C(2,3) of 4 hexyl), 29.1 and 29.0 (8 Me$_3$), 28.6 and 28.5 (CMe_2OMe), 27.9 (C(4) of 4 hexyl), 22.8 (C(5) of 4 hexyl), 14.2 ppm (4 Me); IR (ATR): $\tilde{\nu}_{max}$ = 2962 (m), 2929 (m), 2864 (m), 2210 (w), 1931 (w), 1465 (m), 1449 (m), 1393 (w), 1375 (w), 1360 (m), 1253 (m), 1238 (m), 1208 (w), 1171 (m), 1155 (m), 1076 (m), 1019 (m), 968 (s), 868 (m), 817 (w), 752 (m), 728 (m), 697 (w), 672 (w), 635 cm^{-1} (w). HR-MALDI-MS: m/z (%): 1953.3130 (52, $[M]^+$, calcd. for $C_{132}H_{176}O_{12}^+$: 1953.3156), 1954.3168 (85), 1955.3206 (64); 1976.3030 (69, $[M + Na]^+$, calcd. for $C_{132}H_{176}NaO_{12}^+$: 1976.3054), 1977.3063 (100), 1978.3100 (72), 1979.3155 (37).

9.2.3 Synthesis of Cavitand Scaffold 69

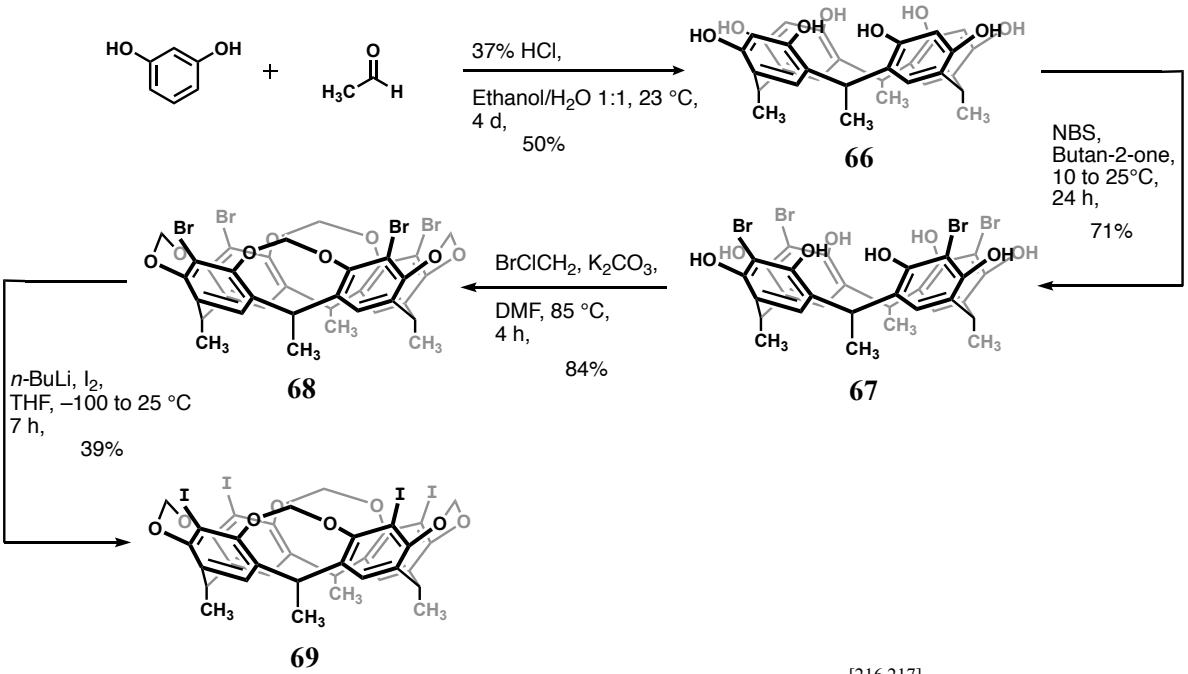

Scheme 21. Synthetic route to tetrabromo resorcin[4]arene cavitand **69**.[216,217]

7,11,15,28-Tetrabromo-1,21,23,25-tetramethyl-2,20:3,19-dimethano-1*H*,21*H*,23*H*,25*H*-bis[1,3]dioxocino[5,4-*i*:5',4'-*i*]benzo[1,2-*d*:5,4-*d*']bis[1,3]benzodioxocin (68)[200]

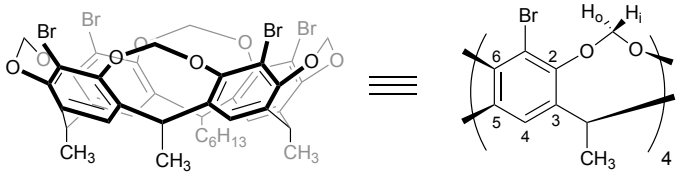

CH_2BrCl (29 mL, 430 mmol) was added to a suspension of tetramethyl octol **67** (11.0 g, 12.8 mmol) and K_2CO_3 (12.2 g, 88.3 mmol) in DMF (70 mL) under a N_2 atmosphere. The mixture was stirred for 5 h at 85 °C. The precipitate was filtered off over a Büchner funnel and washed with DMF (5 mL) and water (3 x 10 mL). MPLC (SiO_2; *n*-hexane/$CHCl_3$ 10:0 to 1:9) afforded **68** as colorless solid (9.72 g, 84%). Spectroscopic properties of **68** were identical to those previously reported.[200]

R_f = 0.65 (SiO_2; cyclohexane/$CHCl_3$ 2:8, UV); m.p. ≥400 °C (lit. > 360 °C)[200]; ^{1}H NMR (400 MHz, $CDCl_3$) δ = 7.17 (s, 4 H; 4 C(4)–H), 5.97 (d, J = 7.3 Hz, 4 H; 4 H_{out} of OCH_2O), 5.08 (q, J = 7.4 Hz, 4H; 4 C*H*Me), 4.41 (d, J = 7.4 Hz, 4 H; 4 H_{in} of OCH_2O), 1.77 ppm (d, J = 7.4 Hz, 12 H; 4 CH*Me*); ^{13}C NMR (100 MHz, $CDCl_3$) δ = 151.8 (4 C(2) and C(6)), 140.3 (4 C(3) and C(5)), 118.6 (4 C(4)), 113.6 (4 C(1)), 98.6 (4 OCH_2O), 32.2 (4 *C*HMe), 16.0 ppm (4 *Me*); IR (ATR): $\tilde{\nu}_{max}$ = 2984 (w), 2942 (w), 1468 (m), 1447 (m), 1414 (m), 1387 (w), 1334 (w), 1293 (m), 1230 (w), 1181 (m), 1143 (w), 1098 (m), 1057 (w), 1018 (m), 980 (s), 943 (s), 896 (m), 882 (m), 841 cm^{-1} (m); HR-MALDI-MS: m/z (%): 903.85032 (14, $[M]^+$, calcd. for $C_{36}H_{38}{}^{79}Br_4O_8{}^+$ 903.85122), 905.84931 (54, $[M]^+$, calcd. for $C_{36}H_{38}{}^{79}Br_3{}^{81}BrO_8{}^+$ 905.84937), 907.84661 (100, $[M]^+$, calcd. for $C_{36}H_{38}{}^{79}Br_2{}^{81}Br_2O_8{}^+$ 907.84763), 909.84232 (46, $[M]^+$, calcd. for $C_{36}H_{38}{}^{79}Br^{81}Br_3O_8{}^+$ 909.84615).

7,11,15,28-Tetraiodo-1,21,23,25-tetramethyl-2,20:3,19-dimethano-1*H*,21*H*,23*H*,25*H*-bis[1,3]dioxocino[5,4-*i*:5',4'-*i*]benzo[1,2-*d*:5,4-*d*']bis[1,3]benzodioxocin (69)[200]

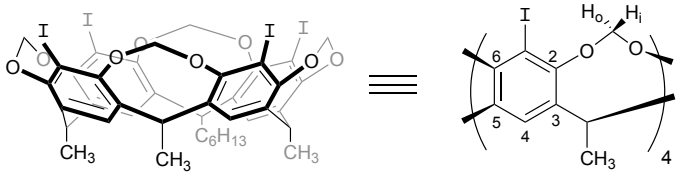

A solution of **68** (500 mg, 551 μmol) in THF (40 mL) was cooled to –100 °C under an argon atmosphere and treated dropwise with 1.6 M *n*-butyllithium (4.0 mL, 6.4 mmol). The mixture was stirred for 15 min at –100 °C, 30 min at –78 °C, and treated with I_2 (1.65 g, 5.5 mmol), stirred for 7 h, and allowed to reach 25 °C. The mixture was treated with an aq. sat. Na_2SO_4

solution (20 mL), and the THF was evaporated. A solution of the residue in $CHCl_3$ (100 mL) was washed with an aq. sat. Na_2SO_4 solution (10 mL) and brine (10 mL), dried over $MgSO_4$, and concentrated *in vacuo*. MPLC (SiO_2; cyclohexane/$CHCl_3$ 10:0 to 2:8) afforded **69** (234 mg, 39%) as a colorless solid. Spectroscopic properties of **69** were identical to those previously reported.

R_f = 0.70 (SiO_2; cyclohexane/$CHCl_3$ 2:8, UV); m.p. ≥ 400 °C (lit. > 360 °C)[200]; ^{1}H NMR (400 MHz, $CDCl_3$, 25 °;assignments based on DFQ COSY and HSQC NMR spectra) δ = 7.20 (s, 4 H; 4 H–C(4)), 5.98 (d, J = 7.4 Hz; 4 H_{out} of OCH_2O), 5.08 (q, J = 7.4 Hz, 4 H; 4 C*H*Me), 4.33 (d, J = 7.4 Hz; 4 H_{in} of OCH_2O) 1.76 ppm (d, J = 7.3 Hz, 12 H; 4 CH*Me*); ^{13}C NMR (101 MHz, $CDCl_3$, 25 °C; assignments based on DFQ COSY, HSQC and HMBC NMR spectra) δ = 154.7 (4 C(2) and C(4 6)), 139.7 (4 C(3) and C(4 5)), 120.3 (4 C(4)), 98.8 (4 OCH_2O), 93.1 (4 C(1)), 32.5 (4 *C*HMe), 16.3 ppm (4 Me); IR (ATR): $\tilde{\nu}_{max}$ = 2987 (w), 2901 (w), 1463 (w), 1442 (m), 1411 (w), 1384 (w), 1227 (w), 1177 (w), 1096 (s), 1057 (w), 1017 (m), 977 (s), 943 (s), 883 (w), 789 (w), 750 (s), 731 (m), 667 (w), 657 (m), 641 cm^{-1} (m); HR-MALDI-MS: *m*/*z* (%):1095.7933 (100, $[M]^+$, calcd. for $C_{36}H_{28}I_4O_8^+$ 1095.7957).

AAC $(P)_4$-and $(M)_4$-70

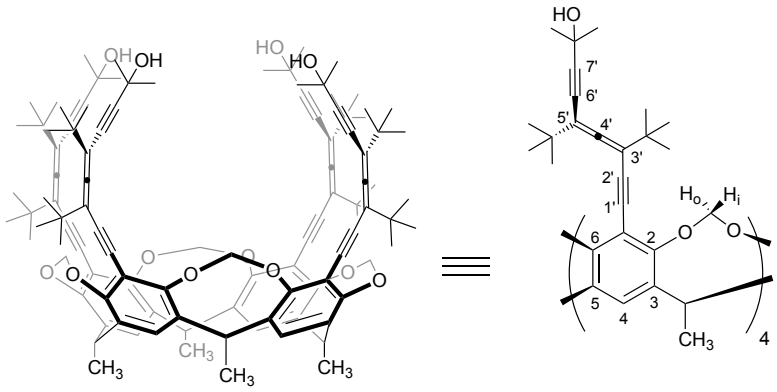

A 10 mL Schlenk tube was loaded with tetraiodo tetramethyl cavitand **69** (30 mg, 27 µmol) and [$Pd(Ph_3P)_4$] (3 mg, 2.7 µmol) and flushed with N_2. Triethylamine (1.0 mL) was added, and the solution was subjected to freeze/pump/N_2 cycles (1x). CuI (1 mg, 3 µmol) was added, and the solution was again subjected a freeze/pump/N_2 cycle. A second 10 mL Schlenk tube was charged with (*P*)-(+)-**27** (35 mg, 0.14 mmol) and flushed with N_2. Triethylamine (0.4 mL) was added, and the solution was subjected to a freeze/pump/N_2 cycle, before adding it dropwise into the first Schlenk tube. The resulting mixture was heated to 100 °C under N_2 for 12 h and diluted with a sat. aq. NH_4Cl solution. The aqueous phase was extracted with EtOAc (3 x 20 mL). The combined organic phases were washed with brine, dried over Na_2SO_4, and

concentrated *in vacuo*. Flash column chromatography (SiO_2; cyclohexane/EtOAc 9:1 to 7:3) afforded the AAC $(P)_4$-**70** (30 mg, 68%) as a white solid.

Same synthetic procedure was applied for $(M)_4$-configured enantiomer.

AAC $(P)_4$-AAC-**70**: $[\alpha]_D^{20} = -694.0$ ($c = 0.22$ in *n*-hexane) and +588.1 ($c = 0.22$ in acetonitrile)

AAC $(M)_4$-AAC-**70**: $[\alpha]_D^{20} = +723.8$ ($c = 0.21$ in *n*-hexane) and –618.5 ($c = 0.22$ in acetonitrile)

$R_f = 0.33$ (SiO_2; cyclohexane/EtOAc 8:2, UV); m.p. 195 °C; ^{1}H NMR (400 MHz, $CDCl_3$, 25 °C; assignments based on DFQ COSY and HSQC NMR spectra): $\delta = 7.15$ (s, 4 H; 4 H–C(4)), 5.87 (d, $J = 7.3$ Hz, 4 H; 4 H_{out} of OCH_2O), 5.02 (q, $J = 7.4$ Hz, 4 H; 4 C*H*Me), 4.51 (d, $J = 7.3$ Hz, 4 H; 4 H_{in} of OCH_2O), 2.34 (br. s, 4 H; 4 OH), 1.75 (d, $J = 7.4$ Hz, 12 H; 4 CH*Me*), 1.55 (s, 24 H; 4 C*Me*$_2$OH), 1.13 (s, 36 H; 4 C*Me*$_3$), 1.10 ppm (s, 36 H; 4 C*Me*$_3$); ^{13}C NMR (101 MHz, $CDCl_3$, 25 °C;assignments based on DFQ COSY, HSQC, and HMBC NMR spectra): δ = 211.4 (4 C(4')), 154.9 and 154.8 (4 C(2,6)), 139.3 and 139.3 (4 C(3,5)), 119.3 (4 C(4)), 113.6 (4 C(1)), 103.4 (4 C(3')), 102.9 (4 C(5')), 98.5 (4 OCH_2O), 97.8 (4 C(7')), 91.6 (4 C(1'), 84.3 (4 C(2'), 75.6 (4 C(6')), 65.8 (4 *C*Me$_2$OH), 35.7 (4 *C*Me$_3$), 35.6 (4 *C*Me$_3$), 31.7 and 31.6 (4 C*Me*$_2$OH), 31.1 (4 *C*HMe), 29.2 and 29.1 (8 C*Me*$_3$), 15.8 ppm (4 CH*Me*); IR (ATR): $\tilde{\nu}_{max} = 3376$ (w, br.), 2964 (m), 2928 (m), 2903 (m), 2863 (m), 1455 (m), 1441 (m), 1393 (w), 1361 (m), 1340 (w), 1309 (w), 1247 /w), 1226 (m), 1157 (m), 1099 (m), 1060 (w), 1019 (m), 982 (s), 954 (s), 891 (m), 845 cm^{-1} (w); HR-MALDI-MS: *m*/*z* (%): 1616.9352 (76, $[M]^+$, calcd. for $C_{108}H_{128}O_{12}^+$: 1616.9400), 1617.9352 (100), 1618.9429 (66).

$(P)_4$-and $(M)_4$-94

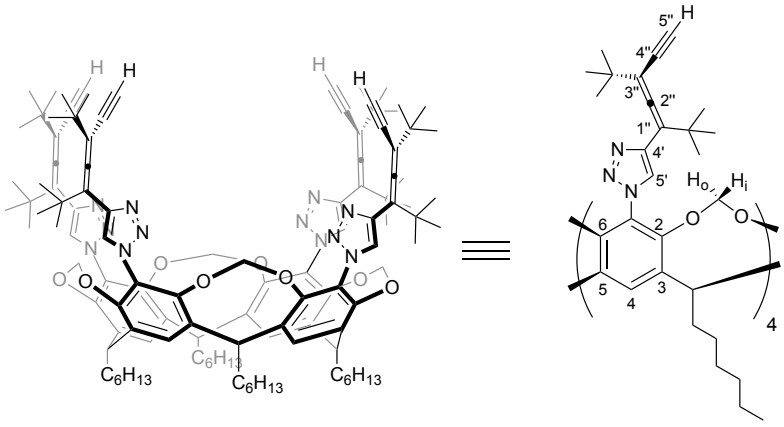

A solution of $(P)_4$-AAC-**61** (40 mg, 19 µmol) in dry toluene (1 mL) under nitrogen atmosphere, was treated with 40 wt% tetrabutylammonium hydroxide in methanol (0.10 mL 0.64 mmol) and heated to 70 °C for 2 h. Additional 40 wt% tetrabutylammonium hydroxide in methanol (0.10 mL 0.64 mmol) was added, stirred for 12 h at 70 °C, treated with 40 wt%

tetrabutylammonium hydroxide in methanol (0.10 mL 0.64 mmol) and stirred for 12 h. The mixture was diluted with water (10 mL) and washed with NH_4Cl (3 x 10 mL). The aqueous layers were extracted with EtOAc (3 x 10 mL). The combined organic layers were dried over Na_2SO_4, concentrated *in vacuo,* and purified by flash column chromatography (SiO_2; cyclohexane/CH_2Cl_2 9:1 to 4:6), affording AAC $(P)_4$-**94** (21 mg, 59%,) as a white solid.

The same synthetic procedure was applied for the $(M)_4$-configured enantiomer.

AAC $(P)_4$-**94**: $[\alpha]_D^{20} = +125.1$ (c = 0.23 in acetonitrile)

AAC $(M)_4$-**94**: $[\alpha]_D^{20} = -123.2$ (c = 0.23 in acetonitrile)

R_f = 0.40 (SiO_2; cyclohexane/ CH_2Cl_2 4:6, UV); m.p. 184 °C; ^{1}H NMR (400 MHz, $CDCl_3$, 25 °C; assignments based on DFQ COSY and HSQC NMR spectra): δ = 7.53 (s, 4 H; 4 H–C(1')), 7.33 (s, 4 H; 4 H–C(5')), 5.32 (d, J = 7.7 Hz, 4 H; 4 H_{out} of OCH_2O), 4.90 (t, J = 8.1 Hz, 4 H; 4 HC–C(3)), 4.64 (d, J = 7.7 Hz, 4 H; 4 H_{in} of OCH_2O), 2.93 (s, 4 H; 4 C≡C–H), 2.25–2.40 (m, 8 H; 4 CH_2(CH_2)$_4$Me), 1.35–1.52 (m, 32 H; 4 CH_2(CH_2)$_4$Me), 1.32 (s, 36 H, 4 CMe_3), 1.14 (s, 36 H, 4 CMe_3), 0.92 ppm (t, J = 6.8 Hz, 12 H; 4 Me); ^{13}C NMR (101 MHz, $CDCl_3$, 25 °C; assignments based on DFQ COSY, HSQC, and HMBC NMR spectra): δ = 207.4 (4 C(2'')), 149.7 and 149.4 (4 C(2,6)), 142.8 (4 C(4')), 139.1 and 139.0 (4 C(3,5)), 125.2 (4 C(1)), 124.9 (4 C(5')), 121.0 (4 C(4)), 109.8 (4 C(1'')), 102.1 (4 C(3'')), 100.9 (4 OCH_2O), 80.0 (4 C(5'')), 78.3 (4 C(4'')), 37.1 (4 *C*H–C(3)), 35.3 (4 *C*Me_3), 35.1 (4 *C*Me_3), 32.0 (C(1) of 4 hexyl), 29.8 (4 C*Me*$_3$), 29.6 (C(2,3) of 4 hexyl), 29.2 (4 C*Me*$_3$), 28.0 (C(4) of 4 hexyl), 22.8 (C(5) of 4 hexyl), 14.2 ppm (4 Me); IR (ATR): $\tilde{\nu}_{max}$ = 3312 (m), 3287 (m), 2960 (m), 2929 (m), 2864 (m), 2096 (w), 1476 (m), 1456 (m), 1390 (w), 1363 (m), 1305 (w), 1230 (w), 1218 (w), 1150 (w), 1084 (m), 1014 (m), 952 (s), 835 (w), 809 (w), 727 (w), 636 (w), 584 cm^{-1} (w); HR-MALDI-MS: *m*/*z* (%): 1860.1429 (76, $[M]^+$, calcd. for $C_{116}H_{148}N_{12}NaO_8^+$: 1860.1435), 1861.1464 (100).

AACs $(P)_4$-and $(M)_4$-89

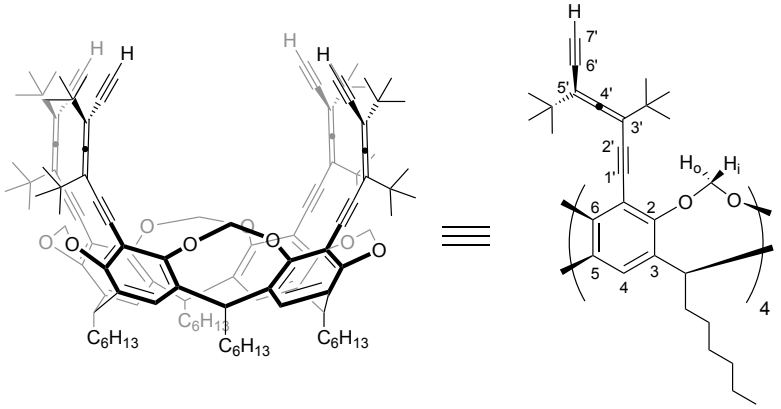

A solution of $(P)_4$-AAC-**62** (60 mg, 32 µmol) was dissolved in dry acetonitrile (1.6 mL) under nitrogen atmosphere, treated with 40 wt% tetrabutylammonium hydroxide in methanol (50 µL 0.32 mmol), heated to 80 °C for 1 h, treated with additional 40 wt% tetrabutylammonium hydroxide in methanol (50 µL 0.32 mmol), and stirred for 1 h at 80 °C. Additional 40 wt% tetrabutylammonium hydroxide in methanol (50 µL 0.32 mmol) was added at 70 °C, and stirring was continued for 30 min. The mixture was diluted with water (10 mL) and washed with NH_4Cl (3 x 10 mL). The aqueous layers were extracted with EtOAc (3 x 10 mL). The combined organic layers were dried over Na_2SO_4, concentrated *in vacuo* and purified by flash column chromatography (SiO_2; cyclohexane/CH_2Cl_2 9:1 to 4:6) to give AAC $(P)_4$-**89** (42 mg, 80%,) as a white solid.

The same synthetic procedure was applied for the $(M)_4$-configured enantiomer.

AAC $(P)_4$-**89**: $[\alpha]_D^{20} = -91.6$ (c = 0.26 in *n*-hexane)

AAC $(M)_4$-**89**: $[\alpha]_D^{20} = +82.1$ (c = 0.25 in *n*-hexane)

R_f = 0.42 (SiO_2; cyclohexane/ CH_2Cl_2 1:1, UV); m.p. 196 °C (with decomp.); ^{1}H NMR (400 MHz, $CDCl_3$, 25 °C; assignments based on DFQ COSY and HSQC NMR spectra): δ = 7.01 (s, 4 H; 4 H–C(4)), 5.86 (d, J = 7.2 Hz, 4 H; 4 H_{out} of OCH_2O), 4.80 (t, J = 8.1 Hz, 4 H; 4 HC–C(3)), 4.51 (d, J = 7.2 Hz, 4 H; 4 H_{in} of OCH_2O), 2.98 (s, 4 H; 4 C≡C–H), 2.15–2.21 (m, 8 H; 4 CH_2(CH_2)$_4$Me), 1.28–1.46 (m, 32 H; 4 CH_2(CH_2)$_4$Me, 1.14 (s, 36 H, 4 CMe_3), 1.12 (s, 36 H, 4 CMe_3), 0.90 ppm (t, J = 6.8 Hz, 12 H; 4 Me); ^{13}C NMR (101 MHz, $CDCl_3$, 25 °C; assignments based on DFQ COSY, HSQC, and HMBC NMR spectra): δ = 212.3 (4 C(4')), 155.3 and 155.3 (4 C(2,6)),138.5 and 138.5 (4 C(3,5)), 120.0 (4 C(4)), 113.6 (4 C(1)), 103.9 (4 C(3')), 102.5 (4 C(5')), 98.5 (4 OCH_2O), 91.3 (4 C(1')), 84.7 (4 C(2')), 80.9 (4 C(7')), 77.3 (4 C(6')), 36.7 (4 *C*H–C(3,5)), 35.6 (4 *C*Me_3), 35.4 (4 *C*Me_3), 32.0 (C(1) of 4 hexyl), 29.9, 29.7, (C(2,3) of 4 hexyl), 29.1 and 29.0 (8 C*Me*$_3$), 27.9 (C(4) of 4 hexyl), 22.8 (C(5) of 4 hexyl), 14.2 ppm (4 Me); IR (ATR): $\tilde{\nu}_{max}$ = 3313 (w), 3286 (w), 2961 (m), 2926 (m), 2858 (m), 1465 (m), 1447

(m), 1393 (w), 1362 (w), 1295 (w), 1241 (w), 1222 (w), 1208 (w), 1156 (m), 1086 (m), 1067 (m), 1019 (m), 969 (s), 806 (w), 734 (m), 677 (w), 642 cm^{-1} (m); HR-MALDI-MS: *m*/*z* (%): 1665.0858 (75, $[M]^+$, calcd. for $C_{116}H_{144}O_8^+$: 1665.0856), 1666.0897 (100), 1667.0933 (70), 1668.0967 (34).

Covalent AAC $(P)_4$-and $(M)_4$-88

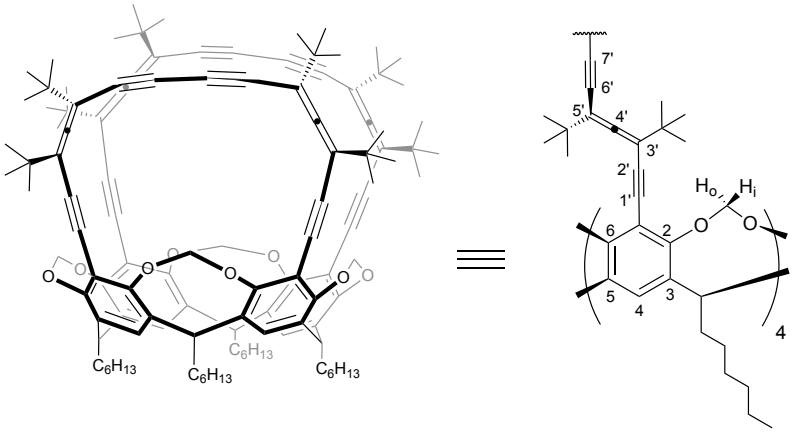

A solution of $(P)_4$-AAC-**89** (38 mg, 23 μmol) in dry pyridine (22 mL) under nitrogen atmosphere was degassed with argon for 20 min. CuCl (169 mg, 1.71 mmol) and $CuCl_2$ (33.7 mg, 0.25 mmol) were added into a second round bottom flask (100 mL), treated with dry pyridine (24 mL), and degassed with argon for 20 min. The Cu(I)/Cu(II)-solution in pyridine was added dropwise (1 mL h^{-1}) to the solution of $(P)_4$-AAC-**89** in pyridine. After complete addition, the resulting mixture was stirred for 3 d at 25 °C, acidified with a 1 M aqueous HCl solution (10 mL), and extracted with CH_2Cl_2 (3 x 10 mL). The combined organic layers were washed with $NaHCO_3$ solution, brine, dried over Na_2SO_4 and concentrated *in vacuo*. Flash column chromatography (SiO_2; cyclohexane/CH_2Cl_2 1:0 to 6:4) gave AAC $(P)_4$-**88** (31 mg, 82%,) as a white solid.

The same synthetic procedure was applied for the $(M)_4$-configured enantiomer.

AAC $(P)_4$-**88**: $[\alpha]_D^{20} = -484.0$ (c = 0.23 in *n*-hexane),

AAC $(M)_4$-**88**: $[\alpha]_D^{20} = +476.6$ (c = 0.24 in *n*-hexane);

R_f = 0.45 (SiO_2; cyclohexane/CH_2Cl_2 7:3, UV); m.p. 240 °C (decomp.); ^{1}H NMR (600 MHz, $CDCl_3$, 25 °C; assignments based on DFQ COSY and HSQC NMR spectra): δ = 7.03 and 7.01 (2 s, 4 H; 4 H–C(4)), 5.92 and 5.81 (2 d, J = 7.5 Hz, 4 H; 4 H_{out} of OCH_2O), 4.84 and 4.74 (2 t, J = 8.1 Hz, 4 H; 4 HC–C(3)), 4.48 and 4.45 (2 d, J = 7.5 Hz, 4 H; 4 H_{in} of OCH_2O), 2.08–2.22 (m, 8 H; 4 CH_2(CH_2)$_4$Me), 1.24–1.47 (m, 32 H; 4 CH_2(CH_2)$_4$Me, 1.18 (s, 18 H, 2 CMe_3), 1.15 (s, 18 H, 2 CMe_3), 1.14 (s, 18 H, 2 CMe_3), 1.04 (s, 18 H, 2 CMe_3), 0.88–0.91 ppm (m, 12

H; 4 Me); ^{13}C NMR (150 MHz, $CDCl_3$, 25 °; assignments based on DFQ COSY, HSQC, and HMBC NMR spectra): δ = 216.7 and 215.19 (4 C(4')), 156.3 and 155.6 (4 C(2,6)), 155.2 (4 C(7')), 138.5, 138.4, 138.3 and 138.1 (4 C(3,5)), 120.1 and 120.0 (4 C(4)), 113.6 and 113.4 (4 C(1)), 104.4, 104.7, 104.5 and 104.1 (4 C(5',3')), 99.0 and 98.8 (4 OCH_2O), 91.3 and 90.4 (4 C(1')), 85.9 and 84.5 (4 C(2')), 78.2 and 78.0 (4 C(6')), 36.7 and 36.7 (4 *C*H–C(3)), 35.6, 35.3, 35.0 and 34.6 (8 *C*Me_3), 32.0 and 32.0 (C(1) of 4 hexyl), 30.3, 29.6, 29.6, 29.5 (C(2,3) of 4 hexyl), 29.1, 29.0 and 29.0 (8 C*Me*$_3$), 28.0 and 27.9 (C(4) of 4 hexyl), 22.8 and 22.8 (C(5) of 4 hexyl), 14.2 and 14.2 (4 Me); IR (ATR): $\tilde{\nu}_{max}$ = 2961 (m), 2928 (m), 2864 (m), 1738 (w), 1463 (m), 1447 (m), 1393 (w), 1363 (m), 1253 (w), 1224 (m), 1153 (m), 1089 (m), 1017 (m), 966 (s), 809 (w), 732 (m), 680 (m), 584 (w), 553 cm^{-1} (m); HR-MALDI-MS: *m*/*z* (%): 1661.05475 (28, $[M]^+$, calcd. for $C_{116}H_{140}O_8^+$: 1661.05427), 1662.05770 (36), 1663.06120 (23); 1684.04389 (80, $[M + Na]^+$, calcd. for $C_{116}H_{140}NaO_8^+$: 1684.04404), 1685.04716 (100), 1686.04986 (64), 1687.05293 (29).

9.2.4 Synthesis of Enantiopure (*P*) and (*M*)-configured 1,3-Diethynylallene 74 and 75

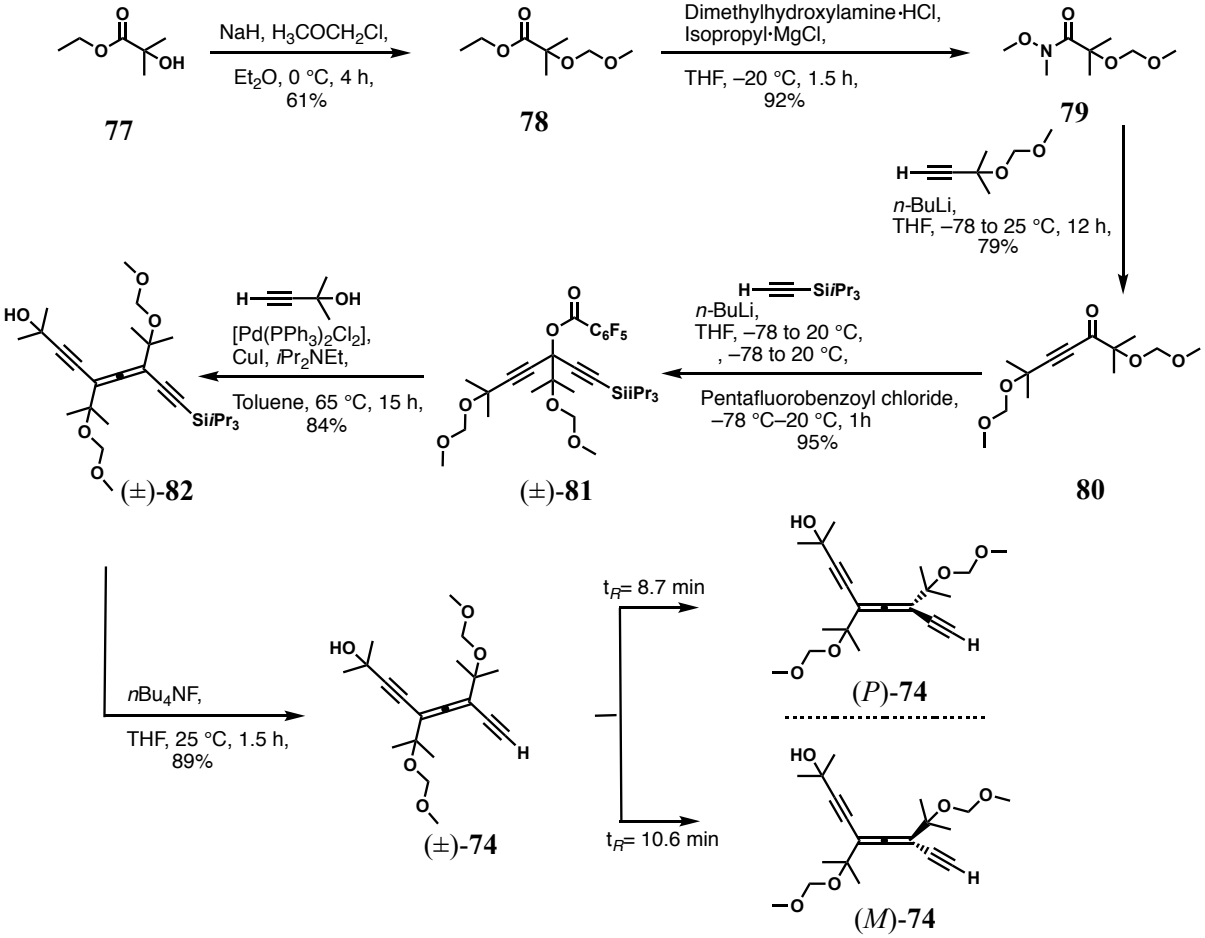

Scheme 22. Synthesis of (*P*)- and (*M*)-configured enantiomers of **74** in their optically pure form. Four to five synthetic steps (27% overall yield) are followed by separation of (±)-**74** in its enantiomers. t_r designates the retention time of the respective enantiomers by preparative HPLC with a CSP Chiralpak® IA in *n*-hexane/*i*PrOH 99.2:0.8.[303]

(±)-5,7-Bis[2-(methoxymethoxy)propan-2-yl]-2-methylnona-5,6-dien-3,8-diyn-2-ol ((±)-74)[303]

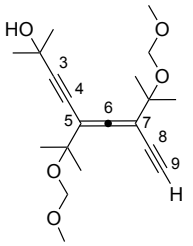

A solution of (±)-**82** (4.76 g, 9.39 mmol) in THF (94 mL) was treated dropwise with 1.0 M tetrabutylammonium fluoride in THF (9.4 mL, 9.4 mmol), stirred for 1.5 h in an open flask, and concentrated *in vacuo*. MPLC (SiO_2; cyclohexane/EtOAc 10:0 to 5:5) gave (±)-**74** (2.93 g, 89%) as an amber oil.

Preparative HPLC using the CSP Diacel Chiralpak® IA (Diacel Chemical Industries Ltd.) gave the enantiomers (*P*)-(+)-**74** and (*M*)-(–)-**74**. Elution was performed with a mixture of *n*-hexane/*i*PrOH 98:2 at a flow of 18 mL min^{-1}. Under these conditions, 1 mL of a solution of (±)-**74** in *n*-hexane (15 mg/mL) was injected.

(*P*)-(+)-**74**: t_R = 8.70 min, e.r. > 99:1; $[\alpha]_D^{20}$ = +72.0 (*c* = 1.0 in acetonitrile)

(*M*)-(–)-**74**: t_R = 10.56 min, e.r. > 99:1; $[\alpha]_D^{20}$ = –71.4 (*c* = 1.0 in acetonitrile)

R_f = 0.29 (SiO_2; hexane/EtOAc 7:3, $KMnO_4$); ^{1}H NMR (400 MHz, $CDCl_3$, 25 °C; assignments based on DFQ COSY and HSQC NMR spectra): δ = 4.73 (s, 2 H; OCH_2O), 4.72–4.68 (m, 2 H; OCH_2O), 3.38 (s, 6 H; 2 OMe), 3.06 (s, 1 H, C≡C–H), 2.39 (s, 1 H; OH), 1.53 (s, 6 H; C*Me*$_2$OH), 1.45, 1.43 and 1.42 ppm (3 s, 12 H; 2 C*Me*$_2$$OCH_2OMe$); ^{13}C NMR (100 MHz, $CDCl_3$, 25 °C; assignments based on COSY, HSQC and HMBC NMR spectra): δ = 214.2 (C(6)), 100.8 (C(5)), 99.8 (C(7)), 99.3 (C(3)), 92.4 and 92.3 (2 OCH_2O), 82.1 (C(9)), 77.4 and 77.3 (2 *C*Me_2OCH_2OMe), 75.8 (C(4)), 73.8 (C(8)), 65.7 (*C*$(Me)_2OH$), 55.7 and 55.7 (2 OMe), 31.4 (*C*Me_2OH), 27.3 and 27.1 (2 C*Me*$_2$$OCH_2OMe$), 26.8 and 26.8 ppm (2 C*Me*$_2$$OCH_2OMe$). IR (ATR): $\tilde{\nu}_{max}$ = 3435 (br. w), 3285 (br. w), 2982 (w), 2934 (w), 1462 (w), 1382 (w), 1364 (w), 1228 (w), 1143 (s), 1086 (m), 1026 (s), 993 (m), 981 (w), 920 (m), 829 (w), 806 (w), 754 (m), 698 (w), 666 cm^{-1} (w); HR-ESI-MS: *m*/*z* (%): 373.1989 (20, $[M + Na]^+$, calcd. for $C_{20}H_{30}NaO_5^+$: 373.1985), 273.1851 (51, $[M – OMOM – OH + H]^+$, calcd. for $C_{18}H_{25}O_2^+$: 273.1849), 259.1694 (100, $[M – OMOM – OMe + H]^+$, calcd. for $C_{17}H_{23}O_2^+$ 259.1693).

(*P*)- and (*M*)-3-Ethynyl-5-(2-hydroxypropan-2-yl)-2,8-dimethylnona-3,4-dien-6-yne-2,8-diol ((*P*)-and (*M*)-75)

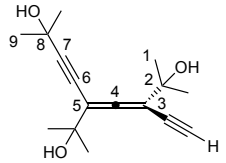

A solution of (*P*)-(–)-**74** (100 mg, 285 μmol) in MeOH (8.0 mL) was treated with 1.25 M HCl in Methanol (2.2 mL, 2.9 mmol), stirred for 4 h in an open flask, and diluted with H_2O (10 mL). The aqueous layer was extracted with CH_2Cl_2 (3 x 30 mL). The combined organic layers were dried over Na_2SO_4 and concentrated *in vacuo*. MPLC (SiO_2; CH_2Cl_2/MeOH 10:0 to 9:1) gave (*P*)-(–)-**75** (62 mg, 83%) as a colorless foam.

The same synthetic procedure was applied for the (*M*)-configured enantiomer.

(*P*)-(–)-**75**: $[\alpha]_D^{20}$ = +84.7 (*c* = 1.5 in acetonitrile),

(*M*)-(–)-**75**: $[\alpha]_D^{20}$ = –88.1 (*c* = 1.5 in acetonitrile);

R_f = 0.50 (SiO_2; CH_2Cl_2/MeOH 9:1, $KMnO_4$); ^{1}H NMR (400 MHz, $CDCl_3$, 25 °C; assignments based on COSY and HSQC NMR spectra): δ = 3.37 (br. s, 3 H; 3 OH), 3.10 (s, 1 H; C≡C–H), 1.54 (s, 6 H; C(7)–*Me*$_2$OH), 1.47 and 1.46 (2 s, 6H; 2 C(3)–*Me*$_2$OH), 1.45 and 1.39 ppm (2 s, 6 H; 2 C(5)–*Me*$_2$OH); ^{13}C NMR (100 MHz, $CDCl_3$, 25 °C; assignments based on COSY, HSQC and HMBC NMR spectra): δ = 210.1 (C(4)), 104.0 (C(5)), 103.5 (C(3)), 99.8 (C(7)), 82.3 (C≡*C*H), 76.2 (*C*≡CH), 74.5 (C(6)), 72.6 (C(3)–*C*Me$_2$OH), 72.4 (C(5)–*C*Me$_2$OH), 65.6 (C(7)–*C*Me$_2$OH), 31.2 and 31.1 (C(7)–C*Me*$_2$OH), 28.8 and 28.7 (C(3)–C*Me*$_2$OH), 28.5 and 28.1 ppm (C(5)–C*Me*$_2$OH); IR (ATR): $\tilde{\nu}_{max}$= 3287 (br. m), 2978 (s), 932 (m), 2901 (m), 1455 (w), 1405 (m), 1377 (m), 1362 (m) 1241 (m), 1196 (m), 1159 (s), 1101 (m), 1066 (s), 1057 (s), 951 (s), 897 (m), 867 (w), 843 cm^{-1}(m); HR-MALDI-MS: *m*/*z* (%): 285.1466 (100, [*M* + Na]$^+$, calcd. for $C_{16}H_{22}NaO_3^+$ 285.1461).

9.2.5 Synthesis of Cavitand Scaffold 96

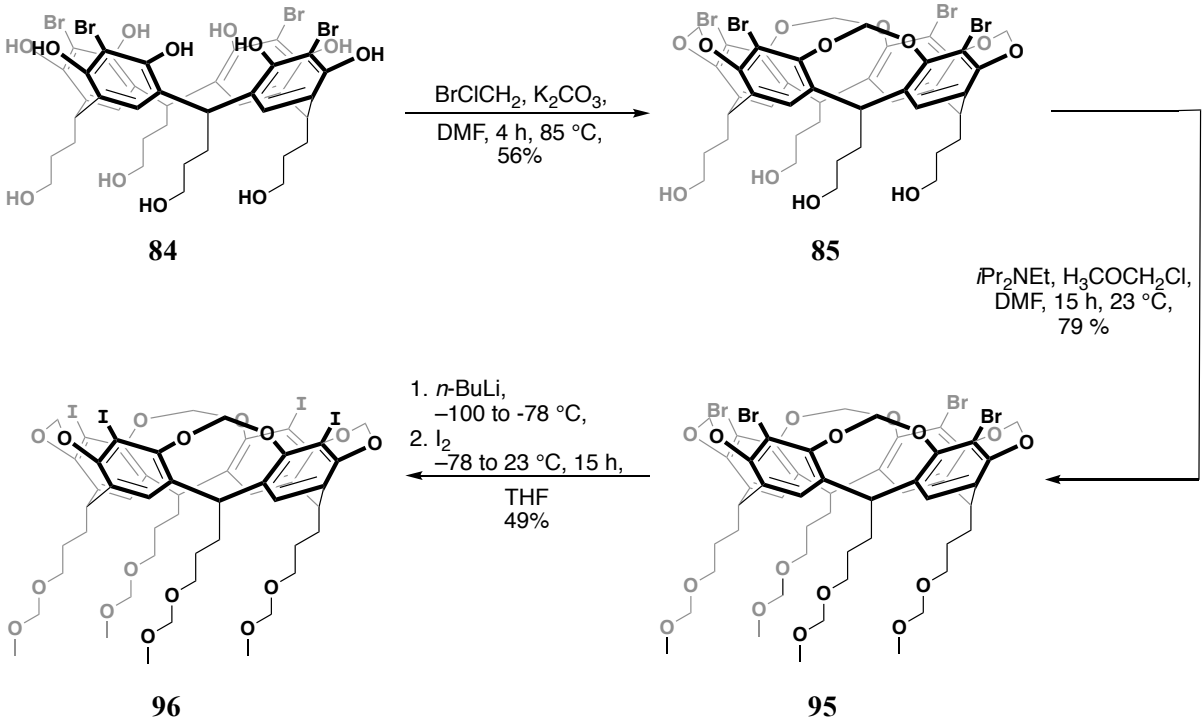

Scheme 23. Synthetic procedure for tetraiodo resorcin[4]arene scaffold **96** from octol **84**.[305]

7,11,15,28-Tetrabromo-1,21,23,25-tetrakis-(4-hydroxypropyl)-2,20:3,19-dimethano-1*H*, 21*H*,23*H*,25*H*-bis[1,3]dioxocino[5,4-*i*:5',4'-*i*]benzo[1,2-*d*:5,4-*d*']bis[1,3]benzodioxocin (85)[304]

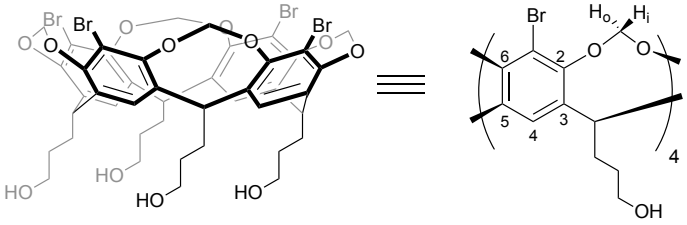

A suspension of tetrabromo octol **84** (5.00 g, 4.82 mmol) and K_2CO_3 (5.33 g, 38.6 mmol) in DMF (35 mL) was treated with $ClCH_2Br$ (12.9 mL, 193 mmol) and stirred for 3 h at 85 °C under an argon atmosphere. The suspension was filtered and the filtrate concentrated *in vacuo* at 60 °C. MPLC (SiO_2; $CHCl_3$/MeOH 10:0 to 8:2) and crystallization from THF (100 mL) and acetonitrile (120 mL) afforded **85** as colorless solid (2.93 g, 56%). Spectroscopic properties of **85** were identical to those previously reported.[304]

R_f = 0.39 (SiO_2; $CHCl_3$/MeOH 9:1, $KMnO_4$); m.p. ≥380 °C (decomp.), lit. > 250 °C);[304] ^{1}H NMR (400 MHz, $(CD_3)_2SO$, 25 °C; assignments based on DFQ COSY and HSQC NMR spectra): δ = 7.66 (s, 4 H; C(4)–H), 6.01 (d, J = 7.6 Hz, 4 H; H_{out} of OCH_2O), 4.70 (t, J = 8.1 Hz, 4 H; C*H*$(CH_2)_3OH$), 4.52 (br. s, 4 H; OH), 4.31 (d, J = 7.6 Hz, 4 H; H_{in} of OCH_2O), 3.51 (t, J = 6.5 Hz, 8 H; $CH(CH_2)_2CH_2OH$), 2.44 (dt, J = 7.5, 6.8 Hz, 8H; $CHCH_2(CH_2)_2OH$), 1.51–1.41 ppm (m, 8H $CHCH_2CH_2CH_2OH$); ^{13}C NMR (100 MHz, $(CD_3)_2SO$, assignments based on DFQ COSY, HSQC and HMBC NMR spectra) δ = 151.2 (4 C(2,6), 139.3 (4 C(3,5), 121.6 (4 C(4)), 112.9 (4 C(1)), 98.0 (4 OCH_2O), 60.2 (4 $CH(CH_2)_2CH_2OH$), 37.6 (4 $CH(CH_2)_3OH$), 30.6 (4 $CHCH_2(CH_2)_2OH$), 25.5 ppm (4 $CHCH_2CH_2CH_2OH$); IR (ATR): $\tilde{\nu}_{max}$ = 3383 (br. w), 2970 (m), 2901 (m), 1469 (m), 1450 (m), 1410 (m), 1394 (m), 1301 (m), 1230 (m), 1186 (w), 1141 (w), 1066 (s), 1047 (s), 1018 (s), 990 (s), 960 (s), 919 (m), 859 (m), 806 cm^{-1}(w); HR-MALDI-MS: *m*/*z* (%): 1102.9465 (16, $[M + Na]^+$, calcd. for $C_{44}H_{44}{}^{79}Br_4NaO_{12}{}^+$: 1102.9459), 1104.9435 (71, $[M + Na]^+$, calcd. for $C_{44}H_{44}{}^{79}Br_3{}^{81}BrNaO_{12}{}^+$: 1104.9441), 1106.9415 (100, $[M + Na]^+$, calcd. for $C_{44}H_{44}{}^{79}Br_3{}^{81}BrNaO_{12}{}^+$: 1106.9425), 1107.9453 (49), 1108.9398 (71, $[M + Na]^+$, calcd. for $C_{44}H_{44}Br_4NaO_{12}{}^+$: 1108.9413), 1109.9425 (33), 1110.9392 (22, $[M + Na]^+$, calcd. for $C_{44}H_{44}{}^{81}Br_4NaO_{12}{}^+$: 1110.9410).

7,11,15,28-Tetrabromo-1,21,23,25-tetrakis-[3-(methoxymethoxy)propyl)]-2,20:3,19-dimethano-1*H*,21*H*,23*H*,25*H*-bis[1,3]dioxocino[5,4-*i*:5',4'-*i*]benzo[1,2-*d*:5,4-*d*']bis[1,3]benzodioxocin (95)[304]

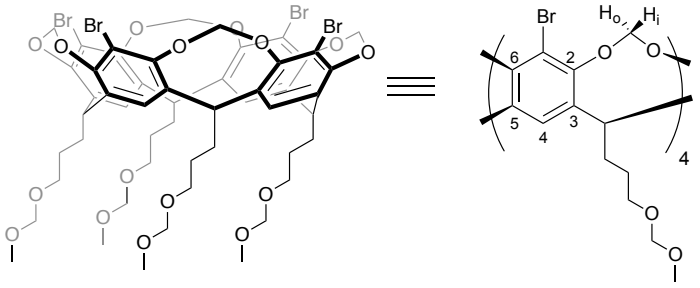

A solution of tetrabromo cavitand **85** (1.00 g, 923 μmol) in DMF (20 mL) and *N,N*-diisopropylethylamine (2.5 mL, 26.1 mmol) under an argon atmosphere was treated with chloromethyl methyl ether (700 μL, 9.2 mmol), stirred for 15 h at 25 °C, and concentrated *in vacuo*. A solution of product in EtOAc (50 mL) was washed with a 0.5 N aq. HCl solution of (20 mL), and the aqueous layer was reextracted with EtOAc (50 mL). The combined organic layers were washed with an aq. sat. $NaHCO_3$ solution (20 mL), dried over $MgSO_4$, and concentrated *in vacuo*. MPLC (SiO_2; cyclohexane/EtOAc 10:0 to 2:8) afforded **95** (962 mg, 83%) as a colorless solid.

R_f = 0.27 (SiO_2; cyclohexane/EtOAc 1:1, UV); m.p. = 250 °C; ^{1}H NMR (400 MHz, $CDCl_3$, 25 °C; assignments based on DFQ COSY and HSQC NMR spectra): δ = 7.07 (s, 4H; 4 H–C(4)), 5.96 (d, J = 7.4 Hz, 4 H; 4 H_{out} of OCH_2O), 4.91 (t, J = 8.2 Hz, 4 H; 4 C*H*$(CH_2)_3O$), 4.66 (s, 8 H; 4 OC*H*$_2$OMe), 4.40 (d, J = 7.4 Hz, 4 H; 4 H_{in} of OCH_2O), 3.62 (t, J = 6.0 Hz, 8 H; 4 $CH(CH_2)_2CH_2O$), 3.40 (s, 12 H; 4 OCH_2OMe), 2.36–2.30 (m, 8 H; 4 $CHCH_2(CH_2)_2O$), 1.65 ppm (m, 8 H; $CHCH_2CH_2CH_2O$); ^{13}C NMR (100 MHz, $CDCl_3$, 25 °C; assignments based on COSY, HSQC and HMBC NMR spectra) δ = 152.3 (4 C(2,6), 139.2 (4 C(3,5), 119.1 (4 C(4)), 113.8 (4 C(1)), 98.6 (4 OCH_2O), 96.6 (4 OCH_2OMe), 67.0 (4 $CH(CH_2)_2CH_2O$), 55.4 (4 OCH_2OMe), 37.5 (4 *C*$H(CH_2)_3O$), 27.9 (4 $CHCH_2CH_2CH_2O$), 26.6 ppm (4 $CHCH_2(CH_2)_2O$); IR (ATR): $\tilde{\nu}_{max}$ = 2935 (w), 2879 (w), 1470 (w), 1450 (m), 1418 (w), 1389 (w), 1298 (w), 1214 (w), 1174 (w), 1144 (m), 1104 (m), 1077 (m), 1036 (s), 1016 (s), 981 (s), 954 (s), 913 (s), 858 (w), 843 (w), 810 cm^{-1} (w); HR-MALDI-MS: *m/z* (%): 1279.0494 (15, $[M + Na]^+$, calcd. for $C_{52}H_{60}{}^{79}Br_4NaO_8{}^+$: 1279.0507), 1281.0482 (63, $[M + Na]^+$, calcd. for $C_{52}H_{60}{}^{79}Br_3{}^{81}BrNaO_8{}^+$: 1281.0491), 1283.0468 (100, $[M + Na]^+$, calcd. for $C_{52}H_{60}{}^{79}Br_2{}^{81}Br_2\ NaO_8{}^+$ 1283.0476), 1284.0504 (53), 1285.0461 (71, $[M + Na]^+$, calcd. for $C_{52}H_{60}{}^{79}Br^{81}Br_3NaO_8{}^+$: 1285.0466), 1287.0463 (23, $[M + Na]^+$, calcd. for $C_{52}H_{60}{}^{81}Br_4NaO_8{}^+$ 1287.0467).

7,11,15,28-Tetraiodo-1,21,23,25-tetra-(3-(methoxymethoxy)propyl)-2,20:3,19-dimethano-1*H*,21*H*,23*H*,25*H*-bis[1,3]dioxocino[5,4-*i*:5',4'-*i*]benzo[1,2-*d*:5,4-*d*']bis[1,3]benzodioxocin (96)[304]

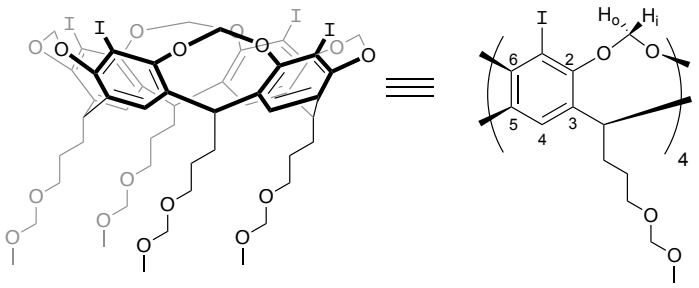

A solution of **95** (500 mg, 397 μmol) in THF (13 mL) as cooled to –100 °C under an argon atmosphere was treated dropwise with 1.6 M *n*-butyllithium in *n*-hexane (2.5 mL, 4.0 mmol), stirred for 15 min and then for 30 min at –78 °C, treated with I_2 (1.08 g, 3.97 mmol), allowed to warm up to 25 °C, and stirred for 14 h. The mixture was treated with aq. sat. $Na_2S_2O_3$ solution (20 mL) and concentrated *in vacuo*. The aqueous mixture was extracted with CH_2Cl_2 (3 x 20 mL). The combined organic layers were washed with aq. sat. $Na_2S_2O_3$ solution (10 mL) and brine (10 mL), dried over $MgSO_4$, and concentrated *in vacuo*. MPLC (SiO_2; cyclohexane/EtOAc 10:0 to 4:6) afforded **96** (462 mg, 81%) as a colorless solid.

R_f = 0.27 (SiO_2; cyclohexane/EtOAc 1:1, UV); m.p. = 265 °C; ^{1}H NMR (400 MHz, $CDCl_3$, 25 °C; assignments based on DFQ COSY and HSQC NMR spectra) δ = 7.10 (s, 4 H; 4 H–C(4)), 5.97 (d, J = 7.4 Hz, 4 H; 4 H_{out} of OCH_2O), 4.91 (t, J = 8.2 Hz, 4 H; 4 C*H*$(CH_2)_3O$), 4.66 (s, 8 H; 4 OCH_2OCH$_3$), 4.32 (d, J = 7.4 Hz, 4 H; 4 H_{in} of OCH_2O), 3.62 (t, J = 6.0 Hz, 8 H; 4 CH$(CH_2)_2CH_2O$), 3.39 (s, 12 H; 4 OCH_2OCH_3), 2.35–2.29 (m, 8 H; 4 $CHCH_2(CH_2)_2O$), 1.81–1.49 ppm (m, 8 H; 4 $CHCH_2CH_2CH_2O$); ^{13}C NMR (100 MHz, $CDCl_3$, 25 °C; assignments based on DFQ COSY, HSQC and HMBC NMR spectra) δ = 152.2 (4 C(2,6), 138.6 (4 C(3,5), 120.7 (4 C(4)), 98.8 (4 OCH_2O), 96.5 (4 OCH_2OCH_3), 93.3 (4 C(1)), 67.0 (4 $CH(CH_2)_2CH_2O$), 55.4 (4 OCH_2OCH_3), 37.8 (4 *C*H$(CH_2)_3O$), 27.9 (4 $CHCH_2CH_2CH_2O$), 26.9 ppm (4 $CHCH_2(CH_2)_2O$); IR (ATR): $\tilde{\nu}_{max}$ = 2934 (w), 2879 (w), 1467 (w), 1447 (m), 1414 (w), 1386 (w), 1299 (w), 1214 (w), 1173 (w), 1146 (m), 1104 (m), 1077 (m), 1036 (s), 1016 (s), 981 (s), 955 (s), 916 (m), 855 (w), 805 cm^{-1}(w); HR-MALDI-MS: *m*/*z* (%): 1470.9989 (100, $[M + Na]^+$, calcd. for $C_{52}H_{60}I_4NaO_{16}^+$: 1470.9953), 1472.0028 (56, $[M + Na]^+$, calcd. for $C_{52}H_{60}I_4NaO_{16}^+$: 1471.9987).

9.2.6 Synthesis of Cavitand Scaffold 83

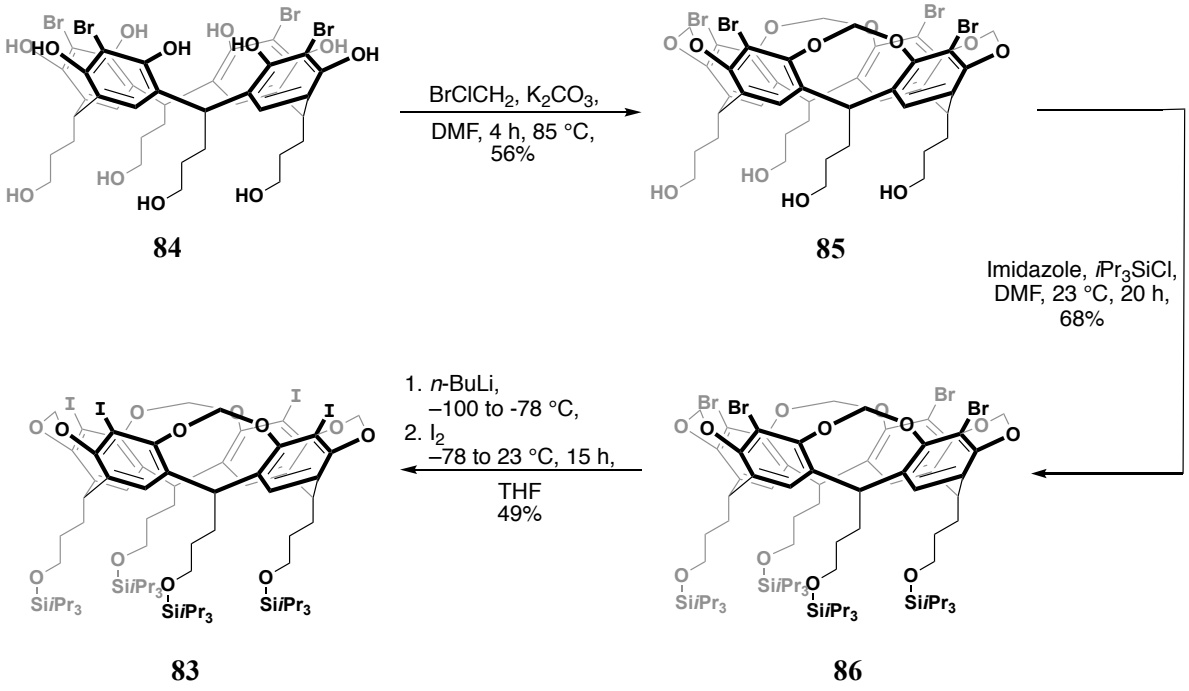

Scheme 24. Synthetic procedure for tetraiodo resorcin[4]arene **83** scaffold from octol **84**.[305]

7,11,15,28-Tetrabromo-1,21,23,25-tetra-(3-((triisopropylsilyl)oxy)propyl)-2,20:3,19-dimetheno-1*H*,21*H*,23*H*,25*H*-bis[1,3]dioxocino[5,4-*i*:5',4'-*i*]benzo[1,2-*d*:5,4-*d*']bis[1,3]benzodioxocin (86)[305]

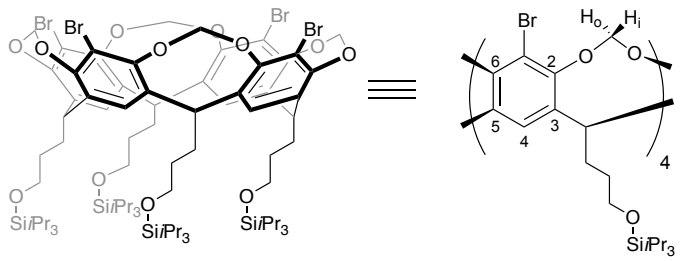

A solution of tetrabromo cavitand **85** (1.00 g, 923 μmol) and imidazole (954 mg, 14.0 mmol) in DMF (10 mL) under an argon atmosphere was treated with triisopropylsilyl chloride (13 mmol, 27 mL), stirred for 20 h at 25 °C, and concentrated *in vacuo*. After addition of H_2O (10 mL), the aqueous layer was extracted with CH_2Cl_2 (2 x 50 mL). The combined organic layers were washed with brine (10 mL), dried over $MgSO_4$, and concentrated *in vacuo*. MPLC (SiO_2; cyclohexane/CH_2Cl_2 10:0 to 3:7) afforded **86** (1.07 g, 68%) as a colorless solid. Spectroscopic properties of **86** were identical to those previously reported.

R_f = 0.51 (SiO_2; cyclohexane/CH_2Cl_2 1:1, UV); m.p. = 115 °C; ^{1}H NMR (400 MHz, $CDCl_3$, 25 °C; assignments based on DFQ COSY and HSQC NMR spectra): δ = 7.06 (s, 4H; 4 C(4)–H), 5.96 (d, J = 7.4 Hz, 4 H; 4 H_{out} of OCH_2O), 4.89 (t, J =8.2 Hz, 4 H; 4 C*H*$(CH_2)_3O$), 4.40

(d, J = 7.4 Hz, 4 H; 4 H_{in} of OCH_2O), 3.77 (*t*, J = 6.3 Hz, 8 H; 4 $CH(CH_2)_2CH_2O$), 2.41–2.12 (m, 8 H; 4 $CHCH_2(CH_2)_2O$), 1.63–1.57 (m, 8 H; 4 $CHCH_2CH_2CH_2O$), 1.09 ppm (1 br. s, 84 H; 4 $Si(CHMe_2)_3$); ^{13}C NMR (100 MHz, $CDCl_3$, assignments based on DFQ COSY, HSQC and HMBC NMR spectra): δ = 152.3 (4 C(2,6), 139.3 (4 C(3,5), 119.2 (4 C(4)), 113.7 (4 C(1)), 98.6 (4 OCH_2O), 62.8 (4 $CH(CH_2)_2CH_2O$), 37.3 (4 $CH(CH_2)_3O$), 30.9 (4 $CHCH_2CH_2CH_2O$), 26.1 (4 $CHCH_2(CH_2)_2O$), 18.2 (4 $Si(CHMe_2)_3$), 12.2 ppm (4 $Si(CHMe_2)_3$); IR (ATR): $\tilde{\nu}_{max}$= 2940 (m), 2890 (w), 2864 (m), 1465 (m), 1450 (m), 1417 (w), 1387 (w), 1366 (w), 1301 (w), 1249 (w), 1229 (w), 1173 (w), 1098 (s), 1069 (m), 1018 (m), 994 (s), 962 (s), 881 (s), 828 (w), 790 (m), 726 (m), 680 (s), 651 cm^{-1} (m); HR-MALDI-MS: m/z (%): 1727.48003 (11, $[M + Na]^+$, calcd. for $C_{80}H_{124}{}^{79}Br_4NaO_{12}Si_4{}^+$: 1727.4796), 1729.4776 (55, $[M + Na]^+$, calcd. for $C_{80}H_{124}{}^{79}Br_3{}^{81}BrNaO_{12}Si_4{}^+$: 1729.4785), 1731.4758 (100, $[M+ Na]^+$, calcd. for $C_{80}H_{124}{}^{79}Br_2{}^{81}Br_2NaO_{12}Si_4{}^+$: 1731.4758), 1733.4744 (93, $[M + Na]^+$, calcd. for $C_{80}H_{124}{}^{79}Br^{81}Br_3NaO_{12}Si_4{}^+$: 1733.4770), 1735.4735 (49, $[M + Na]^+$, calcd. for $C_{80}H_{124}{}^{81}Br_4NaO_{12}Si_4{}^+$ 1735.4769).

7,11,15,28-Tetraiodo-1,21,23,25-tetrakis-(3-((triisopropylsilyl)oxy)propyl)-2,20:3,19-dimethano-1*H*,21*H*,23*H*,25*H*-bis[1,3]dioxocino[5,4-*i*:5',4'-*i*]benzo[1,2-*d*:5,4-*d*']bis[1,3]benzodioxocin (83)[305]

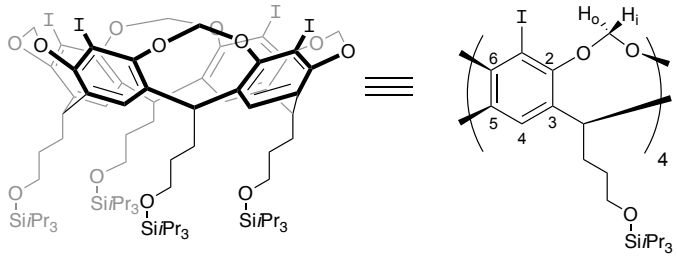

A solution of **86** (500 mg, 292 μmol) in THF (13 mL) was cooled to –100 °C under an argon atmosphere, treated with 1.6 M *n*-butyllithium in *n*-hexane (1.8 mL, 2.9 mmol), stirred for 15 min and for 30 min at –78 °C, treated with I_2 (741 mg, 2.92 mmol), allowed to reach 25 °C, and stirred for 15 h. The mixture was diluted with aq. sat. $Na_2S_2O_3$ (5 mL) and concentrated *in vacuo*. After dilution with H_2O (10 mL), the aqueous layer was extracted with CH_2Cl_2 (2 x 50 mL). The combined organic layers were washed brine (10 mL), dried over $MgSO_4$, and concentrated *in vacuo*. MPLC (SiO_2; cyclohexane/CH_2Cl_2 10:0 to 4:6) afforded **83** (269 mg, 49%) as a colorless solid.

R_f = 0.19 (SiO_2; cyclohexane/CH_2Cl_2 1:1, UV); m.p. = 112 °C; ^1H NMR (400 MHz, $CDCl_3$, 25 °C; assignments based on DFQ COSY and HSQC NMR spectra): δ = 7.09 (s, 4H; 4 H–

C(4)), 5.97 (d, J = 7.4 Hz, 4 H; 4 H_{out} of OCH_2O), 4.89 (t, J =8.2 Hz, 4 H; 4 C*H*$(CH_2)_3O$), 4.32 (d, J = 7.4 Hz, 4 H; 4H_{in} of OCH_2O), 3.77 (*t*, J = 6.3 Hz, 8 H; 4 $CH(CH_2)_2CH_2O$), 2.42–2.19 (m, 8 H; 4 $CHCH_2(CH_2)_2O$), 1.63–1.56 (m, 8 H; 4 $CHCH_2CH_2CH_2O$), 1.09 ppm (1 br. s, 84 H; 4 $Si(CH(Me)_2)_3$); ^{13}C NMR (100 MHz, $CDCl_3$, 25 °C; assignments based on DFQ COSY, HSQC and HMBC NMR spectra): δ = 155.1 (4 C(2,6)), 138.7 (4 C(3,5)), 120.8 (4 C(4)), 98.9 (4 OCH_2O), 93.3 (4 C(1)), 62.8 (4 $CH(CH_2)_2CH_2O$), 37.6 (4 $CH(CH_2)_3O$), 30.9 (4 $CHCH_2CH_2CH_2O$), 26.4 (4 $CHCH_2(CH_2)_2O$), 18.2 (4 $Si(CHMe_2)_3$), 12.2 ppm (4 $Si(CHMe_2)_3$); IR (ATR): $\tilde{\nu}_{max}$= 2941 (m), 2890 (w), 2864 (m), 1464 (m), 1450 (m), 1417 (w), 1387 (w), 1366 (w), 1301 (w), 1249 (w), 1229 (w), 1173 (w), 1098 (s), 1069 (m), 1017 (m), 994 (s), 960 (s), 881 (s), 828 (w), 791 (m), 726 (m), 680 (s), 658 cm^{-1}(s); HR-MALDI-MS: *m/z* (%): 1919.4211 (92, $[M + Na]^+$, calcd. for $C_{80}H_{124}I_4NaO_{12}Si_4^+$: 1919.4241), 1920.4235 (100), 1921.4241 (65).

AACs $(P)_4$-and $(M)_4$-72

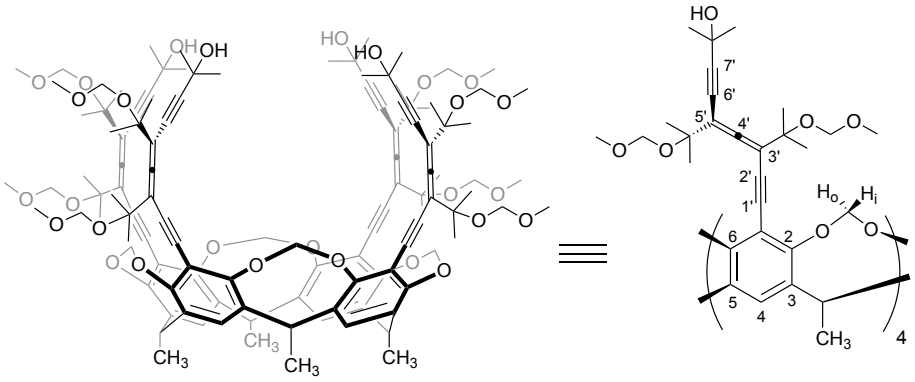

A suspension of cavitand **69** (200 mg, 182 µmol) and $[Pd(Ph_3P)_4]$ (42 mg, 16.4 µmol) in triethylamine (2.5 mL) was degassed with argon for 20 min, treated with CuI (7 mg, 36.4 µmol), and subjected to one freeze/pump/N_2 cycle. A solution of (*P*)-(+)-**74** (320 mg, 912 µmol) in triethylamine (1.5 mL) was degassed with argon for 20 min and added dropwise to the above suspension. The mixture was heated to 100 °C under a N_2 atmosphere for 12 h, diluted with sat. aq. NH_4Cl solution (10 mL), and extracted with EtOAc (3 x 20 mL). The combined organic phases were dried over Na_2SO_4 and concentrated *in vacuo*. MPLC (SiO_2; cyclohexane/EtOAc/MeOH 100:0:0 to 50:47.5:2.5) afforded the AAC $(P)_4$-**72** (231 mg, 64%) as a colorless solid.

The same synthetic procedure was applied for the $(M)_4$-configured enantiomer.

AAC $(P)_4$-**72**: $[\alpha]_D^{20}$ = + 361.8 (c = 0.1 in acetonitrile)

AAC $(M)_4$-**72**: $[\alpha]_D^{20}$ = – 359.0 (c = 0.1 in acetonitrile)

R_f = 0.33 (SiO_2; EtOAc, UV); m.p. 86–89 °C; ^{1}H NMR (400 MHz, $CDCl_3$, 25 °C; assignments based on DFQ COSY and HSQC NMR spectra): δ = 7.16 (s, 4 H; 4 H–C(4)), 5.90 (d, J = 7.3 Hz, 4 H; 4 H_{out} of OCH_2O), 5.01 (q, J = 7.3 Hz, 4 H; 4 C*H*Me), 4.81–4.68 (m, 8 H, 8 OC*H*$_2$OMe), 4.49 (d, J = 7.3 Hz, 4 H; 4 H_{in} of OCH_2O), 4.38 (s, 4 H; 4 OH), 3.40 (s, 12 H; 4 OCH_2O*Me*), 3.37 (s, 12 H; 4 OCH_2O*Me*), 1.73 (d, J = 7.4 Hz, 12 H; 4 CH*Me*), 1.54 and 1.52 (2 s, 24 H; 4 C*Me*$_2$OH), 1.46 and 1.43 (2 s, 24 H; 4 C*Me*$_2$$OCH_2OMe$) and 1.40 ppm (s, 12 H; 4 C*Me*$_2$$OCH_2OMe$); ^{13}C NMR (100 MHz, $CDCl_3$, 25 °C; assignments based on DFQ COSY, HSQC and HMBC NMR spectra): δ = 213.5 (4 C(4')), 155.2 and 154.8 (4 C(2,6), 139.4 and 139.3 (4 C(3,5), 119.7 (4 C(4)), 113.1 (4 C(1)), 101.4 (4 C(3')), 100.4 (4 C(5')), 100.1 (4 C(7')), 98.6 (4 OCH_2O), 92.4 (4 O*C*H_2OMe), 92.2 (4 O*C*H_2OMe), 89.4 (4 C(1')), 86.2 (4 C(2')), 78.2 (4 C(5')*C*Me_2OCH_2OMe), 77.5 (4 C(3')*C*Me_2OCH_2OMe), 73.2 (4 C(6')), 65.1 (4 *C*Me_2OH), 55.9 and 55.6 (8 OCH_2O*Me*), 31.5 and 31.0 (8 C*Me*$_2$OH), 30.9 (4 *C*HMe), 27.7 and 27.2 (8 C*Me*$_2$$OCH_2OMe$), 27.0 and 26.8 (8 C*Me*$_2$$OCH_2OMe$), 15.8 ppm (4 CH*Me*); IR (ATR): $\tilde{\nu}_{max}$= 3434 (br. w), 2979 (w), 2934 (w),1456 (w), 1397 (w), 1382 (w), 1363 (w), 1309 (w), 1229 (w), 1143 (m), 1086 (m), 1059 (w), 1029 (s), 980 (s), 958 (m), 941 (m), 919 cm^{-1}(m); HR-MALDI-MS: *m*/*z* (%): 2007.9752 (82, $[M + Na]^+$, calcd. for $C_{116}H_{144}NaO_{28}^+$: 2007.9742), 2008.9786 (100).

AACs (P)$_4$-and (M)$_4$-73

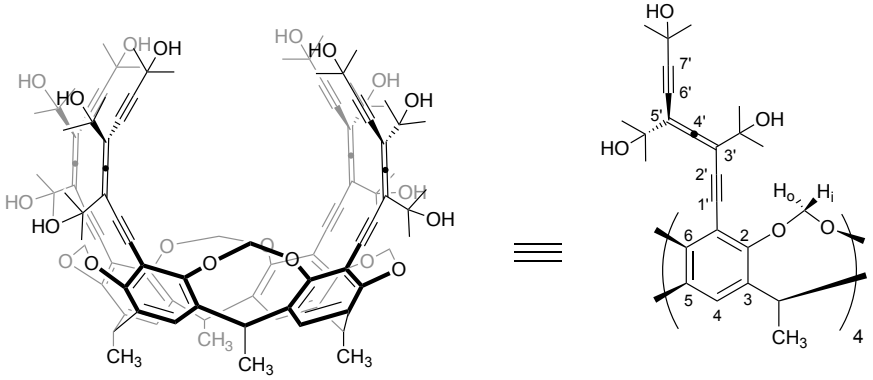

A solution of (P)$_4$-**72** (50 mg, 25 µmol) in MeOH (3.0 mL) in a PTFE (polytetrafluoroethylene) screw-capped glass vial, was treated with 1.25 M HCl in MeOH (1.0 mL, 1.3 mmol) for 3 h, diluted with H_2O (8 mL) and extracted with EtOAc (3 x 10 mL). The combined organic layers were washed with brine (3 mL), dried over Na_2SO_4, and concentrated *in vacuo*. Reverse phase HPLC (LiChrospher® 100 CN (5 µm) CN column; eluent: CH_3CN/H_2O 1:1) afforded AAC (P)$_4$-**73** (27 mg, 66 %) as a colorless solid.

The same synthetic procedure was applied for the (M)$_4$-configured enantiomer.

AAC $(P)_4$-**73**: $[\alpha]_D^{20} = +480.9$ ($c = 0.1$ in acetonitrile)

AAC $(M)_4$-**73**: $[\alpha]_D^{20} = -467.4$ ($c = 0.1$ in acetonitrile)

m.p. ≥ 150 °C (with decomp.); ^{1}H NMR (400 MHz, CD_3CN, 25 °C; assignments based on DFQ COSY and HSQC NMR spectra): $\delta = 7.53$ (s, 4 H; 4 H–C(4)), 5.89 (d, $J = 7.6$ Hz, 4 H; 4 H_{out} of OCH_2O), 4.97 (q, $J = 7.4$ Hz, 4 H; 4 C*H*Me), 4.44 (d, $J = 7.6$ Hz, 4 H; 4 H_{in} of OCH_2O), 3.87 (s, 4 H; 4 C(7')CMe_2*OH*), 3.51 (br. s, 4H; 4 OH), 3.42 (s, 4 H; 4 OH), 1.83 (d, $J = 7.5$ Hz, 12 H; 4 CH*Me*), 1.48 and 1.47 (2 s, 24 H; 4 C(7')C*Me*$_2$OH), 1.37 ppm (br. s, 48 H; 4 C(3')C*Me*$_2$OH and 4 C(5')C*Me*$_2$OH); ^{13}C NMR (100 MHz, CD_3CN, 25 °C; assignments based on COSY, HSQC and HMBC NMR spectra): $\delta = 211.1$ (4 C(4')), 155.6 and 155.5 (4 C(2,6), 140.8 and 140.8 (4 C(3,5), 122.2 (4 C(4)), 114.3 (4 C(1)), 105.0 and 104.8 (4 C(3',5'), 100.9 (4 C(7')), 99.6 (4 OCH_2O), 91.8 (4 C(1')), 85.7 (4 C(2')), 74.3 (4 C(6')), 72.8 and 72.7 (4 C(3',5')*C*Me_2OH and (4 C(5')*C*Me_2OH), 65.7 (4 C(7')*C*Me_2OH), 32.4 (4 *C*HMe), 31.8 and 31.7 (4 C(7')C*Me*$_2$OH), 29.4, 29.4, 29.3 and 29.3 (4 C(3')C*Me*$_2$OH and (4 C(5')C*Me*$_2$OH), 15.7 ppm (4 CH*Me*); IR (ATR): $\tilde{\nu}_{max}$= 3341 (br. w), 2975 (w), 2932 (w), 2886 (w), 1449 (w), 1381 (w), 1364 (w), 1305 (w), 1213 (w), 1143 (m), 1109 (m), 1083 (m), 1028 (s), 991 (m), 962 (s), 918 (m), 824 (w), 809 (w), 753 cm^{-1}(w); HR-MALDI-MS: *m*/*z* (%): 1655.7637 (91, $[M + Na]^+$, calcd. for $C_{100}H_{120}NaO_{20}^+$: 1655.7639), 1656.7672 (100), 1657.7707 (59) 1658.7742 (24).

AAC $(P)_4$-97

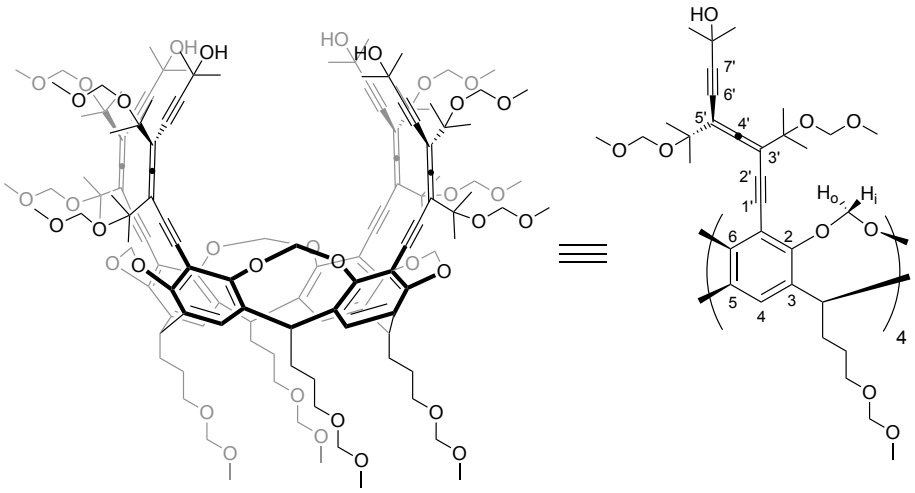

A suspension of cavitand **96** (155 mg, 107 μmol) and $[Pd(Ph_3P)_4]$ (25 mg, 21.4 μmol) in triethylamine (2.5 mL) was degassed with argon for 20 min. CuI (4 mg, 21.4 μmol) was added and the suspension subjected to a freeze/pump/N_2 cycle. A solution of (*P*)-(+)-**74** (200 mg, 567 μmol) in triethylamine (1.5 mL) was degassed with argon for 20 min and added dropwise

to the suspension of the cavitand. The resulting mixture was heated to 100 °C under a N_2 atmosphere for 14 h, diluted with sat. aq. NH_4Cl solution (10 mL), and extracted with EtOAc (3 x 30 mL). The combined organic phases were dried over Na_2SO_4 and concentrated *in vacuo*. MPLC (SiO_2; cyclohexane/EtOAc/MeOH 100:0:0 to 20:76:4) afforded AAC $(P)_4$-**97** (217 mg, 87%) as a pale brownish solid.

AAC $(P)_4$-**97**: $[\alpha]_D^{20} = +314.0$ ($c = 0.1$ in acetonitrile).

$R_f = 0.67$ (SiO_2; EtOAc/MeOH 95:5, UV); m.p. = 79–82 °C; ^{1}H NMR (400 MHz, $CDCl_3$, 25 °C; assignments based on DFQ COSY and HSQC NMR spectra): $\delta = 7.06$ (s, 4 H; 4 H–C(4)), 5.89 (d, $J = 7.2$ Hz, 4 H; 4 H_{out} of OCH_2O), 4.83 (t, $J = 8.2$ Hz, 4 H; 4 C*H*$CH_2CH_2CH_2O$), 4.80–4.68 (m, 16 H; 8 OC*H*$_2$OMe), 4.66 (s, 8 H; 4 OC*H*$_2$OMe), 4.47 (d, $J = 7.2$ Hz, 4 H; 4 H_{in} of OCH_2O), 4.37 (s, 4 H; 4 OH), 3.62 (t, $J = 6.1$ Hz, 8 H; $CHCH_2CH_2CH_2O$), 3.40, 3.39, 3.37 (3 s, 36 H; 12 OCH_2OMe), 2.42–2.22 (m, 8 H; 4 $CHCH_2CH_2CH_2O$), 1.65–1.60 (m, 8 H; 4 $CHCH_2CH_2CH_2O$), 1.53 and 1.52 (2 s, 24 H; 4 C*Me*$_2$OH) 1.46, 1.43 and 1.40 ppm (3 s, 36 H; 4 C*Me*$_2$$OCH_2OMe$); ^{13}C NMR (100 MHz, $CDCl_3$, 25 °C; assignments based on DFQ COSY, HSQC and HMBC NMR spectra): $\delta = 213.5$ (4 C(4')), 155.7 and 155.4 (4 C(2,6), 138.3 and 138.2 (4 C(3,5), 120.12 (4 C(4)), 113.3 (4 C(1)), 101.3 (4 C(3')), 100.4 (4 C(5')), 100.1 (4 C(7')), 98.7 (4 OCH_2O), 96.5 (4 $CH(CH_2)_3OCH_2OMe$), 92.4 and 92.2 (8 O*C*H_2OMe), 89.6 (4 C(1')), 86.1 (4 C(2')), 78.2 (4 C(5')*C*Me_2OCH_2OMe), 77.5 (4 C(3')*C*Me_2OCH_2OMe), 73.2 (4 C(6')), 67.1 (4 $CHCH_2CH_2CH_2O$), 65.1 (4 *C*Me_2OH), 55.9, 55.6 and 55.4 (12 OCH_2OMe), 36.4 (4 *C*$H(CH_2)_3O$), 31.5 and 30.9 (4 C*Me*$_2$OH), 27.9 (4 $CHCH_2CH_2CH_2O$), 27.6, 27.2, 27.0, and 26.8 (8 C*Me*$_2$$OCH_2OMe$), 26.4 ppm (4 $CHCH_2CH_2CH_2O$); IR (ATR): $\tilde{\nu}_{max}$= 3433 (br. w), 2980 (w), 2933 (w), 2886 (w), 1449 (w), 1382 (w), 1363 (w), 1305 (w), 1213 (w), 1143 (m), 1109 (m), 1083 (m), 1028 (s), 991 (m), 963 (s), 918 (m), 824 (w), 809 (w), 753 cm^{-1}(w); HR-MALDI-MS: *m*/*z* (%): 2360.1797 (73, $[M + Na]^+$, calcd. for $C_{132}H_{176}NaO_{36}^+$: 2360.18335), 2361.1854 (100).

AACs $(P)_4$-and $(M)_4$-71

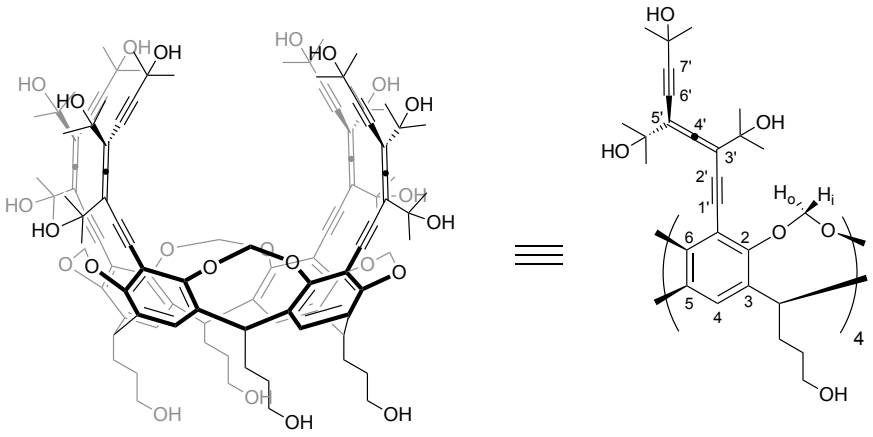

Procedure A:

A solution of AAC $(P)_4$-**97** (100 mg, 42.8 µmol) in MeOH (10 mL) in a PTFE screw-capped glass vial, was treated with a solution of 1.25 M HCl in MeOH (2.5 mL, 3.8 mmol), stirred for 22 h, diluted with brine (20 mL), and extracted with EtOAc (5 x 30 mL). The combined organic layers were dried over Na_2SO_4 and concentrated *in vacuo*. Reverse phase HPLC (LiChrospher® 100 CN (5 µm) CN column; eluent: CH_3CN/H_2O 35:65) afforded AAC $(P)_4$-**71** (17 mg, 22%) as a colorless solid.

Procedure B:

A suspension of cavitand **83** (100 mg, 52.7 µmol) and $[Pd(Ph_3P)_4]$ (12 mg, 10.5 µmol) in triethylamine (1.2 mL) was degassed with argon for 20 min, treated with CuI (2 mg, 10.5 µmol), and subjected to a freeze/pump/N_2 cycle. A solution of (*P*)-(–)-**74** (92 mg, 263 µmol) in triethylamine (0.8 mL) was degassed with argon for 20 min and added dropwise to the suspension of the cavitand. The resulting mixture was heated to 100 °C under a N_2 atmosphere for 15 h, diluted with H_2O (10 mL) and extracted with EtOAc (3 x 30 mL). The combined organic phases were washed with brine (10 mL), dried over Na_2SO_4, and concentrated *in vacuo*. MPLC (SiO_2; cyclohexane/EtOAc/MeOH 100:0:0 to 50:47.5:2.5) gave a crude brownish residue that was dissolved in MeOH (6.0 mL) in a PTFE screw-capped glass vial, treated with 1.25 M HCl in MeOH (2.0 mL, 2.5 mmol), stirred for 3 h, diluted with brine (10 mL), and extracted with EtOAc (4 x 20 mL). The combined organic layers were dried over Na_2SO_4 and concentrated *in vacuo*. Reverse phase HPLC (LiChrospher® 100 CN (5 µm) CN column; eluent: CH_3CN/H_2O 35:65) afforded $(P)_4$-AAC-**71** (38 mg, 40 % over to steps) as a colorless solid.

The same synthetic procedure was applied for the $(M)_4$-configured enantiomer.

$(P)_4$-AAC-**71**: $[\alpha]_D^{20} = +439.0$ (*c* = 0.1 in H_2O/acetonitrile 1:99)

(M)$_4$-AAC-**71**: $[\alpha]_D^{20} = -420.6$ (c = 0.1 in H_2O/acetonitrile 1:99)

m.p. ≥ 150 °C (with decomp.); ^{1}H NMR (400 MHz, CD_3CN/D_2O 98:2, 25 °C; assignments based on COSY and HSQC NMR spectra): δ = 7.47 (s, 4H; 4 H–C(4)), 5.89 (d, J = 7.6 Hz, 4 H; 4 H_{out} of OCH_2O), 4.75 (t, J = 8.2 Hz, 4 H; 4 CH(CH_2)$_3$OH), 4.44 (d, J = 7.6 Hz, 4 H; 4 H_{in} of OCH_2O), 4.14 (s, 4 H; 4 OH), 3.89 (s, 4 H; 4 OH), 3.78 (s, 4 H; 4 OH), 3.64–3.60 (m, 8 H; 4 CH(CH_2)$_2$CH_2OH), 3.23 (t, J = 5.5 Hz, 4H; 4 CH(CH_2)$_3$OH), 2.49–2.40 (m, 8 H; 4 CHCH_2(CH_2)$_2$OH), 1.53–1.49 (m, 8 H; 4 CHCH$_2$CH_2CH$_2$OH), 1.47 (2 s, 24H; 4 C(7')CMe_2OH), 1.37 ppm (br. s, 48H; 4 C(3')CMe_2OH and 4 C(5')CMe_2OH); ^{13}C NMR (100 MHz, CD_3CN/D_2O 98:2, 25 °C; assignments based on COSY, HSQC and HMBC NMR spectra): δ = 210.9 (4 C(4')), 155.9 and 155.8 (4 C(2,6)), 139.6 (4 C(3,5)), 123.0 (4 C(4)), 114.2 (4 C(1)) 104.8 and 104.7 (4 C(3',5')), 100.7 (4 C(7')), 99.6 (4 OCH_2O), 91.6 (4 C(1')), 85.6 (4 C(2')), 74.3 (4 C(6')), 72.7 and 72.6 (4 C(3')CMe$_2$OH and (4 C(5')CMe$_2$OH), 65.6 (4 C(7')CMe$_2$OH), 62.4 (4 CH(CH_2)$_2$$CH_2$OH), 37.9 (4 CH(CH_2)$_3$OH), 31.9, 31.6 and 31.5 (4 (C(7')CMe_2OH and 4 (CHCH$_2$(CH_2)$_2$OH), 29.2, 29.2, 29.2 and 29.1 (4 C(3')CMe_2OH and 4 C(5')CMe_2OH), 26.4 ppm (4 CHCH$_2$$CH_2CH_2$OH); IR (ATR): $\tilde{\nu}_{max}$= 3339 (br., w), 2977 (w), 2934 (w), 1456 (m), 1361 (m), 1308 (w), 1247 (w), 1156 (s), 1099 (m), 1061 (w), 1021 (m), 982 (s), 949 (s), 892 (w), 842 (m), 800 (w), 766 (w), 742 (w), 707 (w), 677 (w), 663 cm^{-1}(m); HR-MALDI-MS: m/z (%): 1831.8639 (84, [M + Na]$^+$, calcd. for $C_{108}H_{128}NaO_{24}^+$: 1831.8639), 1832.8675 (100), 1833.8709 (64).

(*M*)$_4$-98

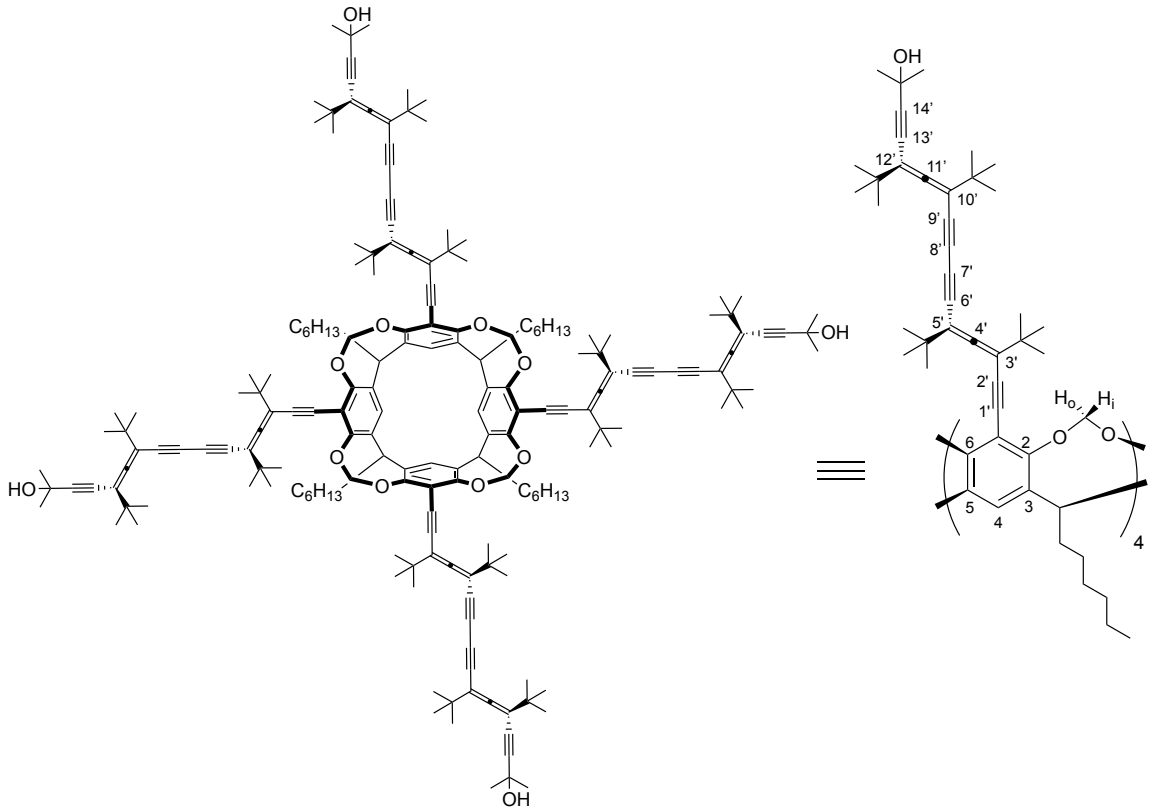

A 10 mL Schlenk tube was loaded with tetraiodo tetrahexyl cavitand **59** (20 mg, 15.0 µmol) and [Pd(Ph$_3$P)$_4$] (2 mg, 1.8 µmol), flushed with N_2, treated with triethylamine (0.6 mL), subjected to a freeze/pump/N_2 cycle, treated with CuI (0.5 mg, 1.8 µmol), and again subjected to freeze/pump/N_2 cycles (2x). A second 10 mL Schlenk tube was charged with (*M*)$_2$-(–)-**99** (27 mg, 58 µmol), flushed with N_2, treated with triethylamine (0.3 mL), subjected to a freeze/pump/N_2 cycle, and added to the first Schlenk tube. The resulting mixture was heated to 100 °C under N_2 for 9 h and washed with a sat. aq. NH_4Cl. The aqueous phase was extracted with EtOAc (3 x 20 mL). The combined organic phases were washed with brine, dried over Na_2SO_4, and concentrated *in vacuo*. Flash column chromatography (SiO_2; cyclohexane/EtOAc 9:1 to 7:3) afforded the (*M*)$_4$-**99** (7 mg, 18%) as a off-white solid.

(*M*)-(–)-**99**: $[\alpha]_D^{20} = -433.8$ (*c* = 0.2 in *n*-hexane).

R_f = 0.25 (SiO_2; cyclohexane/EtOAc 8:2, UV); m.p. 133 °C; ^{1}H NMR (400 MHz, $CDCl_3$, 25 °C; assignments based on DFQ COSY and HSQC NMR spectra): δ = 7.01 (s, 4 H; 4 H–C(4)), 5.87 (d, *J* = 7.2 Hz, 4 H; 4 H_{out} of OCH_2O), 4.79 (t, *J* = 8.1 Hz, 4 H; 4 HC–C(3)), 4.49 (d, *J* = 7.2 Hz, 4 H; 4 H_{in} of OCH_2O), 2.15–2.21 (m, 8 H; 4 CH_2(CH$_2$)$_4$Me), 2.04 (br. s, 4 H, 4 OH), 1.55 (s, 24 H;4 CMe_2OH), 1.28–1.37 (m, 32 H; 4 CH$_2$(CH_2)$_4$Me, 1.15 (s, 36 H, 4 CMe$_3$), 1.14 (s, 36 H, 4 CMe$_3$), 1.12 (s, 72 H, 8 CMe$_3$), 0.90 ppm (t, *J* = 6.7 Hz, 12 H; 4 Me); ^{13}C NMR

(101 MHz, $CDCl_3$, 25 °C; assignments based on DFQ COSY, HSQC, and HMBC NMR spectra): δ = 213.7 and 213.3 (4 C(4',11')), 155.3 and 155.3 (4 C(2,6)), 138.5 and 138.5 (4 C(3,5)), 120.0 (4 C(4)), 113.6 (4 C(1)), 104.5 and 103.4 (4 C(3',10')), 103.1 and 102.9 (4 C(5',12')), 98.5 (4 OCH_2O), 98.0 (4 C(14')), 91.0, 85.1, 75.6, 75.7, 75.5, and 75.0 (4 C(1',2',6',7',8',9'13')), 65.9 (4 *C*Me_2OH), 36.7 (4 *C*H–C(3)), 36.1 (4 *C*Me_3), 36.0 (4 *C*Me_3), 35.9 (4 *C*Me_3), 35.8 (4 *C*Me_3), 32.0 (C(1) of 4 hexyl), 31.6 (4 C*Me*$_2$OH), 29.7, 29.5 (C(2,3) of 4 hexyl), 29.2, 29.0, 29.0 (16 C*Me*$_3$), 27.9 (C(4) of 4 hexyl), 22.8 (C(5) of 4 hexyl), 14.2 (4 Me). IR (ATR): $\tilde{\nu}_{max}$ = 3402 (w, br.), 2962 (m), 2927 (m), 2865 (m), 1950 (w), 1460 (m), 1447 (m), 1437 (m), 1393 (m), 1376 (m), 1362 (m), 1296 (w), 1240 (m), 1155 (m), 1070 (m), 1020 (m), 970 (s), 906 (m), 847 (w), 806 (w), 755 (m), 732 (w), 684 (w), 634 cm^{-1} (w); HR-MALDI-MS: *m*/*z* (%): 2689.8103 (43, $[M]^+$, calcd. for $C_{188}H_{240}O_{12}^+$: 2689.8164), 2690.8140 (93), 2691.8176 (100), 2692.8211 (73), 2693.8247 (40); 2712.8053 (49, $[M + Na]^+$, calcd. for $C_{188}H_{240}O_{12}^+$: 2712.8062), 2713.8091 (98), 2714.8133 (100), 2715.8172 (67).

AAC (*P*)$_4$-90

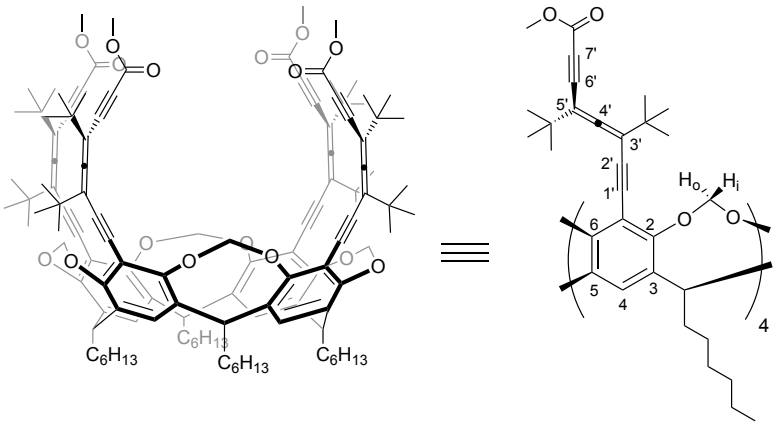

Step 1:

A solution of (*P*)$_4$-**89** (10 mg, 0.42 mmol) in THF (1 mL) under argon was cooled to –100 °C in a methanol/N_2(*l*), treated dropwise with 1.6 M *n*-BuLi in *n*-hexane (45 µL, 72 µmol) while maintaining –100 °C. The solution was warmed to –70 °C over 30 min, cooled to –78 °C, treated with CO_2 bubbling through the solution from dry ice *via* a cannula over 1 h, warmed to 23 °C, acidified with an aqueous 1 M HCl solution, and extracted with EtOAc (3 x 5 mL). The combined organic phases were washed with brine, dried over Na_2SO_4, and concentrated *in vacuo*. After filtration over Celite®, the crude acid was directly subjected to the next step.

Step 2:

A solution o fthe crude acid in dry THF/MeCN 10:3 was treated with K_2CO_3 (8.3 mg, 60 µmol), MeI (38 µL, 60 µmol), stirred for 20 h at 25 °C and diluted with H_2O (10 mL). The aqueous phase was extracted with EtOAc (3 x 10 mL). The combined organic phases were washed with brine, dried over Na_2SO_4, and concentrated *in vacuo*. Flash column chromatography (SiO_2; cyclohexane/EtOAc 95:5 to 9:1) afforded AAC $(P)_4$- 90 (3 mg, 33%) as a white solid.

AAC $(P)_4$- 90: $[\alpha]_D^{20} = -47.6$ (c = 0.10 in *n*-hexane).

R_f = 0.20 (SiO_2; cyclohexane/EtOAc 95:5, UV); m.p. 204 °C; ^{1}H NMR (400 MHz, $CDCl_3$, 25 °C; assignments based on DFQ COSY and HSQC NMR spectra): δ = 7.03 (s, 4 H; 4 H–C(4)), 5.85 (d, J = 7.2 Hz, 4 H; 4 H_{out} of OCH_2O), 4.80 (t, J = 8.1 Hz, 4 H; 4 HC–C(3)), 4.50 (d, J = 7.2 Hz, 4 H; 4 H_{in} of OCH_2O), 3.79 (s, 12 H; 4 CO_2*Me*), 2.15–2.21 (m, 8 H; 4 C*H*$_2$(CH$_2$)$_4$Me), 1.28–1.40 (m, 32 H; 4 CH$_2$(C*H*$_2$)$_4$Me, 1.14 and 1.14 (2 s, 72 H; 8 CMe$_3$), 0.90 ppm (t , J = 6.7 Hz, 12 H; 4 Me); ^{13}C NMR (101 MHz, $CDCl_3$, 25 °C; assignments based on DFQ COSY, HSQC and HMBC NMR spectra): δ = 213.7 (4 C(4')), 155.3 and 155.3 (4 C(2,6)), 154.4 (4 *C*OOMe), 138.6 and 138.5 (4 C(3,5)), 120.3 (4 C(4)), 113.3 (4 C(1)), 105.3 (4 C(3')), 101.2 (4 C(5')), 98.5 (4 OCH_2O), 90.1 (4 C(7')) and 86.1 (4 C(1')), 83.4 (4 C(2')), 80.1 (4 C(6')), 52.8 (4 CO_2*Me*)), 36.7 (4 *C*H–C(3)), 35.9 and 35.9 (8 *C*Me$_3$)), 32.0 (4 C(1) of hexyl), 29.9 and 29.7 (4 C(2,3) of hexyl), 29.1 and 28.9 (8 C*Me*$_3$), 27.9 (C(4) of 4 hexyl), 22.8 (C(5) of 4 hexyl), 14.2 (4 Me); IR (ATR): $\tilde{\nu}_{max}$ = 2962 (m), 2927 (m), 2856 (m), 2793 (w), 2209 (w), 1715 (m), 1697 (w), 1603 (w), 1505 (w), 1461 (m), 1449 (m), 1434 (m), 1395 (w), 1363 (m), 1259 (s), 1234 (m), 1199 (w), 1156 (w), 1090 (s), 971 (s), 873 (w), 797 (s), 748 (w), 694 (w), 639 (w), 621 cm^{-1} (w). HR-MALDI-MS: *m*/*z* (%): 1897.1097 (60, $[M]^+$, calcd. for $C_{124}H_{152}O_{16}^+$: 1897.1075), 1898.1132 (100), 1899.1168 (80), 1900.1205 (40), 1901.1239 (15).

Cyclohexyl Benzoate (100)[324]

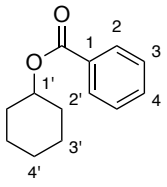

A solution of cyclohexanol (200 mg, 2.00 mmol) in *n*-octane (2.0 mL) in a PTFE screw-capped glass vial, was treated with pyridine (200 µL, 2.4 mmol), benzoyl chloride (280 µL, 2.4 mmol), stirred for 24 h, filtered and washed with 2 mL of *n*-pentane. Evaporation and MPLC (SiO_2; *n*-pentane/Et_2O 10:0 to 9:1) gave cyclohexyl benzoate (**100**) (361 mg, 88%) as a volatile colorless oil. Spectroscopic properties of **100** were identical to those previously reported.[324]

R_f = 0.79 (SiO_2; *n*-pentane/Et_2O 1:9, UV); ^{1}H NMR (400 MHz, $CDCl_3$, 25 °C; assignments based on DFQ COSY and HSQC NMR spectra): δ = 8.30–7.80 (m, 2 H; H–C(2,6)), 7.63–7.49 (m, 1 H; H–C(4)), 7.48–7.36 (m, 2 H; H–C(3,5), 5.04 (tt, J = 8.8, 3.8 Hz, 1 H; H–C(1')), 2.05–1.16 ppm (m, 10 H; C(2',3',4',5',6')H_2); ^{13}C NMR (100 MHz, $CDCl_3$, 25 °C; assignments based on DFQ COSY, HSQC and HMBC NMR spectra): δ = 166.1 (C=O), 132.8 (C(4)), 131.2 (C(1)), 129.7 (C(2,6)), 128.4 (C(3,5)), 73.2 (C(1')), 31.8 (C(2',6')), 25.6 ppm (C(4')), 23.8 (C(3',5'); HR-ESI-MS: *m*/*z* (%): 227.1044 (100, $[M + Na]^+$, calcd. for $C_{13}H_{16}NaO_2^+$: 227.1043).

(±)-*trans*-1,2-Bromomethylcyclohexane 101[325]

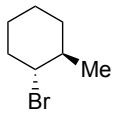

(±)

The synthesis was adapted from the literature.[325] A solution of *cis*-2-Methylcyclohexanol (1g, 8.76 mol) in diethylether (22 mL) was cooled to 0 °C, treated with PPh_3 (4.50 g, 13.2 mol) at 0°C and portionwise with CBr_4 (3.45 g, 13.2 mol) over 10 min. The suspension was stirred at 0 °C for 30 min, warmed to 25 °C, stirred for 20 h, diluted with *n*-pentane (10 mL), stirred for 10 min, and filtered. Evaporation and flash column chromatography (Al_2O_3, activity III; *n*-pentane) gave **101** (280 mg, 18%) as a colorless liquid.

R_f = 0.80 (Al_2O_3; *n*-pentane, $KMnO_4$); ^{1}H NMR (400 MHz, $CDCl_3$, 25 °C; assignments based on DFQ COSY and HSQC NMR spectra): δ = 3.72 (ddd, J = 11.7, 10.4, 4.2 Hz, 1 H; H–C(1)), 2.37–2.31 (m, 1 H; H–C(2)), 1.90–1.79 (m, 2 H; H_{eq}–C(3,6)), 1.77–1.50 (m, 4 H; H–C(4,5)), 1.37–1.23 ppm (m, 2 H; H_{ax}–C(3,6)); ^{13}C NMR (101 MHz, $CDCl_3$, 25 °C; assignments based on DFQ COSY, HSQC, and HMBC NMR spectra): δ = 62.3 (C(1)), 41.8 (C(2)), 39.0 (C(6)), 35.4 (C(3)), 27.7 (C(4)), 25.8 (C(5)), 22.1 ppm (Me); IR (ATR): $\tilde{\nu}_{max}$ = 2975 (m), 2929 (s), 2857 (m), 1447 (s), 1378 (m), 1331 (w), 1261 (m), 1188 (s), 1125 (w), 1077 (w), 1048 (w), 984 (w), 973 (w), 946 (s), 904 (m), 856 (m) cm^{-1} (w).

9.2.7 Synthesis of Alkyl Alcohols and Alkyl Haloalcohols

A summary of the acyclic halogenated and non-halogenated alcohols is shown below (Figure 130). The series of alcohols was prepared by Dr. Stefan Fischer. The synthesis is described in the PhD Thesis of Dr. Stefan Fischer, obtained under the supervision of Prof. Erick M. Carreira.[294] All compounds were synthesized as their racemic mixtures were resolved by

preparative HPLC using the CSP Diacel Chiralpak® IA (Diacel Chemical Industries Ltd.). Elution was performed with a mixture of *n*-hexane/EtOH at a flow of 18 mL min^{-1}.

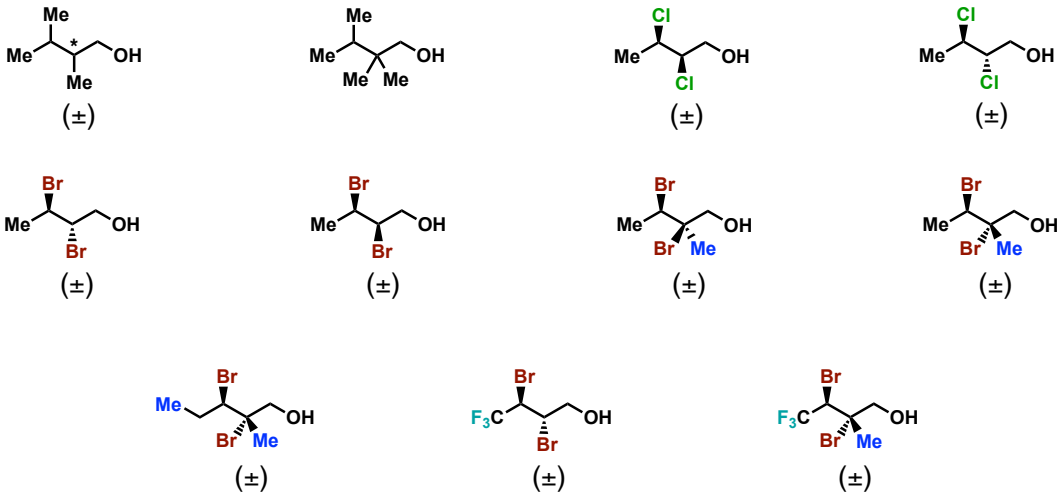

Figure 130. Summary of acyclic non-halogenated and halogenated alcohols, which were synthesized by Dr. Stefan Fischer under the supervision of Prof. E. M. Carreira.

9.3 Methods for Solution Binding Studies

Choice of the solvent system: The choice of an appropriate solvent was evaluated prior to titration in ECD, NMR and ITC titration experiments. The crucial factor was believed to be the usage of non- or weakly competitive solvents, nonetheless maintaining some preorganization of either conformation. Importantly, for ECD titrations it was necessary to choose UV/Vis-silent solvents. We chose *n*-octane as apolar solvent, which is too large and too dynamic to fully enable the closed conformation, but nevertheless assures a certain degree of preorganization of the cage form. In order to show that *n*-octane gives similar binding isotherms to those in the well-established mesitylene as non-competitive solvent for binding studies with resorcin[4]arene cavitands, the binding isotherms of cycloheptane were exemplarily measured in both mesitylene and *n*-octane. Methanol was chosen to provide some degree of preorganization to the open form with the smaller binding cavity. For the more polar AACs, a mixture of methanol and water was chosen.

Determination of binding stoichiometry

At fast exchange on the NMR timescale: The continuous variation method, Job plot, has been the most popular method for determining binding stoichiometry at fast exchange on the NMR time scale.[181] Binding stoichiometry between the AACs and the guest was determined exemplary for cycloheptane with AAC $(P)_4$-**62** by Job's method of continuous variations by the ^{1}H NMR spectroscopy. Stock solutions of AAC $(P)_4$-**62** and cycloheptane were prepared in *n*-octane-d_{18} (~10 mM). Ten samples of different compositions of host-to-guest were measured. The product of the NMR shift ($\Delta\delta$) of H_i of the AAC $(P)_4$-**62** and the guest mole fraction ($\chi_{cycloheptane}$) was plotted against $\chi_{cycloheptane}$ (Figure 54). The maximum of around 0.5 indicated 1:1 host to guest stoichiometry. Together with obtained X-ray co-crystals and NMR studies we assumed a 1:1 host to guest stoichiometry.

At slow exchange on the NMR timescale: At slow exchange the complexed guests showed 1:1 host-guest-ration by integration (see exemplary for AAC $(P)_4$-**62** with *trans*-1,2-bromomethylcyclohexane, Figure 78). After the addition of 13 eq. of *trans*-1,2-dibromocyclohexane AAC $(P)_4$-**62** in *n*-octane-d_{18} at 277 K, 1 equiv. of the guest was complexed, while 12 equiv. were free in solution. In order to verify that the guests were complexed in the interior of the AAC $(P)_4$-**62**, ROESY NMR studies were done with all guests. Hereby, the complexed guests showed ROESY correlations with the H_i-Proton of the host at slow exchange on the NMR time scale. For fast exchange on the NMR time scale, correlation of H_i was observed with the resonance corresponding to the guest molecule. Significant

correlation of the guest with the H_i of the host was only be observed for the complexed guest (see exemplary Figure 75).

Preparation of solutions for ECD titrations: A solution of the AAC, referred to as "host", was prepared gravimetrically (~10 μM) in *n*-octane. The parent solution was used to prepare the stock solution of the varied component, referred to as "guest". All studies were carried out under air atmosphere without drying of the solvents prior to use. Portions of the guest solution were added stepwise, and the ECD spectrum was recorded after each addition. During titration, the change in $\Delta\Delta\varepsilon$ (M^{-1} cm^{-1}) was followed at a specific wavelength (304 nm).

Preparation of solutions for ^{1}H NMR titrations: A solution of the AAC, referred to as "host", was prepared gravimetricically (~1 mM) in *n*-octane-d_{18}. The parent solution was used to prepare the stock solution of the varied component, referred to as "guest". All studies were carried out under air atmosphere without drying of the solvents prior to use. Portions of the guest solution were added stepwise, and the ^{1}H NMR spectrum was recorded after each addition. During titration (fast exchange on the NMR time scale), the change in $\Delta\delta$ (ppm) was followed. At slow host-guest exchange exchange, of the guest binding constants were deduced *via* integration of free and complexed guest or host ^{1}H NMR signals.

Determination of the binding constant: During ECD titrations, the change in $\Delta\Delta\varepsilon$ (M^{-1} cm^{-1}) was followed at 304 nm. The change in $\Delta\Delta\varepsilon$ (M^{-1} cm^{-1}) was plotted against the guest concentration and curve-fitted to a 1:1 binding isotherm (for determination of binding stoichiometry prior to experiment). Determination of the association constant using NMR was performed in a similar manner, following the change in $\Delta\delta$ and plotted against the guest concentration or by integration of the free and complexed host or guest signals. Protons depicted in Figure S1 were followed during NMR titrations. The reported association constant was derived from an average of association constants following the shifts of the highlighted protons in Figure 55.

The data was curve-fitted using the software IGOR Pro V6.12 according to the following equation.[326]

$$\Delta\delta = \frac{\Delta\delta_{sat}}{2}\left[\left(\frac{[G]_0}{[H]_0} + 1 + \frac{1}{K_a[H]_0}\right) - \sqrt{\left(\frac{[G]_0}{[H]_0} + 1 + \frac{1}{K_a[H]_0}\right)^2 + \frac{[G]_0}{[H]_0}}\right]$$

with $\Delta\delta = (\delta_{sat} - \delta_0)\frac{[C]}{[H]_0}$

where the following parameters were applied:

$\Delta\delta$	Change in relative shift to the free host

$\Delta\delta_{sat}$	Calculated change in chemical shift at saturation binding
$[H]_0$	Constant host concentration (M)
$[G]$	Guest concentration (M)
K_a	Association constant (M^{-1})

The overall error in K_a was estimated to be 20%. This error was estimated as we assumed that the errors in the preparation process for the solutions are higher than the actual fitting errors. At slow exchange (e.g. for iodocyclohexane) on the NMR time scale, two distinct signals for the free and the complexed host and guest were observed in the NMR spectrum. Integration of theses signals allowed for determination of the average K_a by applying the following equation:

$$K_a = \frac{[C]}{([H_0] - a[HG])^a . ([G_0] - b[HG])^b}$$

with $[HG] = \frac{n}{n+m}\frac{[H_0]}{a}$

and n = integer of bound guest or host, m = integer of free guest or host and $a = b = 1$.[180]

Determination of dimerization: In order to compare binding isotherms which were acquired at different concentrations by NMR (~10 mM) and ECD (~10 µM), dilution studies were performed on $(P)_4$-AAC in both methanol and *n*-octane. Although various mechanisms of aggregation are possible, we assumed dimerization to occur. A stock solution of the AAC in the respective solvent was prepared gravimetricically (~5 mM) in either *n*-octane-d_{18} or CD_3OD. Portions of the stock solution were added stepwise to the pure solvent, *n*-octane-d_{18} or CD_3OD, and the ^{1}H NMR spectrum was recorded after each addition. During the dilution studies, shifts of the methyl-groups in $\Delta\delta$ (ppm) of the tertiary alcohol moiety was followed, as dimerization is assumed to involve the OH groups.

During the ^{1}H NMR dilution study, the change in δ (ppm) was followed. δ (ppm) was plotted against the guest concentration and curve-fitted to a dimerization isotherm. Protons depicted in Figure 55 were followed during NMR titrations. The data set was curve-fitted using the software IGOR Pro V6.12 according to equation (A) which corresponds to a homodimeric dissociation. $1/K_{dim}$ corresponds to the association constant K_{ass}.

(A) $\delta_{obs} = \delta_{obs} + (\delta_D - \delta_M)\frac{4[M]_0 + K_d - \sqrt{4[M]_0 K_d + {K_d}^2}}{4[M]_0}$

with (B) $K_d = \frac{[M]^2}{[D]} = \frac{([M]_0 - 2[D])^2}{[D]}$ and (C) $\delta_{obs} = \frac{[M]}{2[D]+[M]}\delta_M + \frac{2[D]}{2[D]+[M]}\delta_D$

where (B) is the law mass for a homodimeric species and (C) the observed chemical shift δ_{obs} as weighted average of the chemical shift of the monomeric species δ_M and the dimeric species δ_D.

The following parameters were applied:

δ_{obs}	Observed chemical shift
δ_M	Chemical shift of the monomeric species
δ_D	Chemical shift of the dimeric species
$[M]_0$	Initial concentration (M)
$[M]$	Concentration of monomer (M)
$[D]$	Concentration of dimer (M)
K_d	Dissociation constant (M)

The overall error in K_{ass} was estimated to be 20%.

Preparation of solutions for ITC titrations: A solution of the AAC, referred to as "host", was prepared gravimetrically (~0.1 mM) in *n*-octane. The "guest" solution was prepared in concentration between 1–10 mM depending on the order of magnitude of the expected binding constant. All studies were carried out under air atmosphere without drying of the solvents prior to use at 303 K. From ITC experiments thermodynamic values of K_a, ΔG, ΔH and ΔS were obtained.

9.4 Structures Obtained from Single-Crystal X-ray Diffraction of AACs 62

9.4.1 General Crystallization Protocol

Procedure A: To obtain single crystals suitable for X-ray diffraction, enantiopure AACs $(P)_4$- or $(M)_4$-**62**(~1 mg) were dissolved in acetonitrile:H_2O 9:1 (1mL) and the non-crystalline guest was added (~1–2 mg). The open vial (1 mL) was then placed into a second vial (2 mL) containing H_2O, which was sealed. By slow evaporation of acetonitrile and diffusion of H_2O at room temperature (25°C), crystallization occurred over 1–3 days. The single crystals were studied by single crystal X-ray diffraction.

Procedure B: Enantiopure AACs $(P)_4$- or $(M)_4$-**62** (~1 mg) were dissolved in dry acetonitrile (1mL) and the non-crystalline guest was added (~1–2 mg). The open vial (1 mL) was then placed into a second empty vial (2 mL), which was sealed and the plastic lid was perforated. By slow evaporation of acetonitrile at room temperature (25°C) crystallization occurred over 1–3 days. The single crystals were studied by single crystal X-ray diffraction.

All X-ray co-crystal structures presented herein show $P2_1P2_1P2_1$ or $P2_1$ as space group. These usually exhibited only one cavity occupied by a guest molecule. Occasionally, they showed disorder in the top hydrogen bonding array and alkyl periphery, overall decreasing structure quality. Occasionally, monoclinic structures were found, but these crystals reliably and irreversibly relaxed into the orthorhombic forms shown here upon slow cooling from room temperature (23 °C). For this compound class, the presented X-ray co-crystal structures show comparatively high resolution and low *R* values, meeting generally accepted small molecule crystal structure publication standards.

9.4.2 Disorder and Packing of the AACs $(P)_4$- and $(M)_4$-62 in the Solid-State Structures

Open AACs conformation: disorder and packing of the AAC in the open conformation are very similar for independently crystallized samples. Therefore, disorder of the alkyl chains and the packing of the AAC $(P)_4$-**62** in the open conformation are shown and discussed exemplary for structure CCDC-1496457 (acetonitrile guest). The asymmetric unit contains three acetonitrile molecules, one of which rests within the cavity. This disorder is correlated with another in the terminus of one nearby *n*-hexyl chain, with an occupation of 70% in the main orientation. For more information on the obtained X-ray co-crystal structures, see supplementary data at The Cambridge Crystallographic Data Centre: https://www.ccdc.cam.ac.uk/getstructures.

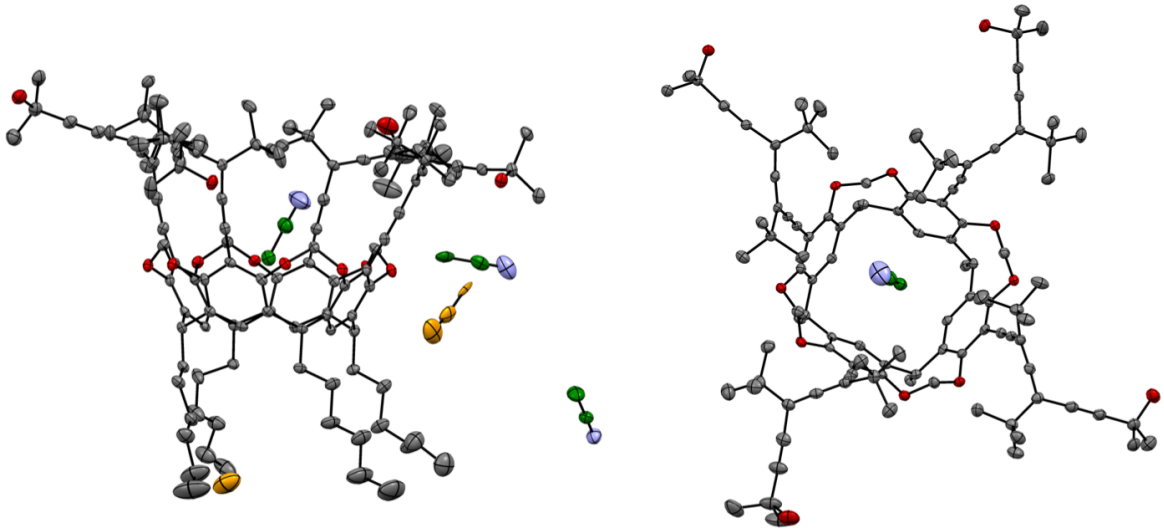

Figure 131. AAC $(P)_4$-**62** in the open conformation with one acetonitrile occupying the cavity and three acetonitrile molecules outside the cavity (green). The minor contribution to the disorder of the X-ray crystal structure is depicted in orange, showing 30% occupancy. Ellipsoids are shown at 50% probability. Right: Top view of the AAC $(P)_4$-**62** in the open conformation with one acetonitrile in the cavity. Acetonitrile molecules outside the cavity are omitted for clarity. *n*-Hexyl chains are omitted for clarity.

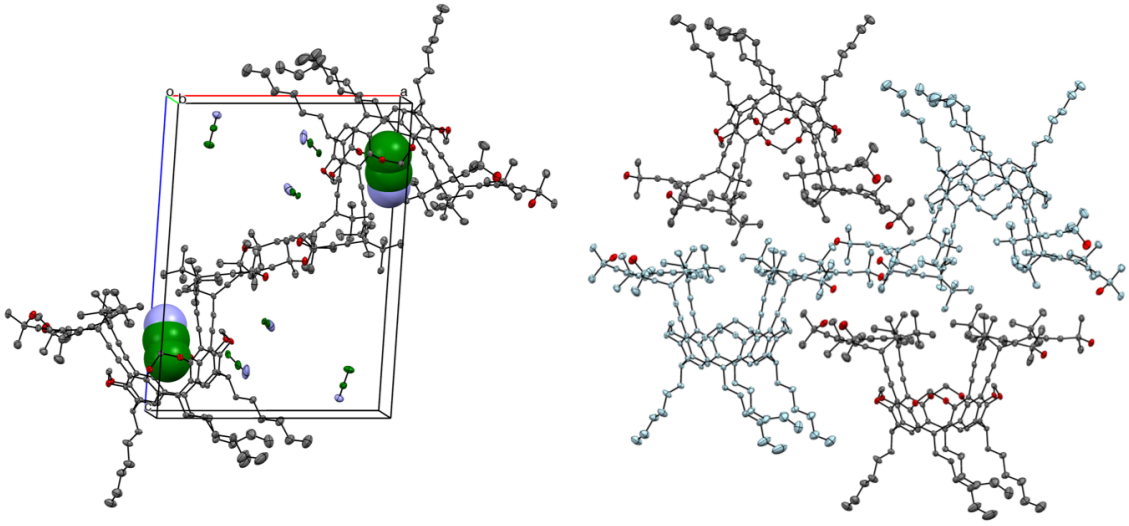

Figure 132. Left: Unit cell of AAC $(P)_4$-**62**⊃acetonitrile. Encapsulated acetonitrile is presented in the space filling representation. Right: Packing of the crystal structure of the AAC $(P)_4$-**62** in the open conformation. AAC $(P)_4$-**62** form dimers, in which the tertiary alcohol of one AAC $(P)_4$-**62** is engaged in hydrogen bonds to the neighboring AAC $(P)_4$-**62**. The extended packing shows layers of AAC $(P)_4$-**62**. The second layer stacks in hydrophobic interactions onto the first layer. Acetonitrile molecules are omitted for clarity.

Closed AAC conformation: since the disorder and packing of the AAC in the closed circular fourfold hydrogen-bonded conformation are very similar for independently crystallized samples, the disorder of the *n*-hexyl chains and the packing of the AAC $(P)_4$-**62** in the closed conformation are shown and discussed exemplary with structure CCDC-1496463 (cycloheptane guest). The asymmetric unit contains one fully occupied and one partially occupied acetonitrile molecule. Three *n*-hexyl chains ends are disordered over two positions, with an occupation of 70% in the main orientation. The minor orientation contains the partially occupied acetonitrile, lodged between two disordered alkyl chains. Weak residual peaks of an additional acetonitrile were also found in almost all other structures of the closed AAC $(P)_4$-**62**, but occupancies were always negligible and thus not modeled. Orientations and even relative occupations of the disordered alkyl chains are very similar in all structures. For more information on the obtained X-ray co-crystal structures, see supplementary data at The Cambridge Crystallographic Data Centre: https://www.ccdc.cam.ac.uk/getstructures.

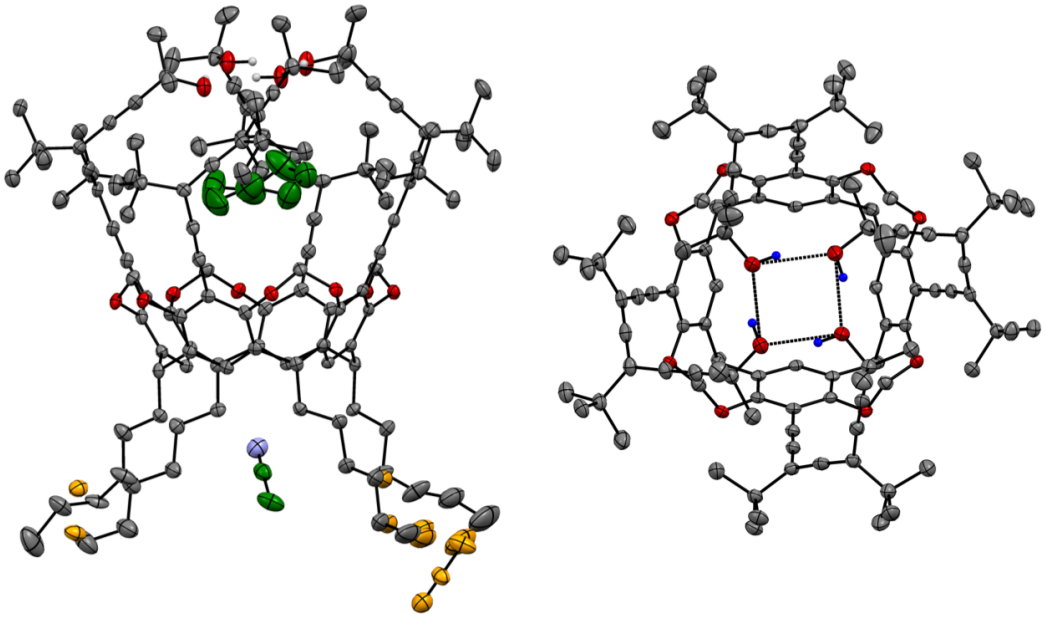

Figure 133. AAC $(P)_4$-**62** in the closed hydrogen-bonded conformation with cycloheptane occupying the cavity and two acetonitrile positions outside the cavity. The minor contribution to the disorder in the X-ray crystal structure is depicted in orange, showing 30% probability. Ellipsoids are shown at 50% probability. Right: Top view of the AAC $(P)_4$-**62** in the closed hydrogen-bonded conformation, the guest is omitted for clarity. The circular hydrogen-bonding array is highlighted in dark blue. Acetonitrile molecules outside the cavity and *n*-hexyl chains are omitted for clarity.

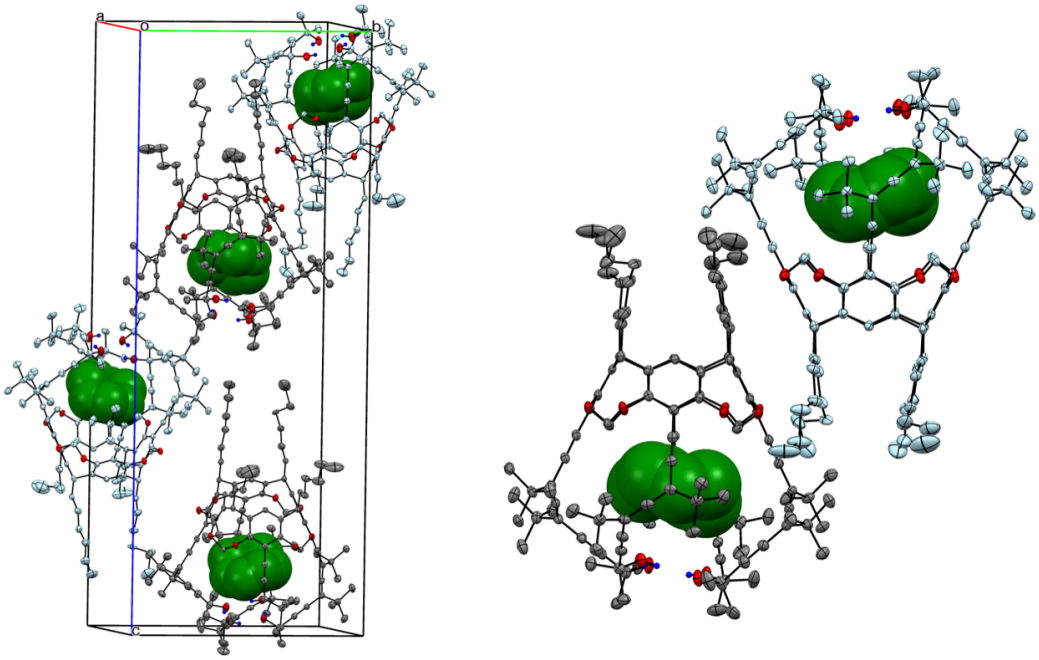

Figure 134. Left: Unit cell of AAC $(P)_4$-**62**⊃cycloheptane. Right: Packing of the crystal structure of the AAC $(P)_4$-**62** in the closed hydrogen-bonded conformation with encapsulated cycloheptane shown in space filling representation. AAC $(P)_4$-**62** are packed in a head-to-tail fashion with hydrophobic contacts. Residual acetonitrile molecules are omitted for clarity.

Adaptability of the host cavity size to the size of the guest: X-ray co-crystal structures of AACs $(P)_4$- and $(M)_4$-**62** revealed adaptability of the size and shape of the cavity based on the guest in our previous study. For smaller guests, AACs $(P)_4$- or $(M)_4$-**62** compensated for the insufficient space filling by the guest by rotating a methyl group of the cyclic tertiary alcohol array (C(*Me*)$_2$OH) into the cavity. When the size of the guest increased, all methyl groups of the tertiary alcohols were rotated outside of the cavity. This effect was also observed with multiple guests and was discussed in detail for specific examples (Figure 57 and 65).

Circular fourfold hydrogen-bonding array: In co-crystal structures of $(P)_4$-configured host **62**, the hydrogen-bonding array followed a clockwise configuration, while in the co-crystal structure of the $(M)_4$-configured enantiomer the array followed a counter-clockwise configuration (see top view, Figure 135). Hydrogen positions could be identified crystallographically for several structures and this is mentioned accordingly. The orientation of the hydrogen-bonding array is directed by the configuration of the AACs $(P)_4$- and $(M)_4$-**62** and is independent of the configuration of the guest.

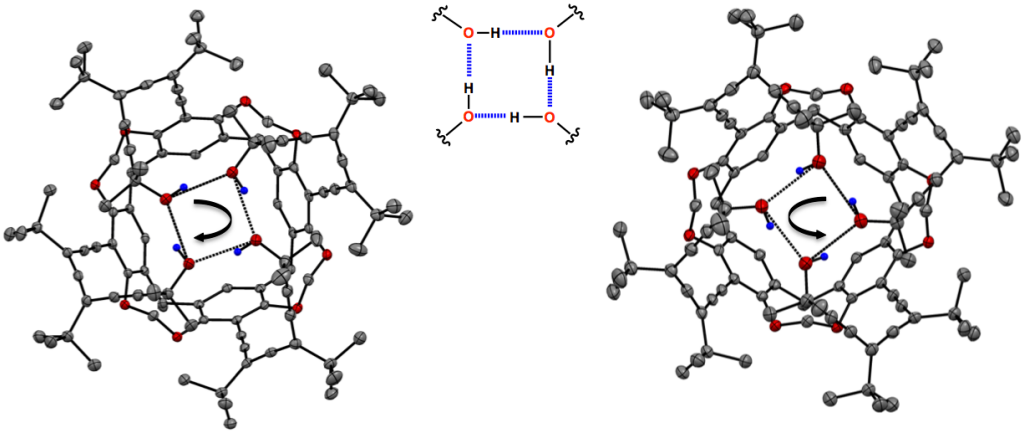

Figure 135. Top view on the fourfold hydrogen-bonding array of AAC $(P)_4$-**62** (left) and AAC $(M)_4$-**62** (right) with the guest (*trans*-1,2-dibromocyclohexane) omitted for clarity. In all complexes of AAC $(P)_4$-**62**, the hydrogen-bonding array follows a clockwise orientation. For AAC $(M)_4$-**62**, the hydrogen-bonding array follows counter-clockwise orientation. The orientation of the H-bonding array is independent of the complexed guest in all structures described herein and in previous work.

Variable temperature X-ray diffraction: In order to study the preference of AAC $(P)_4$-**62** for one enantiomer of (±)-*trans*-1,2-dibromocyclohexane we measured the obtained co-crystal structure (CCDC-1549646) with a (*R*,*R*):(*S*,*S*)-guest ratio of 75:25 at temperatures between 100 K and 280 K in steps of 20 K. We expected the stronger, tighter binding (*R*,*R*)-guest to show suppressed thermal motion and disorder visualized in the size of the thermal ellipsoids compared to the weaker binding (*S*,*S*)-enantiomer. The ellipsoids of the (*R*,*R*)-enantiomer grew

proportional to the AAC $(P)_4$-**62** while the ellipsoids of the (*S*,*S*)-enantiomer showed strong increase. At 220 K a second orientation with low occupancy of the (*S*,*S*)-enantiomer appeard rotated 90° clockwise. Weak residual densities pointing towards the remaining two acetylenic bonds, which can be interpreted as additional bromine positions, appear above 260 K (not shown for clarity). Qualitatively, this can be interpreted as preferential binding of the (*R*,*R*)-enantiomer in the $(P)_4$-configured host, associated with a lowered rotational barrier for the (*S*,*S*)-enantiomer. The comparison of the temperature dependent average sphere volumes (derived from the isotropic displacement parameters = Uequiv.)) is further plotted against the change in temperature in order to visualize that the (*R*,*R*)-enantiomer ellipdoids grew proportional to the AAC $(P)_4$-**62** while the ellipsoids of the (*S*,*S*)-enantiomer showed strong increase.

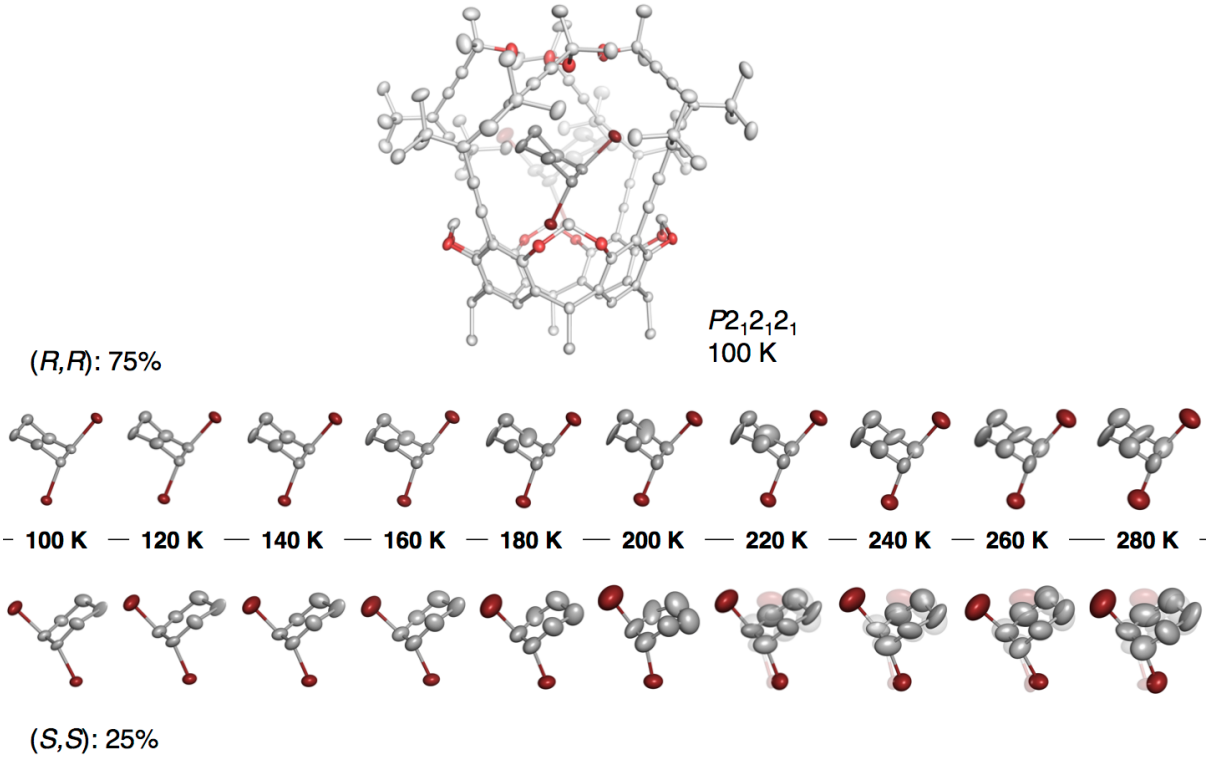

Figure 136. X-ray co-crystal structure of AAC $(P)_4$-**62**⊃*trans*-1,2-dibromocyclohexane crystallized from racemic *trans*-1,2-dibromocyclohexane and AAC $(P)_4$-**62** at 25 °C (CCDC-1549646).

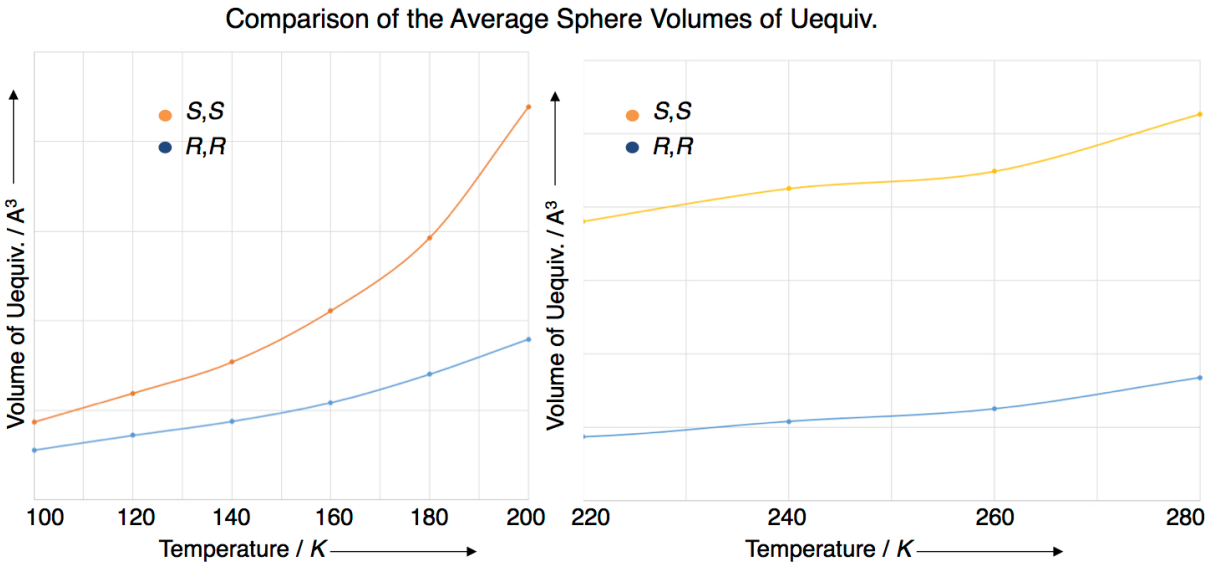

Figure 137. Comparison of the temperature-dependent average sphere volumes (volume of the anisotropic displacement parameter (Uequiv.)) of AAC $(P)_4$-**62**⊃*trans*-1,2-dibromocyclohexane crystallized from (±)-*trans*-1,2-dibromocyclohexane ((*R*,*R*):(*S*,*S*) ratio = 3:1) and AAC $(P)_4$-**62** at 25 °C.

9.5 Determination of the Cavity Size of AACs $(P)_4$- or $(M)_4$-62

The X-ray co-crystal structures were submitted to the program VOIDOO to determine the cavity volumes and the occupancies of the encapsulated guests.[214] A total of six volumes were calculated for the closed cage conformer with three different probe sizes of 1.0 Å, 1.2 Å and 1.4 Å. The volumes of the guests were calculated using the same software.[214] The choice of the adequate probe size is essential for satisfying volume estimations. In this case, a probe size of 1.0 Å was in best agreement with the Mecozzi-Rebek volume occupancy rule of 55%, originally derived for apolar capsules.[59] With a probe size of 1.0 Å, volumes of 190–223 Å^3 were obtained, resulting in packing coefficients varying from 49–58%. The cavity of the AAC showed adaptability to the guest while still maintaining rigidity and preorganization. The cavity size of the host increased from cyclohexane to cycloheptane by 14% (ca. 190 Å^3 → 220 Å^3) optimizing space filling and dispersive interaction to the guest by maintaining the ideal packing coefficient of ca. 55% (see Figure 57).

9.6 Computational Methodology

All theoretical experiments discussed in this Thesis were conducted in collaboration with Tamara Husch and Prof. Markus Reiher at ETH Zurich. The reader is referred to the complete and detailed summary of computational methods in the published manuscript.[241]

Guest structures were optimized with the Perdew–Burke–Ernzerhof density functional (PBE)[327,328] in combination with empirical D3 dispersion corrections (PDB-D3)[329] and with spin-component scaled Møller-Plesset perturbation theory (SCS-MP2).[330] The host–

guest structures ((*P*)$_4$- or (*M*)$_4$-**62**) were optimized with PBE-D3. A def2-TZVPPD basis set on the halogen atoms[330] and a def2-TZVPP basis set,[330] on all other atoms was applied for all PBE-D3 and SCS-MP2 calculations in combination with the corresponding Ahlrichs' density-fitting bases.[331] Subsequent single-point energy evaluations incorportated counterpoise corrections. Additionally, single-point energies for the guest structures were calculated with explicitly correlated density-fitting local coupled cluster theory with single and double excitations and perturbative triple excitations (DF-LCCSD(T0)-F12b)[332] in combination with a cc-pVTZ-F12 basis set.[333] The calculated single-point energy with one method (e.g., DF-LCCSD(T0)-F12b) for a structure and optimized with another method (e.g., SCS-MP2) is denoated by double slash (e.g., DF-LCCSD(T0)-F12b//SCS-MP2). Note that electronic energy differences are presented at 0 Kelvin and without vibrational and temperature corrections in the gas phase for host–guest complexes. Additionally, Gibbs energies for the isolated guest molecules were assessed according to the standard protocol (non-interacting molecules, rigid-rotor-harmonic-oscillator approximation; for details, see Ref.[241]

10. Appendix

10 Appendix

10.1 Crystallographic Data

10.1.1 Summary of Published Structures Determined by Single Crystal X-ray Diffraction

Table 13 gives an overview of the published strcutures obtained by single crystal X-ray diffraction. For more information on the published X-ray co-crystal structures, see supplementary data at The Cambridge Crystallographic Data Centre: https://www.ccdc.cam.ac.uk/getstructures.

Table 13. Summary of published X-ray co-crystal structures. The CCDC code denotes the number assigned to the structures in the Cambridge Crystallographic Data Centre.

CCDC code	X-ray co-crystal structure	R_1 / %	Space group	Guest + Host
1496457	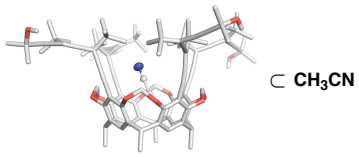	0.0487	$P2_1$	acetonitrile AAC $(P)_4$-**62**
1496458	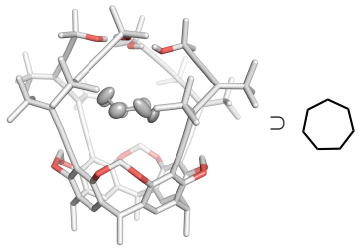	0.0493	$P2_1P2_1P2_1$	cyclohexane AAC $(P)_4$-**62**
1496463	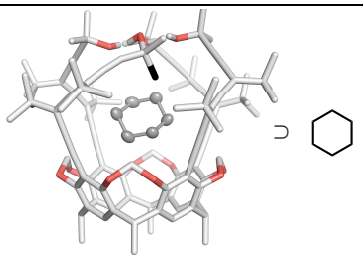	0.0437	$P2_1P2_1P2_1$	cycloheptane AAC $(P)_4$-**62**
1496459	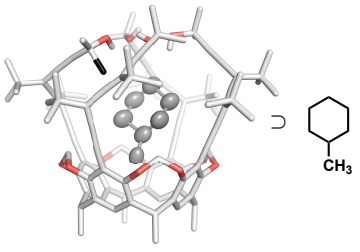	0.0946	$P2_1$	methylcyclohexane (AAC $(P)_4$-**62**

1496461	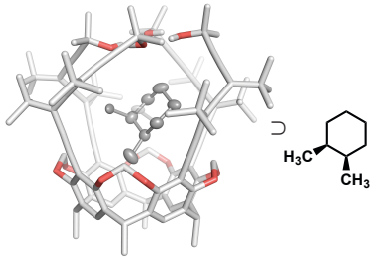	0.0560	$P2_1P2_1P2_1$	*cis*-1,2-dimethylcyclohexane AAC $(P)_4$-**62**
1496462	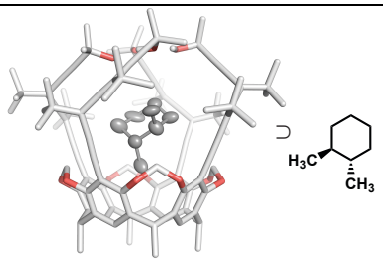	0.0539	$P2_1P2_1P2_1$	*(R,R)-trans*-1,2-dimethylcyclohexane AAC $(P)_4$-**62**
1496460	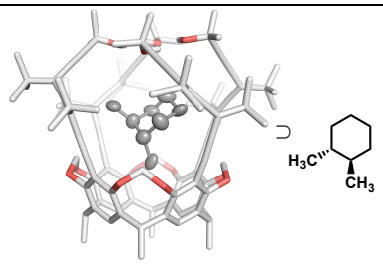	0.0745	$P2_1P2_1P2_1$	*(S,S)-trans*-1,2-dimethylcyclohexane AAC $(M)_4$-**62**
1549644	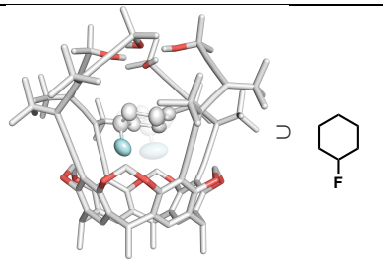	0.0692	$P2_1P2_1P2_1$	fluorocyclohexane AAC $(P)_4$-**62**
1549643	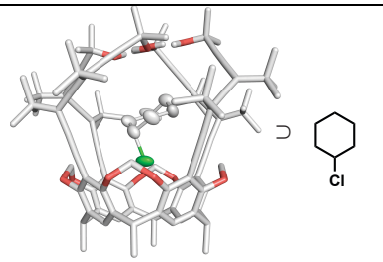	0.0499	$P2_1P2_1P2_1$	chlorocyclohexane AAC $(P)_4$-**62**
1549642	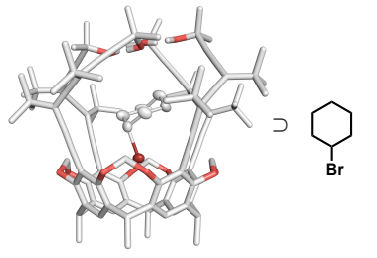	0.0476	$P2_1P2_1P2_1$	bromocyclohexane (AAC $(P)_4$-**62**

1549648	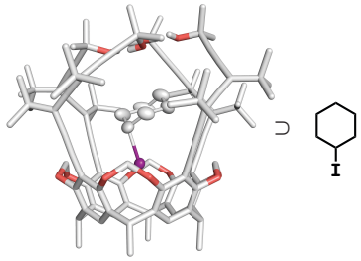	0.0446	$P2_1P2_1P2_1$	iodocyclohexane AAC $(P)_4$-**62**
1549650	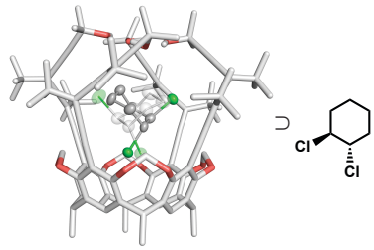	0.0542	$P2_1P2_1P2_1$	*trans*-1,2-dichlorocyclohexane AAC $(P)_4$-**62**
1549645	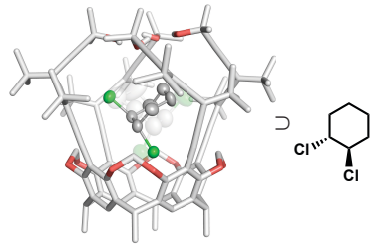	0.0729	$P2_1P2_1P2_1$	*trans*-1,2-dichlorocyclohexane AAC $(M)_4$-**62**
1549646	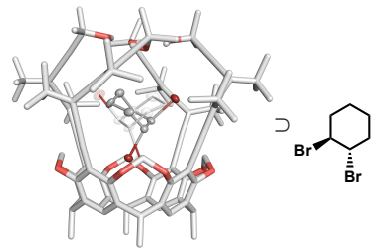	0.0354	$P2_1P2_1P2_1$	*trans*-1,2-dibromocyclohexane AAC $(P)_4$-**62**
1549651	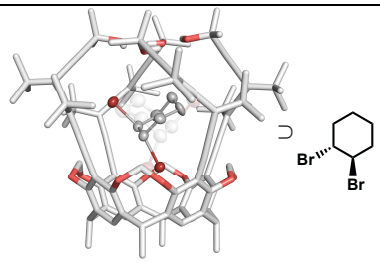	0.0489	$P2_1P2_1P2_1$	*trans*-1,2-dibromocyclohexane AAC $(M)_4$-**62**
1549649	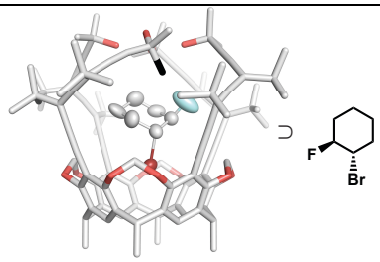	0.0572	$P2_1P2_1P2_1$	*(R,R)-trans*-1,2-bromo-fluorocyclohexane AAC $(P)_4$-**62**

1549641	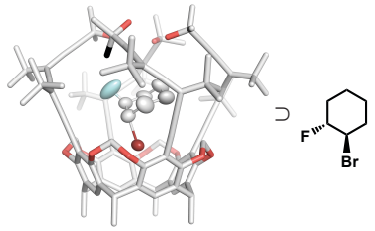	0.0771	$P2_1P2_1P2_1$	*(S,S)-trans*-1,2-bromo-fluorocyclohexane AAC $(M)_4$-**62**
1549647	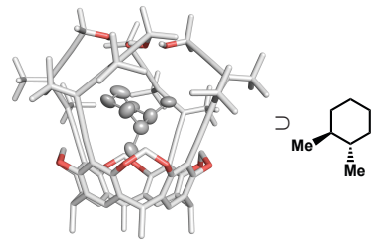	0.0570	$P2_1P2_1P2_1$	*(R,R)-trans*-1,2-dimethylcyclohexane AAC $(P)_4$-**62**

10.1.2 Geometries of AAC $(P)_4$-62-Bound (*R*,*R*)- and (*S*,*S*)-*trans*-Dimethylcyclohexane in a Diaxial Conformation

Table 14. Selected geometric parameters of (*R*,*R*)-*trans*-1,2-dimethylcyclohexane (CCDC-1496462) and (*S*,*S*)-*trans*-1,2-dimethylcyclohexane (CCDC-1496460). Atomic displacement parameters at 100 K are drawn at the 50% probability level. Selected bond lengths (Å), angles (°), and torsion angles (°).

	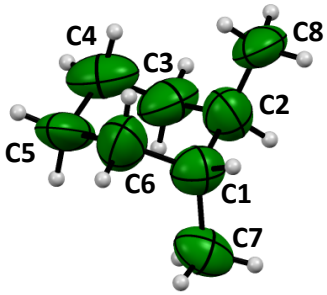	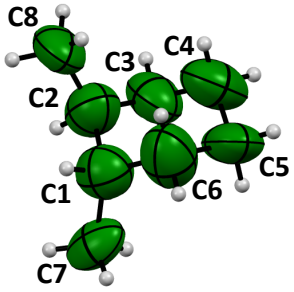
	(*R*,*R*)-*trans*-1,2-dimethylcyclohexane	(*S*,*S*)-*trans*-1,2-dimethylcyclohexane
Bond lengths (Å)		
C1–C2	1.539	1.588
C1–C6	1.581	1.585
C1–C7	1.533	1.557
C2–C3	1.629	1.607
C2–C8	1.459	1.483
C3–C4	1.415	1.512
C4–C5	1.542	1.563

C5–C6	1.639	1.635
Bond angles (°)		
C2-C1-C6	111.3	109.0
C2-C1-C7	114.6	115.4
C6-C1-C7	118.1	119.9
C1-C2-C3	110.2	113.4
C1-C2-C8	115.1	114.4
C3-C2-C8	116.1	118.8
C2-C3-C4	105.5	103.1
C3-C4-C5	115.4	115.8
C4-C5-C6	106.5	108.9
C1-C6-C5	105.9	106.5
Torsion angles (°)		
C1–C2–C3–C4	59.0	–59.6
C2–C3–C4–C5	–65.0	60.6
C3–C4–C5–C6	66.9	–63.3
C4–C5–C6–C1	–57.1	57.1
C5–C6–C1–C2	58.1	–57.8
C6–C1–C2–C3	–59.2	62.7
C7–C1–C2–C3	78.1	–75.6
C7–C1–C2–C8	**–148.4**	**143.7**
C7–C1–C6–C5	–77.5	78.3
C8–C2–C1–C6	74.4	–78.0
C8–C2–C3–C4	74.1	79.3

10.1.3 Unpublished Structures Determined by Single Crystal X-ray Diffraction

Empirical formula	$C_{62}H_{77}N_{15}O_8$
Formula weight	1160.38
Temperature/K	100.0(2)
Crystal system	triclinic
Space group	P-1
a/Å	12.7240(3)
b/Å	15.5481(3)
c/Å	15.9456(3)
α/°	102.2250(10)
β/°	96.9240(10)
γ/°	90.3050(10)
Volume/Å^3	3059.01(11)
Z	2
ρ_{calc}g/cm^3	1.260
μ/mm^{-1}	0.696
F(000)	1236.0
Crystal size/mm^3	0.19 × 0.12 × 0.05
Radiation	CuKα (λ = 1.54178)
2Θ range for data collection/°	5.818 to 133.572
Index ranges	-15 ≤ h ≤ 15, -18 ≤ k ≤ 18, -17 ≤ l ≤ 18
Reflections collected	39131
Independent reflections	10604 [R_{int} = 0.0331, R_{sigma} = 0.0298]
Data/restraints/parameters	10604/187/851
Goodness-of-fit on F^2	1.035
Final R indexes [I>=2σ (I)]	R_1 = 0.0379, wR_2 = 0.0965
Final R indexes [all data]	R_1 = 0.0429, wR_2 = 0.1005
Largest diff. peak/hole / e Å^{-3}	0.39/-0.37

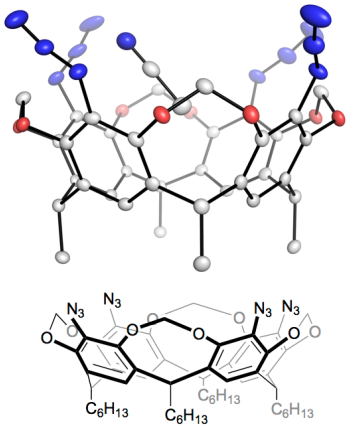

Figure 138. Crystallographic data and ORTEP representation of **60** (50% probability). *n*-Hexyl chains omitted for clarity.

Empirical formula	$C_{130}H_{171}NO_{12}$
Formula weight	1939.67
Temperature/K	100.0(1)
Crystal system	orthorhombic
Space group	$P2_12_12_1$
a/Å	15.68580(10)
b/Å	18.75680(10)
c/Å	42.9926(2)
α/°	90
β/°	90
γ/°	90
Volume/Å^3	12649.09(12)
Z	4
ρ_{calc}g/cm^3	1.019
μ/mm^{-1}	0.494
F(000)	4216.0
Crystal size/mm^3	0.147 × 0.135 × 0.053
Radiation	CuKα (λ = 1.54184)
2Θ range for data collection/°	6.254 to 159.254
Index ranges	-19 ≤ h ≤ 19, -23 ≤ k ≤ 23, -54 ≤ l ≤ 53
Reflections collected	36456
Independent reflections	36456 [R_{int} = 0.0300, R_{sigma} = 0.0201]
Data/restraints/parameters	36456/347/1446
Goodness-of-fit on F^2	1.038
Final R indexes [I>=2σ (I)]	R_1 = 0.0498, wR_2 = 0.1359
Final R indexes [all data]	R_1 = 0.0546, wR_2 = 0.1403
Flack parameter	-0.12(5)

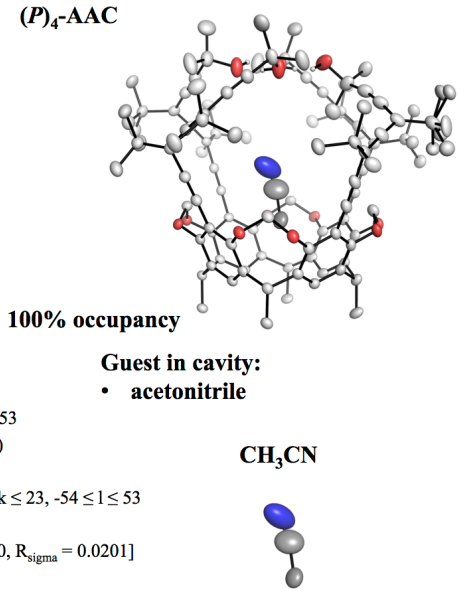

Figure 139. Crystallographic data and ORTEP representation of AAC $(P)_4$-**62**⊃acetonitrile (50% probability). *n*-Hexyl chains omitted for clarity.

Empirical formula	$C_{128.29}H_{168.59}O_{12}S_{0.29}$
Formula weight	1912.09
Temperature/K	100.0(1)
Crystal system	orthorhombic
Space group	$P2_12_12_1$
a/Å	15.6513(11)
b/Å	18.8147(8)
c/Å	42.921(3)
α/°	90
β/°	90
γ/°	90
Volume/Å^3	12639.2(15)
Z	4
ρ_{calc}g/cm^3	1.005
μ/mm^{-1}	0.530
F(000)	4156.0
Crystal size/mm^3	0.13 × 0.093 × 0.03
Radiation	CuKα (λ = 1.54184)
2Θ range for data collection/°	5.128 to 133.2
Index ranges	-16 ≤ h ≤ 18, -16 ≤ k ≤ 22, -51 ≤ l ≤ 50
Reflections collected	55778
Independent reflections	21561 [R_{int} = 0.0461, R_{sigma} = 0.0499]
Data/restraints/parameters	21561/435/1454
Goodness-of-fit on F^2	1.128
Final R indexes [I>=2σ (I)]	R_1 = 0.0443, wR_2 = 0.0987
Final R indexes [all data]	R_1 = 0.0709, wR_2 = 0.1290
Flack parameter	0.04(5)

$(P)_4$-AAC

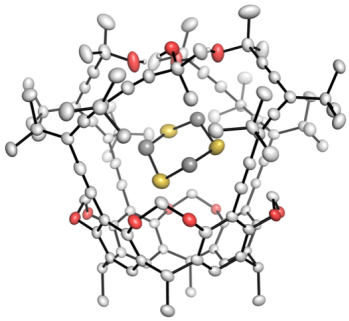

Guest in cavity:

- **1,3,5-trithiane**

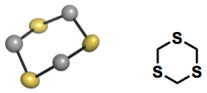

Figure 140. Crystallographic data and ORTEP representation of AAC $(P)_4$-**62**⊃1,3,5-trithiane (50% probability). *n*-Hexyl chains omitted for clarity.

Empirical formula	$C_{129}H_{168}Br_4O_{12}$
Formula weight	2230.26
Temperature/K	100.0(1)
Crystal system	orthorhombic
Space group	$P2_12_12_1$
a/Å	15.58730(10)
b/Å	18.64040(10)
c/Å	44.0290(4)
α/°	90
β/°	90
γ/°	90
Volume/Å^3	12792.78(16)
Z	4
ρ_{calc}g/cm^3	1.158
μ/mm^{-1}	1.956
F(000)	4712.0
Crystal size/mm^3	0.17 × 0.168 × 0.101
Radiation	CuKα (λ = 1.54184)
2Θ range for data collection/°	6.948 to 140.146
Index ranges	-19 ≤ h ≤ 19, -22 ≤ k ≤ 22, -53 ≤ l ≤ 53
Reflections collected	376025
Independent reflections	24275 [R_{int} = 0.0693, R_{sigma} = 0.0262]
Data/restraints/parameters	24275/436/1478
Goodness-of-fit on F^2	1.041
Final R indexes [I>=2σ (I)]	R_1 = 0.0839, wR_2 = 0.2454
Final R indexes [all data]	R_1 = 0.0894, wR_2 = 0.2539
Flack parameter	0.023(4)

$(P)_4$-AAC

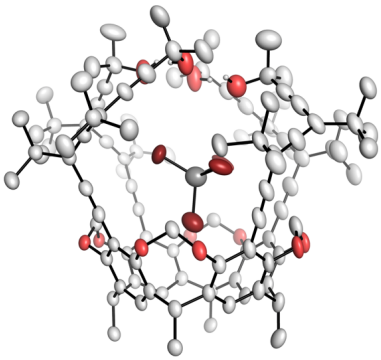

Guest in cavity:

- **tetrabromomethane**

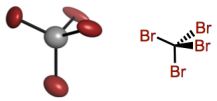

Figure 141. Crystallographic data and ORTEP representation of AAC $(P)_4$-**62**⊃tetrabromomethane (50% probability). *n*-Hexyl chains omitted for clarity.

Empirical formula	$C_{137}H_{183}NO_{12}$
Formula weight	2035.83
Temperature/K	100.0(1)
Crystal system	orthorhombic
Space group	$P2_12_12_1$
a/Å	15.4686(3)
b/Å	18.2645(3)
c/Å	46.3340(11)
α/°	90
β/°	90
γ/°	90
Volume/Å^3	13090.6(5)
Z	4
ρ_{calc}g/cm^3	1.033
μ/mm^{-1}	0.497
F(000)	4432.0
Crystal size/mm^3	0.204 × 0.121 × 0.054
Radiation	CuKα (λ = 1.54184)
2Θ range for data collection/°	5.2 to 134.154
Index ranges	-17 ≤ h ≤ 18, -21 ≤ k ≤ 18, -55 ≤ l ≤ 55
Reflections collected	72862
Independent reflections	23325 [R_{int} = 0.0419, R_{sigma} = 0.0409]
Data/restraints/parameters	23325/459/1512
Goodness-of-fit on F^2	1.065
Final R indexes [I>=2σ (I)]	R_1 = 0.0642, wR_2 = 0.1611
Final R indexes [all data]	R_1 = 0.0948, wR_2 = 0.2081
Flack parameter	-0.20(8)

(*P*)$_4$-AAC

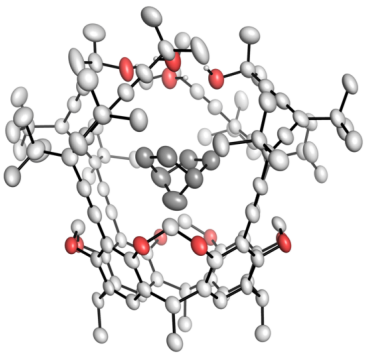

Guest in cavity:

- **norbornane**

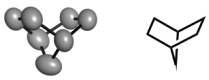

Figure 142. Crystallographic data and ORTEP representation of AAC (*P*)$_4$-**62**⊃nobornane (50% probability). *n*-Hexyl chains omitted for clarity.

Empirical formula	$C_{137}H_{185}NO_{13}$
Formula weight	2053.85
Temperature/K	100.0(2)
Crystal system	monoclinic
Space group	$P2_1$
a/Å	15.4610(6)
b/Å	45.3729(17)
c/Å	18.5239(6)
α/°	90
β/°	91.097(3)
γ/°	90
Volume/Å^3	12992.3(8)
Z	4
ρ_{calc}g/cm^3	1.050
μ/mm^{-1}	0.510
F(000)	4472.0
Crystal size/mm^3	0.16 × 0.1 × 0.04
Radiation	CuKα (λ = 1.54178)
2Θ range for data collection/°	3.894 to 133.746
Index ranges	-18 ≤ h ≤ 14, -53 ≤ k ≤ 52, -22 ≤ l ≤ 15
Reflections collected	167613
Independent reflections	44852 [R_{int} = 0.0613, R_{sigma} = 0.0549]
Data/restraints/parameters	44852/489/2825
Goodness-of-fit on F^2	1.021
Final R indexes [I>=2σ (I)]	R_1 = 0.0677, wR_2 = 0.1769
Final R indexes [all data]	R_1 = 0.0864, wR_2 = 0.1929
Flack parameter	0.18(7)

(*P*)$_4$-AAC

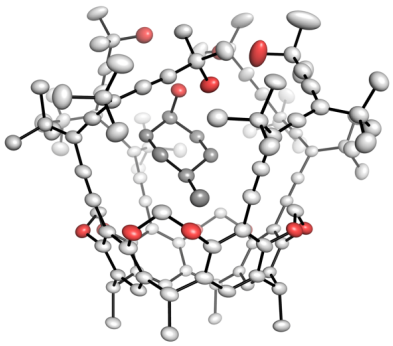

Guest in cavity:

- ***cis*-1,4-methylcyclohexanol**

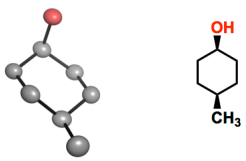

Figure 143. Crystallographic data and ORTEP representation of AAC (*P*)$_4$-**62**⊃*cis*-4-methylcyclohexanol (50% probability). *n*-Hexyl chains omitted for clarity.

Empirical formula	$C_{137}H_{185}NO_{13}$
Formula weight	2053.85
Temperature/K	100.0(2)
Crystal system	orthorhombic
Space group	$P2_12_12_1$
a/Å	15.4730(4)
b/Å	18.2737(4)
c/Å	46.3934(12)
α/°	90
β/°	90
γ/°	90
Volume/Å^3	13117.7(6)
Z	4
ρ_{calc}g/cm^3	1.040
μ/mm^{-1}	0.505
F(000)	4472.0
Crystal size/mm^3	0.18 × 0.1 × 0.02
Radiation	CuKα (λ = 1.54178)
2Θ range for data collection/°	3.808 to 133.452
Index ranges	-18 ≤ h ≤ 9, -21 ≤ k ≤ 21, -54 ≤ l ≤ 55
Reflections collected	154522
Independent reflections	23102 [R_{int} = 0.0733, R_{sigma} = 0.0427]
Data/restraints/parameters	23102/368/1480
Goodness-of-fit on F^2	1.032
Final R indexes [I>=2σ (I)]	R_1 = 0.0541, wR_2 = 0.1312
Final R indexes [all data]	R_1 = 0.0694, wR_2 = 0.1429
Flack parameter	0.04(9)

$(P)_4$-AAC

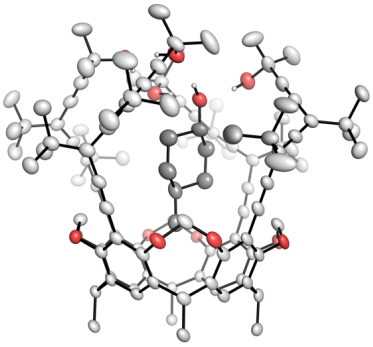

Guest in cavity:

- ***trans*-1,4-methylcyclohexanol**

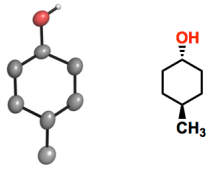

Figure 144. Crystallographic data and ORTEP representation of AAC $(P)_4$-**62**⊃*trans*-4-methylcyclohexanol (50% probability). *n*-Hexyl chains omitted for clarity.

Empirical formula	$C_{136}H_{183}NO_{13}$
Formula weight	2039.82
Temperature/K	100.0(1)
Crystal system	orthorhombic
Space group	$P2_12_12_1$
a/Å	15.43790(10)
b/Å	18.7445(2)
c/Å	44.4789(4)
α/°	90
β/°	90
γ/°	90
Volume/Å^3	12871.1(2)
Z	4
ρ_{calc}g/cm^3	1.053
μ/mm^{-1}	0.512
F(000)	4440.0
Crystal size/mm^3	0.117 × 0.099 × 0.047
Radiation	CuKα (λ = 1.54184)
2Θ range for data collection/°	6.166 to 166.154
Index ranges	-14 ≤ h ≤ 19, -23 ≤ k ≤ 23, -56 ≤ l ≤ 56
Reflections collected	54043
Independent reflections	54043 [R_{int} = ?, R_{sigma} = 0.0378]
Data/restraints/parameters	54043/542/1597
Goodness-of-fit on F^2	1.024
Final R indexes [I>=2σ (I)]	R_1 = 0.1010, wR_2 = 0.2754
Final R indexes [all data]	R_1 = 0.1168, wR_2 = 0.2937
Flack parameter	0.0(2)

$(P)_4$-AAC

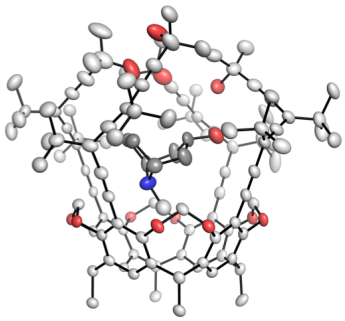

Guest in cavity:

- ***exo*-tropine**

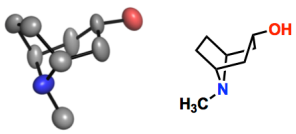

Figure 145. Crystallographic data and ORTEP representation of AAC $(P)_4$-**62**⊃*exo*-tropine (50% probability). *n*-Hexyl chains omitted for clarity.

Empirical formula	$C_{136}H_{183}NO_{13}$
Formula weight	2039.82
Temperature/K	100.0(1)
Crystal system	orthorhombic
Space group	$P2_12_12_1$
a/Å	44.0495(6)
b/Å	18.7600(3)
c/Å	15.5047(2)
α/°	90
β/°	90
γ/°	90
Volume/Å^3	12812.6(3)
Z	4
ρ_{calc}g/cm^3	1.057
μ/mm^{-1}	0.514
F(000)	4440.0
Crystal size/mm^3	0.201 × 0.106 × 0.027
Radiation	CuKα (λ = 1.54184)
2Θ range for data collection/°	6.188 to 160.432
Index ranges	-56 ≤ h ≤ 55, -23 ≤ k ≤ 21, -19 ≤ l ≤ 19
Reflections collected	251403
Independent reflections	27350 [R_{int} = 0.1050, R_{sigma} = 0.0553]
Data/restraints/parameters	27350/877/1606
Goodness-of-fit on F^2	1.038
Final R indexes [I>=2σ (I)]	R_1 = 0.0760, wR_2 = 0.2056
Final R indexes [all data]	R_1 = 0.1064, wR_2 = 0.2309
Flack parameter	0.11(7)

$(P)_4$-AAC

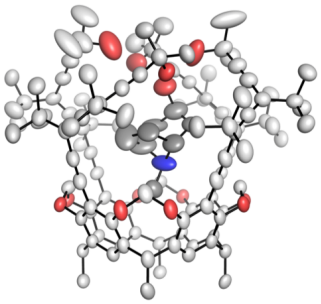

Guest in cavity:

- ***endo*-tropine**

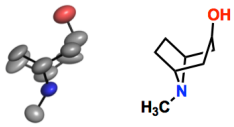

Figure 146. Crystallographic data and ORTEP representation of AAC $(P)_4$-**62**⊃*endo*-tropine (50% probability). *n*-Hexyl chains omitted for clarity.

Empirical formula	$C_{135}H_{184}O_{13}$
Formula weight	2014.81
Temperature/K	100.00(1)
Crystal system	orthorhombic
Space group	$P2_12_12_1$
a/Å	15.5129(4)
b/Å	18.7006(6)
c/Å	44.5116(19)
α/°	90
β/°	90
γ/°	90
Volume/Å^3	12912.8(8)
Z	4
ρ_{calc}g/cm^3	1.036
μ/mm^{-1}	0.502
F(000)	4392.0
Crystal size/mm^3	0.124 × 0.072 × 0.025
Radiation	CuKα (λ = 1.54184)
2Θ range for data collection/°	6.034 to 163.006
Index ranges	-19 ≤ h ≤ 19, -23 ≤ k ≤ 23, -56 ≤ l ≤ 56
Reflections collected	45980
Independent reflections	45980 [R_{int} = 0.1700, R_{sigma} = 0.1333]
Data/restraints/parameters	45980/361/1458
Goodness-of-fit on F^2	1.068
Final R indexes [I>=2σ (I)]	R_1 = 0.1270, wR_2 = 0.3004
Final R indexes [all data]	R_1 = 0.1757, wR_2 = 0.3374
Flack parameter	-0.1(5)

$(P)_4$-AAC

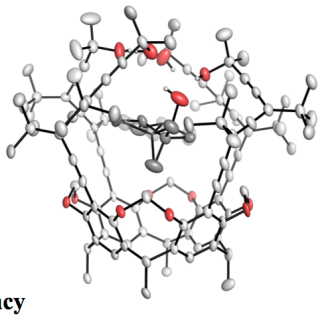

100% occupancy

Guest in cavity:

- **2,2,3-trimethylbutan-1-ol**

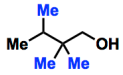

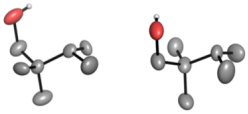

60 : 40

Figure 147. Crystallographic data and ORTEP representation of AAC $(P)_4$-**62**⊃2,2,3-trimethylbutan-1-ol (50% probability). *n*-Hexyl chains omitted for clarity.

Empirical formula	$C_{130.65}H_{173.29}Br_{1.32}O_{12.66}$
Formula weight	2051.95
Temperature/K	100.0(1)
Crystal system	orthorhombic
Space group	$P2_12_12_1$
a/Å	15.56520(10)
b/Å	18.75780(10)
c/Å	43.9214(3)
α/°	90
β/°	90
γ/°	90
Volume/Å^3	12823.68(14)
Z	4
ρ_{calc}g/cm^3	1.063
μ/mm^{-1}	0.977
F(000)	4419.0
Crystal size/mm^3	0.14 × 0.067 × 0.03
Radiation	CuKα (λ = 1.54184)
2Θ range for data collection/°	6.024 to 159.704
Index ranges	-19 ≤ h ≤ 16, -23 ≤ k ≤ 23, -55 ≤ l ≤ 55
Reflections collected	265365
Independent reflections	27728 [R_{int} = 0.0771, R_{sigma} = 0.0357]
Data/restraints/parameters	27728/157/1395
Goodness-of-fit on F^2	1.022
Final R indexes [I>=2σ (I)]	R_1 = 0.0890, wR_2 = 0.2560
Final R indexes [all data]	R_1 = 0.0963, wR_2 = 0.2664
Flack parameter	0.009(4)

$(M)_4$-AAC

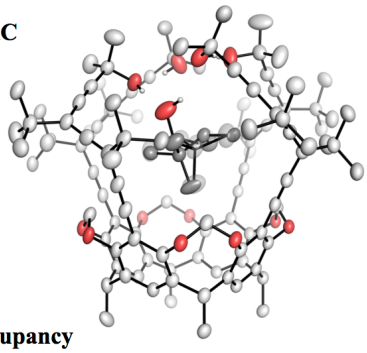

100% occupancy

Guest in cavity:

- **2,2,3-trimethylbutan-1-ol**

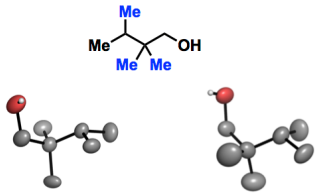

58 : 42

Figure 148. Crystallographic data and ORTEP representation of AAC $(M)_4$-**62**⊃2,2,3-trimethylbutan-1-ol (50% probability). *n*-Hexyl chains omitted for clarity.

Empirical formula	$C_{132}H_{176}Cl_2O_{13}$
Formula weight	2041.62
Temperature/K	100.0(1)
Crystal system	orthorhombic
Space group	$P2_12_12_1$
a/Å	15.61350(10)
b/Å	18.75150(10)
c/Å	43.6512(2)
α/°	90
β/°	90
γ/°	90
Volume/Å^3	12780.05(12)
Z	4
ρ_{calc}g/cm^3	1.061
μ/mm^{-1}	0.889
F(000)	4424.0
Crystal size/mm^3	0.154 × 0.112 × 0.076
Radiation	CuKα (λ = 1.54184)
2Θ range for data collection/°	6.012 to 159.476
Index ranges	-15 ≤ h ≤ 19, -23 ≤ k ≤ 23, -55 ≤ l ≤ 55
Reflections collected	210898
Independent reflections	27582 [R_{int} = 0.0432, R_{sigma} = 0.0227]
Data/restraints/parameters	27582/366/1442
Goodness-of-fit on F^2	1.028
Final R indexes [I>=2σ (I)]	R_1 = 0.0718, wR_2 = 0.2119
Final R indexes [all data]	R_1 = 0.0757, wR_2 = 0.2171
Flack parameter	0.066(4)

$(P)_4$-AAC

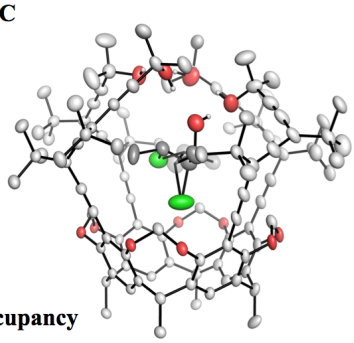

100% occupancy

Guest in cavity:

- **2,3-dichlorobutan-1-ol**

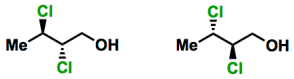

(*S*,*R*) **(*R*,*S*)**

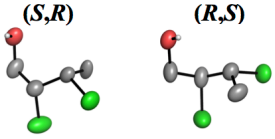

58 : 42

Figure 149. Crystallographic data and ORTEP representation of AAC $(P)_4$-**62**⊃2,3-dichlorobutanol (50% probability). *n*-Hexyl chains omitted for clarity.

Empirical formula	$C_{132}H_{176}Cl_2O_{13}$
Formula weight	2041.62
Temperature/K	100.0(1)
Crystal system	orthorhombic
Space group	$P2_12_12_1$
a/Å	15.59180(10)
b/Å	18.73920(10)
c/Å	43.8114(2)
α/°	90
β/°	90
γ/°	90
Volume/Å^3	12800.72(12)
Z	4
ρ_{calc}g/cm^3	1.059
μ/mm^{-1}	0.888
F(000)	4424.0
Crystal size/mm^3	0.187 × 0.096 × 0.036
Radiation	CuKα (λ = 1.54184)
2Θ range for data collection/°	6.206 to 159.38
Index ranges	-19 ≤ h ≤ 18, -23 ≤ k ≤ 23, -55 ≤ l ≤ 54
Reflections collected	212369
Independent reflections	27540 [R_{int} = 0.0447, R_{sigma} = 0.0236]
Data/restraints/parameters	27540/270/1446
Goodness-of-fit on F^2	1.028
Final R indexes [I>=2σ (I)]	R_1 = 0.0506, wR_2 = 0.1463
Final R indexes [all data]	R_1 = 0.0542, wR_2 = 0.1504
Flack parameter	0.025(4)

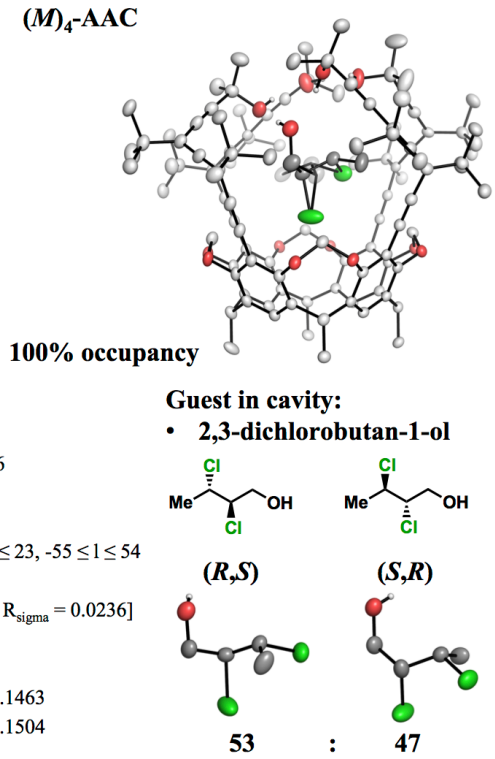

Figure 150. Crystallographic data and ORTEP representation of AAC $(M)_4$-**62**⊃2,3-dichlorobutanol (50% probability). *n*-Hexyl chains omitted for clarity.

Empirical formula	$C_{129.98}H_{171.97}Cl_{0.99}O_{12.49}$
Formula weight	1969.44
Temperature/K	100.0(1)
Crystal system	orthorhombic
Space group	$P2_12_12_1$
a/Å	15.60340(10)
b/Å	18.7470(2)
c/Å	43.6221(4)
α/°	90
β/°	90
γ/°	90
Volume/Å^3	12760.2(2)
Z	4
ρ_{calc}g/cm^3	1.025
μ/mm^{-1}	0.683
F(000)	4275.0
Crystal size/mm^3	0.122 × 0.11 × 0.044
Radiation	CuKα (λ = 1.54184)
2Θ range for data collection/°	6.016 to 160.042
Index ranges	-19 ≤ h ≤ 17, -21 ≤ k ≤ 23, -55 ≤ l ≤ 55
Reflections collected	210282
Independent reflections	27516 [R_{int} = 0.0678, R_{sigma} = 0.0368]
Data/restraints/parameters	27516/263/1419
Goodness-of-fit on F^2	1.036
Final R indexes [I>=2σ (I)]	R_1 = 0.0713, wR_2 = 0.1983
Final R indexes [all data]	R_1 = 0.0837, wR_2 = 0.2112
Flack parameter	0.029(8)

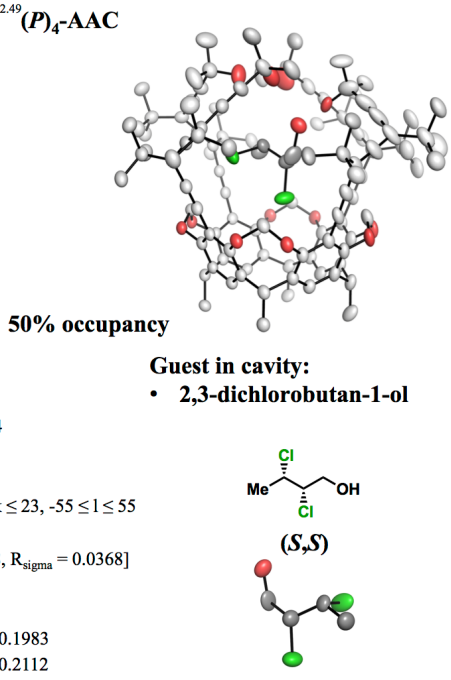

Figure 151. Crystallographic data and ORTEP representation of AAC $(P)_4$-**62**⊃2,3-dichlorobutanol (50% probability). *n*-Hexyl chains omitted for clarity.

Empirical formula	$C_{130.76}H_{173.51}Cl_{1.38}O_{12.69}$
Formula weight	1997.16
Temperature/K	100.0(1)
Crystal system	orthorhombic
Space group	$P2_12_12_1$
a/Å	15.55690(10)
b/Å	18.73900(10)
c/Å	43.9862(3)
α/°	90
β/°	90
γ/°	90
Volume/Å^3	12822.89(14)
Z	4
ρ_{calc}g/cm^3	1.035
μ/mm^{-1}	0.759
F(000)	4332.0
Crystal size/mm^3	0.165 × 0.113 × 0.029
Radiation	CuKα (λ = 1.54184)
2Θ range for data collection/°	6.196 to 159.444
Index ranges	-18 ≤ h ≤ 19, -18 ≤ k ≤ 23, -55 ≤ l ≤ 55
Reflections collected	212820
Independent reflections	27663 [R_{int} = 0.0437, R_{sigma} = 0.0225]
Data/restraints/parameters	27663/249/1411
Goodness-of-fit on F^2	1.031
Final R indexes [I>=2σ (I)]	R_1 = 0.0625, wR_2 = 0.1783
Final R indexes [all data]	R_1 = 0.0686, wR_2 = 0.1853
Flack parameter	0.021(4)

(*M*)$_4$-AAC

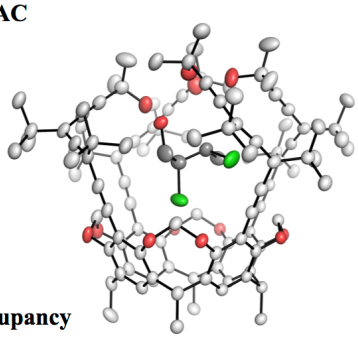

70% occupancy

Guest in cavity:

- **2,3-dichlorobutan-1-ol**

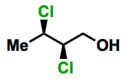

(*R*,*R*)

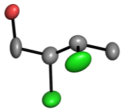

Figure 152. Crystallographic data and ORTEP representation of AAC (*M*)$_4$-**62**⊃2,3-dichlorobutanol (50% probability). *n*-Hexyl chains omitted for clarity.

Empirical formula	$C_{130.13}H_{172.26}Br_{1.07}O_{12.53}$
Formula weight	2022.35
Temperature/K	100.0(1)
Crystal system	orthorhombic
Space group	$P2_12_12_1$
a/Å	15.62340(10)
b/Å	18.76580(10)
c/Å	43.5913(2)
α/°	90
β/°	90
γ/°	90
Volume/Å^3	12780.34(12)
Z	4
ρ_{calc}g/cm^3	1.051
μ/mm^{-1}	0.883
F(000)	4363.0
Crystal size/mm^3	0.168 × 0.144 × 0.036
Radiation	CuKα (λ = 1.54184)
2Θ range for data collection/°	6.01 to 159.66
Index ranges	-15 ≤ h ≤ 19, -23 ≤ k ≤ 23, -55 ≤ l ≤ 55
Reflections collected	266306
Independent reflections	27644 [R_{int} = 0.0620, R_{sigma} = 0.0272]
Data/restraints/parameters	27644/468/1463
Goodness-of-fit on F^2	1.025
Final R indexes [I>=2σ (I)]	R_1 = 0.0733, wR_2 = 0.2104
Final R indexes [all data]	R_1 = 0.0770, wR_2 = 0.2149
Flack parameter	0.012(4)

(*P*)$_4$-AAC

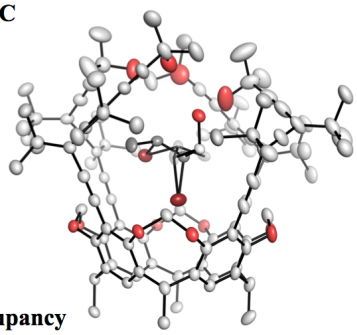

53% occupancy

Guest in cavity:

- **2,3-dibromobutan-1-ol**

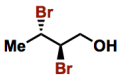

(*R*,*S*)

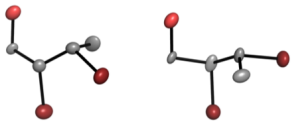

Figure 153. Crystallographic data and ORTEP representation of AAC (*P*)$_4$-**62**⊃2,3-dibromobutanol (50% probability). *n*-Hexyl chains omitted for clarity.

Empirical formula	$C_{132}H_{176}Br_2O_{13}$
Formula weight	2130.54
Temperature/K	100.0(1)
Crystal system	orthorhombic
Space group	$P2_12_12_1$
a/Å	15.60580(10)
b/Å	18.73660(10)
c/Å	43.8709(3)
α/°	90
β/°	90
γ/°	90
Volume/Å^3	12827.84(14)
Z	4
ρ_{calc}g/cm^3	1.103
μ/mm^{-1}	1.233
F(000)	4568.0
Crystal size/mm^3	0.226 × 0.111 × 0.075
Radiation	CuKα (λ = 1.54184)
2Θ range for data collection/°	6.012 to 159.616
Index ranges	-19 ≤ h ≤ 16, -23 ≤ k ≤ 22, -55 ≤ l ≤ 55
Reflections collected	210855
Independent reflections	27662 [R_{int} = 0.0481, R_{sigma} = 0.0256]
Data/restraints/parameters	27662/287/1453
Goodness-of-fit on F^2	1.036
Final R indexes [I>=2σ (I)]	R_1 = 0.0821, wR_2 = 0.2409
Final R indexes [all data]	R_1 = 0.0865, wR_2 = 0.2481
Flack parameter	0.014(4)

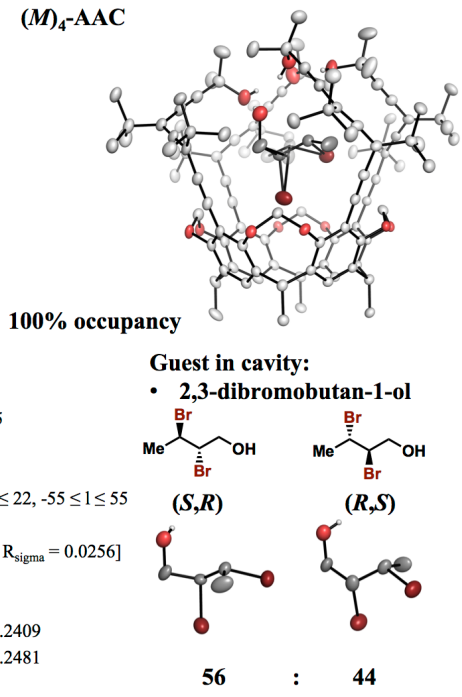

Figure 154. Crystallographic data and ORTEP representation of AAC $(M)_4$-**62**⊃2,3-dibromobutanol (50% probability). *n*-Hexyl chains omitted for clarity.

Empirical formula	$C_{132}H_{176}Br_2O_{13}$
Formula weight	2130.51
Temperature/K	100.0(1)
Crystal system	orthorhombic
Space group	$P2_12_12_1$
a/Å	15.55780(10)
b/Å	18.75530(10)
c/Å	43.8495(3)
α/°	90
β/°	90
γ/°	90
Volume/Å^3	12794.90(14)
Z	4
ρ_{calc}g/cm^3	1.106
μ/mm^{-1}	1.236
F(000)	4568.0
Crystal size/mm^3	0.149 × 0.126 × 0.031
Radiation	CuKα (λ = 1.54184)
2Θ range for data collection/°	6.202 to 160.242
Index ranges	-18 ≤ h ≤ 19, -23 ≤ k ≤ 23, -55 ≤ l ≤ 55
Reflections collected	212525
Independent reflections	27576 [R_{int} = 0.0505, R_{sigma} = 0.0266]
Data/restraints/parameters	27576/303/1507
Goodness-of-fit on F^2	1.034
Final R indexes [I>=2σ (I)]	R_1 = 0.0536, wR_2 = 0.1493
Final R indexes [all data]	R_1 = 0.0601, wR_2 = 0.1554
Flack parameter	-0.007(3)

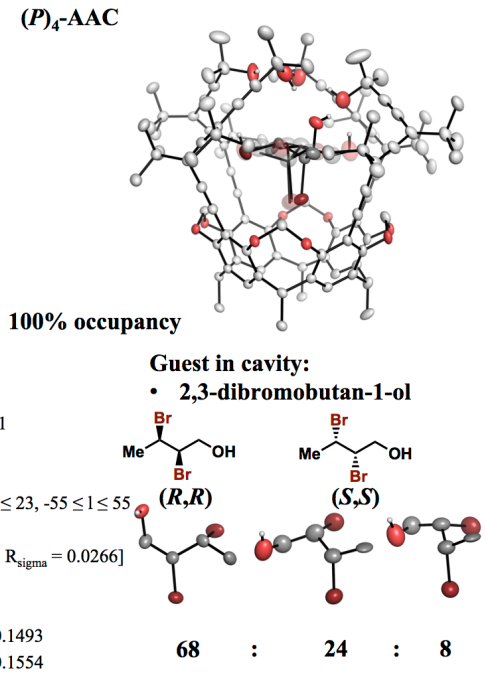

Figure 155. Crystallographic data and ORTEP representation of AAC $(P)_4$-**62**⊃2,3-dibromobutanol (50% probability). *n*-Hexyl chains omitted for clarity.

Empirical formula	$C_{130.65}H_{173.29}Br_{1.32}O_{12.66}$
Formula weight	2051.95
Temperature/K	100.0(1)
Crystal system	orthorhombic
Space group	$P2_12_12_1$
a/Å	15.56520(10)
b/Å	18.75780(10)
c/Å	43.9214(3)
α/°	90
β/°	90
γ/°	90
Volume/Å^3	12823.68(14)
Z	4
ρ_{calc}g/cm^3	1.063
μ/mm^{-1}	0.977
F(000)	4419.0
Crystal size/mm^3	0.14 × 0.067 × 0.03
Radiation	CuKα (λ = 1.54184)
2Θ range for data collection/°	6.024 to 159.704
Index ranges	-19 ≤ h ≤ 16, -23 ≤ k ≤ 23, -55 ≤ l ≤ 55
Reflections collected	265365
Independent reflections	27728 [R_{int} = 0.0771, R_{sigma} = 0.0357]
Data/restraints/parameters	27728/157/1395
Goodness-of-fit on F^2	1.022
Final R indexes [I>=2σ (I)]	R_1 = 0.0890, wR_2 = 0.2560
Final R indexes [all data]	R_1 = 0.0963, wR_2 = 0.2664
Flack parameter	0.009(4)

(*M*)$_4$-AAC

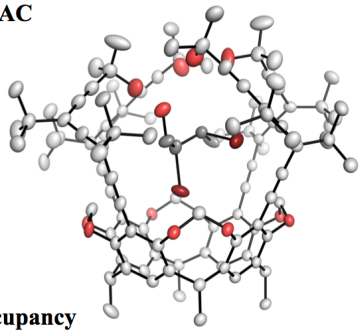

66% occupancy

Guest in cavity:

- **2,3-dibromobutan-1-ol**

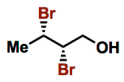

(*S*,*S*)

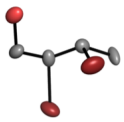

Figure 156. Crystallographic data and ORTEP representation of AAC (*M*)$_4$-**62**⊃2,3-dibromobutanol (50% probability). *n*-Hexyl chains omitted for clarity.

Empirical formula	$C_{133}H_{178}Br_2O_{13}$
Formula weight	2144.56
Temperature/K	100.0(1)
Crystal system	orthorhombic
Space group	$P2_12_12_1$
a/Å	43.9914(3)
b/Å	18.74020(10)
c/Å	15.61220(10)
α/°	90
β/°	90
γ/°	90
Volume/Å^3	12870.82(14)
Z	4
ρ_{calc}g/cm^3	1.107
μ/mm^{-1}	1.231
F(000)	4600.0
Crystal size/mm^3	0.187 × 0.125 × 0.027
Radiation	CuKα (λ = 1.54184)
2Θ range for data collection/°	6.006 to 160.13
Index ranges	-55 ≤ h ≤ 56, -18 ≤ k ≤ 23, -19 ≤ l ≤ 19
Reflections collected	273849
Independent reflections	27806 [R_{int} = 0.0648, R_{sigma} = 0.0264]
Data/restraints/parameters	27806/320/1470
Goodness-of-fit on F^2	1.286
Final R indexes [I>=2σ (I)]	R_1 = 0.0902, wR_2 = 0.2706
Final R indexes [all data]	R_1 = 0.0933, wR_2 = 0.2754
Flack parameter	0.022(4)

(*P*)$_4$-AAC

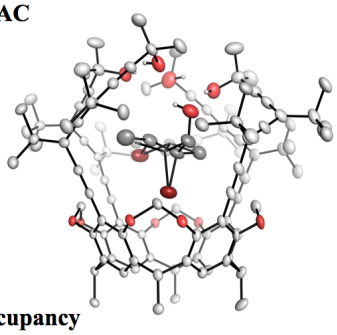

85% occupancy

Guest in cavity:

- **2,3-dibromo-2-methylbutan-1-ol**

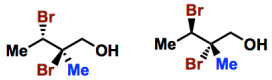

(*R*,*S*) **(*S*,*R*)**

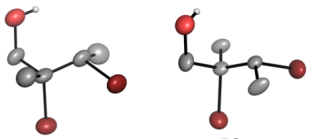

50 : 50

Figure 157. Crystallographic data and ORTEP representation of AAC (*P*)$_4$-**62**⊃2,3-dibromo-2-methylbutanol (50% probability). *n*-Hexyl chains omitted for clarity.

Empirical formula	$C_{133}H_{178}Br_2O_{13}$
Formula weight	2144.56
Temperature/K	100.0(1)
Crystal system	orthorhombic
Space group	$P2_12_12_1$
a/Å	15.60210(10)
b/Å	18.73830(10)
c/Å	44.0011(2)
α/°	90
β/°	90
γ/°	90
Volume/Å^3	12864.02(12)
Z	4
ρ_{calc}g/cm^3	1.107
μ/mm^{-1}	1.232
F(000)	4600.0
Crystal size/mm^3	0.153 × 0.131 × 0.087
Radiation	CuKα (λ = 1.54184)
2Θ range for data collection/°	6.01 to 159.466
Index ranges	-17 ≤ h ≤ 19, -23 ≤ k ≤ 22, -56 ≤ l ≤ 55
Reflections collected	267402
Independent reflections	27796 [R_{int} = 0.0645, R_{sigma} = 0.0268]
Data/restraints/parameters	27796/417/1468
Goodness-of-fit on F^2	1.050
Final R indexes [I>=2σ (I)]	R_1 = 0.0705, wR_2 = 0.2105
Final R indexes [all data]	R_1 = 0.0735, wR_2 = 0.2142
Flack parameter	-0.019(5)

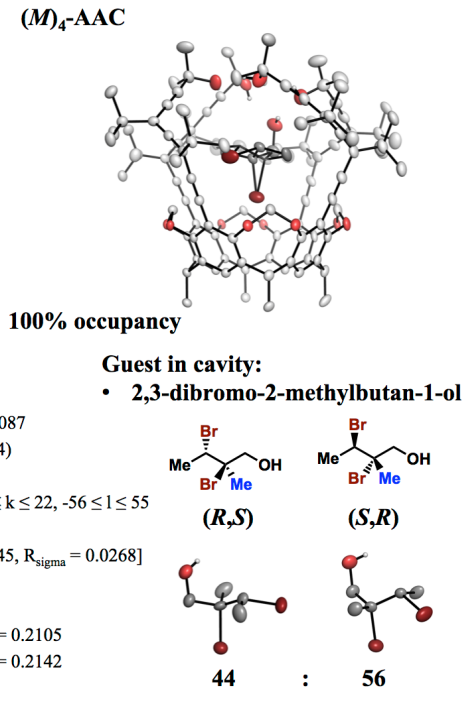

Figure 158. Crystallographic data and ORTEP representation of AAC $(M)_4$-**62**⊃2,3-dibromo-2-methylbutanol (50% probability). *n*-Hexyl chains omitted for clarity.

Empirical formula	$C_{133}H_{178}Br_2O_{13}$
Formula weight	2144.56
Temperature/K	100.0(1)
Crystal system	orthorhombic
Space group	$P2_12_12_1$
a/Å	15.60920(10)
b/Å	18.73600(10)
c/Å	44.0628(3)
α/°	90
β/°	90
γ/°	90
Volume/Å^3	12886.34(14)
Z	4
ρ_{calc}g/cm^3	1.105
μ/mm^{-1}	1.230
F(000)	4600.0
Crystal size/mm^3	0.254 × 0.155 × 0.102
Radiation	CuKα (λ = 1.54184)
2Θ range for data collection/°	6.192 to 160.286
Index ranges	-16 ≤ h ≤ 19, -23 ≤ k ≤ 23, -55 ≤ l ≤ 55
Reflections collected	44246
Independent reflections	44246 [R_{int} = 0.0280, R_{sigma} = 0.0206]
Data/restraints/parameters	44246/315/1461
Goodness-of-fit on F^2	1.024
Final R indexes [I>=2σ (I)]	R_1 = 0.0653, wR_2 = 0.1875
Final R indexes [all data]	R_1 = 0.0679, wR_2 = 0.1912
Flack parameter	-0.024(7)

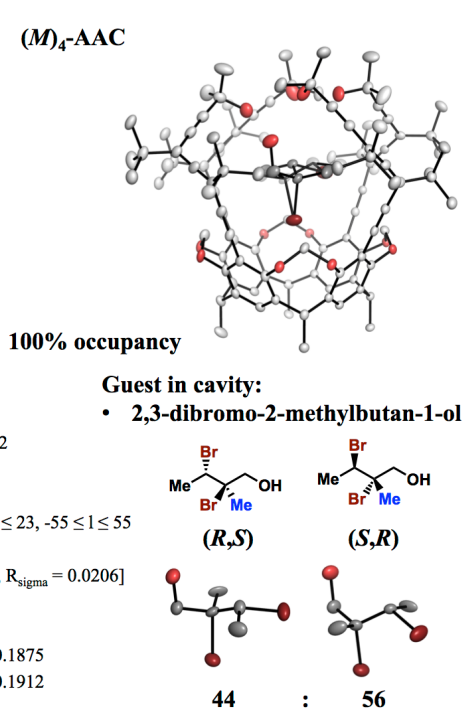

Figure 159. Crystallographic data and ORTEP representation of AAC $(M)_4$-**62**⊃2,3-dibromo-2-methylbutanol (50% probability). *n*-Hexyl chains omitted for clarity.

Empirical formula	$C_{133}H_{178}Br_2O_{13}$
Formula weight	2144.56
Temperature/K	100.0(1)
Crystal system	orthorhombic
Space group	$P2_12_12_1$
a/Å	15.54830(10)
b/Å	18.78360(10)
c/Å	44.2547(3)
α/°	90
β/°	90
γ/°	90
Volume/Å^3	12924.72(14)
Z	4
ρ_{calc}g/cm^3	1.102
μ/mm^{-1}	1.226
F(000)	4600.0
Crystal size/mm^3	0.127 × 0.066 × 0.034
Radiation	CuKα (λ = 1.54184)
2Θ range for data collection/°	6.024 to 159.49
Index ranges	-19 ≤ h ≤ 19, -23 ≤ k ≤ 23, -55 ≤ l ≤ 56
Reflections collected	210259
Independent reflections	27875 [R_{int} = 0.0708, R_{sigma} = 0.0385]
Data/restraints/parameters	27875/317/1464
Goodness-of-fit on F^2	1.027
Final R indexes [I>=2σ (I)]	R_1 = 0.0515, wR_2 = 0.1339
Final R indexes [all data]	R_1 = 0.0647, wR_2 = 0.1432
Flack parameter	-0.014(5)

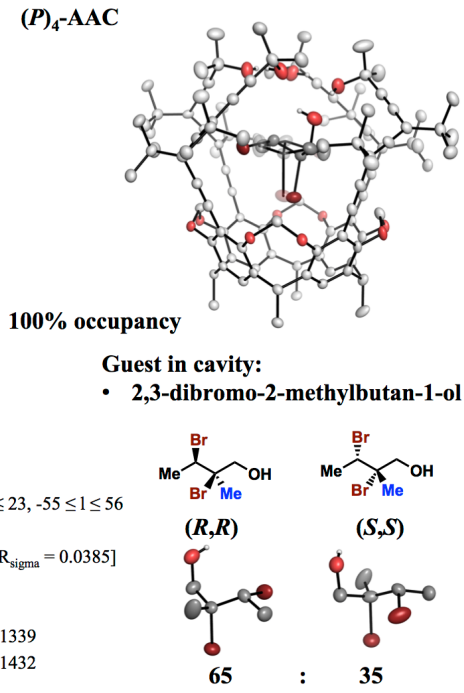

Figure 160. Crystallographic data and ORTEP representation of AAC $(P)_4$-**62**⊃2,3-dibromo-2-methylbutanol (50% probability). *n*-Hexyl chains omitted for clarity.

Empirical formula	$C_{133}H_{178}Br_2O_{13}$
Formula weight	2144.56
Temperature/K	100.0(1)
Crystal system	orthorhombic
Space group	$P2_12_12_1$
a/Å	15.54360(10)
b/Å	18.74790(10)
c/Å	44.4074(2)
α/°	90
β/°	90
γ/°	90
Volume/Å^3	12940.76(12)
Z	4
ρ_{calc}g/cm^3	1.101
μ/mm^{-1}	1.225
F(000)	4600.0
Crystal size/mm^3	0.195 × 0.131 × 0.064
Radiation	CuKα (λ = 1.54184)
2Θ range for data collection/°	6.024 to 159.76
Index ranges	-19 ≤ h ≤ 19, -23 ≤ k ≤ 18, -56 ≤ l ≤ 56
Reflections collected	269776
Independent reflections	27995 [R_{int} = 0.0521, R_{sigma} = 0.0226]
Data/restraints/parameters	27995/350/1438
Goodness-of-fit on F^2	1.018
Final R indexes [I>=2σ (I)]	R_1 = 0.0568, wR_2 = 0.1682
Final R indexes [all data]	R_1 = 0.0593, wR_2 = 0.1709
Flack parameter	0.010(3)

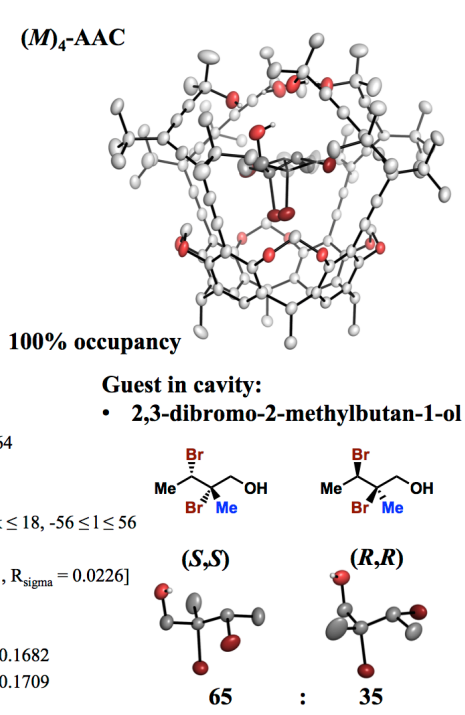

Figure 161. Crystallographic data and ORTEP representation of AAC $(M)_4$-**62**⊃2,3-dibromo-2-methylbutanol (50% probability). *n*-Hexyl chains omitted for clarity.

Empirical formula	$C_{133}H_{178}Br_2O_{13}$
Formula weight	2144.56
Temperature/K	100.0(1)
Crystal system	orthorhombic
Space group	$P2_12_12_1$
a/Å	44.1945(2)
b/Å	18.78150(10)
c/Å	15.55630(10)
α/°	90
β/°	90
γ/°	90
Volume/Å^3	12912.34(12)
Z	4
ρ_{calc}g/cm^3	1.103
μ/mm^{-1}	1.228
F(000)	4600.0
Crystal size/mm^3	0.123 × 0.08 × 0.042
Radiation	CuKα (λ = 1.54184)
2Θ range for data collection/°	6.024 to 159.608
Index ranges	-56 ≤ h ≤ 55, -23 ≤ k ≤ 19, -19 ≤ l ≤ 18
Reflections collected	215132
Independent reflections	27917 [R_{int} = 0.0575, R_{sigma} = 0.0302]
Data/restraints/parameters	27917/353/1436
Goodness-of-fit on F^2	1.024
Final R indexes [I>=2σ (I)]	R_1 = 0.0528, wR_2 = 0.1485
Final R indexes [all data]	R_1 = 0.0570, wR_2 = 0.1522
Flack parameter	-0.005(4)

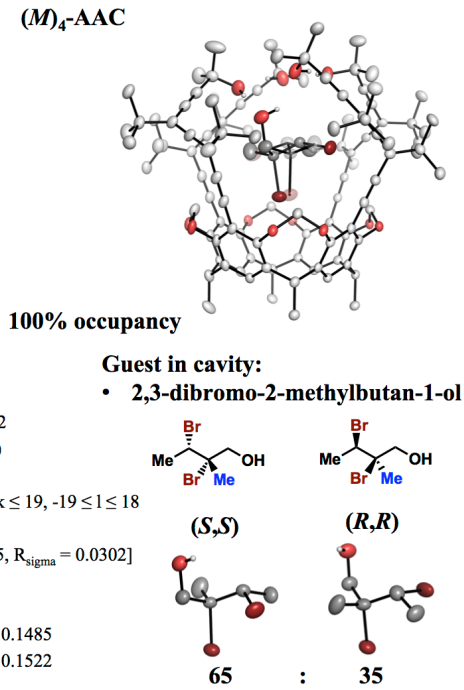

Figure 162. Crystallographic data and ORTEP representation of AAC $(M)_4$-**62**⊃2,3-dibromo-2-methylbutanol (50% probability). *n*-Hexyl chains omitted for clarity.

Empirical formula	$C_{134}H_{182}O_{13}$
Formula weight	2000.79
Temperature/K	100.0(1)
Crystal system	orthorhombic
Space group	$P2_12_12_1$
a/Å	15.41030(10)
b/Å	18.60230(10)
c/Å	44.9029(2)
α/°	90
β/°	90
γ/°	90
Volume/Å^3	12872.18(12)
Z	4
ρ_{calc}g/cm^3	1.032
μ/mm^{-1}	0.501
F(000)	4360.0
Crystal size/mm^3	0.173 × 0.134 × 0.106
Radiation	CuKα (λ = 1.54184)
2Θ range for data collection/°	6.064 to 160.426
Index ranges	-16 ≤ h ≤ 19, -23 ≤ k ≤ 23, -56 ≤ l ≤ 57
Reflections collected	264846
Independent reflections	27814 [R_{int} = 0.0400, R_{sigma} = 0.0170]
Data/restraints/parameters	27814/105/1389
Goodness-of-fit on F^2	1.065
Final R indexes [I>=2σ (I)]	R_1 = 0.0366, wR_2 = 0.0997
Final R indexes [all data]	R_1 = 0.0381, wR_2 = 0.1011
Flack parameter	0.03(3)

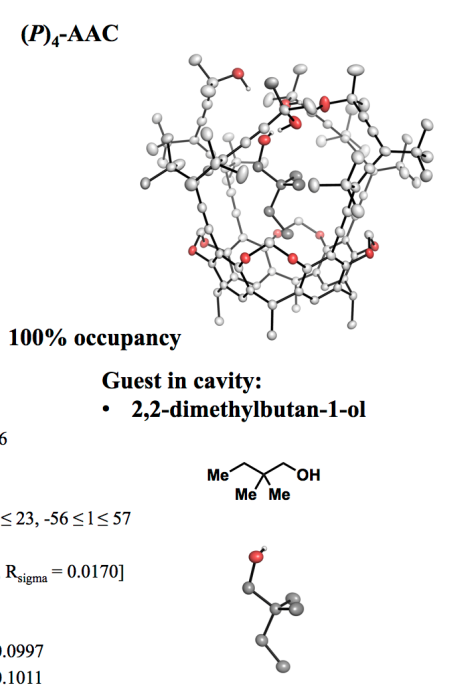

Figure 163. Crystallographic data and ORTEP representation of AAC $(P)_4$-**62**⊃2,2-dimethylbutanol (50% probability). *n*-Hexyl chains omitted for clarity.

Empirical formula	$C_{244.47}H_{297.44}Cl_{7.54}N_{4.97}O_{16}$
Formula weight	3828.64
Temperature/K	100.0(1)
Crystal system	monoclinic
Space group	$P2_1$
a/Å	14.94110(10)
b/Å	47.0639(2)
c/Å	18.02570(10)
α/°	90
β/°	113.5830(10)
γ/°	90
Volume/Å^3	11616.79(14)
Z	2
ρ_{calc}g/cm^3	1.095
μ/mm^{-1}	1.290
F(000)	4110.0
Crystal size/mm^3	0.196 × 0.126 × 0.067
Radiation	CuKα (λ = 1.54184)
2Θ range for data collection/°	6.454 to 158.322
Index ranges	-19 ≤ h ≤ 18, -59 ≤ k ≤ 59, -22 ≤ l ≤ 22
Reflections collected	550996
Independent reflections	49433 [R_{int} = 0.0629, R_{sigma} = 0.0290]
Data/restraints/parameters	49433/454/2737
Goodness-of-fit on F^2	1.023
Final R indexes [I>=2σ (I)]	R_1 = 0.0577, wR_2 = 0.1574
Final R indexes [all data]	R_1 = 0.0637, wR_2 = 0.1628
Flack parameter	0.038(3)

(*P*)$_4$-AAC-Cage

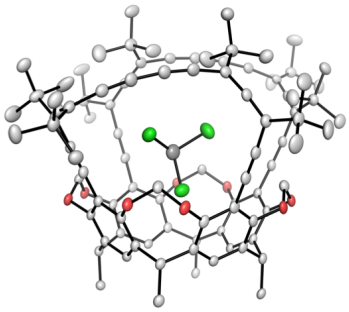

CHCl$_3$

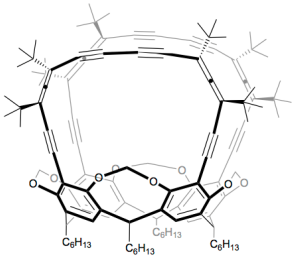

Figure 164. Crystallographic data and ORTEP representation of covalent AAC (*P*)$_4$-**88**⊃chloroform (50% probability). *n*-Hexyl chains omitted for clarity.

Empirical formula	$C_{256}H_{321.43}N_{6.58}O_{16}$
Formula weight	3746.65
Temperature/K	100.0(1)
Crystal system	monoclinic
Space group	$P2_1$
a/Å	15.0054(2)
b/Å	46.9131(4)
c/Å	18.1336(2)
α/°	90
β/°	113.8379(16)
γ/°	90
Volume/Å^3	11676.2(3)
Z	2
ρ_{calc}g/cm^3	1.066
μ/mm^{-1}	0.501
F(000)	4063.0
Crystal size/mm^3	0.112 × 0.049 × 0.03
Radiation	CuKα (λ = 1.54184)
2Θ range for data collection/°	6.44 to 158.23
Index ranges	-15 ≤ h ≤ 18, -59 ≤ k ≤ 59, -23 ≤ l ≤ 22
Reflections collected	399652
Independent reflections	49464 [R_{int} = 0.0804, R_{sigma} = 0.0496]
Data/restraints/parameters	49464/1435/2978
Goodness-of-fit on F^2	1.025
Final R indexes [I>=2σ (I)]	R_1 = 0.0547, wR_2 = 0.1294
Final R indexes [all data]	R_1 = 0.0841, wR_2 = 0.1462
Flack parameter	0.00(5)

(*M*)$_4$-AAC-Cage

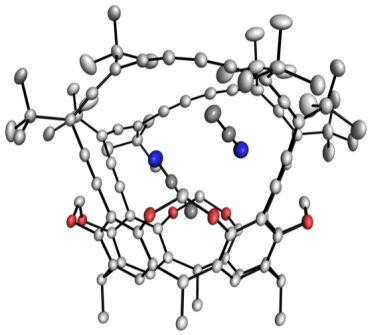

2 x CH$_3$CN

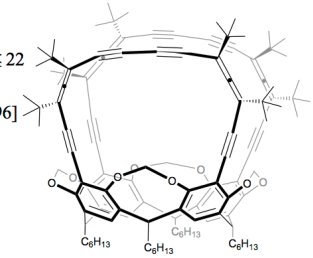

Figure 165. Crystallographic data and ORTEP representation of covalent AAC (*M*)$_4$-**88**⊃chloroform (50% probability). *n*-Hexyl chains omitted for clarity.

Empirical formula	$C_{134}H_{179}N_3O_{13}$
Formula weight	2039.79
Temperature/K	100.0(2)
Crystal system	monoclinic
Space group	$P2_1$
a/Å	15.6574(19)
b/Å	44.298(6)
c/Å	18.431(2)
α/°	90
β/°	91.853(3)
γ/°	90
Volume/Å^3	12777(3)
Z	4
ρ_{calc}g/cm^3	1.060
μ/mm^{-1}	0.067
F(000)	4432.0
Crystal size/mm^3	0.24 × 0.19 × 0.17
Radiation	MoKα (λ = 0.71073)
2Θ range for data collection/°	13.628 to 46.512
Index ranges	-14 ≤ h ≤ 17, -49 ≤ k ≤ 49, -20 ≤ l ≤ 20
Reflections collected	57644
Independent reflections	34480 [R_{int} = 0.0552, R_{sigma} = 0.1172]
Data/restraints/parameters	34480/3285/2859
Goodness-of-fit on F^2	1.017
Final R indexes [I>=2σ (I)]	R_1 = 0.0910, wR_2 = 0.2089
Final R indexes [all data]	R_1 = 0.1346, wR_2 = 0.2368
Flack parameter	0.4(5)

$(P)_4$-AAC

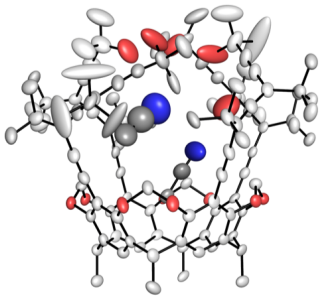

2 x CH_3CN + H_2O

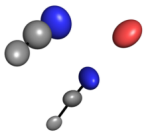

Figure 166. Crystallographic data and ORTEP representation of AAC $(P)_4$-**62**⊃(2 x acetonitrile; 1 x H_2O); (50% probability). *n*-Hexyl chains omitted for clarity.

Empirical formula	$C_{132.3}H_{174.45}F_{2.15}O_{12}$
Formula weight	1997.61
Temperature/K	100.0(1)
Crystal system	orthorhombic
Space group	$P2_12_12_1$
a/Å	15.5493(2)
b/Å	18.5586(2)
c/Å	44.6200(7)
α/°	90
β/°	90
γ/°	90
Volume/Å^3	12876.1(3)
Z	4
ρ_{calc}g/cm^3	1.030
μ/mm^{-1}	0.520
F(000)	4334.0
Crystal size/mm^3	0.236 × 0.178 × 0.106
Radiation	CuKα (λ = 1.54184)
2Θ range for data collection/°	6.194 to 160.252
Index ranges	-19 ≤ h ≤ 19, -18 ≤ k ≤ 23, -56 ≤ l ≤ 55
Reflections collected	212709
Independent reflections	27814 [R_{int} = 0.0483, R_{sigma} = 0.0216]
Data/restraints/parameters	27814/380/1477
Goodness-of-fit on F^2	1.072
Final R indexes [I>=2σ (I)]	R_1 = 0.0815, wR_2 = 0.2234
Final R indexes [all data]	R_1 = 0.0871, wR_2 = 0.2279
Flack parameter	0.04(3)

$(P)_4$-AAC

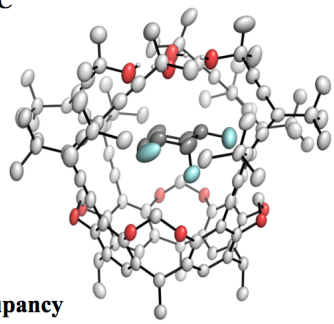

75% occupancy

Guest in cavity:

- **1,2,3-trifluorocyclohexane**

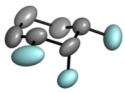

Figure 167. Crystallographic data and ORTEP representation of AAC $(P)_4$-**62**⊃1,2,3-trifluorocyclohexane; (50% probability). *n*-Hexyl chains omitted for clarity.

Empirical formula	$C_{134}H_{177}F_3O_{12}$
Formula weight	2036.75
Temperature/K	100.0(1)
Crystal system	orthorhombic
Space group	$P2_12_12_1$
a/Å	15.5164(2)
b/Å	18.4795(3)
c/Å	45.1097(8)
α/°	90
β/°	90
γ/°	90
Volume/Å^3	12934.5(4)
Z	4
ρ_{calc}g/cm^3	1.046
μ/mm^{-1}	0.535
F(000)	4416.0
Crystal size/mm^3	0.093 × 0.064 × 0.043
Radiation	CuKα (λ = 1.54184)
2Θ range for data collection/°	6.184 to 160.71
Index ranges	-17 ≤ h ≤ 19, -23 ≤ k ≤ 23, -57 ≤ l ≤ 57
Reflections collected	213901
Independent reflections	27970 [R_{int} = 0.0801, R_{sigma} = 0.0438]
Data/restraints/parameters	27970/575/1556
Goodness-of-fit on F^2	1.031
Final R indexes [I>=2σ (I)]	R_1 = 0.0812, wR_2 = 0.2272
Final R indexes [all data]	R_1 = 0.1108, wR_2 = 0.2574
Flack parameter	-0.09(8)

(*P*)$_4$-AAC

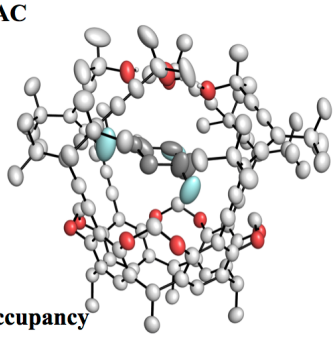

100% occupancy

Guest in cavity:

- **1,3,5-trifluorocyclohexane**

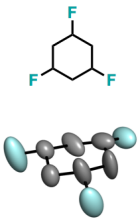

Figure 168. Crystallographic data and ORTEP representation of AAC (*P*)$_4$-**62**⊃1,3,5-trifluorocyclohexane; (50% probability). *n*-Hexyl chains omitted for clarity.

10.2 Selected NMR Spectra

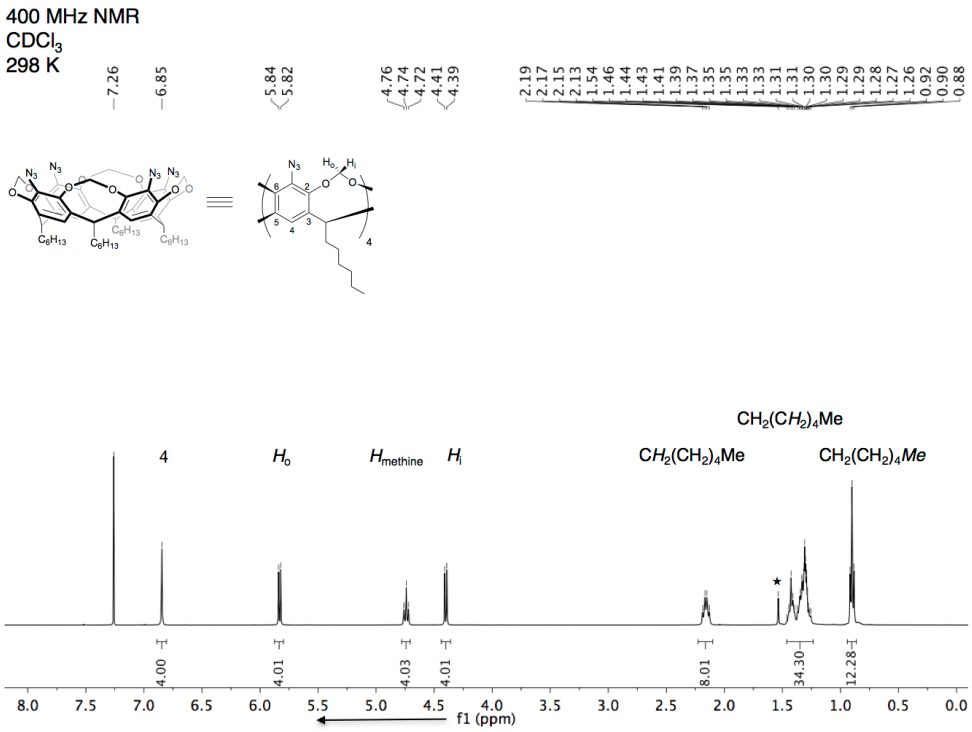

Figure 169. ^{1}H NMR spectrum (400 MHz, 298 K) of **60** in $CDCl_3$.

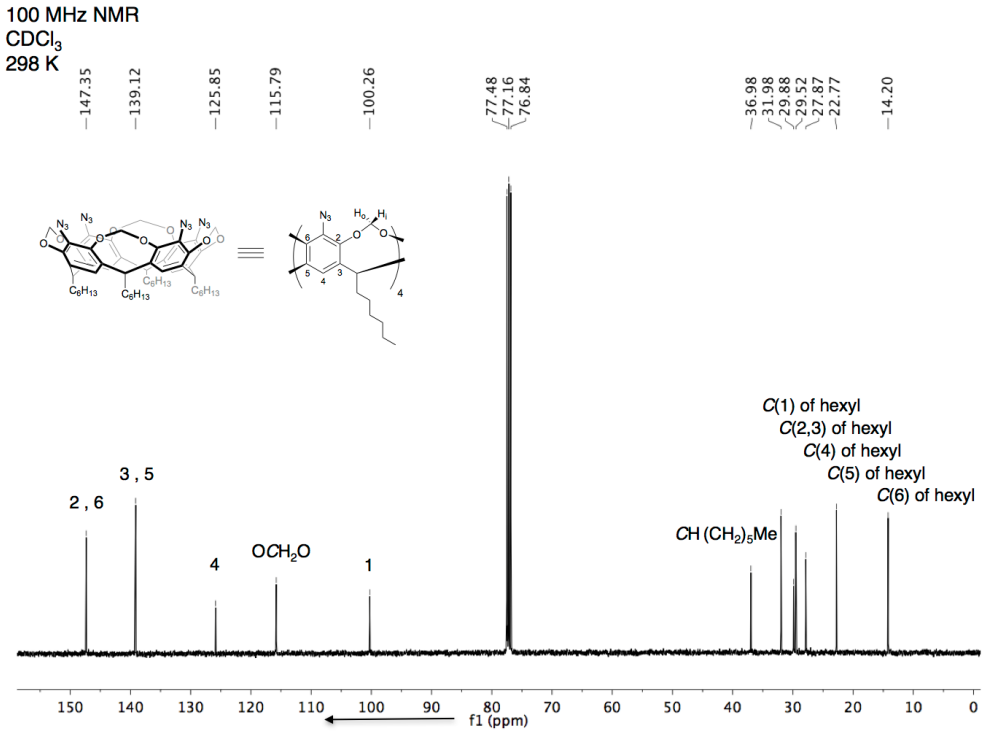

Figure 170. ^{13}C NMR spectrum (100 MHz, 298 K) of **60** in $CDCl_3$.

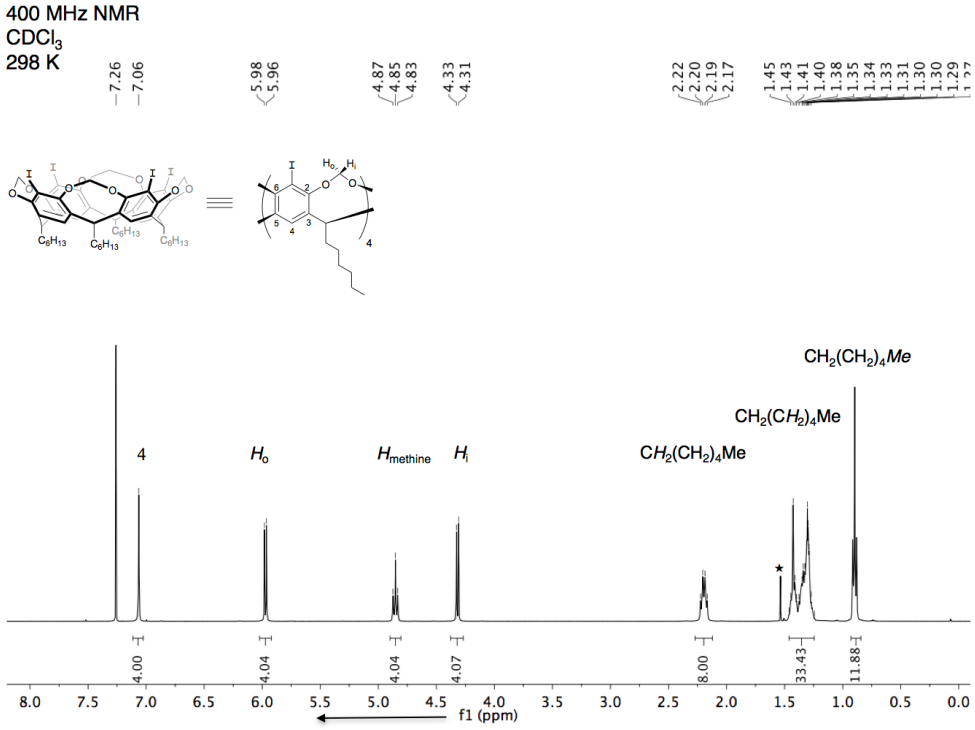

Figure 171. ^{1}H NMR spectrum (400 MHz, 298 K) of **59** in $CDCl_3$.

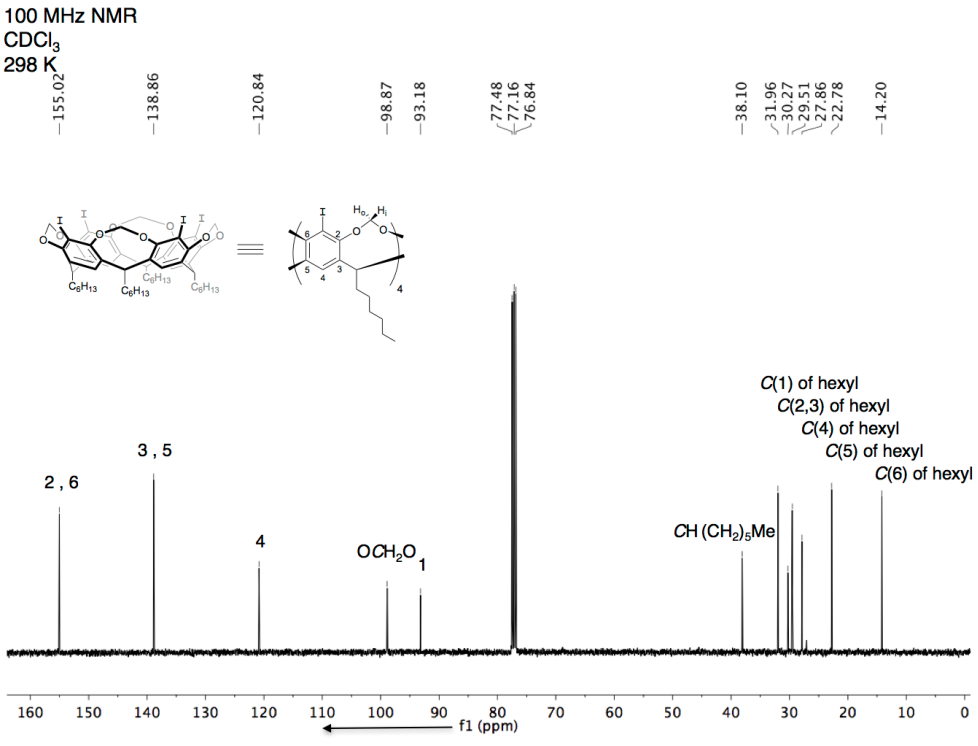

Figure 172. ^{13}C NMR spectrum (100 MHz, 298 K) of **59** in $CDCl_3$.

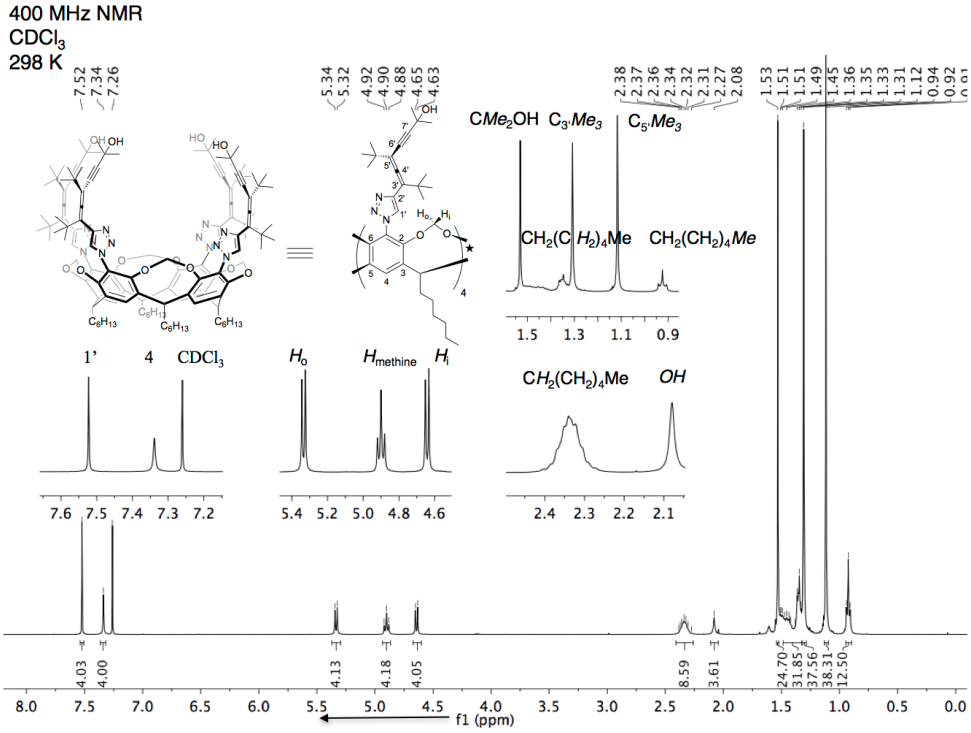

Figure 173. ^{1}H NMR spectrum (400 MHz, 298 K) of **61** in $CDCl_3$.

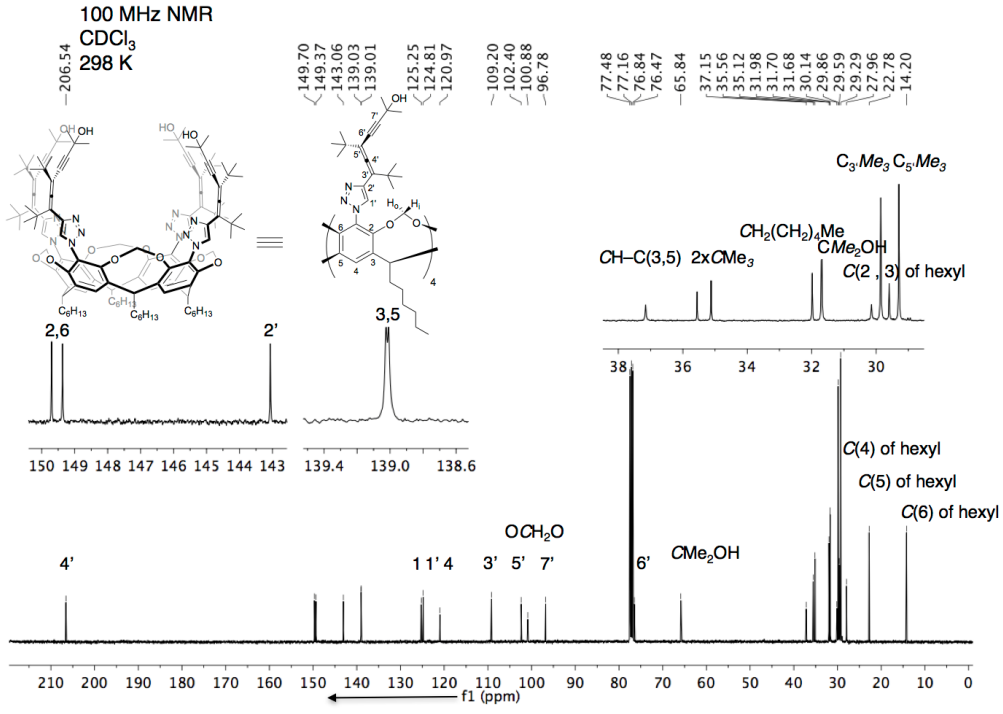

Figure 174. ^{13}C NMR spectrum (100 MHz, 298 K) of AAC $(P)_4$-**61** in $CDCl_3$.

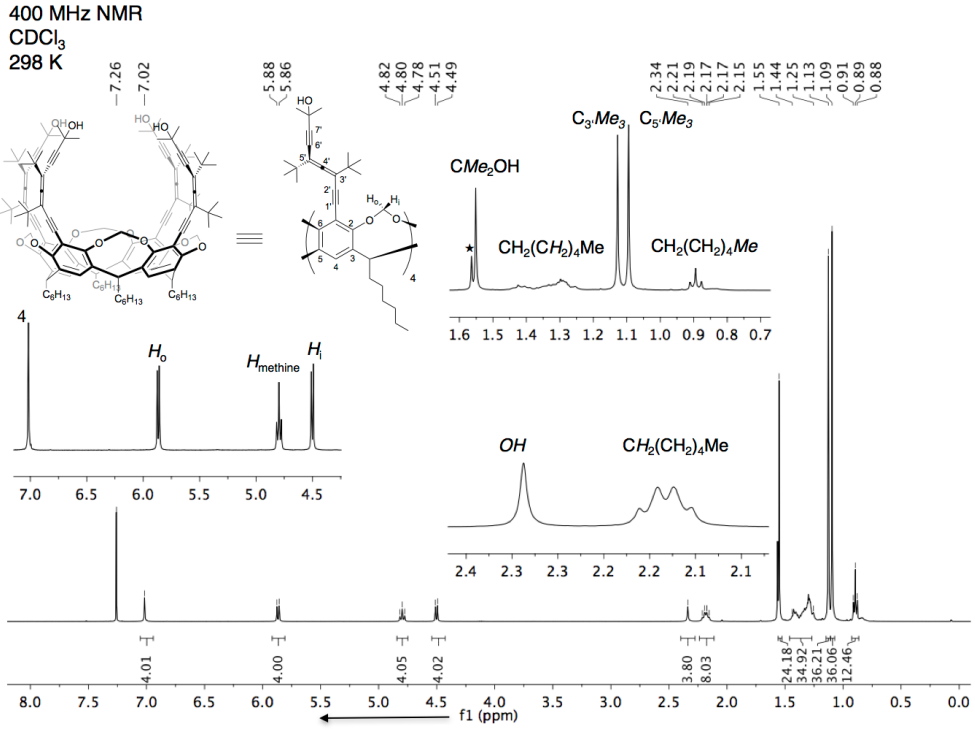

Figure 175. ^{1}H NMR spectrum (400 MHz, 298 K) of AAC $(P)_4$-**62** in $CDCl_3$.

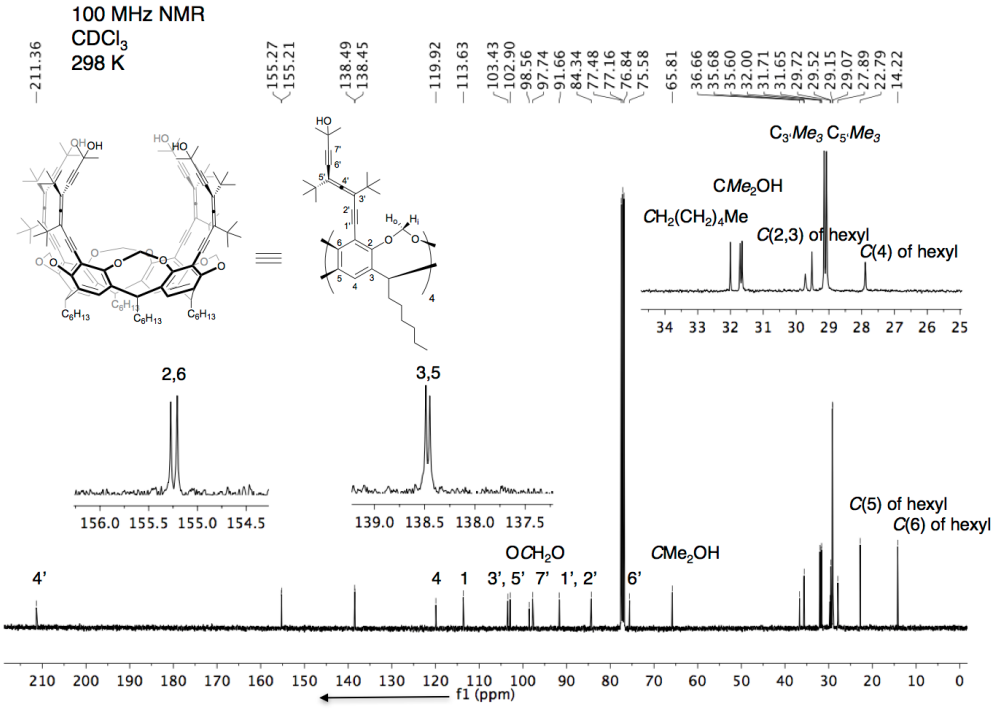

Figure 176. ^{13}C NMR spectrum (100 MHz, 298 K) of AAC $(P)_4$-**62** in $CDCl_3$.

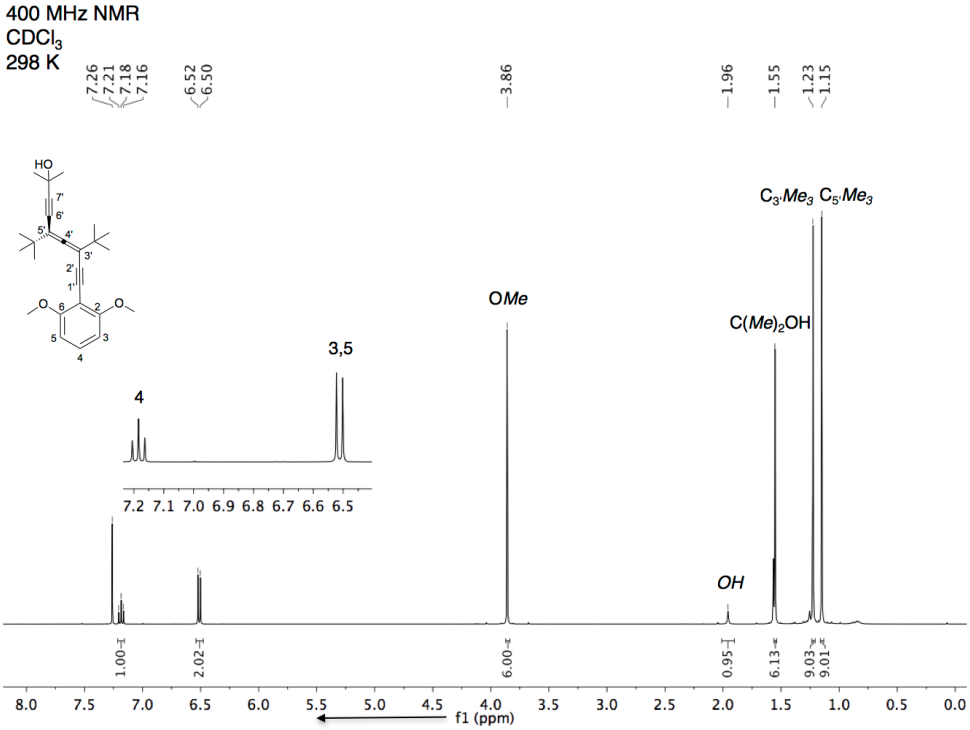

Figure 177. ^{1}H NMR spectrum (400 MHz, 298 K) of (*P*)-**64** in $CDCl_3$.

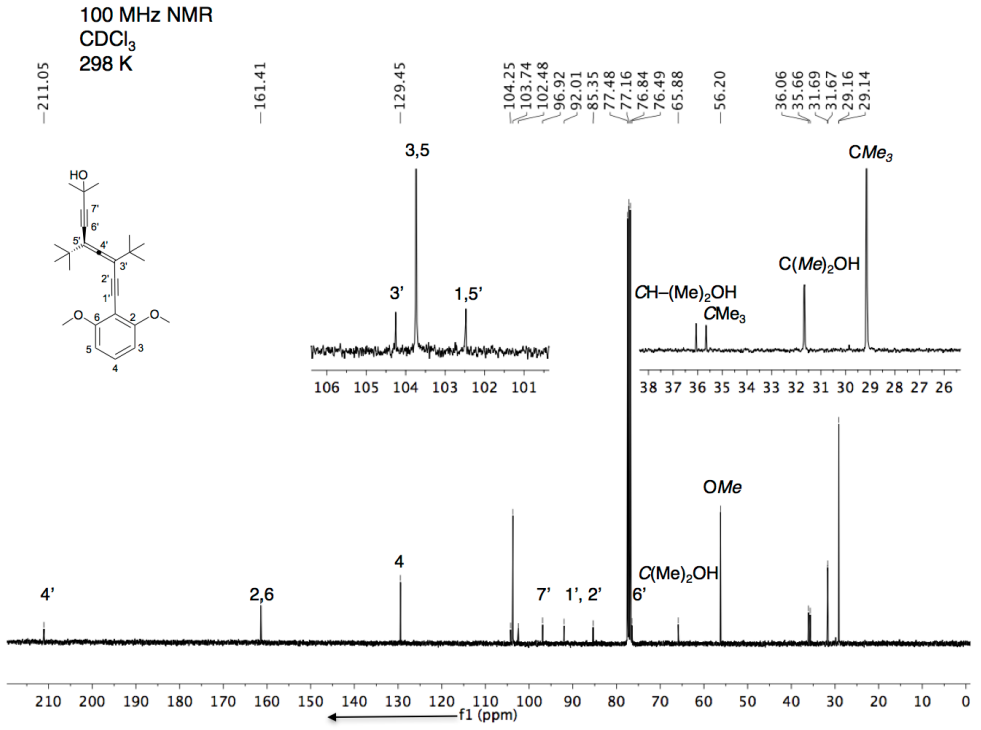

Figure 178. ^{13}C NMR spectrum (100 MHz, 298 K) of (*P*)-**64** in $CDCl_3$.

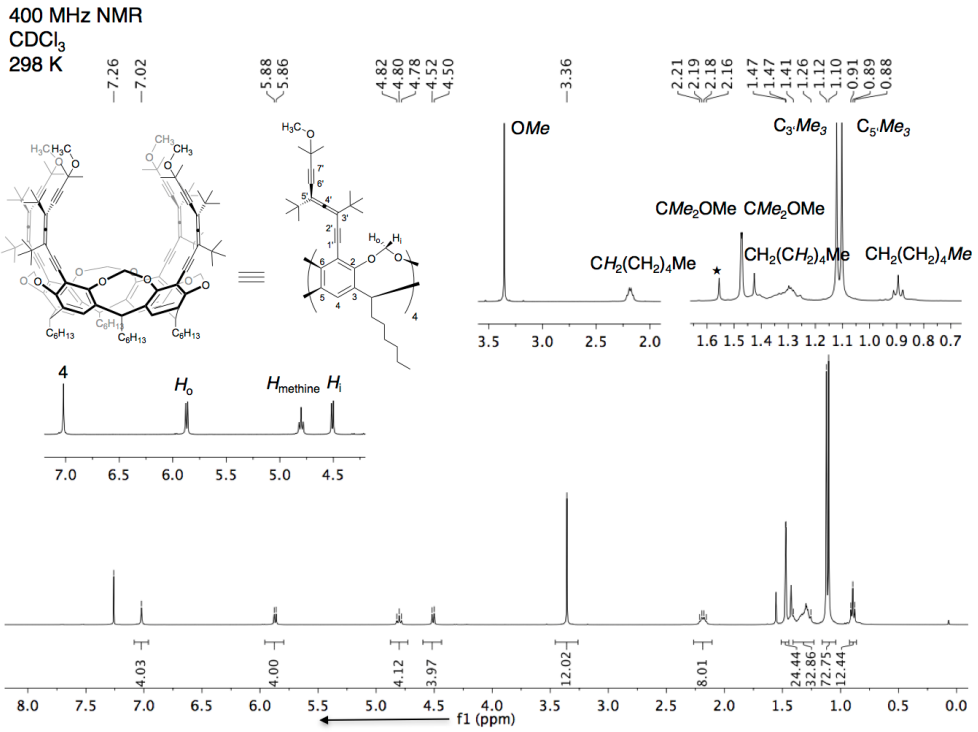

Figure 179. ^{1}H NMR spectrum (400 MHz, 298 K) of $(OMe)_4$-AAC $(P)_4$-**65** in $CDCl_3$.

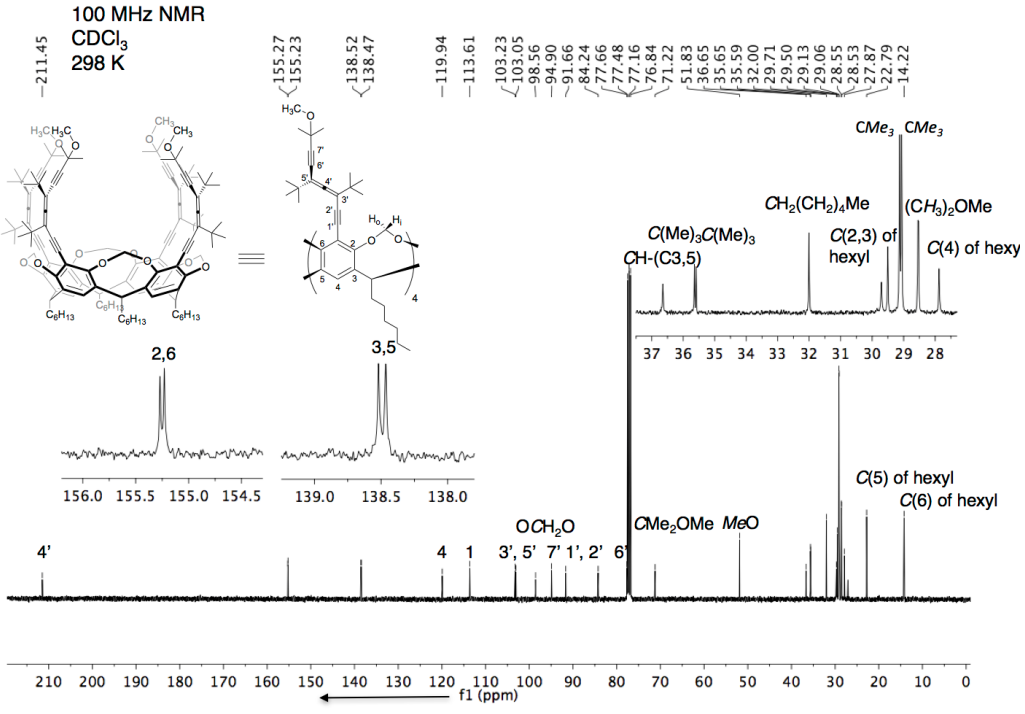

Figure 180. ^{13}C NMR spectrum (100 MHz, 298 K) of $(OMe)_4$-AAC $(P)_4$-**65** in $CDCl_3$.

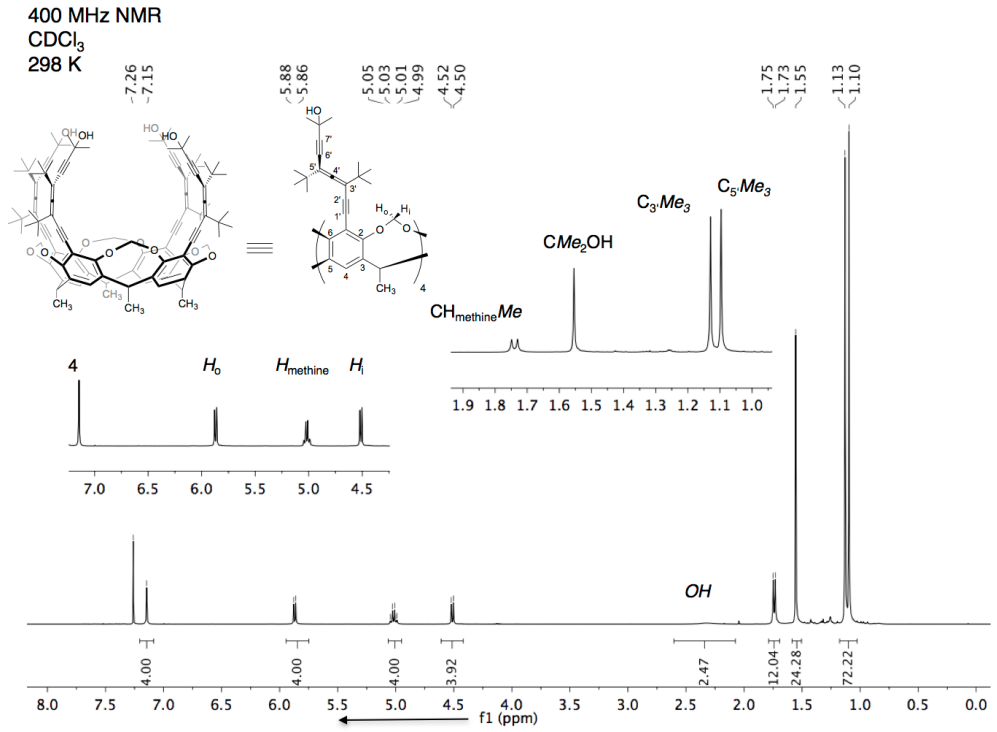

Figure 181. ^{1}H NMR spectrum (400 MHz, 298 K) of AAC $(P)_4$-**70** in $CDCl_3$.

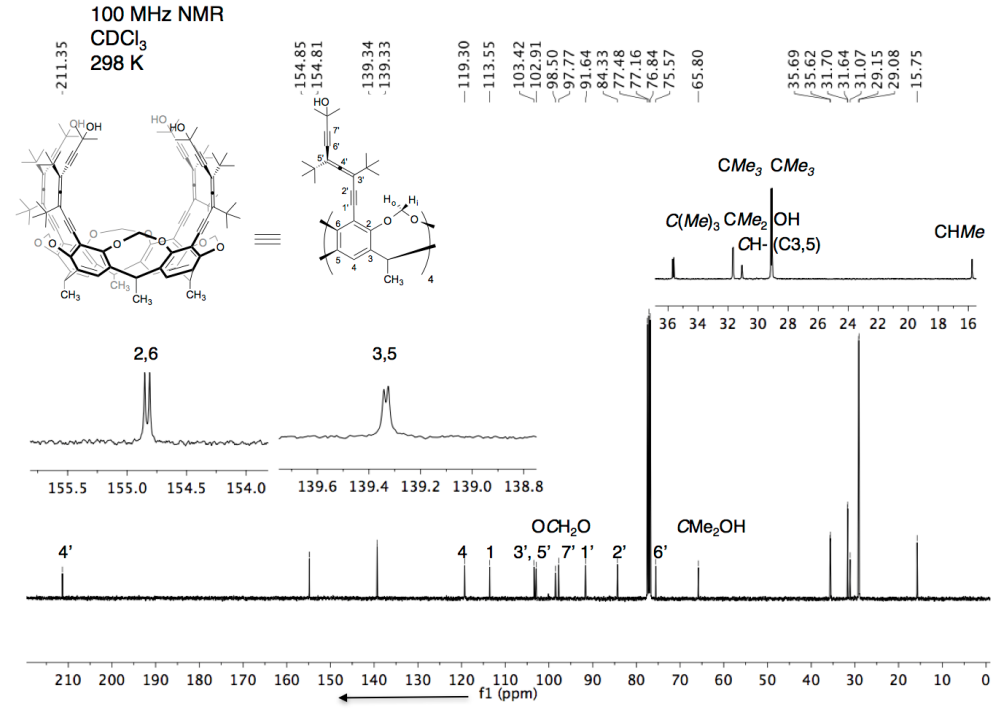

Figure 182. ^{13}C NMR spectrum (100 MHz, 298 K) of AAC $(P)_4$-**70** in $CDCl_3$.

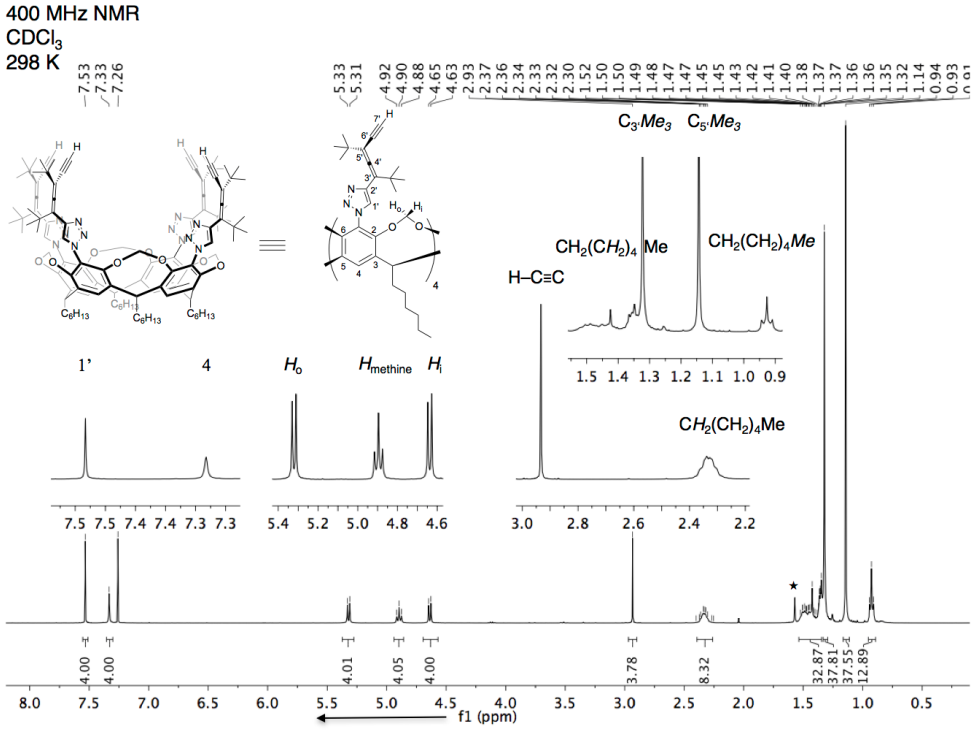

Figure 183. ^{1}H NMR spectrum (400 MHz, 298 K) of AAC $(P)_4$-**94** in $CDCl_3$.

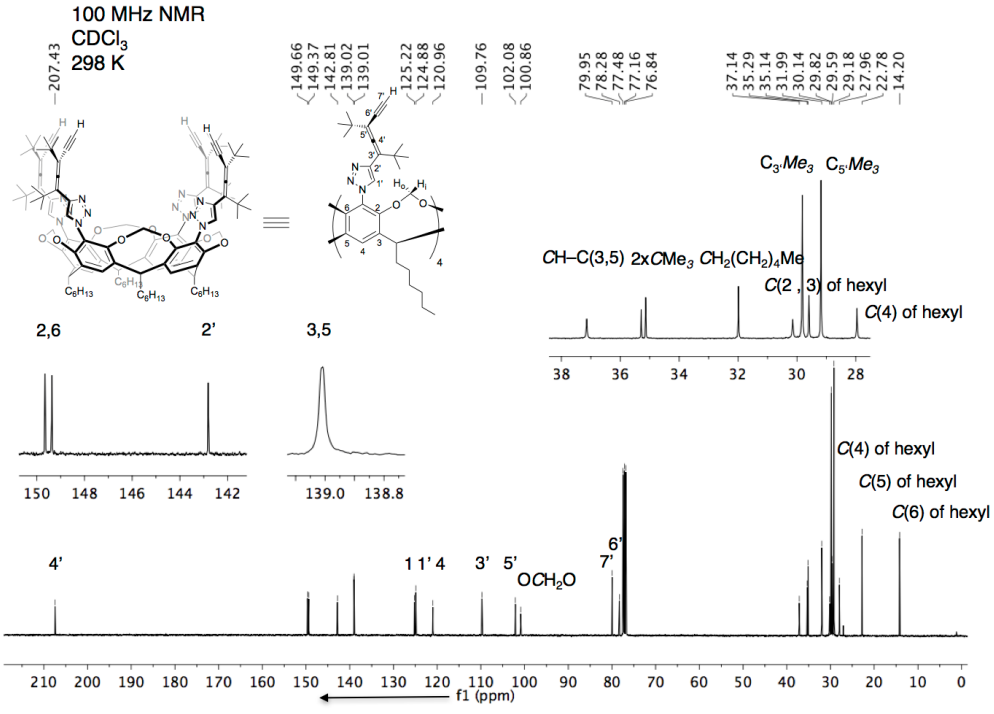

Figure 184. ^{13}C NMR spectrum (100 MHz, 298 K) of AAC $(P)_4$-**94** in $CDCl_3$.

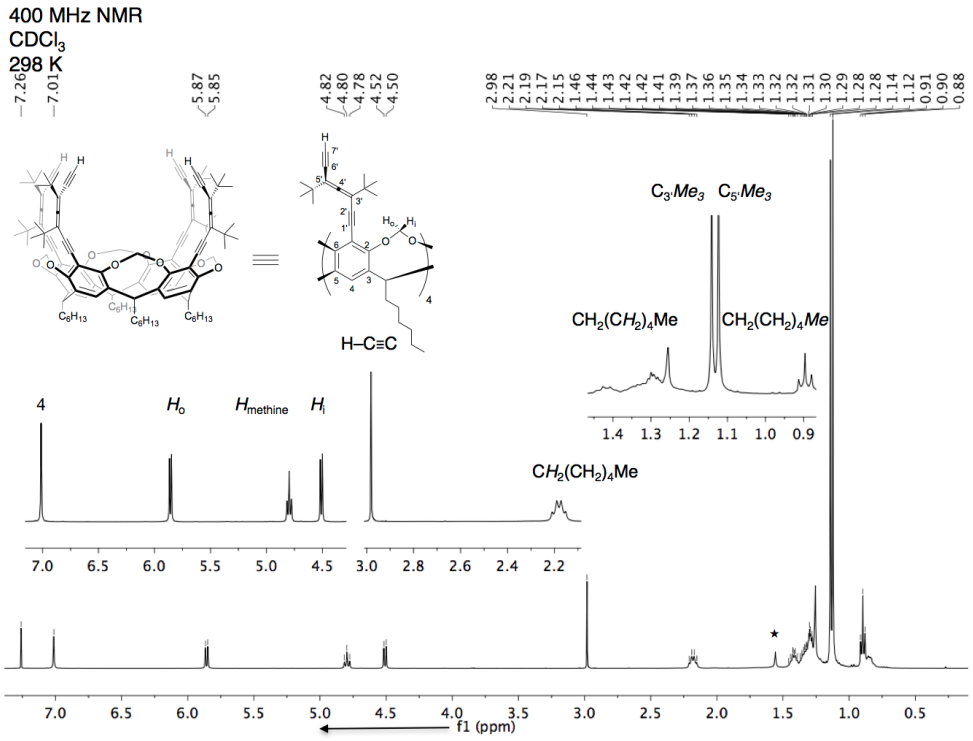

Figure 185. ^{1}H NMR spectrum (400 MHz, 298 K) of AAC $(P)_4$-**89** in $CDCl_3$.

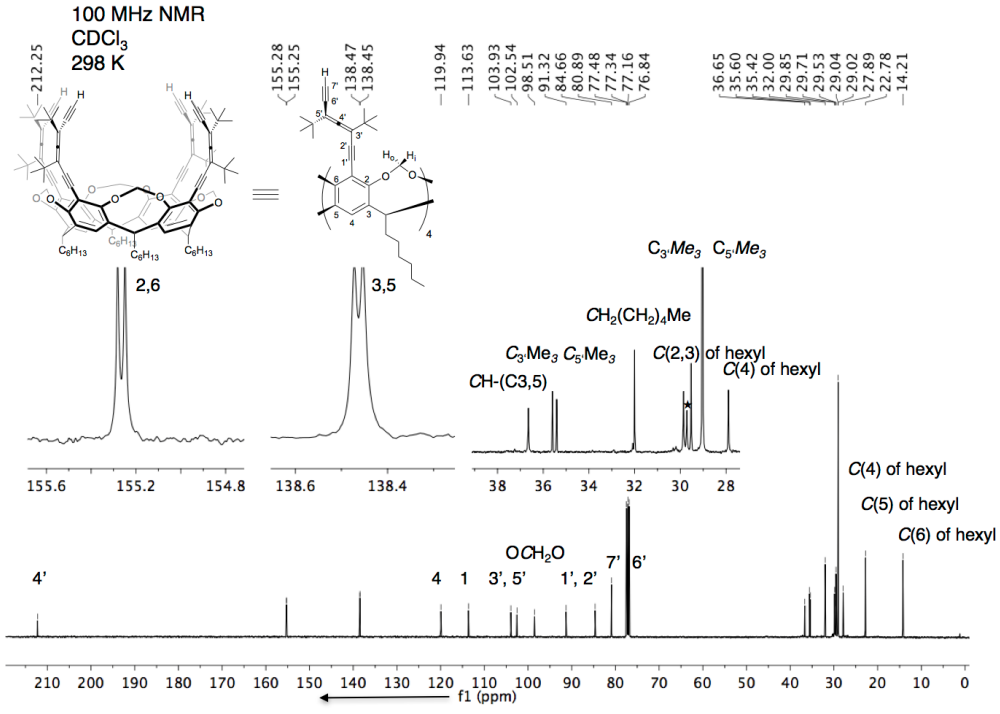

Figure 186. ^{13}C NMR spectrum (400 MHz, 298 K) of AAC $(P)_4$-**89** in $CDCl_3$.

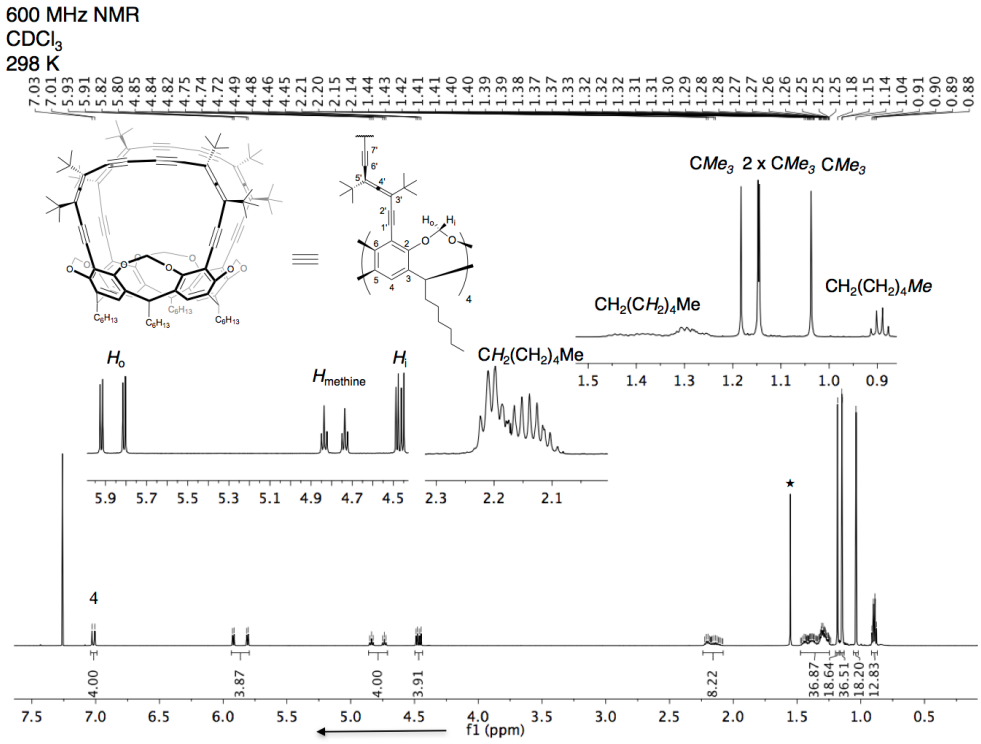

Figure 187. ^{1}H NMR spectrum (600 MHz, 298 K) of covalent AAC $(P)_4$-**88** in $CDCl_3$.

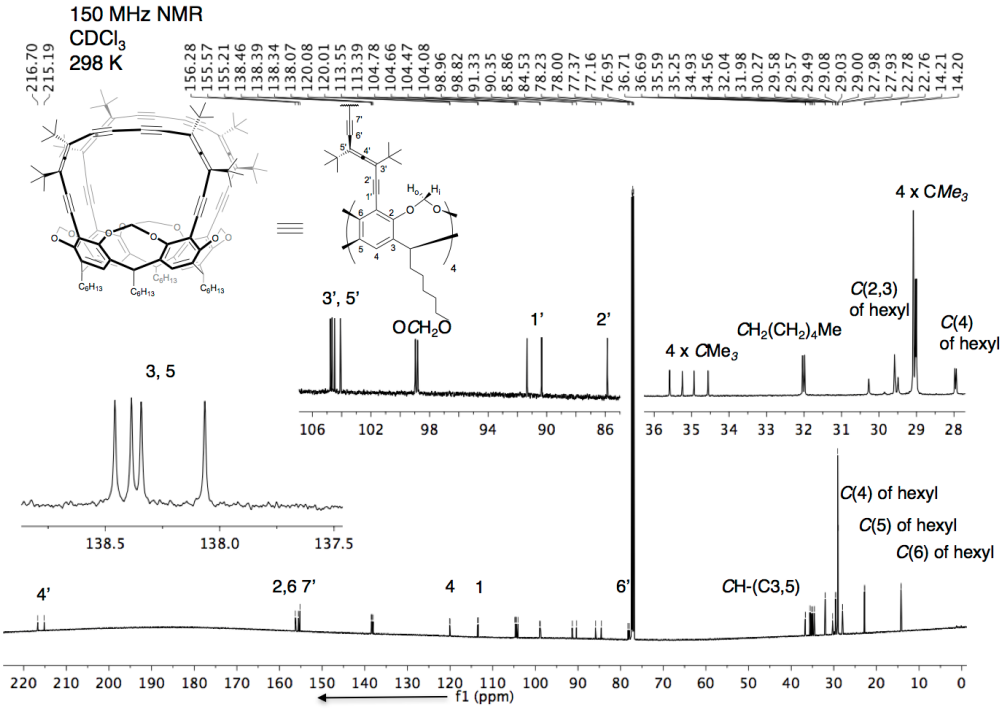

Figure 188. ^{13}C NMR spectrum (150 MHz, 298 K) of covalent AAC $(P)_4$-**88** in $CDCl_3$.

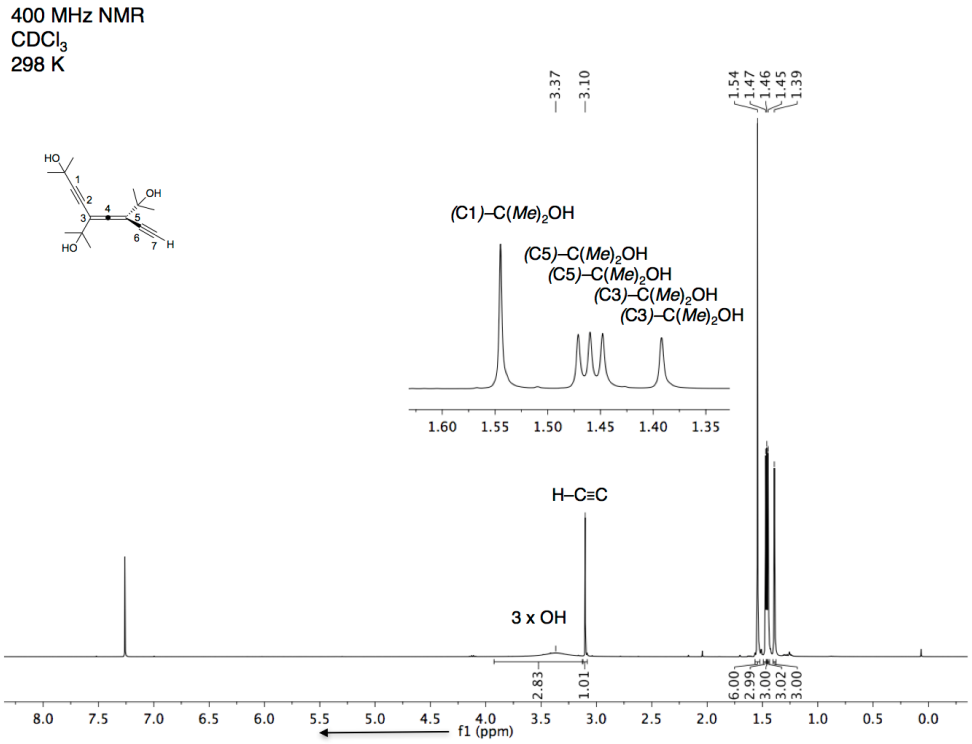

Figure 189. ^{1}H NMR spectrum (400 MHz, 298 K) of (*P*)-**74** in $CDCl_3$.

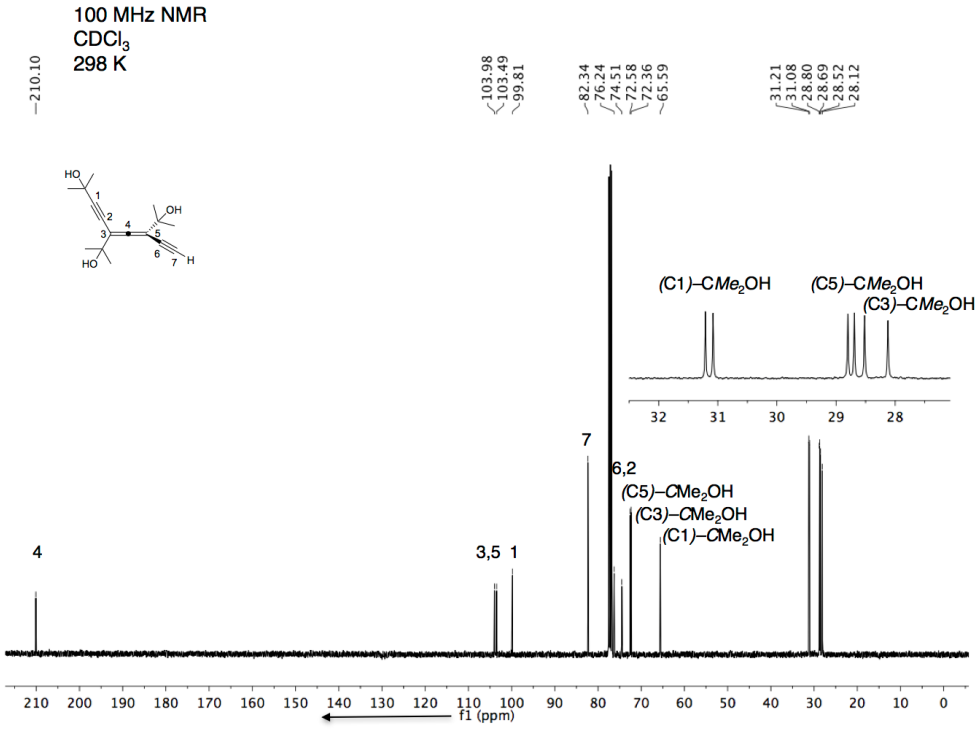

Figure 190. ^{13}C NMR spectrum (100 MHz, 298 K) of of (*P*)-**74** in $CDCl_3$.

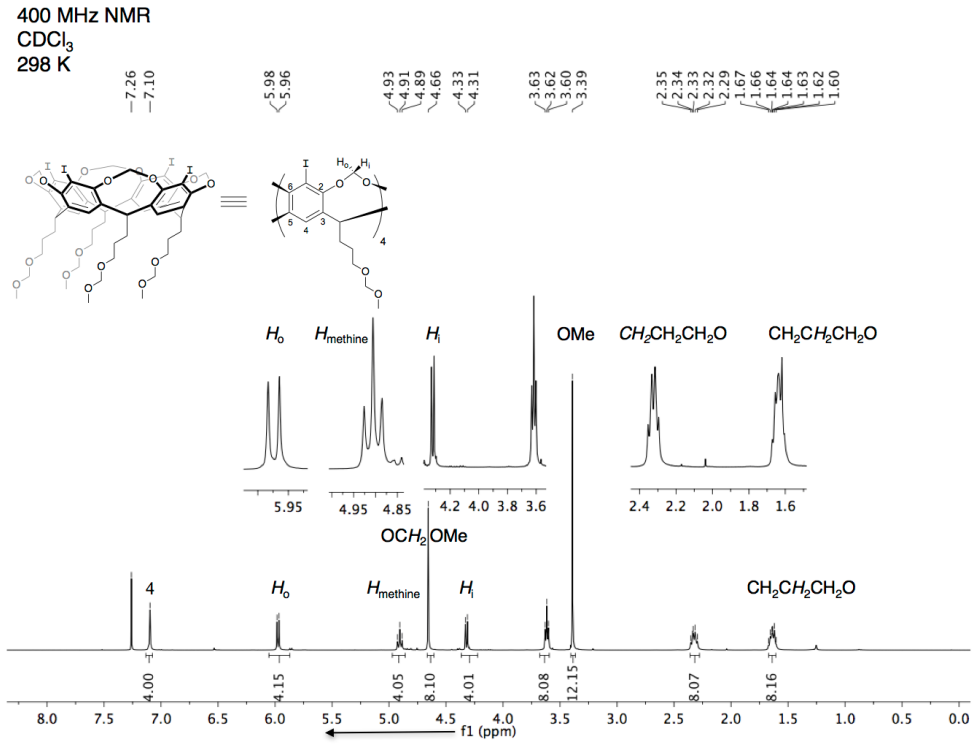

Figure 191. ^{1}H NMR spectrum (400 MHz, 298 K) of **96** in $CDCl_3$.

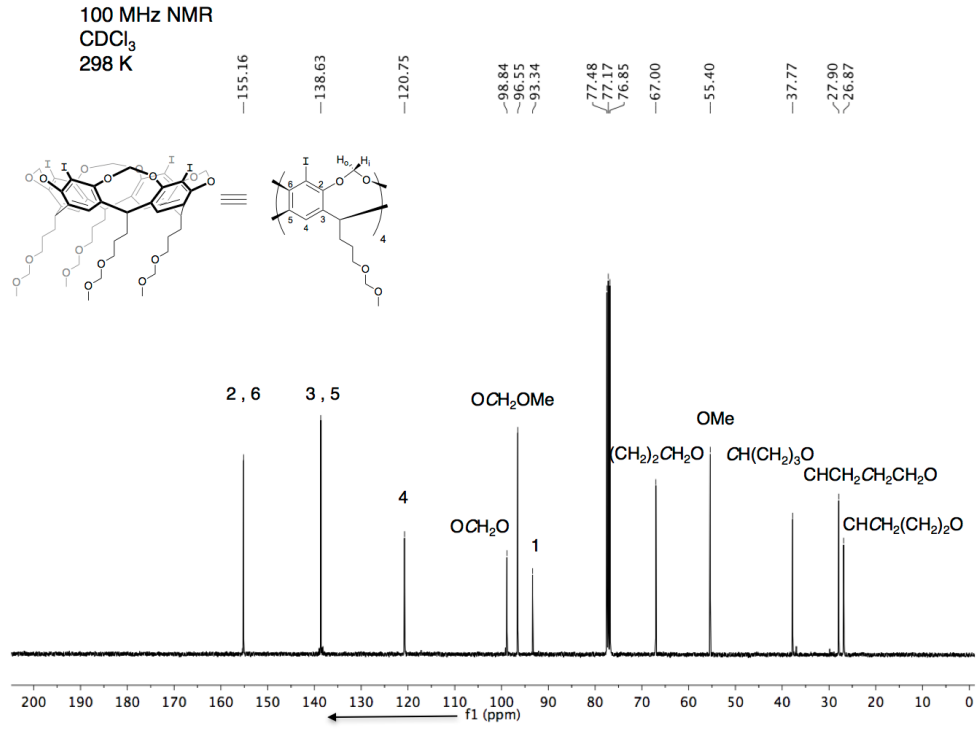

Figure 192. ^{13}C NMR spectrum (100 MHz, 298 K) of **96** in $CDCl_3$.

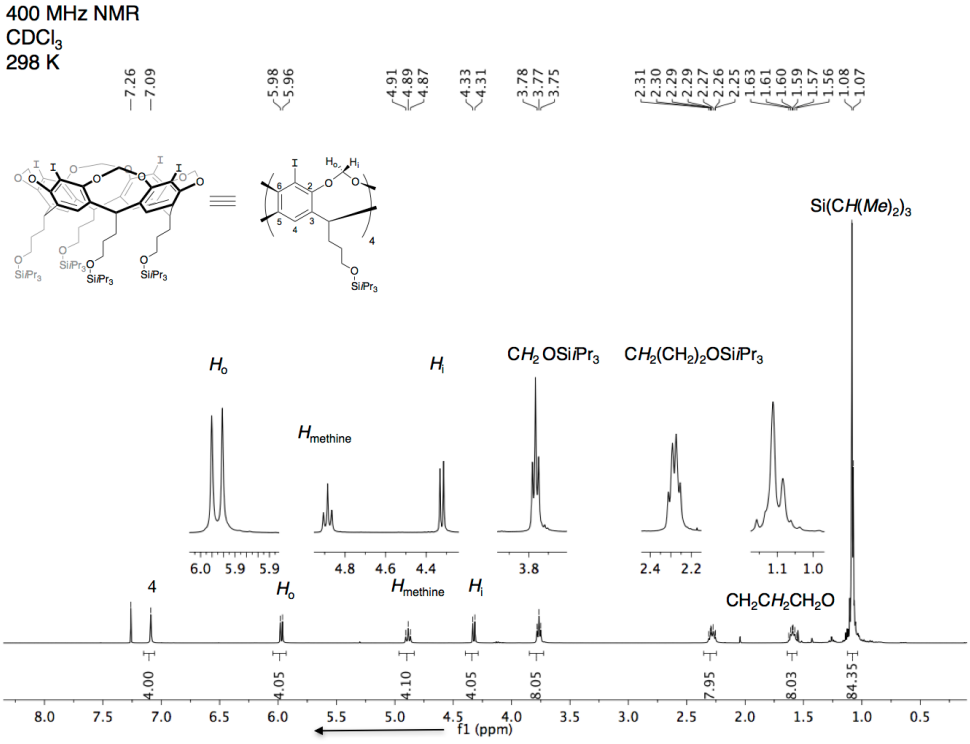

Figure 193. ^{1}H NMR spectrum (400 MHz, 298 K) of **83** in $CDCl_3$.

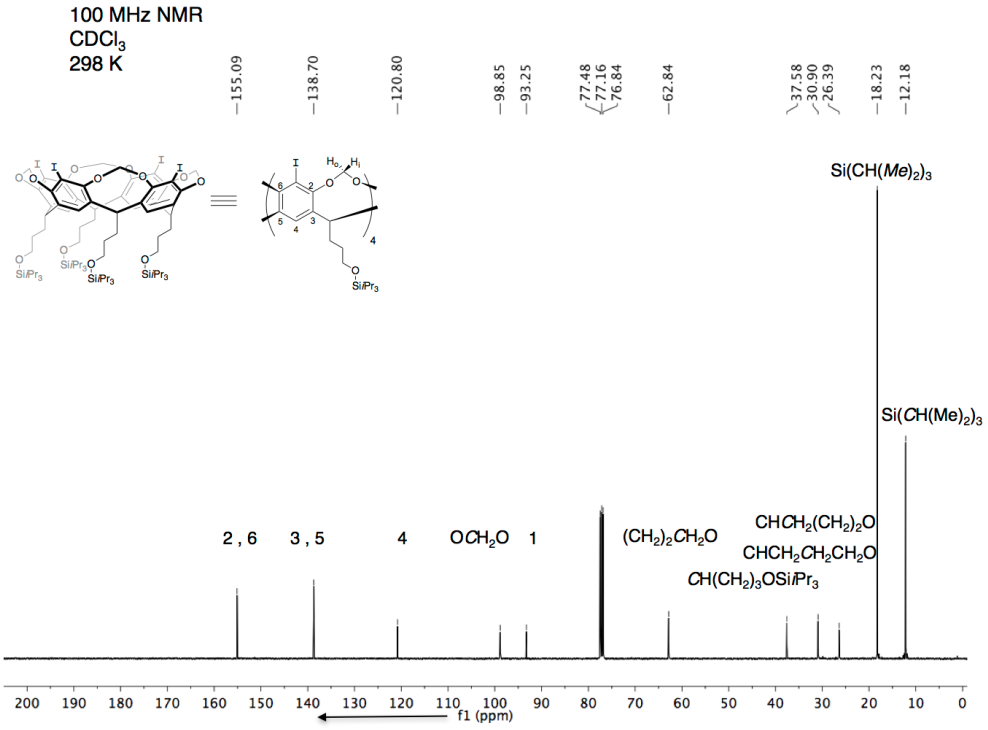

Figure 194. ^{13}C NMR spectrum (100 MHz, 298 K) of **83** in $CDCl_3$.

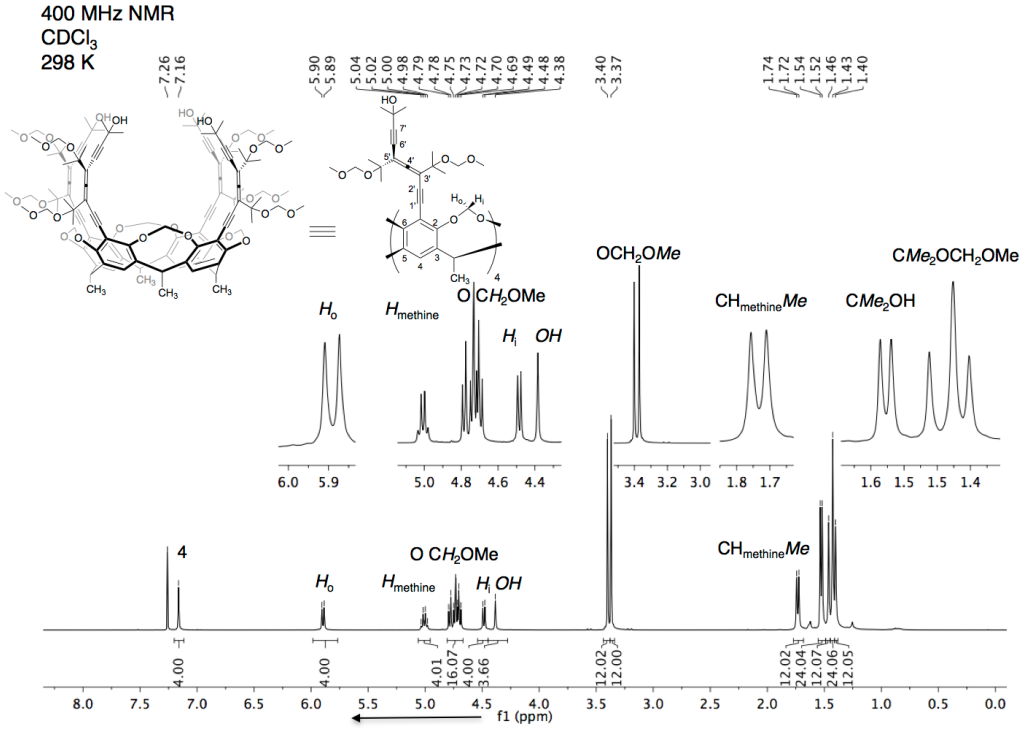

Figure 195. ^{1}H NMR spectrum (400 MHz, 298 K) of AAC $(P)_4$-**72** in $CDCl_3$.

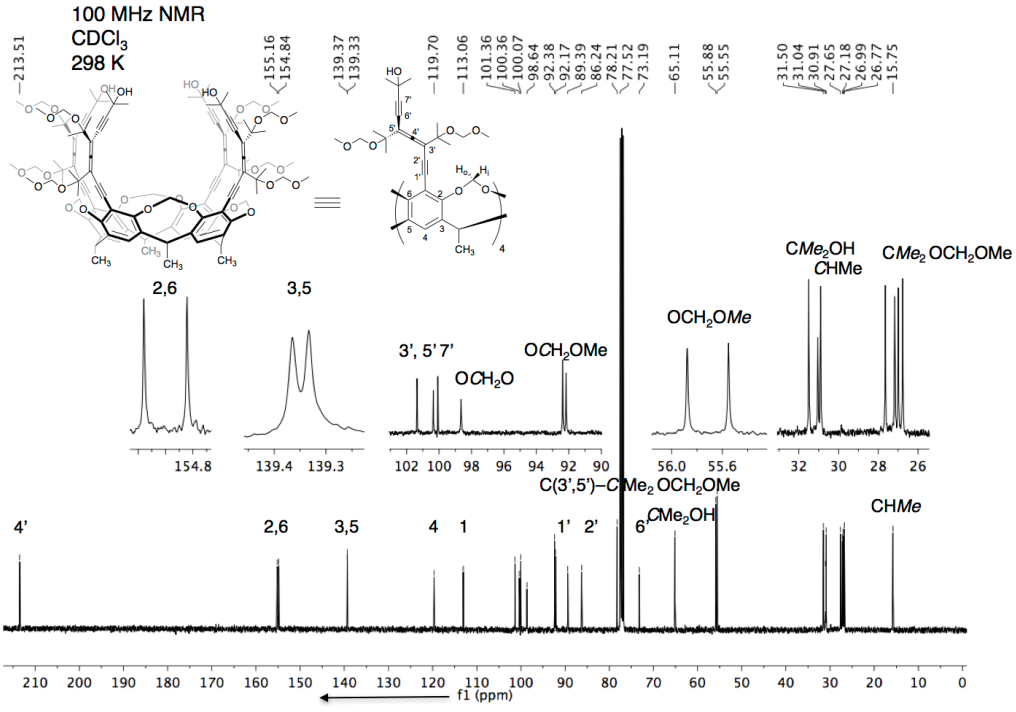

Figure 196. ^{13}C NMR spectrum (100 MHz, 298 K) of AAC $(P)_4$-**72** in $CDCl_3$.

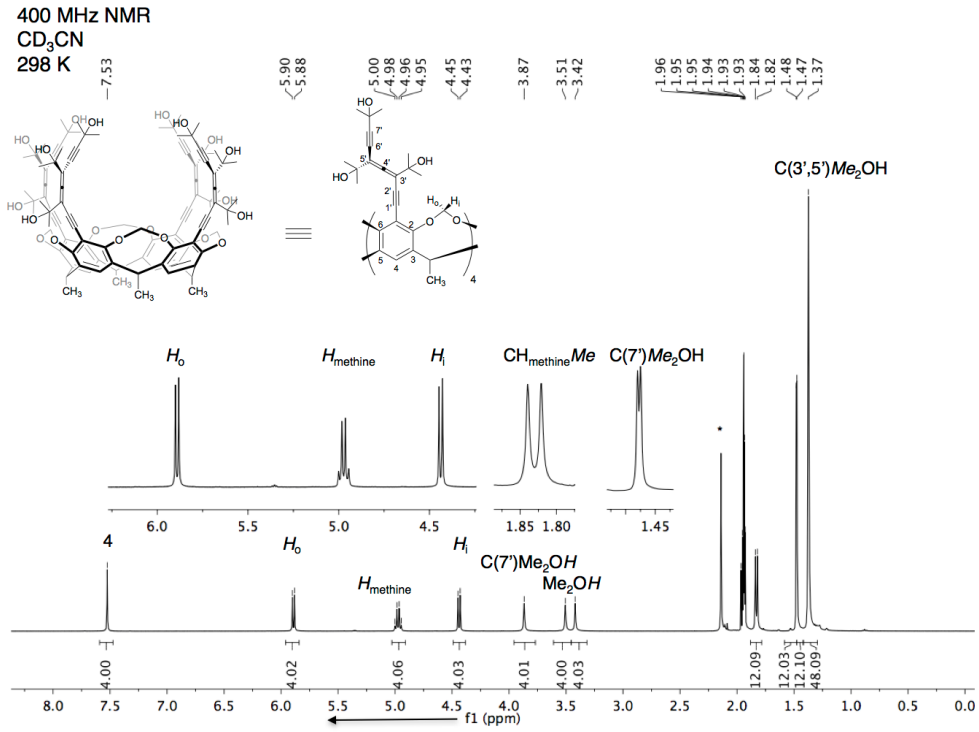

Figure 197. ^{1}H NMR spectrum (400 MHz, 298 K) of AAC $(P)_4$-**73** in acetonitrile-d_3.

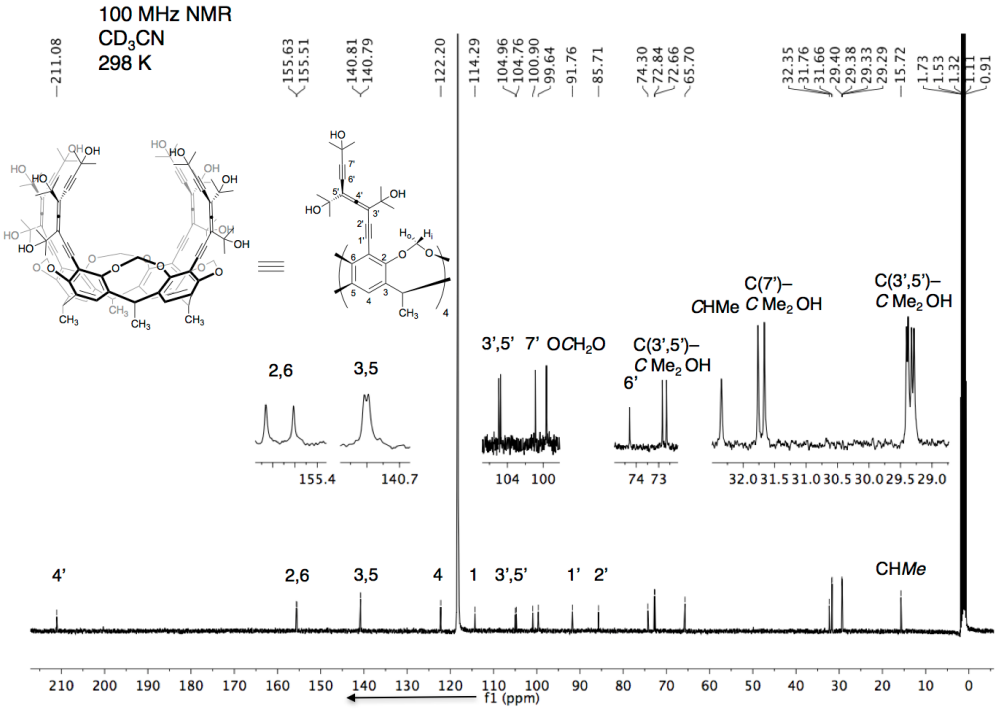

Figure 198. ^{13}C NMR spectrum (100 MHz, 298 K) of AAC $(P)_4$-**73** in acetonitrile-d_3.

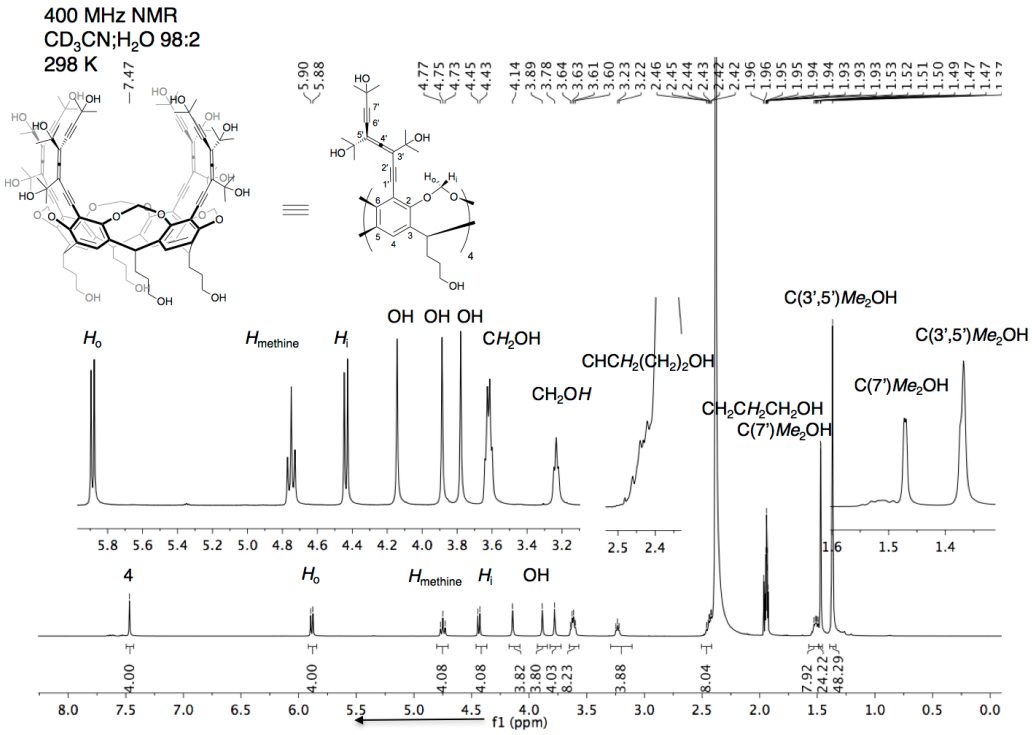

Figure 199. ^{1}H NMR spectrum (400 MHz, 298 K) of AAC $(P)_4$-**71** in acetonitrile-d_3/H_2O 98:2.

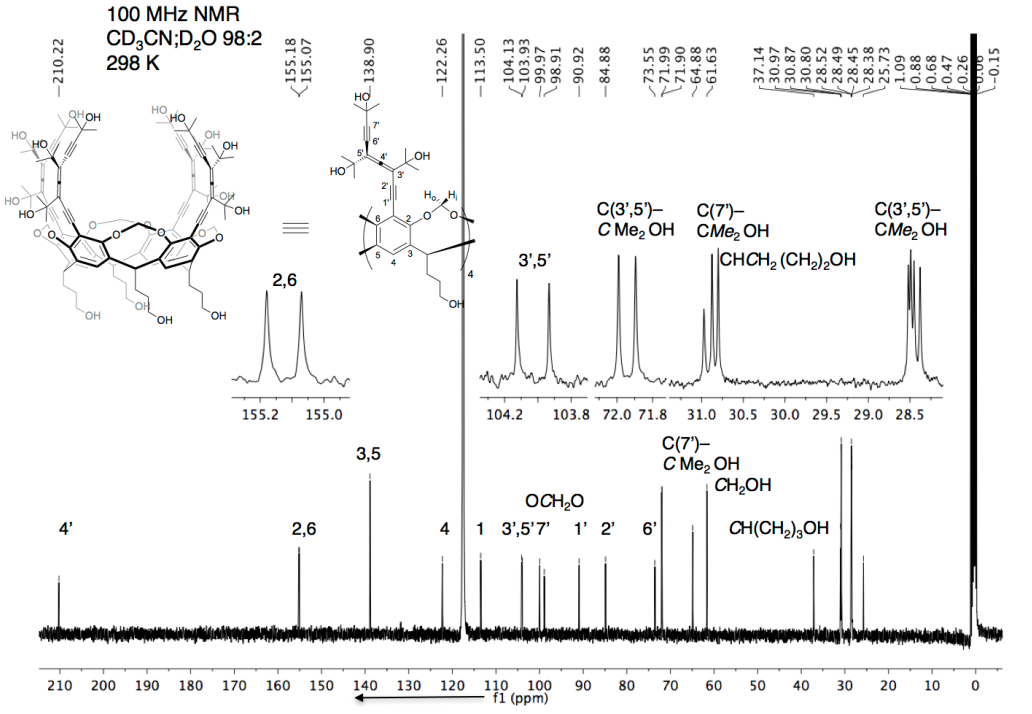

Figure 200. ^{13}C NMR spectrum (100 MHz, 298 K) of AAC $(P)_4$-**71** in acetonitrile-d_3/H_2O 98:2.

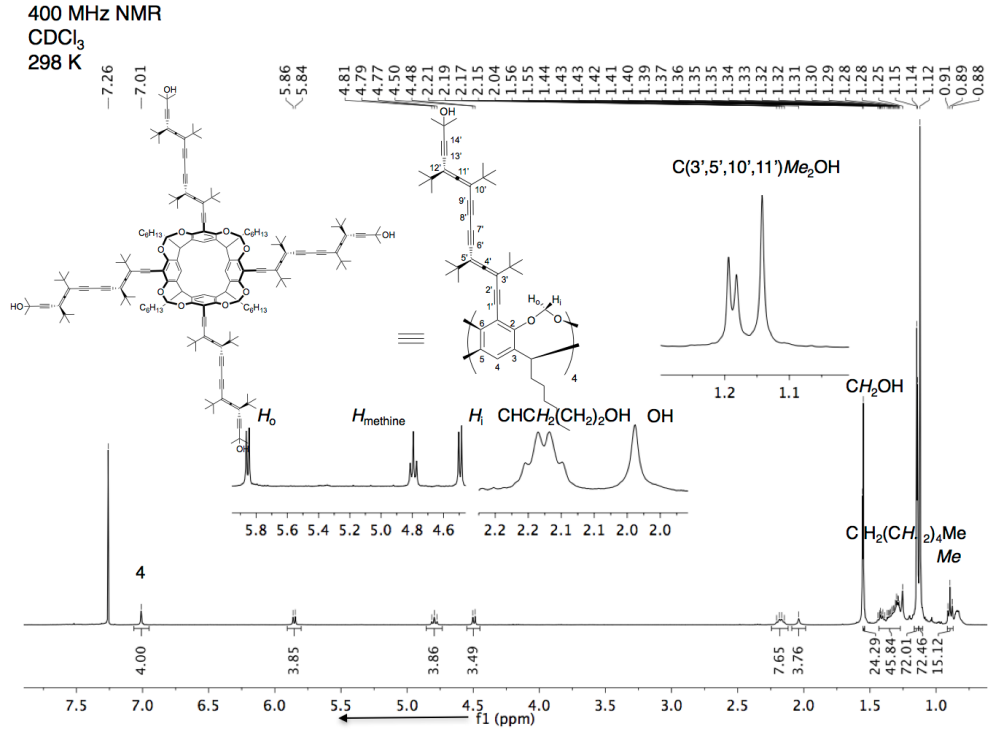

Figure 201. ^{1}H NMR spectrum (400 MHz, 298 K) of AAC $(M)_8$-**98** in $CDCl_3$.

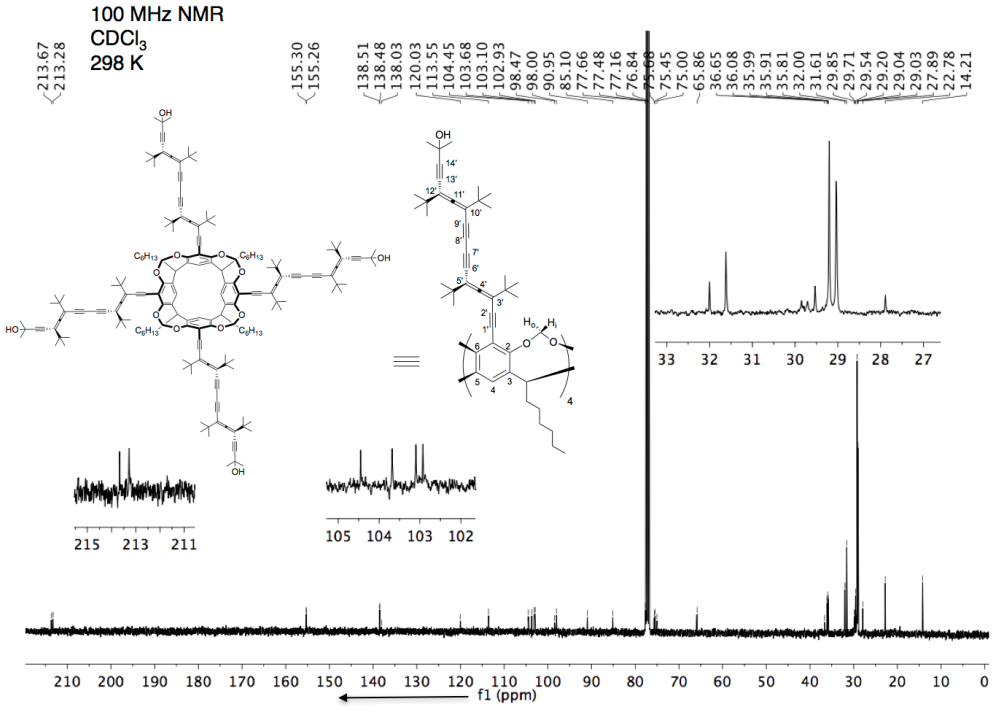

Figure 202. ^{13}C NMR spectrum (100 MHz, 298 K) of AAC $(M)_8$-**98** in $CDCl_3$.

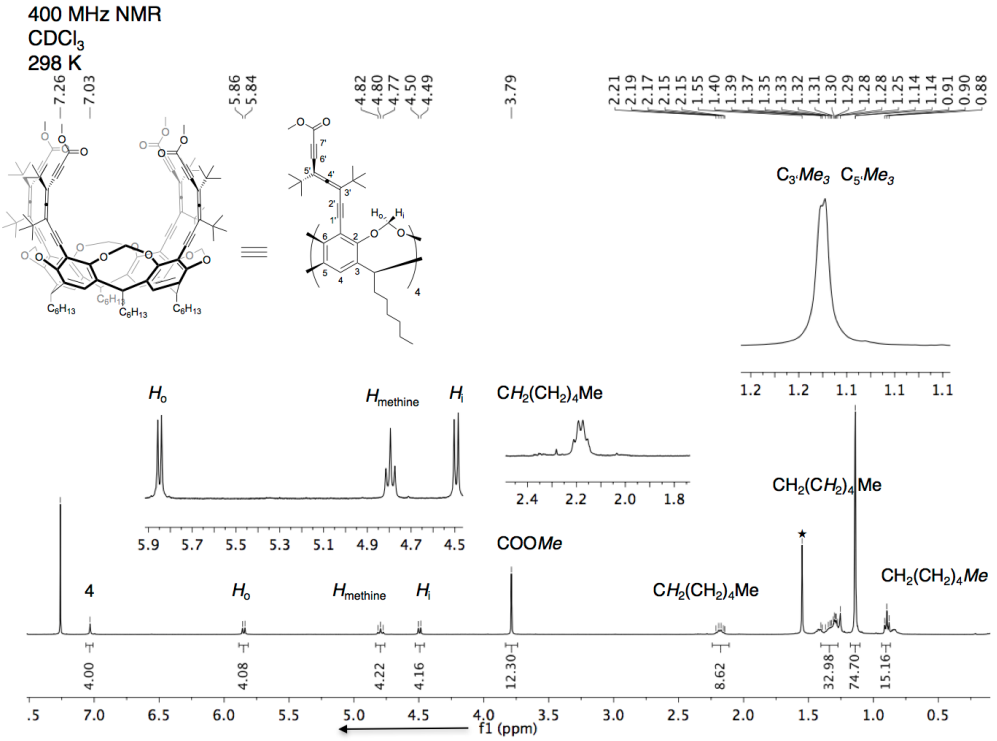

Figure 203. ^{1}H NMR spectrum (400 MHz, 298 K) of AAC $(M)_4$-**90** in $CDCl_3$.

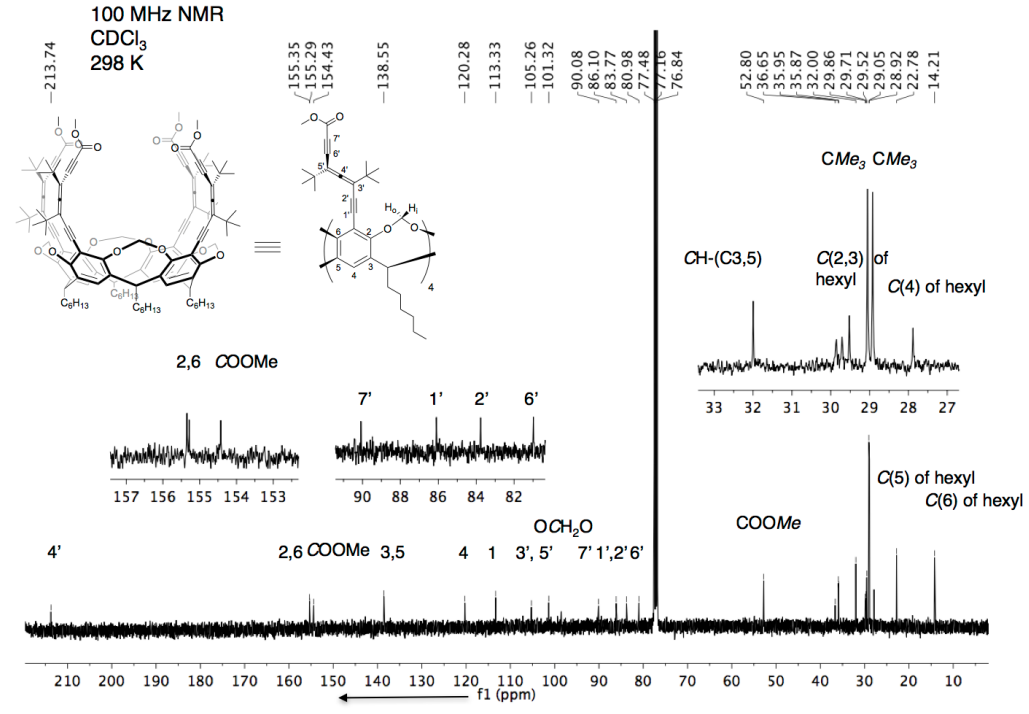

Figure 204. ^{13}C NMR spectrum (100 MHz, 298 K) of AAC $(M)_4$-**90** in $CDCl_3$.

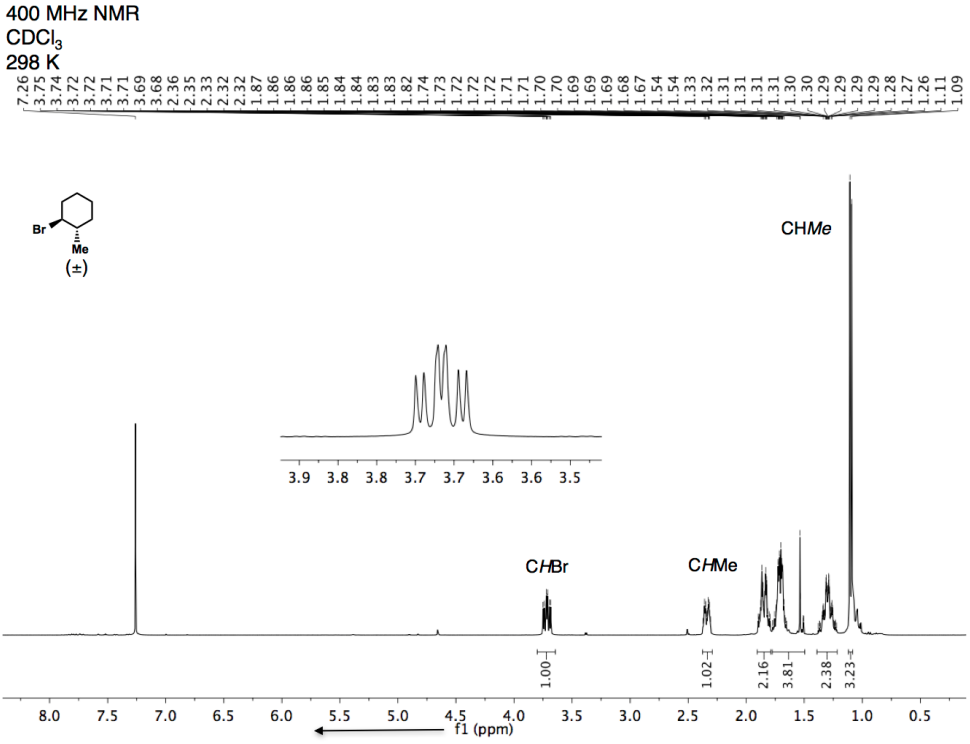

Figure 205. ^{1}H NMR spectrum (400 MHz, 298 K) of (±)-*trans*-1,2-bromomethylcyclohexane $CDCl_3$.

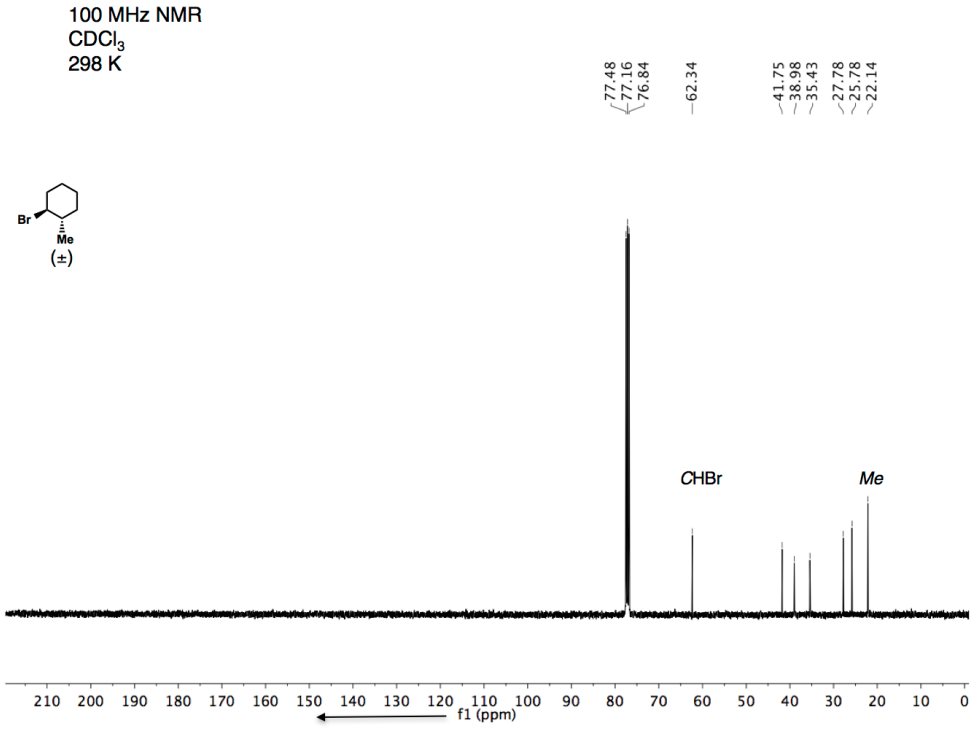

Figure 206. ^{13}C NMR spectrum (100 MHz, 298 K) of (±)-*trans*-1,2-bromomethylcyclohexane $CDCl_3$.

11. References

[1] C. Gropp, B. L. Quigley, F. Diederich, *J. Am. Chem. Soc.* **2018**, *140*, 2705–2717. Molecular Recognition with Resorcin[4]arene Cavitands: Switching, Halogen-Bonded Capsules, and Enantioselective Complexation.

[2] H.-J. Böhm, G. Klebe, *Angew. Chem.* **1996**, *108*, 2750–2778; *Angew. Chem. Int. Ed.* **1996**, *35*, 2588–2614. What Can We Learn from Molecular Recognition in Protein–Ligand Complexes for the Design of New Drugs?

[3] H.-J. Böhm, Protein-ligand Interactions: From Molecular Recognition to Drug Design in *Methods and Principles in Medicinal Chemistry*, (Eds.: R. Mannhold, H. Kubinyi and G. Folkers), Wiley-VCH: Weinheim, **2003**, pp 3–20.

[4] E. Persch, O. Dumele, F. Diederich, *Angew. Chem.* **2015**, *127*, 3341–3382; *Angew. Chem. Int. Ed.* **2015**, *54*, 3290–3327. Molecular Recognition in Chemical and Biological Systems.

[5] D. J. Cram, *Angew. Chem.* **1988**, *100*, 1041–1052; *Angew. Chem. Int. Ed.* **1988**, *27*, 1009–1020. The Design of Molecular Hosts, Guests, and Their Complexes (Nobel Lecture).

[6] D. A. Doyle, J. M. Cabral, R. A. Pfuetzner, A. Kuo, J. M. Gulbis, S. L. Cohen, B. T. Chait, R. MacKinnon, *Science* **1998**, *280*, 69–77. The Structure of the Potassium Channel: Molecular Basis of K^+ Conduction and Selectivity.

[7] Y. Zhou, J. H. Morais-Cabral, A. Kaufman, R. MacKinnon, *Nature* **2001**, *414*, 43–48. Chemistry of Ion Coordination and Hydration Revealed by a K^+ Channel–Fab Complex at 2.0 Å resolution.

[8] R. MacKinnon, *Angew. Chem.* **2004**, *116*, 4363–4376; *Angew. Chem. Int. Ed.* **2004**, *43*, 4265–4277. Potassium Channels and the Atomic Basis of Selective Ion Conduction (Nobel Lecture).

[9] C. J. Pedersen, *J. Am. Chem. Soc.* **1967**, *89*, 2495–2496. Cyclic Polyethers and Their Complexes with Metal Salts.

[10] B. Dietrich, J. M. Lehn, J. P. Sauvage, *Tetrahedron Lett.* **1969**, *10*, 2889–2892. Les Cryptates.

[11] J. M. Lehn, *Acc. Chem. Res.* **1978**, *11*, 49–57. Cryptates: The Chemistry of Macropolycyclic Inclusion Complexes.

[12] C. J. Pedersen, *Angew. Chem.* **1988**, *100*, 1053–1059; *Angew. Chem. Int. Ed.* **1988**, *27*, 1021–1027. The Discovery of Crown Ethers (Nobel Lecture).

[13] J.-M. Lehn, *Angew. Chem.* **1988**, *100*, 91–116; *Angew. Chem. Int. Ed.* **1988**, *27*, 89–112. Supramolecular Chemistry—Scope and Perspectives Molecules, Supermolecules, and Molecular Devices (Nobel Lecture).

[14] J. S. Bradshaw, R. M. Izatt, *Acc. Chem. Res.* **1997**, *30*, 338–345. Crown Ethers: The Search for Selective Ion Ligating Agents.

[15] G. W. Gokel, W. M. Leevy, M. E. Weber, *Chem. Rev.* **2004**, *104*, 2723–2750. Crown Ethers: Sensors for Ions and Molecular Scaffolds for Materials and Biological Models.

[16] L. A. Hardegger, B. Kuhn, B. Spinnler, L. Anselm, R. Ecabert, M. Stihle, B. Gsell, R. Thoma, J. Diez, J. Benz, J.-M. Plancher, G. Hartmann, D. W. Banner, W. Haap, F. Diederich, *Angew. Chem.* **2011**, *123*, 329–334; *Angew. Chem. Int. Ed.* **2011**, *50*, 314–318. Systematic Investigation of Halogen Bonding in Protein–Ligand Interactions.

[17] L. A. Hardegger, B. Kuhn, B. Spinnler, L. Anselm, R. Ecabert, M. Stihle, B. Gsell, R. Thoma, J. Diez, J. Benz, J.-M. Plancher, G. Hartmann, Y. Isshiki, K. Morikami, N. Shimma, W. Haap, D. W. Banner, F. Diederich, *ChemMedChem* **2011**, *6*, 2048–2054. Halogen Bonding at the Active Sites of Human Cathepsin L and MEK1 Kinase: Efficient Interactions in Different Environments.

[18] A. Schwab, B. Illarionov, A. Frank, A. Kunfermann, M. Seet, A. Bacher, M. C. Witschel, M. Fischer, M. Groll, F. Diederich, *ACS Chem. Biol.* **2017**, *12*, 2132–2138. Mechanism of Allosteric Inhibition of the Enzyme IspD by Three Different Classes of Ligands.

[19] O. Dumele, D. Wu, N. Trapp, N. Goroff, F. Diederich, *Org. Lett.* **2014**, *16*, 4722–4725. Halogen Bonding of (Iodoethynyl)benzene Derivatives in Solution.

[20] S. Burley, G. Petsko, *Science* **1985**, *229*, 23–28. Aromatic-Aromatic Interaction: A Mechanism of Protein Structure Stabilization.

[21] S. K. Burley, G. A. Petsko, *Adv. Protein Chem.* **1988**, *39*, 125–189. Weakly Polar Interactions in Proteins.

[22] C. Chipot, R. Jaffe, B. Maigret, D. A. Pearlman, P. A. Kollman, *J. Am. Chem. Soc.* **1996**, *118*, 11217–11224. Benzene Dimer: A Good Model for π–π Interactions in Proteins? A Comparison between the Benzene and the Toluene Dimers in the Gas Phase and in an Aqueous Solution.

[23] E. A. Meyer, R. K. Castellano, F. Diederich, *Angew.Chem.* **2003**, *115*,1244–1287; *Angew. Chem. Int. Ed.* **2003**, *42*, 1210–1250. Interactions with Aromatic Rings in Chemical and Biological Recognition.

[24] S. Paliwal, S. Geib, C. S. Wilcox, *J. Am. Chem. Soc.* **1994**, *116*, 4497–4498. Molecular Torsion Balance for Weak Molecular Recognition Forces. Effects of "Tilted-T" Edge-to-Face Aromatic Interactions on Conformational Selection and Solid-State Structure.

[25] E.-i. Kim, S. Paliwal, C. S. Wilcox, *J. Am. Chem. Soc.* **1998**, *120*, 11192–11193. Measurements of Molecular Electrostatic Field Effects in Edge-to-Face Aromatic Interactions and CH-π Interactions with Implications for Protein Folding and Molecular Recognition.

[26] B. Bhayana, C. S. Wilcox, *Angew. Chem.* **2007**, *119*, 6957–6960; *Angew. Chem. Int. Ed.* **2007**, *46*, 6833–6836. A Minimal Protein Folding Model To Measure Hydrophobic and CH–π Effects on Interactions between Nonpolar Surfaces in Water.

[27] L. M. Salonen, M. Ellermann, F. Diederich, *Angew. Chem.* **2011**, *123*, 4908–4944; *Angew. Chem. Int. Ed.* **2011**, *50*, 4808–4842. Aromatic Rings in Chemical and Biological Recognition: Energetics and Structures.

[28] C. A. Hunter, J. K. M. Sanders, *J. Am. Chem. Soc.* **1990**, *112*, 5525–5534. The Nature of π-π Interactions.

[29] F. R. Fischer, W. B. Schweizer, F. Diederich, *Chem. Commun.* **2008**, 4031–4033. Substituent Effects on the Aromatic Edge-to-face Interaction.

[30] S. E. Wheeler, K. N. Houk, *J. Am. Chem. Soc.* **2008**, *130*, 10854–10855. Substituent Effects in the Benzene Dimer are Due to Direct Interactions of the Substituents with the Unsubstituted Benzene.

[31] L.-J. Riwar, N. Trapp, B. Kuhn, F. Diederich, *Angew.Chem.* **2017**, *129*, 11405–11410; *Angew. Chem., Int. Ed.* **2017**, *56*, 11252–11257. Substituent Effects in Parallel-Displaced π–π Stacking Interactions: Distance Matters.

[32] F. Diederich, *Cyclophanes,* (Eds.: Royal Society of Chemistry, Cambridge, **1991**.

[33] F. Diederich, *Angew. Chem.* **1988**, *100*, 372–396; *Angew. Chem., Int. Ed.* **1988**, *27*, 362–386. Complexation of Neutral Molecules by Cyclophane Hosts.

[34] D. A. Dougherty, D. A. Stauffer, *Science* **1990**, *250*, 1558–1560. Acetylcholine Binding by a Synthetic Receptor – Implications for Biological Recognition.

[35] D. A. Dougherty, *Science* **1996**, *271*, 163–168. Cation–π Interactions in Chemistry and Biology: A New View of Benzene, Phe, Tyr, and Trp.

[36] K. Schärer, M. Morgenthaler, R. Paulini, U. Obst-Sander, D. W. Banner, D. Schlatter, J. Benz, M. Stihle, F. Diederich, *Angew. Chem.* **2005**, *117*, 5203–5207; *Angew. Chem. Int. Ed.* **2005**, *44*, 4400–4404. Quantification of Cation–π Interactions in Protein–

Ligand Complexes: Crystal-Structure Analysis of Factor Xa Bound to a Quaternary Ammonium Ion Ligand.

[37] L. M. Salonen, C. Bucher, D. W. Banner, W. Haap, J.-L. Mary, J. Benz, O. Kuster, P. Seiler, W. B. Schweizer, F. Diederich, *Angew. Chem. Int. Ed.* **2009**, *48*, 811–814. Cation–π Interactions at the Active Site of Factor Xa: Dramatic Enhancement upon Stepwise N-Alkylation of Ammonium Ions.

[38] J. F. Stoddart, *Angew. Chem.* **2017**, *129*, 11244–11277; *Angew. Chem., Int. Ed.* **2017**, *56*, 11094–11125. Mechanically Interlocked Molecules (MIMs)—Molecular Shuttles, Switches, and Machines (Nobel Lecture).

[39] C. R. Kennedy, S. Lin, E. N. Jacobsen, *Angew. Chem.* **2016**, *128*, 12784–12814; *Angew. Chem. Int. Ed.* **2016**, *55*, 12596-12624. The Cation–π Interaction in Small-Molecule Catalysis.

[40] W. P. Jencks, *Catalysis in Chemistry and Enzymology,* McGraw-Hill, New York, **1969**.

[41] S. B. Ferguson, E. M. Seward, F. Diederich, E. M. Sanford, A. Chou, P. Inocencio-Szweda, C. B. Knobler, *J. Org. Chem.* **1988**, *53*, 5593–5595. Strong Enthalpically Driven Complexation of Neutral Benzene Guests in Aqueous Solution.

[42] D. B. Smithrud, F. Diederich, *J. Am. Chem. Soc.* **1990**, *112*, 339–343. Strength of Molecular Complexation of Apolar Solutes in Water and in Organic Solvents is Predictable by Linear Free Energy Relationships: A General Model for Solvation Effects on Apolar Binding.

[43] D. B. Smithrud, T. B. Wyman, F. Diederich, *J. Am. Chem. Soc.* **1991**, *113*, 5420–5426. Enthalpically Driven Cyclophane-Arene Inclusion Complexation: Solvent-dependent Calorimetric Studies.

[44] S. Moghaddam, C. Yang, M. Rekharsky, Y. H. Ko, K. Kim, Y. Inoue, M. K. Gilson, *J. Am. Chem. Soc.* **2011**, *133*, 3570–3581. New Ultrahigh Affinity Host−Guest Complexes of Cucurbit[7]uril with Bicyclo[2.2.2]octane and Adamantane Guests: Thermodynamic Analysis and Evaluation of M2 Affinity Calculations.

[45] F. Biedermann, H.-J. Schneider, *Chem. Rev.* **2016**, *116*, 5216–5300. Experimental Binding Energies in Supramolecular Complexes.

[46] P. S. Cremer, A. H. Flood, B. C. Gibb, D. L. Mobley, *Nat. Chem.* **2017**, *10*, 8–16. Collaborative Routes to Clarifying the Murky Waters of Aqueous Supramolecular Chemistry.

[47] F. Diederich, D. B. Smithrud, E. M. Sanford, T. B. Wyman, S. B. Ferguson, D. R. Carcanague, I. Chao, K. N. Houk, *Acta Chem. Scand.* **1992**, *46*, 205–215. Solvent Effects in Molecular Recognition.

[48] W. L. Jorgensen, J. Pranata, *J. Am. Chem. Soc.* **1990**, *112*, 2008–2010. Importance of Secondary Interactions in Triply Hydrogen Bonded Complexes: Guanine-Cytosine vs Uracil-2,6-diaminopyridine.

[49] T. J. Murray, S. C. Zimmerman, *J. Am. Chem. Soc.* **1992**, *114*, 4010–4011. New Triply Hydrogen Bonded Complexes with Highly Variable Stabilities.

[50] B. A. Blight, C. A. Hunter, D. A. Leigh, H. McNab, P. I. T. Thomson, *Nat. Chem.* **2011**, *3*, 244–248. An AAAA–DDDD Quadruple Hydrogen-Bond Array.

[51] J. D. Dunitz, *Science* **1994**, *264*, 670–670. The Entropic Cost of Bound Water in Crystals and Biomolecules.

[52] M. Ellermann, R. Jakob-Roetne, C. Lerner, E. Borroni, D. Schlatter, D. Roth, A. Ehler, M. G. Rudolph, F. Diederich, *Angew. Chem.* **2009**, *121*, 9256–9260; *Angew. Chem. Int. Ed.* **2009**, *48*, 9092–9096. Molecular Recognition at the Active Site of Catechol-O-Methyltransferase: Energetically Favorable Replacement of a Water Molecule Imported by a Bisubstrate Inhibitor.

[53] J. Michel, J. Tirado-Rives, W. L. Jorgensen, *J. Am. Chem. Soc.* **2009**, *131*, 15403–15411. Energetics of Displacing Water Molecules from Protein Binding Sites: Consequences for Ligand Optimization.

[54] S. Riniker, L. J. Barandun, F. Diederich, O. Krämer, A. Steffen, W. F. van Gunsteren, *J. Comput. Aided Mol. Des.* **2012**, *26*, 1293–1309. Free Enthalpies of Replacing Water Molecules in Protein Binding Pockets.

[55] P. W. Snyder, M. R. Lockett, D. T. Moustakas, G. M. Whitesides, *Eur. Phys. J. Special Topics* **2014**, *223*, 853–891. Is it the Shape of the Cavity, or the Shape of the Water in the Cavity?

[56] M. R. Lockett, H. Lange, B. Breiten, A. Heroux, W. Sherman, D. Rappoport, P. O. Yau, P. W. Snyder, G. M. Whitesides, *Angew. Chem.* **2013**, *125*, 7868–7871; *Angew. Chem. Int. Ed.* **2013**, *52*, 7714–7717. The Binding of Benzoarylsulfonamide Ligands to Human Carbonic Anhydrase is Insensitive to Formal Fluorination of the Ligand.

[57] L. Cao, M. Šekutor, P. Y. Zavalij, K. Mlinarić-Majerski, R. Glaser, L. Isaacs, *Angew. Chem.* **2014**, *126*, 1006–1011; *Angew. Chem, Int. Ed.* **2014**, *53*, 988–993. Cucurbit[7]uril·Guest Pair with an Attomolar Dissociation Constant.

[58] S. G. Krimmer, M. Betz, A. Heine, G. Klebe, *ChemMedChem* **2014**, *9*, 833–846. Methyl, Ethyl, Propyl, Butyl: Futile But Not for Water, as the Correlation of Structure and Thermodynamic Signature Shows in a Congeneric Series of Thermolysin Inhibitors.

[59] S. Mecozzi, J. Rebek, Jr., *Chem. Eur. J.* **1998**, *4*, 1016–1022. The 55% Solution: A Formula for Molecular Recognition in the Liquid State.

[60] J. Hornung, D. Fankhauser, L. D. Shirtcliff, A. Praetorius, W. B. Schweizer, F. Diederich, *Chem. Eur. J.* **2011**, *17*, 12362–12371. Cycloalkane and Alicyclic Heterocycle Complexation by New Switchable Resorcin[4]arene-Based Container Molecules: NMR and ITC Binding Studies.

[61] A. K. H. Hirsch, M. S. Alphey, S. Lauw, M. Seet, L. Barandun, W. Eisenreich, F. Rohdich, W. N. Hunter, A. Bacher, F. Diederich, *Org. Biomol. Chem.* **2008**, *6*, 2719–2730. Inhibitors of the Kinase IspE: Structure-activity Relationships and Co-crystal Structure Analysis.

[62] M. Zürcher, T. Gottschalk, S. Meyer, D. Bur, F. Diederich, *ChemMedChem* **2008**, *3*, 237–240. Exploring the Flap Pocket of the Antimalarial Target Plasmepsin II: The "55% Rule" Applied to Enzymes.

[63] C. S. Leung, S. S. F. Leung, J. Tirado-Rives, W. L. Jorgensen, *J. Med. Chem.* **2012**, *55*, 4489–4500. Methyl Effects on Protein–Ligand Binding.

[64] J. Boström, P. O. Norrby, T. Liljefors, *J. Comput. Aided Mol. Des.* **1998**, *12*, 383–396. Conformational Energy Penalties of Protein-Bound Ligands.

[65] K. A. Brameld, B. Kuhn, D. C. Reuter, M. Stahl, *J. Chem. Inf. Model.* **2008**, *48*, 1–24. Small Molecule Conformational Preferences Derived from Crystal Structure Data. A Medicinal Chemistry Focused Analysis.

[66] J. Rebek, Jr., *Acc. Chem. Res.* **2009**, *42*, 1660–1668. Molecular Behavior in Small Spaces.

[67] A. Galan, P. Ballester, *Chem. Soc. Rev.* **2016**, *45*, 1720–1737. Stabilization of Reactive Species by Supramolecular Encapsulation.

[68] L. Yang, C. Adam, S. L. Cockroft, *J. Am. Chem. Soc.* **2015**, *137*, 10084–10087. Quantifying Solvophobic Effects in Nonpolar Cohesive Interactions.

[69] L. Yang, J. B. Brazier, T. A. Hubbard, D. M. Rogers, S. L. Cockroft, *Angew. Chem.* **2016**, *128*, 924–928; *Angew. Chem. Int. Ed.* **2016**, *55*, 912–916. Can Dispersion Forces Govern Aromatic Stacking in an Organic Solvent?

[70] R. Paulini, K. Müller, F. Diederich, *Angew. Chem. Int. Ed.* **2005**, *44*, 1788–1805. Orthogonal Multipolar Interactions in Structural Chemistry and Biology.

[71] M. G. Holl, C. R. Pitts, T. Lectka, *Angew. Chem. Int. Ed.* **2018**, *130*, 2806–2815; *Angew. Chem. Int. Ed.* **2018**, *57*, 2758–2766. Fluorine in a C−F Bond as the Key to Cage Formation.

[72] M. Harder, B. Kuhn, F. Diederich, *ChemMedChem* **2013**, *8*, 397–404. vEfficient Stacking on Protein Amide Fragments.

[73] M. Harder, M. A. C. Corrales, N. Trapp, B. Kuhn, F. Diederich, *Chem. Eur. J.* **2015**, *21*, 8455–8463. Rebek Imide Platforms as Model Systems for the Investigation of Weak Intermolecular Interactions.

[74] L. C. Gilday, S. W. Robinson, T. A. Barendt, M. J. Langton, B. R. Mullaney, P. D. Beer, *Chem. Rev.* **2015**, *115*, 7118–7195. Halogen Bonding in Supramolecular Chemistry.

[75] G. Cavallo, P. Metrangolo, R. Milani, T. Pilati, A. Priimagi, G. Resnati, G. Terraneo, *Chem. Rev.* **2016**, *116*, 2478–2601. The Halogen Bond.

[76] B. R. Beno, K.-S. Yeung, M. D. Bartberger, L. D. Pennington, N. A. Meanwell, *J. Med. Chem.* **2015**, *58*, 4383–4438. A Survey of the Role of Noncovalent Sulfur Interactions in Drug Design.

[77] D. J. Pascoe, K. B. Ling, S. L. Cockroft, *J. Am. Chem. Soc.* **2017**, *139*, 15160–15167. The Origin of Chalcogen-Bonding Interactions.

[78] G. R. Desiraju, P. S. Ho, L. Kloo, A. C. Legon, R. Marquardt, P. Metrangolo, P. Politzer, G. Resnati, K. Rissanen, *Pure Appl. Chem.* **2013**, *85*, 1711–1713. Definition of the Halogen Bond (IUPAC Recommendations 2013).

[79] T. Dipaolo, C. Sandorfy, *Can. J. Chem.* **1974**, *52*, 3612–3622. Hydrogen-Bond Breaking Ability of Fluorocarbons Containing Higher Halogens.

[80] M. H. Kolář, P. Hobza, *Chem. Rev.* **2016**, *116*, 5155–5187. Computer Modeling of Halogen Bonds and Other σ-Hole Interactions.

[81] N. Ramasubbu, R. Parthasarathy, P. Murray-Rust, *J. Am. Chem. Soc.* **1986**, *108*, 4308–4314. Angular Preferences of Intermolecular Forces around Halogen Centers: Preferred Directions of Approach of Electrophiles and Nucleophiles around Carbon-Halogen Bond.

[82] J. P. M. Lommerse, A. J. Stone, R. Taylor, F. H. Allen, *J. Am. Chem. Soc.* **1996**, *118*, 3108–3116. The Nature and Geometry of Intermolecular Interactions between Halogens and Oxygen or Nitrogen.

[83] S. M. Huber, J. D. Scanlon, E. Jimenez-Izal, J. M. Ugalde, I. Infante, *Phys. Chem. Chem. Phys.* **2013**, *15*, 10350–10357. On the Directionality of Halogen Bonding.

[84] O. Hassel, *Science* **1970**, *170*, 497–502. Structural Aspects of Interatomic Charge-Transfer Bonding.

[85] P. Metrangolo, F. Meyer, T. Pilati, G. Resnati, G. Terraneo, *Angew. Chem.* **2008**, *120*, 6206–6220; *Angew. Chem. Int. Ed.* **2008**, *47*, 6114–6127. Halogen Bonding in Supramolecular Chemistry.

[86] R. Cabot, C. A. Hunter, *Chem. Commun.* **2009**, 2005–2007. Non-covalent Interactions between Iodo-perfluorocarbons and Hydrogen Bond Acceptors.

[87] M. G. Sarwar, B. Dragisic, L. J. Salsberg, C. Gouliaras, M. S. Taylor, *J. Am. Chem. Soc.* **2010**, *132*, 1646–1653. Thermodynamics of Halogen Bonding in Solution: Substituent, Structural, and Solvent Effects.

[88] P. Auffinger, F. A. Hays, E. Westhof, P. S. Ho, *Proc. Natl. Acad. Sci. USA* **2004**, *101*, 16789–16794. Halogen Bonds in Biological Molecules.

[89] D. J. Cram, *Angew. Chem.* **1986**, *98*, 1041–1060; *Angew. Chem. Int. Ed.* **1986**, *25*, 1039–1057. Preorganization—From Solvents to Spherands.

[90] R. Wyler, J. de Mendoza, J. Rebek, Jr., *Angew. Chem.* **1993**, *105*, 1820–1823; *Angew. Chem., Int. Ed.* **1993**, *32*, 1699–1701. A Synthetic Cavity Assembles Through Self-Complementary Hydrogen Bonds.

[91] R. S. Meissner, J. Rebek, Jr., J. de Mendoza, *Science* **1995**, *270*, 1485–1488. Autoencapsulation Through Intermolecular Forces: A Synthetic Self-Assembling Spherical Complex.

[92] T. Heinz, D. M. Rudkevich, J. Rebek, Jr., *Nature* **1998**, *394*, 764–766. Pairwise Selection of Guests in a Cylindrical Molecular Capsule of Nanometre Dimensions.

[93] C. L. D. Gibb, B. C. Gibb, *J. Am. Chem. Soc.* **2004**, *126*, 11408–11409. Well-Defined, Organic Nanoenvironments in Water: The Hydrophobic Effect Drives a Capsular Assembly.

[94] J. H. Jordan, B. C. Gibb, *Chem. Soc. Rev.* **2015**, *44*, 547–585. Molecular Containers Assembled through the Hydrophobic Effect.

[95] D. J. Cram, H. J. Choi, J. A. Bryant, C. B. Knobler, *J. Am. Chem. Soc.* **1992**, *114*, 7748–7765. Host–Guest Complexation. 62. Solvophobic and Entropic Driving Forces for Forming Velcraplexes, which are 4-fold, Lock-key Dimers in Organic Media.

[96] O. Dumele, N. Trapp, F. Diederich, *Angew. Chem.* **2015**, *127*, 12516–12521; *Angew. Chem. Int. Ed.* **2015**, *54*, 12339–12344. Halogen Bonding Molecular Capsules.

[97] O. Dumele, B. Schreib, U. Warzok, N. Trapp, C. A. Schalley, F. Diederich, *Angew. Chem.* **2017**, *129*, 1172–1177; *Angew. Chem. Int. Ed.* **2017**, *56*, 1152–1157. Halogen-Bonded Supramolecular Capsules in the Solid State, in Solution, and in the Gas Phase.

[98] S. H. Wilen, L. N. Mander, E. L. Eliel, *Stereochemistry of Organic Compounds,* John Wiley & Sons, New York, **1994**.

[99] V. Prelog, *Science* **1976**, *193*, 17–24. Chirality in Chemistry.

[100] E. Fischer, *Chem. Ber.* **1894**, *27*, 2985–2993. Einfluss der Configuration auf die Wirkung der Enzyme.

[101] L. H. Easson, E. Stedman, *Biochem. J.* **1933**, *27*, 1257–1266. Studies on the Relationship between Chemical Constitution and Physiological Action: Molecular Dissymmetry and Physiological Activity.

[102] A. G. Ogston, *Nature* **1948**, *162*, 963–963. Interpretation of Experiments on Metabolic Processes, Using Isotopic Tracer Elements.

[103] R. C. Helgeson, J. M. Timko, P. Moreau, S. C. Peacock, J. M. Mayer, D. J. Cram, *J. Am. Chem. Soc.* **1974**, *96*, 6762–6763. Models for Chiral Recognition in Molecular Complexation.

[104] E. B. Kyba, K. Koga, L. R. Sousa, M. G. Siegel, D. J. Cram, *J. Am. Chem. Soc.* **1973**, *95*, 2692–2693. Chiral Recognition in Molecular Complexing.

[105] S. C. Peacock, L. A. Domeier, F. C. A. Gaeta, R. C. Helgeson, J. M. Timko, D. J. Cram, *J. Am. Chem. Soc.* **1978**, *100*, 8190–8202. Host-guest Complexation. 13. High Chiral Recognition of Amino Esters by Dilocular Hosts Containing Extended Steric Barriers.

[106] V. Prelog, *Pure Appl. Chem.* **1978**, *50*, 893–904. Chiral Ionophores.

[107] V. Prelog, S. Mutak, *Helv. Chim. Acta* **1983**, *66*, 2274–2278. Über die Stereoselektivität der 9,9′-Spirobifluoren-Kronenäther gegenüber α-Aminoalkoholen.

[108] I. Goldberg, *J. Am. Chem. Soc.* **1977**, *99*, 6049–6057. Structure and Binding in Molecular Complexes of Cyclic Polyethers. 4. Crystallographic Study of a Chiral System: An Inclusion Complex of a Macrocyclic Ligand with Phenylglycine Methyl Ester.

[109] A. Collet, J. P. Dutasta, B. Lozach, J. Canceill, *Top. Curr. Chem.* **1993**, *165*, 103–129. Cyclotriveratrylenes and Cryptophanes – Their Synthesis and Applications to Host-Guest Chemistry and to the Design of New Materials.

[110] D. J. Cram, J. M. Cram, *Container Molecules and Their Guests,* Royal Society of Chemistry, Cambridge, **1994**.

[111] J. L. Sessler, P. A. Gale, W. S. Cho, Anion Receptor Chemistry in *Anion Receptor Chemistry*, (Ed.: J. F. Stoddart), Royal Society of Chemistry: Cambridge, **2006**, pp 1–26.

[112] A. E. Hargrove, S. Nieto, T. Zhang, J. L. Sessler, E. V. Anslyn, *Chem. Rev.* **2011**, *111*, 6603–6782. Artificial Receptors for the Recognition of Phosphorylated Molecules.

[113] P. A. Gale, E. N. W. Howe, X. A. Wu, *Chem.* **2016**, *1*, 351–422. Anion Receptor Chemistry.

[114] H. E. Simmons, C. H. Park, *J. Am. Chem. Soc.* **1968**, *90*, 2428–2429. Macrobicyclic Amines. I. Out-in Isomerism of 1,(k+2)-Diazabicyclo[k.l.m]alkanes.

[115] F. P. Schmidtchen, *Angew. Chem.* **1977**, *89*, 751–756; *Angew. Chem. Int. Ed.* **1977**, *16*, 720–721. Inclusion of Anions in Macrotricyclic Quaternary Ammonium Salts.

[116] J. L. Sessler, A. Andrievsky, V. Král, V. Lynch, *J. Am. Chem. Soc.* **1997**, *119*, 9385–9392. Chiral Recognition of Dicarboxylate Anions by Sapphyrin-Based Receptors.

[117] J. Y. C. Lim, I. Marques, V. Félix, P. D. Beer, *J. Am. Chem. Soc.* **2017**, *139*, 12228–12239. Enantioselective Anion Recognition by Chiral Halogen-Bonding [2]Rotaxanes.

[118] J. Y. C. Lim, I. Marques, V. Félix, P. D. Beer, *Angew. Chem.* **2017**, *130*, 593–597; *Angew. Chem. Int. Ed.* **2018**, *57*, 584–588. A Chiral Halogen-Bonding [3]Rotaxane for the Recognition and Sensing of Biologically Relevant Dicarboxylate Anions.

[119] S. Topiol, M. Sabio, *J. Am. Chem. Soc.* **1989**, *111*, 4109–4110. Interactions between Eight Centers are Required for Chiral Recognition.

[120] J. K. Judice, D. J. Cram, *J. Am. Chem. Soc.* **1991**, *113*, 2790–2791. Stereoselectivity in Guest Release from Constrictive Binding in a Hemicarceplex.

[121] J. Y. Yoon, D. J. Cram, *J. Am. Chem. Soc.* **1997**, *119*, 11796–11806. Chiral Recognition Properties in Complexation of two Asymmetric Hemicarcerands.

[122] J. Gabard, A. Collet, *J. Chem. Soc., Chem. Commun.* **1981**, 1137–1139. Synthesis of a (D_3)-Bis(cyclotriveratrylenyl) Macrocage by Stereospecific Replication of a (C_3)-subunit.

[123] J. Canceill, L. Lacombe, A. Collet, *J. Am. Chem. Soc.* **1985**, *107*, 6993–6996. Analytical Optical Resolution of Bromochlorofluoromethane by Enantioselective Inclusion into a Tailor-made Cryptophane and Determination of its Maximum Rotation.

[124] T. Brotin, L. Guy, A. Martinez, J. P. Dutasta, *Top. Curr. Chem.* **2013**, *341*, 177–230. Enantiopure Supramolecular Cages: Synthesis and Chiral Recognition Properties.

[125] A. Schmitt, B. Chatelet, S. Collin, J. P. Dutasta, A. Martinez, *Chirality* **2013**, *25*, 475–479. Chiral Discrimination of Ammonium Neurotransmitters by C3-Symmetric Enantiopure Hemicryptophane Hosts.

[126] S. Lefevre, D. Zhang, E. Godart, M. Jean, N. Vanthuyne, J.-C. Mulatier, J.-P. Dutasta, L. Guy, A. Martinez, *Chem. Eur. J.* **2016**, *22*, 2068–2074. Large-Scale Synthesis of Enantiopure Molecular Cages: Chiroptical and Recognition Properties.

[127] D. Zhang, J.-C. Mulatier, J. R. Cochrane, L. Guy, G. Gao, J.-P. Dutasta, A. Martinez, *Chem. Eur. J.* **2016**, *22*, 8038–8042. Helical, Axial, and Central Chirality Combined in a Single Cage: Synthesis, Absolute Configuration, and Recognition Properties.

[128] L. R. MacGillivray, J. L. Atwood, *Nature* **1997**, *389*, 469–472. A Chiral Spherical Molecular Assembly held together by 60 Hydrogen Bonds.

[129] R. K. Castellano, B. H. Kim, J. Rebek, Jr., *J. Am. Chem. Soc.* **1997**, *119*, 12671–12672. Chiral Capsules: Asymmetric Binding in Calixarene-Based Dimers.

[130] J. M. Rivera, T. Martin, J. Rebek, Jr., *Science* **1998**, *279*, 1021–1023. Chiral Spaces: Dissymmetric Capsules through Self-assembly.

[131] J. M. Rivera, J. Rebek, Jr., *J. Am. Chem. Soc.* **2000**, *122*, 7811–7812. Chiral Space in a Unimolecular Capsule.

[132] J. M. Rivera, S. L. Craig, T. Martín, J. Rebek, Jr., *Angew. Chem.* **2000**, *112,* 2214–2216; *Angew. Chem. Int. Ed.* **2000**, *39*, 2130–2132. Chiral Guests and Their Ghosts in Reversibly Assembled Hosts.

[133] J. J. González, R. Ferdani, E. Albertini, J. M. Blasco, A. Arduini, A. Pochini, P. Prados, J. de Mendoza, *Chem. Eur. J.* **2000**, *6*, 73–80. Dimeric Capsules by the Self-Assembly of Triureidocalix.

[134] A. Szumna, *Chem. Soc. Rev.* **2010**, *39*, 4274–4285. Inherently Chiral Concave Molecules – From Synthesis to Applications.

[135] K. Kobayashi, M. Yamanaka, *Chem. Soc. Rev.* **2015**, *44*, 449–466. Self-assembled Capsules Based on Tetrafunctionalized Calix[4]resorcinarene Cavitands.

[136] D. Fiedler, D. H. Leung, R. G. Bergman, K. N. Raymond, *Acc. Chem. Res.* **2005**, *38*, 349–358. Selective Molecular Recognition, C−H Bond Activation, and Catalysis in Nanoscale Reaction Vessels.

[137] M. Fujita, M. Tominaga, A. Hori, B. Therrien, *Acc. Chem. Res.* **2005**, *38*, 369–378. Coordination Assemblies from a Pd(II)-Cornered Square Complex.

[138] A. M. Castilla, W. J. Ramsay, J. R. Nitschke, *Acc. Chem. Res.* **2014**, *47*, 2063–2073. Stereochemistry in Subcomponent Self-Assembly.

[139] L.-J. Chen, H.-B. Yang, M. Shionoya, *Chem. Soc. Rev.* **2017**, *46*, 2555–2576. Chiral Metallosupramolecular Architectures.

[140] D. Xu, R. Warmuth, *J. Am. Chem. Soc.* **2008**, *130*, 7520–7521. Edge-Directed Dynamic Covalent Synthesis of a Chiral Nanocube.

[141] M. Mastalerz, *Angew. Chem.* **2010**, *122,* 5164–5175; *Angew. Chem. Int. Ed.* **2010**, *49*, 5042–5053. Shape-Persistent Organic Cage Compounds by Dynamic Covalent Bond Formation.

[142] G. Zhang, M. Mastalerz, *Chem. Soc. Rev.* **2014**, *43*, 1934–1947. Organic Cage Compounds – From Shape-Persistency to Function.

[143] D. Beaudoin, F. Rominger, M. Mastalerz, *Angew. Chem.* **2017**, *129,* 1264–1268; *Angew. Chem. Int. Ed.* **2017**, *56*, 1244–1248. Chiral Self-Sorting of [2+3] Salicylimine Cage Compounds.

[144] T. Hasell, M. A. Little, S. Y. Chong, M. Schmidtmann, M. E. Briggs, V. Santolini, K. E. Jelfs, A. I. Cooper, *Nanoscale* **2017**, *9*, 6783–6790. Chirality as a Tool for Function in Porous Organic Cages.

[145] D. Beaudoin, F. Rominger, M. Mastalerz, *Angew. Chem.* **2016**, *128,* 18828–15832; *Angew. Chem. Int. Ed.* **2016**, *55*, 15599–15603. Chirality-Assisted Synthesis of a Very Large Octameric Hydrogen-Bonded Capsule.

[146] D. Fiedler, D. H. Leung, R. G. Bergman, K. N. Raymond, *J. Am. Chem. Soc.* **2004**, *126*, 3674–3675. Enantioselective Guest Binding and Dynamic Resolution of Cationic Ruthenium Complexes by a Chiral Metal−Ligand Assembly.

[147] T. Liu, Y. Liu, W. Xuan, Y. Cui, *Angew. Chem.* **2010**, *122*, 4215–4218; *Angew. Chem., Int. Ed.* **2010**, *49*, 4121–4124. Chiral Nanoscale Metal–Organic Tetrahedral Cages: Diastereoselective Self-Assembly and Enantioselective Separation.

[148] C. Tan, J. Jiao, Z. Li, Y. Liu, X. Han, Y. Cui, *Angew. Chem.* **2018**, *130*, 2107–2112; *Angew. Chem., Int. Ed.* **2018**, *57*, 2085–2090. Design and Assembly of a Chiral Metallosalen-Based Octahedral Coordination Cage for Supramolecular Asymmetric Catalysis.

[149] F. Diederich, *Nature* **1994**, *369*, 199–207. Carbon Scaffolding: Building Acetylenic All-Carbon and Carbon-Rich Compounds.

[150] U. H. F. Bunz, Y. Rubin, Y. Tobe, *Chem. Soc. Rev.* **1999**, *28*, 107–119. Polyethynylated Cyclic π-Systems: Scaffoldings for Novel two and three-Dimensional Carbon Networks.

[151] R. H. Baughman, D. S. Galvão, *Nature* **1993**, *365*, 735. Crystalline Networks with Unusual Predicted Mechanical and Thermal Properties.

[152] J. H. van't Hoff, *La chimie dans l'Espace,* (Eds.: Bazemdijk, Rotterdam, **1875**.

[153] P. Maitland, W. H. Mills, *Nature* **1935**, *135*, 994–994. Experimental Demonstration of the Allene Asymmetry.

[154] R. C. Livingston, L. R. Cox, V. Gramlich, F. Diederich, *Angew. Chem.* **2001**, *113*, 2396–2399; *Angew. Chem. Int. Ed.* **2001**, *40*, 2334–2336. 1,3-Diethynylallenes : New Modules for Three-Dimensional Acetylenic Scaffolding.

[155] R. Livingston, L. R. Cox, S. Odermatt, F. Diederich, *Helv. Chim. Acta* **2002**, *85*, 3052–3077. 1,3-Diethynylallenes: Carbon-rich Modules for Three-dimensional Acetylenic Scaffolding.

[156] P. Rivera-Fuentes, F. Diederich, *Angew. Chem.* **2012**, *124*, 2872–2882; *Angew. Chem. Int. Ed.* **2012**, *51*, 2818–2828. Allenes in Molecular Materials.

[157] S. Odermatt, J. L. Alonso-Gómez, P. Seiler, M. M. Cid, F. Diederich, *Angew. Chem.* **2005**, *117*, 5203–5207; *Angew. Chem. Int. Ed.* **2005**, *44*, 5074–5078. Shape-Persistent Chiral Alleno-Acetylenic Macrocycles and Cyclophanes by Acetylenic Scaffolding with 1,3-Diethynylallenes.

[158] M. K. J. ter Wiel, S. Odermatt, P. Schanen, P. Seiler, F. Diederich, *Eur. J. Org. Chem.* **2007**, *21*, 3449–3462. 1,3-Diethynylallenes: Stable Monomers, Length-Defined Oligomers, Asymmetric Synthesis, and Optical Resolution.

[159] C. He, J. Ke, H. Xu, A. Lei, *Angew. Chem.* **2013**, 125, 1567–1570; *Angew. Chem., Int. Ed.* **2013**, *52*, 1527–1530. Synergistic Catalysis in the Sonogashira Coupling Reaction: Quantitative Kinetic Investigation of Transmetalation.

[160] P. Rivera-Fuentes, B. Nieto-Ortega, W. B. Schweizer, J. T. L. Navarrete, J. Casado, F. Diederich, *Chem. Eur. J.* **2011**, *17*, 3876–3885. Enantiopure, Monodisperse Alleno-acetylenic Cyclooligomers: Effect of Symmetry and Conformational Flexibility on the Chiroptical Properties of Carbon-Rich Compounds.

[161] J. L. Alonso-Gómez, P. Schanen, P. Rivera-Fuentes, P. Seiler, F. Diederich, *Chem. – Eur. J.* **2008**, *14*, 10564–10568. 1,3-Diethynylallenes (DEAs): Enantioselective Synthesis, Absolute Configuration, and Chiral Induction in 1,1,4,4-Tetracyanobuta-1,3-dienes (TCBDs).

[162] S. Thorand, F. Vögtle, N. Krause, *Angew. Chem.* **1999**, *111*, 3929–3931; *Angew. Chem., Int. Ed.* **1999**, *38*, 3721–3723. Synthesis of the First [34]Allenophane:

1,3,10,12,19,21,28,30-Octamethyl[3.3.3.3]paracyclophan-1,2,10,11,19,20,28,29-octaene.

[163] M. D. Clay, A. G. Fallis, *Angew. Chem.* **2005**, *117*, 4107–4110; *Angew. Chem. Int. Ed.* **2005**, *44*, 4039–4042. Acetylenic Allenophanes: An Asymmetric Synthesis of a Bis(alleno)-bis(butadiynyl)-meta-cyclophane.

[164] M. Leclère, A. G. Fallis, *Angew. Chem.* **2008**, *120,* 578–582; *Angew. Chem. Int. Ed.* **2008**, *47*, 568–572. Asymmetric Allenophanes: Synthesis of a Tris-Meta-Allenophane and Tetrakis-Meta-Allenophane by Sequential Cross-Coupling.

[165] J. L. Alonso-Gómez, A. Navarro-Vázquez, M. M. Cid, *Chem. Eur. J.* **2009**, *15*, 6495–6503. Chiral (2,5)Pyrido[74]allenoacetylenic Cyclophanes: Synthesis and Characterization.

[166] P. Rivera-Fuentes, J. L. Alonso-Gómez, A. G. Petrovic, F. Santoro, N. Harada, N. Berova, F. Diederich, *Angew. Chem.* **2010**, *122*, 2296–2300; *Angew. Chem., Int. Ed.* **2010**, *49*, 2247–2250. Amplification of Chirality in Monodisperse, Enantiopure Alleno-Acetylenic Oligomers.

[167] E. J. Donckele, O. Gidron, N. Trapp, F. Diederich, *Chem. Eur. J.* **2014**, *20*, 9558–9566. Outstanding Chiroptical Properties: A Signature of Enantiomerically Pure Alleno-Acetylenic Macrocycles and Monodisperse Acyclic Oligomers.

[168] I.-E. S. Müller, B. Bernet, C. Dengiz, W. B. Schweizer, F. Diederich, *Eur. J. Org. Chem.* **2014**, *2014*, 941–953. Towards Stapling of Helical Alleno-Acetylene Oligomers – Synthesis of an Enantiopure Bis(ethynylvinylidene)-Substituted Cyclohexadeca-1,3,9,11-tetrayne.

[169] Cornelius Gropp, Master Thesis, **2014**, Diederich Group, ETHZ Zurich

[170] J. L. Alonso-Gómez, P. Rivera-Fuentes, N. Harada, N. Berova, F. Diederich, *Angew. Chem.* **2009**, *121*, 5653–5656; *Angew. Chem., Int. Ed.* **2009**, *48*, 5545–5548. An Enantiomerically Pure Alleno-Acetylenic Macrocycle: Synthesis and Rationalization of its Outstanding Chiroptical Response.

[171] S. Castro-Fernández, I. R. Lahoz, A. L. Llamas-Saiz, J. L. Alonso-Gómez, M.-M. Cid, A. Navarro-Vázquez, *Org. Lett.* **2014**, *16*, 1136–1139. Preparation and Characterization of a Halogen-Bonded Shape-Persistent Chiral Alleno-acetylenic Inclusion Complex.

[172] S. Míguez-Lago, A. L. Llamas-Saiz, M.-M. Cid, J. L. Alonso-Gómez, *Chem. – Eur. J.* **2015**, *21*, 18085–18088. A Covalent Organic Helical Cage with Remarkable Chiroptical Amplification.

[173] S. J. Wezenberg, F. Ferroni, S. Pieraccini, W. B. Schweizer, A. Ferrarini, G. P. Spada, F. Diederich, *RSC Adv.* **2013**, *3*, 22845–22848. Effective Cholesteric Liquid Crystal Inducers Based on Axially Chiral Alleno-Acetylenes.

[174] M. D. Tzirakis, N. Marion, W. B. Schweizer, F. Diederich, *Chem. Comm.* **2013**, *49*, 7605–7607. A Shape-persistent Alleno-Acetylenic Macrocycle with a Modifiable Periphery: Synthesis, Chiroptical Properties and H-bond-Driven Self-Assembly into a Homochiral Columnar Structure.

[175] M. D. Tzirakis, M. N. Alberti, H. Weissman, B. Rybtchinski, F. Diederich, *Chem. Eur. J.* **2014**, *20*, 16070–16073. Enantiopure Laterally Functionalized Alleno-Acetylenic Macrocycles: Synthesis, Chiroptical Properties, and Self-Assembly in Aqueous Media.

[176] O. Gidron, M.-O. Ebert, N. Trapp, F. Diederich, *Angew. Chem.* **2014**, *126*, 13833–13837; *Angew. Chem. Int. Ed.* **2014**, *53*, 13614–13618. Chiroptical Detection of Nonchromophoric, Achiral Guests by Enantiopure Alleno-Acetylenic Helicages.

[177] O. Gidron, M. Jirásek, M. Wörle, F. Diederich, *Chem. Eur. J.* **2016**, *22*, 16172–16177. Enantiopure Alleno-Acetylenic Helicages Containing Multiple Binding Sites.

[178] O. Gidron, M. Jirásek, N. Trapp, M.-O. Ebert, X. Zhang, F. Diederich, *J. Am. Chem. Soc.* **2015**, *137*, 12502–12505. Homochiral [2]Catenane and Bis[2]catenane from Alleno-Acetylenic Helicates – A Highly Selective Narcissistic Self-Sorting Process.

[179] *Analytical Methods in Supramolecular Chemistry,* (Eds.: C. A. Schalley), Wiley-VCH, Weinheim, **2012**.

[180] K. Hirose, Quantitative Analysis of Binding Properties in *Analytical Methods in Supramolecular Chemistry*, (Ed.: C. A. Schalley), Wiley-VCH: Weinheim, **2012**, *Vol. 1*, pp 27–66.

[181] F. Ulatowski, K. Dąbrowa, T. Bałakier, J. Jurczak, *J. Org. Chem.* **2016**, *81*, 1746–1756. Recognizing the Limited Applicability of Job Plots in Studying Host–Guest Interactions in Supramolecular Chemistry.

[182] P. Thordarson, *Chem. Soc. Rev.* **2011**, *40*, 1305–1323. Determining Association Constants from Titration Experiments in Supramolecular Chemistry.

[183] P. Thordarson, Binding Constants and Their Measurement in *Supramolecular Chemistry: From Molecules to Nanomaterials*, (Eds.: P. A. Gale and J. W. Steed), Wiley: Chichester, **2012**, *Vol. 2*, pp 239–274.

[184] M. Urbanová, P. Maloň, Circular Dichroism Spectroscopy in *Analytical Methods in Supramolecular Chemistry*, (Eds.: C. A. Schalley), Wiley-VCH: Weinheim, **2007**, pp 265-304.

[185] N. Berova, L. Di Bari, G. Pescitelli, *Chem. Soc. Rev.* **2007**, *36*, 914–931. Application of Electronic Circular Dichroism in Configurational and Conformational Analysis of Organic Compounds.

[186] G. A. Hembury, V. V. Borovkov, Y. Inoue, *Chem. Rev.* **2008**, *108*, 1–73. Chirality-Sensing Supramolecular Systems.

[187] G. Pescitelli, L. Bari, N. Berova, *Chem. Soc. Rev.* **2014**, *43*, 5211–5233. Application of Electronic Circular Dichroism in the Study of Supramolecular Systems.

[188] F. P. Schmidtchen, Isothermal Titration Calorimetry in Supramolecular Chemistry in *Analytical Methods in Supramolecular Chemistry*, (Ed.: C. A. Schalley), Wiley-VCH: **2007**, pp 55-78.

[189] D. A. Stauffer, R. E. Barrans, D. A. Dougherty, *J. Org. Chem.* **1990**, *55*, 2762–2767. Concerning the Thermodynamics of Molecular Recognition in Aqueous and Organic Media. Evidence for Significant Heat Capacity Effects.

[190] K. Rissanen, Crystallography and Crystal Engineering in *Analytical Methods in Supramolecular Chemistry*, (Ed.: C. A. Schalley), Wiley-VCH: **2007**, pp 305-336.

[191] B. Kirchner, M. Reiher, Theoretical Methods for Supramolecular Chemistry in *Analytical Methods in Supramolecular Chemistry*, (Ed.: C. A. Schalley), Wiley-VCH: **2007**, pp 419-471.

[192] C. Gropp, N. Trapp, F. Diederich, *Angew. Chem.* **2016**, *128*, 14659–14664; *Angew. Chem. Int. Ed.* **2016**, *55*, 14444–14449. Alleno-Acetylenic Cage (AAC) Receptors: Chiroptical Switching and Enantioselective Complexation of *trans*-1,2-Dimethylcyclohexane in a Diaxial Conformation.

[193] J. B. Niederl, H. J. Vogel, *J. Am. Chem. Soc.* **1940**, *62*, 2512–2514. Aldehyde-Resorcinol Condensations.

[194] A. G. S. Högberg, *J. Org. Chem.* **1980**, *45*, 4498–4500. Two Stereoisomeric Macrocyclic Resorcinol-acetaldehyde Condensation Products.

[195] E. S. Barrett, J. L. Irwin, P. Turner, M. S. Sherburn, *J. Org. Chem.* **2001**, *66*, 8227–8229. Efficient Distal-Difunctionalization of Cavitand Bowls.

[196] J. L. Irwin, M. S. Sherburn, *J. Org. Chem.* **2000**, *65*, 602–605. Practical Synthesis of Selectively Functionalized Cavitands.

[197] A. Jasat, J. C. Sherman, *Chem. Rev.* **1999**, *99*, 931–968. Carceplexes and Hemicarceplexes.

[198] M. P. Scott, M. S. Sherburn, Resorcinarenes and Pyrogallolarenes in *Comprehensive Supramolecular Chemistry II*, (Eds.: J. L. Atwood and G. W. Gokel), Elsevier: Oxford, **2017**, *1*, pp 337–374.

[199] S. K. Kurdistani, R. C. Helgeson, D. J. Cram, *J. Am. Chem. Soc.* **1995**, *117*, 1659–1660. Stepwise Shell Closures Provide Hosts That Expose or Protect Guests from Outer-Phase Reactants.

[200] D. J. Cram, S. Karbach, H. E. Kim, C. B. Knobler, E. F. Maverick, J. L. Ericson, R. C. Helgeson, *J. Am. Chem. Soc.* **1988**, *110*, 2229-2237. Host-guest Complexation. 46. Cavitands as Open Molecular Vessels Form Solvates.

[201] Y. Aoyama, Y. Tanaka, H. Toi, H. Ogoshi, *J. Am. Chem. Soc.* **1988**, *110*, 634–635. Polar Host–Guest Interaction. Binding of Nonionic Polar Compounds with a Resorcinol-Aldehyde Cyclooligomer as a Lipophilic Polar Host.

[202] J. R. Moran, J. L. Ericson, E. Dalcanale, J. A. Bryant, C. B. Knobler, D. J. Cram, *J. Am. Chem. Soc.* **1991**, *113*, 5707–5714. Vases and Kites as Cavitands.

[203] D. J. Cram, H. J. Choi, J. A. Bryant, C. B. Knobler, *J. Am. Chem. Soc.* **1992**, *114*, 7748–7765. Host–Guest Complexation .62. Solvophobic and Entropic Driving Forces for Forming Velcraplexes, Which are 4-Fold, Lock-Key Dimers in Organic Media.

[204] O. Middel, W. Verboom, David N. Reinhoudt, *Eur. J. Org. Chem.* **2002**, *2002*, 2587–2597. Water-Soluble Cavitands − Synthesis, Solubilities and Binding Properties.

[205] M. Frei, F. Marotti, F. Diederich, *Chem. Commun.* **2004**, 1362–1363. Zn(II)-induced Conformational Control of Amphiphilic Cavitands in Langmuir Monolayers.

[206] J. H. Jordan, B. C. Gibb, Water-Soluble Cavitands in *Comprehensive Supramolecular Chemistry II*, (Eds.: J. L. Atwood and G. W. Gokel), Elsevier: Oxford, **2017**, pp 387–404.

[207] Y. Yamakoshi, R. R. Schlittler, J. K. Gimzewski, F. Diederich, *J. Mater. Chem.* **2001**, *11*, 2895–2897. Synthesis of Molecular-Gripper-Type Dynamic Receptors and STM-Imaging of Self-Assembled Monolayers on Gold.

[208] R. Huisgen, *Angew. Chem.* **1963**, *75*, 604–637; *Angew. Chem. Int. Ed.* **1963**, *2*, 565–598. 1,3-Dipolar Cycloadditions. Past and Future.

[209] Z. P. Demko, K. B. Sharpless, *Angew. Chem.* **2002**, *114*, 2217–2220; *Angew. Chem. Int. Ed.* **2002**, *41*, 2113–2116. A Click Chemistry Approach to Tetrazoles by Huisgen 1,3-Dipolar Cycloaddition: Synthesis of 5-Acyltetrazoles from Azides and Acyl Cyanides.

[210] H. C. Kolb, M. G. Finn, K. B. Sharpless, *Angew. Chem.* **2001**, *113*, 2056–2075; *Angew. Chem. Int. Ed.* **2001**, *40*, 2004–2021. Click Chemistry: Diverse Chemical Function from a Few Good Reactions.

[211] J. C. Jewett, C. R. Bertozzi, *Chem. Soc. Rev.* **2010**, *39*, 1272–1279. Cu-free Click Cycloaddition Reactions in Chemical Biology.

[212] Y. H. Lau, P. J. Rutledge, M. Watkinson, M. H. Todd, *Chem. Soc. Rev.* **2011**, *40*, 2848–2866. Chemical Sensors that Incorporate Click-derived Triazoles.

[213] L. Xu, Y. Li, Y. Li, *As. J. Org. Chem.* **2014**, *3*, 582–602. Application of "Click" Chemistry to the Construction of Supramolecular Functional Systems.

[214] G. J. Kleywegt, VIODOO, Version 3.3.4, Uppsala Software Factory: Uppsala, **2007**.

[215] L. Abis, E. Dalcanale, A. Du Vosel, S. Spera, *J. Org. Chem.* **1988**, *53*, 5475–5479. Structurally New Macrocycles from the Resorcinol-Aldehyde Condensation. Configurational and Conformational Analyses by Means of Dynamic NMR, NOE, and T1 Experiments.

[216] F. Gruppi, F. Boccini, L. Elviri, E. Dalcanale, *Tetrahedron* **2009**, *65*, 7289–7295. Self-assembly of a Cavitand-based Heteronuclear Coordination Cage.

[217] X. Liu, R. Warmuth, *Nat. Protocols* **2007**, *2*, 1288–1296. A simple One-pot Multicomponent Synthesis of an Octahedral Nanocontainer Molecule.

[218] L. Sebo, F. Diederich, V. Gramlich, *Helv. Chim. Acta* **2000**, *83*, 93–113. Tetrakis(phenylamidinium)-substituted Resorcin[4]arene Receptors for the Complexation of Dicarboxylates and Phosphates in Protic Solvents.

[219] A. Gorbunov, D. Cheshkov, V. Kovalev, I. Vatsouro, *Chem. Eur. J.* **2015**, *21*, 9528–9534. Copper(I)-Catalyzed Cycloaddition of Azides to Multiple Alkynes: A Selectivity Study Using a Calixarene Framework.

[220] B. Schulze, U. S. Schubert, *Chem. Soc. Rev.* **2014**, *43*, 2522–2571. Beyond Click Chemistry - Supramolecular Interactions of 1,2,3-Triazoles.

[221] S. Díez-González, A. Correa, L. Cavallo, S. P. Nolan, *Chem. Eur. J.* **2006**, *12*, 7558–7564. (NHC)Copper(I)-Catalyzed [3+2] Cycloaddition of Azides and Mono- or Disubstituted Alkynes.

[222] S. Díez-González, S. P. Nolan, *Angew. Chem.* **2008**, *120*, 9013–9016; *Angew. Chem. Int. Ed.* **2008**, *47*, 8881–8884. [(NHC)2Cu]X Complexes as Efficient Catalysts for Azide–Alkyne Click Chemistry at Low Catalyst Loadings.

[223] I. Stengel, C. A. Strassert, L. De Cola, P. Bäuerle, *Organometallics* **2014**, *33*, 1345–1355. Tracking Intramolecular Interactions in Flexibly Linked Binuclear Platinum(II) Complexes.

[224] E. Shirakawa, T. Kitabata, H. Otsuka, T. Tsuchimoto, *Tetrahedron* **2005**, *61*, 9878–9885. A Simple Catalyst System for the Palladium-catalyzed Coupling of Aryl Halides with Terminal Alkynes.

[225] D. Gelman, S. L. Buchwald, *Angew. Chem.* **2003**, *115*, 6175–6178; *Angew. Chem. Int. Ed.* **2003**, *42*, 5993–5996. Efficient Palladium-Catalyzed Coupling of Aryl Chlorides and Tosylates with Terminal Alkynes: Use of a Copper Cocatalyst Inhibits the Reaction.

[226] Schrödinger, MacroModel, Version 9.1, New York, **2010**.

[227] R. S. Walters, C. M. Kraml, N. Byrne, D. M. Ho, Q. Qin, F. J. Coughlin, S. Bernhard, R. A. Pascal, *J. Am. Chem. Soc.* **2008**, *130*, 16435–16441. Configurationally Stable Longitudinally Twisted Polycyclic Aromatic Compounds.

[228] H. Langhals, J. Gold, *Liebigs Ann.* **1997**, *1997*, 1151–1153. Chiral Bifluorophoric Perylene Dyes with Unusually High CD Effects – a Simple Model for the Photosynthesis Reaction Center.

[229] C. Reichardt, T. Welton, *Solvents and Solvent Effects in Organic Chemistry,* Wiley-VCH, Weinheim, **2011**.

[230] H.-B. Bürgi, J. D. Dunitz, *Helv. Chim. Acta* **1993**, *76*, 1115–1166. Structural Chemistry in Helvetica Chimica Acta, 1917–1992.

[231] J. D. Dunitz, *X-ray Analysis and the Structure of Organic Molecules,* Cornell University Press, Ithaca, **1995**.

[232] L.-l. Ooi, *Principles of X-ray Crystallography,* Oxford University Press, Oxford, **2010**.

[233] F. Diederich, N. Trapp, M. Wörle, *Isr. J. Chem.* **2017**, *57*, 39–54. Small Molecule Crystallography in the Laboratory of Organic Chemistry at ETH Zürich.

[234] K. Rissanen, *Chem. Soc. Rev.* **2017**, *46*, 2638–2648. Crystallography of Encapsulated Molecules.

[235] A. Holden, P. Morrison, *Crystals and Crystal Growing,* MIT Press, Cambridge - Mass., **1982**.

[236] *Inclusion Compounds,* (Eds.: J. L. Atwood, J. E. D. Davies and D. D. MacNicol), Academic Press, London, **1984**.

[237] F. Toda, *Pure Appl. Chem.* **2001**, *73*, 1137–1145. Crystalline Inclusion Complexes as Media of Molecular Recognitions and Selective Reactions.

[238] S. Lee, E. A. Kapustin, O. M. Yaghi, *Science* **2016**, *353*, 808–811. Coordinative Alignment of Molecules in Chiral Metal–Organic Frameworks.

[239] Y. Inokuma, S. Yoshioka, J. Ariyoshi, T. Arai, Y. Hitora, K. Takada, S. Matsunaga, K. Rissanen, M. Fujita, *Nature* **2013**, *495*, 461–466. X-ray Analysis on the Nanogram to Microgram Scale Using Porous Complexes.

[240] Y.-M. Legrand, A. van der Lee, M. Barboiu, *Science* **2010**, *329*, 299–302. Single-Crystal X-ray Structure of 1,3-Dimethylcyclobutadiene by Confinement in a Crystalline Matrix.

[241] C. Gropp, T. Husch, N. Trapp, M. Reiher, F. Diederich, *J. Am. Chem. Soc.* **2017**, *139*, 12190–12200. Dispersion and Halogen-Bonding Interactions: Binding of the Axial Conformers of Monohalo- and (±)-*trans*-1,2-Dihalocyclohexanes in Enantiopure Alleno-Acetylenic Cages.

[242] C. Gropp, N. Trapp, *Chimia* **2018**, *72*, 245–248. Complexation and Structure Elucidation of the Axial Conformers of Mono- and (±)-*trans*-1,2-Disubstituted Cyclohexanes by Enantiopure Alleno-Acetylenic Cage Receptors.

[243] E. L. Eliel, *Angew. Chem.* **1965**, *77*, 784–797; *Angew. Chem. Int. Ed.* **1965**, *4*, 761–774. Conformational Analysis in Mobile Cyclohexane Systems.

[244] M. Manoharan, E. L. Eliel, W. R. Kenan, *Tetrahedron Lett.* **1983**, *24*, 453–456. The Gauche Interaction in *trans*-1,2-Dimethylcyclohexane.

[245] H. Booth, T. B. Grindley, *J. Chem. Soc., Chem. Comm.* **1983**, 1013–1014. A Direct Determination of the Position of Equilibrium in *trans*-1,2-Dimethylcyclohexane.

[246] P. Klaeboe, J. J. Lothe, K. Lunde, *Acta Chem. Scand.* **1956**, *10*, 1465–1474. Spectroscopic Conformational Analysis of Some Monohalogenated Cyclohexanes.

[247] L. W. Reeves, K. O. Strømme, *Can. J. Chem.* **1960**, *38*, 1241–1248. Studies of Rates of Conversion and Populations of Various Conformations of Saturated Ring Compounds by NMR: I: Chlorocyclohexane and Bromocyclohexane.

[248] D. H. R. Barton, *Experientia* **1950**, *6*, 316–320. The Conformation of the Steroid Nucleus.

[249] F. R. Jensen, C. H. Bushweller, Conformational Preferences in Cyclohexanes and Cyclohexenes in *Advances in Alicyclic Chemistry*, (Eds.: H. Harold and G. J. Karabatsos), Elsevier: **1971**, *3*, pp 139–194.

[250] M. Kato, K. Tanaka, F. Toda, *Supramol. Chem.* **2001**, *13*, 175–180. Stereoselective Inclusion and Structure of Equatorial *trans*-1,2-Dichlorocyclohexane.

[251] S. Hirano, S. Toyota, M. Kato, F. Toda, *Chem. Commun.* **2005**, 3646–3648. Isolation of Axial Conformers of Chloro- and Bromocyclohexane in a Pure State as Inclusion Complexes with 9,9'-Bianthryl, and the Discovery of a Novel 1,3 Diaxial Cl···H weak interaction.

[252] S. Hirano, S. Toyota, F. Toda, *Chem. Commun.* **2004**, 2354–2355. Isolation of Equatorial Conformers of Chloro- and Bromocyclohexane in a Pure State as Inclusion Complexes with a Host Compound.

[253] Y.-X. Lu, J.-W. Zou, Y.-H. Wang, Q.-S. Yu, *Chem. Phys.* **2007**, *334*, 1–7. Theoretical Investigations of the C–X···π Interactions between Benzene and some Model Halocarbons.

[254] A. Forni, S. Pieraccini, S. Rendine, F. Gabas, M. Sironi, *ChemPhysChem* **2012**, *13*, 4224–4234. Halogen-Bonding Interactions with π Systems: CCSD(T), MP2, and DFT Calculations.

[255] A. Forni, S. Pieraccini, S. Rendine, M. Sironi, *J. Comput. Chem.* **2014**, *35*, 386–394. Halogen Bonds with Benzene: An Assessment of DFT Functionals.

[256] K. E. Riley, C. L. Ford, Jr, K. Demouchet, *Chem. Phys. Lett.* **2015**, *621*, 165–170. Comparison of Hydrogen Bonds, Halogen Bonds, CH···π Interactions, and C–X···π Interactions using High-level ab Initio Methods.

[257] K. E. Riley, M. Vazquez, C. Umemura, C. Miller, K.-A. Tran, *Chem. Eur. J.* **2016**, *22*, 17690–17695. Exploring the (Very Flat) Potential Energy Landscape of R−Br···π Interactions with Accurate CCSD(T) and SAPT Techniques.

[258] H. Sun, A. Horatscheck, V. Martos, M. Bartetzko, U. Uhrig, D. Lentz, P. Schmieder, M. Nazaré, *Angew. Chem.* **2017**, *129*, 6554–6558; *Angew. Chem., Int. Ed.* **2017**, *56*, 6454–6458. Direct Experimental Evidence for Halogen–Aryl π Interactions in Solution from Molecular Torsion Balances.

[259] N. S. Zefirov, L. G. Gurvich, A. S. Shashkov, M. Z. Krimer, E. A. Vorob'eva, *Tetrahedron* **1976**, *32*, 1211–1219. Stereochemical studies—XX: Conformations of 1,2-*trans*-Disubstituted Cyclohexanes.

[260] N. S. Zefirov, V. V. Samoshin, O. A. Subbotin, V. I. Baranenkov, S. Wolfe, *Tetrahedron* **1978**, *34*, 2953–2959. The Gauche Effect : On the Nature of the

Interaction between Electronegative Substituents in *trans*-1,2-Disubstituted Cyclohexanes.

[261] K. B. Wiberg, *J. Org. Chem.* **1999**, *64*, 6387–6393. Conformational Studies in the Cyclohexane Series. 3. The Dihalocyclohexanes.

[262] M. P. Freitas, R. Rittner, C. F. Tormena, R. J. Abraham, *Spectrochim. Acta A* **2005**, *61*, 1771–1776. Conformational Analysis and Stereoelectronic Effects in *trans*-1,2-Dihalocyclohexanes: ^{1}H NMR and Theoretical Investigation.

[263] C. J. Adams, L. E. Bowen, *Dalton Trans.* **2005**, 2239–2240. I–π Halogen-Bonding in the Structures of Platinum-alkynyl Compounds: an Overlooked Supramolecular Interaction.

[264] M. Baldrighi, D. Bartesaghi, G. Cavallo, M. R. Chierotti, R. Gobetto, P. Metrangolo, T. Pilati, G. Resnati, G. Terraneo, *CrystEngComm.* **2014**, *16*, 5897–5904. Polymorphs and Co-crystals of Haloprogin: an Antifungal Agent.

[265] K. J. Miller, *J. Am. Chem. Soc.* **1990**, *112*, 8533–8542. Additivity Methods in Molecular Polarizability.

[266] E. R. Johnson, S. Keinan, P. Mori-Sánchez, J. Contreras-García, A. J. Cohen, W. Yang, *J. Am. Chem. Soc.* **2010**, *132*, 6498–6506. Revealing Noncovalent Interactions.

[267] H. B. Bürgi, S. C. Capelli, *Acta Cryst.* **2000**, *A56*, 403–412. Dynamics of Molecules in Crystals from Multi-Temperature Anisotropic Displacement Parameters. I. Theory.

[268] B. L. McClain, D. Ben-Amotz, *J. Phys. Chem. B* **2002**, *106*, 7882–7888. Global Quantitation of Solvent Effects on the Isomerization Thermodynamics of 1,2-Dichloroethane and *trans*-1,2-Dichlorocyclohexane.

[269] K. B. Wiberg, W. Hinz, R. M. Jarret, K. B. Aubrecht, *J. Org. Chem.* **2005**, *70*, 8381–8384. Conformational Preferences for 1,2- and 1,4-Difluorocyclohexane.

[270] M. P. Freitas, C. F. Tormena, P. R. Oliveira, R. Rittner, *J. Mol. Struct.: THEOCHEM* **2002**, *589–590*, 147–151. Halogenated Six-membered Rings: A Theoretical Approach for Substituent Effects in Conformational Analysis.

[271] J. Nochebuena, C. Cuautli, J. Ireta, *Phys. Chem. Chem. Phys.* **2017**, *19*, 15256–15263. Origin of Cooperativity in Hydrogen Bonding.

[272] S. S. Xantheas, *Chem. Phys.* **2000**, *258*, 225–231. Cooperativity and Hydrogen Bonding Network in Water Clusters.

[273] K. Müller, C. Faeh, F. Diederich, *Science* **2007**, *317*, 1881–1886. Fluorine in Pharmaceuticals: Looking Beyond Intuition.

[274] *Modern Alkaloids Structure, Isolation, Synthesis and Biology,* (Eds.: E. Fattorusso), Wiley-VCH, Weinheim, **2008**.

[275] R. Lazny, A. Ratkiewicz, A. Nodzewska, A. Wynimko, L. Siergiejczyk, *Tetrahedron* **2012**, *68*, 6158–6163. Determination of the *N*-methyl Stereochemistry in Tropane and Granatane Derivatives in Solution: A Computational and NMR Spectroscopic Study.

[276] R. J. Hrynchuk, R. J. Barton, B. E. Robertson, *Can. J. Chem.* **1983**, *61*, 481–487. The Crystal Structure of Free Base Cocaine, $C_{17}H_{21}NO_4$.

[277] R. Glaser, D. Shiftan, M. Drouin, *Can. J. Chem.* **2000**, *78*, 212–223. The Solid-State Structures of (–)-Scopolamine Free Base, (–)-Scopolamine Methobromide, (–)-Scopolamine Hydrobromide Trihydrate, and of the Pseudopolymorphic Forms of (–)-Scopolamine Hydrochloride Anhydrate and 1.66 Hydrate.

[278] H. Schenk, C. H. MacGillavry, S. Skolnik, J. Laan, *Acta Cryst.* **1967**, *23*, 423–426. Crystal and Molecular Structure of Pseudotropine.

[279] J. Cramer, S. G. Krimmer, A. Heine, G. Klebe, *J. Med. Chem.* **2017**, *60*, 5791–5799. Paying the Price of Desolvation in Solvent-Exposed Protein Pockets: Impact of Distal Solubilizing Groups on Affinity and Binding Thermodynamics in a Series of Thermolysin Inhibitors.

[280] A. Biela, N. N. Nasief, M. Betz, A. Heine, D. Hangauer, G. Klebe, *Angew. Chem.* **2013**, *125*, 1868–1876; *Angew. Chem. Int. Ed.* **2013**, *52*, 1822–1828. Dissecting the Hydrophobic Effect on the Molecular Level: The Role of Water, Enthalpy, and Entropy in Ligand Binding to Thermolysin.

[281] A. Shivanyuk, K. Rissanen, S. K. Körner, D. M. Rudkevich, J. Rebek, Jr., *Helv. Chim. Acta* **2000**, *83*, 1778–1790. Structural Studies of Self-Folding Cavitands.

[282] S. Saito, C. Nuckolls, J. Rebek, Jr., *J. Am. Chem. Soc.* **2000**, *122*, 9628–9630. New Molecular Vessels: Synthesis and Chiroselective Recognition.

[283] J. L. Atwood, A. Szumna, *J. Am. Chem. Soc.* **2002**, *124*, 10646–10647. Hydrogen Bonds Seal Single-molecule Capsules.

[284] B. Kuberski, M. Pecul, A. Szumna, *Eur. J. Org. Chem.* **2008**, *2008*, 3069–3078. A Chiral "Frozen" Hydrogen Bonding in C_4-Symmetric Inherently Chiral Resorcin[4]arenes: NMR, X-ray, Circular Dichroism, and Theoretical Study.

[285] A. Szumna, *Org. Biomol. Chem.* **2007**, *5*, 1358–1368. Cyclochiral Conformers of Resorcin[4]arenes Stabilized by Hydrogen Bonds.

[286] D. F. Brougham, R. Caciuffo, A. J. Horsewill, *Nature* **1999**, *397*, 241–243. Coordinated Proton Tunnelling in a Cyclic Network of Four Hydrogen Bonds in the Solid State.

[287] J. Meisner, J. Kästner, *Angew. Chem.* **2016**, *128*, 5488–5502; *Angew. Chem. Int. Ed.* **2016**, *55*, 5400–5413. Atom Tunneling in Chemistry.

[288] K. Ueda, M. Oguni, *J. Phys. Chem. B* **2012**, *116*, 14470–14476. Quantum Tunneling in the Quadruple Proton Rearrangement on a Hydroxyl Hydrogen Bond Ring in Calix[4]arene.

[289] K. Ueda, M. Oguni, *J. Phys. Chem. B* **2013**, *117*, 14157–14162. Effect of *p-tert*-Butyl Group Substitution on the Quantum Tunneling Rate in Quadruple Proton Rearrangement of Calix[4]arene.

[290] C. Nilewski, R. W. Geisser, E. M. Carreira, *Nature* **2009**, *457*, 573–576. Total Synthesis of a Chlorosulpholipid Cytotoxin Associated with Seafood Poisoning.

[291] C. Nilewski, R. W. Geisser, M.-O. Ebert, E. M. Carreira, *J. Am. Chem. Soc.* **2009**, *131*, 15866–15876. Conformational and Configurational Analysis in the Study and Synthesis of Chlorinated Natural Products.

[292] S. Fischer, N. Huwyler, S. Wolfrum, E. M. Carreira, *Angew. Chem.* **2016**, *128*, 2601–2604; *Angew. Chem. Int. Ed.* **2016**, *55*, 2555–2558. Synthesis and Biological Evaluation of Bromo- and Fluorodanicalipin A.

[293] S. Krautwald, C. Nilewski, M. Mori, K. Shiomi, S. Ōmura, E. M. Carreira, *Angew. Chem.* **2016**, *128*, 4117–4121; *Angew. Chem. Int. Ed.* **2016**, *55*, 4049–4053. Bioisosteric Exchange of C_{sp3}-Chloro and Methyl Substituents: Synthesis and Initial Biological Studies of Atpenin A5 Analogues.

[294] S. Fischer, ETH Zurich, Zurich, Switzerland, **2018**.

[295] B. Breiten, M. R. Lockett, W. Sherman, S. Fujita, M. Al-Sayah, H. Lange, C. M. Bowers, A. Heroux, G. Krilov, G. M. Whitesides, *J. Am. Chem. Soc.* **2013**, *135*, 15579–15584. Water Networks Contribute to Enthalpy/Entropy Compensation in Protein–Ligand Binding.

[296] D. A. Dougherty, *Acc. Chem. Res.* **2013**, *46*, 885–893. The Cation−π Interaction.

[297] J. C. Ma, D. A. Dougherty, *Chem. Rev.* **1997**, *97*, 1303–1324. The Cation−π Interaction.

[298] G. W. Collie, R. Bailly, K. Pulka-Ziach, C. M. Lombardo, L. Mauran, N. Taib-Maamar, J. Dessolin, C. D. Mackereth, G. Guichard, *J. Am. Chem. Soc.* **2017**, *139*, 6128–6137.

Molecular Recognition within the Cavity of a Foldamer Helix Bundle: Encapsulation of Primary Alcohols in Aqueous Conditions.

[299] N. Giri, M. G. Del Pópolo, G. Melaugh, R. L. Greenaway, K. Rätzke, T. Koschine, L. Pison, M. F. C. Gomes, A. I. Cooper, S. L. James, *Nature* **2015**, *527*, 216–220. Liquids with Permanent Porosity.

[300] M. Mastalerz, *Nature* **2015**, *527*, 174–176. Liquefied Molecular Holes.

[301] J. Yoon, D. J. Cram, *Chem. Commun.* **1997**, 497–498. The First Water-Soluble Hermicarceplexes.

[302] T. Haino, D. M. Rudkevich, A. Shivanyuk, K. Rissanen, J. Rebek, Jr, *Chem. Eur. J.* **2000**, *6*, 3797–3805. Induced-Fit Molecular Recognition with Water-Soluble Cavitands.

[303] E. J. Donckele, Macrocyclic and Acylic Alleno-Acetylenic Scaffolds ith Outstanding Chiroptical Properties and Expansion of the Chemical Space of Electron–Poor Alkenes for the [2+2] Cycloaddition–Retroelectrocyclization (CA–RE) and Related Reactions, No. 23743, ETH Zurich, Zurich, Switzerland, **2016**.

[304] B. C. Gibb, R. G. Chapman, J. C. Sherman, *J. Org. Chem.* **1996**, *61*, 1505–1509. Synthesis of Hydroxyl-Footed Cavitands.

[305] S. Rat, J. Gout, O. Bistri, O. Reinaud, *Org. Biomol. Chem.* **2015**, *13*, 3194–3197. The First Water-soluble Bowl Complex: Molecular Recognition of Acetate by the Biomimetic Tris(imidazole) Zn(II) System at pH 7.4.

[306] R. F. Cunico, L. Bedell, *J. Org. Chem.* **1980**, *45*, 4797–4798. The Triisopropylsilyl Group as a Hydroxyl-protecting Function.

[307] P. Siemsen, R. C. Livingston, F. Diederich, *Angew. Chem.* **2000**, *112*, 2740–2767; *Angew. Chem., Int. Ed.* **2000**, *39*, 2632–2657. Acetylenic Coupling: A Powerful Tool in Molecular Construction.

[308] R. Chinchilla, C. Nájera, *Chem. Rev.* **2007**, *107*, 874–922. The Sonogashira Reaction: A Booming Methodology in Synthetic Organic Chemistry.

[309] C. Seel, F. Vögtle, *Angew. Chem.* **1992**, *104*, 542–563; *Angew. Chem., Int. Ed.* **1992**, *31*, 528–549. Molecules with Large Cavities in Supramolecular Chemistry.

[310] T. Hasell, A. I. Cooper, *Nat. Rev. Mat.* **2016**, *1*, 1–14. Porous Organic Cages: Soluble, Modular and Molecular Pores.

[311] D. O'Krongly, S. R. Denmeade, M. Y. Chiang, R. Breslow, *J. Am. Chem. Soc.* **1985**, *107*, 5544–5545. Efficient Triple Coupling Reaction to Produce a Self-adjusting Molecular Cage.

[312] D. J. Cram, R. Jaeger, K. Deshayes, *J. Am. Chem. Soc.* **1993**, *115*, 10111–10116. Host–Guest Complexation. 65. Hemicarcerands that Encapsulate Hydrocarbons with Molecular Weights Greater than Two Hundred.

[313] F. Vögtle, R. Berscheid, W. Schnick, *J. Chem. Soc., Chem. Commun.* **1991**, 414–416. Inclusion of Acetonitrile in a Macrobicyclic Host Molecule.

[314] F. Beuerle, B. Gole, *Angew. Chem. Int. Ed.* doi:10.1002/anie.201710190. Covalent Organic Frameworks and Cage Compounds: Design and Applications of Polymeric and Discrete Organic Scaffolds.

[315] M. P. Wiesenfeldt, Z. Nairoukh, W. Li, F. Glorius, *Science* **2017**, *357*, 908–912. Hydrogenation of Fluoroarenes: Direct Access to all-*cis*-(Multi)fluorinated Cycloalkanes.

[316] P. Nagy, *Antioxidants & Redox Signaling* **2013**, *18*, 1623–1641. Kinetics and Mechanisms of Thiol–Disulfide Exchange Covering Direct Substitution and Thiol Oxidation-Mediated Pathways.

[317] A. Najer, D. Wu, M. G. Nussbaumer, G. Schwertz, A. Schwab, M. C. Witschel, A. Schafer, F. Diederich, M. Rottmann, C. G. Palivan, H.-P. Beck, W. Meier, *Nanoscale* **2016**, *8*, 14858–14869. An Amphiphilic Graft Copolymer-based Nanoparticle Platform for Reduction-responsive Anticancer and Antimalarial Drug Delivery.

[318] L. You, D. Zha, E. V. Anslyn, *Chem. Rev.* **2015**, *115*, 7840–7892. Recent Advances in Supramolecular Analytical Chemistry Using Optical Sensing.

[319] T. Lange, J.-D. v. Loon, R. R. Tykwinski, M. Schreiber, F. Diederich, *Synthesis* **1996**, *4*, 537–550. Towards the Synthesis of Tetraethynylallene.

[320] J. D. v. Loon, P. Seiler, F. Diederich, *Angew. Chem.* **1993**, *105*, 1817–1820; *Angew. Chem. Int. Ed.* **1993**, *32*, 1706–1709. Tricyclo[6.2.0.03,6]deca-1,3,6,8-tetraene: A Remarkably Stable *para*-Quinodimethane from a Novel Rearrangement Reaction.

[321] CrysAlisPro, Rigaku Oxford Diffraction, **2015–2017**.

[322] O. V. Dolomanov, L. J. Bourhis, R. J. Gildea, J. A. K. Howard, H. Puschmann, *J. Appl. Cryst.* **2009**, *42*, 339–341. OLEX2: A Complete Structure Solution, Refinement and Analysis Program.

[323] G. M. Sheldrick, *Acta Cryst. A* **2008**, *64*, 112–122. A Short History of SHELX.

[324] M. Ochiai, T. Ito, H. Takahashi, A. Nakanishi, M. Toyonari, T. Sueda, S. Goto, M. Shiro, *J. Am. Chem. Soc.* **1996**, *118*, 7716–7730. Hypervalent (tert-Butylperoxy)iodanes Generate Iodine-Centered Radicals at Room Temperature in Solution: Oxidation and Deprotection of Benzyl and Allyl Ethers, and Evidence for Generation of α-Oxy Carbon Radicals.

[325] S. Nicolai, P. Swallow, J. Waser, *Tetrahedron* **2015**, *71*, 5959–5964. Intramolecular Palladium-Catalyzed Alkene Carboalkynylation.

[326] IgorPro, Wavemetrics, Portland, USA, **2009**.

[327] J. P. Perdew, Y. Wang, *Phys. Rev. B* **1992**, *45*, 13244–13249. Accurate and Simple Analytic Representation of the Electron-Gas Correlation Energy.

[328] J. P. Perdew, K. Burke, M. Ernzerhof, *Phys. Rev. Lett.* **1996**, *77*, 3865–3868. Generalized Gradient Approximation Made Simple.

[329] S. Grimme, J. Antony, S. Ehrlich, H. Krieg, *J. Chem. Phys.* **2010**, *132*, 154104. A Consistent and Accurate *ab initio* Parametrization of Density Functional Dispersion Correction (DFT-D) for the 94 Elements H-Pu.

[330] S. Grimme, *J. Chem. Phys.* **2003**, *118*, 9095–9102. Improved Second-Order Møller–Plesset Perturbation Theory by Separate Scaling of Parallel- and Antiparallel-Spin Pair Correlation Energies.

[331] S. F. Boys, F. Bernardi, *Mol. Phys.* **1970**, *19*, 553–566. The Calculation of Small Molecular Interactions by the Differences of Separate Total Energies. Some Procedures with Reduced Errors.

[332] T. B. Adler, H.-J. Werner, *J. Phys. Chem.* **2011**, *135*, 144117. An Explicitly Correlated Local Coupled Cluster Method for Calculations of Large Molecules Close to the Basis Set Limit.

[333] K. A. Peterson, T. B. Adler, H.-J. Werner, *J. Chem. Phys.* **2008**, *128*, 084102. Systematically Convergent Basis Sets for Explicitly Correlated Wavefunctions: The Atoms H, He, B–Ne, and Al–Ar.

Curriculum Vitae

1988	Born on July 30 in Munich, Germany

Education

2014–2018	Ph.D. in Chemistry at ETH Zurich, Switzerland Supervisor: Prof. F. Diederich
2013–2014	M.Sc. in Chemistry at the ETH Zurich M.Sc. Thesis supervisor: Prof. F. Diederich
2012–2013	Visiting researcher at the Scripps Research Institute, La Jolla, USA; Supervisor: Prof. P.S. Baran
2011–2012	Exchange student at the École Polytechnique, Palaiseau, France B.Sc. Thesis supervisor: Prof. F. Gagosz and Prof. A.S.K. Hashmi
2009–2012	B.Sc. in Chemistry at the University of Heidelberg, Germany
2008	German Diploma, Wilhelmsgymnasium Munich, Germany

Work experience

2014 (4 months)	Research internship at Novartis NIBR, Basel, Switzerland
2008–2009 (12 months)	Civil Service at the Chaitanya Special School, Karnataka, India (Weltwärts fellowship of the German government)

Fellowships and Awards

2018	Nominee: Forbes 30 under 30 in Science & Healthcare Europe
2017	Swiss Chemical Society Fall Meeting: Poster Prize & Travel Award in Organic Chemistry
2017	Participant in the 67th Lindau Nobel Laureate Meeting (Chemistry), Lindau, Germany
2009–2018	Fellow of the Studienstiftung des Deutschen Volkes (B.Sc., M.Sc., and Ph.D. fellowship)
2014	Biogen Idec Innovation Award, ETH Zurich

Zurich, May 2018 Cornelius Gropp